



300
YEARS of SPbU

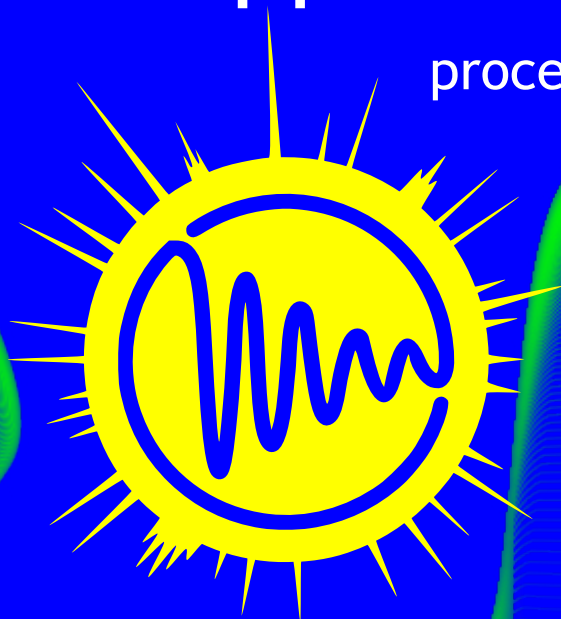
ISSN 2542-2049

Saint-Petersburg State University

21th International School-Conference

Magnetic resonance and its applications

proceedings



Spinus

1 April – 5 April 2024

Saint-Petersburg, Russia

SAINT PETERSBURG STATE UNIVERSITY
Department of Nuclear Physics Research Methods

21th International School-Conference

MAGNETIC RESONANCE AND ITS APPLICATIONS

Proceedings

April 1 – 5, 2024
Saint Petersburg, Russia

Magnetic Resonance and its Applications. Spinus-2024.
Proceedings. Saint Petersburg State University, 2024. 355 pp.
ISSN 2542-2049

Reviewer of Proceedings: Vasily T. Lebedev, Doctor of Physics and Mathematics, Head of Laboratory of Neutron Physicochemical Research, PNPI RAS

Schola Spinus



**21st International School-Conference
MAGNETIC RESONANCE AND ITS APPLICATIONS
SPINUS-2024**

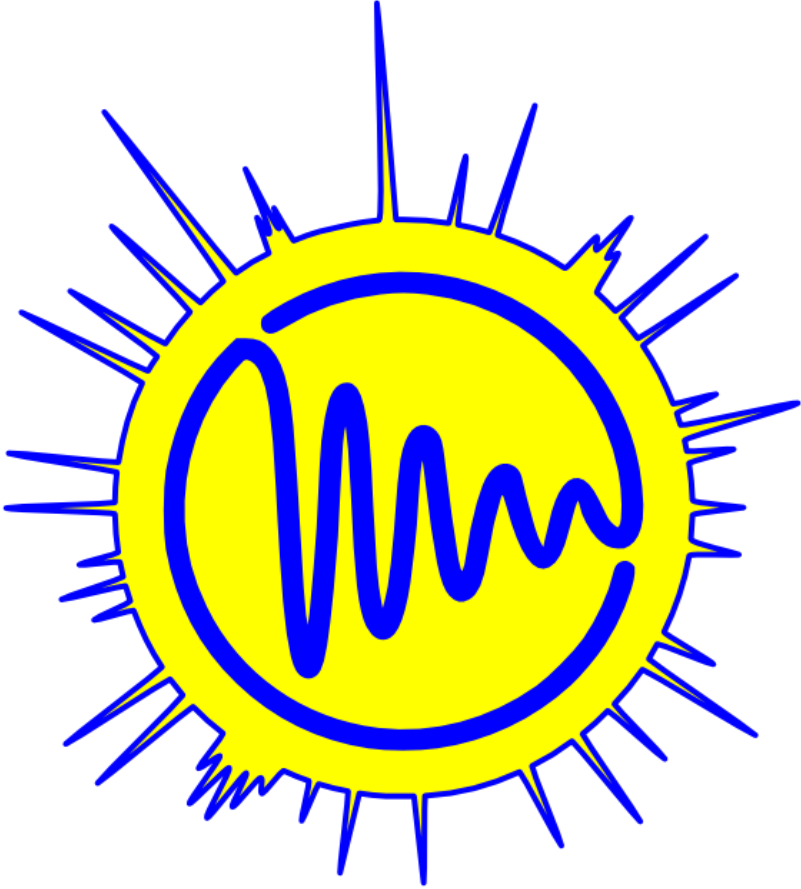
ORGANIZING COMMITTEE

Chairman	Prof. Denis Markelov, SPSU
Vice-chairman	M. Sc. Alexandr Ievlev, researcher, SPSU
Committee members	Dr. Andrey Egorov, associate professor, SPSU Dr. Andrey Komolkin, associate professor, SPSU Prof. Marina Shelyapina, SPSU Dr. Pavel Kupriyanov, associate professor, GTU (Gebze, Turkey) Dr. Nadezhda Sheveleva, assistant, SPSU M. Sc. Timofey Popov, SPSU
Layout of proceedings	M. Sc. Aleksandra Koroleva
Reviewer of Proceedings	Vasily T. Lebedev, Doctor of Physics and Mathematics, Head of Laboratory of Neutron Physicochemical Research, PNPI RAS

CONTACTS

1, Ulyanovskay st., Peterhof, 198504, St. Petersburg, Russia
Department of Nuclear Physics Research Methods
St. Petersburg State University

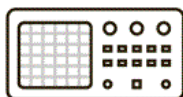
Tel.:	+7-953-350-0640
E-mail:	spinus@spinus.spb.ru
Website:	spinus.spb.ru



SPINUS



Saint-Petersburg State University
spbu.ru



P&L
Scientific

P&L Scientific Company
plscientific.se



ЭЛЕМЕНТ

ELEMENT Company
element-msc.ru



MagicPlot

Magicplot Systems, LCC
magicplot.com



TerraQuanTech, LCC

Contents

SCHEDULE	19
THE SCHOOL-CONFERENCE “SPINUS” OF SAINT PETERSBURG STATE UNIVERSITY	29
LECTURES	31
 <i>Vladimir I. Chizhik</i> 300 years of St. Petersburg State University and 80 years of radiospectroscopy in it.....	 32
 <i>Roman Babunts</i> Spin-dependent phenomena in wide-gap materials and based nanostructures and development of the instrumentation for these studies	 34
 <i>Elena V. Charnaya, Denis Yu. Nefedov, Allisher A. Vasilev, Andrei V. Uskov</i> Liquid-liquid phase transition in metallic melts	 35
 <i>Yury Bunkov</i> Qubit on magnon BEC state Yury Bunkov.....	 37
 <i>Leonid Grunin, Maria Ivanova, Ivan Kirilov</i> Systematic View on the Dynamics and Structure Analysis of Solids by Time-Domain	 39
 <i>Dr.Lu Shuntian</i> The ZHONGTAI 94 GHz pulsed EPR spectrometer.....	 40
 <i>Yury A. Pirogov</i> Novel approaches in magnetic resonance imaging	 41
 <i>K.M. Salikhov</i> The effect of exchange narrowing of the electron paramagnetic resonance (EPR) spectra of dilute radical solutions indicates the formation of a Bose-Einstein condensate (BEC).....	 43
 <i>M.G. Shelyapina</i> Nanoconfined water in zeolites with hierarchical porosity probed by ¹ H NMR	 45
 <i>Janez Stepišnik</i> Why biopolymers fold in glycerol-water mixture: NMR study of diffusion in glycerol-water mixture.....	 46
 <i>Sandeep Kumar Mishra, Bikash Baishya and N. Suryaprakash</i> Clean Sequences for Complete Eradication of Unwanted Evolution and Accurate Determination of Spectral Parameters	 47
 <i>Pavel Yushmanov</i> Electrophoretic NMR and applications.....	 48

ORAL REPORTS	53
<i>Alonso Geli, Yamirka; García Cruz, Claudia C.; Cruz Vadell, Haydee; Torres-Martínez, Leisbelys R.; Delgado Tamayo, Fabian; Somoano Delgado, Lilian M.; Suarez Beyries, Lidia C.; Araujo Duran, Yomaidis; Lores Guevara, Manuel A.</i> Assessment of blood serum dynamic viscosity by NMR in sickle cell disease	54
<i>Nikolay V. Anisimov, Arina A. Tarasova, Lev L. Gervits</i> Visualization of the internal structure of coils used in MRI studies	58
<i>Alina S. Arkhipova, Maya Ulyanova, Olga Yu. Selyutina, Nikolay E. Polyakov, Olga A. Chinak, Evgeniya V. Grigorieva, Elena V. Dmitrienko</i> Interaction of a Quinone-Quinoline and its chelate complexes with nucleic bases in dark and photoinduced processes	61
<i>Zilya Badrieva, Ekaterina Brui</i> Dictionary-based T ₂ -mapping with multi-echo turbo-spin echo	63
<i>Anastasia V. Batueva, Roman A. Babunts, Alexander S. Gurin, Kirill V. Likhachev, Pavel G. Baranov</i> Mn Related Paramagnetic Centres in a Bulk GaS and GaSe Van der Waals Semiconductors with High-Frequency EPR Method	66
<i>Vladimir Y. Bazaikin, Andrei V. Komolkin, Denis A. Markelov</i> Investigation of poly-m-phenylene isophthalamide polymer membrane modified by UiO-66 (NH ₂) MOF for separation of toluene/methanol mixture using molecular dynamics method .	68
<i>Bystrov S. S., Kirilenko V. D., Zolotov D. R., Khrustalev A.A.</i> NMR to Industry: Development of modern universal control software for TD-NMR spectrometers, validation using fertilizer samples as an example	71
<i>U.J. Yolchuyeva, R.A. Japharova, S.H. Eldarova, A.F. Alieva, G.A. Hajiyeva, F.T. Alizadeh</i> Study of the chemical composition of Azerbaijani crude oil using infrared spectroscopy and nuclear magnetic resonance methods.	74
<i>Edward B. Fel'dman, Elena I. Kuznetsova, Ilia D. Lazarev, Sergey G. Vasil'ev</i> Multiple quantum NMR in problems of quantum informatics: many-spin entanglement and scrambling	77
<i>P.A. Fetin, M.V. Kadnikov, V.I. Fetina, I.M. Zorin</i> Polymerization kinetic and catalytic properties of resulted comb-like polyelectrolytes by ¹ H NMR	79
<i>Eduardo Garea-Llano, Evelio Gonzalez Dalmau and Carlos Cabal Mirabal</i> Artificial Intelligence tools for the reconstruction and enhancement of MR imaging	82
<i>Carlos Cabal Mirabal, Evelio Gonzalez Dalmau</i> System to ensure the reproducibility of the legs positions during the Magnetic Resonance Imaging (MRI) studies.	85

<i>Naira R. Gromova, Denis A. Markelov</i> Cell size dependence of hydrodynamic radius of carbosilane dendrimers in chloroform	88
<i>Alexander V. Ievlev, Konstantin V. Tyutyukin, Nadezhda V. Pokhvishecheva</i> Molecular and ionic mobility of ionic liquids with complex anions containing metals	91
<i>Boris B. Kharkov, Ivan S. Podkorytov, Stanislav A. Bondarev, Mikhail V. Belousov, Vladislav A. Salikov, Galina A. Zhouravleva, Nikolai R. Skrynnikov</i> The Role of Rotational Motion in Diffusion NMR Experiments on Supramolecular Assemblies	94
<i>Alexey Kiryutin, Vitaly Kozinenko, Alexandra Yurkovskaya</i> SLIC-SABRE at Earth's Magnetic fields: Simple and Effective Method of getting Strong ¹⁵ N NMR Polarization	96
<i>Elizaveta S. Kononenko, Alexandra I. Trepakova, Oleg B. Shevelev, Larisa M. Kovtunova, Dudari B. Burueva and Igor V. Koptug</i> In vivo MR imaging of murine bronchial tree using hyperpolarized propane produced with parahydrogen	100
<i>Polina A. Kononova, Olga Yu. Selyutina, Nikolay E. Polyakov, Vladislav V. Fomenko, Nariman F. Salakhutdinov</i> The ¹ H NMR spectroscopy in the study of the interaction of membrane proteins of enveloped viruses and potential antiviral agents	102
<i>Vladimir E. Koshman, Olga Yu. Selyutina, Alexei A. Dmitriev, Nikolay E. Polyakov</i> Redox activity and membrane interaction of novel thiosemicarbazones	104
<i>Ilya A. Kostyukov, Yury G. Kolyagin</i> Determination of crystallographic positions of aluminum atoms in BEA zeolites using high-quality ²⁷ Al MAS NMR	106
<i>Vitaly P. Kozinenko, Alexey S. Kiryutin, Alexandra V. Yurkovskaya</i> Probing Weak Ligand-Protein Binding Using Long-Lived Spin Order Relaxometry	109
<i>Galina Kupriyanova, Ivan Mershev, George Mozhukhin, Bulat Rameev</i> ¹⁴ N magnetic relaxation in solids and liquids	112
<i>Kuzmichev Alexey, Vetoshko Peter</i> Improved Low-Temperature Damping of Epitaxial Yttrium Iron Garnet Film	116
<i>Manuel Arsenio Lores Guevara, Evelio Rafael Gonzalez Dalmau, Carlos Alberto Cabal Mirabal</i> Proposal for a detachable Phantom for MRI-qMRI	119
<i>Lilian Somoano Delgado, Fabián Tamayo Delgado, Claudia Camila García Cruz, Abel Tobías Suárez Olivares, Diana Esperanza Monet Alvarez, Alina Salabert Revilla, Haydee Cruz Vadell, Lidia Clara Suárez Beyries, Yomaidis Araujo Durán, Yamirka Alonso Geli, Manuel Arsenio Lores Guevara</i> Blood dynamic viscosity measured using NMR	122

<i>Néstor Juan Rodríguez de la Cruz, Manuel Arsenio Lores Guevara, Carlos Alberto Cabal Mirabal, Robert N. Muller, Sophie Laurent, Fabián Tamayo Delgado, Juan Carlos García Naranjo</i> Modelling proton magnetic relaxation in hemoglobin solutions: spherical and ellipsoidal approaches	124
<i>Dmitrii A. Luzik, Irene Ceccolini, Boris B. Kharkov, Alexandra D. Levkina, Ivan S. Podkorytov, Lewis E. Kay, Nikolai R. Skrynnikov</i> NMR study of small protein asymmetric dimer	125
<i>Markelov D. A., Kozinenko V. P., Kiryutin A. S., Yurkovskaya A. V.</i> New methods for SABRE hyperpolarization at high magnetic field	126
<i>G. Mozhukhin, P. Kupriyanov, E. Doğan, A. Maraşlı, B. Çolak, B. Rameev</i> Design of large volume RF probe for NQR Detection applications.....	129
<i>Kirill A. Mukhin, Olga N. Pestova, Vladimir V. Matveev</i> NMR Study of Ion Behavior in lithium acetate – cesium acetate aqueous solutions.....	133
<i>Eugeny M. Pestryaev</i> Applicability limits of the Anderson-Weiss approach	136
<i>Alexander Fedotov, Vladimir Pugovkin, Denis Burov, Anna Hurshkainen and Carlos Cabal Mirabal</i> An alternative proposal of gradient coils configuration for ultra-low field magnetic resonance imaging	139
<i>Margarita A. Sadovnikova, George V. Mamin, Fadis F. Murzakhanov, Nataliya V. Petrakova, Vladimir S. Komlev, Marat R. Gafurov</i> Study of the hydroxyapatite doped with gadolinium and cerium ions using EPR spectroscopy	143
<i>L.V. Sharipova, A.V. Shchelokova, E.A. Brui</i> Experimental investigation of a metasurface for cardiac magnetic resonance imaging at 3 T.....	146
<i>Leonid V. Skripnikov</i> Use of molecules to measure the parity conserving and parity violating nuclear moments ..	150
<i>Polina V. Skvortsova, Arina V. Pergat, Bulat I. Khairutdinov</i> NMR study of liquid–liquid phase separation in pillar[5]arene-oligonucleotide system.....	151
<i>Alexander V. Snadin, Alexey S. Kiryutin, Nikita N. Lukzen, Alexandra V. Yurkovskaya</i> Singlet-triplet conversion in molecular hydrogen on a homogeneous catalyst in parahydrogen induced polarization experiments	152
<i>Alexander Sónora Mengana</i> Assesment of timing parameters of Cuban NMR console	154

<i>Sergey V. Sviyazov, Simon V. BabenkoI, Ivan V. Skovpin, Nikita V. Chukanov, Dudari B. Burueva and Igor V. Koptyug</i> Manipulating Stereoselectivity of Parahydrogen Addition to Acetylene to Unravel Interconversion of Ethylene Nuclear Spin Isomers	156
<i>Timofei T. Taran, Olga S. Pavlova, Mikhail V. Gulyaev, Dmitry S. Dmitriev, Aleksandr G. Pistrak, Kirill N. Ryabikov, Viktor P. Tarasov, Yury A. Pirogov</i> Non-contrast MRI for ventilation and perfusion study of the lungs	159
<i>Anna A. Titova, Maxim A. Skakun, Elena Yu. Tupikina</i> Investigation of the use of hydrogen bonds for association of polymer blocks with different substituents by means of quantum chemistry	161
<i>Aleksandr S. Tomilov, Anastasiya A. Yazikova, Artem S. Poryvaev, Matvey V. Fedin</i> Nitroxide radical sorption on MOF-808 for quantum bits.....	163
<i>Milosh Ubovich, Vladimir V. Matveev, Vladimir I. Chizhik</i> Ionic Liquid Systems “[bmim]Cl/AlCl ₃ /H ₂ O” Studied by NMR and Quantum Chemistry..	164
<i>A.A. Vasilev, D.Yu. Nefedov, A.V. Uskov, E.V. CharnayaI, Yu.A. Kumzerov, A. V. Fokin</i> Liquid-liquid phase transition in the nanoconfined Ga-In-Sn eutectic alloy.....	166
<i>Sergey G. Vasil'ev, Ksenia Panicheva, Edward Fel'dman</i> Dissipative dynamics of multiple-quantum NMR coherences in two-spin systems.....	168
<i>Vedernikov L. S., Stashkevich A. A., Tatsenko I. Y. Ustinov A. B.</i> Excitation of black spin wave solitons in an active ring resonator based on a ferromagnetic film.....	171
<i>Ilya V. Yakovlev, Aleksandr A. Shubin, Evgeniy S. Papulovskiy, Aleksandr V. Toktarev, Olga B. Lapina</i> Ordering of water molecules in hydrated aluminophosphate AIPO-11 according to ²⁷ Al solid-state NMR and DFT calculations	174
<i>Valentina V. Yakovleva, Kirill V. Likhachev, Roman A. Babunts, Sergey V. Titkov, Pavel G. Baranov</i> Scanning NV spectroscopy as a tool for the study of natural diamonds.....	175
<i>Anna P. Yi, Oleg G. Sannikov, Dudari B. Burueva, Nikita V. Chukanov, Igor V. Koptyug</i> Solvent effects in hyperpolarization of ¹⁵ N nuclei in metronidazole and nimorazole antibiotics via SABRE-SHEATH	178
POSTER SESSION.....	185
<i>Adyukov I. S., Pelipko V. V., Baichurin R. I., Makarenko S. V.</i> The geometric configuration determination of 2-(1-aryl-1-oxopropan-2-ylidene)hydrazinecarboxamides with 1H-1H NOESY	186

<i>Arseniy A. Alekseev, Ivan V. Pleshakov, Efim E. Bibik, Igor V. Ilichev</i> Behavior of magnetic nanoparticles of ferrofluid in a focused laser beam	188
<i>Dmitry V. Alimov, Artem S. Poryvaev, Matvey V. Fedin</i> UiO-66 framework with encapsulated spin probe: mechanistic study of sensitivity to mechanical pressure and guest molecules	191
<i>Omar Alkhuder, Peter M. Tolstoy, Mikhail A. Kostin</i> Using NMR to establish experimental correlations between hydrogen bond strength and the chemical shift of the ^{31}P in complexes with phosphine oxide	194
<i>Nikolay V. Anisimov, Arina A. Tarasova, Lev L. Gervits</i> Study of the gastrointestinal tract using ^{19}F MRI	197
<i>Kev M. Salikhov, Marcel M. Bakirov, Ruslan B. Zaripov, Iskander T. Khairutdinov</i> Manifestations of spin coherence transfer in EPR spectra of nitroxide free radical solutions.....	199
<i>E.E. Batueva, A.R. Sharipova, E.N. Frolova, L.I. Savostina, L.V. Bazan, M.A. Cherosov, R.G. Batulin, O.A. Turanova, A.N. Turanov</i> The effect of the counterion and substituent in the ligand on the properties of the Fe(II)–Fe(III) heptanuclear complex	201
<i>Valeriy V. Bezrodnyi, Sofia E. Mikhtaniuk, Emil I. Fatullaev, Oleg V. Shavykin, Igor M. Neelov and Nadezhda N. Sheveleva</i> Molecular dynamic simulation of complexes lysine-based dendrimers with fullerenes C_{60} ..	202
<i>K.V. Bozhenko I, A.N. Utenyshev I, L.G. Gutsev I, S.M. Aldoshin, and G.L. Gutsev</i> Spin-Dependent Interactions of Fe_2O_n ($n=1-6$) Clusters	205
<i>Cheremensky S.O., Egorov A.V.</i> Microstructure and molecular mobility in the LiCl-CsCl-H ₂ O ternary system according to molecular dynamics simulations	207
<i>Dmitry A. Cheshkov, Dmitry O. Sinitsyn, Vyacheslav A. Chertkov</i> ANATOLIA: NMR Software for Total Lineshape Analysis	209
<i>Viktor N. Demidov, Alexandra G. Ivanova, Alexandr A. Matveev, Tatiana B. Pakhomova, Irina B. Glebova, Anna Yu. Mylnikova, Sofia V. Paston, Evgenya V. Bogomolova</i> ^1H and ^{13}C NMR spectra of bioactive glassy polymorphic N-heterobiphenylene acetate binuclear complexes of Zn^{2+} and Cd^{2+}	211
<i>Viktor N. Demidov, Alexandra G. Ivanova, Irina N. Tsvetkova, Evgeny M. Kosobuko, Evgenya V. Bogomolova, Sofia V. Paston, Vadim I. Voschikov, Yaroslav A. Khamidulin, Larisa N. Efimova, Tatiana B. Pakhomova</i> Effect of the coordination centers and the solvents on the parameters of the ^1H and ^{13}C NMR spectra of Zn^{+2} and Cd^{2+} acetate mononuclear complexes with 1,10-phenanthroline	215

<i>Maria E. Dmitrenko, Anna I. Kuzminova, Roman R. Dubovenko, Alexandra M. Korovina, Anton S. Mazur, Konstantin N. Semenov, Tatiana V. Plisko, Anastasia V. Penkova</i> Preparation and characterization of pervaporation membranes based on sodium alginate modified by Zn(BIM).....	218
<i>Anastasia S. Dmitrieva, Boris P. Nikolaev, Ludmila Yu. Yakovleva, Viacheslav S. Fedorov, Maxim Shevtsov</i> Low-field bench-top NMR study of magnetic cellulose microspheres for spiking of circulating tumor cells.....	219
<i>Roman Dubovenko, Mariia Dmitrenko, Anna Kuzminova, Anna Mikulan, Margarita Puzikova, Artem Selyutin, Anton Mazur, Anastasia Penkova</i> Structure and physicochemical properties of carboxymethyl cellulose/Zn-based MOF membrane.....	222
<i>Pavel Shandybin, Anna Dyatlovich, Anna Hurshkainen, C. Cabal Mirabal</i> Device for determining the characteristics of the magnetic field of a permanent magnet. Preliminary results.	223
<i>M.I. Egorova, D.A. Mizyulin, A.V. Egorov, M.G. Shelyapina</i> Local ordering and mobility of water molecules in the micropores of a 3D zeolite with mordenite structure by molecular dynamics simulation	226
<i>A.M. Garaeva, E.M. Alakshin, E.I. Boltenkova, K.R. Safiullin, I.V. Romanova, M.S. Tagirov</i> The effect of DyF ₃ particles on the magnetic relaxation of ³ He nuclei	227
<i>Dilyara R. Gareeva</i> Automated method of MRI image segmentation.....	228
<i>Gomonov K. A., Pelipko V. V., Baichurin R. I., Makarenko S. V.</i> Nuclear Overhauser effect in determining the configuration of nitrofuran-3-carboxylates semicarbazones	231
<i>Ilya A. Grishanovich, Semyon L. Shestakov, Yuliya A. Sypalova, Alexander Yu. Kozhevnikov</i> The detecting of correlations between NMR spectra of ligno-carbohydrate complexes in dissolved and solid state.....	233
<i>Islamov T.R., Aganova O.V., Julmetov A.R., Klochkov V.V.</i> Investigation of Lovastatine with transition metal by NMR.....	235
<i>Ivanov A. A., Skirda V. D., Alexandrov A. S., Ivanov D. S., Doroginizky M. M., Valiullin A. L., Berdnikov V. A.</i> Multi-point magnetic field mapping device to passive shimming of NMR permanent magnet.....	237
<i>M.V. Kadnikov, P.A. Fetin, I.M. Zorin, N.V. Tsvetkov</i> Synthesis and macromonomer structure analysis by ¹ H NMR spectroscopy	240

<i>Anna S. Kariakina, Anna I. Kuzminova, Roman R. Dubovenko, Maria E. Dmitrenko, Konstantin N. Semenov, Anastasia V. Penkova</i> Synthesis and characterization of membranes based on polyether block amide modified by MIL-125	241
<i>Regina E. Dashko, Darya L. Kolosova, Anton S. Mazur, Alexandr V. Ievlev</i> Structural transformations of pore water based on nuclear magnetic resonance in the filtration consolidation theory of fine-grained soils	242
<i>Alexandr V. Kondrashov, Mikhail Kostylev, Alexey B. Ustinov</i> Influence of the operating regime on performances of the magnonic reservoir computer.....	245
<i>Vasilij G. Vasil'ev, Anzhelika V. Sheremeta, Vasilij A. Ivlev, Sergey V. Goryainov, Luitza A. Miridonova, Alina Y. Polukhina, Anastasia A. Murtazina, Ekaterina A. Krivosheeva</i> Identification of glucofrangulin A in <i>Rhamnus frangula</i> L. by ¹ H NMR spectroscopy.	248
<i>Anna I. Kuzminova, Anna S. Karyakina, Maria E. Dmitrenko, Semen S. Egorov, Anton S. Mazur, Anastasia V. Penkova</i> Novel membranes based on poly(ester-block-amide) modified with Ho-MOFs.	251
<i>Olga S. Lezova, Ruslan I. Baichurin, Olga A. Shilova, Alexandra G. Ivanova, Stanislav I. Selivanov</i> Investigation of the interaction of polyvinyl alcohol and tetraethoxysilane in dimethyl sulfoxide by NMR spectroscopy	252
<i>Kirill V. Likhachev, Igor.P. Veyshtort, Maxim.V. Uchaev, Anastasia.V. Batueva, Valentina.V. Yakovleva, Alexander.S. Gurin, Roman.A. Babunts, Pavel.G. Baranov</i> All-optical scanning spectroscopy of anti crossing of electron and nuclear spin levels in a SiC crystal of hexagonal polytype.....	256
<i>Lobova A.M., Egorova A.V., Egorov D.M., Baichurin R.I.</i> Synthesis and 1H-1H spectroscopy NOESY studies of (E)-(2-chloro-2-phenylvinyl)diaminophosphine oxide	259
<i>Kenan K. Mammadhasanov, Andrei V. Komolkin, Sabina A. Seidova, Minaver D. Ibragimova, Vagif M. Abbasov, Huseyn J. Huseynov</i> Molecular dynamics simulation of sulfur compound extraction from a model fuel	261
<i>V. A. Ryzhov, V. V. Deriglazov, D. S. Grouzdev, V. V. Koziyeva, I. A. KiselevI, I. I. Larionov, K. G. Gareev, N. O. Sitkov, T. M. Zimina, Ya. Yu. Marchenko, V. S. Fedorov, M. A. Shevtsov</i> Magnetic parameters of magnetosomes inside Magnetotactic Bacteria Magnetospirillum spp.	264
<i>Yulianela Mengana Torres, Manuel A. Lores Guevara, Juan C. García Naranjo, Yamilka Alonso Geli, Fabián Tamayo Delgado</i> Theoretical relationship between proton spin-spin magnetic relaxation time (T ₂) and dynamic viscosity.	266

<i>Olga Mikhailovskaya, Xeniya Sushkova, Anna Kuzminova, Roman Dubovenko, Anton Mazur, Anastasia Penkova, Mariia Dmitrenko</i> Study of pervaporation membranes based on polyelectrolyte complex of sodium alginate/polyethylenimine modified with graphene oxide.....	270
<i>Anna I. Mikulan, Anna I. Kuzminova, Maria E. Dmitrenko, Roman R. Dubovenko, Anton S. Mazur, Anastasia V. Penkova</i> Novel composite carboxymethyl cellulose/MIL-125 pervaporation membranes: synthesis and characterization	271
<i>Guzel A. Minnullina, Sergey V. Efimov, Vladimir V. Klochkov</i> Cis-trans isomerization in cyclosporin C dissolved in acetonitrile.....	272
<i>Vasilii G. Vasil'ev, Anzhelika V. Sheremeta, Vasilii A. Ivlev, Sergey V. Goryainov, Luiza A. Miridonova, Alina Y. Polukhina, Anastasia A. Murtazina, Ekaterina A. Krivosheeva</i> Determination of diosmin in <i>Hyssopus officinalis</i> L.: opportunity of ¹ H NMR spectroscopy.....	274
<i>Amina D. Muratova, Andrey V. Komolkin, Denis A. Markelov</i> Cell size dependence of hydrodynamic radius of PAMAM dendrimers G2 in methanol	277
<i>Nichugovskiy A.I., Cheshkov D.A.</i> From Theory to Practice: Extracting spin-spin coupling constants from highly complex NMR multiplets.....	280
<i>Yury V. Bogachev, Vasilii I. Zubkov, Anna V. Solomnikova, Anastasiya V. Nikitina, Stanislav M. Suharzevskiy</i> Studies of EPR relaxation of NV centers in diamonds	282
<i>Yury V. Bogachev, Marina N. Shishkina, Anastasiya V. Nikitina</i> EPR of magnetic nanoparticles in water dispersions	285
<i>Daria S. Novikova, Ammar Al Mustafa, Vyacheslav G. Tribulovich, Ruslan I. Baichurin, Stanislav I. Selivanov</i> Analysis of NOESY spectra to obtain accurate information on the structure and dynamics of some 5,7-substituted pyrazolo[1,5-a]pyrimidine derivatives in solution	287
<i>Daria A. Osetrina, Aydar G. Bikmullin, Aydar R. Yulmetov, Timur A. Mukhametzyanov, Vladimir V. Klochkov1, Dmitriy S. Blokhin</i> Structural Investigations of Fibril-Forming Peptide Fragments of Semenogelin Protein	290
<i>I.V. Ozhogin, A.S. Kozlenko, A.D. Pugachev, V.S. Dmitriev, P.B. Chepurnoy, G.S. Borodkin</i> Study of the thermochromic behavior of nitro-substituted symmetric bis-spiropyran of the indoline series using dynamic NMR methods	293
<i>Ksenia Panicheva, Sergey G. Vasil'ev, Edward Fel'dman</i> Relaxation of the ¹ H multiple-quantum (MQ) NMR coherences during the excitation period in gypsum single crystal.	296

<i>Vasily G. Vasil'ev, Anzhelika V. Sheremeta, Vasily A. Ivlev, Sergey V. Goryainov, Luiza A. Miridonova, Alina Y. Polukhina, Anastasia A. Murtazina, Ekaterina A. Krivosheeva</i> Determination of regio- and stereochemistry of spiropyrrolizine oxindoles using NMR spectroscopy methods.....	298
<i>Alina Petrova, Fadis Murzakhanov, George Mamin, Oleg Gnezdilov, Inna Fadeeva, Marat Gafurov</i> Investigation of polyvinylpyrrolidone—hydroxyapatite composites by NMR and EPR methods.....	301
<i>Pilipenko I. A., Selivanov S. I., Pelipko V.V., Baichurin R. I., Makarenko S. V.</i> Application of 2D NMR experiments for identification of alkyl 5-nitro-7,12-dioxo-7,12-dihydroindeno[1,2-a]fluorene-6-carboxylates.....	305
<i>Margarita E. Puzikova, Anna I. Kuzminova, Maria E. Dmitrenko, Roman R. Dubovenko, Alexandra M. Korovina, Anton S. Mazur, Anastasia V. Penkova</i> Development and characterization of novel nanofiltration membranes based on polyacrylonitrile modified with Zr-MOFs.....	307
<i>Andrey M. Rochev, Vladimir M. Mikushev, Elena V. Charnaya, Akim D. Zagovorich</i> Temperature evolution of spin-phonon coupling efficiency under magnetic saturation for sodium quadrupole nuclei in a NaF crystal.....	308
<i>Alexey V. Salin, Andrey A. Shabanov, Elizaveta V. Kartashova</i> Organocatalytic synthesis of Michael adducts of the sesquiterpene lactone arglabin and their 2D NMR structural analysis.....	311
<i>Kirill A. Salomatin, Anna I. Kuzminova, Danila D. Myznikov, Mariia E. Dmitrenko, Roman R. Dubovenko, Artem A. Selyutin, Anton S. Mazur, Alexandra Yu. Pulyalina, Anastasi V. Penkova</i> Characterization of novel dense membranes based on chitosan modified by MIL-125	314
<i>A.N. Sashina, A.R. Khakimzyanova, A.M. Khakimov, A.V. Filippov, A.V. Khaliullina</i> Structure and mobility of the lipid system in water-ionic liquid mixtures: magnetic resonance measurements and molecular dynamics simulations.....	315
<i>Sabina A. Seidova, Minaver D. Ibragimova, Vagif M. Abbasov, Huseyn J. Huseynov, Ulviya J. Yolchueva</i> Study of ionic-liquid extraction of arenes from petroleum fractions by UV spectroscopy method	317
<i>Amina F. Shaidullina, Michael Yu. Volkov, Alsu R. Sharipova, Olga A. Turanova, Ludmila I. Savostina, and Alexander N. Turanov</i> Study of intramolecular dynamics of β -enaminone using NMR, UV and DFT methods	319
<i>M.G. Shelyapina, E.P. Maksimova, A.V. Egorov</i> Adsorption of glycerol at Brønsted sites in mordenite: A density functional theory study ...	320

<i>Xeniya D. Sushkova, Maria E. Dmitrenko, Anna I. Kuzminova, Anna Y. Mikulan, Anton S. Mazur, Roman R. Dubovenko, Anastasia V. Penkova</i> Study on biodegradability of carrageenan/starch/nanocellulose food films	323
<i>Artyom S. Tarasov, Sergey V. Efimov, Vladimir V. Klochkov</i> Spectral characteristics of the complex of cyclosporin C (CsC) with Dy ³⁺ ions and DPC micelles in aqueous solution determined by NMR spectroscopy	324
<i>Roman P. Terekhov, Amir Taldaev, Eduard V. Bocharov, Denis I. Pankov, Anastasiya D. Savina, Irina A. Selivanova</i> Spatial structure of taxifolin's diastereomers via NMR analysis.....	327
<i>Anastasia A. Troshkina, Dmitriy S. Blokhin, Vladimir V. Klochkov</i> Structure of the amyloidogenic peptide SEM2(49-107) by NMR spectroscopy	330
<i>Daria Tsukhlova, Daria Melnikova, Vladimir Skirda</i> Investigation of the features of the interaction of water molecules and saccharides in aqueous solutions by NMR	333
<i>Milosh Ubovich, Andrei V. Egorov, Vladimir. I. Chizhik</i> Molecular Mobility in Mixtures of Ethylammonium and Aluminum Nitrates by Molecular Dynamics Simulations in Interests of Interpreting NMR Data.....	335
<i>Yu. A. Uspenskaya, A. S. Gurin, D. D. Kramushchenko, I. V. Ilyin, A. V. Batueva, P. G. Baranov, R. A. Babunts</i> Transition metals in wide-band-gap semiconductor β -Ga ₂ O ₃ identified by high-frequency electron paramagnetic resonance	338
<i>Lyudmila A. Kayukova, Azamat Yerlanuly, Aidana M. Duisenali, Anna V. Vologzhanina, Yelizaveta O. Belyankova</i> Formation of 2-aminospiropyrazolinium and linear compounds at β -aminopropioamidoximes alkylsulfochlorination	340
<i>Ruslan B. Zaripov, Iskander T. Khairutdinov</i> Using Microwave and Field Gradient Pulses for binary coding of the Transverse Magnetization.....	343
<i>Ivan Zhukov, Anton Popov, Alexander Baranchikov, Yulia Gorbunova, and Alexandra Yurkovskaya</i> Relaxation dispersion of water protons in magnetic fields ranging from 10 mT to 16.4 T for Gd-containing materials proposed as new MRI contrast agents.....	345
POEMS ABOUT SCHOOL	348
AUTHOR INDEX	351

Schedule

21st International School-Conference

«Magnetic Resonance and its Applications.

Spinus-2024»

April 1 - 5, 2024

St. Petersburg



MONDAY –April 1, 2024	
Chairman	Professor Denis Markelov (Saint-Petersburg, Russia)
10:00 – 10:15	Opening
10:15– 11:00	Vladimir Chizhik (Saint-Petersburg, Russia) Lecture: 300 years of St. Petersburg State University and 80 years of radiospectroscopy in it
11:00 – 11:40	Janez Stepišnik (Ljubljana, Slovenia) Lecture: Why biopolymers fold in glycerol-water mixture: NMR study of diffusion in glycerol-water mixture
11:40 – 12:10	‘COFFEE’ BREAK
Chairman	Professor Carlos Cabal-Mirabal (Havana, Cuba)
12:10 – 12:50	Yury Pirogov (Moscow, Russia) Lecture: Novel approaches in magnetic resonance imaging
12:50 – 13:05	Leila Sharipova (Saint-Petersburg, Russia) Oral report: Experimental investigation of a metasurface for cardiac magnetic resonance imaging at 3 T
13:05 – 13:20	Elizaveta Kononenko (Novosibirsk, Russia) Oral report: In vivo MR imaging of murine bronchial tree using hyperpolarized propane produced with parahydrogen

13:20 – 13:35	Anna Hurshkainen (Saint-Petersburg, Russia) Oral report: Ultra-low field portable MRI for a human head: preliminary results
13:35– 13:50	Vladimir Pugovkin (Saint-Petersburg, Russia) Oral report: An alternative proposal of gradient coils configuration for ultra-low field magnetic resonance imaging
13:50– 14:10	Nikolay Anisimov (Moscow, Russia) Oral report: Visualization of the internal structure of coils used in MRI studies
14:10 – 15:30	LUNCH
Chairman	Professor Yury Pirogov (Moscow, Russia)
15:30 – 15:50	Carlos Cabal-Mirabal (Havana, Cuba) Oral report: Quantitative MRI studies of the kinetics of the wound healing process. Case of diabetic foot ulcer. Towards a model.
15:50 – 16:05	Timofei Taran (Moscow, Russia) Oral report: Non-contrast MRI for ventilation and perfusion study of the lungs
16:05 – 16:20	Dmitrii Luzik (Saint-Petersburg, Russia) Oral report: NMR study of small protein assymmetric dimer
16:20 – 16:35	Vitaly Kozinenko (Novosibirsk, Russia) Oral report: Probing Weak Ligand-Protein Binding Using Long-Lived Spin Order Relaxometry
16:35 – 16:50	Polina Kononova (Novosibirsk, Russia) Oral report: spectroscopy in the study of the interaction of membrane proteins of enveloped viruses and potential antiviral agents
16:50– 17:10	Manuel Arsenio Lores Guevara (Santiago de Cuba, Cuba) Oral report: Blood dynamic viscosity measured using NMR
17:10 – 17:30	'COFFEE' BREAK
Chairman	Professor Carlos Cabal-Mirabal (Havana, Cuba)
17:30 – 17:45	Manuel Arsenio Lores Guevara (Santiago de Cuba, Cuba) Oral report: Proposal for a detachable Phantom for MRI-qMRI
17:45 – 18:00	Zilya Badrieva (Saint-Petersburg, Russia) Oral report: Dictionary-based T ₂ -mapping with multi-echo turbo-spin echo
18:00–18:15	Eduardo Garea-Llano (Havana, Cuba) Oral report: Artificial Intelligence tools for the reconstruction and enhancement of MR imaging
18:15 – 18:30	Yamirka Alonso (Santiago de Cuba, Cuba) Oral report: Assessment of blood serum dynamic viscosity by NMR in sickle cell disease
18:30 – 18:45	Evelio Gonzalez-Dalmau (Havana, Cuba) Oral report: System to ensure the reproducibility of the legs positions during the Magnetic Resonance Imaging (MRI) studies
19:30 – 22:00	Welcome Party

TUESDAY – April 2, 2024	
Chairman	Professor Yury Bunkov (Moscow, Russia)
10:00 – 10:40	Roman Babunts (Saint-Petersburg, Russia) Lecture: Spin-dependent phenomena in wide-gap materials and based nanostructures and development of the instrumentation for these studies
10:40 – 10:55	Anastasia Batueva (Saint-Petersburg, Russia) Oral report: Mn Related Paramagnetic Centres in a Bulk GaS and GaSe Van der Waals Semiconductors with High-Frequency EPR Method
10:55 – 11:10	Ilya Kostyukov (Moscow, Russia) Oral report: Determination of crystallographic positions of aluminum atoms in BEA zeolites using high-quality ²⁷ Al MAS NMR
11:10 – 11:25	Alexander Snadin (Novosibirsk, Russia) Oral report: Singlet-triplet conversion in molecular hydrogen on a homogeneous catalyst in parahydrogen induced polarization experiments
11:25 – 11:40	Sergey Sviyazov (Novosibirsk, Russia) Oral report: Manipulating Stereoselectivity of Parahydrogen Addition to Acetylene to Unravel Interconversion of Ethylene Nuclear Spin Isomers
11:40 – 12:10	‘COFFEE’ BREAK
Chairman	Professor Yury Bunkov (Moscow, Russia)
12:10 – 12:40	Shutian Lu (ZHONGTAI, Hefei, China) Ilya Chazov (sales director of the company "ELEMENT", Ekaterenburg, Russia) Lecture: The ZHONGTAI 94 GHz pulsed EPR spectrometer
12:40 – 12:55	Margarita Sadovnikova (Kazan, Russia) Oral report: Study of the hydroxyapatite doped with gadolinium and cerium ions using EPR spectroscopy
12:55 – 13:10	Valentina Yakovleva (Saint-Petersburg, Russia) Oral report: Scanning NV spectroscopy as a tool for the study of natural diamonds
13:10 – 13:25	Leonid Vedernikov (Saint-Petersburg, Russia) Oral report: Excitation of black spin wave solitons in an active ring resonator based on a ferromagnetic film
13:25– 14:05	Kev Salikhov (Kazan, Russia) Lecture: The effect of exchange narrowing of the electron paramagnetic resonance (EPR) spectra of dilute radical solutions indicates the formation of a Bose-Einstein condensate (BEC)
14:05 – 15:30	LUNCH
Chairman	Professor Vladimir Chizhik (Saint-Petersburg, Russia)

15:30 – 16:10	Leonid Grunin (Yoshkar-Ola, Russia) Lecture: Systematic View on the Dynamics and Structure Analysis of Solids by Time-Domain NMR
16:10– 16:30	Boris Kharkov (Saint-Petersburg, Russia) Oral report: The Role of Rotational Motion in Diffusion NMR Experiments on Supramolecular Assemblies
16:30– 16:50	Galina Kupriyanova (Kaliningrad, Russia) Oral report: ^{14}N magnetic relaxation in solids and liquids.
	CONFERENCE PHOTO
16:50– 18:50	Oral blitz reports of young scientists POSTER SESSION I
	WEDNESDAY – April 3, 2024
10:00 – 14:30	Excursion
14:30 – 15:30	LUNCH
Chairman	Professor Marina Shelyapina (Saint-Petersburg, Russia)
15: 30 – 16:10	Suryaprakash Nagarajarao (Bangalore, India) Lecture: Clean Sequences for Complete Eradication of Unwanted Evolution and Accurate Determination of Spectral Parameters
16:10 – 16:40	Edward Fel'dman (Chernogolovka, Russia) Oral report: Multiple quantum NMR in problems of quantum informatics: many-spin entanglement and scrambling
16:40 – 16:55	Aleksandr Tomilov (Novosibirsk, Russia) Oral report: Nitroxide radical sorption on MOF-808 for quantum bits
16:55– 17:15	Sergey Vasil'ev (Chernogolovka, Russia) Oral report: Dissipative dynamics of multiple-quantum NMR coherences in two-spin systems
17:15– 17:35	'COFFEE' BREAK
Chairman	Professor Marina Shelyapina (Saint-Petersburg, Russia)
17: 35 – 17: 50	Sergei Bystrov (Batumi, Georgia) Oral report: NMR to Industry: Development of modern universal control software for TD-NMR spectrometers, validation using fertilizer samples as an example
17: 50– 18:10	Alexander Sónora Mengana (Santiago de Cuba, Cuba) Oral report: Assessment of timing parameters of cuban NMR console

18:10– 18:30	Manuel Arsenio Lores Guevara (Santiago de Cuba, Cuba) Oral report: Modelling proton magnetic relaxation in hemoglobin solutions: spherical and ellipsoidal approaches
18:30– 18:50	Georgy Mozzhukhin (Gebze-Kocaeli, Turkey) Oral report: Design of large volume RF probe for NQR Detection applications
THURSDAY – April 4, 2024	
Chairman	Associate Professor Andrei Komolkin (Saint-Petersburg, Russia)
10:00 – 10:40	Elena Charnaya (Saint-Petersburg, Russia) Lecture: Liquid-liquid phase transition in metallic melts
10:40 – 11:00	Polina Skvortsova (Kazan, Russia) Oral report: NMR study of liquid–liquid phase separation in pillar[5]arene-oligonucleotide system
11:00– 11:15	Allisher Vasilev (Saint-Petersburg, Russia) Oral report: Liquid-liquid phase transition in the nanoconfined Ga-In-Sn eutectic alloy
11:15 – 11:40	Marina Shelyapina (Saint-Petersburg, Russia) Lecture: Nanoconfined water in zeolites with hierarchical porosity probed
11:40 – 12:10	‘COFFEE’ BREAK
Chairman	Professor Elena Charnaya (Saint-Petersburg, Russia)
12:10 – 12:50	Yury Bunkov (Moscow, Russia) Oral report: Qubit on magnon BEC state
12:50 – 13:05	Alexey Kuzmichev (Moscow, Russia) Oral report: Improved Low-Temperature Damping of Epitaxial Yttrium Iron Garnet Film
13:05– 13:25	Alexey Kiryutin (Novosibirsk, Russia) Oral report: SLIC-SABRE at Earth’s Magnetic fields: Simple and Effective Method of getting Strong ^{15}N NMR Polarization
13:25 – 13:40	Danil Markelov (Novosibirsk, Russia) Oral report: New methods for SABRE hyperpolarization at high magnetic field
13:40– 13:55	Anna Yi (Novosibirsk, Russia) Oral report: Solvent effects in hyperpolarization of ^{15}N nuclei in metronidazole and nimorazole antibiotics via SABRE-SHEATH
13:55 – 14: 10	Leonid Skripnikov (Saint-Petersburg, Russia) Oral report: Use of molecules to measure the parity conserving and parity violating nuclear moments
14:10 – 15:30	LUNCH
Chairman	Professor Denis Markelov (Saint-Petersburg, Russia)

15: 30 – 15:50	Ilya Yakovlev (Novosibirsk, Russia) Oral report: Ordering of water molecules in hydrated aluminophosphate AlPO-11 according to ^{27}Al solid-state NMR and DFT calculations
15: 50 – 16:05	Naira Gromova (Saint-Petersburg, Russia) Oral report: Cell size dependence of hydrodynamic radius of carbosilane dendrimers in chloroform
16:05– 16:20	Anna Titova (Saint-Petersburg, Russia) Oral report: Investigation of the use of hydrogen bonds for association of polymer blocks with different substituents by means of quantum chemistry
16:20– 16:35	Vladimir Bazaikin (Saint-Petersburg, Russia) Oral report: Investigation of poly-m-phenylene isophthalamide polymer membrane modified by UiO-66 (NH_2) MOF for separation of toluene/methanol mixture using molecular dynamics method
16:35– 16:55	Eugeny Pestryaev (Ufa, Russia) Oral report: Applicability limits of the Anderson-Weiss approach to polymer melts
16:55– 18:50	Oral blitz reports of young scientists POSTER SESSION II
20:00– 23:00	Conference Dinner
FRIDAY – April 5, 2024	
Chairman	Professor Peter Tolstoy (Saint-Petersburg, Russia)
10:45 – 11:05	Alina Arkhipova (Novosibirsk, Russia) Oral report: Interaction of the anthraquinone derivative and its chelate complexes with nucleic bases in dark and photoinduced processes
11:05 – 11:20	Vladimir Koshman (Novosibirsk, Russia) Oral report: Redox activity and membrane interaction of novel thiosemicarbazones
11:20– 11:40	Sabina Eldarova (Baku, Azerbaijan) Oral report: Study of the chemical composition of azerbaijani crude oil using infrared spectroscopy and nuclear magnetic resonance methods.
11:40 – 12:10	‘COFFEE’ BREAK
Chairman	Associate Professor Vladimir Matveev (Saint-Petersburg, Russia)
12:10 – 12:50	Pavel Yushmanov (Stockholm, Sweden) Lecture: Electrophoretic NMR and applications
12:50– 13:05	Petr Fetin (Saint-Petersburg, Russia) Oral report: Polymerization kinetics and catalytic properties of resulted comb-like polyelectrolytes by ^1H NMR

13:05 – 13:20	Milosh Ubovich (Saint-Petersburg, Russia) Oral report: Ionic Liquid Systems “[bmim]Cl/AlCl ₃ /H ₂ O” Studied by NMR and Quantum Chemistry
13:20 – 13:35	Kirill Mukhin (Saint-Petersburg, Russia) Oral report: NMR Study of Ion Behavior in lithium acetate – cesium acetate aqueous solutions
13:35– 13:55	Alexandr Ievlev (Saint-Petersburg, Russia) Oral report: Molecular and ionic mobility of ionic liquids with complex anions containing metals
13:55– 16:00	MEETING OF AWARDING COMMISSION
16:00– 16:30	Awarding, Closing and “Related Phenomena”

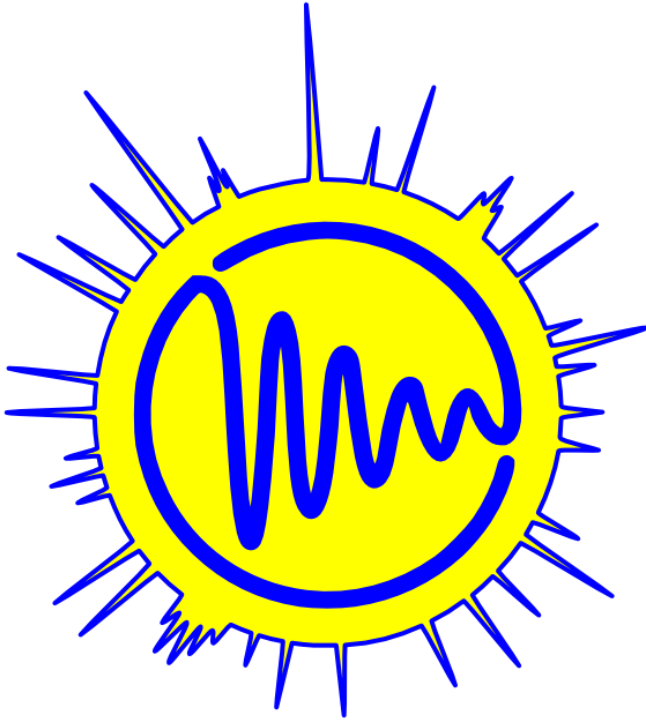
POSTER SESSION I (TUESDAY, 16:50 – 18:50)			
1	Ivan	Adyukov	The geometric configuration determination of 2-(1-aryl-1-oxopropan-2-ylidene)hydrazinecarboxamides with ¹ H- ¹ H NOESY
2	Arseniy	Alekseev	Behavior of magnetic nanoparticles of ferrofluid in a focused laser beam
3	Dmitry	Alimov	UiO-66 framework with encapsulated spin probe: mechanistic study of sensitivity to mechanical pressure and guest molecules
4	Omar	Alkhuder	Using NMR to establish experimental correlations between hydrogen bond strength and the chemical shift of the ³¹ P in complexes with phosphine oxide.
5	Ekaterina	Batueva	The effect of the counterion and substituent in the ligand on the properties of the Fe(II)–Fe(III) heptanuclear complex
6	Valerii	Bezrodnyi	Molecular dynamic simulation of complexes lysine-based dendrimers with fullerenes
7	Sergey	Cheremensky	Microstructure and molecular mobility in the LiCl-CsCl-H ₂ O system according to molecular dynamics simulations
8	Mariia	Dmitrenko	Preparation and characterization of pervaporation membranes based on sodium alginate modified by Zn(BIM)
9	Anastasia	Dmitrieva	Low-field bench-top NMR study of magnetic cellulose microspheres for spiking of circulating tumor cells
10	Roman	Dubovenko	Structure and physicochemical properties of carboxymethyl cellulose/Zn-based MOF membrane
11	Anna	Dyatlovich	Device for determining the characteristics of the magnetic field of a permanent magnet. Preliminary results.
12	Maria	Egorova	Local ordering and mobility of water molecules in the micropores of a 3D zeolite with mordenite structure by molecular dynamics simulation
13	Adeliya	Garaeva	The effect of DyF ₃ particles on the magnetic relaxation of ³ He nuclei
14	Dilyara	Gareeva	Segmentation of MRI images of the spine using ML
15	Kirill	Gomonov	Nuclear Overhauser effect in determining the configuration of nitrofurans-3-carboxylates semicarbazones
16	Timur	Islamov	Investigation of Lovastatin with transition metal by NMR
17	Matvei	Kadnikov	Synthesis and macromonomer structure analysis by ¹ H NMR spectroscopy
18	Anna	Kariakina	Synthesis and characterization of membranes based on polyether block amide modified by MIL-125

19	Mamedgasanov	Kenan	Molecular dynamics simulation of sulfur compound extraction from a model fuel.
20	Amina	Muratova	Cell size dependence of hydrodynamic radius of PAMAM dendrimers G2 in methanol
21	Dariya	Kolosova	Structural transformations of pore water based on NMR in the consolidation theory of fine-grained soils.
22	Ekaterina	Krivosheeva	Identification of glucofrangulin A in <i>Rhamnus frangula</i> L. by ^1H NMR spectroscopy.
23	Anna	Kuzminova	Novel membranes based on poly(ester-block-amide) modified with Ho-MOFs
24	Olga	Lezova	Investigation of the interaction of polyvinyl alcohol and tetraethoxysilane in dimethyl sulfoxide by NMR spectroscopy
25	Kirill	Likhachev	All-optical scanning spectroscopy of anti-crossing of electron and nuclear spin levels in a SiC crystal of hexagonal polytype
26	Anastasia	Lobova	Synthesis and ^1H - ^1H spectroscopy NOESY studies of (E)-(2-chloro-2-phenylvinyl)diaminophosphine oxide
27	Olga	Mikhailovskaya	Study of pervaporation membranes based on polyelectrolyte complex of sodium alginate/polyethylenimine modified with graphene oxide
28	Anna	Mikulan	Novel composite carboxymethyl cellulose/MIL-125 pervaporation membranes: synthesis and characterization
29	Guzel	Minnullina	Cis-Trans Isomerization in Cyclosporin C Dissolved in Acetonitrile
30	Viktor	Demidov	^1H and ^{13}C NMR spectra of bioactive glassy polymorphic N-heterobiphenylene acetate binuclear complexes of Zn^{2+} and Cd^{2+}
31	Viktor	Demidov	Effect of the coordination centers and the solvents on the parameters of the ^1H and ^{13}C NMR spectra of bioactive Zn^{+2} and Cd^{2+} acetate mononuclear complexes with 1,10-phenanthroline
32	Alexey	Salin	Organocatalytic synthesis of Michael adducts of the sesquiterpene lactone arglabin and their 2D NMR structural analysis
33	Anastasia	Nikitina	Studies of EPR relaxation of NV centers in diamonds
34	Anastasia	Nikitina	EPR of magnetic nanoparticles in water dispersions
35	Nikolay	Anisimov	Study of the gastrointestinal tract using ^{19}F MRI
36	Dmitry	Cheshkov	ANATOLIA: NMR Software for Total Lineshape Analysis
37	Ruslan	Zaripov	Using Microwave and Field Gradient Pulses for binary coding of the Transverse Magnetization
38	Ilya	Ozhogin	Study of the thermochromic behavior of nitro-substituted symmetric bis-spiropyran of the indoline series using dynamic NMR methods
39	Ilya	Grishanovich	The detectig of correlations between NMR spectra of ligno-carbohydrate complexes in dissolved and solid state
40	Alexandr	Kondrashov	Influence of the operating regime on performances of the magnonic reservoir computer

POSTER SESSION II (THURSDAY, 16:55 – 18:50)

1	Luiza	Miridonova	Determination of diosmin in <i>Hyssopus officinalis</i> L.: opportunity of ^1H NMR spectroscopy.
2	Artemiy	Nichugovskiy	From Theory to Practice: Extracting spin-spin coupling constants from highly complex NMR multiplets
3	Daria	Novikova	Analysis of NOESY spectra to obtain accurate information on the structure and dynamics of some 5,7-substituted pyrazolo[1,5-a]pyrimidine derivatives in solution
4	Daria	Osetrina	Structural studies of fibril-forming peptide fragments of the semenogelin1 protein using NMR spectroscopy and molecular modeling

5	Ksenia	Panicheva	Relaxation of the ^1H multiple-quantum (MQ) NMR coherences during the excitation period in gypsum single crystal.
6	Vasili	Pelipko	Determination of regio- and stereochemistry of spiropyrrolizine oxindoles using NMR spectroscopy methods
7	Alina	Petrova	Investigation of polyvinylpyrrolidone—hydroxyapatite composites by NMR and EPR methods
8	Ilya	Pilipenko	Application of 2D NMR experiments for identification of alkyl 5-nitro-7,12-dioxo-7,12-dihydroindeno[1,2-a]fluorene-6-carboxylates
9	Margarita	Puzikova	Development and characterization of novel nanofiltration membranes based on polyacrylonitrile modified with Zr-MOFs.
10	Andrej	Rochev	Temperature evolution of spin-phonon coupling efficiency under magnetic saturation for sodium quadrupole nuclei in a NaF crystal
11	Kirill	Salomatin	Characterization of novel dense membranes based on chitosan modified by MIL-125
12	Aleksandra	Sashina	Structure and mobility of the lipid system in water-ionic liquid mixtures: magnetic resonance measurements and molecular dynamics simulations
13	Sabina	Seyidova	Study of ionic-liquid extraction of arenes from petroleum fractions by UV spectroscopy method.
14	Amina	Shaidullina	Study of intramolecular dynamics of β -enaminone using NMR, UV and DFT methods
15	Xeniya	Sushkova	Study on biodegradability of carrageenan/starch/nanocellulose food films
16	Artyom	Tarasov	Spectral characteristics of the complex of cyclosporin C (CsC) with Dy^{3+} ions and DPC micelles in aqueous solution determined by NMR spectroscopy
17	Roman	Terekhov	Spatial structure of taxifolin's diastereomers via NMR analysis
18	Anastasia	Troshkina	Structure of the amyloidogenic peptide SEM2(49-107) by NMR spectroscopy
19	Daria	Tsukhlova	Investigation of the features of the interaction of water molecules and saccharides in aqueous solutions by NMR
20	Milosh	Ubovich	Molecular Mobility in Mixtures of Ethylammonium and Aluminum Nitrates by Molecular Dynamics Simulations in Interests of Interpreting NMR Data
21	Yulia	Uspenskaya	Transition metals in wide-band-gap semiconductor β - Ga_2O_3 identified by high-frequency electron paramagnetic resonance
22	Azamat	Yerlanuly	Formation of 2-aminospiropyrazolinium and linear compounds at β -aminopropioamidoximes alkylsulfchlorination
23	Ivan	Zhukov	Relaxation dispersion of water protons in magnetic fields ranging from 10 mT to 16.4 T for Gd-containing materials proposed as new MRI contrast agents.
24	Marcel	Bakirov	Manifestations of spin coherence transfer in EPR spectra of nitroxide free radical solutions
25	Yaroslav	Marchenko	Magnetic parameters of magnetosomes inside Magnetotactic Bacteria <i>Magnetospirillum</i> spp.
26	Marina	Shelyapina	Adsorption of glycerol at Brønsted sites in mordenite: A density functional theory study
27	Yuliana	Mengana	Theoretical relationship between proton spin-spin magnetic relaxation time (T_2) and dynamic viscosity.
28	Anatoly	Ivanov	Multi-point magnetic field mapping device to passive shimming of NMR permanent magnet
29	Konstantin	Bozhenko	Spin-Dependent Interactions of Fe_2O_n ($n=1-6$) Clusters with H_2 and O_2 Molecules



SPINUS

The School-Conference “Spinus” of Saint Petersburg State University

The St. Petersburg State University (SPbSU) holds International School-Conference “Magnetic resonance and its application” (Spinus) since 2004. “Spinus” is organized in accordance to the subjects of researches and educational programs, which have been developed and implemented in the SPbSU. In modern physics, the term “magnetic resonance” refers to a set of phenomena accompanied with the emission or absorption of electromagnetic waves of the radiofrequency diapason by quantum systems (nuclei, electrons, atoms, molecules, etc.). These phenomena, the physical nature of which is of independent interest, provided the basis of radiospectroscopic methods for studying the structure of matter and physical-chemical processes in it. They are also used for the creation of quantum generators, amplifiers, and magnetometers. For the development of ideas and applications of magnetic resonance six Nobel Prizes were awarded in the areas of physics, chemistry, biology, physiology and medicine (the latter was in 2003).

Primarily, magnetic resonance methods are:

- Nuclear Magnetic Resonance (NMR)
- Electron Paramagnetic Resonance (EPR)
- Nuclear Quadrupole Resonance (NQR)

These methods, being contactless, do not destroy an object under a study, that makes them unique and in demand not only in physics and chemistry, but also in medicine, geology, biology, archeology. Now, any medical center with high reputation has a magnetic resonance imaging (MRI). In Russia, NMR is used in oil well logging, laboratory analysis of the productivity of oil-bearing reservoirs, analysis of oil content and moisture of seeds; EPR technique is used for geological research, non-destructive control of precious stones, as well as for the dating of paleontological artifacts; there are NQR applications for remote detection of solid explosives and narcotics. Magnetometry methods based on magnetic resonance are indispensable for carrying out archaeological researches.

Earlier the school organizers worked at the Department of quantum magnetic phenomena (QMPh) of the St. Petersburg State University, which was founded in 1993 on the initiative of Professor V. I. Chizhik on the basis of the laboratory, created in the 50s of the last century by F. I. Skripov at the Department of Radio Physics (the branch “Quantum Radiophysics”). On January 1, 2014, the Department of QMPh joined the united Department of nuclear-physics research methods (Head of the Department is Corresponding Member of the Russian Academy of Sciences, Professor Mikhail Kovalchuk). The QMPh collective has a number of priority works in the field of nuclear magnetic resonance. One of the most significant achievements was the first in the world implementation (in 1958) of the Fourier transform of a free induction signal in order to obtain a NMR spectrum (see the details in [1]). Concurrently with the research activity, the staff of the department are actively involved in the development of practical applications of magnetic resonance. The department graduates work not only in Russia and the CIS, but also in Sweden, USA, New Zealand, England, Cuba, Germany, France, Italy, Turkey, occupying positions from a highly advanced operator of radiospectrometers to a professor.

The main research areas developing in the team of quantum magnetic phenomena:

- Nuclear magnetic resonance in liquids (spectra, relaxation, diffusometry, ...);
- Nuclear magnetic resonance in solids;
- NMR in liquid crystals;
- NMR in heterogeneous systems;
- The quantum magnetometry in archeology and industry;

- Nuclear magnetic resonance in the magnetic field of the Earth;
- Computing modeling in magnetic resonance.

It is evident from the above that the scope of our research interests is quite wide. We are always open for the collaboration with researchers from various fields of science.

Our team has published a series of monographs, textbooks and training manuals on Magnetic Resonance. For example:

1. Vladimir I. Chizhik, Yuri S. Chernyshev, Alexey V. Donets, Viatcheslav Frolov, Andrei Komolkin, Marina G. Shelyapina. *Magnetic Resonance and Its Applications*. 2014, Springer-Verlag. 782 pp. (*Now about 40000 chapter downloads*).
2. Квантовая радиофизика: магнитный резонанс и его приложения. Учеб. пособие. 2-е изд., перераб. Под ред. В. И. Чижики. – СПб.: Изд-во С.-Петербур. ун-та, 2009. 700 с.
3. В. И. Чижик. Ядерная магнитная релаксация. Учеб. пособие. 3-е изд. – СПб.: Изд-во С.-Петербур. ун-та, 2004. 388 с.
4. Практикум по магнитному резонансу. Учебное пособие. Под ред. В. И. Чижики. – СПб.: Изд-во С.-Петербур. ун-та, 2003. 184 с.

The goal of “Spinus” is to provide a forum for young scientists to discuss the use of all aspects of magnetic resonance methods and techniques, as well as computational and theoretical approaches, for the solving of fundamental and applied problems in physics, chemistry, medicine and biology.

In 2024, the conference will be held in “face-to-face” format. The online participation in the conference (oral presentation only) will be organized for foreign participants, who will not be able to participate in person, and for Russian participants under exceptional circumstances.

Annually, selected papers of participants are published in a special issue of the journal “Applied Magnetic Resonance”

Welcome to the annual “Spinus”!



*Dr. Sci., Professor, SPbSU, Denis A. Markelov
Chairman of Organizing committee of the 21th School-
conference
“Magnetic resonance and its applications” Spinus-2024*

1. V.I. Chizhik. On the history of the Fourier transform in NMR spectroscopy. 2018, BULLETIN DU GROUPEMENT AMPERE, 67, № 4 (273), p 5-6.

Lectures

300 years of St. Petersburg State University and 80 years of radiospectroscopy in it

Vladimir I. Chizhik

Faculty of Physics, Saint-Petersburg State University, Ulianovskaya 1, 198504, Saint-Petersburg, Russia

E-mail: v.chizhik@spbu.ru

St Petersburg University is the oldest university in Russia. January 28 (February 8), 1724 Emperor Peter the Great issued a decree on the establishment of the St. Petersburg Academy of Sciences, and for the training of Russian scientists it was supposed to organize the University and gymnasium. When the Academy and the University opened, leading foreign scientists were invited. Among them were mathematicians Leonhard Euler; Nikolaus and Daniel Bernoulli; Christian Goldbach; astronomer and geographer Jean Delisle; and physicist Georg Krafft to name just a few. In 1758, Mikhail Lomonosov is ordered to lead the research and education. From 1758 to 1764, the scientist prepared and realized a number of projects to bring the Academy of Sciences to a good state, including proposals for the charter of the University. Since the end of the 1860s, scientific societies started to appear at the University. In 1868, the Society of Naturalists was formed. In 1869, the Russian Chemical Society was opened with the active participation of Dmitri Mendeleev.

Our university has a complicated destiny: it traces its history back to the Academic University of Peter the Great, changed its official name 15 times, but the structure of education in it has always corresponded to the "university canons".

The special status of the first higher education institution of Russia is enshrined in the Federal Law "On Lomonosov Moscow State University and St. Petersburg State University" 10.11.2009 N 259-FZ.

The tradition that existed at the University from 1835 to 1918 was restored. Since 1 September 2016, in accordance with the Federal Law, St Petersburg University was granted the right to defend dissertations according to their own rules and to award their own academic degrees that are also recognised by the state. A year later, dissertations were defended for the first time in Russia to be awarded an academic degree from St Petersburg University.

Alumni of the University have been awarded Nobel Prizes in different areas:

1904 **Ivan Pavlov**, for the discoveries in physiology or medicine that led to benefit for humankind.

1908 **Ilya Mechnikov**, "for his works on immunity" (physiology or medicine).

1956 **Nikolay Semenov**, for developing the theory of chain reactions.

1962 **Lev Landau**, for his pioneering theories for condensed matter, especially liquid helium.

1964 **Alexander Prokhorov**, for fundamental work in the field of quantum electronics.

1973 **Wassily Leontief**, for the development of the input-output method and for its application to important economic problems.

1975 **Leonid Kantorovich**, for his contribution to the theory of optimal resource allocation (economics)

2023 **Alexey Ekimov**, for the discovery and research of quantum dots.

Initially the University consisted of 3 faculties: History and Philology, Philosophy and Law (later Law), Physics and Mathematics; in 1854 the Faculty of Oriental Languages was opened and in this form SPbSU existed until 1918.

Currently, the University has 16 faculties and 11 institutes, that is, 27 units which combine educational and scientific activity.

The Faculty of Physics was established by the order of the Rector of the Leningrad (in that time) State University No. 191 of April 14, 1933 on the basis of the Physics Department of the Faculty of Physics and Mathematics at the improvement (reorganization) of the faculty structure at the University. Currently, there are 17 Chairs at the Faculty of Physics.

In 1945, the Chair of Radiophysics was created at the University. The organizer and the first head of the Chair in 1946-1957 was Professor Leonid Myasnikov, who initiated research in the field of radiospectroscopy. In the 50s, these studies were headed by Fyodor Skripov (1921-1961). He stimulated works on magnetic resonance (NMR, EPR, and NQR) in condensed media.

Earlier the **organizers** of “Spinus” worked at the Chair of Quantum Magnetic Phenomena (QMPH), which was founded in 1993 on the initiative of Professor Vladimir Chizhik on the basis of the laboratory, created by F. I. Skripov at the Chair of Radiophysics (the branch “Quantum Radiophysics”). On January 1, 2014, the Chair of QMPH joined the united Chair of Nuclear-physics Research Methods (Head of the Chair is Corresponding Member of the Russian Academy of Sciences, Professor Mikhail Kovalchuk). The QMPH collective has a number of priority works in the field of nuclear magnetic resonance. One of the most significant achievements was the first in the world implementation (in 1958) of the Fourier transform of a free induction signal in order to obtain a NMR spectrum. Concurrently with the research activity, the QMPH collective is actively involved in the development of practical applications of magnetic resonance. The lecture will provide a brief overview of the traditional and new research directions of the QMPH team in the field of nuclear magnetic resonance: high-resolution NMR spectroscopy, NMR in solids and heterogeneous systems, NMR relaxation, NMR in the Earth's magnetic field and some others.

Gradually, the application of magnetic resonance methods was realized at other departments of the Physics Faculty (primarily at the Chair of Solid State Physics and the Chair of Molecular Spectroscopy) and at other faculties of SPbSU (Chemical and Geological), as well as in the new Laboratory of Biomolecular Nuclear Magnetic Resonance (formed in 2013 at SPbSU after the first competition for the organization of scientific laboratories under the guidance of leading scientists). The lecture is planned to reflect the main directions of scientific activity in this aspect.

Currently, 23 resource centers have been opened in the Science Park of SPbSU. They are united in groups according to the main directions of the SPbSU Development Program: “Nanotechnology and Materials Science”, “Biomedicine and Human Health”, “Ecology and Environmental Management”, “Information Systems and Technologies”.

The group “Nanotechnology and Materials Science” includes the Resource Center “Magnetic Resonance Research Methods”. The Resource Center “Magnetic Resonance Research Methods” is an interdepartmental and interdisciplinary laboratory that provides access to equipment, infrastructure and practical experience of its staff to perform and support research in all natural science fields and in fundamental and innovative projects using the capabilities of nuclear magnetic, nuclear quadrupole and electron paramagnetic resonance spectroscopy, as well as microtomography (7 modern spectrometers).

Spin-dependent phenomena in wide-gap materials and based nanostructures and development of the instrumentation for these studies

Roman Babunts

Ioffe Institute, St. Petersburg

E-mail: roman.babunts@mail.ioffe.ru

The series of high-frequency EPR/optically detected magnetic resonance (ODMR) spectrometers developed at the Ioffe Institute can operate in continuous and pulsed modes at wavelengths of 2 and 3 mm. We use a cryogenic-free magneto-optical system with a superconducting split-coil magnet that creates a horizontal magnetic field of up to 7 Tesla.

The basis of the spectrometer is a series of unified microwave bridges, operating in the W and D bands. The program controls the operation of the spectrometer and monitors all the basic parameters of the spectrometer around the clock. The spectrometers can operate in continuous and pulsed modes and have many features and original, patented solutions.

We have also created two similar spectrometers based on confocal AF microscopes from the NT-MDT company. One, for the visible range, uses a blue or green laser for excitation - for a study of NV centers in diamond. The second one operates in the near infrared range - for silicon carbide.

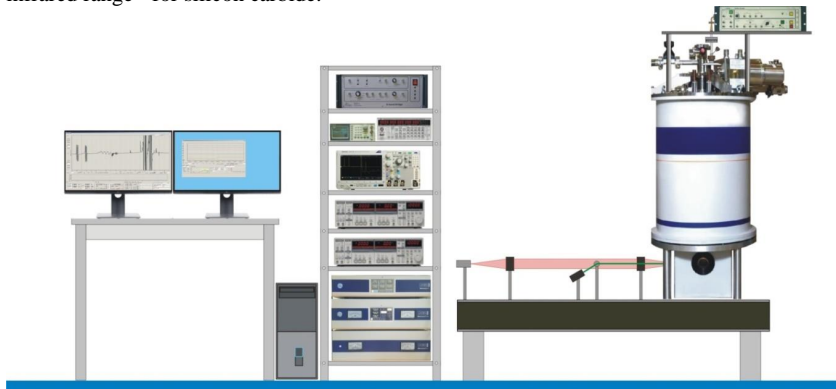


Figure 1. A line of high-frequency EPR/ODMR spectrometers operating at W and D bands

Application examples include the study of NV⁻ centers in diamond, vacancy centers in silicon carbide, 2D materials, and non-Cramer ions.

Acknowledgments

This study was supported by a grant from the Russian Science Foundation (project No. 23-12-00152), <https://rscf.ru/project/23-12-00152/>.

Liquid-liquid phase transition in metallic melts

Elena V. Charnaya, Denis Yu. Nefedov, Allisher A. Vasilev, Andrei V. Uskov

Faculty of Physics, St. Petersburg State University, St. Petersburg 198504 Russia

E-mail: e.charnaya@spbu.ru

Introduction

Structural transformations in liquids pose severe challenges to condensed matter physics. Conclusive theoretical and experimental evidences of a phase transition between different structures in liquids (liquid-liquid phase transition (LLPT)) were obtained for water and few other liquids. However, the nature of LLPT is poorly understood and even its occurrence in many substances is in doubt. It was suggested that LLPT at ambient pressure takes place under strong supercooling. Therefore, LLPT in bulk is disguised by crystallization or vitrification processes. In contrast, liquids confined to nanoporous matrices are easy to supercool to temperatures much lower than the melting temperatures. This raises expectations that LLPT can be found in liquids under nanoconfinement.

Generally, they tried to reveal LLPT using various experimental techniques. Among them, neutron scattering and x-ray diffraction provided the most convincing evidences due to their sensitivity to the short-range order. However, solidification often masks the alterations in neutron and x-ray patterns induced by LLPT.

Here we review our recent results on LLPT in metallic melts using NMR [1-3]. It should be emphasized that applications of NMR to LLPT were not reported until these studies. Up to now only one other publication was devoted to LLPT investigations by NMR [4], as far as we know.

Experimental

For metallic substances NMR acts as a powerful experimental technique, which gives valuable information about the structure of metallic liquids through measurements of the shift in the resonance frequency, the Knight shift, and the nuclear spin-lattice relaxation rate caused by coupling with conduction electrons. Moreover, NMR allows studying properties of metallic melts confined to nanoporous templates, in which liquid metals and alloys can be strongly supercooled much below their melting temperatures. The nanostructured Ga metal, ternary Ga-In-Sn and binary Ga-In alloys were obtained by embedding the melts into opal matrices, porous glasses and porous alumina under pressure up to 10 kbar in Ioffe Institute RAS.

Studies were carried out using NMR Bruker Avance 400, Avance 500, and Avance 750 pulse spectrometers within a broad temperature range. We observed the variations with temperature of the Knight shift, integral intensity of the NMR lines, and relaxation rate for the isotopes ^{69}Ga , ^{71}Ga , and ^{115}In in the melts. At each target temperature the samples were stabilized for about 20 min. The rate of changing temperature did not exceed 0.5 K/min to prevent the temperature overshoots. Note that at ambient conditions the confined gallium and gallium alloys were totally in the liquid state in agreement with their phase diagrams and the general reduction of the melting temperatures under nanoconfinement.

Results and discussion

At room and higher temperatures the NMR spectra for both gallium isotopes and indium in confined melts consisted of a single quite narrow Lorentzian line. Upon cooling and partial freezing the lines first moved to high frequency and then split into two signals at lower temperatures. Upon further cooling only one signal survived. Signals from solid gallium and gallium alloys were not observed because of strong broadening the NMR lines due to the Knight shift anisotropy and quadrupole coupling.

The evolution of the NMR spectra for the ^{71}Ga isotope observed at cooling from room temperature is illustrated in Fig. 1 for the Ga-In alloy under nanoconfinement.

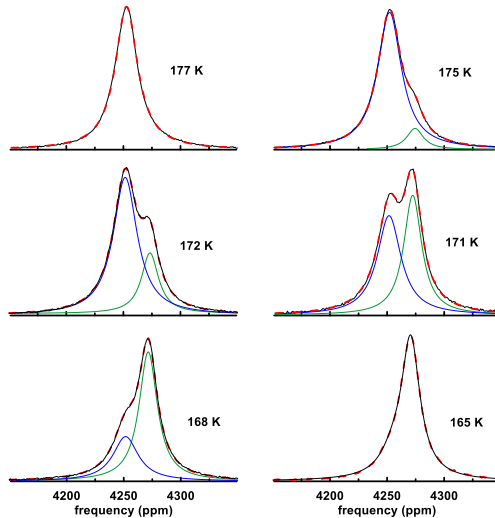


Figure 1. ^{71}Ga NMR lines in the binary Ga-In alloy confined to opal.

From the NMR spectra the Knight shift dependences on temperature were found. The emergence of a second ^{71}Ga NMR signals and the coexistence of two signals within some temperature ranges prove unambiguously the appearance of a new liquid state at supercooling and segregation of liquids into two parts.

NMR studies showed that LLPT is characterized by a large thermal hysteresis. The transition upon cooling is associated with the step-like change in the Knight shift which corresponds to the step-like changes in the structure of confined liquid. While at warming the phase transition is continuous in agreement with gradual changes in the Knight shift. This thermal asymmetry can arise in the case when the upper limit of the hysteresis loop coincides to the critical point of the boundary line between two liquid phases.

Acknowledgements

This work is supported by RSF (grant 21-72-20038). Part of measurements was carried out using the equipment of "Center for Diagnostics of Functional Materials for Medicine, Pharmacology and Nanoelectronics, SPbGU.

References

1. C. Tien, E. V. Charnaya, W. Wang, Y. A. Kumzerov, D. Michel. – *Phys. Rev. B*, 74, 024116 (2006).
2. D. Yu. Nefedov, E. V. Charnaya, A. V. Uskov, et al. – *Phys. Solid State*, 60, 2640-2644 (2018).
3. D. Y. Nefedov, D. Y. Podorozhkin, E. V. Charnaya, et al. – *J. Phys.: Condens. Matter*, 31, 255101 (2019).
4. W. Xu, M. T. Sandor, Y. Yu, et al. – *Nat. Commun.*, 6, 7696 (2015).

Qubit on magnon BEC state

Yury Bunkov

Laboratory of Quantum Magnonics, RQC, Moscow, 121205, Skolkovo, B. Boulevard 30
e-mail: y.bunkov@rqc.ru

The coherent quantum state of matter obtained in recent decades - the Bose-Einstein Condensate (BEC) - is a very promising state of aggregation, which, undoubtedly, should find its application in quantum technologies. Due to the possibility of excitation of magnons sufficiently high density, as well as their low effective mass it turned out to be possible to obtain quantum state of BEC magnons even at room temperature as was shown in [1].

In particular, in an Yttrium Iron Garnet (YIG) film magnetized perpendicular to the plane, the formation of MBEC was confirmed by direct optical detection. [2, 3]. Here we consider the formation of a real magnon BEC for magnons with wave vector $k=0$. Such an MBEC was first discovered 40 years ago in superfluid $^3\text{He-B}$ [4,5]. A signal of coherent precession of magnetization was obtained even in a highly inhomogeneous magnetic field. It is described by a single wave function, the frequency of which changes over time due to a decrease in the number of magnons and, accordingly, a change in the chemical potential. Fig. 1.

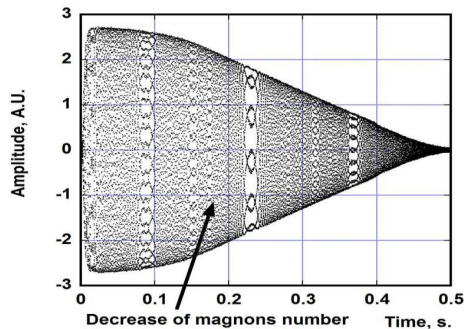


Fig.1 Stroboscopic recording of the induction signal of magnon BEC in $^3\text{He-B}$

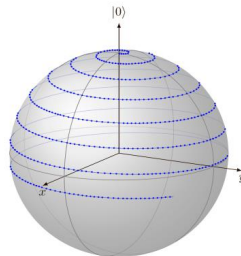


Fig.2. Evolution of a coherent BEC signal on a Bloch sphere

The evolution of this state can be represented on the Bloch sphere. Fig. 2. It is important to note that the amplitude of the signal corresponds to the number of magnons, that is, the number of spins in the excited state $|1\rangle$. Typically, a spin qubit consists of a single

spin. In the process of quantum computing, one-qubit and two-qubit operations are applied to them. The result of the calculations comes down to measuring the final state of qubit $|1\rangle$ or $|0\rangle$ for each qubit. A single calculation results in one of these states, and for the final result it is necessary to repeat the calculation procedure many times and obtain the probability value.

We propose to use the coherent state of magnons to instantly determine the probability of the formation of state $|1\rangle$ after undergoing single-qubit operations immediately with a macroscopic ensemble of spins. In other words, we propose to replace the process of determining the probability of formation of state $|1\rangle$ after a large number of repeated operations by measuring the probability of formation of state $|1\rangle$ on an ensemble of spins after a single calculation procedure.

Previously, the possibility of using a package of spin qubits for quantum operations was considered. The main problem was the interaction of spins and the spread of their frequencies (homogeneous and inhomogeneous line broadening). In addition, difficulties arose when independently reading the quantum states of qubits. As our experiments have shown, the magnon Bose condensate compensates for the inhomogeneous broadening. It also lacks spin-spin relaxation processes. Therefore, we have the opportunity to measure the density of magnons, that is, states $|1\rangle$ in a sample after performing single-qubit operations on an ensemble of spins. Naturally, the time of quantum operations should be less than the time of formation of the Bose condensate of the resulting magnons. To perform two-qubit operations, a signal amplifier can be used to interact Bose condensates in different samples.

We recently discovered a strong acoustic coupling between two Bose condensates formed in two YIG samples located on a single substrate [6]. We are currently investigating whether this coupling can be used for two-qubit operations.

Acknowledgements

This work is supported by Russian Science Foundation (grant # 22-12-00322).

References

1. Yu. M. Bunkov, V. L. Safonov, Journal M.M.M., 452, 30 (2018).
2. P. E. Petrov, G. A. Knyazev, A. N. Kuzmichev, P. M. Vetoshko, V. I. Belotelov, and Yu. M. Bunkov, *JETP Letters*, 119, 118 (2024).
3. G. A. Knyazev, A. N. Kuzmichev, P. E. Petrov, I. V. Savochkin, P. M. Vetoshko, V. I. Belotelov, and Yu.M.Bunkov, <https://doi.org/10.1364/opticaopen.24591147> (2023).
4. A. S. Borovik-Romanov, Yu. M. Bunkov, V. V. Dmitriev, and Yu. M. Mukharskii, *JETP Lett.* 40, 1033 (1984).
5. Yu.M. Bunkov and G.E. Volovik «Bose-Einstein condensation of magnons in superfluid ^3He » *J. of Low Temp. Phys.* 150, 135, (2008)
6. G. A. Knyazev, A. N. Kuzmichev, P. E. Petrov, P. M. Vetoshko, V. I. Belotelov and Yu. M. Bunkov, *JETP Letters*, 118, 603, (2023).

Systematic View on the Dynamics and Structure Analysis of Solids by Time-Domain

Leonid Grunin, Maria Ivanova, Ivan Kirilov

Resonance Systems, Yoshkar-Ola, Russia

E-mail: mobilenmr@hotmail.com

http://www.nmr-design.com

The lecture pretends to embrace all possible techniques for deriving structural and dynamics information of solids by a modern Time-Domain NMR relaxometer.

Besides talking about transverse and longitudinal relaxation, polarization transfer and multiple-quantum transitions, the new Second Moment Approximation theory will be reported. As the basic principle it is taken the assumption that any complex NMR spectral line can be characterized with the phantom Gaussian shape having similar value of the second moment M_2 .

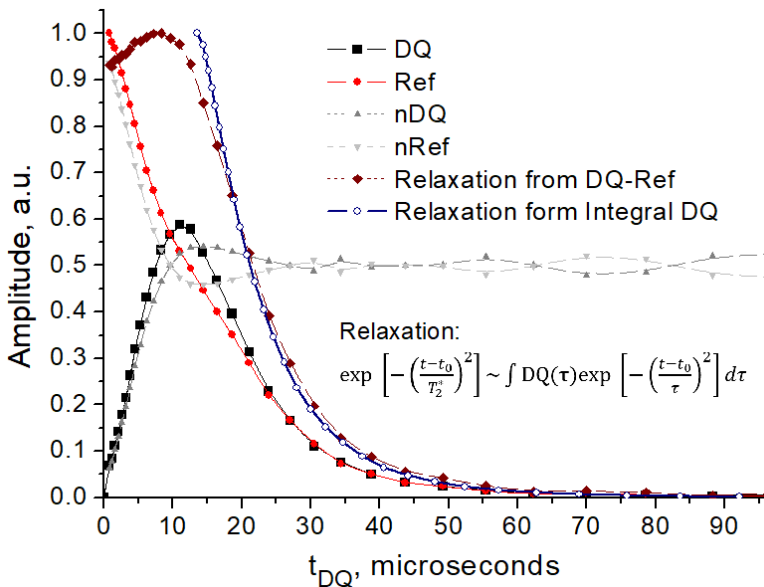


Fig.1. DQ-MQ experiment on an Ibuprofen sample the distribution of T_2^*

This M_2 is considered to introduce the effective relaxation time T_2^* which rather precisely follows BPP predictions and, in turn, can be used directly to estimate dynamics and structure of a sample.

$$T_2^* = \sqrt{2/M_2}$$

The Double-Quantum build-up curve, in this frame, represents the distribution of effective relaxation time, that in the most cases is logarithmically normal.

The ZHONGTAI 94 GHz pulsed EPR spectrometer

Dr. Lu Shuntian, PhD, EPR application engineer ZHONGTAI

Abstract

The design and performance of a W-band EPR spectrometer are presented. The spectrometer features continuous-wave (CW) and pulsed EPR experiments, including electron-nuclear double resonance (ENDOR) capacity. The instrument contains a microwave bridge, a hybrid magnet system, a TE₀₁₁ resonator with RF coil, a variable-temperature system as well as the control system and software. The magnet system consists of a 6 T horizontal split-coil superconducting magnet and a fast sweep coil with the range of ± 1000 Gauss. The magnet system is cooled by two cryocoolers. The frequency range is 93.5 – 94.5 GHz. The maximum microwave power is 50 mW at CW-EPR mode and 1 W at pulsed-EPR mode. A second microwave source for ELDOR experiment is equipped. In pulsed-EPR mode, the length of $\pi/2$ pulse is 12 ns at a resonator Q-value of 2000. The variable-temperature system is a continuous flow-type with a working range from 4 to 300 K.

Novel approaches in magnetic resonance imaging

Yury A. Pirogov

Faculty of Physics, Lomonosov Moscow State University, Russia

E-mail: yupi937@gmail.com

http://www.physics.msu.ru

Introduction

Magnetic resonance imaging (MRI) is an important method of medical diagnostics due to its high informativeness and safety of the study. MRI does not use harmful radiation, and the RF fields used in MRI to excite spins are low. This distinguishes the MRI method from other radiological methods, especially X-ray computed tomography (CT), which uses intense ionizing radiation and makes repeated application of the method difficult. We also note that the CT method only detects changes in the density of a substance; it is not very effective for analyzing soft tissues and, unlike MRI, is not capable of diagnosing the molecular structure and metabolic processes in the body. MRI is used not only in medicine, but also in other fields of science and technology. The method is based on the phenomenon of nuclear magnetic resonance (NMR) [1-5].

MRI as the unique visualization technique

This lecture is dedicated to the most promising modern directions of research in the field of magnetic resonance imaging. These include multinuclear studies, the use of new contrast agents that improve the quality of MRI images, electrodynamic elements that increase the signal-to-noise ratio, hyperpolarization techniques that allow increasing the sensitivity of MRI measurements by several orders of magnitude, MRI methods for registering pharmaceuticals introduced into the body. If we talk about multinuclear approaches in medical MRI diagnostics, then, first of all, it should be noted that all clinical MRI scanners operate with radio frequency tuning exclusively to the Larmor frequency of protons and cannot register signals from tissues with a low content of them, and even more so from tissues and injected into the body of pharmaceuticals that do not contain hydrogen atoms.

At the same time, knowledge of the content in the body of a number of such biomedically significant atoms as sodium-23, fluorine-19, carbon-13, deuterium, boron-11, phosphorus-31, etc. is of particular practical interest. Some of these atoms, for example, fluorine and deuterium, are practically absent in the body, but they are contained in pharmaceuticals for various purposes and their localization after injection should be established using MRI. An important application of fluorinated gases is the visualization of the internal structure of the lungs with their help and the study of gas exchange processes in the alveolar system of the respiratory tract [6].

Of particular interest is knowledge about the content and localization of sodium in the organs, the excess or lack of which in the body is the cause of blood pressure disorders, diabetic manifestations, renal failure, salt metabolism in the body, etc. [7,8]. The presence of phosphorus in the body is responsible for the bioenergetics of cells and phospholipid metabolism, the structural characteristics of cell membranes, the pH level in cells and the magnesium content [2]. MRI also provides a unique opportunity to determine the place and degree of neuronal excitation in response to the presentation of one or another stimulus - tactile, visual, sound, etc. and control the functional activity of the brain (fMRI method) [2].

Some words will be said about the magnetization transfer method of detecting defects in myelination of axons in the brain, leading to neurodegenerative disorders in the activity of the brain. Under normal conditions of medical diagnostics, MRI (especially on heavy, heavier than protons, nuclei) has a low sensitivity, the most effective way to increase it by several

orders of magnitude is nuclear hyperpolarization in a magnetic field. Hyperpolarized nuclei of gaseous helium-3 [9] or xenon-129 [10] are successfully used to visualize the lungs, which are poorly visible in MRI due to the low content of protons in the lung tissues. The use of xenon and helium is very effective, but due to the high cost of these gases, one has to look for them a replacement, for example, with cheaper krypton-83 [11].

Acknowledgements

Described investigations were carried out with the support of grants from the Russian Foundation for Basic Research No. 19-29-10015 and 20-52-10004, and the Interdisciplinary Scientific and Educational School of Moscow University “Photonics and Quantum Technologies. Digital Medicine” and with participation of my Russian colleagues Nikolay V. Anisimov, Mikhail V. Gulyaev, Olga S. Pavlova, Lev L. Gervits, Nataliya A. Semenova, Dmitry B. Lebedev, and foreign ones Galina E. Pavlovskaya (Great Britain), Vasily L. Yarnykh (USA), Anna V. Naumova (USA), Carlos Cabal Mirabal (Cuba).

References

1. Joseph P. Hornak. The Basics of MRI. - Interactive Learning Software, 2004. www.cis.rit.edu/htbooks/mri.
2. V. I. Chizhik. Quantum Radio Physics. Magnetic resonance and its applications (in Russian). - SPb State University Publ., SPb, 2009.
3. Yu. A. Pirogov, N. V. Anisimov, O. S. Pavlova, M. V. Gulyaev et al. Advances in magnetic resonance tomography // Magnetic Materials and Technologies for Medical Applications. Ed. A. Tishin, 1st issue, Elsevier, 107-152 (2022).
4. N. V. Anisimov, S. S. Batova, Yu. A. Pirogov. Contrast control in magnetic resonance imaging (in Russian) – MAKS Press Publ., Moscow, 2013.
5. M. A. Zubkov, A. E. Andreychenko, E. I. Kretov, and al. MRI in superhigh fields: new problems and novel possibilities (in Russian) - Uspekhi physicheskikh nauk, 189, No.12, 1293-1314 (2019).
6. O. S. Pavlova, N. V. Anisimov, M. V. Gulyaev, L. L. Gervits, Yu. A. Pirogov, V. Ya. Panchenko. 19F MRI of human lungs at 0.5 Tesla using octafluorocyclobutane // Magnetic Resonance in Medicine, 84, No.4, 2117-2123 (2020).
7. T. Henzler, S. Konstantin, G. Schmid-Bindert et al. Imaging of Tumor Viability in Lung Cancer: Initial Results Using ^{23}Na -MRI - Fortschritte auf dem Gebiete der Röntgenstrahlen und der Nuklearmedizin, 340-344 (2012).
8. Mark Bydder, W Zaaraoui, Ben Ridley, et al. Dynamic ^{23}Na MRI - A non-invasive window on neuroglial-vascular mechanisms underlying brain function - NeuroImage, 184, No.1, 771-780 (2019).
9. S. Fain, M. L. Schiebler, D. G. McCormack et al. Imaging of Lung Function Using Hyperpolarized Helium-3 Magnetic Resonance Imaging: Review of Current and Emerging Translational Methods and Applications - Journal of MRI, 32, No.6, 1398-1408 (2010).
10. K. Ruppert, H. Hamedani, F. Amzajerdian et al. Assessment of Pulmonary Gas Transport in Rabbits Using Hyperpolarized Xenon-129 Magnetic Resonance Imaging - Scientific reports, 8, 7310 (2018).
11. J. S. Six, Th. Hughes-Riley et al. Pulmonary MRI contrast using Surface Quadrupolar Relaxation (SQUARE) of hyperpolarized ^{83}Kr - Magnetic Resonance Imaging, 32, 48–53 (2014).

The effect of exchange narrowing of the electron paramagnetic resonance (EPR) spectra of dilute radical solutions indicates the formation of a Bose-Einstein condensate (BEC).

K.M. Salikhov

Zavoisky physical-technical institute of the Federal research center "Kazan scientific center of the Russian academy of sciences".

Address: Russia, Tatarstan, 420043 Kazan, Sibirsky trakt str. 10/7

It is shown that under conditions of exchange narrowing of the EPR spectra of dilute solutions of paramagnetic particles, conditions are created and Bose-Einstein condensation of quasiparticles can be realized. These quasiparticles are elementary excitations of collective modes of motion of spins of unpaired electrons of paramagnetic particles. These collective modes are formed due to the effect of the transfer of spin coherence from the collision partner (the "recoil effect") as a result of the Heisenberg exchange interaction between particles during random bimolecular collisions of particles. It is shown that elementary excitations (quasiparticles) associated with these collective modes are bosons. Thus, under the conditions of electron paramagnetic resonance spectroscopy experiments, a mixture of Bose quasiparticles is created. With an increase in the rate of spin coherence transfer, the spectrum collapses into a narrow homogeneously broadened Lorentzian line (the effect of an exchange narrowing of the spectrum), the microwave field pumps quasiparticles of only one of the collective modes. And this creates the prerequisites for the Bose-Einstein condensation of identical quasiparticles. The conclusions of this work can be extended to other mechanisms of paramagnetic relaxation as the so-called chemical exchange or any other mechanism of spectral diffusion. The statement follows from the fact that in all these cases, the kinetic equations for the partial magnetization of spins are linear equations of the same kind as the kinetic equations for paramagnetic relaxation caused by spin exchange for dilute solutions of paramagnetic particles.

The Bose-Einstein condensate (BEC) is the state of atoms at very low temperatures when a sufficiently large number of atoms are in the ground electronic state.

BEC is formed not only by atoms, but also by quasiparticles (collective excited states). Today, many examples of the formation of BEC quasiparticles are known, for example, magnons in magnetically ordered solids. The formation of BEC quasiparticles means that photons pump excited collective states in the system, which are all in the same quantum state. As a result, the coherence of the quasiparticle state is manifested in the system on a macroscopic scale.

To form a BEC, quasiparticles must satisfy several conditions:

- Quasiparticles must be bosons so that many identical quasiparticles can be in the same state.
- Quasiparticles must be sufficiently long-lived.
- There must be a sufficiently high concentration of quasiparticles so that the Bose gas of quasiparticles can turn into condensate.

In this work, it is shown that the formation of BEC of magnetic excited states can occur not only in magnetically ordered solids, but also in dilute solutions of paramagnetic particles.

Based on the modern paradigm of spin exchange in dilute solutions of paramagnetic particles [4-6], it is shown in this article that in the situation of exchange narrowing of the EPR spectrum, the above necessary conditions for the formation of BEC quasiparticles are fulfilled. The quasiparticles are the excited states of the collective modes of motion of the

partial magnetization of the spins of unpaired electrons of paramagnetic particles in a dilute solution. Electronic paramagnetic resonance (EPR) is used to pump these quasi-particles.

Where do quasiparticles with a coherent state of partial magnetization of electron spins in dilute solutions of paramagnetic particles come from?

Paramagnetic particles in the liquid diffuse rapidly. From time to time, pairs of particles randomly collide. In case of collisions, the exchange interaction is switched on. As a result of the collision, the states of electron spins of both colliding particles change. And at first glance, it is difficult to imagine that these random collisions can lead to any observable consistency, coherence, in the motion of the spins of different radicals. In this regard, it is possible to note the remark of A. Abragam in his book (see, pp. 277-278): "...one does not expect phase coherence to be introduced into a system through a coupling described by a random Hamiltonian". But it turns out it's possible!

Collective modes of motion are highlighted if we switch from a considering the motion of individual spins in the phase space of resonant frequencies to analyzing the motion of averaged partial magnetizations of sub-assemblies of spins with specified resonant frequencies. This transition in the description of the spin state is achieved using the methods of kinetic theory.

Under the exchange narrowing conditions, the prerequisites for the formation of a BEC are created.

Under exchange narrowing conditions, only long-living quasiparticles are excited.

These quasiparticles obey Bose-Einstein statistics, and there can be many identical quasiparticles in the system at the same time. And they, in principle, can form a BEC.

References

1. K.M. Salikhov. Current state of theory of spin exchange in dilute solutions of paramagnetic particles. New paradigm of spin exchange. *Physics Uspekhi*, 189, 1017-1043 (2019),
2. K.M. Salikhov. Fundamentals of spin exchange. Story of a paradigm shift. Springer (2019)
3. B.L. Bales, M. Peric, I. Dagutan, M.K. Bowman, M.M. Bakirov, R.N. Schwartz. Experimental Observation of a Peculiar Effect in Saturated Electron Paramagnetic Resonance Spectra Undergoing Spin Exchange. *Magnetic Polariton? J. Phys. Chem. Letters* 13, 10952-1057 (2022)
4. K. M. Salikhov, M. M. Bakirov, R. B. Zaripov and I. T. Khairutdinov. Experimental confirmation of the formation of a spin polariton in dilute solutions of paramagnetic particles. *Phys.Chem. Chem.Phys.* 25, 17966 (2023)
5. B.L. Bales, M. Peric, R.N. Schwartz. Experimental Observation of a Peculiar Effect in Electron Paramagnetic Resonance Spectra for Nitroxides Undergoing Fast Spin Exchange: Emission. *J. Phys. Chem. Letters* (2024)

Nanoconfined water in zeolites with hierarchical porosity probed by ^1H NMR

M.G. Shelyapina

Saint Petersburg State University, 7/9 Universitetskaya nab., Saint Petersburg 199034, Russia
E-mail: marina.shelyapina@spbu.ru

The effects of confinement in porous media, which are experienced by adsorbed water molecules, lead to significant deviations from volumetric diffusion. Under conditions of limited geometry, the adsorbed molecules can also interact with the inner surface of the porous matrix. Competition between the interactions of surface molecules with each other and with the surface can lead to the appearance of new elements of the water structure. Mesoporous silicon dioxide or zeolites [1] are impressive examples of the effect of nanoconfinement in pores on the structure and behavior of water.

Proton nuclear magnetic resonance (NMR) is a unique tool for studying both the structure and dynamics of water. Since the proton chemical shift is sensitive to the structure and bonding of water molecules, it can be used to study the local environment.

In turn, the main problems responsible for NMR relaxation in water are fluctuations in the strength of the proton-proton dipole coupling. Since these interactions depend on the relative position of the interacting nuclear spins, they change as a result of motion processes. This allows the use of proton relaxation to study the dynamics of water. The temperature dependences of the spin-lattice relaxation rates of protons, in addition to providing information about the motion parameters of water molecules (activation energies and correlation time values), reflect the phase that closed water undergoes with temperature [2]. In particular, the spin-lattice relaxation rate of protons and the low-temperature transition point of conformed water in mesoporous materials linearly correlate with the inverse pore radius in these materials [3-4].

In this lecture we provide a brief overview of our results of proton NMR studies of the dynamics of water molecules enclosed in microporous and micro/mesoporous zeolites with different topologies. The influence of the order of secondary porosity on the water dynamics is discussed.

Acknowledgements

This work was supported by the Russian Science Foundation (grant No 23-23-00448).

References

1. E.W.Hansen, R. Schmidt, M. Sticker, D. Akporiaye. – J. Chem. Phys. 99, 4148 (1995).
2. M.G. Shelyapina, D.Y. Nefedov, A.O. Antonenko, G.A. Valkovskiy, R.I. Yocupicio-Gaxiola, V. Petranovskii. – Int. J. Mol. Sci. 24, 15898 (2023).
3. D. Akporiaye, E.W. Hamen, R. Schmidt, W. Stiicker. – J. Phys. Chem. 84, 1926 (1994).
4. K. Overloop, L. Van Gerven. – J. Magn. Reson. Ser. A 101, 179 (1993).

Why biopolymers fold in glycerol-water mixture: NMR study of diffusion in glycerol-water mixture

Janez Stepišnik

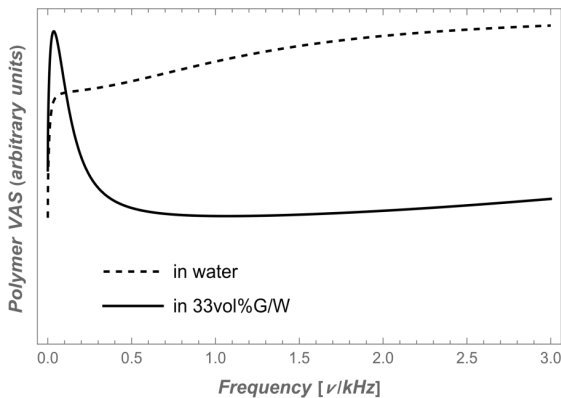
¹Faculty of mathematics and physics, University of Ljubljana, Slovenia,

E-mail: janez.stepisnik@fmf.uni-lj.si

<https://users.fmf.uni-lj.si/stepisnik/index.html>

Abstract

Velocity correlation spectra in binary mixtures of water and glycerol obtained by the use of measurement with the modulated gradient spin echo NMR method, were explained by the interactions of water molecules with clusters formed around the hydrophilic glycerol molecule, which drastically changes the molecular dynamics and rheology of the mixture. It indicates a thickening of the shear viscosity, which could affect the dynamics of submerged macromolecules. The calculation of the polymer dynamics with the Langevin equations according to the Rouse model, where the friction was replaced by the memory function of the retarded friction, gave the dependence of the polymer dynamics on the rate of shear viscous properties of the solvent. The obtained formula enables to calculate the segmental velocity correlation spectrum of the polymer when immersed in pure water and in a mixture of water with 33 vol% glycerol, taking into account the inverse proportionality between the solvent velocity correlation spectrum and friction as shown on the picture. The spectrum indicates a strong inhibition of the fast segmental motions in the glycerol-water mixture, which could create the conditions for slow processes caused by the internal interaction between the polymer segments, such as interactions that lead to the spontaneous folding of disordered polypeptides into biologically active protein molecules are immersed in such a solvent.



Polymer velocity autocorrelation spectra in water and G/W mixture

Clean Sequences for Complete Eradication of Unwanted Evolution and Accurate Determination of Spectral Parameters

Sandeep Kumar Mishra¹, Bikash Baishya² and N. Suryaprakash^{3}*

1Department of Physics and NMR Research Centre, Indian Institute of Science Education and Research, Pune 411008, India

2Centre of Biomedical Research (Formerly Centre of Biomedical Magnetic Resonance), SGPGIMS Campus, Raebareli Road, Lucknow 226014, India

3Solid State and Structural Chemistry Unit, Indian Institute of Science, Bangalore 560012, India

Tel: +91 9845124802; +9180 23607344; Fax: +9180 23601550

Novel techniques have been designed for the simplification of NMR spectral complexity, enhancing the sensitivity of detection, unravelling of the spectral overlap and the facile extraction of spectral parameters. The clean sequences also result in the prevention of the evolution of unwanted couplings, eradication of axial peaks, in addition to enhancing the spectral resolution.

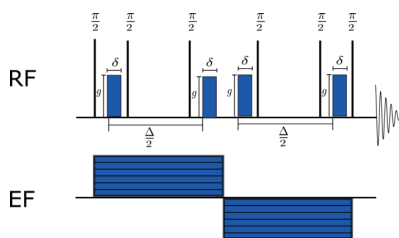
Electrophoretic NMR and applications

Pavel Yushmanov

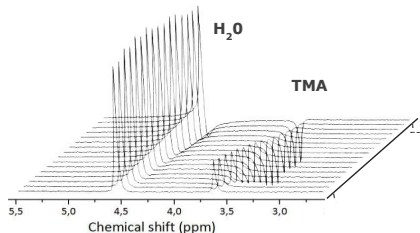
P&L Scientific, Stockholm, Sweden

E-mail: pavel@plscientific.se

Electrophoretic NMR (eNMR), having been introduced more than 30 years ago, is a useful yet not very widespread methodology. It is based upon applying a voltage and thereby an electric field across the sample volume. When done so, ionic species are set into motion that can be detected by experiments exploiting pulses of magnetic field gradients that are parallel to the direction of the applied electric field. Hence, pulse sequences of eNMR experiments are often similar to those of diffusion NMR experiments with the major differences being (i) the need for electric field pulses and (ii) the information in the form of electrophoretic mobilities μ extracted from the signal phase instead of signal attenuation[1,2].



Electrophoretic NMR (eNMR) pulse sequence is based on pulsed field gradients, akin to diffusion NMR



Resulting series of spectra for TMA in D_2O solvent

eNMR is a desirable methodology for determining μ because of the unparalleled chemical selectivity of the detection method NMR. Also, based on the results of the e-NMR experiment, one can determine the electrophoretic mobility of particles, their charge, and belonging (association with other particles, etc.). A wide range of materials studied - electrolytes, gels, ionic liquids, and all kinds of ionic solutions - determines the great practical importance of this method.

Possible applications include:

- optimization of electrolyte parameters for modern batteries, in particular, those based on ionic liquids and gels
- determination of the structure of substances, in particular, complex ionic solutions
- determination of properties and search for hidden phase transitions of process fluids
- study of biomolecules and their association
- study of the structure of supramolecular complexes according to the degree of their charge
- study of proton conductivity in Nafion membranes
- study of solid electrolytes

Thus, the e-NMR method is of great importance for the following applications [2]:

- Fundamental and applied research in the field of physical, organometallic, and analytical chemistry, as well as biotechnology
- The pharmaceutical industry and applied research of properties and materials

- Development of battery and fuel cell technology
- Studying the properties of various process fluids used as cleaning, lubricants, etc.

While the capability of applying field-gradient pulses is commonplace in modern NMR spectrometers, applying electric field pulses requires additional instrumentation that is commercially less widespread. The additional instrumentation encompasses both suitable power supplies providing the electric field pulses and probe arrangements that enable the electric field to be applied over the chosen sample volume.

Our company has developed the complete set of eNMR equipment that is presently distributed worldwide in various NMR research laboratories and research centers [3].



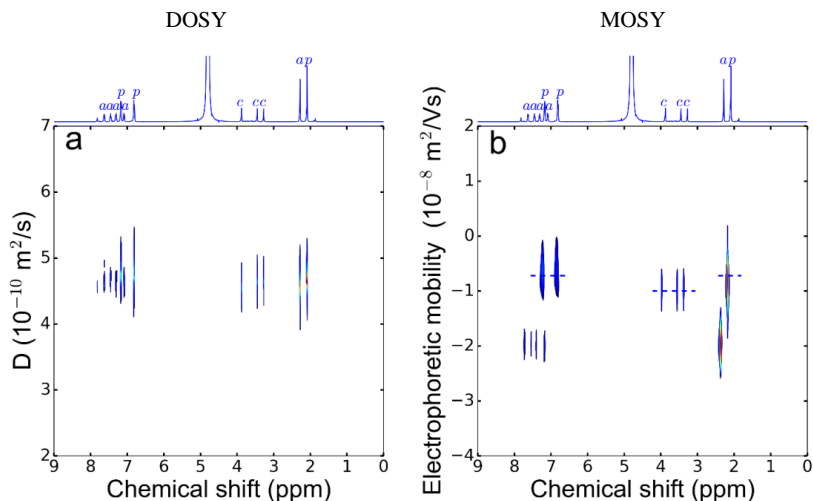
The complete set of eNMR equipment including Bruker NMR spectrometer and magnet

However, even when the required instrumentation is at hand, eNMR suffers from some limitations that, so far, severely restrict eNMR experiments in terms of permissible samples and phenomena. Various forms of motional artifacts constitute the most important limitations. In very conductive samples, the electric field, while setting the ions into motion, also generates an electric current that leads to Joule heating and, typically, to a temperature gradient that in turn results in thermal convection [5,6]. This constitutes the first motional artifact. The second artifact is electroosmosis which appears in a manner that is strongly dependent on the sample, and the material and dimensions of the sample container [4]. The third major artifact is the electrode reactions that also produce gases and yield bubbles that may detach from the electrodes and travel through the signal-yielding volume.

Various solutions were developed to diminish those artifacts. Among others, those are:

- Coating the sample tube with the slightly conductive media to reduce electroosmosis [5]
- Using the Carr-Parcell version of eNMR pulse sequence [4]
- Well-symmetric construction of eNMR cell [2]
- Installation of the porous plug in the bottom of the eNMR sample and performing the experiment in current stabilization mode [1]

As a result, the achieved values of the recorded phase shifts may allow the so-called 2D electrophoretic mobility ordered spectroscopy (2D-MOSY) where the resulting 2D spectra are provided by Fourier transform in the F1 direction. For certain samples, this approach is beneficial vs. DOSY providing a better selection of the components in the F1 axis[7].



2D-MOSY vs. 2D-DOSY analysis of components of Thomapyrin medical substance

References

1. Yuan Fang, Pavel V. Yushmanov, István Furó, Improved accuracy and precision in electrophoretic NMR experiments. Current control and sample cell design. *Journal of Magnetic Resonance* 318 (2020) 106796
2. P. Stilbs, *Diffusion and electrophoretic NMR*, De Gruyter, Berlin, Boston, 2019.
3. <http://plscientific.se/?eNMR/References-and-selected-literature>
4. M. Bielejewski, M. Giesecke, I. Furó, On electrophoretic NMR. Exploring high conductivity samples, *J. Magn. Reson.* 243 (2014) 17–24.
5. F. Hallberg, I. Furó, P.V. Yushmanov, P. Stilbs, Sensitive and robust electrophoretic NMR: instrumentation and experiments, *J. Magn. Reson.* 192 (2008) 69–77.
6. E. Pettersson, I. Furó, P. Stilbs, On experimental aspects of electrophoretic NMR, *Concepts Magn. Reson., Part A* 22A (2004) 61–68.
7. Y. Fang, P. V. Yushmanov, and I. Furó, Assessing 2D electrophoretic mobility spectroscopy (2D MOSY) for analytical applications, *Magn. Reson. Chem.* 55 DOI: 10.1002/mrc.4558 (2017).



Element

official distributor



ZHONGTAI

The company "ELEMENT" officially presents in Russia devices manufactured ZHONGTAI (China). ZHONGTAI specializes in research and developments in the field of magnetic resonance, quantum precision measurements, quantum computing, scanning electron microscopy, etc.

Fields of application of the developed devices: creation of promising materials, semiconductors, quantum science, life sciences, medicine, clinical research and more. We present you a line of electron spectrometers paramagnetic resonance, which includes four devices:



ZT6500

Desktop EPR spectrometer



ZT15C

Research Grade Floor Standing
EPR Spectrometer



ZT15P

Research Grade Pulsed
EPR Spectrometer



ZT60W

High Frequency EPR Spectrometer



More information on our website element-msc.ru



Element

official distributor



ZHONGTAI

Quantum Diamond Atomic Force Microscope



Quantum Diamond Atomic Force Microscope (QDAFM) is a magnetic imaging instrument based on both NV center in diamond and AFM scanning imaging technology. By quantum control and readout of the spin state in the diamond probe, the magnetic property of samples is acquired quantitatively and non-invasively. With nanoscale spatial resolution and ultra-high detection sensitivity, QDAFM is an innovative technology to develop and study magnetic textures, high-density magnetic storage, and spintronics.

QDAFM has extensive applications in material science, biology, physics and so on.

element-msc.ru

Moscow
(495) 514-00-47
msc@element-msc.ru

Ekaterinburg
(343) 278-34-64 (-65-69)
ekb@element-msc.ru

Novosibirsk
(383) 21-12-726
nsk@element-msc.ru

Oral Reports

Assessment of blood serum dynamic viscosity by NMR in sickle cell disease

Alonso Geli, Yamirka^{1}; García Cruz, Claudia C.¹; Cruz Vadell, Haydee²; Torres-Martínez, Leisbelys R.¹; Delgado Tamayo, Fabian¹; Somoano Delgado, Lilian M.¹; Suarez Beyries, Lidia C.³; Araujo Duran, Yomaidis³; Lores Guevara, Manuel A.¹*

¹ Centro de Biofísica Médica, Patricio Lumumba 507, Altos de Quintero, Santiago de Cuba, Cuba

² Laboratory of Biomedical Basic Science, Universidad de Ciencias Médicas, Santiago de Cuba, Cuba

³ Hospital General Docente "Dr. Juan Bruno Zayas Alfonso", Santiago de Cuba, Cuba.

E-mail: yamirka.alonso@uo.edu.cu

Introduction

The increase in blood viscosity can predict some clinical manifestations in diseases characterized by significant vascular dysfunction. The clinical utility of viscosity measurements in risk factor analysis requires reference values established from a healthy, disease-free population and a steady-state patient population. Particularly, the determination of the blood serum dynamic viscosity (η_s) is very important for the clinical assessment of patients suffering medical condition in one of these three categories as follows: pleocytosis, in which there is an excess number of blood formed elements, such as polycythemia vera and leukemia; sieric, in which there is an abnormality of plasma proteins such as myeloma, Waldenström's macroglobulinemia, and cryoglobulinemia; and sclerocitic, in which there is an abnormality in the deformability of red cells, such as sickle cell disease (SCD) [1, 2]. Lores *et al.* developed several methods to determine dynamic viscosity in protein solution, by proton magnetic relaxation, and developed the physical model used to explain the relation between of the transverse proton magnetic relaxation rate ($1/T_2$) and η [3, 4, 5]. These methods to determine η based on Magnetic Resonance have advantages over traditional methods, since last ones, have a limited clinical application, because of the sample volume needed, the necessity of to wash the viscometer to be used in different patients and the additional determinations required to convert the kinematic viscosity in absolute dynamic viscosity [6, 7]. These methods based on nuclear magnetic relaxation significantly reduce the needed sample volume, allow directly obtain the value of η without additional experimental procedures, and avoids the viscometer washing between determinations.

From theoretical relation between $1/T_2$ and water translational diffusion coefficient is possible to obtain η_s . In this work we assess of blood serum dynamic viscosity by NMR in healthy disease-free individuals and SCD patients in steady state.

Materials and Methods

Blood serum samples were obtained from venous whole blood of healthy disease-free individuals and SCD disease patients in steady state. 60 healthy individuals were randomized selected from blood donors in Blood Bank «Renato Guitart» in Santiago de Cuba and 64 SCD patients were selected in Hematologic service of the «Juan Bruno Zayas Alfonso» general hospital of Santiago de Cuba. All the ethical rules included in the Helsinki convention of the World Medical Association for research with human beings were accomplished (1964, updated until 2013).

Whole blood is collected in dry tubes and allowed to stand for 10 minutes at 37°C; then centrifuged at 3000 rpm for 10 minutes and supernatant decanting [1]. Samples were frozen at -80°C until use.

For the measurement of transverse proton magnetic relaxation time (T_2) was used a LapNMR magnetic resonance console (Tecmag, Houston, USA) coupled to a magnet ($B_0 = 0.095$ T,

$\nu_0 = 4.03 \text{ MHz}$) and the Carr-Purcell-Meiboom-Gill (CPMG) pulse sequence (90° and 180° radio frequency pulses of 6 and 12 μ respectively, 15000 echoes and echo time (TE) of 1600 μ s). η_S was calculated from T_2 according to the previously reported linear regression [8]. For blood serum samples were plotted experimental values of the transverse proton magnetic relaxation rate ($1/T_2$) as a function of the η_S values determined by Ostwald viscometer at 20°C , and was observed a linear behavior represented for the following equation:

$$\frac{1}{T_{2e}} = 0.003\eta_S - 0.0019 \quad (1)$$

All the experiments were performed at 20°C and η_S were reported in mPa s, according with the clinical practice [9, 10].

To compare mean values a student test (t-test) was used with $\alpha=0.05$. The Shapiro-Wilk test was used to test the normality of the data, and F-test for equality of variances-test.

Results and Discussion

T_2 values were determined in blood serum samples from 60 healthy and disease-free individuals and 64 SCD patients under steady state; η_S was calculated by interpolation from the linear regression previously presented for the relationship of the experimental values of the transverse proton magnetic relaxation rate ($1/T_2$) as a function of the values of η_S determined by the Ostwald viscometer at 20°C . Ошибка! Закладка не определена. This relation is described by equation 1.

Since we wanted to compare the means using the t student test, determining the distribution of η_S was important to verify the assumptions of the parametric tests about our data. A Shapiro-Wilk test was performed to test the normality of data. For both samples (healthy disease-free individual and SCD patients under steady state), Shapiro-Wilk test did not show a significant departure from normality for 0.05 significance level; p-value $> \alpha$, therefore, the H_0 is not rejected and it is assumed that the data is normally distributed, potentially symmetric and mesokurtic (Table 1). Also, F-Test to test equality of variances shows there is a significant difference between healthy group ($SD_1 = 0.2$) and SCD (Steady state) group ($SD_2 = 0.09$), $F(63,59) = 2.7$, p-value < 0.001 . Due the p-value $< \alpha$, H_0 is rejected and the difference between groups variance ratios is statistically significant.

Table 1. Skewness, kurtosis, and normality tests for mean η_S (mPa s).

Samples	Skewness		Kurtosis		Normality	
	Z	p-value	Z	p-value	W	p-value
Healthy disease-free individuals N=60	-0.0819	0.791	0.439	0.471	0.98	0.453
SCD patients (Steady state) N=64	-0.0319	0.915	0.976	0.098	0.98	0.426

The Student's t test was used to compare the η_S means between our results in frozen/thawed serum and fresh serum results obtained by Mengana *et al.* Ошибка! Закладка не определена. η_S values in frozen/thawed serum for healthy individuals do not statistically match with those obtained in fresh serum by Mengana *et al.* (Table 2) in healthy individuals under the same experimental conditions, except for the additional step of freezing the sample before use. The mean of our data set is significantly different from $\mu_0=1.29 \text{ mPa s}$ at 0.05 significance level.

Table 2. Student's T test comparison of η_S means between frozen/thawed and fresh serum 0.05 significance level.

Samples	n	η_S (mPa s)	t	p-value
Healthy disease-free individuals (fresh serum)	20	1.29±0.07	-14.4905	0.037*
Healthy disease-free individuals	60	1.12±0.02		

(frozen/thawed serum)				
-----------------------	--	--	--	--

* Statistically significant differences

Some studies have showed several blood serum metabolites such as aminotransferases, glucose, cholesterol, triglycerides, high density lipoprotein (HDL) are stable during and after frozen, but others metabolites change significantly, for example, blood urea nitrogen, uric acid, total protein, albumin [11, 12]. Other studies found changes in cord blood serum metabolites after slow freezing and subsequent thawing, indicating protein conformational changes. For retaining the properties of blood serum proteins it is necessary to freeze at high rate (not less than 100°C/min) and store the sample at -80°C or lower temperature [13].

η_s values of frozen/thawed serum are lower than fresh serum by 15%. Although this difference was statistically significant, it may not be physiologically relevant. Hence, serum may be used for η_s determination, because we are interested in characterize this kind of sample.

The Table 2 summarize the values of η_s obtained in of healthy disease-free individuals and SCD disease patients in steady state.

Table 3. T_2 and η_s values from healthy disease-free individuals and SCD disease patients under steady state. Values are showed as mean \pm standard error of mean (SEM)

Samples	n	T2 (s)	η_s (mPa s)
Healthy disease-free individuals	60	0.41 \pm 0.01	1.12 \pm 0.02
SCD patients (Steady state)	64	0.38 \pm 0.01	1.22 \pm 0.04

According to Student's t test, η_s is significantly higher in SCD patients than in healthy individuals. The p-value < 0.0001 and this difference is considered to be extremely statistically significant (t=4.1795, p-value= 0.00006053). The differences between η_s values of healthy and sick subjects may be due to differences in main plasma proteins, mainly fibrinogen, which is the main determinant of blood viscosity [14] due to its elongated shape and the influence of shape on viscosity [3]. It was found that fibrinogen concentrations and viscosity were higher in SCD patients at steady state and during pain crisis than in healthy subjects [15]. In some specific cases, residual fibrinogen and its fractionated products can be found in the blood serum, for example in cases of prolonged venous occlusion [16], as may occur in sickle cell anemia, due to accumulated damage as a result of repeated oxygenation-deoxygenation and polymerization-depolymerization cycles.

To sum up, the presence of fibrinogen in the serum of SCD patients may be due to (1) residual fibrinogen due to the high starting concentration in the plasma, and (2) residual fibrinogen and fibrinogen fractionated products due to prolonged venous occlusion.

Acknowledgements

This work was supported by the Belgian Development Cooperation through VLIR-UOS, MRI Centre of the University of New Brunswick in Canada and Project Program "Productos y Servicios de Salud" of Cuban Ministry of Science, Technology and Environment of Cuba in Santiago de Cuba.

References

- Reeves, J. H. (2009). CHAPTER 277 - Plasmapheresis in Critical Illness. In C. Ronco, R. Bellomo, J. A. Kellum (Eds.), Critical Care Nephrology (2nd Edition) (pp. 1519-1524). Philadelphia: W.B. Saunders.
- Stone, Marvin J. (2009). Clinical Lymphoma and Myeloma, 9(1), 97–99.
- Lores, MA., Mengana, Y., García, JC., Rodríguez, N., Suárez, LC., ... Phillippé. (2018). Appl. Magn. Reson., 49, 1075-83.
- Mengana, Y., Lores, MA., García, JC., Ricardo, BT., Suárez, LC.,... Araujo, Y. (2019). Int J Biochem Biophysics Mol Bio, 4, 25-30.
- Mengana, Y., Lores, MA., Ferrer, H., Suarez, LC., Rosales, SJ.,... Alonso, Y. (2024). Appl. Magn. Reson. (in press).

6. Hong, R., Cima, MJ., Weissleder, R., Josephson, L. (2008). *Magnetic Resonance in Medicine*, 59(3), 515-520.
7. Lores, M.; Cabal, C.; Nascimento, O.; Gennaro A.M. (2006). *Appl. Magn. Reson* 30(1), 121–128.
8. Tuck MK, Chan DW, Chia D, Godwin AK, Grizle WE., . . . Brenner DE. (2009). *J. proteome res.*, 8(1), 113-7.
9. Javadi, E., & Jamali, S. (2021). *Soft matter*, 17(37), 8446-8458.
10. Yamamoto, H., Yabuta, T., Negi, Y., Horikawa, D., Kawamura, K., Tamura. (2020). *Heliyon*, 6(9): e04792.
11. Cuhadar, S., Koseoglu, M., Atay, A., & Dirican, A. (2013). *Biochemia medica*, 23(1), 70-77.
12. Abraham,A., Rana, G., Agrawal, PK., Johnston, R., Sarna, A., ., . . . Kurundkar, S. B. (2021). *J. Lab. Physicians*, 13(01), 006-013.
13. Nardid, E., Rozanova, E., Tsymbal, L., Zinchenko, A., Nardid, O., Grishcheko, V. (2009). *Biophysics*, 54, 621-25.
14. Toros Xavier, H., Castellanos, R., & Fernández-Britto, J. E. (2005). *Rev. Cub.Invest.Biomed.* 24(3), 0-0.
15. Nasimuzzaman M, Malik P. (2019). *Blood Adv.*, 22;3 (20):3170-80.
16. Merskey, C., Kleiner, G. J., & Johnson, A. J. (1966). *Blood*, 28(1), 1-18.

Visualization of the internal structure of coils used in MRI studies

Nikolay V. Anisimov¹, Arina A. Tarasova², Lev L. Gervits³

¹*Faculty of Fundamental Medicine, Lomonosov Moscow State University, 119991, Russia*

²*Faculty of Physics, Lomonosov Moscow State University, 119991, Moscow, Russia*

³*Nesmeyanov Institute of Organoelement Compounds of the Russian Academy of Sciences, Moscow, Russia*

E-mail: anisimovmv@mail.ru

Introduction/Purpose

In addition to medical diagnostics, MRI is also used for technological purposes. In particular, for visualizing inanimate objects, including those from which it is impossible to directly obtain an NMR signal. For this purpose, ¹H and ¹⁹F MRI methods can be used [1]. In this work, we show how these non-invasive and non-destructive techniques can be used to visualize scanner electronics. In particular, for visualizing the internal contents of coils that are used as NMR probes and/or transmitting antennas. This is relevant if there is insufficient information about the location of conductors, the placement of electronic components and fasteners inside the coil body, and the design of the coil body does not allow visual inspection of its internal parts or access to them, for example, by dismantling the facing elements.

The simplest way to visualize the coil's contents is to perform a proton scan. In this case, the signal can be received from the case and fastening elements, since they are usually made of hydrogen-containing materials - plastic or textolite. This is possible if their relaxation times are acceptable for recording an NMR signal, in particular T2, and are not too short. If the excitation and/or reception of the NMR signal is carried out by the same coil under study, then the distribution of conductors can also be identified - the intensity of the signal from hydrogen-containing materials depends on the distance to the conductor from which the radio frequency field is generated and/or in which the NMR signal is induced - the closer to the conductor, the higher the signal. Typically, the range of materials used in an MRI coil for mounting and coating is not very diverse. The combination of these materials can be considered as an imaging medium, and a significant increase in the signal in some zone of this medium can be associated with the presence in this zone of a conductor involved in transmitting radio frequency power and/or receiving the signal.

This method of detecting conductors works well if the signal from the imaging medium is strong enough and the media itself is evenly distributed, at least in the vicinity of the conductors. Otherwise, the distribution of conductors on the MR image will be fragmented and therefore difficult to interpret.

To overcome these limitations, we use fluoride liquid as the imaging medium. We immerse the coil under study in a container with so-called "dry water" – CF₃CF₂C(O)CF(CF₃) [2] and carry out an MR scan with detection of signals from fluorine (¹⁹F) nuclei.

The specified liquid is a commercial product of the "3M" company called Novek-1230. Its boiling point is 49.2 °C. This fluid has fills the space inside the body of the coil used in MRI studies, including the conductors and other structural elements. This liquid gives a strong NMR signal - its spin density for fluorine nuclei is only 2 times less than for protons in ordinary water. At the same time, the relaxation times of dry and ordinary water are comparable. But the proton spectrum of ordinary water is singlet, and the fluorine spectrum of dry water is represented by 4 groups of lines with different chemical shifts in the range of 100 ppm. Therefore, with MR scanning, the detection of fluoride nuclei from dry water requires a wider receiver bandwidth than when registering protons from ordinary water, with a corresponding decrease in sensitivity.

As a visualization medium, ordinary water can only be used for a limited range of objects - sinks, glass and plastic products. But for a number of objects - food, paper products, etc. - this is unacceptable - after being in it they undergo irreversible changes. Ordinary water is also unacceptable for visualizing coils - it has conductivity, which distorts the current distribution map - in addition to the conductors, additional conducting channels appear. When using dry water, such problems do not arise - it has very low conductivity and moderate dielectric constant - $\epsilon = 2.3$, while ordinary water has $\epsilon = 80$. For these reasons, dry water does not interfere with the operation of electronics, and the frequency tuning of the coil has little effect on its presence or absence.

Materials and Methods

Experiments were conducted on 0.5T clinical scanner Bruker Tomikon S50. For ^{19}F MRI, proprietary coils were used. The scanned coils were immersed in a 12-liter container of dry water. At the same time, they themselves detected the MR signal. We used a 3D GRE sequence with parameters: $\text{TR}/\text{TE}=47/3.5$ ms, $\text{FA}=15^\circ$. Data processing, including 3D reconstruction and sensitivity map construction, was carried out using proprietary software – XWinNMR v.1 and ParaVision v.1, as well as the ImageJ v.1.48 program.

Results

We obtained ^{19}F MR images of a number of coils, including dual-channel quadrature coils. The resulting material was used to construct volumetric reconstructions and sensitivity maps. Figure 1 shows an ^{19}F MRI of a coil used to examine the knee joint. This is a saddle type quadrature coil. Panel B shows its simplified electrical circuit. Panel C shows one of the coronal slices passing through the geometric center of the coil. Based on the signal intensity distribution in this image, a 2D sensitivity map can be constructed. Panel D shows 1D signal plots for mutually perpendicular X and Y directions. The latter are of interest for zones not near conductors, but, on the contrary, at a distance from them - where the distribution of the NMR signal is most uniform. This is where the object examined by MRI is located.

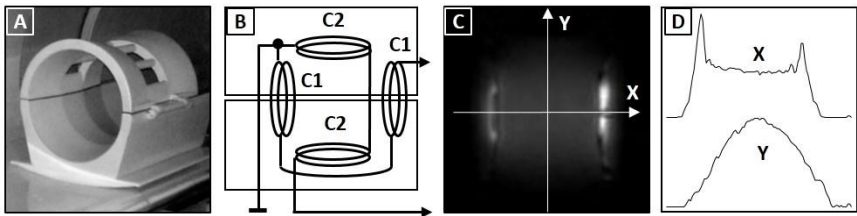


Figure 1 A - photograph of the coil under study; B - its electrical diagram: two pairs of coils C1 and C2, oriented mutually perpendicular, are indicated; C - ^{19}F MRI of one of the coronal slices. The lines X and Y are indicated, along which the signal graphs presented in panel D are constructed

Figure 4 shows reconstructions using the 3D rendering method at different angles - axial, sagittal and coronal projections for the C1 channel - Fig. 4A, 4B, 4C and the same projections for channel C2 - Fig. 4E, 4F, 4G. In addition, reconstructions with angular displacements are presented - Fig. 4G and 4Z.

Discussion/Conclusion

We have implemented a method to visualize the internal structure of a coil using simple tools. Let us note that “dry water” not only does not interfere with the operation of electronics, does not spoil objects filled with it, but also does not itself undergo changes. Therefore, the same volume of dry water can be used repeatedly. In this case, small losses due

to overflows are possible, especially if the volume being filled contains porous materials. There is also some slight loss during scanning due to liquid evaporation. In this regard, it is of interest to use as a visualization medium a close analogue of “dry water”, also a product of the “3M” company - Novek-774 - $(CF_3)_2CF-CO-CF(CF_3)_2$. Its spin density is only 2.8 % less than that of Novek-1230, but its boiling point is higher – 76 °C.

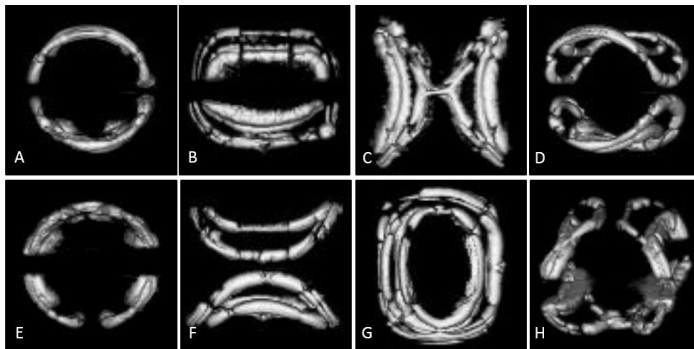


Figure 2 Volumetric reconstructions for the knee coil. 3D renderings are presented in different projections for winding C1 (top row) and C2 (bottom row)

It is important that the conductors inside the coil body are not filled with epoxy resin or other filler, otherwise the imaging medium (dry water) cannot be placed in close proximity to them. In addition, the coil design must not contain ferromagnetic materials. This specificity is typical for MRI sensors - due to this, the coil body is lighter, which is convenient when manipulating it in preparation for a diagnostic study, and there is no distortion of the magnetic field due to ferromagnetic material. These features may not be present in coils used in non-NMR technical applications, making the application of our method problematic.

Information about the internal structure of the coil can also be obtained using X-ray methods. But in this case it is impossible to obtain information about the sensitivity maps. It is impossible to determine the performance of the coil. Typically, there are electronic components inside the coil for switching the windings, for example, to turn off the receiving coil while the transmitting coil is generating an RF pulse. The windings may contain decoupling capacitors to reduce the inductance of the circuit. If these electronic components and/or capacitors are faulty, the coil will not function. But it is impossible to determine this from X-rays. Using X-ray to identify individual windings in a multi-channel coil is also problematic. Since the MRI electronics allow you to connect each channel separately, carrying out such identification using our method does not present any problems.

Acknowledgements

This work is supported by the Interdisciplinary Scientific and Educational Schools of Moscow University «Molecular Technologies of the Living Systems and Synthetic Biology» and «Photonic and quantum technologies. Digital medicine». Access to electronic scientific resources was provided by Nesmeyanov Institute of Organoelement Compounds of the Russian Academy of Sciences with the support of Ministry of Science and Higher Education of the Russian Federation.

References

1. N. V. Anisimov, et al. – Appl. Magn. Reson., 54, 895-904 (2023).
2. Perfluoro(2-methyl-3-pentanone) [https://en.wikipedia.org/wiki/Perfluoro\(2-methyl-3-pentanone\)](https://en.wikipedia.org/wiki/Perfluoro(2-methyl-3-pentanone)).

Interaction of a Quinone-Quinoline and its chelate complexes with nucleic bases in dark and photoinduced processes

*Alina S. Arkhipova*¹, *Maya Ulyanova*^{1,2}, *Olga Yu. Selyutina*¹, *Nikolay E. Polyakov*¹, *Olga A. Chinak*³, *Evgeniya V. Grigorieva*³, *Elena V. Dmitrienko*³

¹*Voevodsky Institute of Chemical Kinetics and Combustion, Novosibirsk, Russia*

²*Novosibirsk State University*

³*Institute of Chemical Biology and Fundamental Medicine*

E-mail: arkhipova@kinetics.nsc.ru

Introduction

The quinone-quinoline chelator 2-phenyl-4-(butylamino) naphtho [2,3-h]quinoline-7,12-dione (Q1, Fig. 1) is an anthraquinone derivative. Many compounds of this class have biological activity, including anticancer activity. For example, doxorubicin and idarubicin are widely used as antitumor agents [1]. The main mechanism of the anticancer effect of anthracyclines is DNA intercalation; studies have also shown that another mechanism is associated with the generation of reactive oxygen radicals [2]. Anthraquinones are capable of forming chelate complexes with metal ions, which may affect their anticancer properties and cytotoxicity. For some anthraquinones, an increase in their anticancer activity was detected when irradiated with light [3]. This work consider the interaction of Q1, as well as its chelate complexes, with nucleic bases in the light and dark conditions, which is the first step for studying the anticancer mechanism associated with interaction with DNA.

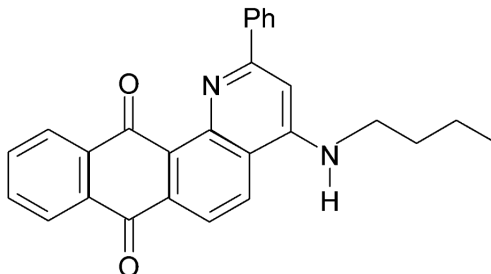


Figure 1. The chemical structure of the 2-phenyl-4-(butylamino) naphtho [2,3-h]quinoline-7,12-dione (Q1)

Methods

The binding of Q1 to nucleic bases was studied using optical spectroscopy and NMR relaxation techniques (T_2 relaxation). Spectra were recorded on Bruker Avance III (500 MHz). Photoinduced reactions were investigated using the chemically induced dynamic nuclear polarization (CIDNP) method on Bruker DPX-200 spectrometer using excimer Lambda Physik laser ($\lambda=308\text{nm}$).

Results and discussion

Optical absorption spectra were recorded for the mixture of 0.05 mM of Q1 and nucleic bases: guanosine monophosphate (GMP), adenosine monophosphate (AMP), thymidine monophosphate (TMP), cytidine monophosphate (CMP), uridine monophosphate (UMP) with the concentration in the range of 0-0.8 mM in mixture ACN 50% and H₂O 50%. Analysis of optical absorption spectra shown that all nucleic bases bind with Q1. The higher binding constants were obtained for AMP and GMP. In addition, binding constants were

calculated. Fig. 2 shows optical absorption spectra of mixture of Q1 and AMP in different concentrations.

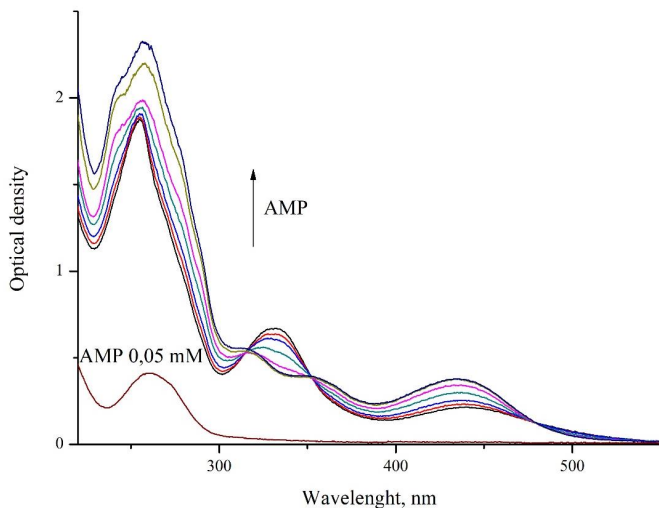


Figure 2. Optical absorption spectra of the samples containing 0.05 mM of Q1 and adenosine monophosphate (AMP) with the concentration in the range of 0-0.8 mM

Photoinduced reactions of Q1 with the nucleic bases listed above were studied using ^1H NMR and chemically induced dynamic nuclear polarization (CIDNP) methods. The presence of the signal at CIDNP spectrum of the mixture of Q1 and its chelate complexes with GMP indicate that photoinduced radical reaction between Q1 and GMP takes place. The mixtures of Q1 with the other nucleic bases turned out to be photostable.

The cytotoxicity of quinone and its chelate complexes was measured by MMT test using cell lines A549 and MDA-MB-231. It was revealed that Q1 demonstrates cytotoxic activity and its cytotoxicity increases under the light irradiation.

Acknowledgements

The reported study was funded by the Russian Science Foundation (grant No. 21-73-10037).

References

1. Mattioli, Roberto, et al. "Doxorubicin and other anthracyclines in cancers: Activity, chemoresistance and its overcoming." *Molecular Aspects of Medicine* 93 (2023).
2. Tewey, Kathleen M., et al. "Intercalative antitumor drugs interfere with the breakage-reunion reaction of mammalian DNA topoisomerase II." *Journal of Biological Chemistry* 259.14 (1984).
3. Selyutina, Olga Yu, et al. "Increased Free Radical Generation during the Interaction of a Quinone-Quinoline Chelator with Metal Ions and the Enhancing Effect of Light." *Pharmaceuticals* 16.8 (2023).

Dictionary-based T2-mapping with multi-echo turbo-spin echo

Zilva Badrieva¹, Ekaterina Brui¹

¹School of Physics and Engineering, ITMO University, Saint Petersburg, Russian Federation
E-mail: zilia.badrieva@metalab.ifmo.ru

Spin-spin relaxation time (T2) of water protons in tissues may provide an important quantitative information about inflammation and hydration processes in many diseases [1]. This parameter can be mapped in vivo in magnetic resonance imaging (MRI). One of the most frequently used technique is based on acquisition of a set of images using multi-echo spin-echo (MESE) pulse sequence. This sequence allows collecting data on time evolution of transverse component of magnetization vector (echo-modulation curve - EMC). However, in some applications, for example, in a breath-hold scanning of abdominal organs, acquisition time becomes a critical factor, and MESE-based technique becomes unacceptable. Acceleration may be achieved by combining several echoes from the echo train using a multi-echo turbo-spin echo sequence (ME-TSE) [2]. However, similarly to MESE sequences, ME-TSE provides stimulated echo signals that contribute to the echo modulation curve. In this case, the EMCs strongly deviate from the expected exponential decay, leading to an incorrect estimate of the T2 relaxation time after exponential approximation [3]. In addition, in multi-slice scanning, direct saturation between neighboring slices affects measured T2 values. As a result, it affects the accuracy of the T2 measurement. Previously both of these problems were solved by using a dictionary-based method for reconstruction of T2 maps from multi-slice MESE images [4].

In this work, we aim to create an accurate and fast method for obtaining multi-slice T2 maps from ME-TSE MR-images. For this purpose, we have investigated how the choice of effective echo times affects the T2 mapping results when a dictionary-based fitting method is used. We have also compared the measured inter-slice T2 variation when using single-slice and multi-slice dictionaries for fitting multi-slice data.

Experiment

Agarose-based phantoms (Eurospin, Diagnostic Sonar, UK) with calibrated (reference) $T_{1,ref}$ and $T_{2,ref}$ values (Table 1) were scanned at 3T (Magnetom Vida, Siemens, Erlangen). The parameters of the ME-TSE pulse sequence were as follows: TR = 2 s, first TE = 10.3 ms, inter-echo time = 10.3 ms, turbo factor = 3, number of contrasts = 3, slice thickness = 2 mm, number of slices = 5, inter-slice gap = 0 and 100% (100% gap was used for reference T2 maps, as this gap provides negligible direct saturation between slices [4]).

Table 1. Reference T1 and T2 values for phantoms

Phantom #	1	2	3	4	5
T2, ms	97.2	118.5	170.5	158.7	131.6
T1, ms	336.1	672.5	1235.2	1288.9	1407.7

In ME-TSE, the k-space for each image is filled with data from different echo times, the number of such echoes is called turbo-factor. Figure 1 illustrates a diagram of an ME-TSE sequence with a turbo factor = 3. The central part of k-space of the first image in a series (first contrast) is filled with the data from echo #1 (and thus, in this case, the first echo time is considered as an effective - TE_{eff}), the outer parts of this k-space are filled with data from the echo #2 and #3. The k-spaces for rest of the contrasts are filled in the same manner: with the echoes #4-6 and #7-9 for contrasts 2 and 3, respectively. In our work, we used three variants of TE_{eff} combinations: first-first-first (FFF), first-second-third (FST) and first-third-third (FTT).

The proposed T2-mapping pipeline is illustrated in Figure 1. First, experimental EMCs were obtained from the MR images. Then, dictionaries of echo modulation curves, containing 9 echo signals, were generated using the ME-TSE pulse sequence diagram with the relevant parameters, by our previously reported dictionary generator, which took into account inter-slice interactions [4]. We generated a separate dictionary for the single slice case, and 5 separate dictionaries for the multi-slice case. Each experimental EMC contained only 3 points. Thus, they were matched only with the corresponding points in the generated EMCs.

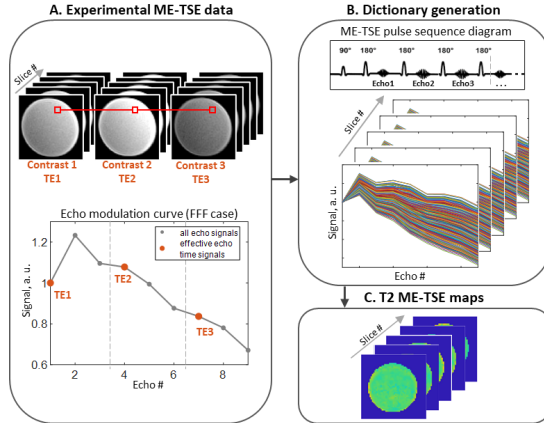


Figure 1. A block diagram of T2 map reconstruction algorithm, using a multi-echo turbo-spin echo pulse sequence in a multi-slice mode.

Figure 2 shows T2 maps of the phantoms #4 ($T_{2ref} = 158.73ms$) obtained by matching experimental data (gap 100%) with the single slice dictionary.

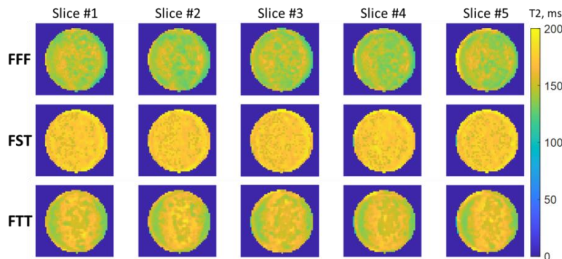


Figure 2. T2 maps of phantom #4 based on multi-slice ME-TSE with gap 100% acquired with different TE_{eff} combinations.

The worst fitting result was observed for the FTT case: T2 maps were inhomogeneous and biased in comparison to T_{2ref} . The most homogeneous maps with the smallest errors of T2 estimation were obtained for the FST case. Thus, only FST data were further used to analyze the effect of multi-slice dictionary on the inter-slice T2 variation. As expected, no inter-slice T2 variation was observed for this case.

Multi-slice T2 maps based on zero gap ME-TSE were obtained for each phantom: when multi-slice data were fitted with the single-slice dictionary (MS), and when multi-slice data were fitted with the multi-slice dictionary (MM) (Figure 3-A – T2 maps for phantom #4). Figure 3-B depicts the mean T2 values measured in the phantoms. In MS case, the largest and lowest T2 values were consistently obtained for slices #1 or #5 (bordering) and slice #3

(central), respectively. Intermediate T2 values were observed for the other slices. For MM fitting, a visible improvement of inter-slice T2 reproducibility is clearly observed for most of the phantoms.

In addition, relative error of T2 estimation was calculated as:

$$\Delta T2_{ref} = \frac{\sum_{i=1}^N (T2_i - T2_{ref})}{N * T2_{ref}}$$

where $N=5$ (number of slices). The results are depicted in Figure 3-C as a function of $T1_{ref}$ values. In MS case, an increased error for higher T1 values was observed. These errors decreased in MM case.

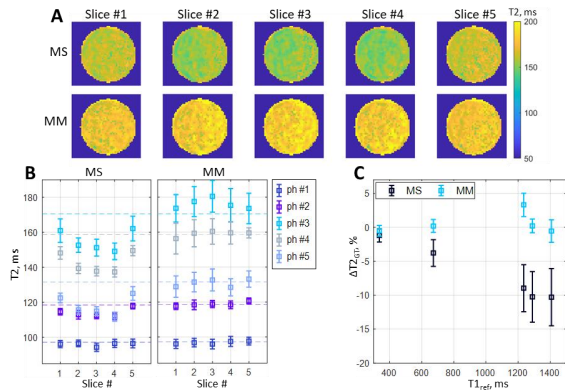


Figure 3. A) T2 maps of phantom #4 based on multi-slice ME-TSE with gap 0, TE_{eff} combination – FST; B) Mean T2 values extracted from T2 maps based on multi-slice MESE. Horizontal dashed lines correspond to reference T2 values. C) Errors of the multi-slice T2 estimation with respect to the ground truth T2 values.

Conclusions

In this work, an improved EMC-dictionary method for ME-TSE-based T2 mapping has been proposed. The combination of TE_{eff} that provided the lowest T2 estimation error was identified. The use of the improved EMC method, which considers direct saturation effects for T2 maps reconstruction from multi-slice data, resulted in a reduction of both T2 variation between slices and the relative error of T2 measurement.

Acknowledgements

The work was supported by state assignment No. FSER-2022–0010 within the framework of the national project “Science and Universities”.

References

1. Kim HK, et al, T2 mapping in Duchenne muscular dystrophy: distribution of disease activity and correlation with clinical assessments. *Radiology*. 2010; 255(3):899–908.
2. Hoffman DH, et al, T1 mapping, T2 mapping and MR elastography of the liver for detection and staging of liver fibrosis. *Abdominal Radiology*. 2020; 45:692-700.
3. Majumdar S, et al, Errors in the measurements of T2 using multiple-echo MRI techniques. I. Effects of radiofrequency pulse imperfections. *Magn Reson Med*. 1986;3(3):397–417. doi: 10.1002/mrm.1910030305.
4. Brui EA., et al, Mitigating slice cross talk in multi slice multi echo spin echo T2 mapping. *Magn Reson Med*. 2023.

Mn Related Paramagnetic Centres in a Bulk GaS and GaSe Van der Waals Semiconductors with High-Frequency EPR Method

Anastasia V. Batueva, Roman A. Babunts, Alexander S. Gurin, Kirill V. Likhachev, Pavel G. Baranov

Ioffe Institute, 194021, St. Petersburg, Russia

E-mail: rarain1345@yandex.ru

https://ioffe.ru/labmsc/ru/main.html

Introduction

Layered semiconductors, in particular GaS and GaSe, consisting of quasi-two-dimensional S-Ga-Ga-S and Se-Ga-Ga-Se layers with a hexagonal structure, appear to be extremely promising for optoelectronics and spintronics applications. The highly anisotropic structure leads to interesting properties, such as naturally formation of layers with up to a monolayer thicknesses and a band structure that differs sharply compared to bulk samples. From both theoretical and practical points of view (in light of the possibility of creating semi-insulating and magnetic materials by doping with transition elements to form spin centers that can be used as information carriers for spintronics devices), it seems important to study the features of the formation of paramagnetic centers in such materials. For these purposes, the electron paramagnetic resonance (EPR) method is extremely informative, allowing one to determine the type of center, charge state, and lattice position.

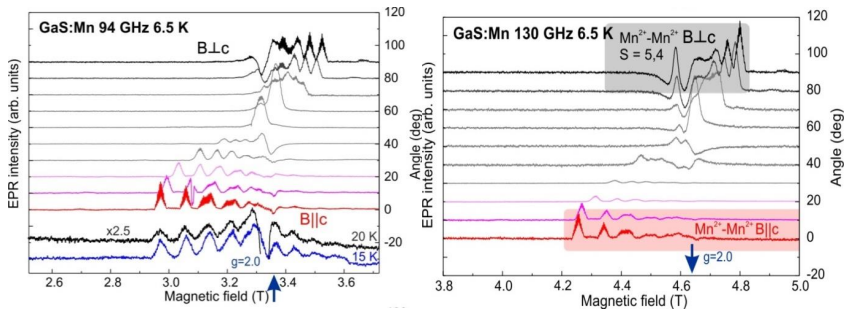


Figure 1. Orientation dependence of EPR signals related to Mn centers in a GaS:Mn sample, recorded at 94 GHz and 130 GHz at a temperature of 6.5 K.

Results

The results of this work include EPR study on Mn-doped bulk GaS and GaSe samples at frequencies of 94 and 130 GHz and temperature of about 6 K with the EPR/ODMR spectrometer developed at the Ioffe Institute [1].

For GaS:Mn sample, spectra (Fig. 1) of ferromagnetically coupled Mn^{2+} - Mn^{2+} pairs embedded in the positions of covalently bound Ga^{2+} atoms located along the c-axis of the crystal were obtained [2]. The fine structure parameters and the isotropic exchange interaction parameter are determined in conformity with the selected effective spin Hamiltonian. For the GaSe:Mn crystal, spectra for two types of centers with effective spin $S=2$ were recorded, presumably related to Mn-Mn pairs occupying Ga sites of two types. The parameters of the effective spin Hamiltonian [3] have been determined for them. For both GaS and GaSe, signals from single Mn^{2+} ions with $g \approx 2.0$ and $S = 5/2$ in different positions are observed. For all signals, a well-resolved hyperfine structure is observed (Fig. 2) - 6 equidistant lines for single Mn^{2+} centers and 11 equidistant lines for Mn^{2+} - Mn^{2+} pairs. The set of hyperfine

structure lines for the center with $S=2$ in GaSe is more complex, which suggests that the interacting centers are not equivalent.

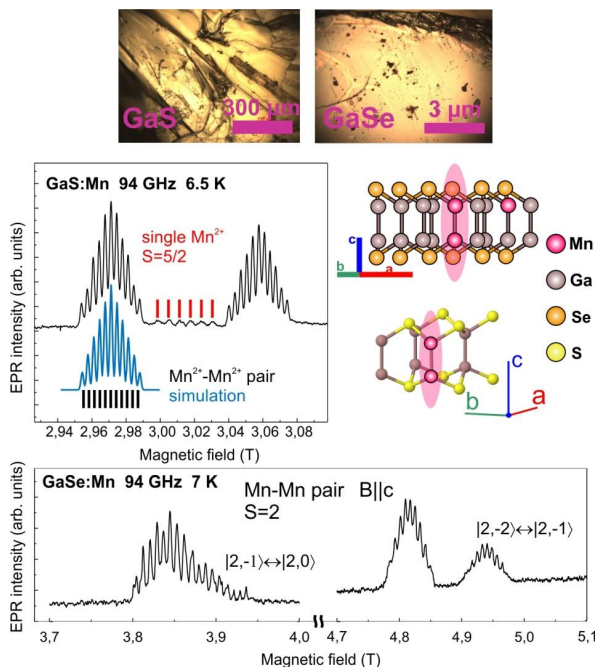


Figure 2. EPR spectra fragments for Mn-Mn pairs in a GaS:Mn and GaSe:Mn, recorded at 94 GHz. On inserts – microscope pictures of GaS:Mn and GaSe:Mn samples and sketch of the 2H-GaS and β -GaSe crystal structure, manganese Mn-Mn pairs and single Mn^{2+} ions.

Acknowledgements

This study was supported by a grant from the Russian Science Foundation (project No. 23-12-00152), <https://rscf.ru/project/23-12-00152/>.

References

1. R.A. Babunts et al., Appl. Magn. Reson. 51, 1125–1143 (2020)
2. Roman A. Babunts et al.; Evidence of ferromagnetic coupling for manganese pairs in a layered van der Waals GaS semiconductor. J. Appl. Phys. 28 October 2023; 134 (16): 165705. <https://doi.org/10.1063/5.0147197>
3. A. Bencini and D. Gatteschi, Electron Paramagnetic Resonance of Exchange Coupled Systems (Springer, Heidelberg, 1990)

Investigation of poly-m-phenylene isophthalamide polymer membrane modified by UiO-66 (NH₂) MOF for separation of toluene/methanol mixture using molecular dynamics method

Vladimir Y. Bazaikin I, Andrei V. Komolkin I, Denis A. Markelov I.

vbazaikin@icloud.com

¹Saint Petersburg State University, 7/9 Universitetskaya nab., St. Petersburg 199034, Russia

Introduction

Today, there are many important industrial processes that use membrane technologies, which have become widespread primarily due to their efficiency, low energy consumption and environmental friendliness.

One of the central membrane technologies is the pervaporation method, which is used to separate liquids. The essence of the method is that the cell is separated into two parts by a semi-permeable polymer membrane, then a pressure gradient is created, leading to selective evaporation of liquids. To improve this method, polymers are modified with metal-organic framework structures (MOFs) embedded inside the polymer.

In this work, the transport and equilibrium properties of methanol and toluene inside a poly-m-phenylene isophthalamide (PMIA) polymer membrane with and without the addition of UiO-66 (NH₂) MOF nanoparticles were investigated using molecular dynamics method (MD) with a full atomistic resolution.

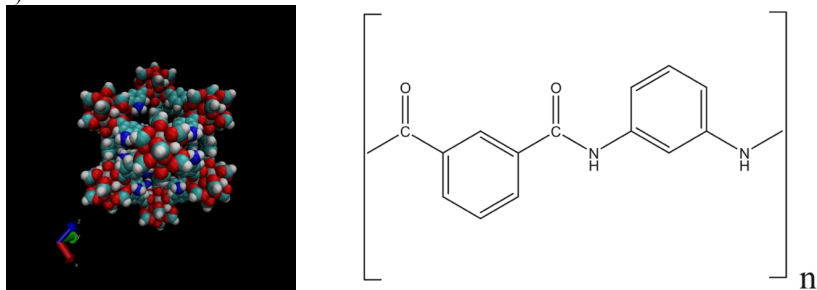


Fig. 1. A snapshot of simulation box with the MOF nanoparticle (left), The molecular structure of poly-m-phenylene isophthalamide (PMIA) (right) [1].

Details of simulating

We have simulated two systems which contained 210 linear chains of PMIA, MOF nanoparticle (only in of them), 130 molecules of methanol, and 221 molecules of toluene. For simulation GROMACS and OPLS forcefield [2] were used. Systems were simulated in the NPT ensemble using V-rescale thermostat [3] and Berendsen barostat [4].

At first, we have equilibrated the systems at high temperature of 700 K (above glass transition temperature) with 200 ns trajectories length. This length was enough to mix all the components of the systems, which means that there wouldn't artefacts of simulating found. Then, systems were cooled to 300 K with a cooling rate of 1 K/ns.

And finally, simulations were carried out at temperature of 300 K with 1 ms trajectories length. These trajectories were used for analysis of equilibrium and transport properties.

Table 1 [1] Some details of the simulated systems. PMIA is poly-m-phenylene isophthalamide; the nanoparticle of UiO-66 (NH₂) metal-organic framework.

Name	Chemical formula	The number of molecules	Molecular weight, a.e.m.
PMIA	[C ₁₄ H ₁₀ N ₂ O ₂] ₁₀	210	500740
MOF*	C ₃₇₂ H ₃₁₆ N ₃₆ O ₄₁₆ Zr ₇₈	1	19062
Methanol	CH ₃ OH	130	4160
Toluene	C ₆ H ₅ CH ₃	221	20332

* Only for the system which includes the MOF nanoparticle.

Results and discussion

Equilibrium properties

We have established that methanol molecules are evenly distributed inside membrane, they don't form clusters or pairs. It happens because energetically beneficial for the methanol molecules to interact with PMIA than with each other. This is confirmed by the presence of hydrogen bonds between methanol molecules and polymer chains. In the volume of the MOF nanoparticle the methanol molecules are evenly distributed too.

Toluene molecules showed fundamentally different behavior. About half of toluene molecules form clusters inside the polymer matrix consisting of 2-10 molecules. The average size of the cluster is 1 nm. It was established the absence of hydrogen bonds between PMIA and toluene, because of that the formation of toluene clusters is energetically more beneficial than the interaction of toluene with polymer membrane. Also, it was established that toluene molecules get stuck on the surface and inside the MOF nanoparticle. It is explained by the presence of T-configuration which is characteristic of crystalline benzene.

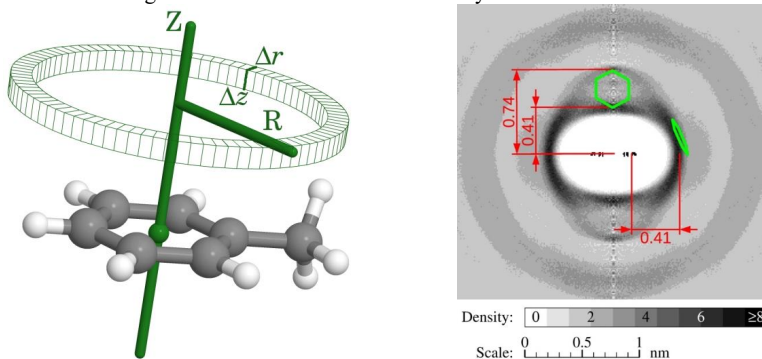


Fig. 2. The definition of cylindrical distribution function (CDF) (left), The cylindrical distribution function of carbon atoms of the aromatics rings in aminoterephthalic acid (ATPA) of UiO-66 (NH₂) MOF (right) [1].

Translation mobility

We have established that the methanol molecules penetrate well through the polymer matrix. The methanol molecules shift by their own radius of gyration, R_g , in an average of 0.35 ps. Also, it was found that the addition of MOF nanoparticle accelerates the mobility of methanol in the system. Despite high mobility, molecules don't reach the diffusion regime ($\text{MSD} \sim \text{time}$), because of that it is not possible to compare the diffusion coefficients of the

systems. For comparison, a displacement of $5R_g$ was used, it showed that in presence of MOF the mobility of methanol increases in 4 times ($40\text{ ns}/10\text{ ns}$).

It was found that the mobility of toluene molecules is reduced only to the movement within the clusters of toluene molecules. Single molecules do not penetrate through the membrane. The mobility of toluene decreases in the presence of MOF nanoparticle, because molecules get stuck on the surface or inside the MOF.

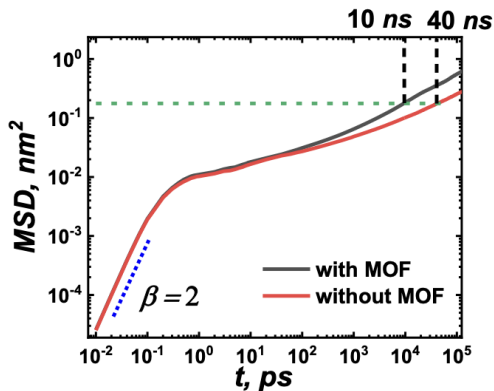


Fig. 8. The time dependences of the mean square displacement in a double logarithmic scale for methanol molecules in the pure (40ns) and composite (10ns) polymer membranes [1].

Conclusion

Summarizing, we showed the differences in distribution and translational mobility between solvent molecules. Also, it was established that MOF nanoparticle improve the polymer properties for separation of a toluene/methanol mixture.

Thus, considered polymer (PMIA) and MOF nanoparticle show high efficiency for separation toluene/methanol mixture. Our results are in good agreement with experimental data [5].

Acknowledgments

The authors thank Anastasia V. Penkova for fruitful discussions. The simulations have been performed by using the Computer Resources Center of Saint Petersburg State University.

References

1. V.Y. Bazaikin, A.V. Komolkin, D.A. Markelov, Journal of Molecular Liquids 383 (2023) 122188.
2. W.L. Jorgensen, J. Tirado-Rives, Potential energy functions for atomic-level simulations of water and organic and biomolecular systems, Proc. Natl. Acad. Sci. 102 (19) (2005) 6665–6670, <https://doi.org/10.1073/pnas.0408037102>.
3. G. Bussi, D. Donadio, M. Parrinello, Canonical sampling through velocity rescaling, J. Chem. Phys. 126 (2007), 014101
4. H.J.C. Berendsen, J.P.M. Postma, W.F. van Gunsteren, A. DiNola, J.R. Haak, Molecular dynamics with coupling to an external bath, J. Chem. Phys. 81 (1984) 3684–3690
5. A.V. Penkova, A.I. Kuzminova, M.E. Dmitrenko, V.A. Surkova, V.P. Liamin, D.A. Markelov, A.V. Komolkin, D.Y. Poloneeva, A.V. Laptenkova, A.A. Selyutin, A.S. Mazur, A.V. Emeline, S.Thomas, S.S. Ermakov / Sep. Purif. Technol., 2021, 263, 118370.

NMR to Industry: Development of modern universal control software for TD-NMR spectrometers, validation using fertilizer samples as an example

Bystrov S. S.^{1,2}, Kirilenko V. D.³, Zolotov D. R.⁴, Khrustalev A.A.⁵

¹*Dept. Nuclear-Physics Research Methods, St. Petersburg State University*

²*TerraQuantTech LLC (VAT Number: 400372342), Tbilisi, Georgia*

³*Wydział Matematyki i Informatyki, Uniwersytet Łódzki, Łódź, Poland*

⁴*TRASSIR GLOBAL FZC, LLC “DSSL” (Digital Security Systems Lab), Moscow, Russia*

⁵*Bachelor of Engineering in Mechatronics and Robotics, ITMO University*

E-mail: terraquanttech@gmail.com

https://terraquant.tech

Introduction

Over recent decades, Nuclear Magnetic Resonance (NMR) has emerged as an indispensable tool for chemical and structural research, showcasing its versatility across various domains. From aiding in disease diagnosis to elucidating molecular structures in intricate biological systems, NMR has proven unmatched in its capabilities.

However, its widespread application beyond research settings faces significant hurdles, primarily due to the exorbitant costs associated with acquiring and maintaining NMR facilities. The prohibitive expenses, and the ongoing need for skilled personnel and equipment upkeep, pose substantial barriers to leveraging NMR for routine problem-solving in industrial contexts.

Nonetheless, there exists an opportunity to integrate NMR methodologies into various stages of technological processes across diverse industries, ranging from food production to oil refining [1-3]. This avenue, albeit often underestimated, holds promise for reducing product costs for consumers and enhancing production quality control minimizing the regular costs on the part of manufacturers. The key challenge lies in balancing between NMR's costliness and amount of potential benefits for practical applications.

Despite the existing challenges, researchers and entrepreneurs worldwide still persist in their endeavors to harness nuclear magnetic resonance (NMR) technologies, albeit with a focus on a highly specialized niche. A notable development aimed at increasing the overall availability of NMR spectrometers for small enterprises is the emergence of benchtop NMR solutions. Market leaders such as Magritek, Nanalysis, Oxford Instruments, and Bruker have introduced their variations of these devices, such as Magritek's Spinsolve and Bruker Fourier 80, among others. From a broad perspective, these benchtop NMR spectrometers share a core design, typically featuring powerful electromagnetic coils or permanent magnets tuned to resonant frequencies between 20-90 MHz, corresponding to magnetic field strengths of 0.3-1.5 Tesla. However, despite their smaller size and lower cost compared to traditional superconducting spectrometers, they still do not provide a convenient tool specifically for industry representatives, mimicking the user interaction experience of full-scale superconducting spectrometers, i.e. still require a high level of qualification for the device operator, an understanding of the operating principles of both the NMR spectrometer itself, and the presence of at least a general understanding of physics and chemistry, which is often extremely disadvantageous for product manufacturers, i.e. to the end user in the industrial sector.

One notable gap in the current landscape of benchtop NMR solutions is the lack of comprehensive software tailored for industrial applications, which could significantly enhance their utility and impact in practical settings.

Modern solution

A more modern approach to expanding the coverage of nuclear magnetic resonance applications for industrial needs is to maintain the focus while developing solution on a particular specific consumer demand, leading, as a consequence, to an overall increase of the appearance of such devices in various enterprises workflow.

In various industries, the determination of product quality within production chains relies on distinct metrics tailored to the specific needs of each sector. For instance, in the peat industry, chemical analysis plays a pivotal role in assessing concentrations of crucial elements such as carbon, fluorine, nitrogen, sodium, and phosphorus. Similarly, in the petroleum industry, the focus often shifts towards determining the hydrogen content in fuels, essential for assessing combustion efficiency and overall product performance. Conversely, in the rubber industry, the quality of vulcanization at the end of the manufacturing process emerges as a critical concern, with parameters such as crosslink density and polymer chain structure being indicative of product integrity.

Despite these diverse metrics, the ultimate goal across these industries remains consistent: the classification of products into categories such as "good" or "bad" based on predetermined quality standards. However, many challenges persist in achieving accurate and efficient quality assessment using conventional methods, prompting the exploration of alternative approaches. By harnessing NMR technology, industries can potentially overcome limitations associated with traditional analytical techniques and streamline quality control processes.

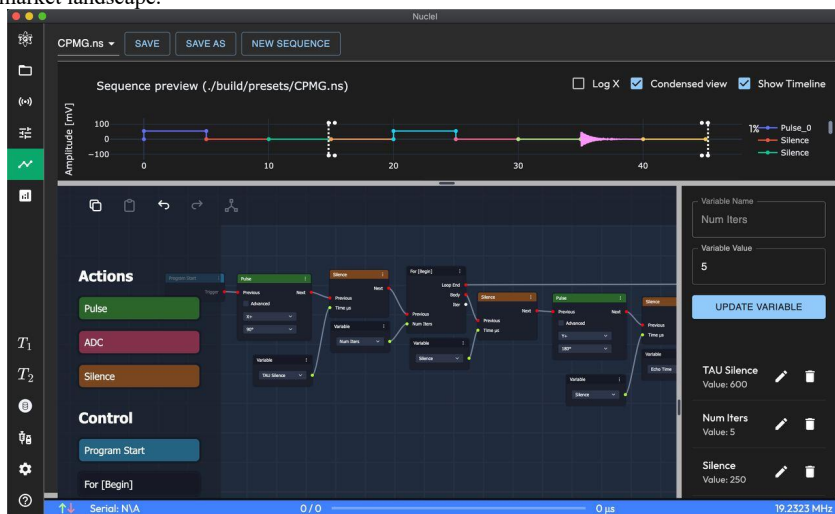
To facilitate the practical application of NMR in industrial settings, TerraQuantTech LLC aims to develop a consumer-oriented approach leveraging classification neural networks tailored with labeling of the NMR data using the classical area-specific laboratory methods. This innovative methodology promises to deliver fast and reliable quality assessment results tailored to the specific needs of various industrial sectors.

As a foundational step towards realizing this vision, TerraQuantTech LLC, in collaboration with Resonance Systems GmbH, has developed TQT Nuclei, a modern software platform designed for conducting NMR experiments and structuring the sample information. The developed solution is optimized for use in tandem with a Resonance Systems "Spin Track" 20 MHz NMR spectrometer, renowned for its robust performance and reliability in industrial environments. However, owing to its modular design, the software can seamlessly integrate with any NMR spectrometer, provided there is an appropriate Dynamic Link Library (DLL) available to control the device. This versatility ensures compatibility with a wide range of NMR instrumentation, offering flexibility and scalability to meet the diverse needs of industrial applications. By providing intuitive interfaces and advanced data analysis capabilities, TQT Nuclei empowers users to interpret NMR results effectively and extract actionable insights in a language that resonates with their respective industries.

Unfortunately, current NMR controlling software solutions primarily emphasize conducting "classical" NMR experiments, lacking the ability to structure different experiments within a cohesive system. As a result, the outputs provided by these software packages may not be readily applicable or obvious to the target users in industrial applications. In many cases, the results generated may require further interpretation or processing before they can be effectively utilized in industrial decision-making processes. This limitation underscores the critical need for a software solution like TQT Nuclei, which not only facilitates NMR experimentation but also offers clear and distinct results tailored to the specific needs of industrial users. By providing intuitive interfaces and actionable insights, TQT Nuclei aims to bridge the gap between NMR technology and industrial application, empowering users to derive meaningful conclusions and drive actionable outcomes in real-world scenarios.

To achieve accurate predictions of target labels using machine learning techniques, it is imperative to gather a substantial amount of NMR data paired with meaningful metrics specific to each industry. In the case of the peat industry, this may involve collecting NMR data alongside complementary information obtained from other research methods, such as chemical analysis to determine concentrations of essential elements. This holistic approach ensures that the machine learning algorithms have access to comprehensive datasets, enabling them to discern patterns and relationships effectively. By leveraging a combination of NMR data and complementary metrics, the developed software can enhance the quality and reliability of predictions, thereby empowering industries to make informed decisions and optimize their production processes.

Through the integration of advanced NMR technology and cutting-edge software solutions, TerraQuantTech LLC and Resonance Systems GmbH seek to revolutionize quality control processes across diverse industrial domains. By bridging the gap between scientific innovation and practical application, this collaborative effort promises to unlock new opportunities for enhancing product quality, efficiency, and competitiveness in the global market landscape.



Acknowledgements

The author would like to thank every team member of TerraQuantTech company and show my deepest gratitude for all the hard work that each of you put into our project, and for your desire to create and strive for the best despite any external circumstances. N.B. I would also like to thank my dear mom and dad for the unquenchable faith in our deed.

References

1. "A Review of Applications of NMR Spectroscopy in Petroleum Chemistry" John C. Edwards, ASTM Books, 2011.
2. J. Braz. Chem. Soc. vol.32 no.7 São Paulo, July 02, 2021 [10.21577/0103-5053.20210039]
3. "Process and Quality control in food and agroindustry using TD-NMR", D. Consalter, Proceedings of the conference "BENCHTOP NMR: FROM ACADEMIA TO INDUSTRY"

Study of the chemical composition of Azerbaijani crude oil using infrared spectroscopy and nuclear magnetic resonance methods.

U.J. Yolchuyeva^{1,2}, R.A. Japharova¹, S.H. Eldarova¹, A.F. Alieva¹, G.A. Hajiyyeva¹, F.T. Alizadeh¹

¹Institute of Petrochemical Processes, Azerbaijan National Academy of Sciences, 30, Khojaly Ave., AZ1025, Baku, Azerbaijan

²Zazar University, School of Science and Engineering department, Mahsati Str.41, AZ1096, Baku, Azerbaijan

E-mail: u.jeyhunzde@gmail.com

The amount of paraffins, naphthenes, aromatic hydrocarbons of heteroatomic structure, resinous asphaltene and mineral substances contained in crude oil is different and varies over a wide range. The quality of petroleum products depends on its fraction and hydrocarbon content, such as gasoline. As the amount of isoparaffins and aromatic hydrocarbons in gasoline increases, its octane number and grade increase. The cetane number of diesel fuels is associated with a higher content of normal paraffins in them compared to isoparaffins. The chemical, physical and operational properties of naphthenic hydrocarbons (NH) vary depending on their structure. The boiling point of HC increases with increasing number of rings in them, and the viscosity index increases with increasing side chain length. An increase in the degree of branching of carbon atoms in the side chain leads to a decrease in the freezing point. The nature and quantity of aromatic hydrocarbons (AH) mainly depend on the nature of the raw material. Most of them have a hybrid structure.

In the work we presented, comparative studies of the aromaticity and degree of branching of the Zagly, Surakhani and Balakhani oils, as well as their hydrocarbon group composition, were carried out using infrared (IR) spectroscopy and nuclear magnetic resonance (NMR) methods. The physical and chemical properties of oils from the Absheron fields are given in Table 1.

Table 1. Physico-chemical properties of Surakhani, Balakhani and Zagly oil

Physicochemical characteristics	Oilfield		
	Surakhany	Balakhany	Zagly
Density at 200C, kg/m ³	841.7	887.8	847.9
Specific resistance at 40 ⁰ C, mm ² /s	6.33	17.05	5.0298
Freezing temperature, ⁰ C	-40	-50	-30
Amount of sulfur,%	0.7809	0.1685	0.1588

As can be seen from Table 1, Surakhani and Zagly oils have lower density and viscosity compared to Balakhani oil. Balakhani oil is classified as heavy oil by density and contains more sulfur than Surakhani oil.

To conduct oil research, Surakhany, Balakhany and Zagly were divided according to their hydrocarbon composition. In Surakhani and Balakhani oils, a predominance of paraffin-naphthenic hydrocarbons (PNH) is observed (75.4% and 66%, respectively). The amount of PHC in Zagly oil is 40.5%, and the amount of aromatic hydrocarbons (AH) is 47.6%. The hydrocarbon composition of oils was studied using IR spectroscopy and NMR. The results are presented in Tables 2 and 3.

Table 2. Analysis of hydrocarbon content in oil according to IR spectra

Comments	Wavenumber, cm ⁻¹
Deformation and valence vibration of the C-H bond of CH ₃ and CH ₂ groups	1375, 1376, 1451, 1453, 1456, 1457, 2851, 2854, 2920, 2921, 2949, 2951,
valence vibration of the C-H bond of CH ₃ and CH ₂ groups of naphthenic hydrocarbons	1032, 1033, 1034, 1035, 1036, 1037, 1044, 1075
valence vibration of the C-H bond of the –HC=C– (benzene ring) group (AK).	3013, 3015, 3017, 3018, 3019, 3020, 3021, 3041, 3044, 3045, 3049, 3052, 3053, 3055
deformation vibration of the C-H bond of the aromatic ring	632, 744, 745, 748, 749, 783, 813, 814, 815, 816, 873, 874, 882, 885, 891, 896, 901, 912
deformation vibration of the C-H bond of CH ₃ and CH ₂ groups of naphthenic hydrocarbons	960, 962, 964, 970
valence vibration of the C-C bond of the aromatic ring	1601, 1602, 1603, 1604

Table 3. Structural parameters of oils and their hydrocarbon components, calculated by NMR method

Samples		Raw oil	Paraffin-naphthene	I AH	II AH	IIIAH	IVAH	Resins	
Distribution of hydrogen atoms across various structural groups	Surakhan i	H _{Ar}	1,2	–	9.3	15.0	16.0	13.6	4.5
	Balakhan y		3.7	–	4.9	11.4	4.9	12.4	5.8
	Zagly		15,1		9.52	18.09	20.20	4.82	6.3
	Surakhan i	H _α	3.4	–	16.1	26.4	24.6	16.0	11.3
	Balakhan y		4.9	–	8.9	20.3	9.3	19.8	13.2
	Zagly		7.1		14.13	25.38	26.28	6.36	12.1
	Surakhan i	H _{saturated}	65.6	~100	90.7	85.0	84.0	86.4	95.5
	Balakhan y		58.5	64.2	63.1	47.1	56.5	50.4	58.8
	Zagly		79.3	73.5	53.71	39.17	36.84	58.34	52.1
	Surakhan i	H _γ	35.0	34.0	22.3	19.4	19.6	24.4	24.9
	Balakhan y		33.7	35.8	29.1	21.2	29.3	17.4	22.2
	Zagly		30.5	40.1	22.64	17.36	16.68	30.48	19.8
Degree of aromatization	Surakhan i	f _a	0.01	–	0.331	0.402	0.43	0.36	0.34
	Balakhan y		0.04	–	0.22	0.35	0.38	0.37	0.28
	Zagly		0.16	-	30.2	47.0	50.0	21.0	0.44
Degree of branching	Surakhan i	J	0.83	0.42	0.40	0.45	0.46	0.46	0.43
	Balakhan y		0.85	0.49	0.53	0.50	0.53	0.51	0.54
	Zagly		0.61	0.51	0.36	0.46	0.50	0.43	0.41

Paraffinic hydrocarbons of these oils have a normal and branched structure, and their amount varies depending on the type of oil. Branched paraffins are unevenly distributed in oil fractions. The amount of paraffins with an isoprenoid structure varies depending on the oil. Naphthenes occupy a special place among the natural organic compounds of oil. These oils contain mono-, bi-, tri- and polycyclic naphthenes and AH. The amount of AH varies depending on the type of oil.

The structural parameters of these oils, including the components isolated from them, were determined by the NMR method, and the content of hydrocarbons and the values of the most important structural parameters characterizing them were determined. The majority of hydrogen atoms in average molecules (~more than 84%) belong to saturated structures. Relatively high values of the degree of aromaticity (f_a) are observed in the heavy and medium-heavy fractions (~40-45%). The presence of isostructure in the paraffin chains of the middle molecules of the studied oils can be judged by the values of other parameters (J , $H\gamma$).

The calculation results are consistent with the physicochemical parameters of the studied oils, and the presence of a high number of alkane structures is confirmed by their spectral characteristics. In these oils, especially in Balakhan and Surakhan, PNU predominates. The calculated parameters confirm the paraffin-naphthenic basis of the oils we studied. Surakhani oil is characterized by a relatively large amount of naphthenic hydrocarbons. Therefore, a mixture of naphthenic hydrocarbons obtained from the components of Surakhan oil and having antimicrobial properties can be used in medicine to treat some skin and oncological diseases.

The calculation results are consistent with the physicochemical parameters of the studied oils, and the presence of a high number of alkane structures is confirmed by their spectral characteristics. In these oils, especially in Balakhan and Surakhan, PNU predominates. The calculated parameters confirm the paraffin-naphthenic basis of the oils we studied. Surakhani oil is characterized by a relatively large amount of naphthenic hydrocarbons. Therefore, a mixture of naphthenic hydrocarbons obtained from the components of Surakhan oil and having antimicrobial properties can be used in medicine to treat some skin and oncological diseases.

Thus, in oils, as a result of the interaction of components, patterns of physical indicators are revealed, which makes it possible to interpret the functional composition of oil due to spectral coefficients. The most important is the study of oil at the molecular level using IR spectroscopy and NMR.

Multiple quantum NMR in problems of quantum informatics: many-spin entanglement and scrambling

Edward B. Fel'dman, Elena I. Kuznetsova, Ilia D. Lazarev, Sergey G. Vasil'ev

Federal Research Center of Problems of Chemical Physics and Medicinal Chemistry RAS, Chernogolovka, Moscow Region 142432, Russia

E-mail: efeldman@icp.ac.ru

Introduction

Although multiple quantum (MQ) NMR spectroscopy [1] was introduced for the investigation of nuclear spin distributions in various materials (liquid crystals [2], simple organic systems [1], amorphous hydrogenated silicon [3], etc.), it also turned out useful for probing the decoherence rate in highly correlated spin clusters [4], a study of many-spin entanglement [5], and scrambling [6]. It is very important that MQ NMR dynamics allows us to quantify the development of MQ coherences starting from the z -polarization and ending with a collective state of all spins. The spreading rate of correlations can be described through out-of-time-ordered correlations (OTOCs), which are related to the distribution of the MQ NMR coherences.

Many-spin entanglement

Investigations of many-spin entanglement are performed on the basis of the quantum Fisher Information [7] and the Wigner-Yanase information [8], well-known witnesses of multi-particle entanglement. Essentially, the second moment of the distribution of the intensities of the MQ NMR coherences provides a lower bound on the quantum Fisher information [5,6] and the exact value of the Wigner – Yanase information in some cases [9]. This property opens up possibilities of MQ NMR for the study of many-spin entanglement. However, possibilities of MQ NMR are not restricted in such a way. We worked out a code allowing us to calculate the quantum Fisher information for an arbitrary system of interacting spins.

In order to investigate many-spin entanglement we used two models of interacting spins, in which many-spin dynamics can be studied at low temperatures. One of them is a nano-cavity filled with spin-carrying atoms (molecules). We developed [5] a theory of MQ NMR in a nano-cavity at low temperatures. The theory [5] is based on the idea that molecular diffusion is substantially faster than the time of the spin flip-flop processes. As a result, the problem is reduced to a system of equivalent spins [10,11], which can be analyzed in the basis of the common eigenstates of the total spin angular momentum and its projection on the external magnetic field. The developed approach allowed us to extract information about many-spin entanglement from the MQ NMR spectrum. The temperature dependence of many-spin entanglement was also investigated.

The second model is a one-dimensional zigzag chain consisting of up to 12 spins $\frac{1}{2}$ with nearest neighbor and next nearest neighbor interactions at high and low temperatures in the MQ NMR experiment. The dependence of the number of the entangled spins on the temperature and the chain length was obtained.

Scrambling

Many-spin correlations in MQ NMR dynamics are responsible for delocalization of quantum information, which is known as scrambling. Scrambling implies that information about the input cannot be deduced from any local measurement of the output. The scrambling rate can be quantified through OTOCs, which are closely related to MQ NMR coherences [6]. Thus, MQ NMR is a powerful tool for investigations of scrambling in many-spin systems experimentally [6].

Conclusions

Thus, MQ NMR spectroscopy is an effective method for the investigation of different problems of quantum informatics. It can be used for experimental investigations of quantum information processing in solids.

Acknowledgements

This work is performed as a part of a state task, State Registration No.124013000760-0

References

1. J. Baum, M. Munowitz, A. N. Garroway, A. Pines. – *Journal of Chemical Physics* **83**, 2015 (1985).
2. J. Baum, A. Pines. – *Journal of American Chemical Society* **108**, 7447 (1986).
3. J. Baum, K. K. Gleason, A. Pines, A. N. Garroway, J. A. Reimer. – *Physical Review Letters* **56**, 1377 (1986).
4. H. G. Krojanski, D. Suter. – *Physical Review Letters* **93**, 090501 (2004).
5. S. I. Doronin, E. B. Fel'dman, I. D. Lazarev. – *Physical Review A* **100**, 022330 (2019).
6. M. Garttner, P. Hauke, A. M. Rey. - *Physical Review Letters* **120**, 040402 (2018).
7. G. Toth, I. Apellaniz. – *Journal of Physics A* **47**, 424006 (2014).
8. Z. Chen. – *Physical Review A* **71**, 052302 (2005).
9. S. I. Doronin, E. B. Fel'dman, I. D. Lazarev. – *Physics Letters A* **406**, 127458 (2021).
10. J. Baugh, A. Kleinhammes, D. Han, Q. Wang, Y. Wu, - *Science* **294**,1505 (2001).
11. S. I. Doronin, A. V. Fedorova, E. B. Fel'dman, A. I. Zenchuk. - *Journal of Chemical Physics* **131**, 104109 (2009).

Polymerization kinetic and catalytic properties of resulted comb-like polyelectrolytes by ^1H NMR

P.A. Fetin¹, M.V.Kadnikov,^{1,2} V.I. Fetina¹, I.M. Zorin¹

¹ Department of Macromolecular Chemistry, Institute of Chemistry, St. Petersburg State University, Universitetskaya Nab., 7/9, St. Petersburg 199034, Russian Federation

² Department of Molecular Biophysics and Polymer Physics, Faculty of Physics, St. Petersburg State University, Universitetskaya Nab., 7/9, St. Petersburg 199034, Russian Federation

Introduction

The term polymeric surfactants refer to a whole series of macromolecular structures in the modern scientific community [1]. We mean comb-like polyelectrolytes as polymeric surfactant in which the polar group is located at the end of the side aliphatic groups. The most common method for the synthesis of such compounds is the polymerization of surface-active monomers bearing polymerizable group in the tail (type C [2]). The kinetics of free radical polymerization of such surface-active monomers will be in the focus of this work. Such polymerization is complicated by the association of monomers into micelles in an aqueous solution, therefore the laws of classical free radical polymerization may not hold true in this case. The literature describes the features of the polymerization kinetics of anionic monomers [3], as well as the case when the polymerizable group is a part of the counterion and is associated with the micelle [4], [5]. These works indicate that the preliminary association of the monomer into a micelle, as well as the association of the growing macroradical with monomer micelles, lead to at least an acceleration of polymerization. The properties of the polymer differ from the properties of the polymer obtained in a homogeneous solution in the absence of micelles. In this report, using the *in situ* ^1H NMR spectroscopy method, the features of the polymerization kinetics of cationic surface-active monomers with the polar groups of triethylammonium, pyridinium and quinolinium will be discussed. Cationic comb-like polyelectrolytes obtained by this method are promising micellar catalysts for Suzuki and Heck cross-coupling reactions in water without any other solvents. Features of using the ^1H NMR method for analysis of catalytic activity in these reactions will also be the focus of the report.

In-situ ^1H NMR polymerization

Polymerizations were carried out in standard 5-mm NMR tubes in D_2O solvents. Measuring cell was preheated to temperature 60°C . Monomer and initiator solution of desired concentration were placed in chromatographic vial with septum and bubbled with argon for 15 min, then, using an argon flow, the polymerization solution was transferred into the NMR tube. After placing the tube into the spectrometer (60°C), shimming was performed and ^1H NMR spectra were recorded every 18 s (4 scans per spectrum). Monomer conversion was calculated from the decreasing intensity of signals corresponding to the double bond hydrogens at 6.8 – 6.2 ppm (Fig. 1). Signal of $\text{H}_2\text{C}=\text{CH}$ - fragment from first scan was used as internal standard for calculation of conversion. Conversion was calculated as $p = (1 - I_t/I_0) \times 100\%$, where I_t and I_0 are integral intensities of hydrogen signals of double bond. The data was processed with Bruker Topsin Dynamics Centrum software.

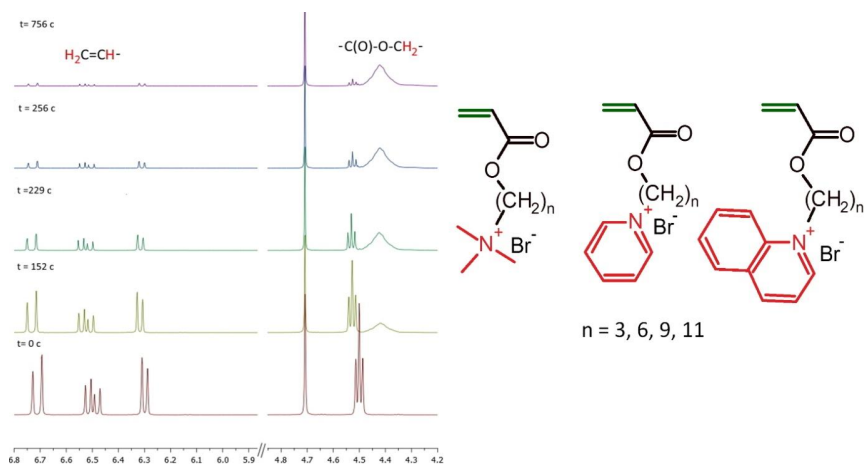


Fig 1. Chemical structures of surface-active monomers and a fragments of the ^1H NMR spectra of the polymerization mixture at different times

The discussion of the results

The possibility of association of the monomer into a micelle at different lengths of the aliphatic spacer was established using the methods of conductometry and solubilization of a low-polar dye (Fig 1). Unlike samples with the trimethylammonium group, samples with the aromatic groups are capable to association in water solution even with a spacer of three methylene units ($n=3$). It is possible that for these samples the association is carried out predominantly by the pi-pi interaction mechanism.

Decrease in the polymerization rate is observed for all samples with a decrease in the length of the aliphatic spacer between the polar group and the polymerizable group. The introduction of aromatic groups into the surfactant structure leads to a sharp slowdown in the polymerization rate ((by two orders of magnitude in the case of the quinolinium cation) in comparison with samples with a trimethylammonium groups. For samples with aromatic cations, the order of the polymerization reaction with respect to the monomer has a value less than one (the one value is classical value from the theory of free radical polymerization). The detected anomalies in the kinetics of polymerization of surface-active monomers with aromatic groups are most likely due to the long life times of surfactant molecules in monomer micelles. The monomers can associate to micelles not only by hydrophobic interactions in water but also by pi-pi mechanism.

One of the applications of the obtained comb-like polyelectrolytes is micellar catalysis. Due to the phenomenon of solubilization in the presence of these substances, many organic substrates are able to overcome the boundaries of hydrophobicity and enter into a chemical reaction in the absence of suitable organic solvents. In this case, the comb-like polyelectrolyte acts as nanoreactor in water.

According to the mechanism of solubilization and ionic attraction, both hydrophobic and anionic reagents are concentrated in micellar pseudophase. This facilitates the carrying out of important organic reactions in environmentally friendly conditions using water as the only solvent. Analysis of the intensity of chemical shifts in a mixture of products and reagents allowed us to test the catalytic activity of these compounds in model reactions of Suzuki and Heck (fig 2) under model conditions.

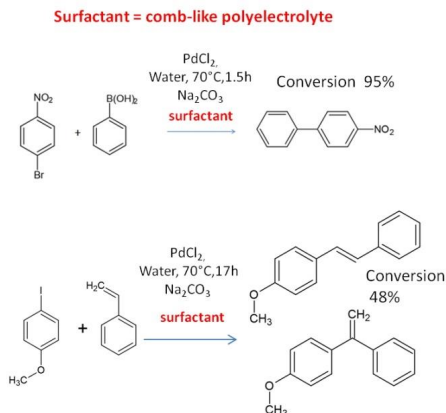


Fig. 2. Schemes of model catalytic reactions of Suzuki (top) and Heck (bottom) for testing the micellar-catalytic activity of the resulting compounds.

The best catalytic activity is demonstrated by a sample with a trimethylammonium group and a hydrocarbon space containing 11 methylene fragments.

Acknowledgements

This work was supported by the RSF № 21-73-10132.

Authors are grateful St. Petersburg state university: RC of Magnetic resonance and cryogenic department. The authors express personal gratitude to Mikhail Andreevich Vovk for recording the NMR spectra

References

1. P. Raffa. Polymeric surfactants: Synthesis, properties, and links to applications – Chem. Rev., 115, №16, 8504–8563 (2015).
2. I.M. Zorin, N.A. Zorina, P.A. Fetin. Polymerization of Micelle-Forming Monomers. – Polym. Sci. - Ser. C., 64, №2, 123–134 (2022).
3. I.M. Zorin, E.P. Podolskaya, A.Yu. Bilibin. On the kinetics of micellar polymerization. Acryloylaminoalkanoates case study. – European Polymer Journal., 110, 355–363 (2019).
4. I. M. Zorin et.al. Polyelectrolyte-colloid complex formation via polymerization: reaction kinetics in direct micelles, inverted micelles and homogeneous solution studied by NMR and conductometry. – Colloid and Polymer Science., 297, 1169–1176 (2019).
5. Yu. V. Shulevich et.al. Matrix polymerization of trimethyl metacryloyloxy ethylethylammonium methyl sulfate in sodium dodecyl sulfate micellar solutions. – Polymer Science, Series B, 61, № 6,715–724 (2019).

Artificial Intelligence tools for the reconstruction and enhancement of MR imaging

Eduardo Garea-Llano¹, Evelio Gonzalez Dalmau¹ and Carlos Cabal Mirabal¹

¹Cuban Neuroscience Center, 190 No. 1520, Playa 11600, Havana, Cuba.

Email: eduardo.garea@cneuro.edu.cu

Introduction

In this work we present a comparative study between different techniques based on deep learning for image reconstruction in high and low field brain MRI. We analyze methods based on convolutional networks, adversarial generative networks and propose a reconstruction model based on the concepts of semantic genesis [1]. The experiments developed in neuro-images taken by high and low field magnetic resonance scanners demonstrated a superior performance of the proposed architecture based on semantic genesis in terms of correlation and signal to noise ratio.

Methods

Aliasing and blur are two of the most common effects that occur in MRI images due to patient movement or reduced scanning, but other mechanisms such as low-resolution scanning that occur in MRI low-field images lead to image blurring [2]. Aliasing effect is obtained by subsampling the low frequencies. To obtain the effect of the image subsampling, we use the implementation of the method proposed in [3] and publicly available (<https://github.com/Corey-Zumar/MRI-Reconstruction>). The implemented scheme simulates the aliasing effect that can occur as a consequence of reducing the patient's exposure time in the scanner. It begins with the transformation of the original image to the frequency domain or k-space by the fast Fourier transform, then an operation is performed to shift the zero frequency of the image towards its center to facilitate the subsampling process, next some low frequencies in the k-space are eliminated, this is done through two parameters that regulate the amount of frequencies to eliminate, the subsampling step and the percentage of low frequencies to retain in the output image. Finally, the inverse Fourier transform is applied to the resulting image to obtain the subsampled image. In the case of our study we apply the same parameters used in the implementation of [3], `substep=4` and `low_freq_percent=0.04`.

Gaussian blur describes the blur of an image using a Gaussian function. This is an effect widely used in computer vision, typically to reduce image noise and reduce details. The visual effect of this blur technique is a soft blur similar to viewing the image through a translucent screen. In our study we used a Gaussian blurring filter to simulate the effect produced in the image by movement of the patient. Figure 1 show an example of effect of subsampling (b) and Gaussian blurring (c) in a MR image.

Image reconstruction schemes and deep neural networks

The first scheme is designed for image reconstruction from the aliasing effect caused by the subsampling process. As pre-processing, the unmeasured region of the subsampled data is first padded with zeros. Then, by means of the inverse Fourier transform, its absolute value is taken and the folded image is obtained. After this pre-processing the folded image is used as the input of the pre-trained network and produce the output. The network retrieves the zero-padded portion of the k-space data. The Fourier transform is obtained and the unpadded parts are replaced by the original k-space data to preserve the original measured data. Finally, the output image is obtained by applying the inverse Fourier transform and the absolute value. In the second scheme, the simulation of the effect of blurring is carried out by means of the Gaussian filtering of the original image, the image resulting from the filtering is the input to

the pretrained deep learning model (for the task of reconstruction from the blurred image), finally the output of the network is the reconstructed image.

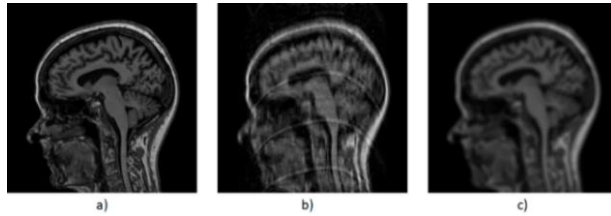


Figure 1. *Subsampling (b) and Gaussian blurring (c) on a high field MR image (a)*

As the main baseline we use the Unet convolutional network, which is the one used in the original scheme proposed in [3]. Unet is a fully convolutional neural network model. This model was originally developed for medical images segmentation [4]. As the second deep learning framework for this study we propose the Pix2pix architecture. It is a Generative Adversarial Network (GAN) [4]. As a third framework to be evaluated, we propose the semantic genesis approach [1]. In this work we propose the adaptation of this approach to the task of reconstruction of MRI (Figure 2). The framework consists of three components: 1) Pseudo-labeling of anatomical patterns, 2) Anatomical Pattern Classification, and 3) Restoration of anatomical patterns. The Semantic Genesis is conceptually simple: an encoder-decoder structure with skip connections between (Unet) and a classification head at the end of the encoder.

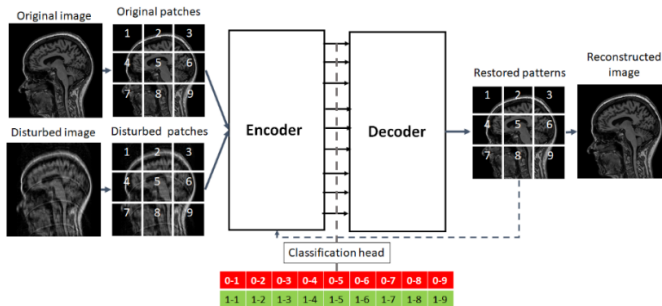


Figure 2. *Framework for MRI reconstruction based on Semantic Genesis [1]*

Experimental results and discussion

Data used in the preparation of this article were obtained from the Alzheimer’s Disease Neuroimaging Initiative* (ADNI) database (adni.loni.usc.edu), available at <http://adni.loni.usc.edu/about/>. The experiments were developed in neuro-images taken by high and low field magnetic resonance scanners. For model training, the dataset obtained from ADNI cohort was divided into three sets with randomly selected images: Training: 1899. Validation: 594 and Test: 475. An additional test set was implemented with the 100 low-field images. Previously, their corresponding pairs of disturbed images by aliasing and blurring were obtained. The performance of the experimented models was measured in terms of correlation (NC) and signal to noise ratio (SNR). Table 1 shows the average results obtained by each model in the 4-fold cross-validation scheme. Figure. 3 show some examples of the obtained results for each of the experimented frameworks. As can be seen, all the methods

studied have a good performance in the task of image reconstruction. However, the reconstruction methods that are developed in the k-space obtain a better recovery

Conclusion

The proposed architecture based on semantic genesis demonstrated superior performance than other deep learning methods. This fact, together with its simplicity, allows it to be used in applications with different levels of complexity in the intelligent units of MRI equipment (Consoles, computers, etc). Our group works on the development of tools applicable to the pre-processing and post-processing of noisy MR high and low field images.

Table 1. Results obtained in the 4-fold cross-validation scheme in low field MRI

No.	Exp. scheme	DL.Framew.	SNR _o	SNR _d	SNR _r	Std (SNR _r)	NC	Std (NC)
1	Aliasing	Unet	5.02	4.774	5.525	0.028	0.645	0.003
2		Pix2Pix			6.216	0.161	0.649	0.002
3		Sem.Gen.			6.152	0.003	0.674	0.002
4	Blurring	Unet	6.521	6.521	5.165	0.064	0.683	0.029
5		Pix2Pix			5.816	0.024	0.658	0.005
6		Sem. Gen.			6.349	0.005	0.692	0.004

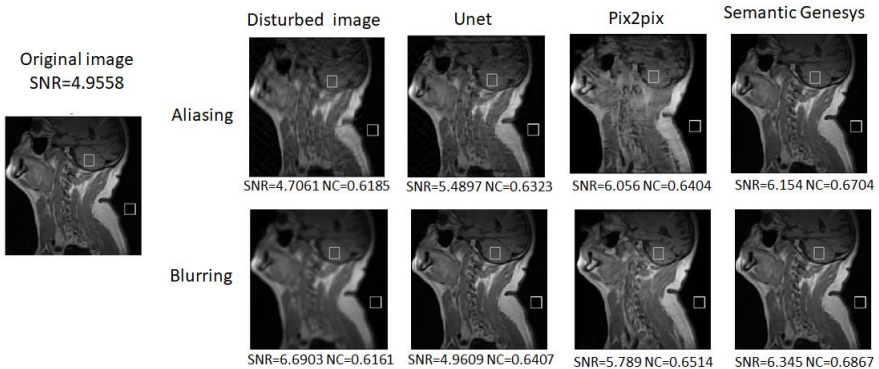


Figure 3. Example, results for each of the experimented frameworks in a low field MRI.

References

- Haghighi, F., et al. (2020). Learning Semantics-Enriched Representation via Self-discovery, Self-classification, and Self-restoration. MICCAI 2020. LNCS, vol 12261. Springer, Cham.
- D. Mehta, D. Padalia, K. Vora and N. Mehendale (2020). MRI image denoising using U-Net and Image Processing Techniques. ICAST, Mumbai, India.
- Hyun C.M. et al. (2018). Deep learning for undersampled MRI reconstruction. Physics in Medicine & Biology.
- Ronneberger, O., Fischer, P., Brox, T (2015). U-Net: Convolutional Networks for Biomedical Image Segmentation. MICCAI 2015. LNCS 9351. Springer, Cham.
- Odena, A.; Olah, C.; Shlens, J. (2017) Conditional image synthesis with auxiliary classifier gans. ICML, Sydney, NSW, Australia.

System to ensure the reproducibility of the legs positions during the Magnetic Resonance Imaging (MRI) studies.

Carlos Cabal Mirabal¹, Evelio Gonzalez Dalmau¹

¹*Cuban Neurosciences Center*
carlos.cabal@cneuro.edu.cu

Introduction

A large set of inflammatory, degenerative, traumatic, infectious, autoimmune, orthopedic, vascular and neurological diseases are affecting the anatomy and physiology of the feet and the lower parts of the legs. The feet diseases disturb in varying degrees the body. There are growing numbers of people during their professional activities (sportsmen, artists, military), that subject the lower extremities, to high stress. Methods of diagnosis of foot diseases and legs are still insufficient. [1]

The majority of MRI reports perform a qualitative assessment of the status of the feet, without giving continuity to the evolution (longitudinal studies), and those that do it, do not show guarantees of making it under equal conditions. In MRI foot studies the main problem is to obtain evolutionary and quantitative information of the several feet diseases, (including inflammatory processes that alter the sizes and relative locations of the anatomical structures) requiring that a fixed and reproducible position be achieved, along the different tests. This is not yet solved problem. [1,2].

In this paper a device for controlling of the feet's orientation with respect to MRI equipment to guarantee its reproducibility is presented. This described device guarantee the feet position reproducibility during successive MRI studies. [2-5].

Materials and Method

Our group have developed a stereotaxic frame (SF) to better assist in reproducibility (Fig. 1).

The device is inserted into a radiofrequency (RF) coil of MRI system (in this case Symphony 1,5T Siemens). Fig. 2. [2]. With the device immobilization and reproducibility of the position of feet and the legs is guaranteed. This device is constructed such that it is mechanically and electromagnetically compatible with MRI equipment. The material for the construction of the device must be rigid, lightweight, not rugged, and resistant to frequent cleanings and disinfections.

To check for any changes in the electromagnetic characteristics of the RF coil (the uniformity and intensity of the RF field, and the quality factor) when going to use the device for the first and only time. MRI were recorded with a phantom before placing, and once placed. There are measured on the MRI phantom, the RF field homogeneity, the signal-to-noise and contrast-to-noise ratios in accordance with NEMA international standards [6].

A cardinal element of the device is shown in Fig.1 with number 7. There are four external markers, which are parallel ampules (containing paramagnetic solution) and at the same level of the supporting surface 1.

Results and discussion

The L_0 distance and it perpendicular segment connecting the two external markers determine exactly one plane. Both distances were measured from sagittal sections of MRI (Fig. 3 D-E). In Table 1 the values of $L1$ and $L2$ are shown, measured on images from 10 healthy volunteers, recorded at two different times, in which the feet were always placed in identical positions. As shown in Table 1, the mean changes $\Delta L1$ and $\Delta L2$ (variation between two successive positions in two different studies), are less than 1 mm. The maximum variation was 6.7% [2].

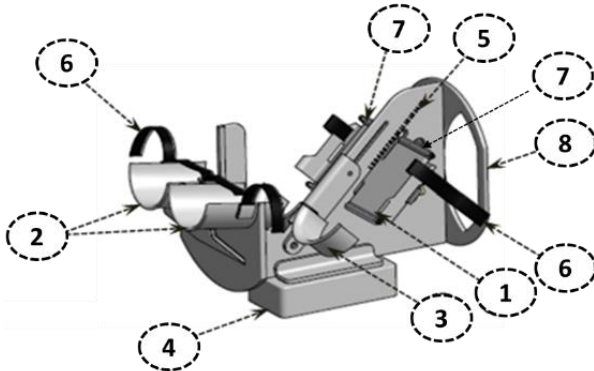


Figure 1. Two support surfaces for the foot (1), so as to secure the position of both feet (2), and let both to be in the same plane, the same orientation, and in the best of homogeneity RF field of the coil. In addition, the device has arches for the heel (3), to ensure the location of the calcaneus of both feet. The heel arches (3) are coated with a soft material. It is shown the base of the device (4) which permits to fix regarding the RF coil, or the patient's bed, as appropriate, according to the MRI model. The support surfaces of the foot (1) slide, and their position is marked according to the scale (5). Fixing bands (6). External markers 7, with a paramagnetic solution. (8) structure support.

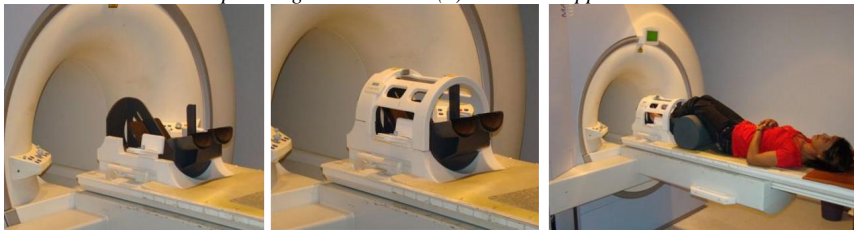


Figure 2. Views of how the frame is placed on the skull RF coil (a and b) and how the patient's extremities are placed in the SF (c)

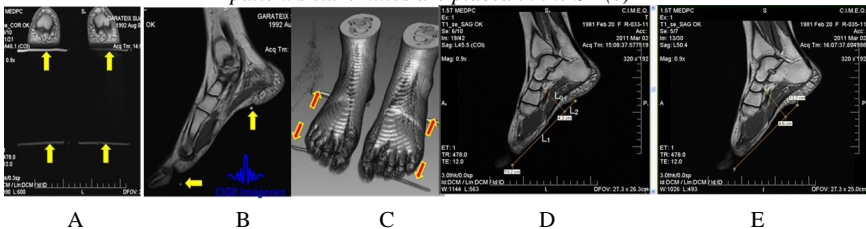


Figure 3. MRI of feet from a healthy volunteer. The external markers are identified using arrows. (A) Coronal slice; (B) sagittal slice; (C) 3D reconstruction. In (D-E) are show Sagittal slices taken at two different times, to the same healthy volunteer. L_1 - L_2 distance between the two external makers and L_2 - L_0 , distance between external and internal marker are controlled in two different scan moments. As an internal marker it was defined an anatomical structure of the foot, in this case have been selected the tocalcaneum interosseum ligament.

Table 1. Feet Correct positioning criteria. Measurements L_1 and L_2 in the sagittal MRI orientation of 10 healthy volunteers studied on two separate occasions.

Volunteer N°		1	2	3	4	5	6	7	8	9	10	
Length (mm)	Study 1 (S_1)	L_1	71	54	58	64	65	69	60	44	68	55
		L_2	13	5	7	7	8	20	16	31	13,5	16
	Study 2 (S_2)	L_1	70	54	57	62	65	69	58	42	66	54
		L_2	13	5	7	7	8	19	15	31	14	17
	Δ between studies ($\Delta L_x = L_{xS1} - L_{xS2}$) $x = 1 \text{ ó } 2$)	ΔL_1	1	0	1	2	0	0	2	3	2	1
		ΔL_2	0	0	0	0	0	1	1	0	-1	-1
% Variation ($\Delta L_x / L_{xS2} * 100$)	ΔL_1	1,4	0	1,8	3,2	0	0	3,4	4,5	3,0	1,9	
	ΔL_2	0	0	0	0	0	5,3	6,7	0	3,6	5,9	

Similarly, the area of the calcaneus of the foot at different heights of the sagittal slice on two different occasions was measured. The root mean square value of the maximum variation was 4.5%. Both results confirm the robustness of the positioning of both feet throughout different MRI studies, which allows following the kinetics of complex processes related to the pathophysiology of the lower extremities [2,5].

The SF has been applied in the quantitative study of DFU under treatment, determining with high precision the kinetics of healing from the variations in the areas and volumes of the lesions, the volume of edema, the variation of the Apparent Diffusion Coefficient (ADC) [2,3].

Conclusion

A device created and validated that guarantees the reproducibility of the positions of both feet longitudinal MRI studies.

Acknowledgements

The authors thank the CIGB plastic workshop, Cuba

References.

1. T. Gorbachova “Magnetic resonance imaging of the ankle and foot” Pol J Radiol. 2020; 85: e 532–e549. doi: 10.5114/pjr.2020.99472
2. C. Cabal Mirabal, et al “Feet Positioning System for MRI studies” US Patent Application Publication US 2016/0157750, 2016.
3. C. Cabal-Mirabal, E. González Dalmau, J. Berlanga Acosta, D. Darias Zayas, et al (2014), “Quantitative Studies of the Evolution of Diabetic Foot Lesions under EGF Treatment by Magnetic Resonance Imaging.” Journal of Radiology Research and Practice Vol. 2014 (2014), Article ID 783980, DOI: 10.5171/2014.783980
4. Cabal Mirabal, C., Fernández García, A., Lores Guevara, M. et al. “Kinetics of Complex Biomedical Problems by Magnetic Resonance. Cuban Experiences”. Appl Magn Reson (2018) pp.1/10 <https://doi.org/10.1007/s00723-018-0985-2>
5. C. Cabal Mirabal, J. Berlanga Acosta, J. Fernández Montequín, L. Oramas Díaz, E. González et al “Quantitative Studies of Diabetic Foot Ulcer Evolution Under Treatment by Digital Stereotactic Photography” Journal of Diabetes Science and Technology, 2019, 1-6 doi.org/10.1177/1932296819853843
6. MS 6-2008; MS 8-2008: “MS 9-2008, NEMA

Cell size dependence of hydrodynamic radius of carboxilane dendrimers in chloroform

Naira R. Gromova,¹ Denis A. Markelov¹

St Petersburg University, 7-9 Universitetskaya Emb., St Petersburg 199034, Russia

E-mail: nai.khus@yandex.ru

Introduction

Dendrimers are multifunctional macromolecules that have unique structures and properties that distinguish them from other classes of polymers. They consist of a central point (core), from which branches of various lengths extend radially, at the ends of which there are functional groups. Currently, dendrimers are attracting more and more attention from researchers and industry in various fields such as medicine, materials science, optics, catalysis, and others. Their unique properties, such as controlled size and shape, high functionality, and the possibility of modification, make dendrimers promising objects for creating new materials and drugs, as well as for various biotechnological applications.

Since dendrimers are rather large macromolecules that have a complex branching structure, even the main method of their study, computer simulation, still faces a number of problems, such as the need to accumulate a large amount of data, longer simulation time (on the order of microseconds with step of femtoseconds).

We study chloroform solution CSD dendrimer of fourth generation ($G = 4$) at 300 K by molecular dynamics (MD) simulations.

Computer simulation details and results

Detailed description of the atomic model, the modeling method, including procedures for preparing and balancing the system, for dendrimers are given in [1].

Simulation cells with single CSD dendrimer of 4th generation and different number of molecules of chloroform were simulated. Periodic boundary conditions and the force field Gromos53a6 were used in the Gromacs 2021.4 package[2]. The equilibration of dendrimer was carried out for 200ns. And after the MD simulations were continued for 3000 ns to collect data to calculate system performance. Main simulations were performed in the NPT ensemble using Berendsen barostat and V-rescale thermostat (B/V pair) [3]. Additionally, simulation were carried out in the NPT ensemble using Nose–Hoover (NH) thermostat - Rahman (PR) barostat [4].

After simulation in cells of various sizes, hydrodynamic radii, R_h , were calculated using various methods: through the coefficient of translational and rotational diffusion (1,2). As well as using formula (3) proposed in ref. [5] to correct the influence of boundaries on the calculation of the diffusion coefficient and, accordingly, hydrodynamic radius.

$$R_h = \frac{k_B T}{6\pi\eta_{sol} D} \quad (1)$$

$$R_h = \left(\frac{3\tau_{rot} k_B T}{4\pi\eta_{(sol)}} \right)^{1/3} \quad (2)$$

$$D_L \approx D_{MD} + 2.837 \frac{k_B T}{6\pi\eta_{sol} L} \quad (3)$$

The results were presented in the form of the dependence of the hydrodynamic radius values on the cell size. It is worth noting here that the 11 nm cell was chosen as the most efficient - large enough to avoid boundary effects and at the same time not too slowing down and complicating the calculations due to the multiple increase in solvent molecules (8000 chloroform molecules).

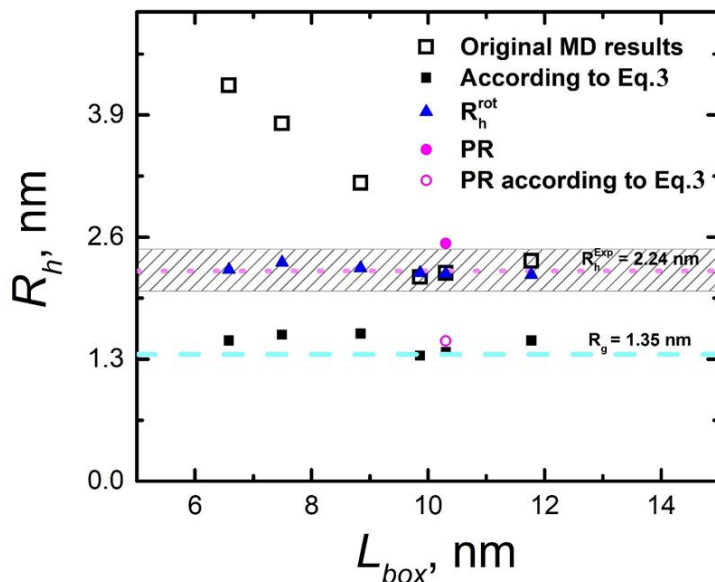


Figure 1. R_h calculated from diffusion coefficients obtained by different methods (see legend) depending on simulated box sizes, experimental range of R_h ($R_h \pm 10\%$) is indicated by shading. For reproduction of material from [1]. —Published by the PCCP Owner Societies

The figure (1) shows the values calculated through the MSD and the Einstein equation, using rotational diffusion, and also the values marked with circles were obtained by the first and second methods, but when modeling with the Parrinello-Rahman barostat. It can be seen in the figure that the hydrodynamic radius differs significantly from both the experimental and calculated using rotational diffusion, but it is noticeable that the parameters fall into the general range of values with a small difference, hence the idea that this formula can work when the coefficient changes.

Conclusions

Thus, we simulated the fourth generation of a carbosilane dendrimer in a chloroform solution under different conditions, including different cell sizes (from 7 to 12 nm), different barostats and thermostats. Afterwards, different calculation methods were used - translational and rotational diffusion and a formula for taking into account the cell size. The closest to the experimental values were the hydrodynamic radii calculated using the rotational diffusion

method, as well as those calculated using the Stokes-Einstein formula, but only for box sizes above 10 nm (10 times the gyration radius).

Acknowledgements

This work is supported by the Russian Science Foundation (grants no. 23-13-00144). The simulations were performed at the Computer Resource Center of Saint Petersburg State University.

References

1. Khusnutdinova N.R., Markelov D.A. Hydrodynamic radius of dendrimers in solvents // Phys. Chem. Chem. Phys. The Royal Society of Chemistry, 2023. Vol. 25, № 41. P. 28220–28229.
2. Abraham M.J. et al. Gromacs: High performance molecular simulations through multi-level parallelism from laptops to supercomputers // SoftwareX. 2015.
3. Berendsen H.J.C. et al. Molecular dynamics with coupling to an external bath // J Chem Phys. 1984.
4. Parrinello M., Rahman A. Crystal structure and pair potentials: A molecular-dynamics study // Phys Rev Lett. 1980.
5. Dünweg B., Kremer K. Molecular dynamics simulation of a polymer chain in solution // Journal of Chemical Physics. 1993. Vol. 99. P. 6983–6997.

Molecular and ionic mobility of ionic liquids with complex anions containing metals

Alexander V. Ievlev, Konstantin V. Tyutyukin, Nadezhda V. Pokhyishcheva
 Department of Nuclear Physics Research Methods, Saint Petersburg State University,
 St. Petersburg State University, St. Petersburg 198504 Russia
 E-mail: a.ievlev@spbu.ru

Introduction

In continuation of a series of works [1], [2] on the study of molecular mobility in ionic liquids with complex anions containing metals based on 1 butyl, 3 methyl imidazolium thiocyanate, this work will consider the influence of the metal forming the complex anion on the mobility of anions and cations, as well as on others physicochemical properties of IL.

Results and discussions

Spectra

The first figure shows a set of carbon spectra showing how the position of the carbon line included in the thiocyanate changes depending on the metal that acts as the center of the complex anion; in addition, for comparison, the spectrum of the basic [Bmim⁺] [SCN⁻] is given. For convenience, only the range of chemical shifts related to the imidazole ring is given. It is in this interval that the carbon line in the thiocyanate ion can be observed, due to the influence of the nitrogen atom associated with it by a triple bond. Depending on the metal, the thiocyanate line can be observed both to the right and to the left of the standard position in the base IL. The remaining lines of the spectrum practically do not change their position, except for carbon, which is located between two nitrogen atoms in the imidazole ring, which accounts for the main charge of the cation electrostatically interacting with the complex anion.

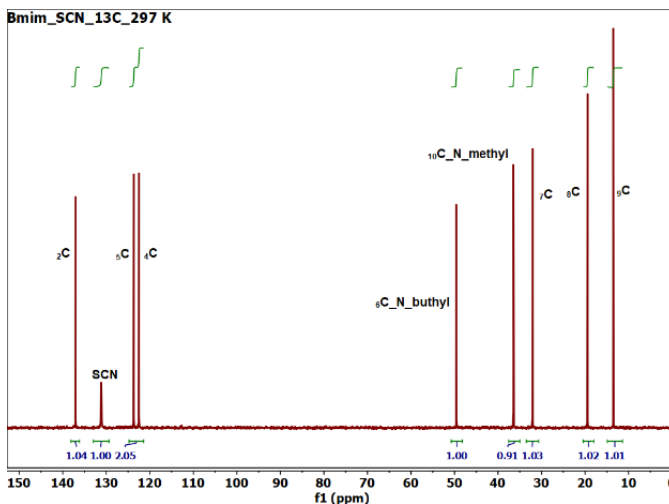


Figure 1. ^{13}C spectrum for pure IL Bmim⁺ SCN⁻.

Figure 1 shows, the complete carbon spectrum of the pure ionic liquid 1-butyl, 3-methyl imidazolium thiocyanate, which was used as a base for the synthesis of a series of

ionic liquids with complex anions. As can be seen from figure 2, it is quite convenient to simultaneously survey the carbon of both in the cation and the anion.

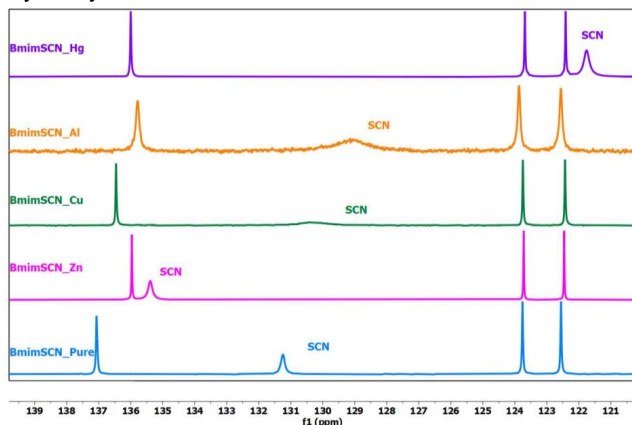


Figure 2. Stack of ^{13}C spectra for ILs based on the Bmim^+ cation with complex anions, which include SCN and various metal ions.

The data was received on the Bruker Avance III NMR spectrometer 500 MHz (^1H) at frequency 125.8 MHz (^{13}C).

Diffusion

In table 1 you can see that the mobility of the anion in the main liquid is higher than the mobility of the cation, which is explained by their size. In the case of complex anions, the situation is the opposite, since the size of the anion increases sharply, while the size of the cation remains unchanged.

Table 1. Summary data on diffusion coefficients at a temperature of 298 K, measurements at ^{13}C are given.

Sample	Line position in the carbon NMR spectrum 2, 4, 5 numbers of carbon atoms in the imidazole ring (ppm)				$D_{\text{Bmim}}/D_{\text{SCN}}$	$D \cdot 10^{12}, \text{m}^2 \cdot \text{s}^{-1}$	
	(2) C	(4) C	(5) C	SCN		Bmim^+	SCN^-
$\text{Bmim}_2\text{Hg}(\text{SCN})_4$	136,01	123,69	122,41	121,76	1,5	15,01	10,08
$\text{Bmim}_3\text{Al}(\text{SCN})_6$	135,78	123,88	122,58	129,16	4,9	0,93	0,19
$\text{Bmim}_3\text{Cu}(\text{SCN})_4$	136,46	123,75	122,43	130,28	1,3	7,52	5,86
BmimSCN	137,07	123,76	122,56	131,25	0,4	16,42	38,71
$\text{Bmim}_2\text{Zn}(\text{SCN})_4$	135,96	123,72	122,46	135,39	2,6	11,93	4,52

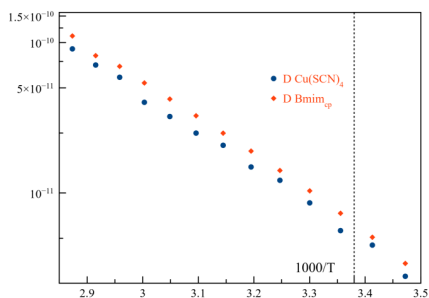


Figure 3. Temperature dependence D of anion and cation in complex with copper.

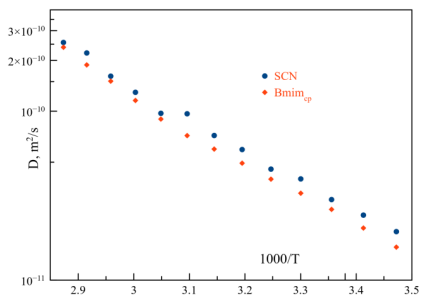


Figure 4. Temperature dependence D of anion and cation in the base IL $BmimSCN$.

Comparing the data from figures 3 and 4, it is easy to verify that the thiocyanate ion actually forms a stable complex with the metal, since in the base IL its mobility is greater than that of the cation, and in the complex it is already much lower, which confirms the data previously obtained for complexes with Al and Hg [2] in both cases, a very stable anionic complex is formed from thiocyanate and metal ions, the mobility of which slows down compared to the cation by 1.5 and 3.9 times for the complex with mercury and aluminum, respectively. This directly gives us information about the change in the size of the anion from the relatively small thiocyanate to a large complex ion with a coordinating metal in the center.

Conclusions

Using the data obtained on the mobility of ions in the described series of samples, we can predict changes in physicochemical properties in similar systems.

Acknowledgements

This work is supported by Russian Science Foundation (RSF): grant № 23-23-00430. Thanks to the staff of Center for Magnetic Resonance of Research Park of St. Petersburg State University for fast and high-quality measurements.

References

1. A. V. Ievlev, A. V. Koroleva, K. V. Tyutyukin, V. V. Matveev, O. Cabeza, and L. M. Varela, "NMR and X-ray photoelectron spectroscopy possibilities for study complex ionic liquids," in *MAGNETIC RESONANCE AND ITS APPLICATIONS*, Saint-Petersburg: St. Petersburg University Publishing House, 2020, pp. 89–91.
2. O. Cabeza *et al.*, "Strange behaviour of transport properties in novel metal thiocyanate based ionic liquids," *J. Mol. Liq.*, vol. 340, p. 117164, Oct. 2021, doi: 10.1016/J.MOLLIQ.2021.117164.

The Role of Rotational Motion in Diffusion NMR Experiments on Supramolecular Assemblies

Boris B. Kharkov¹, Ivan S. Podkorytov¹, Stanislav A. Bondarev², Mikhail V. Belousov^{2,3}, Vladislav A. Salikov¹, Galina A. Zhouravleva², Nikolai R. Skrynnikov¹

¹ *Laboratory of Biomolecular NMR, St. Petersburg State University, St. Petersburg 199034, Russia*

² *Department of Genetics and Biotechnology, St. Petersburg State University, St. Petersburg 199034, Russia*

³ *Laboratory for Proteomics of Supra-Organismal Systems, ARRIAM, St. Petersburg 196608, Russia*

E-mail: b.kharkov@spbu.ru

Introduction

Pulsed-field gradient NMR is an important tool to measure diffusion of proteins and protein assemblies and thus obtain insight into their structure and dynamics. For extended objects, such as amyloid fibrils, these experiments become difficult to interpret because in addition to translational diffusion they are also sensitive to rotational diffusion.

We have constructed a mathematical theory describing the outcome of PFG NMR experiments on rod-like fibrils. The analytical results proved to be in excellent agreement with the predictions from our random walk Monte-Carlo simulations. The effect of rotational diffusion is indeed significant, accounting for up to 30% of the diffusion-induced signal loss. However, just like translational diffusion, rotational diffusion of heavy fibril particles is a slow process and registers as such in the PFG NMR experiments. Contrary to certain literature claims, this allows one to separate spectral signals from fibrils and other species that may be present in the sample (monomers, proteolytic fragments, etc.) based on their different diffusion properties.

Results

To test the validity of our theory, we have studied fibrils formed by Sup35NM fragment derived from yeast translation termination factor Sup35. The M-domain of Sup35NM when molecules are stacked in a fibril remains highly mobile and flexible, which makes it possible to observe spectral signals from the fibrils by means of solution-state NMR. As usually the case in most practical applications, along with fibrils, the sample also contains a small fraction of proteolytic fragments, as schematically illustrated in Figure 1A. The fibril lengths in the sample are not uniform and typically follow the log-normal distribution. Fibril length histogram (blue bars) obtained by processing of the TEM images is shown in Figure 1B. The results of an NMR diffusion experiment on this sample are shown in Figure 1C. The experimental data have been fitted using our new theory [1] that considers the effect of rotational motion of fibrils taking into account the distribution of fibril diffusion properties due to length variation. Furthermore, the fit accounts for the presence of 11% of small-size soluble fragments broadly resembling the M-domain of Sup35NM. The amount of proteolytic fragments was confirmed with SDS-PAGE. Notably, no adjustable parameters were used in the fitting of NMR diffusion data and the theoretical curve is fully predicted from the known sample characteristics.

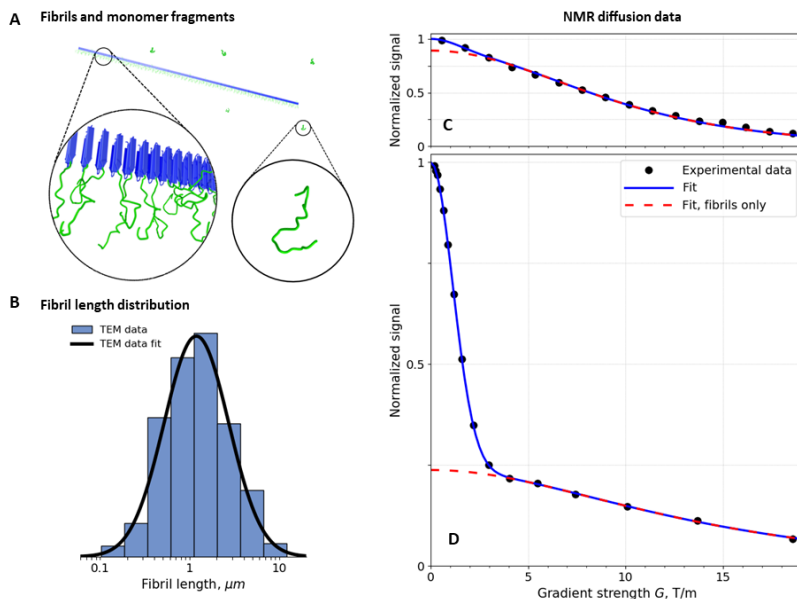


Figure 1. (A) Fibrils and proteolytic fragments coexist in Sup35NM sample. (B) Fibril length distribution as obtained from TEM images. (C) Data from STE measurements on the sample of Sup35NM fibrils fitted by means of the new theory. (D) Data from STE measurements on another sample of Sup35NM fibrils spiked with recombinant Sup35M.

To further address the presence of the rapidly diffusing species, we have spiked the sample of Sup35NM fibrils with recombinant Sup35M. The STE diffusion data from this sample are shown in Fig. 1D. The fast diffusion component is prominent in this graph, suggesting that various versions of diffusion ordered spectroscopy [2] can be readily implemented for multicomponent samples containing amyloid fibrils. This should facilitate future NMR studies of complex and intricate molecular processes underlying protein amyloidogenesis

Acknowledgements

The authors acknowledge Saint-Petersburg State University for a research project 116883049.

References

1. Kharkov B.B., Podkorytov I.S., Bondarev S.A., Belousov M.V., Salikov V.A., Zhouravleva G.A., Skrynnikov N.R. *Angew. Chem. Int. Ed.* 60, 15445-51 (2021).
2. Johnson C.S. *Prog. NMR Spectrosc.* 34, 203-56 (1999).

SLIC-SABRE at Earth's Magnetic fields: Simple and Effective Method of getting Strong ^{15}N NMR Polarization

Alexey Kiryutin^{1,2}, Vitaly Kozinenko^{1,2}, Alexandra Yurkovskaya¹

¹International Tomography Center SB RAS, Institutskaya Str. 3A, Novosibirsk, 630090, Russia

²Novosibirsk State University, Pirogova Str. 2, Novosibirsk, 630090, Russia

E-mail: kalex@tomo.nsc.ru

Introduction

Parahydrogen induced polarization (PHIP) stands out among various NMR hyperpolarization techniques due to its versatility and cost-effectiveness, offering significant signal enhancement for NMR spectroscopy. Unlike dynamic nuclear polarization (DNP), PHIP utilizes parahydrogen (pH_2), a form of H_2 with zero nuclear spin, to transfer non-equilibrium spin order to the target substrate magnetization. In the SABRE (Signal Amplification By Reversible Exchange) approach, this conversion occurs during the reversible coordination of pH_2 and substrate at specialized organometallic Ir-complexes. Efficient polarization transfer to substrate nuclei can be achieved using radiofrequency (RF) excitation at high magnetic field or low/ultralow (mT/ μT) static magnetic field. Despite advancements in high-field SABRE, low and ultralow-field methods were found to be more reliable and efficient, thus preferable for research.

In practice, ^{13}C or ^{15}N nuclei of the substrate molecule are commonly targeted for polarization transfer due to background-free detection and their ability to retain magnetization for minutes, crucial for in vivo studies. Spontaneous polarization transfer from pH_2 to these isotopes typically occurs at magnetic field range, significantly lower than Earth's magnetic field (tens of μT). By SHEATH-SABRE (SABRE in shield enables alignment transfer to heteronuclei) it is possible to achieve polarization transfer within a specialized magnetic shield, enabling to control magnetic fields below microtesla levels. For over a decade, SHEATH-SABRE was the most efficient technique¹. However, recently it has been shown that polarization transfer by a weak oscillating transverse field resonant with the heteronuclear spin in a static field of around 50-100 microtesla gives similar or even better results than SHEATH-SABRE². This approach is very similar to the methods of low irradiation at high field or spin-lock induced crossing- (SLIC-)SABRE, but without the adverse effects of the high field, such as singlet-triplet conversion and the necessity of selective irradiation of the bound and free substrate. LF-SLIC-SABRE has only been used for enhancing polarization in ^{13}C nuclei of pyruvate³.

Results and Discussion

We report the first result of the application of LF-SLIC-SABRE method with substantially high levels of ^{15}N polarization at a field of 100 μT without sophisticated magnetic field shielding. Our simple and easy approach utilizes a homemade device that costs less than 100\$ comprising magnetic coils for generating static longitudinal field and oscillating transverse field. We tested two approaches for SLIC-SABRE – with resonant and slightly off-resonant excitation of the heteronuclear spin. We tested new approach with pyridine and biocompatible substrates (metronidazole, tinidazole, secnidazole, and ornidazole) for SABRE. SLIC-SABRE approach reproducibly yields two-fold increase in polarization levels compared to SHEATH-SABRE.

To perform SABRE experiments at low field we utilized a self-made device, consisting of two Z coils for creating static field (for adjusting and for gradient compensating) and two X,Y coils for applying oscillating transverse field (Fig. 1A). The coils are hand-wound on a 3D-printed plastic frame. The design of this SLIC-device allows generating static magnetic fields around hundreds of microtesla with good homogeneity and apply oscillating transverse

fields of the desired configuration. The current generating the transverse field was produced with an integrated sound card of the desktop computer without any further amplification. This approach ensures the high quality of the applied pulses, although at the cost of their power. Thus, the maximum achievable B_1 field was equal to around $10 \mu\text{T}$. The polarization of the transverse field was circular, which provided with the additional factor of two in the B_1 amplitude, as compared to linear polarization. To optimize the SLIC-SABRE experiments we fixed the B_0 field in the polarization creation region equal to $97 \mu\text{T}$ (420 Hz of ^{15}N Larmor frequency) and varied the frequency and the amplitude of the SLIC pulse. To transfer the sample between the SLIC coils above the cryomagnet and the NMR probe, we used a motorized sample shuttling and parahydrogen bubbling setup described previously.

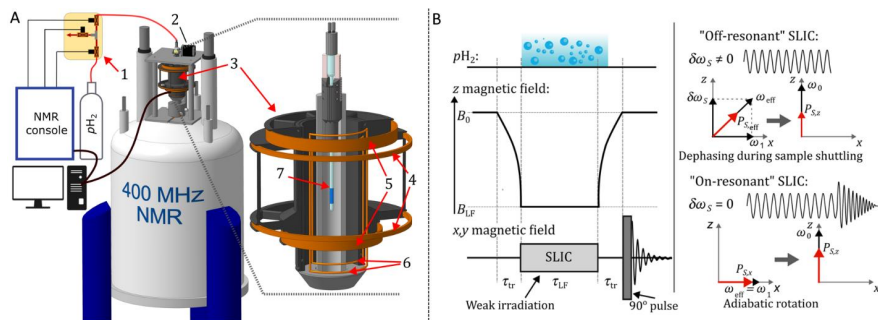


Fig. 1. (A) Experimental setup for SLIC-SABRE at low field: (1) automated $p\text{H}_2$ bubbling unit, controlled by a standard NMR console, (2) stepper motor for sample shuttling, (3) self-made device for performing LF-SLIC-SABRE, (4) Helmholtz coil for the static Z magnetic field, (5) "anti-Helmholtz" coil compensating the Z field gradient, (6) saddle-shaped coils generating the oscillating transverse field, (7) NMR sample. (B) Experimental scheme of LF-SLIC-SABRE (left). Protocols for the "off-resonant" and "on-resonant" variants of SLIC-SABRE (right).

The LF-SLIC-SABRE experiment involved: (1) relaxation at high field, (2) sample transfer to a low field area, (3) bubbling $p\text{H}_2$ while irradiating with a transverse field, (4) returning to the high field for spectrum detection using a nonselective RF pulse (Fig. 1B left).

There are two ways of harnessing SLIC pulse in SABRE experiments (Fig. 1B right). In the first approach, hereafter referred to as "off-resonant", the pulse is applied with a small detuning from the resonance of the target heteronuclei, which leads to the creation of polarization along the effective field, which has non-zero components both along the static field B_0 and the oscillating B_1 field. In contrast to high-field experiments, at low magnetic fields the Larmor frequencies of the heteronuclei in the bound and free forms of the substrate coincide, which allows accumulating the polarization along the effective field in the free form. In the second approach, called "on-resonant", the SLIC pulse frequency exactly equals the Larmor frequency and the polarization build-up occurs along the B_1 field. By varying the amplitude and frequency of the SLIC excitation to leave the resonance condition, this polarization can be adiabatically rotated coaxially with the static field. This allows preserving the entire created polarization when the sample is transferred to the high field, making the "on-resonant" approach more effective than the "off-resonant". However, the experimental procedure for "off-resonant" SLIC-SABRE is more straightforward, as it requires only a CW pulse, without any amplitude or frequency sweep.

As a reference for assessing the efficiency of SLIC-SABRE we measured the magnetic field dependence of ^{15}N polarization in SHEATH-SABRE experiments. As a result, the maximum polarization for protonated pyridine was equal to 10%, while for deuterated compound it was only 7%. In “off-resonant” SLIC method with the nutation frequency of the SLIC pulse equal to 15 Hz the maximum ^{15}N polarization of protonated pyridine increases up to 12.4%. For deuterated pyridine “off-resonant” SLIC performs even better, providing 14% polarization with 5 Hz SLIC pulse. The dependence of the resulting polarization on the SLIC frequency has an antisymmetric shape with two maxima, occurring when the effective field fulfils the LAC condition: $\omega_{S,\text{eff}} = 2\pi J_{12}$. However, one should notice that chemical exchange in SABRE method affects the coherent spin dynamics, shifting the optimal LAC conditions. Utilizing “on-resonance” variant of SLIC method with 25 Hz nutation frequency allowed us to obtain 16.2% polarization for protonated pyridine and 12.2% for deuterated one. As expected, the SLIC frequency dependence in that case has a single maximum, corresponding to zero detuning from the ^{15}N resonance. To sum up, for protonated pyridine both variants of SLIC-SABRE provide higher ^{15}N polarization than SHEATH-SABRE, with “on-resonant” SLIC excitation being advantageous to “off-resonant”.

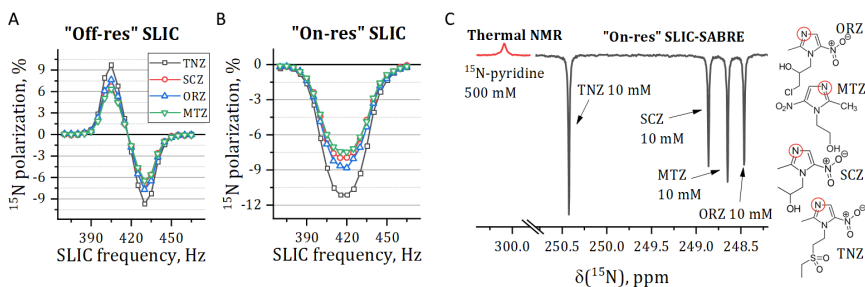


Fig. 2. Dependence of ^{15}N polarization on the frequency B_1 field in SLIC-SABRE experiment for ornidazole (ORZ), metronidazole (MTZ), secnidazole (SCZ) and tinidazole (TNZ) for “off-resonant” (A) and “on-resonant” (B) SLIC. $^{15}\text{N}\{1\text{H}\}$ NMR spectra of the sample after performing “on-resonant” SLIC-SABRE. The thermal NMR spectrum (red) of 500 mM of ^{15}N labelled pyridine, used as a reference (C). The sample contains 10 mM of each of the substrates, 100 mM $\text{DMSO-}d_6$ and 2 mM of SABRE catalyst dissolved in 500 μL of methanol- d_4 .

We also performed experiments on polarization of ^{15}N nuclei with the equimolar (10mM) mixture of four compounds: metronidazole (MTZ), tinidazole (TNZ), secnidazole (SCZ), and ornidazole (ORZ) on the natural abundance of ^{15}N isotope. These compounds are used as antimicrobial drugs, they all have similar structure and are suitable substrates for SABRE experiments. However, the chemical shifts of the ^{15}N nuclei of these molecules differ in both free and bound forms. Performing SLIC-SABRE experiments at 100 μT field we created remarkably high polarization of ^{15}N nuclei for mixture of them. (Fig. 2). The highest polarization was observed for tinidazole, which can be caused by the better matching conditions between the exchange rate and spin coupling of ^{15}N and hydride protons withing the active complex for this compound. As in the experiments with pyridine, the “on-resonant” variant of the SLIC method (plot B in Fig 3) allowed us to achieve noticeably greater polarization than the “off-resonant” (plot A in Fig.3).

Acknowledgements

This work was supported by the Russian Science Foundation (project #23-73-10103)

References

1. Kiryutin, A. S.; Yurkovskaya, A. V.; Ivanov, K. L., ^{15}N SABRE Hyperpolarization of Metronidazole at Natural Isotope Abundance. *ChemPhysChem* **2021**, *22* (14), 1470-1477.
2. Pravdivtsev, A. N.; Buckenmaier, K.; Kempf, N.; Stevanato, G.; Scheffler, K.; Engelmann, J.; Plaumann, M.; Koerber, R.; Hövener, J.-B.; Theis, T., LIGHT-SABRE Hyperpolarizes $1\text{-}^{13}\text{C}$ -Pyruvate Continuously without Magnetic Field Cycling. *J. Phys. Chem. C* **2023**, *127* (14), 6744-6753.
3. de Maissin, H.; Groß, P. R.; Mohiuddin, O.; Weigt, M.; Nagel, L.; Herzog, M.; Wang, Z.; Willing, R.; Reichardt, W.; Pichotka, M.; Heß, L.; Reinheckel, T.; Jessen, H. J.; Zeiser, R.; Bock, M.; von Elverfeldt, D.; Zaitsev, M.; Korchak, S.; Glöggler, S.; Hövener, J.-B.; Chekmenev, E. Y.; Schilling, F.; Knecht, S.; Schmidt, A. B., In Vivo Metabolic Imaging of $[1\text{-}^{13}\text{C}]\text{Pyruvate-d}_3$ Hyperpolarized By Reversible Exchange With Parahydrogen. *Angewandte Chemie International Edition* **2023**, *62* (36), e202306654

In vivo MR imaging of murine bronchial tree using hyperpolarized propane produced with parahydrogen

Elizaveta S. Kononenko^{1,2}, Alexandra I. Trepakova^{1,2}, Oleg B. Shevelev^{1,3}, Larisa M. Kovtunova^{1,4}, Dudari B. Burueva¹ and Igor V. Koptiyug¹

¹ International Tomography Center, SB RAS, Novosibirsk 630090, Russia

² Novosibirsk State University, Novosibirsk 630090, Russia

³ Institute of Cytology and Genetics, SB RAS, Novosibirsk 630090, Russia

⁴ Boreskov Institute of Catalysis, SB RAS, Novosibirsk 630090, Russia

E-mail: elizaveta.kononenko@tomo.nsc.ru

Introduction

Lung diseases are among the main mortality factors in the world. In the context of public health, early diagnosis of lung diseases becomes crucial. Traditional diagnostic methods such as computed tomography (CT) and spirometry, due to several limitations, cannot detect diseases at early stages. While spirometry is completely safe for humans, it cannot provide information about the internal structure of the lungs. For this purpose, CT is utilized, which uses ionizing radiation, limiting its applicability for tracking the disease progression. Magnetic resonance imaging (MRI) is a safe alternative method. It can provide information about morphological changes in the lungs and ventilation without exposure of the body to ionizing radiation. [1] Nowadays, there are several contrast agents for obtaining lung MRI with image quality comparable to CT, e.g., noble gases hyperpolarized by spin-exchange optical pumping (SEOP). However, contrast agents hyperpolarized by SEOP could not become widespread due to the complexity and high cost of the additional equipment. To overcome these limitations, the development of new methods is of considerable interest. In this work we present an approach that relies on parahydrogen-induced polarization via heterogeneous catalysts (HET-PHIP) for creating a contrast agent compatible with in vivo studies. This method does not require complex equipment for obtaining hyperpolarized gas. And in contrast to SEOP, in PHIP the polarization is observed on ¹H nuclei, eliminating the need for additional coils tuned to heteronuclei. A promising gaseous contrast agent that can be created by HET-PHIP is propane (C₃H₈). [2] In this work, we present an approach for creating hyperpolarized propane for lung contrast in MR images, which is compatible with in vivo studies.

Setup optimization

For in vivo experiments, it is important to design a catalytic reactor that ensures stable long-term operation. Gas pressure, temperature, and catalyst loading were optimized for this purpose. Also, for continuous and stable operation, the gas system for premixing and supplying the gas mixture to the reactor was improved. For a more efficient heat transfer and to avoid compaction and sintering of the catalyst, silicon carbide and copper granules were added to the catalyst layer. This made it possible to achieve conversion of propylene to propane up to 97±3% with a 7-fold increase in signal intensity by hyperpolarization. For in vivo experiments, the oxygen is needed in the gas mixture; therefore, we made sure that there was no dramatic effect of oxygen and anesthetic (isoflurane) on the signal intensity of hyperpolarized propane.

To obtain MR image, we chose a pulse sequence based on a gradient echo with the breath cycle synchronization. The signals of the CH₂- and CH₃-groups of propane produced by PHIP have the opposite signs; their mutual cancellation was avoided due by a proper choice of the time delay between the excitation RF pulse and signal acquisition (TE).

MRI results

In this work, for the first time, we demonstrate *in vivo* ^1H MR visualization of hyperpolarized propane in the mouse lungs (Fig. 1 A). The utilization of propane allowed us to observe the bronchial tree of the lungs, which was not possible with the use of conventional ^1H MRI (Fig. 1 B). To assess the clarity of the bronchial tree area of interest, the contrast-to-noise ratio (CNR) was calculated. The area with the visible signal from the bronchial tree was highlighted (Fig. 1 C and D). In our case the CNR of MR image obtained with air is 0.1, it indicates the absence of any signal in the region of interest. At the same time, the CNR of the image obtained with hyperpolarized propane is equal to 7.5, which indicates a sufficient amount of signal in the area of the bronchial structure.

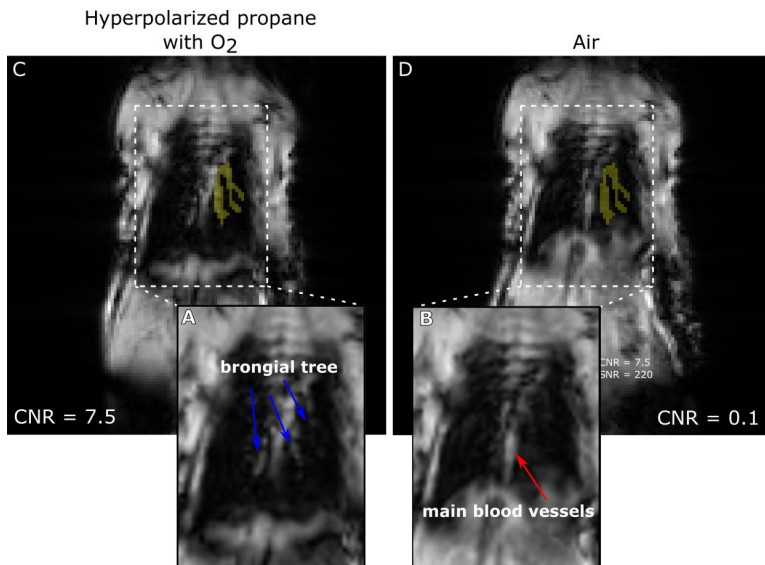


Figure 1. ^1H MRI of a mouse upon inhalation of the mixture of hyperpolarized propane and O_2 (A) and air only (B). MRI of a mouse upon inhalation of the mixture of hyperpolarized propane and O_2 and only air with the highlighted area of the bronchial tree (C) and (D), respectively. Number of averages was 32, TE was 2.5 ms, acquisition matrix was 128×128 , field of view was $4 \times 4 \text{ cm}^2$, slice thickness was 3 mm, delay between trigger and RF pulse was 100 ms, flip angle was 90° , receiver gain was 101.

The performed study is an essential step for implementation of PHIP-hyperpolarized propane for *in vivo* MRI studies. In this study, we obtained images with $\text{CNR} \sim 10$ with the use of hyperpolarized propane. This value is enough for further improvements of the MRI image quality and content that will allow performing more detailed visualization of the respiratory system structure at different stages of breathing.

Acknowledgements

This work was supported by the Russian Science Foundation (grant # 23-23-00394).

References

1. J. Biederer, Y. Ohno et al. *Eur. J. Radiol.* 2017, 86, 353–360.
2. N. M. Ariyasingha, A. Samoilenko et al. *ACS Sensors* 2023, 8, 10, 3845–3854.

The ^1H NMR spectroscopy in the study of the interaction of membrane proteins of enveloped viruses and potential antiviral agents

Polina A. Kononova^{1,4}, *Olga Yu. Selyutina*^{1,2}, *Nikolay E. Polyakov*^{1,2}, *Vladislav V. Fomenko*³,
*Nariman F. Salakhutdinov*³

¹ Voevodsky Institute of Chemical Kinetics and Combustion, Novosibirsk, Russia

² Institute of solid state chemistry and mechanochemistry, Novosibirsk, Russia

³ Vorozhtsov Institute of Organic Chemistry, Novosibirsk, Russia

⁴ Novosibirsk State University, Novosibirsk, Russia

E-mail: kononova_polina@bk.ru

Introduction

The viruses that have caused the most recent major outbreaks—Middle East respiratory syndrome (2012), Ebola hemorrhagic fever (2014), Zika fever (2015), COVID-19 (2019) are enveloped. The lipid membrane of the virion is a potential target for antiviral drugs, as it plays a critical role in the fusion of the viral and cellular membranes. Moreover, a promising approach is to study the ways in which conserved transmembrane domains of viral envelope proteins are affected.

SARS-CoV-2 is an enveloped single-stranded (+)RNA virus. Like other coronaviruses, SARS-CoV-2 has four structural proteins known as proteins S, E, M and N; the N protein contains the RNA genome, and the S, E and M proteins together create the viral envelope. Inhibition of E protein reduces viral pathogenicity, suggesting that E protein is a potential antiviral target. The SARS-CoV-2 E protein consists of three domains: a transmembrane domain (TMD), an intermediate helical domain, and an N- and C-terminal domain. The E protein forms a homopentameric cation channel in the lipid membrane, which is important for the pathogenicity of the virus. The E-protein TMD was used in this work.

Glycyrrhizic acid (GA) is a triterpene saponin from licorice root (*Glycyrrhiza glabra*), an amphiphilic molecule. GA and its derivatives are promising biologically active compounds for the creation of broad-spectrum antiviral agents. In this work, GA and GA derivatives (glycivir) obtained by acylation with nicotinic acid were studied. Glycivir is a multicomponent mixture containing mainly mono-, di-, tri- and tetranicotinates. There is data on the activity of GA and glycivir against SARS-CoV-2 in vitro.

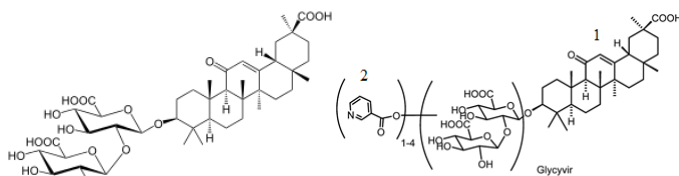


Figure 1. Glycyrrhizic acid and Glycivir.

Methods

The studies were carried out on a model of a lipid membrane - lipid bicelles (disc-shaped model of a biomembrane). Classic bicelles were used - a mixture of DMPC (dimyristoylphosphatidylcholine) and DHPC (dihexanoylphosphatidylcholine) in a ratio 1:1.

NMR spectroscopy methods were used in this work. Using the selective Nuclear Overhauser Effect Correlation Spectroscopy (sNOESY) method, the spatial proximity (<0.5 nm) of different groups of atoms was studied. Changes in mobility were assessed by changes in relaxation times (T_1). ^1H NMR and sNOESY spectra were recorded in D_2O on a Bruker

Avance HD III NMR spectrometer (500 MHz ^1H operating frequency). T_1 relaxation times were measured using a standard inversion-recovery pulse sequence. NMR spectra were processed in the TopSpin software. These methods allow one to determine the localization and distribution of molecules in membranes. In the present study, we applied this method to study the interaction of GA/Glycyvir and ETM with bicelles. During the measurements, the temperature was kept at 303 K.

Results

It was found that at pH 3 GA was located inside the lipid bilayer, whereas at pH 7.4 GA was located on the surface of the bilayer. Selective NOESY showed the effect of the transmembrane domain of the coronavirus E-protein on the localization of GA in the lipid bilayer. The presence of the transmembrane domain of the coronavirus contributes to the deep penetration of GA into the center of the bilayer at both acidic and neutral pH. In addition, ETM promotes self-association of GA molecules, and phenylalanine residues interact with GA inside the lipid bilayer at a neutral pH. GA, in turn, affects the localization of ETM inside the lipid bilayer. Moreover, GA affects the mobility of ETM protons inside the bilayer. Changes in the mobility of the transmembrane domain can affect the activity of the E-protein. It was found that in all cases there was a mutual influence of GA and ETM on their localization, while direct interaction of GA and ETM was observed only at a high concentration of ETM at pH = 7.4. Thus, the presence of GA leads to the movement of phenylalanine protons from the center of the bilayer to its surface.

It has been shown that the glycyvir molecule is anchored in the lipid membrane by nicotinic acid residues in both protonated and deprotonated states. In the presence of ETM, the terpene moiety of glycyvir is also immersed in the lipid bilayer. A mutual influence on the localization of the E protein of SARS-CoV-2 and glycyvir was also observed. The presence of ETM leads to deeper penetration of the glycyvir molecule into the bilayer, and the presence of glycyvir, in turn, leads to deeper immersion of ETM into the lipid bilayer. No specific interaction of glycyvir with ETM was detected. The ETM pentamer is oriented parallel to the bilayer normal, and the phenylalanine residue is located in the middle of the bilayer, while in the monomeric form of TMD the phenylalanine residue is displaced towards the bilayer surface.

Discussion and Conclusions

The interaction of the transmembrane domain of SARS-CoV-2 E-protein with GA/Glycyvir in model lipid bilayer has been demonstrated by various NMR techniques. Changes in the mobility of the transmembrane domain can affect E protein activity. The results obtained for GA are published in the article [1].

Acknowledgements

The study was financially supported by the Council for grants of the President of the Russian Federation (grant № MK-1580.2021.1.3)

References

1. Kononova, Polina & Selyutina, Olga & Polyakov, Nikolay. (2023). The Interaction of the Transmembrane Domain of SARS-CoV-2 E-Protein with Glycyrrhizic Acid in Lipid Bilayer. *Membranes*. 13. 505. 10.3390/membranes13050505.

Redox activity and membrane interaction of novel thiosemicarbazones

Vladimir E. Koshman^{1,2}, Olga Yu. Selyutina¹, Alexei A. Dmitriev¹, Nikolay E. Polyakov¹

¹Voevodsky Institute of Chemical Kinetics and Combustion SB RAS, Novosibirsk, Russia

²Faculty of Physics, Novosibirsk State University, Novosibirsk, Russia

E-mail: kosmanvova2010@mail.ru

Introduction

Thiosemicarbazones (TSCs, general structural formula, Fig. 1) represent an important class of N, S-donor compounds that demonstrate a wide range of biological activities, including anticancer, and are of great interest to scientists from various fields of science. Their anticancer activity has long been attributed to their ability to inhibit ribonucleotide reductase. However, recent studies indicate a significant role of oxidative stress in the anti-tumor activity of TSCs. This aspect of their biological activity is currently very poorly understood and is of great interest to medicinal chemistry [1]. In this work, the processes of lipid peroxidation involving chelate complexes with iron and copper ions using the thiosemicarbazones di-2-pyridylketone-4,4-dimethyl-3-thiosemicarbazone (Dp44mT), di-2-pyridylketone 4-cyclohexyl-4-methyl-3-thiosemicarbazone (DpC) and novel thiosemicarbazones AOBP and AODP as examples and their interaction with model lipid membranes were studied.

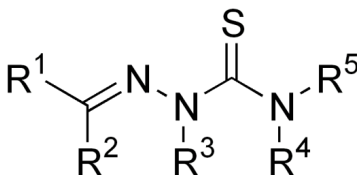


Figure 1: General structural formula of thiosemicarbazones

Methods

As a model membrane, micelles of linoleic acid (LA) and bicelles of DLPC/DHPC phospholipids were chosen. The interaction of chelate complexes with the lipid bilayer and their role in the lipid peroxidation reaction were studied on model systems by ¹H NMR methods and molecular dynamic simulation using GROMACS 2021.4 package and GROMOS54a7 force field.

Results

The redox properties of Dp44mT, DpC, AOBP, and AODP complexes with iron and copper in the lipid peroxidation reaction and the role of the natural antioxidant ascorbic acid in this process and the interaction of TSC complexes with the lipid membrane were studied. It was found that the complexation of Dp44mT with iron almost completely inhibits the peroxidation reaction, while complexes with copper retain oxidative activity. At the same time, in the presence of ascorbic acid the activity of Dp44mT complexes with iron increases significantly. It was revealed that the complexation of Dp44mT with iron ions inhibits the formation of OH-radical in the Fenton reaction. OH-radical formation was observed in the presence of ascorbic acid. The increase in the oxidative activity of Dp44mT complexes with iron ions in the presence of ascorbic acid is due to the cyclic redox reaction with Dp44mT complexes. Iron complexation with DpC also inhibits lipid peroxidation. Complex of iron with AOBP is redox active and ascorbic acid enhances its influence on the lipid peroxidation reaction. According to ¹H NMR correlation spectroscopy measurements and molecular dynamic simulation the Dp44mT molecule is located on the surface of the lipid bilayer, while

the DpC, AOBP and AODP molecules can penetrate the membrane. The AODP molecule is located closer to the surface of the bilayer than AOBP.

Discussion and Conclusions

The current investigation has examined the redox activity and interaction of the thiosemicarbazones Dp44mT, DpC, AOBP and AODP with model lipid membrane.

It was shown that AOBP and AODP are able to penetrate into lipid membrane, but their localization is different while Dp44mT is located on the surface of the lipid bilayer. Whereas DpC passes inside the membrane and is located beneath the lipid heads with little or no exposure to the membrane surface. Results were obtained by the combination of NMR, quantum chemical calculations and molecular dynamics simulation.

The mechanism of anti-proliferative activity of some TSCs is related to the penetration through lysosomal membrane and formation of cytotoxic metal complexes, which generate ROS resulting in lysosomal membrane permeabilization and cell death [2]. Therefore, the results obtained may improve the understanding of the mechanisms of anticancer activity of thiosemicarbazones.

References

1. B. Lu, X. B. Chen, M. D. Ying, Q. J. He, J. Cao, B. Yang. The Role of Ferroptosis in Cancer Development and Treatment Response. - "Frontiers in Pharmacology", 2018
2. A.E. Stacy, D Palanimuthu, P.V. Bernhardt, D.S. Kalinowski, P.J. Jansson, D.R. Richardson. Zinc(II)-Thiosemicarbazone Complexes Are Localized to the Lysosomal Compartment Where They Transmetallate with Copper Ions to Induce Cytotoxicity.- "J. Med. Chem", 2016

Determination of crystallographic positions of aluminum atoms in BEA zeolites using high-quality ^{27}Al MAS NMR

Ilya A. Kostyukov¹, Yury G. Kolyagin²

¹*Department of Chemistry, Lomonosov Moscow State University, Moscow, 119991 Russia*

²*Université de Lille, CNRS, Centrale Lille, Université Artois, UMR 8181, UCCS - Unit of Catalysis and Chemistry of Solids, Lille, France*

E-mail: elikosst98@gmail.com

Introduction

Zeolites are crystalline porous aluminosilicates. They are widely used as catalysts in industrial processes of petrochemistry, fine organic synthesis and biomass processing. Aluminum atoms can be located in the zeolite crystal lattice in nonequivalent crystallographic positions (T-positions) and they are associated with catalytic acid sites. There are 9 such positions in BEA zeolite. Depending on the location, the acid sites may have different catalytic activity [1-2]. Therefore, the purpose of this work was to determine the distribution of aluminum over crystallographic positions by the high-quality ^{27}Al MAS NMR method in BEA zeolites synthesized in different media. The samples studied are denoted as following: BEA-X-Y, where X = 50, 200 or 250 ($\text{SiO}_2/\text{Al}_2\text{O}_3$ ratio), Y = F (fluoride medium) or OH (alkaline medium). BEA-X-OH samples were supplied by Zeolyst company; BEA-X-F samples were synthesized by us.

The problem of direct determination of the aluminum atoms crystallographic positions

Aluminum atoms have spin $5/2$, because of it the ^{27}Al MAS NMR spectrum is often greatly affected by the second-order quadrupole interactions. For example, in BEA zeolites Al atoms in different T-positions undergo quadrupole interactions with quadrupole coupling constants ranging from 3 to 17 MHz (Fig. 1) at fields of 9.4 T [3]. However, in spectra obtained at high fields of 18 T and above of fully hydrated BEA zeolites, the line broadening due to the second quadrupole interaction can be ignored and the ^{27}Al MAS NMR spectra can be deconvoluted with simple Gaussian/Lorentzian lines to determine the Al T-site distribution [3].

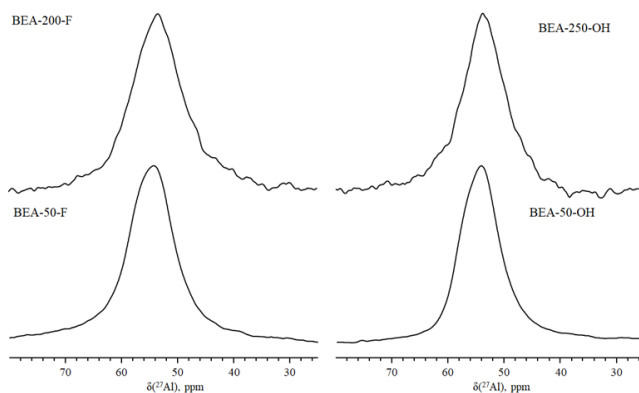


Figure 1. ^{27}Al MAS NMR spectra obtained at fields of 9.4 T for zeolites under study

Aluminum T-sites identification in high-quality ^{27}Al MAS NMR

The distribution of aluminum atoms over T-positions in the zeolite structure was determined from the analysis of high-quality ^{27}Al MAS NMR spectra (Fig. 2). The NMR spectra on ^{27}Al nuclei predominantly contained a group of overlapping signals in the region of 50-60 ppm related to tetrahedral aluminum atoms in the structure of BEA zeolites. The difference in the geometry of the environment of atoms located in different crystallographic positions leads to the appearance of small shifts in the signals of 4-coordinated aluminum within the group. This allows us to determine Al T-positions. Based on work [3], the decomposition of the spectra was carried out using lines of the Gauss/Lorentz shape, since at a magnetic field of 18.8 T central lines almost represent the true chemical shift. Width and shape of the lines were preserved within each spectrum. Chemical shifts and the number of lines were chosen based on the work [4] and the crystallographic positions of polymorph A of the zeolite [5].

In the MAS NMR spectra, 7 signals of aluminum atoms in non-equivalent crystallographic positions with $\delta(^{27}\text{Al})$ circa 53.5, 54.7, 55.6, 57.6, 58.7, 60.2 ppm were identified. These signals were assigned according to the results of Vjunov's work [4] using Newsam's nomenclature [5] to crystallographic positions T8, T5, T9, T1+T2, T6, T7 and T3, respectively (Fig. 2). The T4 position signal is absent in all spectra; its maximum should be located at 62.5 ppm. The spectra of samples synthesized in a fluoride medium contain a signal at 51.2 (BEA-50-F) and 52.1 (BEA-200-F) ppm; it is rather wide, which could be explained by a distortion of the tetrahedral environment of aluminum atoms and which may be associated with increased hydrophobicity owing to the ideal aluminosilicate framework of zeolites [6].

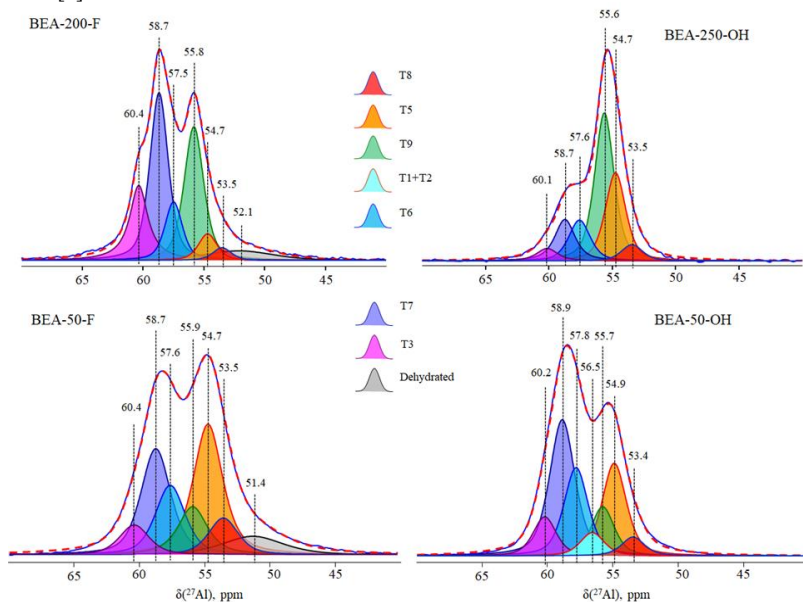


Figure 2. ^{27}Al MAS NMR spectra obtained at high fields of 18.8 T (blue line – original spectrum; red line – calculated spectrum) and the results of their deconvolution for zeolites under study

The distribution of T-positions strongly depends on the aluminum content in the zeolite structure or the synthesis technique. Thus, with a low aluminum content in the zeolite, T9 position turns out to be the most significant. With a decrease in zeolite modulus ($\text{SiO}_2/\text{Al}_2\text{O}_3$ ratio) for samples synthesized in a fluoride medium the contribution of signals corresponding to positions T5 and T6 increases, while for BEA zeolites obtained in an alkaline medium lower amounts of Al positions T6 and T7 are the most preferential. Difference in aluminum distribution can be controlled by thermodynamic and kinetic factors [4]. The increase in the contribution of positions T5 and T6 in BEA obtained by direct synthesis in a fluoride medium with increasing aluminum content may be due to the fact that the crystallization time of samples with low $\text{SiO}_2/\text{Al}_2\text{O}_3$ is significantly longer compared to high-modulus zeolites, so the distribution of aluminum over crystallographic positions in them approaches thermodynamic. Recent calculations carried out by the authors of [7] showed that positions T5, T6, T7 and T8 according to Newsam's nomenclature [5] are the most thermodynamically stable. In the case of high-modulus zeolites, the distribution of Al atoms over crystallographic positions can be determined by a kinetic factor. It should be noted that the BEA-250-OH sample was most likely obtained by dealumination, since it is not possible to synthesize this zeolite in an alkaline medium by direct synthesis [8]. The dealumination stage, based on calculations carried out in [7], can lead to the selective removal of aluminum from positions T3, T6 and T7, while the authors note that dealumination of position T6 is very difficult, and aluminum atoms located in positions T7 and T8 are easily removed from the framework. It is worth outlining that the dealumination stage can be carried out in various ways, which can greatly affect the removal of aluminum from the structure.

Conclusions

Thus, the high-quality ^{27}Al MAS NMR spectra recorded at 18 T and above can be decomposed into signals of individual crystallographic positions of aluminum atoms in zeolite framework. This makes it possible to determine the most stable sites for further prediction of catalyst activity.

Acknowledgements

This work is supported by the Russian Science Foundation (RSF grant no. 20-13-00203, <https://rscf.ru/project/20-13-00203/>).

References

1. Zhao R., Zhao Z., Li S., Zhang, W. – The Journal of Physical Chemistry Letters. 8, 10, 2323-2327 (2017).
2. Li S., Zhao Z., Zhao R., Zhou D., Zhang W. – ChemCatChem. 9, 8, 1494-1502 (2017).
3. Hu J. Z., Wan C., Vjunov A., Wang M., Zhao Z., Hu M. Y., Lercher J. A. – The Journal of Physical Chemistry C. 121, 23, 12849-12854 (2017).
4. Vjunov A., Fulton J. L., Huthwelker T., Pin S., Mei D., Schenter G. K., Niranjan Govind, Camaioni D. M., Jian Zhi Hu, Lercher J. A. – Journal of the American Chemical Society. 136, 23, 8296-8306 (2014).
5. Newsam J. M., Treacy M. M., Koetsier W. T., Gruyter C. D. – Proceedings of the Royal Society of London. A. Mathematical and physical sciences. 420, 1859, 375-405 (1988).
6. van Bokhoven J. A., Koningsberger D. C., Kunkeler P., van Bekkum H., Kentgens A. P. M. – Journal of the American Chemical Society. 122, 51, 12842-12847 (2000).
7. Li C., Dong X., Yu H., Yu Y. – Physical Chemistry Chemical Physics. 25, 36, 24547-24562 (2023).
8. Cambor M. A., Mifsud A., Pérez-Pariente J. – Zeolites. 11, 8, 792-797 (1991).

Probing Weak Ligand-Protein Binding Using Long-Lived Spin Order Relaxometry

Vitaly P. Kozinenko, Alexey S. Kiryutin, Alexandra V. Yurkovskaya

International Tomography Center SB RAS, Novosibirsk, Russia

E-mail: kozinenko@tomo.nsc.ru

Introduction

Among the diverse NMR techniques, the investigation of spin relaxation stands out as a well-developed method for probing molecular motions. Relaxation in NMR is a result of stochastic fluctuations in local magnetic fields induced by thermal motions of molecules, with relaxation rates dependent on the external magnetic field strength, commonly known as nuclear magnetic relaxation dispersion (NMRD). The measurement and analysis of NMRD curves, forming the field of NMR relaxometry, provide a means to extract both dynamical and structural information for various molecular systems, with a list of applications in fundamental and practical studies across disciplines such as biology, food science, and soil science [1,2]. Notably, recent work by Wang and co-workers demonstrated the effectiveness of combining NMR relaxometry with high-resolution detection in studying metabolite-protein interactions in biological fluids [3].

One challenge in NMR relaxometry is the limited timescale of nuclear spin relaxation, typically spanning several seconds, restricting studies to faster processes. Overcoming this limitation involves exploiting the symmetric properties of a specific spin state, such as the singlet state of a pair of protons, which corresponds to zero total spin. Storing initial magnetization as a population imbalance between singlet and triplet states, known as singlet order (SO), has shown promise in overcoming fast relaxation limits, as demonstrated in previous research on ligand-protein interactions [4].

In our investigation, we analyze the field dependence of singlet order relaxation time T_{SO} in a small molecule (alanine-glycine, Ala-Gly) engaged in weak binding with a protein (human serum albumin, HSA). We establish a connection between the observed NMRD data and the parameters of the ligand-protein interaction by fitting it with a theoretical model grounded on established analytical expressions for the field dependence of T_1 and T_{SO} . Furthermore, our findings reveal that the contrast, indicating the relative change in relaxation time in the presence of the protein, offered by T_{SO} surpasses that provided by T_1 across all field ranges.

Methods

The application of NMR relaxometry to investigate ligand-protein interactions relies on the sensitivity of spin relaxation to molecular motion timescales. Typically, a protein's slower overall rotation compared to a ligand's results in faster relaxation of nuclei in the ligand-protein complex at low magnetic fields. When binding is reversible, the measured relaxation time is an average over both bound and free forms of the ligand, with the bound form often undetectable (Fig. 1).

For most types of motions associated with biomolecules, the dispersion of relaxation times occurs in the range of magnetic fields around 0.1 T. A common technique to measure relaxation at such fields exploits the stray magnetic field of a superconducting NMR magnet. In our study we use a custom-build experimental setup based on 700 MHz Bruker Avance HD NMR spectrometer, with a stepper motor placed at the top of the spectrometer bore. The motor drives a plastic rail with a carriage for a standard 5 mm NMR sample tube. This allows shuttling the sample in the range of fields from 4 mT to 16.4 T with transfer time shorter than 0.4 s.

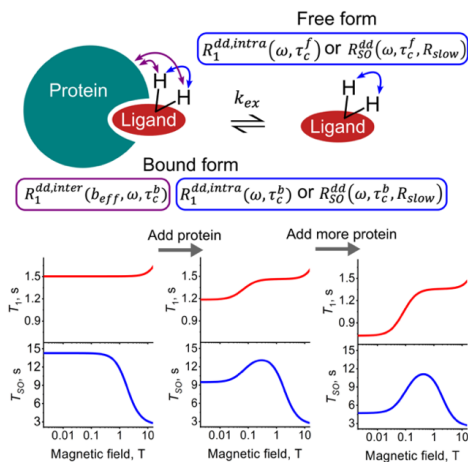


Figure 1. Schematic process of the weak ligand-protein interaction with the indication of the T_1 and T_{S0} relaxation mechanisms, accounted in the fitting model (top). Typical effect of the addition of protein on the T_1 and T_{S0} magnetic field dependences (bottom).

Results

The experiments yielded a collection of relaxation kinetics measured across a range of magnetic fields, specifically probing ten field values logarithmically distributed from 4 mT to 16 T. To extract the relaxation times from the kinetics, a least square fitting procedure with a single exponential function was conducted. We obtained NMRD curves for a sample containing only the ligand molecule and for samples containing 50, 100, 200 and 300 μM of added HSA. The fitting results exhibit strong conformity with the experimental data for both Ala-Gly (Fig. 2.A). The T_1 NMRD curves, observed in the presence of protein, manifest the expected behavior, reaching their maximum at high fields and experiencing a significant decline as the magnetic field decreases. Consistent with the model, an increase in protein concentration leads to a faster relaxation at low fields.

The shape of the T_{S0} NMRD curves presents a more complex pattern (Fig. 2.B). Upon decreasing the field from 16 T to 1 T, the lifetime of the singlet order notably extends as it aligns with the eigenstate of the methylene protons, where the difference in their Larmor frequencies approaches their J-coupling. Subsequently, as the magnetic field further diminishes, the rapid relaxation of the bound form becomes evident, leading to a reduction in the observed singlet order lifetime.

The reported procedure not only confirms the occurrence of ligand-protein interactions but also offers qualitative insights into this process. However, given the significant disparity between relaxation times of magnetization and long-lived spin order, visualizing the binding effect on NMRD curves is best achieved by considering the "relaxation contrast" $C = (T_{1,SO}^0 - T_{1,SO}^{HSA})/T_{1,SO}^0$, indicating the relative change in relaxation time upon protein addition. Analysis of relaxation contrast as a function of magnetic field reveals that NMRD curves obtained with the singlet order exhibit greater sensitivity to ligand-protein binding compared to T_1 NMRD curves. Thus, employing the singlet order results in approximately a 10% enhancement in relaxation contrast for various concentrations of HSA (Fig. 2.C). This increased relaxation contrast enables the detection and quantification of the binding process with lower concentrations of the protein.

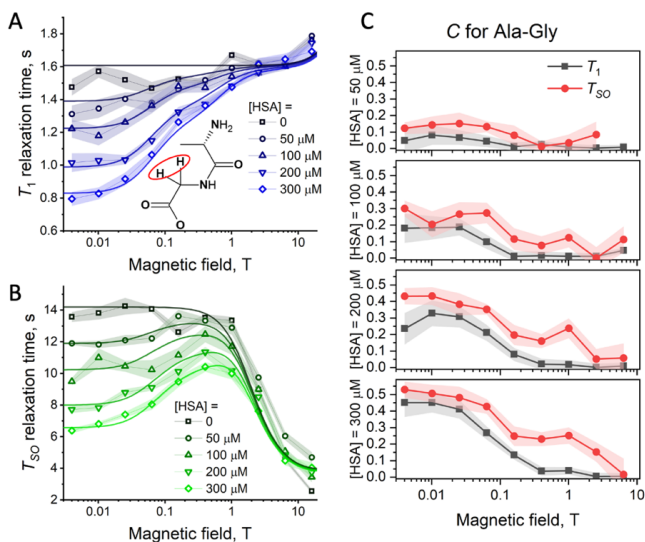


Figure 2. Experimental (symbols) and fitted (solid lines) field dependence of T_1 (A) and T_{SO} (B) relaxation times of Ala-Gly methylene protons (highlighted with a red ellipse) in samples containing 0, 50, 100, 200 and 300 μM of HSA. Relaxation contrast C measured as the function of the magnetic field for the cases of T_1 (rectangles, black) and T_{SO} (circles) relaxation of Ala-Gly methylene proton (C). The coloured areas around the experimental points indicate the values of fitting uncertainties for the corresponding relaxation kinetics.

In addition to investigations carried out with thermally polarized samples, the application of relaxometry to long-lived spin order holds substantial promise when combined with NMR hyperpolarization techniques. Experiments involving Dynamic Nuclear Polarization (DNP) or Parahydrogen-Induced Polarization (PHIP) offer the direct hyperpolarization of long-lived spin order, providing a valuable avenue for exploring ligand-protein interactions, particularly at exceptionally low concentrations.

Acknowledgements

This work is supported by the Russian Science Foundation (Grant #23-73-10103).

References

1. D.P. Cistola, M.D. Robinson, Compact NMR relaxometry of human blood and blood components, *TrAC Trends in Analytical Chemistry* 83 (2016) 53–64.
2. E.G. Ates et al., Field-dependent NMR relaxometry for Food Science: Applications and perspectives, *Trends in Food Science & Technology* 110 (2021) 513–524.
3. Z. Wang et al., Detection of Metabolite–Protein Interactions in Complex Biological Samples by High-Resolution Relaxometry: Toward Interactomics by NMR, *J. Am. Chem. Soc.* 143 (2021) 9393–9404.
4. N. Salvi et al., Boosting the Sensitivity of Ligand–Protein Screening by NMR of Long-Lived States, *J. Am. Chem. Soc.* 134 (2012) 11076–11079.

^{14}N magnetic relaxation in solids and liquids

Galina Kupriyanova¹, Ivan Mershiev¹, George Mozzhukhin², Bulat Rameev^{2,3,4}

¹*I. Kant Baltic Federal University, Kaliningrad 236041, Russian Federation*

²*Department of Physics, Gebze Technical University, 41400 Gebze/Kocaeli, Turkey*

³*Kazan State Power Engineering University, 420066 Kazan/Tatarstan, Russian Federation*

⁴*Zavoisky Physical-Technical Institute, FRC Kazan Scientific Center of RAS, 420029*

Kazan/Tatarstan, Russian Federation

E-mail: galkupr@yandex.ru

Abstract

In this study, dynamic information has been extracted from relaxation data with the aid of the Inverse Laplace Transform (ILT). The two-component relaxation decay of the longitudinal relaxation of ^{14}N nuclei in NQR measurements has been observed in accordance with quantum mechanical calculations. A two-component transverse relaxation decay of ^{14}N NQR signal has been observed in the NaNO_2 sample with the use of ILT. The Gierer and Wirtz (GW) method has been used to calculate molecular motion correlation times. Quadrupole coupling constants have been obtained from ^{14}N NMR relaxation times of various liquids: NH_4NO_3 , HNO_3 , $\text{Pb}(\text{NO}_3)_2$, $\text{Mg}(\text{NO}_3)_2$. A two-dimensional ^{14}N NMR relaxation method to determine the relaxation time T_2 and the diffusion coefficient within one experiment has been proposed.

Introduction

Nitrogen is one of the most important elements in chemistry and biology. Most medications and biologically active compounds contain nitrogen in their structure. Dynamic processes involving nitrogen are of particular importance since they largely determine the biological activity of the nitrogen-containing compounds. One of the important magnetic resonance techniques to probe dynamic properties is the study of nitrogen relaxation processes. Even though the abundance of ^{14}N is 99.6%, it remains the least studied Nuclear Magnetic Resonance (NMR) active nucleus. This is largely due to the fact that ^{14}N is a quadrupole nucleus with integer spin I . In solids, single-quantum transitions of nuclei with spin $I=1$ in a magnetic field are affected by first-order quadrupolar broadening which in most materials is on the order of a few megahertz. As a rule, information about dynamic processes in solids (relaxation characteristics and the dynamics of molecular motion) obtained from studying the width and shape of the ^{14}N NMR line is rather labor-intensive and, in many cases, non-accurate. The main issue is the need to know the exact value of the quadrupole constant C_q . Reliable C_q values can be obtained only for the case of $C_q < 1$ MHz. On the other hand, accurate values of C_q in solids and powders can be obtained by the ^{14}N Nuclear Quadrupole Resonance (NQR) method. The symmetry of the crystal uniquely determines the magnetic nonequivalence of the nuclei and, consequently, the intensity and frequency of NQR lines. The main advantage of ^{14}N NQR is the ability to trace the dynamic behaviour of all non-equivalent nuclei and obtain detailed information about the nature of dynamic processes. Traditional pulse sequences are used in ^{14}N NQR to measure the T_1 and T_2 relaxation times. Such studies are especially important for highly nitrogenous compounds, for example, tetrazole derivatives, the ring of which contains four nitrogen atoms [1]. The study of tetrazole derivatives using double ^{14}N NQR-NMR resonance and pulsed ^{14}N NQR methods made it possible to establish an unambiguous assignment of NQR signals to a specific atom in the tetrazole molecule and to measure the relaxation times T_1 and T_2 for each nucleus [1,2].

¹⁴N NQR Relaxometry with Inverse Laplace Transform

To enhance the ability to extract dynamic information from relaxation data, the Inverse Laplace Transform (ILT) method can be applied. The use of the ILT made it possible to identify the two-component relaxation decay of the longitudinal relaxation of ¹⁴N nuclei in accordance with quantum mechanical calculations. A difference was revealed in the dynamic behaviour of the N₂ and N₃ ring atoms [1]. This difference was explained within the framework of a model that takes into account that ring atoms are involved not only in ring vibration but also in torsional motion. The difference in the inertia moments relative to the axes of the electric field gradient leads to the difference in dynamic behaviour for N₂ and N₃. The shortest ¹⁴N T₁ relaxation time was found in the NH₂ group (T₁=700ms). This fact is explained within the framework of the model of the occurrence of the process of polarization transfer between nuclei that have the same frequencies, but the main axes of the gradient electric field do not coincide. To explain the relaxation process for N₆ (NH₂), two factors are taken into account: dipole-dipole interaction and the polarization transfer process that occurs for nuclei that have the same frequency but different directions of the principal axes of the EFG tensor.

The use of the ILT method made it possible to obtain more detailed information about the dynamics of various polymorphic forms of sulfanilamide such as α -, β - and γ -polymorphs. The most stable polymorph of sulfanilamide is the beta form. Sulfanilamide is a well-known medicament having various polymorphic forms such as α -, β - and γ -polymorphs. The most stable polymorph is the beta form. Measuring the T₁ relaxation times using the ¹⁴N NQR method, it was found that the T₁ relaxation times at frequencies $\nu = 2495$ kHz (N₁) $\nu = 2565$ kHz (N₂) are 25 ms and 400 ms, respectively [3]. However, using the ILT allows us to obtain a picture of the distribution of relaxation times for each polymorphic form. The T_{1(A)} distribution was obtained for amine nitrogen, consisting of 4 groups of T₁ relaxation times at a frequency $\nu = 2495$ kHz [4]. This indicates the presence in the crystal lattice of several pairs of amino groups with different mobility. On the other hand, the T₁ distribution for sulfonamide nitrogen at frequency $\nu = 2565$ kHz has a wide relaxation spectrum centered at T₁ = 700 ms. Whereas the spectrum of relaxation times for T₂ consists of one line. This can be explained by the fact that the relaxation time is determined by another mechanism - spin-spin interaction, which can be weak under the conditions of the crystal lattice [2].

The use of the ILT allowed not only to expand knowledge about dynamic processes but also to observe diffusion processes of polarization transfer caused by dimensional and surface effects. These effects were first noticed in work [5]. We have studied of the relaxation times of ¹⁴N NQR in NaNO₂ after prolonged grinding of the powder. The use of ILT made it possible to identify a two-component transverse relaxation decay. The following values were obtained for NaNO₂ at a frequency of 4.64 MHz at room temperature (25^oC) T₁ = 173 ms and T₂₁ = 18.2 ms, T₂₂ = 72.5 ms.

¹⁴N NMR relaxation in liquids

The ¹⁴N NMR method has an important advantage in studying the dynamics of molecules in liquids. Quadrupole interactions make a dominant contribution to the NMR relaxation process [6]. The T₁ and T₂ relaxation times depend on the quadrupole interaction constant and the molecular motion correlation function. However, obtaining data on molecular motion encounters a number of difficulties associated with the lack of exact values of the quadrupole interaction constant. The use of data on the quadrupole constant obtained for a solid is not the correct procedure due to the absence of long-range order in liquids. On the other hand, constructing an adequate model of molecular motion and calculating the correlation time of molecular motion using mathematical models can make it possible to determine the quadrupole interaction constant in liquids, thereby obtaining experimental

values about the distribution of electron density in a molecule. Using the Gierer and Wirtz (GW) method to calculate molecular motion correlation times, quadrupole coupling constants were obtained from ^{14}N NMR relaxation times in liquids for the ^{14}N in NO_3 group (e.g. compounds, such as NH_4NO_3 , HNO_3 , $\text{Pb}(\text{NO}_3)_2$, $\text{Mg}(\text{NO}_3)_2$). In the works [7,8], the ^{14}N Cq parameter was obtained for a number of polycrystalline nitrate samples using the MAS ^{14}N NMR method at two different magnetic field strengths and introducing f-correction parameter characterizing the ratio between the powder-averaged second-order shift and the maximum shift caused by the second order quadrupolar interaction. It should be noted that the values of Cq obtained for $\text{Pb}(\text{NO}_3)_2$ in solution ($\text{Cq}(\text{Pb}(\text{NO}_3)_2) = 0.75\text{MHz}$) are higher than the values obtained by solid-state ^{14}N MAS NMR $\text{Cq} = 510\text{ kHz}$ [7] and $\text{Cq} = 652.9\text{ kHz}$ [8]. Anomalously small values of the quadrupole interaction constants in nitrates, such as AgNO_3 , $\text{Ba}(\text{NO}_3)_2$ (538.1 kHz), and $\text{Pb}(\text{NO}_3)_2$ (652.9 kHz) are explained in [7] multidirectional molecular and lattice contributions. Therefore, significant variations in Cq are caused precisely by molecular effects, while lattice contributions experience small fluctuations. The values of the quadrupole interaction constants we obtained confirm this concept. A decrease in the lattice contribution in liquids should lead to an increase in the quadrupole interaction constant, in accordance with the results of our experiment. However, the values for $\text{Cq}(\text{Mg}(\text{NO}_3)_2) = 0.56\text{ MHz}$ and $\text{Cq}(\text{KNO}_3) = 0.660\text{ MHz}$ are slightly lower than the values $\text{Cq}(\text{Mg}(\text{NO}_3)_2) = 0.877\text{ MHz}$ and $\text{Cq}(\text{KNO}_3) = 0.726\text{ MHz}$ obtained for solid-state samples accordingly. To obtain additional data on molecular motion, we propose a two-dimensional ^{14}N NMR relaxation method, which allows one to determine the relaxation time T_2 and the diffusion coefficient within one experiment. These data make it possible to correct the model calculation of dynamic parameters and extract data on the quadrupole constant.

Conclusions

We have shown that dynamic information can be efficiently extracted from the ^{14}N NQR and NMR relaxation data with the aid of the Inverse Laplace Transform (ILT). The two-component relaxation decay of the longitudinal relaxation of ^{14}N nuclei in NQR measurements has been observed. The dynamics of various polymorphic forms of sulfanilamide (α -, β - and γ -polymorphs) have been studied and the distribution of relaxation times for each polymorphic form has been established. The two-component transverse relaxation decay of the ^{14}N NQR signal has been also observed in NaNO_2 . We have also shown that the dynamics of molecules in liquids can be probed by T_1 and T_2 ^{14}N NMR relaxation measurements, which depend on the quadrupole interaction constant and the molecular motion correlation function. We have also discussed the quadrupole interaction constant for the ^{14}N nuclei in liquids which are somewhat different from ^{14}N NQR for solids due to the absence of long-range order in liquids. The model, taking into account the molecular motion and calculations of the correlation times, for determining the quadrupole interaction constants in NMR has been proposed. Correct data on quadrupole coupling constants have been obtained from the ^{14}N NMR relaxation times of various liquids.

References

1. S. Mamadazizov, M.G. Shelyapina, G.S. Kupriyanova, G.V. Mozzhukhin. – *Chem. Phys.*, 506, 52–60 (2018); doi: 10.1016/j.chemphys.2018.03.030
2. J. Pirnat, J. Luznik, V. Jazbinsek, V. Zagar, J. Seliger, T.M. Klapotke, Z. Trontelj, *Chem. Phys.* 364 (1–3) (2009) 98–104
3. Trontelj Z, Pirnat J, Jazbinšek V, Lužnik J, Srčič S, Lavrič Z, Beguš S, Apih T, Žagar V, Seliger J. Nuclear Quadrupole Resonance (NQR)—A Useful Spectroscopic Tool in Pharmacy for the Study of Polymorphism. *Crystals* **10**(6), 450 (2020);doi: 10.3390/cryst10060450

4. M. Fedotov, I. Mershev, G. Kupriyanova, N. Sinyavsky. Conference on “Modern Development of Magnetic Resonance”, MDMR-2021, Kazan, Russian Federation, November 1-5, 2021, p. 174-175
5. S.R. Rabbani, D. T. Edmonds. *Phys. Rev. B* **50**(9), 6184-6188 (1994); doi: 10.1103/PhysRevB.50.6184
6. G.V. Mozhukhin, G.S. Kupriyanova, S.Sh. Mamadazizov, A. Maraşlı, B.Z. Rameev. Low-field ^{14}N nuclear magnetic resonance for detection of dangerous liquids. – *Chem. Phys.* **513**, 129–134 (2018); doi: 10.1016/j.chemphys.2018.07.032
7. S. P. Marburger, B. M. Fung, A. K. Khitrin. ^{14}N Chemical Shifts and Quadrupole Coupling Constants of Inorganic Nitrates – *J. Magn. Reson.* **154**, 205–209 (2002); doi: 10.1006/jmre.2001.2490
8. R. A. Santos, P. Tang, W.-J. Chien, S. Kwan, and G. S. Harbison , *J. Phys. Chem.* **94**, 2717–2721 (1990).

Improved Low-Temperature Damping of Epitaxial Yttrium Iron Garnet Film

Kuzmichev Alexey¹, Vetoshko Peter²

¹*Russian Quantum Center, Skolkovo, Moscow 121205, Russia*

²*Vernadsky Crimean Federal University, Simferopol 295007, Russia*

E-mail: a.kuzmichev@rqc.ru

Introduction

In 1956, an event occurred in the world of magnetism that defined a new era - the discovery of yttrium iron garnet (YIG). Dielectric, with a record low Hilbert damping constant of the order of 10^{-5} . The material has great compositional flexibility, which allows the addition of various ions to the lattice and even complete modification while maintaining only the valency and oxygen-based stoichiometry. YIG immediately came into use among researchers around the world, and many discoveries in magnetism were made thanks to it. Ch. Kittel called this material the “fruit fly of magnetism,” emphasizing its important role, since fruit flies are the main working material for genetics. The record-breaking small width of the ferromagnetic resonance line made it possible to create low-noise tunable microwave signal generators, narrow-band filters, and delay lines with advanced characteristics at that time. But how narrow can this line be? Spencer and LeCrow tried to find an answer to this question back in 1961 [1], where for a YIG sphere upon cooling to 4K they managed to obtain hundredths of an oersted and this, apparently, is still not the limit [2]. Unfortunately, technologies on spheres have a number of disadvantages, the main ones being large size and high technological costs. Obtaining such a narrow line and low Hilbert attenuation constant on film structures, which, in addition to their compact size, are also well compatible with planar geometry, will open new horizons for next-generation microwave devices.

Magnetic Resonance Damping

The traditional tool for determining the quality of YIG is ferromagnetic resonance (FMR). This phenomenon is theoretically described by the well-known Landau-Lifshitz-Hilbert equation:

$$\frac{\partial M}{\partial t} = -\gamma[M \times H_{eff}] + \frac{\alpha}{M_s} \left[M \times \frac{\partial M}{\partial t} \right] \quad (1)$$

On the basis of which, Kittel has already derived equations describing the dependence of the resonance frequency on the external field, the shape of the magnet and anisotropy:

$$\omega_{res} = \gamma H_{eff} \quad (2)$$

For garnet, the gyromagnetic constant is $\gamma = 2.8$ MHz/Oe, while the width of the resonance line consists of two components - uniform and inhomogeneous broadening.

$$\Delta f_{res} = \Delta f_o + \frac{\alpha\gamma H}{\pi}; \Delta H_{res} = \Delta H_o + \frac{\alpha 4\pi f}{\gamma} \quad (3)$$

Δf_o и ΔH_o - line broadening associated with the structure of the material (non-uniform broadening). Components linearly dependent on frequency or field are associated with uniform broadening, the mechanism of which is determined by the internal magnetic properties of the material. The constant α in these relations is an indicator of the damping of magnetic dynamics.

As it turned out, if you get rid of magnetic impurities and the paramagnetic substrate in YIG films, you can observe a sharp decrease in the uniform broadening upon cooling below 5 K, down to zero values with an accuracy limited by the capabilities of the equipment [6]. Thus, to obtain ultra-narrow lines it is necessary to get rid of inhomogeneous broadening. The first attempts to obtain high-quality material on a YSGG substrate are described in [7]. The

next step in the development of technology is the production of films with a narrow FMR line and the absence of uniform broadening. To date, it has been possible to achieve record values from those described in the literature for films grown by the LPE method (Fig. 1).

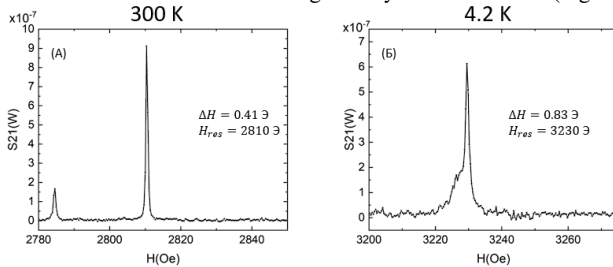


Figure 1: FMR at 3.125 GHz for a YIG disk with a diameter of 1 mm and a thickness of 2 μm (A) for a temperature of 300 K and (B) for a temperature of 4.2 K.

The line width at room is approximately 2 times less than at liquid helium temperature. This behavior is due to the presence of impurities due to insufficiently pure iron and yttrium oxides - the main components of the film containing magnetic ions such as dysprosium and nickel. The preparation of pure oxides is one of the most important steps in this work. Figure 2 shows the dependence of the resonance width on the pump frequency at two temperatures. Approximating the dependencies with straight lines allows one to calculate the values of the attenuation constant α .

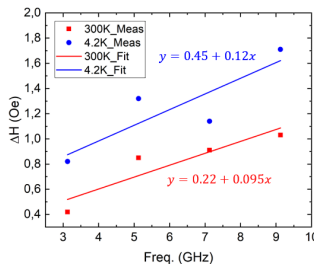


Figure 2: Dependence of the resonance width on the pump frequency for temperatures of 300 K and 4.2 K. From the equations for the corresponding linear approximations, we can obtain the inhomogeneous broadening components of 0.22 Oe and 0.45 Oe, respectively, as well as the components for uniform broadening - 0.095 and 0.12.

Let us calculate for the given data the values of the damping constant at room temperature and at 4.2 K, using relations (3). Then for 300 K $\alpha = 2.11 \cdot 10^{-5}$, and at the temperature of liquid helium $\alpha = 2.67 \cdot 10^{-5}$. These values are very close to the threshold values found in [7], while the inhomogeneous broadening is more than 20 times smaller. Recent measurements of new samples of epitaxial structures at room temperature showed that we were able to overcome the threshold of the damping constant of 10^{-6} , which no one has been able to demonstrate to date (Fig. 3).

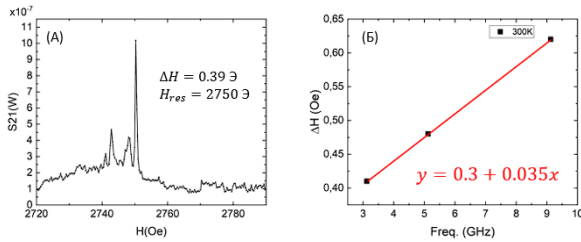


Figure 3: (A) FMR of a 2 μm thick film at a frequency of 3.125 GHz at room temperature. (B) Linewidth as a function of pump frequency. From the equation for linear approximation, we can obtain a component of inhomogeneous broadening of 0.3 Oe and a component for uniform broadening of 0.035.

From relation (5) we obtain $\alpha = 7.78 \cdot 10^{-6}$. The data obtained suggest that in the near future it will be possible to achieve linewidths on the order of a hundredth of an oersted at cryogenic temperatures on iron garnet films grown by the LPE method, and that this method is the most suitable for this.

Acknowledgements

This work was supported by the Russian Science Foundation (project no. 22-12-00322).

References

1. Spencer, E. G., LeCraw, R. C., & Linares, R. C., Physical Review, 123(6), 1937–1938, (1961). doi:10.1103/physrev.123.1937
2. Dionne, Gerald F.; Fitch, George L., Journal of Applied Physics, 87(9), 4963 (2000). doi:10.1063/1.373216
3. Mihalceanu, Laura; Vasyuchka, Vitaliy I.; Bozhko, Dmytro A.; Langner, Thomas; Nechiporuk, Alexey Yu.; Romanyuk, Vladyslav F.; Hillebrands, Burkard; Serga, Alexander A., Physical Review B, 97(21), 214405, (2018). doi:10.1103/PhysRevB.97.214405
4. A.N. Kuzmichev, V.I. Belotelov, Y.M. Bunkov, P.M. Vetoshko, A.I. Popov, V.N. Berzhansky, A.N. Shaposhnikov, Ch.K. Sabdenov, A.V. Koshelev, A.A. Fedorenko, , Materials Research Bulletin, Volume 149, 111691, (2022), <https://doi.org/10.1016/j.materresbull.2021.111691>
5. Golovchanskiy, I.A.; Abramov, N.N.; Pfirmann, M.; Piskor, T.; Voss, J.N.; Baranov, D.S.; Hovhannissyan, R.A.; Stolyarov, V.S.; Dubs, C.; Golubov, A.A.; Ryazanov, V.V.; Ustinov, A.V.; Weides, M., Physical Review Applied, 11(4), 044076, (2019). doi:10.1103/PhysRevApplied.11.044076
6. Side Guo et al., Nano Lett., 23, 11, 5055–5060, (2023) <https://doi.org/10.1021/acs.nanolett.3c00959>
7. Nadezhda E. Kupchinskaya, Petr M. Vetoshko, Alexey N. Kuzmichev, Sergey N. Polulyakh, Eugeny Y. Semuk, Alexander S. Pakhomov, Fedor M. Maksimov, Vladimir N. Berzhansky, Vladimir I. Belotelov, Alexander I. Chernov, Journal of Magnetism and Magnetic Materials, Volume 591, 171623, (2024). <https://doi.org/10.1016/j.jmmm.2023.171623>

Proposal for a detachable Phantom for MRI-qMRI

Manuel Arsenio Lores Guevara^{1,2}, Evelio Rafael Gonzalez Dalmau^{1,2}, Carlos Alberto Cabal Mirabal^{1,2}

¹ Laboratorio de Resonancia Magnética de Imágenes. Centro de Neurociencias de Cuba (CNEURO). Avenida 25 y 158, No. 15202, Cubanacán, Playa. La Habana. Cuba.

² Laboratorio de Relajación Magnética Nuclear. Centro de Biofísica Médica. Universidad de Oriente. Santiago de Cuba. Cuba.

Introduction

Magnetic Resonance Imaging (MRI) is a leading technology in imaging diagnosis today thanks to its non-invasive nature [1,2] and its ability to obtain adequate contrast between human tissues on the basis of the different values of the proton magnetic relaxation times (T_1 and T_2), the proton density (ρ) and the diffusion of these nuclei [1, 3, 4]. It is used for the diagnosis of soft tissue pathologies, the diagnosis of tumors, for the design of implants and tissue substitutes individualized for each patient and is essential in the early diagnosis of ICTUS [1, 2, 4-6].

To characterize the accuracy, stability and comparability of an MRI machine (scanner), both in the qualitative (MRI) and quantitative (qMRI) modality, phantoms are essential [1, 7]. These are inanimate and artificial objects, manufactured by man, that allow the quantification of parameters directly related to the operation of the scanner or the quality of the images it produces: intensity, non-uniformity and stability of static (B_0) and radio frequencies (B_1) magnetic fields; geometric linearity; amplitude of the gradients; position and profile of the slides; image uniformity; resolution; signal to noise ratio; contrast to noise ratio; and the longitudinal (T_1) and transverse (T_2) proton magnetic relaxation times; as well as the accuracy and precision in the determination of ρ [1]. They also enable the development, calibration and validation of new software, pulse sequence design and hardware technologies within MRI, as well as the development of new physical methods and procedures [1].

Usually the MRI and qMRI Phantoms are designed and produced separately or the Phantom includes only one type of qMRI application. In this work we suggest a phantom including a main structure oriented to the scanner characterization coupled to a detachable structure oriented to qMRI determination, which can include different qMRI options.

Proposal of Design

The Phantom will be divided into a fixed part (MRI) and a removable and interchangeable part (qMRI) with coupling guides between them (figure 1). Both parts (fixed and interchangeable) will be hollow polycarbonate cylinders with common external (200 mm) and internal (195 mm) diameters and thickness (2.5 mm). The height of the MRI cylinder will be 150 mm and the qMRI cylinder will be 50 mm. The fixed part (MRI) will be filled with distilled and deionized water and will contain an internal support structure formed by 5 polypropylene sulfide plates (190 mm in diameter and thickness 8 mm) fixed and stabilized by a structure of cylindrical rods (diameter 5 mm, height 23 mm) also made of polypropylene sulfide. The plates are arranged from 1 to 5, from bottom to top, and contain: the arrangement of fiducial elements (PVC spheres with external and internal diameters of 15 mm and 10 mm respectively) filled with CuSO_4 that are distributed in each plate (8 in the 180 mm diameter and 1 in the center); the resolution inserts (prisms on plates 3 and 5 filled with CuSO_4) and plane profile (prism on plate 3) and the arrangements for signal-to-noise ratio and proton density evaluations in plate 2 (4 polypropylene spheres, internal diameter 5 mm and external diameter 7 mm filled with mixtures of H_2O and D_2O).

The Phantom of qMRI will be made up of 5 cylindrical sections or compartments of common height (40 mm) arranged from the center outwards as: section 1 (diameter 38 mm),

section 2 (internal diameter 40 mm and external diameter 78 mm), section 3 (internal diameter 80 mm, external diameter 118 mm), section 4 (internal diameter 120 mm, external diameter 158 mm) and section 5 (internal diameter 160 mm, external diameter 190 mm). Each of these sections is separated from the adjacent one by a 2mm polycarbonate sheet.

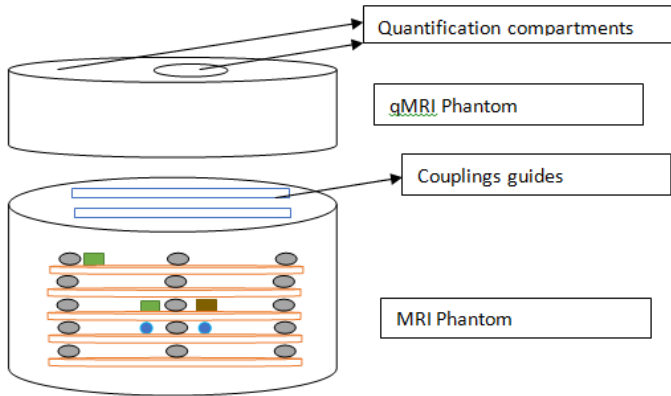


Figure 1. General scheme of the Phantom MRI-qMRI (interchangeable). Side view. Cylindrical geometry. Divided into a fixed part (MRI) and a removable and interchangeable part (qMRI) with coupling guides between the fixed part (in blue, upper cover) and the mobile part (identical to those of the fixed part, lower cover, not shown). The fixed part (MRI) will be filled with distilled and deionized water and will contain a support structure formed by 5 cylindrical plates (edges in red) that will allow fixing the set of fiducial elements (spheres in olive green), the 2 resolution inserts (rectangular prism in orange), the insertion of the slide profile (rectangular prism in dark violet) and the arrangement of the signal-to-noise ratio (spheres in aquamarine blue).

Discussion

The MRI Phantom would allow determination of non-uniformity in image intensity; the inhomogeneities of B_1 , nutation angle and inversion efficiency; as well as geometric distortion, proton density and signal-to-noise ratio. The mobile and interchangeable part (or Phantom of qMRI) can be variable, that is, it can be a Phantom to quantify T_1 and T_2 , or one to quantify diffusion metrics (ADC, TrD, FA, RD, AD, RK, AK), or one to quantify anisotropy of magnetic susceptibility, or one to quantify perfusion, etc. Actually you can have a group made up of all those Phantoms that are (each one) attachable to the fixed part (MRI). Likewise, the Phantom would also be upgradeable with new developments related to the qMRI part. On the other hand, if desired, the qMRI Phantoms and the RMI Phantom can be used independently.

The content of each section at the qMRI phantom will change depending on the type of qMRI phantom used. To quantify T_1 and T_2 it is possible to use solutions of 5 different concentrations of $MnCl_2$, solutions of 5 different concentrations of gels and paramagnetic substances, or solutions of 5 different concentrations of gels and dispersing elements (silica, wood, evaporate milk) mimicking each one: gray matter, white matter, cerebrospinal fluid, bone and skin. Another option could be to eliminate the polycarbonate sheets between the 5 compartments and to use a 3D-printed anthropomorphic phantom.

To quantify diffusion metrics (ADC, FA, TrD, RD, AD, RK and AK) can be used 5 different wood types, 5 different fiber types, or a single fiber type with 5 different densities. To quantify the anisotropy of magnetic susceptibility it is possible to fill the compartment 1 with air, compartment 2 with content mimicking the bone, compartment 3 with content mimicking the muscle, compartment 4 with content mimicking the skin and compartment 5 with content mimicking the mucus.

Conclusions

It was possible to design a phantom for magnetic resonance imaging which included a main part oriented to the evaluation of the scanner performance and an attachable and exchangeable part focused in qMRI characterization. The attachable and exchangeable part supports the possibility of to have different phantoms in one Phantom, allowing the continuous update of the qMRI part with new developments.

Acknowledgements

This work has been supported by the Centro de Neurociencias de Cuba (CNEURO) y el Centro de Biofísica Médica (Cbiomed).

References:

1. D. Kilian, W. Kilian, A. Troia, T. D. Nguyen, B. Ittermann, L. Zilberti, M. Gelinsky. ACS Appl. Mater. Interfaces. A14, 48397 (2022).
2. A. Sekowska, D. Majchrowicz, A. Sabisz, M. Ficek, B. Butto-Piontecka, M. Kosowska, L. Jing, R. Bogdanowicz, M. Szczerska. Scientific Reports. A10, 6446 (2020). <https://doi.org/10.1038/s41598-020-63581-9>.
3. A. Valladares, T. Beyer, I. Rausch Med. Phys. A47, 2023 (2020).
4. M. Suzuki, S. Moriya, J. Hata, A. Tachibana, A. Senoo, M. Niitsu. Magnetic Resonance Materials in Physics, Biology and Medicine. A32, 539 (2019). <https://doi.org/10.1007/s10334-019-00761-3>.
5. H. L. Lutsep, G. W. Albers, A. DeCrespigny, G. N. Kamat, M. P. Marks, M. E. Moseley Ann. Neurol. A41, 574 (1997).
6. S. Warach, D. Chien, W. Li, M. Ronthal, R. R. Edelman. Neurology. A42, 1717 (1992).
7. K. F. Stupic et al. Magn. Reson. Med. A86, 1194 (2021). doi: 10.1002/mrm.28779.

Blood dynamic viscosity measured using NMR

Lilian Somoano Delgado¹, Fabián Tamayo Delgado¹, Claudia Camila García Cruz¹, Abel Tobías Suárez Olivares², Diana Esperanza Monet Alvarez², Alina Salabert Revilla², Haydee Cruz Vadell³, Lidia Clara Suárez Beyries⁴, Yomaidis Araujo Durán⁴, Yamirka Alonso Geli¹, Manuel Arsenio Lores Guevara^{1,2}

¹Laboratorio de Relajación Magnética Nuclear. Centro de Biofísica Médica. Universidad de Oriente. Santiago de Cuba. Cuba.

²Hospital Ginecoobstétrico Mariana Grajales Coello, Santiago de Cuba, Cuba.

³Facultad de Enfermería-tecnología. Instituto Superior de Ciencias Médicas. Santiago de Cuba.

⁴Hospital General “Juan Bruno Zayas Alfonso”, Santiago de Cuba, Cuba.

Introduction

Blood dynamic viscosity (η_b) is a recognized medical tool for the clinical evaluation of different diseases [1, 2]. Nevertheless, the experimental method used for its determination (rotational Viscometry) is limited by the volume of sample used, the need of washing the instrument between measurements and the time needed for each measurement [1]. Proton Magnetic Relaxation (PMR) has been proposed as an alternative tool to measure the dynamic viscosity in protein solution [3, 4] allowing the determination of η_b according to:

$$\eta_b = \eta_p \left(1 - H \left[\frac{\left(\frac{\eta_{Hb} + 0.4}{\eta_p} \right)}{\left(\frac{\eta_{Hb} + 1}{\eta_p} \right)} \right] \right)^{-2.5} \quad (1)$$

Where H is the haematocrit, η_p the viscosity of blood plasma and η_{Hb} the viscosity of the intracellular hemoglobin (Hb) solution.

In this work we have used proton magnetic relaxation to evaluate η_b in healthy individuals (HI), pregnant women (PW) and patient sufferin Sickle Cell Disease (SCD).

Materials and Methods

The venous whole blood samples (HI: 27, PW: 13 and SCD: 6) were voluntary obtained using venipuncture and processed to obtain blood plasma and Hb after centrifuging (2500 rpm, 10 min), decanting and cycles of frezind and thawing [3, 4]. H was determined using classical methods.

For the measurement of the proton transverse relaxation time (T_2), a LapNMR console (Tecmag, Houston, USA) was used coupled to a permanent magnet ($B_0 = 0.095$ T, $\nu_0 = 4.03$ MHz) and the Carr-Purcell-Meiboon-Gill (CPMG) pulse sequence was employed [3, 4]. η_p and η_{Hb} were determined using PMR through the experimental relation between dynamic viscosity and T_2 [3, 4], η_b was calculated from Eq. (1) using also the H values. All the experiments were performed at 293 K. To compare mean values a student test (t-test) was used with $\alpha=0.05$. All the ethical rules included in the Helsinki convention for research with human beings were accomplished.

Results and discussion

The values of all the measured parameters in HI match with previous determinations at the lilerature [1-4] considering the temperature of measurement for the case of dynamic viscosities. This analysis should be performed carefully for the case of η_b , considering that previous determination were performed using rotational Viscometry and the reports do not specify the temperature of measurement [1, 2]. The value of η_b determined using PMR could be

interpreted as a value for zero shear stress, which means that is not affected by rouleaux formation and red blood cell deformability [1].

Table 1 summarizes the values of η_P , η_{Hb} , H and η_b obtained in HI, PW and patients with SCD.

Table 1. Values of η_P , η_{Hb} , H and η_b obtained in HI, PW and patients with SCD

Condition	η_P (mPa s)	η_{Hb} (mPa s)	H (L/L)	η_b (mPa s)
HI	2.15±0.05	18.62±1.67	0.46±0.02	8.93±0.85
PW	2.01±0.09	12.59±1.43	0.33±0.02	5.11±0.54
SCD	2.15±0.18	11.55±4.54	0.25±0.03	4.04±0.55

For the case of PW all the measured parameters are statistically diminished with respect to the HI. The decreasing of H is due to the gestational anemia characteristic of the studied cases. The observed general decreasing of the protein viscosities and hematocrite could be analyzed as a protection mechanism during pregnancy [1].

In the SCD patients the significant decreasing of η_b is related with the severe anemia which is characteristic of this hemolytic disease.

Conclusions

Proton magnetic resonance shows utility to measure blood dynamic viscosity, being the obtained results coherent with previous determinations. Was possible to evaluate this parameter in pregnant women and asymptomatic patients, suffering Sickle Cell Disease, and the method was able to follow the physiological changes concerning the condition of the studied individuals.

Acknowledgements

This work has been supported by the Belgian Development Cooperation through VLIR-UOS. The authors also wish to thank the MRI Centre of the University of New Brunswick in Canada, for the support received for the completion of this work. At the same time, the authors want to recognize the support received by the Program from the Cuban Science and Technology Ministry to develop products and services for health in Santiago de Cuba, Cuba.

References:

1. C., Huamaní, L., Cruz-Huanca, R., Herrera-Aedo, P., Damián-Saavedra, R., Marmanillo-Valenza, D., Antonio, J., De la Jara, I., Hanco, P., Anjum. *Acta Med Peru*, A40 (2), 161 (2023)
2. M. A. Gertz. *Blood*, A132, 1379(2018)
3. Y., Mengana-Torres, M. A., Lores-Guevara, J. C., García-Naranjo, B. T., Ricardo-Ferro, L. C. Suárez-Beyries, I. C. Rodríguez-Reyes, J. Philippé. *International Journal of Biochemistry, Biophysics & Molecular Biology*, 4(2), 25 (2019)
4. M.A. Lores Guevara, Y. Mengana Torres, J.C. García Naranjo, N. Rodríguez Suárez, L.C. Suárez Beyries, M.A. Marichal Feliu, T. Simón Boada, I.C. Rodríguez Reyes, J. Philippé. *Appl. Magn. Reson.* A49, 1075 (2018)

Modelling proton magnetic relaxation in hemoglobin solutions: spherical and ellipsoidal approaches

Néstor Juan Rodríguez de la Cruz¹, Manuel Arsenio Lores Guevara², Carlos Alberto Cabal Mirabal³, Robert N. Muller⁴, Sophie Laurent⁴, Fabián Tamayo Delgado¹, Juan Carlos García Naranjo¹

¹ *Universidad Autónoma de Santo Domingo, República Dominicana.*

² *Centro de Biofísica Médica, Cuba.*

³ *Centro de Neurociencias de Cuba, Cuba.*

⁴ *University of Mons, Mons, Belgium.*

Abstract:

Proton Magnetic Relaxation (PMR) has shown potential medical utility, which needs to be perfected and maximized through an adequate theoretical description, especially in hemoglobin (Hb) solutions. To model the RMP in Hb solutions we have used the dispersion curves, obtained in previous experiment in Hb solutions of intracellular concentrations and 37°C, which were fitted using a 2-sites water molecule exchange model and considering the protein as a sphere and as an ellipsoid. A significant improvement was obtained in the description of the RMP using the spherical geometry by considering the relaxation of the solvent different from that of pure water and considering this as a variable parameter in the fit. The ellipsoidal geometry constituted an even greater improvement, increasing the adjusted correlation coefficient and bringing the values of the determined parameters closer to the theoretical predictions. The use of ellipsoidal geometry to describe the Hb molecule significantly improved the description of PMR in solutions of this protein with a concentration close to the intracellular concentration and at 37°C, especially at the intermediate frequencies where the main medical applications have been developed.

Keywords: Relaxation; Hemoglobin; Protons; Magnetic.

NMR study of small protein asymmetric dimer

Dmitrii A. Luzik¹, Irene Ceccolini², Boris B. Kharkov¹, Alexandra D. Levkina¹, Ivan S. Podkorytov¹, Lewis E. Kay^{3,4,5}, Nikolai R. Skrynnikov^{1,6}

¹Laboratory of Biomolecular NMR, St. Petersburg State University, St. Petersburg 199034, Russia

²Department of Structural and Computational Biology, University of Vienna, Max F. Perutz Laboratories Vienna Biocenter Campus 5, 1030 Vienna, Austria

³Department of Molecular Genetics, University of Toronto, Toronto, ON M5S 1A8, Canada

⁴Department of Chemistry, University of Toronto, Toronto, ON M5S 3H6, Canada

⁵Department of Biochemistry, University of Toronto, Toronto, ON M5S 1A8, Canada 6 Program in Molecular Medicine, Hospital for Sick Children Research Institute, Toronto, ON M5G 0A4, Canada

⁶Department of Chemistry, Purdue University, West Lafayette, Indiana 47907, United States

LCB3 is a de novo designed small three-helix bundle protein with a molecular weight of ~7.7 kDa [1], demonstrating capability to efficiently block S protein receptor binding domain of the coronavirus SARS-CoV2 binding to human ACE2. In order to improve LCB3 affinity for mutant variants of target protein, we proposed a mini-protein mutant with the point replacement of threonine 10 to tyrosine - LCB3 T10Y.

When assessing the structural properties of LCB3 T10Y using heteronuclear NMR spectroscopy, we found that the ¹H-¹⁵N HSQC spectrum of this protein contains a set of peaks almost twice as large as expected from the amino acid sequence. This observation led us to propose that LCB3 T10Y is an asymmetric homodimer undergoing a slow conformational or monomer-dimer exchange. We performed PFG measurement of protein diffusion coefficient and relaxation rates (T₁ and T_{1ρ}) for this protein in order to estimate the size of the molecule.

Results of these measurements confirmed our dimer hypothesis, showing narrow distribution of R_{1ρ} rates corresponding to approximate protein molecular weight ~14.2 kDa (while theoretical LCB3 T10Y monomer molecular weight is 7.8 kDa) and hydrodynamic radius [2] about 22.3 Å, which is also characteristic for the dimeric form. Finally, we measured dimerization K_d using isothermal titration calorimetry and found it to be equal to be 47.9±7.7 μM.

In order to assess structural features of LCB3 T10Y at more detailed level we acquired a set of 3D-NMR spectra for double-labeled (¹³C, ¹⁵N) samples and assigned the most part of backbone and sidechain signals. Chemical shifts-based TALOS+ secondary structure prediction shows that both subunits in dimer retain monomer-like three-helix structure. In the future we plan to obtain and validate structural model of the dimer using docking and/or molecular dynamics guided by spatial restraints (solvent PRE and NOE data) and chemical shifts from NMR spectroscopy. We also plan to crystallize the LCB3 T10Y sample followed by obtaining a high-resolution structure using X-ray diffraction analysis. We hope that our study will contribute to development of methodology of NMR-based studies of such interesting systems and shed some light on mechanisms of protein asymmetric dimers formation.

Acknowledgments

The authors acknowledge Saint-Petersburg State University for a research project 15.61.2221.2013

References

1. Cao, L., Goresnik, I., Coventry, B., Case, J. B., Miller, L., Kozodoy, L., Chen, R. E., Carter, L., Walls, A. C., Park, Y.-J., Strauch, E.-M., Stewart, L., Diamond, M. S., Velesler, D., & Baker, D. (2020). De novo design of picomolar SARS-CoV-2 miniprotein inhibitors. In *Science* (Vol. 370, Issue 6515, pp. 426–431). American Association for the Advancement of Science (AAAS). <https://doi.org/10.1126/science.abd9909>
2. Wilkins, D. K., Grimshaw, S. B., Receveur, V., Dobson, C. M., Jones, J. A., & Smith, L. J. (1999). Hydrodynamic Radii of Native and Denatured Proteins Measured by Pulse Field Gradient NMR Techniques. In *Biochemistry* (Vol. 38, Issue 50, pp. 16424–16431). American Chemical Society (ACS). <https://doi.org/10.1021/bi991765g>

New methods for SABRE hyperpolarization at high magnetic field

Markelov D. A.^{1,2}, Kozinenko V. P.¹, Kiryutin A. S.¹, Yurkovskaya A. V.¹

¹*International Tomography Center, Siberian Branch of the Russian Academy of Science, Novosibirsk, 630090, Russia*

²*Novosibirsk State University, Novosibirsk, 630090, Russia*

E-mail: d.markelov@tomo.nsc.ru

Signal Amplification By Reversible Exchange (SABRE) is a member of the family of Parahydrogen Induced Polarization (PHIP) techniques aimed to enhance tremendously weak NMR-signals of heteronuclei as ^{13}C , ^{15}N , exploiting non-equilibrium singlet spin order of parahydrogen. SABRE polarization transfer takes place in metalorganic complexes in which hydrogen nuclear spins are coupled with the spins of substrate while they are transiently bound to the complex.

There are two general approaches to perform heteronuclear SABRE polarization transfer. The first one is to exploit ultralow ($\leq 1 \mu\text{T}$) magnetic fields in order for the spin system to become strongly coupled. In this regime, the difference in Larmor frequencies of nuclear spins is comparable with the spin-coupling constant. Therefore, SABRE polarization transfer from parahydrogen to the substrate occurs not inside an NMR-spectrometer, but rather inside a magnetic shield aimed to provide ultralow magnetic fields (SABRE-SHEATH, Signal Amplification by Reversible Exchange in SHield Enables Alignment Transfer to Heteronuclei) [1].

The second approach is to fulfill conditions for strong spin coupling inside the high field of NMR-spectrometer exploiting radiofrequency magnetic field pulses without an additional magnetic shield equipment. However, SABRE at high magnetic field requires RF-pulse sequence engineering. In contrast to the SABRE-SHEATH, SLIC-SABRE (SLIC, Spin Lock Induced Crossing) [2], which is the most efficient pulse sequence for heteronuclear SABRE hyperpolarization at high field, strongly depends on the symmetry of the SABRE polarization transfer complex demonstrated in fig. 1.

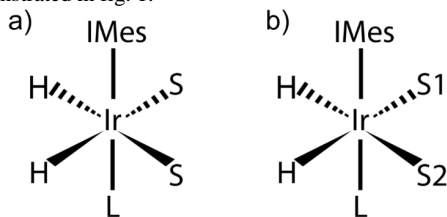


Fig. 1. (a) Symmetrical SABRE-complex, where both equatorial ligands are identical; (b) Non-symmetrical SABRE complex, where equatorial ligands are different, $S_1 \neq S_2$.

The SABRE complex is either symmetrical, i.e., the equatorial ligands of the complex are the same, therefore, hydride protons have identical resonant frequencies (fig. 1 a). The other situation is also possible, when the polarization transfer complex is non-symmetrical, i.e., it contains different equatorial ligands, therefore, hydride protons have significantly different resonant frequencies. SLIC-SABRE pulse sequence is efficient only for symmetrical SABRE-complexes [3]. Therefore, an efficient heteronuclear hyperpolarization takes place only for the substrate molecules which are able to form a symmetrical SABRE-complex, which leads to the strong restrictions on the samples.

In our work, we focus on the design of new pulse-sequences which provide an efficient ^{15}N hyperpolarization for non-symmetrical SABRE complexes. These pulse-sequences presented in fig. 2 are based on the simultaneous RF excitation of ^1H and ^{15}N nuclear spins in the SABRE complex.

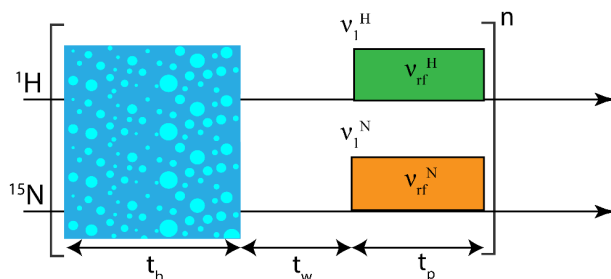


Fig. 2. Pulse sequence used for SABRE hyperpolarization at high magnetic fields for non-symmetrical complexes. One polarization cycle of the pulse sequence consists of pH₂-bubbling the sample during the time t_b , time-delay t_w necessary for removing the bubbles from the sample and then simultaneous RF excitation of ^1H and ^{15}N spins during the time period t_p . The polarization cycles is sequentially repeated n times.

We found that exploiting weak RF magnetic fields allows one to efficiently hyperpolarize ^{15}N nuclei, that is, ^{15}N signal enhancement relative to the thermal signal acquired at 9.4 T was equal to 2500. Due to its high selectivity, we also consider proposed pulse sequences as a very precise method for obtaining heteronuclear ^{15}N - ^1H correlations in the non-symmetrical SABRE complexes. We tested our method on the sample which consisted of two biologically relevant molecules (antibiotics) as a substrate on the natural isotopic abundance of ^{15}N (0.36%): tinidazole (TNZ) and secnidazole (SCZ) in the presence of DMSO as a co-substrate. The structure of the substrates is demonstrated in fig. 3.

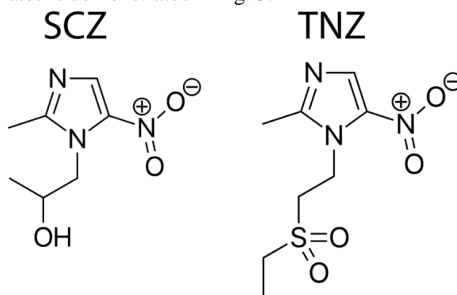


Fig. 3. The structure of the substrates used for hyperpolarization at high field: secnidazole (left) and tinidazole (right).

Using high selectivity of the proposed pulse sequence, we were able to detect the heteronuclear correlations with the difference in 30 Hz between the hydride protons resonant frequencies and 20 Hz difference between the complexes-bound ^{15}N resonant frequencies, as demonstrated in fig. 4.

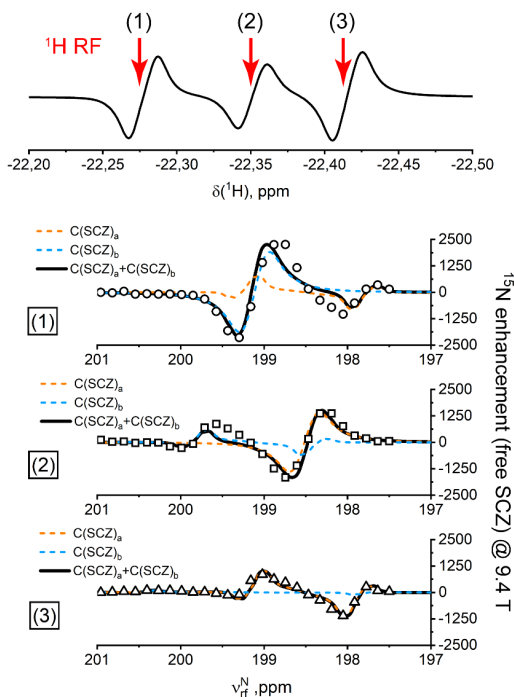


Fig. 4. Dependence of ^{15}N enhancement of SCZ on the frequency of ^{15}N RF-field. ^1H RF frequency was resonant towards (1) -22.277 hydride proton; (2) -22.35 hydride proton; (3) -22.415 hydride proton. From the comparison of calculations with the experiment we determined the following ^{15}N - ^1H SCZ correlations: (198.52 ppm; -22.35 ppm) and (199.12 ppm; -22.28 ppm). While for TNZ we obtain (200.9 ppm; -22.42 ppm). The sample was consisted of 30 mM of SCZ and 37 mM of TNZ at natural ^{15}N isotopic abundance. Experimental parameters: $\nu_1^{\text{N}} = \nu_1^{\text{H}} = 8 \text{ Hz}$, $t_p = 0.5 \text{ s}$, $t_w = 0.5 \text{ s}$, $t_b = 0.5 \text{ s}$, $n = 30$.

Acknowledgements

This work is supported by the Russian Science Foundation (№ 23-73-10103).

References

- M.L. Truong, T. Theis, A.M. Coffey, R.V. Shchepin, K.W. Waddell, F. Shi, B.M. Goodson, W.S. Warren, E.Y. Chekmenev, ^{15}N Hyperpolarization by Reversible Exchange Using SABRE-SHEATH, *The Journal of Physical Chemistry C*, 119 (2015) 8786-8797.
- S. Knecht, A.S. Kiryutin, A.V. Yurkovskaya, K.L. Ivanov, Efficient conversion of anti-phase spin order of protons into ^{15}N magnetisation using SLIC-SABRE, *Molecular Physics*, 2018 (2018) 1-10.
- J.R. Lindale, S.L. Eriksson, W.S. Warren, Phase coherent excitation of SABRE permits simultaneous hyperpolarization of multiple targets at high magnetic field, *Physical Chemistry Chemical Physics*, 24 (2022) 7214-7223.

Design of large volume RF probe for NQR Detection applications

G. Mozzhukhin¹, P. Kupriyanov¹, E. Doğan¹, A. Maraşlı¹, B. Çolak¹, B. Rameev^{1,2,3}

¹Gebze Technical University, 41400 Gebze/Kocaeli, Turkey

²Kazan State Power Engineering University, 420066 Kazan/Tatarstan, Russian Federation

³Zavoisky Physical-Technical Institute, FRC Kazan Scientific Center of RAS, 420029

Kazan/Tatarstan, Russian Federation

E-mail: mgeorge@gtu.edu.tr

Abstract

Nuclear quadrupole resonance (NQR) is an efficient method of the reliable identification of nitrogen-containing explosives because it probes a chemically specific NQR spectrum. However, it is characterized by an inherently low signal-to-noise ratio and the effect of radiofrequency interference. Furthermore, the technical realization of the approaches for scanning large volumes or distances is not a trivial task. In this work, the design of a large-volume RF probe for the NQR detection of ammonium nitrate in large volumes is presented. The most efficient design of the RF probe has been proposed and an NQR signal of AN has been successfully detected. The NQR signal magnitude depending on the AN sample position has been measured. Furthermore, detection of the NQR signal for the cases of a partially shielded volume and conducting bodies placed near a sample have been demonstrated.

Introduction

Nuclear Quadrupole Resonance (NQR) is a well-known technique for the bulk detection of solid nitrogen-based explosives. ¹⁴N isotope of nitrogen is a quadrupolar nucleus with the spin I=1 and 99.6% natural abundance. The transition frequencies of ¹⁴N quadrupole splitting energy levels for most nitrogen compounds lie in the frequency range of 0.06-5.5 MHz. Detection of explosives with the use of the NQR technique usually relies on the registration of one of three NQR lines NQR spectrum. The signal intensity depends strongly on material features (frequency of an NQR line and specific relaxation conditions), technical realization conditions (detector parameters, electronics, etc.) and post-detection signal processing (filtering, identification/classification and noise mitigation). In the case of large volume or large distance scanning, the design of an RF detector becomes an extremely important issue because it has very specific features rather different from the case of a typical solenoidal RF probe used in research NQR/NMR spectrometers.

In this work, we report on the design of an NQR probe with an effective detection volume of 130 liters and a small sample filling factor. The probe is designed for a low-frequency range (~500 kHz), that corresponds to the highest frequency NQR line of Ammonium Nitrate (AN).

Experimental Methods, Results and Discussion

NQR detection of ammonium nitrate

Ammonium nitrate NH₄NO₃ (AN) is widely used in mining as an industrial explosive and in agriculture as fertilizer. Most examples of improvised explosive devices (IEDs) have been made of fertilizer AN due to relatively easy access to this material. A pure AN has the form of colourless crystallites which are pressed in the form of granules for fertilizing applications. Depending on temperature, five crystalline forms of AN are possible, of which only two at ambient temperatures are important for explosive detection. The β form is stable from -16.9°C to +32.2°C, while the γ form is stable from +32.2°C to +84.2°C [1]. The most suitable frequencies for the detection of AN are ν_{-} = 424 kHz and ν_{+} = 496 kHz at room temperature with the temperature coefficients, $\Delta\nu/\Delta T$ = +100 Hz/K and -300 Hz/K, relatively.

The T_1 relaxation parameter is 13 s for the ν_+ line and it is 16 s for the ν_- transition. A long spin lattice (T_1) relaxation time does not allow a short detection time. The detection of NQR by Spin-Locking Spin Echo (SLSE) sequence provides the shortest detection time (optimal scan time) T_{opt} [2]. The pulsed magnetic fields can be applied to decrease the detection time by acceleration of relaxation processes [3]. It should be noted that AN is usually used in rather large quantities because it has smaller explosive power in comparison with other explosives. Thus, a low sensitivity of NQR detection of AN is compensated by typically large AN quantities used in IEDs.

The electronic system consists of a *Tecmag Apollo* NQR console, a 4 kW *Tomco* pulse amplifier and homemade additional electronic units. The resonance frequency of the RF probe is tunable in the range of several kHz. The quality factor for the loaded coil is near 180-200. Spin-locking spin echo (SLSE) pulse sequence has been used for the detection of NQR. We used the pulse sequence which includes phase cycling in two successive series of spin-locking pulses: $t_i - (\tau - t_i^{+90^\circ} - \tau)^n - relax - t_i^{+180^\circ} - (\tau - t_i^{+90^\circ} - \tau)^n - relax$, where t_i is a pulse duration, n is a number of pulses, τ is an interval between pulses, and *relax* time is typically in the range of $(3-5)T_1$ [4].

Design criteria

The design of the probe for scanning large volumes is defined by the following limitations: maximum sensitivity with high signal-to-noise ratio (SNR), maximally possible noise resiliency for outside interference, and needed detection threshold for a given material in a given volume with a known (usually low) sample filling factor. The sensitivity of NQR/NMR resonance probe mainly defined by quality factor Q as $SNR \sim \sqrt{Q}$ [5]. However, high Q increases the unwanted ringing process t_D in resonance circuit defined by the approximate formula $t_D = 20 Q / \pi \nu_0$ for power of pulses near 1 kW, where ν_0 is resonance frequency of circuit [6]. This transient process is important obstacle in the AN detection because for high Q values it masks the NQR signal. Thus, we need to design a special Q-switch device to attenuate the unwanted oscillations process while saving a high Q value at the receiving stage. Our experience shows that Q approximately equals 200 is enough for successful detection of AN. This Q value, however, results in the ringing process with duration of at least 2.5 ms after the end of radiofrequency pulse, that makes the detection NQR signal by the multipulse sequences [Ошибка! Закладка не определена.] impossible without Q-switch. A special Q-switch with a property of scaling of the attenuation of transition processes in dependence of applying power is highly desirable. Currently our system is tested for 130 liters of the detection volume. The next step would be scanning volume of 8000 liters.

The SNR of NQR signals is also depends from average radiofrequency induction B applied to ^{14}N nuclei. The design of coil has to provide homogeneous radiofrequency induction over of all big effective volume of coil. Additional property of this coil is a maximum resilience to outside interference because it is very difficult and expensive to shield large objects electrically. The level of outside interference is defined by surrounding media including broadcasting signals and technological signals. We need also additional tools for active attenuation of outside interference for the value of $>20-30$ db

Solutions

For the remote detection of NQR there are following types: planar and volume gradiometers [6, 7], solenoid coil with big volume of 160 liters [2], and semi-toroidal coil [8]. We used semi-toroidal coil because this coil has distribution of field concentrated inside the gap of coil and homogeneous distribution of field. We made modeling of this coil by the finite element method (FEM). This coil for effective volume of detection of 130 liters is presented in Fig. 1a.

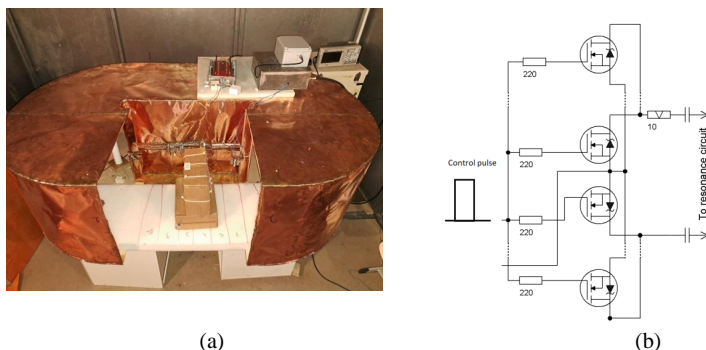


Figure 1. a) Semitoroidal coil for the detection of AN; b) simplified diagram of final stage of Q-switch.

For switching of Q we used silicon carbide MOSFET's G2R1000MT (from 8 to 24 items parallel) with low device capacitances and low direct resistance (see Fig.1b). Q-switch is controlled via optocoupler and galvanic isolated from other devices. To exclude additional noise, we used a car accumulator as electrical power supply. The loaded Q of our parallel circuit is near 190. The results of application is presented in Fig. 2.

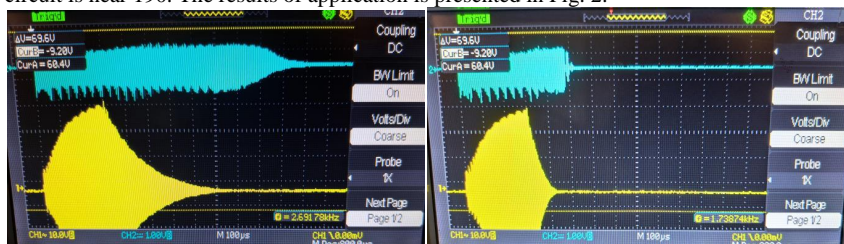


Figure 2. Application of Q-switch in probe: (a) signals without Q-switch, yellow is a signal from probe antenna, blue is a signal after preamplifier of receiver; (b) signals with Q-switch, yellow is a signal from probe antenna, blue is a signal after preamplifier of receiver

Finally, the dead time for transmitting power of radiofrequency pulses 3 kW is 700 μ s. We also designed the second channel for attenuation outside interference. This system includes solenoid antenna in parallel resonance circuit, preamplifier with tuning gain up to 30 dB, phase shifter 0-180°, and simple subtractor with use of transformer. The results are also affected by the level of outside interference. The attenuation with aid of the second channel is in the range of 20-30 dB.

Conclusions

Thus, we designed a radio-frequency probe for the NQR detection of AN in a large volume. Our system allows detecting both pure AN and different AN mixtures. We have demonstrated a successful NQR detection signal of AN with the detection time of 1 minute for the case of the 4 kg of the AN fertilizer (the filling coefficient is near 0.013).

Acknowledgements

The current research has been supported by the Technology Transfer Office (TTO) of Gebze Technical University.

References

1. J. Seliger, V. Žagar, R. Blinc, ^{14}N NQR study of the structural phase transitions in NH_4NO_3 , *Z. Physik B. Condensed Matter* 77, 3, (1989) 439-443;
2. G.V.Mozzhukhin, S.V.Molchanov, G.S.Kupriyanova, A.V.Bodnya, V.V.Fedotov, Hao Guoxin, Jin Yanbo, Ren Tianliang, Zhang Guojin.- In book:Explosives Detection using Magnetic and Nuclear Resonance Techniques. Series: NATO Science for Peace and Security Series. Springer 2009, 231-244
3. G.V. Mozzhukhin, B.Z.Ramev, G.S.Kupriyanova, B.Aktaş, Cross-Relaxation Enhanced NQR of Ammonium Nitrate in Low Magnetic Field, In: Explosives Detection using Magnetic and Nuclear Resonance Techniques. Series: NATO Science for Peace and Security Series. Eds: Tomaz Apih, Bulat Rameev, Georgy Mozzhukhin, and Jamie Barras, Springer, 2014, 45-59.
4. J.Smith, N.Pierson. Patent No.: US 6,208,136 B1.,Aug.22,1997
5. Т.Фарраp, Э.Беккер. Импульсная и фурье-спектроскопия. Изд. «Мир». М. 1973
6. Allen N. Garroway, Michael L. Buess, Joel B. Miller, Bryan H. Suits, Andrew D. Hibbs, Geoffrey A. Barrall, Robert Matthews, and Lowell J. Burnett, Remote Sensing by Nuclear Quadrupole Resonance, *IEEE Trans. Geosci. Remote Sens.* 39(6) (2001) 1108-1118.
7. G. V. Mozzhukhin, A. V. Efremov, A. V. Bodnya and V. V. Fedotov, A Two-Spiral Flat Coil for Detecting ^{14}N NQR Signals, *Russian physics Journal*,2005, Volume 48, Number 9, Pages 978-983
8. J. Barras, M. J. Gaskell, N. Hunt, R. I. Jenkinson, K. R. Mann, D. A. G. Pedder, G. N. Shilstone, J. A. S. Smith. Detection of ammonium nitrate inside vehicles by nuclear quadrupole resonance , *Applied Magnetic Resonance*, 2004, Volume 25, Number 3-4, Page 411

NMR Study of Ion Behavior in lithium acetate – cesium acetate aqueous solutions.

Kirill A. Mukhin^{1,2}, *Olga N. Pestova*¹, *Vladimir V. Matveev*²

¹ *Department of General and Inorganic Chemistry, Chemistry Institute, Saint Petersburg State University*

² *Department of Nuclear Physics Research Methods, Saint Petersburg State University,*

E-mail: st085268@student.spbu.ru, v.matveev@spbu.ru

Introduction

The search for environmentally friendly, safe electrolytes for lithium-ion batteries (LIBs) are still being researched today by many researchers. Ternary water-acetate systems based on alkali metal acetates are being actively studied. In this case, acetate salts with higher solubility is added to lithium acetate (LiOAc). Systems with potassium acetate (KOAc) [1, 2] and cesium acetate (CsOAc) [3, 4] were studied. In the system with CsOAc, the properties of such ternary systems at the molecular level, namely the ions mobility in solution, have not been emphasized. In addition, there is a problem associated with the establishment of the limiting concentration of cesium acetate both in water and in the ternary system lithium acetate - cesium acetate - water. We attribute this to the existence of cesium acetate solvate, so the synthesis of anhydrous CsOAc deserves special attention.

CsOAc synthesis and system preparation

Synthesis of cesium acetate crystalline solvate (CsOAc*HOAc) was carried out from glacial acetic acid and cesium carbonate with subsequent crystallization at evaporation and cooling of the mixture. The synthesis of anhydrous cesium acetate was carried out according to the method [5], slightly modified for laboratory synthesis.

Using the synthesized CsOAc a set of ternary $7\ m\ \text{LiOAc} - x\ m\ \text{CsOAc} - \text{H}_2\text{O}$ ($x = 1, 3, 5, 7$) systems was prepared. Also, samples of $5\ m$ both cesium salts in water were prepared to confirm the differences in composition between the anhydrous salt and the solvate. Concentrations of all samples were confirmed by integration of ^1H NMR spectrum by the ratio of water and CH_3 -group signals, part of the results are given in Table 1.

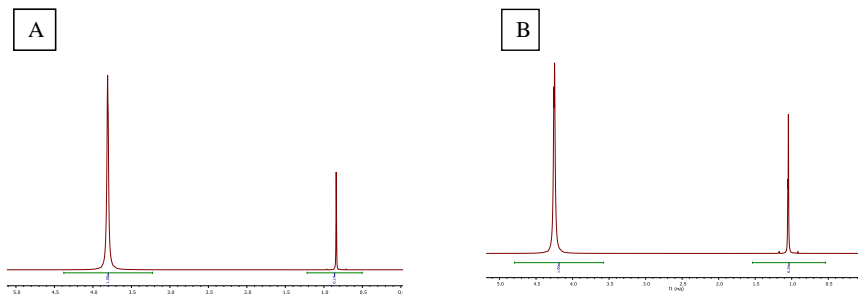


Figure 1. ^1H NMR spectra of samples $5\ m\ \text{CsOAc}$ (A) and $5\ m\ \text{CsOAc*HOAc}$ (B)

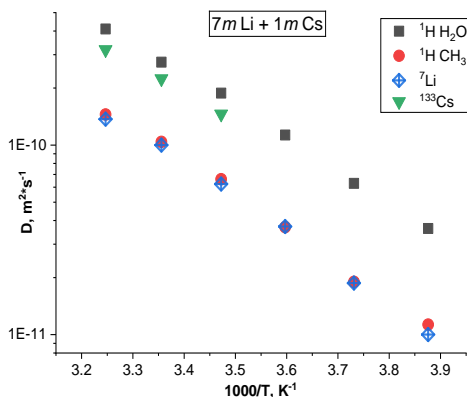
Table 4. Comparison of sample concentrations

Sample	5m CsOAc	5mCsOAc*HOAc	7m Li + 1m Cs	7m Li + 5m Cs
Total <i>m</i> salt (by preparation), mol/kg H ₂ O	5.0	5.0	8.0	12.0
Total <i>m</i> salt (NMR data), mol/kg H ₂ O	5.1	5.0	8.0	11.9

As shown in Table 1, the concentration determined by NMR coincides with the concentration by preparation.

Diffusion and viscosity

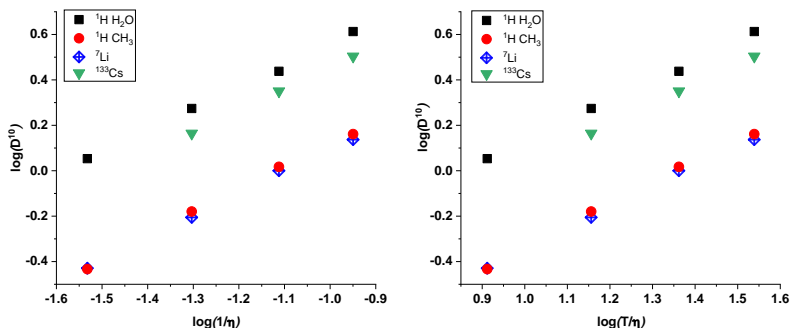
Temperature dependences of diffusion coefficients were measured using NMR diffusometry on ¹H, ⁷Li and ¹³³Cs nuclei for ternary systems. Temperature dependences of solution viscosities were also obtained.



The figure on the left shows temperature dependences of diffusion coefficients for a sample of 7 *m* LiOAc + 1 *m* CsOAc. It can be clearly seen that $D(\text{Cs}^+)$ is larger than $D(\text{Li}^+)$ and $D(\text{CH}_3\text{COO}^-)$.

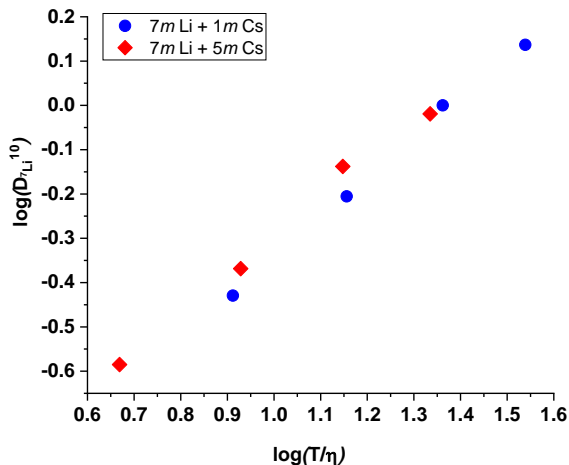
Apparently, it is related to the strong solvation of lithium cation and practically no solvation of cesium cation. It would be of undoubted interest to compare the electrical conductivity of the sample with the ion diffusion coefficients.

Then we decided to compare mobilities at the bulk and molecular level. We plotted the dependences of diffusion coefficients on the inverse viscosity and on the value of (T/η) . As is known, the linear dependence of $\lg D$ against $\lg (T/\eta)$ corresponds to the fulfillment of the Stokes-Einstein or fractional Stokes-Einstein ratios.



Diffusion factors vs. fluidity and (T/η) for the 7m LiOAc + 1m CsOAc sample.

We also compared systems with different contents of cesium acetate using such dependences. The figure below shows the logarithm of lithium ion diffusion from (T/η) for samples $7m$ LiOAc + $1m$ CsOAc and $7m$ LiOAc + $5m$ CsOAc.



Note also that the dependences $D(\text{Li}^+)$ vs. (T/η) for both systems have similar behavior, which may indicate the invariance of the effective radius for Li-ions, which means that the nearest environment of lithium ions does not change.

Acknowledgements

This work was supported by the Russian Science Foundation (project № 23-23-00049). NMR measurements were carrying out in Centre for Magnetic Resonance of Research Park of St. Petersburg State University.

References

1. Lukatskaya M.R., Feldblyum J.I., Mackanic D.G. *et al.* – Energy Environ Sci. 2018. V. 11. No. 3. P. 2876. doi:10.1039/c8ee00833g
2. Matveev V.V., Pestova O.N., Tyutyukin K.V. & Chizhik V.I. – Applied Magnetic Resonance 2023. V. 54. No. 10 P. 971. doi:10.1007/s00723-023-01558-3
3. Chen S., Lan R., Humphreys J., and Tao S. – Applied Materials Today 2020. V. 20. P. 100728. DOI:10.1016/j.apmt.2020.100728.
4. Liu S., Dr. Stettner T., Klukas R. *et al.* – ChemElectroChem. 2022. V. 9. No. 22. e20220071. doi:10.1002/celec.202200711
5. L. Liangbin, Ye Ming, W. Meng *et al.* Patent CN, no. CN116283548A, 2023.

Applicability limits of the Anderson-Weiss approach to polymer melts

Eugeny M. Pestrvaev

Department of Physics, Ufa State Petroleum Technological University, Ufa, Kosmonavtov St., 1, 450062, Russian Federation

E-mail: physics_usptu@mail.ru

Simulating the FID by definition

The conceptually simplest response of a spin system to 90°-pulse impact, FID, is described by a non-analytical expression representing the normalized statistical summation over all spins of the system [1]: for the sake of discussion and without loss of generality, it is written in discrete form for a freely jointed polymer chain in an isotropic model entangled melt [2]:

$$g(t) = \frac{2}{N} \sum_{i=1}^{N/2} \langle \cos \left\{ b_i \int_0^t [3 \cos^2 \theta_i(t'/\tau_i) - 1] dt' \right\} \rangle; \quad (1a)$$

$$b_i \approx S'(i) \cdot S_K(64) \cdot b_K(64); \quad \tau_i \approx \tau'(i) \cdot \tau_K(64); \quad (1b)$$

$$S_K(64) \approx 0.037; \quad b_K(64) \approx 0.035, 0.25; \quad \tau_K(64) \approx 2.8; \quad N = 127. \quad (1c)$$

Here θ_i is the angle of the i -th Kuhn segment coinciding with the inter-spin vector relative to the external constant magnetic field, B_0 . Fluctuations of the i -th Kuhn segment, characterized by the correlation time τ_i , control the dipole coupling (DC), b_i , with a maximum value for the middle segment of the entangled chain $b_K(64)=0.035$ in computer modeling of a high-temperature melt and 0.25 for a low-temperature melt. The non-analytical functions $\tau'(i)$ and $S'(i)$ are characterized by the similar behavior and describe the heterogeneity of dynamics and anisotropy of conformational fluctuations, i.e., the dependences of τ_i and b_i on the segment position along chain: $2 \cdot N_E$ segments at each of the two chain ends move freely and for them $S(i \leq N_E) < 1$; the remaining middle segments of the chain are inhibited and for them $S(i > N_E) = 1$, where N_E is the number of segments between adjacent entanglements along a chain of $N=127$. Angle brackets indicate melt averaging.

Simulating the FID by the Anderson-Weiss approach

Obviously, (1a) does not allow analyzing $g(t)$ with changes in temperature and chain-length, even a relatively short one, that is in fact for a low-molecular-weight liquid. Therefore, even at the dawn of the liquids study by NMR-relaxation, the Anderson-Weiss approach (AWA) was derived [1], which provides a powerful analytical tool in which the main characteristic of molecular motion – an orientation autocorrelation function (OACF), $C(t)$ – is transformed in the FID by a simple convolution with time:

$$g(t) = \frac{2}{N} \sum_{i=1}^{N/2} \langle \exp \left[-\Delta\omega_i^2 \int_0^t (t-t') C_i(t'/\tau_i) dt' \right] \rangle; \quad (2a)$$

$$\Delta\omega_i^2 = \frac{4}{5} b_i^2; \quad (2b)$$

$$g(t) = \exp \left\{ - \left(\frac{2}{N} \sum_{i=1}^{N/2} \Delta\omega_i^2 \right) \int_0^t \left[\left(\frac{2}{N} \sum_{i=1}^{N/2} C_i(t'/\tau_i) \right) \right] (t-t') dt' \right\}. \quad (2c)$$

Here, the factor 4/5 relates the intra-segmental DC with the NMR second moment, $\Delta\omega_i^2$. Unlike low-molecular liquids, where in most situations a single exponential OACF $C(t) \sim \exp(-t/\tau)$, is sufficient, the kinetic units of the polymer chain in the melt participate in several types of motion with very different correlation times, as a consequence of which the resulting OACF in (2a) can be split into a sum and the FID into a product, respectively.

Equation (2a), even in using the simplest exponential OACF for any kind of motion, makes it possible to approximate and analytically describe the FID transformation for many systems in a wide range of changes in thermodynamic parameters, especially if release from

summation by averaging the DC and OACF along the chain, as is option (2c). In theoretical calculations, it is (2c) that is used based on the ergodicity assumption for the spin system of chains in the melt [3] and being absence the dynamic heterogeneity of segments along the chain. However, the latter is not true even in a high-temperature melt [4], as can be seen in the figure.

Comparing with typical experimental FIDs

The left panel shows solid-phase low-temperature FIDs, and the right panel shows liquid-phase high-temperature ones. The three curves in each panel have the same numbering: 1 is according to formula (1a), 2 is according to formula (2a), and 3 is according to formula (2c).

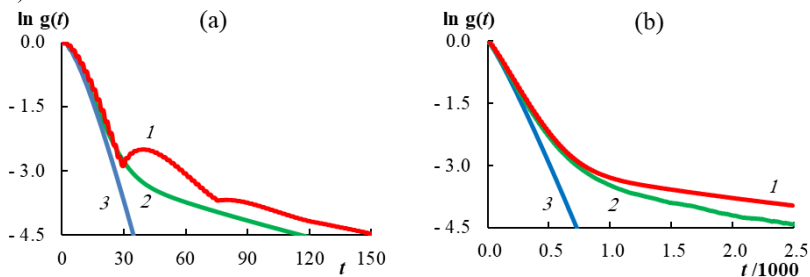


Figure 1. Low-temperature solid-phase (a) and high-temperature liquid-phase (b) FID in the melt of chains of 127 Kuhn segments, obtained by the definition in equation (1a) (curves 1); using the Anderson-Weiss transformation when averaging the signal in equation (2a) (curves 2) and when averaging the OACF in equation (2c) (curves 3)

The curves comparison of all three pairs shows that, within the typical experimental accuracy, the initial component in its most part is satisfactorily described by all three options, but oscillations in the low-temperature melt are reproduced only by the FID definition (a, curve 1). The FID tails – with slower damping due to freely motion of two chain ends – are reproduced only when taking into account the dynamic heterogeneity along the chain (curves 1 and 2), both at low and high temperatures. Averaging the DC and OACF over the entire chain leads to a dominant contribution from the hindered middle segments, and information about the dynamics of the end dangling fragments is lost in these FID approximations (curves 3).

Another limitation on using the AWA to polymer melts is due to the fact that in some time intervals related to different regimes of chain diffusion, the OACF is described by a power function $C(t) \sim (t/\tau_K)^{-\alpha}$, which was revealed relatively recently when reconstructing the OACF from the dispersion of spin-lattice relaxation [5] and in computer modeling [6]. To find out the interval α at which the AWA is applicable, consider the exponent (2a):

$$\ln g(t) \sim -\Delta\omega_K^2 \int_0^t (t-t') \left(\frac{t'}{\tau_K}\right)^{-\alpha} dt' = \frac{-\Delta\omega_K^2 \tau_K^2}{(1-\alpha)(2-\alpha)} \left(\frac{t}{\tau_K}\right)^{2-\alpha} = \frac{-\Delta\omega_K^2 \tau_K^2}{\beta(1-\alpha)} \left(\frac{t}{\tau_K}\right)^\beta. \quad (3)$$

The first value $\alpha=0$ in the table corresponds to a static or quasi-static state, for example Kuhn segments, and gives the exact Gaussian form of the FID with $\beta=2$. Increasing values of α (columns 3÷6) give a Gaussian-like FID in the form of the Weibull exponential $\exp[-const \cdot (t/T_2)^\beta]$ with $1 < \beta < 2$ [7], respectively. However, the value $\alpha \geq 1$ (columns 7 and 8) is not included in the AWA applicability range, since it gives not a damped, but an increasing FID due to the exponent in (3) becomes negative. Since results of the OACF reconstruction from the spin-lattice-relaxation dispersion [5] and computer modeling [6] in polymer melts give an interval of $0.3 < \alpha \leq 1.5$ over the vast majority of its duration – a tail

of 4 decimal orders out of 7 – then it becomes obvious that the FID approximation on the terminal stage by the AWA, where the intermolecular contribution to the OACF with $\alpha > 1$ dominates [6], provides highly distorted information about the structural and dynamic characteristics of the chain.

The exponents α & β in equation (3)							
l	2	3	4	5	6	7	8
α	0	1/4	1/2	3/4	1	3/2	7/4
$\beta = 2 - \alpha$	2	7/4	3/2	5/4	1	1/2	1/4

Let us illustrate the necessity and fruitfulness of taking into account the latter circumstance with a recent theoretical description of FID in an entangled melt [8], based on solving the stochastic equation of the

primitive segment one-dimensional self-diffusion in a tube and definition (1a), that is, without the AWA use. The resulting solution showed that the magnetization of the chain middle inhibited segments decays in two stages: the main part as the initial Gaussian-like component of the FID (4a); the remaining part with an amplitude below the noise level (4b) and therefore has never been observed before to the best my knowledge [9]. This last component is controlled by the primitive segment residual DC, inherited from the previous highly anisotropic diffusion regime.

$$g_P(t < 3\tau_E) \sim \exp \left[-const \cdot (t/\tau_K)^{\frac{7}{4}} \right], \quad \tau_E \text{ is the entanglement time}; \quad (4a)$$

$$g_T(3\tau_E < t) \sim \exp \left[-const \cdot (t/\tau_K)^{\frac{1}{4}} \right]. \quad (4b)$$

It is interesting to note that the first stage of the transverse magnetization decay (4a) corresponds to the hydrodynamic form of the Kuhn segment OACF in this interval $C(t) \sim (t/\tau_K)^{-1/4}$ [2] and is described by the AWA (column 3); however, the second stage (4b) leaves the AWA definition domain, since it corresponds to $\alpha = 7/4$ (column 8).

Conclusion

Experimental FIDs in polymer melts, approximated by AWA, produce fairly correct information about the structural and dynamic characteristics of macromolecules, provided that the tail and initial component are considered separately. In the low-temperature region, approximation of the oscillating FID using the AWA provides highly distorted information about the dynamics of the macromolecule, which is now dominated by the quasi-static residual DC, which is a small part of the intrasegmental DC, but is still used in the FID being approximated.

The long-time tails in the figure (curves 1 and 2) are due to the dynamic heterogeneity of the chain in entangled melt and are described by a simple superposition of the partial FIDs for the Kuhn segments even in the frame of AWA.

Comparing the definition domain for the standard AWA with the latest theoretical solution which is confirmed in experiment [8] and simulation [9], says that the standard AWA can only be used to describe the FID initial part. At the same time, to describe the reptation tail (4b) with a small amplitude the FID definition must be used.

References

1. A. Abragam. The principles of Nuclear Magnetism – Clarendon pr., Oxford, 1961.
2. E.M. Pestryaev – J. Phys.: Conf. Ser., 324, 012031 (2011).
3. E.M. Pestryaev – Polym. Sci.: Ser. A, 60, 530-551 (2018).
4. E.M. Pestryaev – Polym. Sci.: Ser. A, 62, 766-778, 779-792 (2020).
5. A. Herrmann et al □ Macromolecules, 45, 6516-6525 (2012).
6. P. Henritzi et al □ Solid State Nucl. Magn. Reson., 54, 32-40 (2013).
7. S. Kaufman and D.J. Bunker – J. Magn. Reson., 2, 218-222 (1970).
8. N.F. Fatkullin, T. Korber, E.A. Rossler – Polymer, 142, 310-315 (2018).
9. E.M. Pestryaev – Polym. Sci.: Ser. A, 61, 283-288 (2019).

An alternative proposal of gradient coils configuration for ultra-low field magnetic resonance imaging

Alexander Fedotov¹, Vladimir Pugovkin¹, Denis Burov¹, Anna Hurshkainen¹ and Carlos Cabal Mirabal^{1,2}.

¹Department of Physics, ITMO University, St. Petersburg, Russian Federation

²MRI Department, Cuban Neuroscience Center, Havana, Cuba

E-mail: aleksandr.fedotov@metalab.ifmo.ru

<https://physics.itmo.ru/>

Introduction

Gradient coils play a determinant role in implementing spatial encoding magnetic resonance imaging (MRI) for achieving high quality. In the context, of ultra-low field MRI systems with permanent magnets present specific problems: the existence of little space between the poles of the permanent magnet is associated with Eddy currents (EC), mutual inductances, and heating on the patient which are critical factors to take into consideration.[1]

In modern low-field MRI systems, a prevalent solution involves planar gradient coils positioned at the magnet poles to generate the three gradients (G_x, G_y, G_z). This configuration partially preserves free space within the magnet. However, it introduces challenges related to induced EC, and attempts to mitigate their impact may compromise gradient coil efficiency and linearity. [1, 2]. Fortunately, there are also known approaches that propose the design of gradient systems of arbitrary, including cylindrical, geometry, allowing coils to be located near the area of interest [3]. These coils reduce the occurrence of EC and also have good efficiency. However, the dense conductor arrangement and intricate geometry in such systems result in increased mutual inductance. Finally, classical gradient field formation, using Maxwell and Helmholtz coils, requires additional optimization for parameters like linearity and gradient intensity within the area of interest while maintaining good efficiency. [4, 5]

In this work, knowing the restrictions of flat coils, another possible configuration is presented. Numerical simulations show that the coils have good gradient efficiency and linearity.

Material and methods.

In this study, specific requirements and initial parameters were followed depending on the magnet configuration. These dimensions encompass a 27 cm distance between poles and a 70 cm width. The proposed configuration has non-local coils for gradients along the Y-axis and two local cylindrical coils for gradients along the X and Z axes chosen coordinate system. The general view is shown in Fig. 1.

This configuration has potential advantages. It has more free space inside magnet because relocating Y gradient coil. It also may reduce issues related to EC, heating effects, and mutual inductance.

Non-local coils.

To describe the system of the non-local coils used the following target function:

$$Q = \omega_1 \frac{ROI^2}{2\mu_0} \sum_{i=1}^N (G_i - G_0|_{z=0})^2 + \omega_2 \frac{1}{2} \sum_{i,j}^N L_{ij} I_i I_j + \omega_3 \tau \sum_i^N R_i I_i^2 - \omega_4 \left| \frac{ROI^2}{2\mu_0} \sum_i^N \left(\frac{dB_i}{dy} \right)^2 \right|$$

Formula 1. Target function: w_i – the weight coefficients chosen so that different components of the target function contribute equally to the optimization of the parameters, L_{ij} – self-inductance of coil, I_i – current of coil, G_i – the value of gradient intensity at some point, G_0 – the value of gradient intensity at the isocenter.

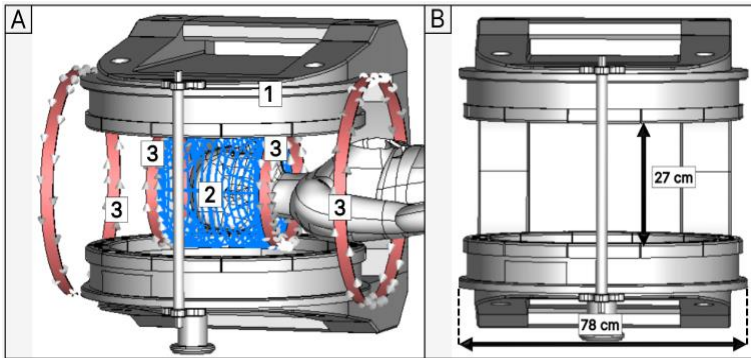


Figure 1, A. Main view of the proposed configuration, 1 – magnet, 2 – local-coil, 3 – non-local coil;
B. Magnet dimensions.

Python script was used to optimize the geometry parameters: currents, inductances, radius of rings, and distance between pairs of rings. To select an algorithm for this optimization problem, it was selected several candidate algorithms that could handle this task: BFGS, TNC, and JADE. Then optimization was performed with each of the algorithms, as a result of which we found out that BFGS, TNC algorithms fall into local minimum. It was founded by changing the optimization starting point and obtaining different optimization parameters under the same boundary conditions. The JADE algorithm showed stability with respect to the change of the initial optimization point and produced the point of global minimum of the target function. The program code consisted of several stages. At the beginning, the parameters to be optimized were entered: currents, radii of rings and distances between rings. Then, enough points were generated in the ROI space to produce correct optimization. Then target function was calculated at the points and optimized. As a result, the optimized data was obtained. CST Studio 2022 software (Dassault Systèmes) was used to magnetostatic numerical simulations. Based on the data obtained, it is possible to estimate the efficiency and linearity of the gradient.

Local coils.

Local coils were designed using an algorithm based on the boundary element method (BEM). The target field method involves creating a wire geometry such that the required magnetic field gradient is created in the region of interest (ROI) - a sphere with a radius of 20 cm. In general, the process of designing gradient coils can be divided into the optimization stage and the post-processing stage. For optimization, the electric current density or its scalar flux function (SF) satisfying optimization conditions is calculated. Subsequently, the current density is approximated by discrete loops, and these disconnected parts are then connected into a unified coil conductor, represented as a sequence of three-dimensional (3D) coordinates. Numerical calculations were carried out Matlab 2022b (The Math Works) using an open-source code – CoilGen [6]. Based on the results of constructing an array of conductor points for a given cylindrical configuration, magnetostatic numerical simulations were performed using CST Studio. The points were combined into a single current path. As a result of the simulation, magnetic field distribution maps were obtained, as well as efficiency and linearity of the gradient.

Result and discussion

All the optimization results for local and non-local coils shown in Table 1.

It is worth noting that a gradient Z coil is obtained by slightly increasing the radius of the X coil and rotating the system 90 degrees along the axis of symmetry. Thus, the combination of local and non-local coils represents the proposed configuration of the gradient system described in Fig. 2.

Table 1. Obtained results.

	Resistance	Inductance	Coil efficiency	Linearity
Non local coil (Y) (10 turns for each ring, diameter of wire 3 mm)	36 mOhm	148 uH	0.31 mT/m/A	3,6 %
Local coils (X and Z) (length of wire 26m, diameter of wire 3 mm)	60 mOhm	132 uH	0.32 mT/m/A	4.05 %

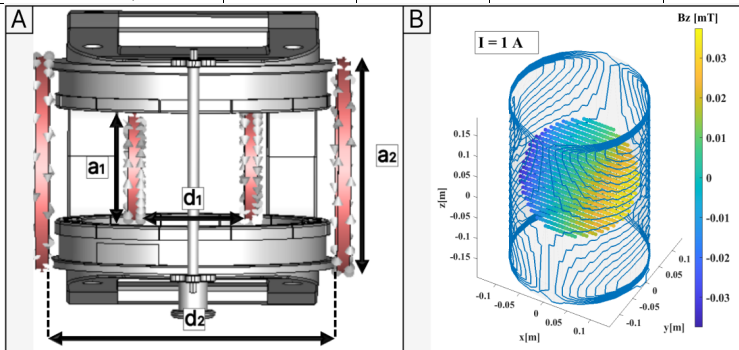


Figure 2. A. Non-local coil geometry: $a_1 = 0.128\text{ m}$, $a_2 = 0.25\text{ m}$ – radius of internal/ external coils; $d_1 = 0.26\text{ m}$, $d_2 = 0.78\text{ m}$ – distance between coils; $I_1 = 80\text{ A}$, $I_2 = 10\text{ A}$ – currents.; B. Local X coil (diameter 0.26 m, height 0.35 m), as example. B_z distribution along axis X with 1 A current.

If the results of numerical calculations for the proposed configuration will be compared with planar coils, it can be noted that the gradient efficiency of the resulting system has a good value for the same values of resistance and inductance. The high efficiency of the system makes it possible to reduce the requirements for a gradient power amplifier. As a result, at lower currents, less heat will be generated inside the system. Moving Y gradient coil outside the magnet allows to reduce EC, as well as the influence of mutual induction. Also, do not forget about the prospects for using the algorithm for non-local coils in problems of homogeneity correction, which is especially important in ultra-low fields.

Conclusion

An alternative and viable variant of coil configuration, for the generation of magnetic field gradients in MRI equipment with permanent magnets is presented. Obtained inductances and impedance of the coils as well as the linearity and effectiveness of the coils described make them a competitive option. Likewise, these configurations mitigate the demands and difficulties presented by flat coils and allow successive enhancements. An additional pair of Maxwell coils opens the option of improving homogeneity, increasing field strength and allowing the application of pre-polarization in situations where it is desirable. New modeling and calculations for the specific case are under development.

Acknowledgements

We express gratitude to staff of our Low-field MRI laboratory. Priority 2030 Federal Academic Leadership Program supported this research.

References

1. Shen, S., Koonjoo, N., Kong, X., Rosen, M. S., & Xu, Z. (2022). Gradient coil design and optimization for an ultra-low-field MRI system. *Applied Magnetic Resonance*, 53(6), 895–914. <https://doi.org/10.1007/s00723-022-01470-2>
2. Kong, X., Xu, Z., Shen, S., Wu, J., He, Y., & Igarashi, H. (2023). Z-gradient coil design with improved anti-eddy performance for MRI system with opposed permanent magnets. *Applied Magnetic Resonance*, 54(9), 869–890. <https://doi.org/10.1007/s00723-023-01577-0>
3. Poole, M., & Bowtell, R. (2007). Novel gradient coils designed using a boundary element method. *Concepts in Magnetic Resonance. Part B, Magnetic Resonance Engineering*, 31B(3), 162–175. <https://doi.org/10.1002/cmr.b.20091>
4. Hidalgo-Tobon, S. S. (2010). Theory of gradient coil design methods for magnetic resonance imaging. *Concepts in Magnetic Resonance. Part A, Bridging Education and Research*, 36A(4), 223–242. <https://doi.org/10.1002/cmr.a.20163>
5. Ueno, T., & Lopez, H. S. (2023). Method for designing gradient coil and gradient coil (Patent No. 20230039826:A1). In US Patent (20230039826:A1).
6. CoilGen – an open source MR coil layout generator. (n.d.). [Opensesourceimaging.org](https://opensesourceimaging.org).

Study of the hydroxyapatite doped with gadolinium and cerium ions using EPR spectroscopy

Margarita A. Sadovnikova¹, George V. Mamin¹, Fadis F. Murzakhonov¹, Nataliya V. Petrakova², Vladimir S. Komlev², Marat R. Gafurov¹

¹ *Institute of Physics, Kazan Federal University, Kremlyovskaya 18, 420008 Kazan, Russia*

² *A.A. Baikov Institute of Metallurgy and Materials Science, Russian Academy of Sciences, Leninsky pr. 49, 119334 Moscow, Russia*

E-mail: margaritaasadov@gmail.com

Introduction

Hydroxyapatite (HAp, $\text{Ca}_{10}(\text{PO}_4)_6(\text{OH})_2$) is a member in the family of calcium phosphate (CaPs) materials, and the major inorganic components of human bone, dentine, and enamel. The most widely explored area of CaPs research is biomedical applications, namely tissue engineering for bone regeneration due to their osteoconductivity, biocompatibility, and chemical similarity to natural bone [1]. However, its intrinsic and surface set of properties enable to use HAp also for other purposes such as catalysts for chemical reactions, ion conductors, gas sensors, absorbers for the water treatment processes and for the remediation of heavy metal polluted soils [2]. HAp has a highly flexible structure that can easily incorporate foreign ions into the crystal lattice, leading to changes in its physical-chemical properties. Ionic substitutions affect the crystallinity degree, lattice parameters, porosity, composition, and morphology of HAp, providing the appearance development of materials with new properties such as chemical, thermal and mechanical stability, cytocompatibility, solubility, bioactivity, and antibacterial properties.

The gadolinium (Gd^{3+}) doped HAp has been proposed as multifunctional or theragnostic material possessing a great potential as contrast agents for magnetic resonance imaging, and computed tomography. The replacement of calcium ions in the HAp lattice with cerium ions (Ce^{3+} and/or Ce^{4+}) is an interesting subject in medical sciences. Ce^{3+} -HAp has been reported to have antibacterial properties, where the ability of cerium to luminesce allows also it to be used as a fluorescent marker [3].

Thus, the present study focuses on the characterization of synthetic HAp doped with rare earth (Gd and Ce) ions. We demonstrate the capabilities of various continuous and pulsed electron paramagnetic resonance (EPR) techniques for studying electron-nuclear interactions. The synthesis of HAp containing rare earth ions was carried out by precipitation from aqueous salt solutions. EPR spectra were recorded on a Bruker Elexsys E680 spectrometer with the frequency $\nu_{\text{MW}} = 9.7$ GHz.

Result and discussion

The EPR spectrum for gadolinium-doped HAp (Fig. 1a red, top) and cerium-doped HAp (Fig. 1a green, bottom) was recorded at $T = 10$ K using a two-pulse Hahn sequence with a time $\tau = 0.18$ μs between the $\pi/2$ and π pulses. The resulting resonance microwave absorption corresponds to the spectrum of a powder sample with a broad line. Based on the characteristic g-factors, it was revealed that the spectrum corresponds to the gadolinium and cerium ions. The spin-lattice and spin-spin relaxation rates were measured at a magnetic field value B_0 (Table 1) correspond to contributions from different paramagnetic centers.

Table 1. Relaxation times recorded at $T = 10$ K

	$T_1, \mu\text{s}$	$T_2, \mu\text{s}$
HAp-Gd	17.4 ($B_0 = 346$ mT)	0.69 ($B_0 = 346$ mT)
HAp-Ce	127 ($B_0 = 352$ mT)	2.4 ($B_0 = 352$ mT)

Electron spin echo envelope modulation (ESEEM) techniques have become an important asset of the EPR toolbox. ESEEM method is a so-called hyperfine spectroscopy and hence targeted to the detection of nuclear frequencies in paramagnetic systems. The presence of magnetic nuclei in CaPs samples often leads to the appearance of modulations in the decay curves of transverse magnetization. This effect is caused by neighboring nuclei. Information about these nuclei can be obtained from the Fourier transform, which connects the time characteristic of a spin system with its frequency spectrum. (Fig. 1b). The most informative results of ESEEM spectroscopy in the frequency domain after appropriate signal processing are shown in Fig. 1b (red, top) for HAp-Gd. The spectra show a ^{31}P signal centered at the Larmor frequency for the magnetic field $B_0 = 346$ mT, the frequency $\nu_{\text{Larm}}(^{31}\text{P}) = 6$ MHz, and for $B_0 = 346$ mT, respectively, $\nu_{\text{Larm}}(^1\text{H}) = 14.7$ MHz. This information indicates that the paramagnetic center (Gd^{3+}) is located in the structure of the sample (HAp). The spectra (Fig. 1b. green, bottom) show a ^{31}P signal centered at the Larmor frequency for the magnetic field $B_0 = 352$ mT, the frequency $\nu_{\text{Larm}}(^{31}\text{P}) = 6.06$ MHz, and for $B_0 = 352$ mT, respectively, $\nu_{\text{Larm}}(^1\text{H}) = 14.9$ MHz. Consequently, it was found that cerium ions are also successfully incorporated into the HAp crystal lattice.

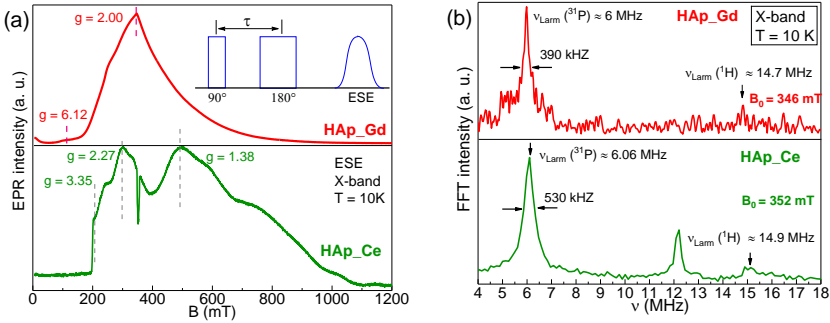


Figure 1. (a) EPR spectrum for HAp-Gd after heat treatment in air at 1300° (red, top); EPR spectrum for HAp-Ce after heat treatment in air at 1300° (green, bottom); (b) Spectrum of nuclear transitions in the frequency range after Fourier transform for various fixed B_0 of HAp-Gd (red, top), and HAp-Ce (green, bottom) samples

From the full linewidth at half-maximum corresponding to the anisotropic hyperfine interaction value (A_{d-d}), the distance (r) from paramagnetic ions (Ce^{3+} and Gd^{3+}) to ^{31}P was calculated in the dipole-dipole approximation (Table 2) using equation:

$$A_{d-d} \sim \frac{g_n g_e \mu_N \mu_B}{r^3},$$

where $g_n = 2.2632$ is a nuclear g-factor of phosphorus ^{31}P , $g_e = 2.0023$ is an electron g-factor.

Table 2. Distance between calcium and phosphorus as derived from the analysis of ESEEM peaks

	B_0 , mT	r_{exp} (Å)	r_{theory} (Å) [4]
HAp-Gd	346	3.0 ± 0.4	3.2 (Ca1 – P)
HAp-Ce	352	3.9 ± 0.3	3.4 (Ca2 – P)

Using HAp powders as an example, it is shown that the EPR method is effective experimental tool for studying cationic doping. Based on the obtained results using the capabilities of modern methods of pulsed EPR spectroscopy, it can be used for the comprehensive study of functional biomaterials doped with rare earth elements.

Acknowledgements

This research was funded by the RSF grant No 23-63-10056

References

1. Q. R. T. Lim, X. Y. Cheng, C. Y. Wee. – *Advanced Materials Science and Technology*, 5 (2) (2023).
2. B. Nasiri-Tabrizi, W. J. Basirun, C. H. Yeong, W. M. Thein. – *Ceramics International*, 49 (5), 7142-7179 (2023).
3. J. Gao, L. Feng, B. Chen, B. Fu, M. Zhu. – *Composites Part B: Engineering*, 235, 109758 (2022).
4. Y. Tang, H. F. Chappell, M. T. Dove, R. J. Reeder, Y. J. Lee. – *Biomaterials*, 30 (15), 2864-2872 (2009).

Experimental investigation of a metasurface for cardiac magnetic resonance imaging at 3 T

L.V. Sharipova, A.V. Shchelokova, E.A. Brui

School of Physics and Engineering, ITMO University, Saint Petersburg, 197101, Russia

E-mail: lv.sharipova@yandex.ru

Introduction

Magnetic resonance imaging (MRI) is a valuable tool for acquiring precise information regarding the morphological and functional characteristics of tissues, thereby enhancing diagnostic accuracy, prognostication of disease progression, and treatment efficacy. Given the critical importance of early detection in cardiovascular diseases, enhancing the quality of cardiac MRI is imperative. At 3 Tesla MRI, the radiofrequency (RF) wavelength approaches the dimensions of the human body, leading to localized signal voids in cardiac images that compromise diagnostic quality. Extensive research has demonstrated that RF metamaterials can enhance RF magnetic field homogeneity [1], improve image resolution [2], and mitigate specific absorption rate of electromagnetic energy in the human body [3].

The purpose of this study is to investigate the effect of metasurface-based pads on cardiac MR imaging parameters: signal-to-noise ratio (SNR) and relaxation time maps of left ventricular myocardium.

Experiment

Cardiac MRI was carried out for a group of 20 healthy volunteers (10 men, 10 women, age range 21-33 years; average age = 26.25 years old). Experimental data on quantitative MRI were obtained on a 3T Magnetom Trio Scanner (Siemens) using a surface matrix body coil. MR images were acquired using GRE (TR = 120 ms; TE = 2.2; 3.24; 4.28; 5.32; 6.36; 7.4; 8.44; 9.48; 10, 52; 11.56; 12.6; 13.64 ms; FA = 20°; FOV = 337×450 mm²; acquisition matrix = 256×192; slice thickness = 10 mm) and MOLLI (TR = 895.46 ms; TE = 3.35 ms; FA = 12°; FOV = 399×399 mm²; acquisition matrix = 144×138; slice thickness = 5 mm) pulse sequences.

For each volunteer, the scan was performed in two steps: with and without metasurface-based pads [4]. The pad was a flexible-printed circuit board with a periodic structure deposited on it in the form of plane-parallel capacitors connected by flat copper conductors. For scanning, one of the pads was placed under the patient's torso, beneath the heart area. The second pad was placed on top of the patient's torso under a flexible multichannel body coil, exactly above the lower pad. Scanning was performed with cardiac synchronization and breath-holding.

The SNR is a very important parameter of MRI images, and it is measured as a ratio of the mean pixel intensity within a region of interest and standard deviation of the background noise. To minimize the influence of differences in susceptibility between heart and lungs, a region in the interventricular septum was selected.

Experimental quantitative MRI data were analysed using a toolbox based on MATLAB software (The MathWorks Inc, Natick, MA). To process the data, the home-built scripts were used to reconstruct relaxation time maps based on MR images acquired with different T₁ and T₂-weighting. The reconstruction method was based on a pixel-by-pixel approximation of the signal by exponential curves ($f_1 = 1 - 2\exp(-TI/T_1) + \exp(-TR/T_1)$ - for T₁, and $f_2 = \exp(-TE/T_2^*)$ - for T₂^{*}), where TI – inversion time, TR – repetition time, TE – echo time). From the obtained values of relaxation times, quantitative maps T₁ and T₂^{*} were constructed for each pixel in the image. Afterward, in the obtained T₁ and T₂^{*} maps, a tissue area of at least 1 cm² was selected in myocardium. In this case, the region of interest was the same for both maps - with and without pads - for each individual volunteer.

Results

Experimentally obtained T_1 -weighted cardiac MR images with/without the pads are shown in Figure 1 for one of the volunteers (female, 24 years old). The distributions of the SNR measured in T_1 - and T_2^* - weighted images in a sample of healthy volunteers are depicted in Figure 2. In average, when the pads were utilized, a significantly higher ($p > 0.05$, in a paired t-test) SNR was obtained, that resulted in an enhanced image quality. Note that the interquartile range of the distribution increased when the pads were used, that means that the effect of pads was not the same for different volunteers.

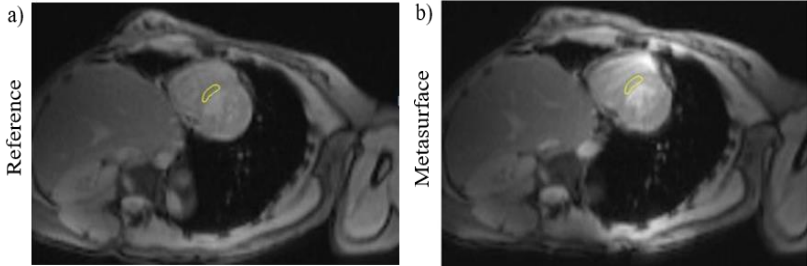


Figure 1. An example of T_1 -weighted MR images of the heart with a highlighted region of interest: a) without pads b) with pads

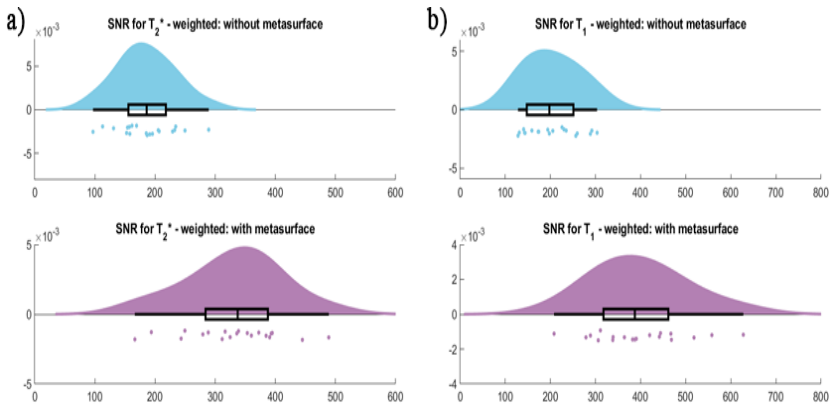


Figure 2. Distributions of the SNR measured in T_2^* (a) and T_1 (b)- weighted images in a sample of healthy volunteers without the metasurface-based pads (upper insets), and with them (lower insets)

The SNR values averaged in a sample of volunteers are summarized Table 1. Compared to the reference case, the mean SNR increased up to 2 times in the presence of the metasurfaces.

It was also of interest to evaluate the effect of pads on the measured quantitative parameters of the myocardium, using reconstructed relaxation maps (Fig. 3). The hypothesis was that if the pads improve the homogeneity of B_1^+ in the heart area, the distributions of quantitative parameters within the region of interest, which are sensitive to B_1^+ , should become narrower, resulting in lower interquartile ranges. The distribution of T_1 relaxation times measured in identical regions of interest in a healthy myocardium of one of the

volunteers is presented in Figure 3 c. This distribution narrowed in case of using metamaterial pads. At the same time, this was not the case for T_2^* mapping (Fig. 2 f). The interquartile ranges, averaged in a sample of volunteers are summarized in Table 1. Indeed, the magnetic field inhomogeneities, which can also be related to the flip angle, directly affect the signal dependence on TI in MOLLI pulse sequence, thereby, bias final T_1 maps, as our approximation considers homogeneous distribution of the B_1^+ within the sample. At the same time, if we consider GRE pulse sequence, the term of the equation associated with the flip angle do not contribute to the T_2^* decay. Thus, the inhomogeneities of the field introduce inaccuracies to T_1 mapping technique, that can be reduced by utilization of metamaterial pads.

Table 1. SNR, and interquartile ranges of T_1 and T_2^* times measured in the regions of interest, averaged within the sample of volunteers. SD – standard deviation.

	T ₁ -weighted/ T ₁ -maps		T ₂ [*] -weighted/T ₂ [*] maps	
	Without pads	With pads	Without pads	With pads
Mean SNR	204.2±47.3	396.8±73.8	184.9±38.6	331.6±70.9
Mean interquartile ranges of relaxation times, ms	133.3±90.3	103.6±59.1	10.3±3.4	11.4±2.7

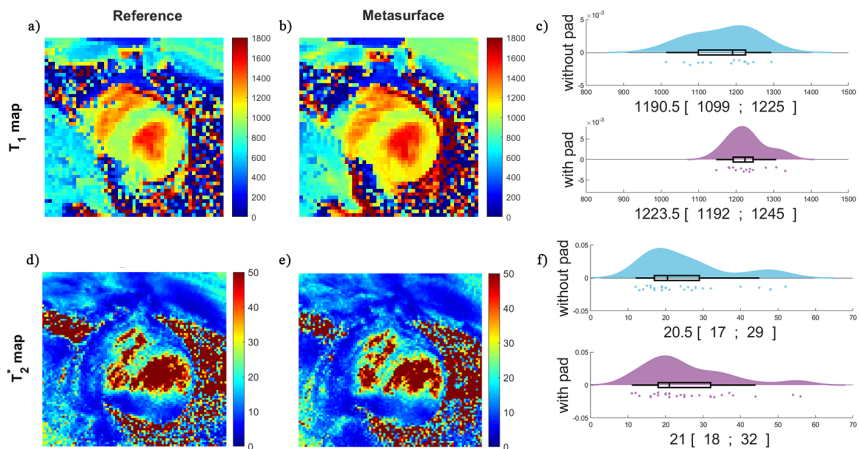


Figure 3. An example of the obtained T_1 maps (a,b) and T_2^* maps (d,e) of one of the volunteers, and corresponding raincloud plots for distributions of T_1 (c) and T_2^* (f) in the regions of interest marked with the black ellipses.

Discussion and conclusion

This paper presents the results of assessing the influence of metasurface-based pads on the transmit RF magnetic field homogeneity in the heart region via analysis of T_1 - and T_2^* -maps; and on the receive RF magnetic field – via analysis of SNR. It was found that the inaccuracies of T_1 mapping can be reduced when the pads are utilized. At the same time, SNR of the MR images drastically improved. Thus, the metasurface-based pads increase the quality of cardiac MRI, both conventional and quantitative.

Acknowledgements

This work was supported by the Russian Science Foundation (grant No. 23-75-10045)

References

1. Koloskov V., et al., Improving detection of fMRI activation at 1.5 T using high permittivity ceramics. *Journal of Magnetic Resonance*, 2023, 348, 107390.
2. Shchelokova A. V., et al., Locally enhanced image quality with tunable hybrid metasurfaces. *Physical Review Applied*, 2018, 9(1), 014020.
3. Shchelokova A. V., et al., Volumetric wireless coil based on periodically coupled split loop resonators for clinical wrist imaging. *Magnetic resonance in medicine*, 2018, 80(4), 1726-1737.
4. Vorobyev V., et al., Improving B1+ homogeneity in abdominal imaging at 3 T with light, flexible, and compact metasurface. *Magnetic resonance in medicine*, 2021, 87(1), 496-508.

Use of molecules to measure the parity conserving and parity violating nuclear moments

Leonid V. Skripnikov^{1,2}

¹Petersburg Nuclear Physics Institute named by B.P. Konstantinov of National Research Center "Kurchatov Institute", 1 Orlova roscha, Gatchina, 188300 Leningrad region, Russia

²Saint Petersburg State University, 7/9 Universitetskaya nab., St. Petersburg, 199034, Russia

E-mail: leonidos239@gmail.com

<http://qchem.pnpi.spb.ru>

Molecules can be used for precision measurements of nuclear properties, such as magnetic dipole, electric quadrupole and other moments. These fundamental properties of nuclei are necessary for solving various atomic problems, developing the theory of nuclear structure, etc. In [1], a strong discrepancy was discovered between the theoretical prediction [2] of hyperfine splitting in highly charged ^{209}Bi ions and experiment. This discrepancy is called the "puzzle of the hyperfine structure of bismuth." We have established [3] that the reason for the discrepancy is the incorrect reference value of the magnetic moment of the ^{209}Bi nucleus. To solve this problem, we have developed a fully relativistic approach to calculating the shielding constants needed to extract magnetic moment values from data from NMR experiments on heavy element compounds. This approach was further applied to refine the magnetic moments of the ^{207}Pb [4], ^{185}Re , ^{187}Re [5] nuclei. In [5], we were the first to take into account the contribution of the finite nuclear magnetization distribution effect to the shielding constant and showed that this effect can be more important than the solvent effect.

In [6], we proposed a new method for measuring the anapole moment of a nucleus. This nuclear moment arises as a result of violation of spatial parity P in intranuclear interactions and was measured only once. The approach is based on measuring the P -violating contribution to the spin-spin interaction between the nuclei (J -coupling) of the molecule. The theoretical method we have developed is the most accurate for solving the problem of interpreting this experiment in terms of the anapole moment of the nucleus.

Acknowledgements

The work was supported by the Russian Science Foundation grant 19-72-10019-P.

References

1. J. Ullmann, Z. Andelkovic, et al., Nat. Commun., 8, 15484 (2017).
2. V.M. Shabaev et al, Phys. Rev. Lett., 86, 3959 (2001).
3. L.V. Skripnikov, S. Schmidt, J. Ullmann, C. Geppert, F. Kraus, et al, Phys. Rev. Lett., 120, 093001 (2018).
4. V. Fella, L.V. Skripnikov, W. Nörtershäuser, et al. Phys. Rev. Res. 2, 013368 (2020).
5. L. V. Skripnikov, S. D. Prosnjak, Phys. Rev. C 106, 054303 (2022).
6. J.W. Blanchard, D. Budker, D. DeMille, M.G. Kozlov, L.V. Skripnikov, Phys. Rev. Research 5, 013191 (2023).

NMR study of liquid–liquid phase separation in pillar[5]arene-oligonucleotide system

*Polina V. Skvortsova*¹, *Arina V. Pergat*^{1,2}, *Bulat I. Khairutdinov*^{1,2}

¹*Kazan Institute of Biochemistry and Biophysics, FRC Kazan Scientific Center of RAS, Kazan, Russian Federation*

²*Kazan Federal University, Kazan, Russian Federation*

E-mail: skvpolina@gmail.com

The spatio-temporal organization of biochemical processes in cells is provided by organelles. Organelles have boundaries that separate the environment with unique properties inside from the outside space. Cells contain both membrane-bound and non-membrane-bound (membraneless) organelles. Membraneless organelles have liquid-like properties and are formed by liquid-liquid phase separation (LLPS) [1]. They include large range of polyvalent biomolecules such as proteins, DNA and RNA [2].

The study of real systems of membraneless organelles found in living cells is complicated by their multi-component composition and the complexity of preparation. It can be helpful to use model systems to determine the physicochemical principles of their formation. In our work, we studied a system containing polycationic pillar[5]arene derivatives and polyanionic DNA oligonucleotide that undergo LLPS.

NMR spectroscopy and computer modeling showed that polycationic pillar[5]arene derivatives form a complex with a polyanionic DNA oligonucleotide due to electrostatic interaction. In the 1:1 complex formation 4-5 charged functional groups of pillar[5]arene involves. The remaining 5-6 pillar[5]arene cationic groups can interact with other oligonucleotide molecules. This behavior promotes the formation of supramolecular complexes and leads to liquid-liquid phase separation.

Acknowledgements

This work is supported by the Russian Science Foundation grant No.23-23-00632.

References

1. J. Berry, S.C. Weber, N. Vaidya, M. Haataja, C.P. Brangwynne – *Proc. Natl. Acad. Sci. U.S.A.*, 112 (2015).
2. P. Li, S. Banjade, H.-C. Cheng, S. Kim, B. Chen, L. Guo, M. Llaguno, J.V. Hollingsworth, D.S. King, S.F. Banani, P.S. Russo, Q.-X. Jiang, B.T. Nixon, M.K. Rosen. – *Nature.*, 483, 336–340 (2012).

Singlet-triplet conversion in molecular hydrogen on a homogeneous catalyst in parahydrogen induced polarization experiments

Alexander V. Snadin^{1,2}, Alexey S. Kiryutin², Nikita N. Lukzen^{1,2}, Alexandra V. Yurkovskaya²

¹*Department of Physics, Novosibirsk State University, Novosibirsk, Russia*

²*International Tomography Center, Siberian Branch of the Russian Academy of Sciences, Novosibirsk, Russia*

E-mail: a.snadin@tomo.nsc.ru

Introduction

SABRE (Signal amplification by reversible exchange) belongs to the family of methods for induced hydrogen-parahydrogen polarization of nuclei (PHIP). Pure parahydrogen potentially contains a huge stock of nonequilibrium polarization, and it can be stored for up to several weeks. One of the problems in PHIP applications is the singlet-triplet conversion in the H₂ molecule, which reduces the lifetime of the singlet spin order of H₂ in solution. In the presence of a catalyst, this conversion is significantly accelerated (up to several seconds), which negatively affects the enhancement of NMR signals.

It became apparent that, despite the significant importance of the para-ortho conversion process in PHIP, there is a lack of systematic data in the literature regarding the relationship between the conversion rate and the magnetic field, as well as a consistent theoretical explanation of the conversion mechanism. In order to address this gap, we conducted both experimental and theoretical research on this correlation. Our findings allowed us to identify the factors influencing the decrease of singlet spin order lifetime of H₂ nuclei and, ultimately, suggested methods to enhance the level of spin polarization and the intensity of NMR signals in PHIP and SABRE experiments utilizing parahydrogen. In this study, we examined the dynamics of para-ortho transitions of molecular hydrogen when dissolved in a solution with the presence of a SABRE catalyst.

Para-ortho conversion is an important process and has previously been studied in the presence of paramagnetic metal ions to develop efficient catalysts for the liquefaction of molecular hydrogen (e.g., MOFs with paramagnetic metal ions [1]).

Methods

We introduced a new experimental method utilizing magnetic field cycling (Fig. 1) to assess the rate of para-ortho conversion of molecular hydrogen in a solution and utilized it in non-hydrogenative PHIP signal enhancement through reversible exchange (SABRE) experiments.

The para-ortho conversion rate was determined across a broad magnetic field range spanning from 0.5 mT to 9.4 T. The research revealed that the conversion rate is significantly influenced by the magnetic field within which the reaction takes place, as well as by the concentrations of the reactants. The rate decreases as the concentration of the pyridine ligand increases and increases as the concentration of the iridium catalyst rises. It might be expected that the intensity of the NMR signal from orthohydrogen would rise and reach at a constant value, as there is initially little orthohydrogen in the system and its amount increases as the conversion progresses. However, this anticipated trend is not observed because the conversion of parahydrogen leads to the production of hyperpolarized orthohydrogen, whose signal intensity decreases exponentially toward the thermally equilibrated hydrogen signal intensity as the concentration of parahydrogen in the system decreases. Nevertheless, we believe that this observed exponential decay accurately reflects the rate of conversion from para- to orthohydrogen in the magnetic field with which the delay persists.

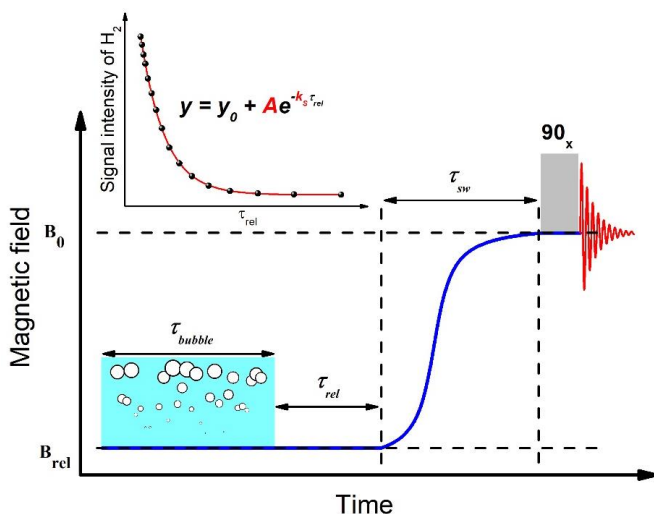


Figure 1. Schematic of experiments to measure the field dependences. τ_{bubble} – time of sample bubbling with parahydrogen (10 s), τ_{rel} – time of varying delay

The theoretical model considers the reversible exchange of molecular hydrogen with the catalyst, the nuclear spin-spin interaction of hydride protons with the nuclei of ligands within the catalytic complex, and the nuclear Zeeman interactions, providing a qualitative description of the experimental results. To calculate the para-ortho conversion rate, we have constructed and solved equations [2] on hydrogen density operators in free and bound forms, taking into account both spin dynamics and exchange between components. The conversion of molecular hydrogen is influenced by two types of complexes with different spin system symmetry. In asymmetric complexes with hydride protons having distinct chemical shifts due to the presence of a chlorine anion ligand, the para-ortho conversion rate increases with the magnetic field, while this mechanism does not apply to symmetric complexes. A resonant feature in the rate of para-ortho conversion is observed in the magnetic field where the level anti-crossing takes place. The findings of this study can be used to determine the optimal conditions that lead to maximum hyperpolarization in experiments using parahydrogen.

Acknowledgements

This work is supported by the Russian Science Foundation (Contract No. 23-73-10103).

References

1. D.M. Polyukhov, N.A. Kudriavych, S.A. Gromilov, A.S. Kiryutin, A.S. Poryvaev, M.V. Fedin, Efficient MOF-Catalyzed Ortho-Para Hydrogen Conversion for Practical Liquefaction and Energy Storage, ACS Energy Letters, (2022) 4336-4341.
2. S. Knecht, K.L. Ivanov, Quantitative Quantum Mechanical Approach to Sabre Hyperpolarization at High Magnetic Fields, J. Chem. Phys, 150 (2019) 124106.

Assesment of timing parameters of Cuban NMR console

Alexander Sónora Mengana¹

¹*Departamento de Bioingeniería. Centro de Biofísica Médica. Universidad de Oriente. Santiago de Cuba. Cuba.*

Introduction

A console for Nuclear Magnetic Resonance (NMR) applications is a hardware capable of generating most of the signals needed during a NMR experiment. The complexity of a console can be determined by the field of its application, i.e. spectroscopy, imaging, relaxometry or other. In all cases, it includes a block called event sequencer or pulse programmer, which synchronizes all the events needed during the experiment. [1, 2]

The pulse programmer has to be precise, compact and flexible. To fulfill those requirements, the NMR hardware designed in Centro de Biofísica Médica (CBM) is based on field-programmable gate arrays (FPGA), a powerful reconfigurable technology. Due to the high standards of timing needed in NMR, the implementation of the pulse programmer must be evaluated.

The objective of this work is to assess the evaluation of timing parameters of a pulse programmer designed for a NMR console implemented in an FPGA.

Materials and Methods

The pulse programmer under evaluation is coded in VHDL language, and was designed to generate pulses with maximum width of 60 minutes with 0.1 μ s of precision and 512 lines in the k-space for imaging applications. The process of implementing and evaluation of the pulse programmer is done using Vivado 18.2 (AMD, California, USA) running on a Ubuntu installed laptop.

The internal memory of the pulse programmer, was initialized with files containing the definition do the pulse series. In this work only two series were tested, a Carr-Purcell-Meiboon-Gil (CPMG) and a spin-echo series. The process was repeated several times for values selected in an arbitrary manner. Because of the enormous amount of parameter combinations, the values were selected to verify the requirements.

A cmod S7-25 evaluation board is used as testing platform. It contains an xc7s25 Spartan 7 FPGA and other functionalities.

Results and discussion

Ошибка! Источник ссылки не найден. shows the events generated for an spin-cho and a CPMG series. In both caserfs, `rf_event` is the habilitation of radiofrequency (RF) excitation, `rfo_event` is the gating of the `rf` power amplifier, `gx_event`, `gy_event`, `gz_event` and `g0_event` controls the magnetic field gradiens and `adq_event` controls the acquisition event.

The whole system works synchronously with the main clock signal and setting the main frequency to 10 MHz, the precision is completely fulfilled. The verification was performed changing the less significant bit on the control words. The maximum pulse width was achieved selecting the adequate values during pulse serie programming.

Ошибка! Источник ссылки не найден. shows a CPMG with five 180-degrees pulse and was tested with a maximum of twenty pulses because it was difficult to visualize and identify a high number of pulses.

Despite of that situation, the implementation of the pulse programmer allows to extend the possibilities beyond the requested initial parameters. On the other hand, the design can be easily improved if needed, because it is based on programmable technology.

As can be seen from

Table , the implementation of the design of the xc2s-25, shows a low percentage of device usage. The main internal components of the FPGA used to evaluate the use of the device are the look-up tables (LUT) and the flip-flops (FF). This design uses less than 1 % of LUTs and FFs. For the case of the RAM (BRAM) only one block is partially used

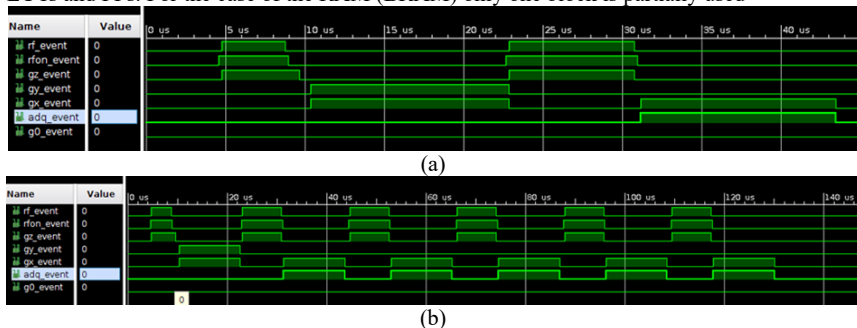


Figure 1. Sample of pulse series generated by the pulse programmer. a) Spin-echo pulse serie, b) CPMG pulse serie.

Table 1. Summarizes the resources used by the pulse programmer in the FPGA

Resource	Utilization	Available	Utilization %
LUT	117	14600	0,80
FF	83	29200	0,28
BRAM	0,50	45	1,11

From the timing summary made by the synthesis tool, the implemented design, has a worst negative slack (WNS) of 94.626 ns and a worst pulse width slack (WPWS) of 49.500 ns. These values represent how much time delay can be accommodate within a clock period without affecting the performance of the pulse programmer. In the case of WNS, the value is near the clock period (100 ns) and the WPWS reflects the maximum duration of a pulse.

Conclusions

The pulse programmer under evaluation fulfill the requirements for what it was designed with high possibilities of increase in performance.

Due to it is a low resource demanding hardware, the pulse programmer can be integrated within the FPGA with other NMR hardware without critically affecting the performance.

References:

- Chen, H.-Y.; Kim, Y.; Nath, P. & Hilty, C. An ultra-low cost NMR device with arbitrary pulse programming, *Journal of Magnetic Resonance*, 2015, 255, 100-105
- Yong, J. R. J.; Kupče, E. & Claridge, T. D. W. Modular Pulse Program Generation for NMR Supersequences, *Analytical Chemistry*, 2022, 94, 2271-2278

Manipulating Stereoselectivity of Parahydrogen Addition to Acetylene to Unravel Interconversion of Ethylene Nuclear Spin Isomers

Sergey V. Sviyazov^{1,2}, *Simon V. Babenko*¹, *Ivan V. Skovpin*¹, *Nikita V. Chukanov*^{1,2}, *Dudari B. Burueva*^{1,2} and *Igor V. Kopytug*¹

¹International Tomography Center SB RAS, Novosibirsk 630090, Russia

²Novosibirsk State University, Novosibirsk 630090, Russia

E-mail: s.sviyazov@tomo.nsc.ru

Introduction

In symmetric molecules, different sets of rotational levels are allowed for nuclear states of different symmetry leading to the appearance of discrete nuclear spin isomers of molecules (NSIMs). Nowadays, the problem of separating nuclear spin isomers on a scale suitable for practical applications has been solved for only one molecule - dihydrogen. This work is devoted to the enrichment of nuclear spin isomers of ethylene via chemical synthesis.

Previous Work

The ethylene molecule has four nuclear spin isomers: A_g , B_{3g} , B_{1u} , B_{2u} . One of the promising methods for enriching NSIMS of ethylene is the scalable chemical synthesis proposed by Zhivonitko et al. [1]. In this approach, ethylene with non-equilibrium distribution of NSIMs was produced via heterogeneous hydrogenation of acetylene with parahydrogen, spin isomer of hydrogen with the total nuclear spin $I=0$. Note that the ratio of ethylene NSIMs depends on the stereoselectivity of the addition of parahydrogen (shown in the figure below). To break the magnetic equivalence of ethylene protons and, therefore, study the NSIMs, ethylene was introduced into the electrophilic addition reaction. Also, Zhivonitko et al. investigated interconversion of ethylene NSIMs and showed that the equilibration kinetics is biexponential [1].

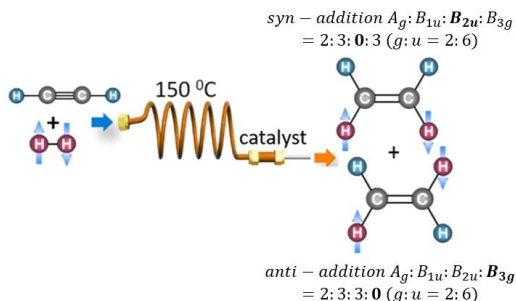


Figure 1. Method of chemical synthesis of ethylene NSIMs (illustration adapted from [1]). p - H_2 -derived protons in ethylene can be in *cis*-configuration (*Z*-ethylene) or in *trans*-configuration (*E*-ethylene).

Assessing Initial Imbalance of Ethylene NSIMs

In this work, three heterogeneous catalysts (monometallic Pd/TiO₂, bimetallic Pd-In/Al₂O₃, and immobilized Ir-P-SiO₂, where P is the phosphine-containing linker on silica gel) were used. To assess the non-equilibrium ratio of ethylene NSIMs by NMR, the symmetry-breaking reaction is required, here in this work the reaction with bromine water with the formation of 2-bromoethanol was proposed. The utilization of readily accessible

chemicals was essential for obtaining new results reported in this work as they required numerous repetitions of the symmetry-breaking reaction.

Thus, the hydrogenation products mixture was bubbled through bromine water and the ^1H NMR spectrum was then recorded. For all three catalysts the enhanced antiphase signals of 2-bromoethanol were observed, which confirms the non-equilibrium ratio of ethylene NSIMs. It was found that the lineshape of the hyperpolarized signals is different for all three catalysts. We demonstrate that the stereoselectivity of p- H_2 addition to acetylene (*syn*- vs. *anti*-addition) can be accessed via analysis of ^1H NMR spectra of produced hyperpolarized 2-bromoethanol (the experimental and simulated NMR spectra for each catalyst are presented below). Moreover, we demonstrate experimentally that stereoselectivity of p- H_2 addition controls the produced distribution of ethylene NSIMs.

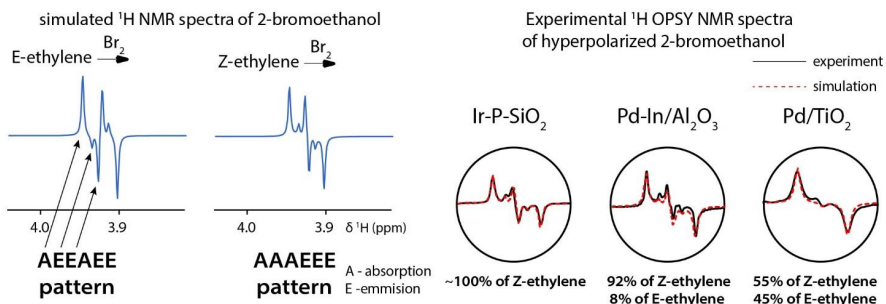


Figure 2. Simulated ^1H NMR spectra of the produced hyperpolarized 2-bromoethanol differ significantly for the two cases (*syn*- or *anti*-addition): the AAEEEE pattern corresponds to 2-bromoethanol produced from Z-ethylene, while the AEEAAE – E-ethylene. The experimental ^1H OPSY NMR spectra of 2-bromoethanol. Different catalysts were used for ethylene production.

Interconversion of Ethylene NSIMs

The kinetics of ethylene NSIMs equilibration was studied by storing produced ethylene for variable times before subjecting it to the symmetry-breaking reaction. A monoexponential equilibration with $T_{\text{short}}=6.5\pm 0.5$ s was found for Ir-P-SiO₂. Since this catalyst renders $\sim 100\%$ *syn*-addition and thus does not produce any *g* : *u* imbalance of ethylene NSIMs, T_{short} is the characteristic time of equilibration between NSIMs with the same inversion symmetry (i.e., $A_g \rightleftharpoons B_{3g}$, $B_{1u} \rightleftharpoons B_{2u}$, or both). In contrast, for Pd/TiO₂ and Pd-In/Al₂O₃ catalysts the equilibration kinetics was biexponential, with T_{short} of 3-6 s for both catalysts and T_{long} of 1700 ± 1200 s and 2200 ± 1300 s for Pd-In/Al₂O₃ and Pd/TiO₂, respectively. Based on the results described above, The T_{long} time can be assigned to the equilibration between NSIMs with different inversion symmetries ($g \rightleftharpoons u$).

Moreover, based on the modeling of experimental spectra under the assumption of partial equilibration of nuclear spin isomers, it was found that during 30 second of storage, ethylene isomers are balanced within the same spatial symmetry classes (*g* and *u*). With further storage (more than 30 s), interconversion between isomers of classes *g* and *u* occurs. Thus, we can conclude that the evolution of the lineshape of 2-bromoethanol with ethylene storage time reflects the dynamics of the equilibration processes of ethylene NSIMs and further supports the assignment of NSIMs equilibration processes established in this study.

It was found that the hyperpolarized signals from 2-bromoethanol are observed after 1 h of ethylene storage (for ethylene produced over Pd-In/Al₂O₃). Thus, we observe that the equilibration time of nuclear spin isomers (1700-2200 s) exceeds T₁ (in experimental conditions T₁ is about 300 ms) by 3 orders of magnitude, which is the longest reported lifetime for proton long-lived states (besides H₂).

Results of this work were recently published in [2].

Acknowledgements

This work was supported by the Russian Science Foundation (grant #21-73-10105).

References

1. V.V. Zhivonitko, K.V. Kovtunov, P.L. Chapovsky, I.V. Koptyug. *Angew. Chem. Int. Ed.* 52 (2013) 13251-13255.
2. S.V. Sviyazov, S.V. Babenko, I.V. Skovpin, L.M. Kovtunova, N.V. Chukanov, A.Yu. Stakheev, D.B. Burueva, I.V. Koptyug. *Physical Chemistry Chemical Physics* 2024, DOI: 10.1039/D3CP04983C

Non-contrast MRI for ventilation and perfusion study of the lungs

Timofei T. Taran¹, Olga S. Pavlova^{1,2}, Mikhail V. Gulyaev², Dmitry S. Dmitriev³, Aleksandr G. Pistrak³, Kirill N. Ryabikov³, Viktor P. Tarasov^{3,4}, Yury A. Pirogov¹

¹*Faculty of Physics, Lomonosov Moscow State University, 119991, Moscow, Russia*

²*Faculty of Medicine, Lomonosov Moscow State University, 119991, Moscow, Russia*

³*«S.P. HELPIC» LTD, 117485, Moscow, Russia*

⁴*Federal Research Center of Problems of Chemical Physics and Medicinal Chemistry Russian Academy of Sciences, 142432, Moscow region, Chernogolovka, Russia*

E-mail: tarantimofey@mail.ru

Introduction

Currently, there are several methods in ¹H MRI concerning functional assessment of lung ventilation and perfusion [1]. One of this methods is PREFUL MRI – Phase Resolved Functional Lung MRI [2]. It does not use any contrasting agents and can be implemented on already existent clinical and preclinical equipment.

The idea behind PREFUL is that on a MRI time-series with high temporal resolution (less than 0.6 s) during free-breathing of a patient, variance of signal intensity could be seen. This is due to changes in oxygen concentrations resulting from perfusion and ventilation cycles of the lungs. Acquired MR images could be sorted according to their phase in each of those cycles. Then, fractional ventilation (*FV*) and perfusion (*Q_n*) maps could be calculated by using the formulas (1) and (2):

$$FV = \frac{S_{avg}}{S_{inh}} - \frac{S_{avg}}{S_{exh}} \quad (1),$$

where *S_{inh}* and *S_{exh}* are the signal intensities on the inhalation and exhalation (or 0 and π phases) images, respectively, and *S_{avg}* is the averaged signal intensity over the entire time series.

$$Q_n = \frac{100\%}{S_{blood}} |S_{sys} - S_{dias}| \quad (2),$$

where *S_{sys}* and *S_{dias}* are the average signal intensities on the MRI images corresponding to the systole (0) and diastole (π) phases of the cardiac cycle, respectively; and *S_{blood}* is the signal intensity in the voxel during blood inflow.

This work is aimed at implementing PREFUL method, optimization of scanning parameters and developing an automated program which could be used in clinical practice to calculate ventilation and perfusion maps from MRI data.

Materials and methods

Ten healthy subjects participated in this study. MR images were acquired at 1.5 T MR scanner developed by «S.P. HELPIC» LTD using 2D GE pulse sequence with the following scan parameters: TR = 4.4 ms, TE = 1.2 ms, FA = 9°, matrix = 80 × 80, number of slices = 1, number of averages = 1. FOV was adjusted to each subject ranging from 300 × 300 mm² to 400 × 400 mm². Three time-series consisting of 600 ¹H MR images of the lungs were acquired for each subject (corresponding to three different coronal slices of lungs). Total experiment time for a subject was ~13 minutes. In Fig. 1, the experimental data are presented.

Data processing for each sequence was applied as follows. Firstly, all of the images underwent lung segmentation using pre-trained U-net convolutional neural network [3]. Then, corresponding lung heights were used as measures of a position in ventilation cycle. Next, this data were fitted by a sine function and phases were assigned to each image. Images were sorted according to their phase and then mean inspiration, expiration and mid-phase images were calculated and used in formula (1) in order to acquire ventilation maps. The process for

creating perfusion maps was analogous except signal intensity in the aorta was chosen as a measure of perfusion cycle's position and formula (2) used for calculating results.

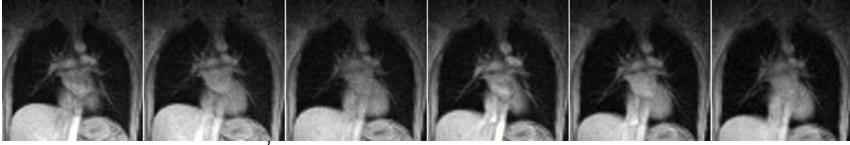


Figure 1. Six sequential ^1H MR images of human lungs obtained from one of the time sequence

Results

A computer program which implements PREFUL method was developed. An analysis concerning optimal scan parameters was carried out. We can conclude that a matrix size of 80×80 with a TR of 4.4 ms, resulting in a scanning time of 352 ms per image, is optimal for the accurate assessment of both ventilation and perfusion cycles.

A series of 30 time sequences from 10 healthy subjects were obtained and processed. Fractional ventilation and perfusion maps for each of these sequences were calculated. In Fig. 2, FV-maps and Q_n -maps build for one of the volunteer are presented.

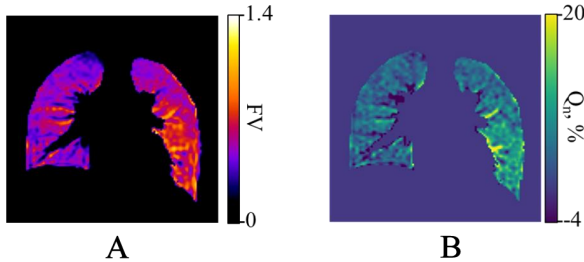


Figure 2. Functional maps of the lungs calculated for one of the volunteer. A: Fractional ventilation map (FV-map). B: Perfusion map (Q_n -map)

Conclusion

In this study, we applied the PREFUL method, developed an automated program for generating fractional ventilation and perfusion maps, and evaluated its performance using data from 10 healthy subjects. Further research will involve scanning subjects with pulmonary diseases to evaluate the method's effectiveness.

Acknowledgements

This work is supported by Russian Science Foundation grant #21-75-10038, the Interdisciplinary Scientific and Educational Schools of Moscow University «Molecular Technologies of the Living Systems and Synthetic Biology» and «Photonic and quantum technologies. Digital medicine».

References

1. A. Voskrebenezov et al - *J Magn Reson Imaging*, **53**, 1344-1357 (2020).
2. A. Voskrebenezov et al - *Magn Reson Med*, **79**, 2306-2314 (2018).
3. O. Ronneberger et al. MICCAI, (2015)

Investigation of the use of hydrogen bonds for association of polymer blocks with different substituents by means of quantum chemistry

Anna A. Titova, Maxim A. Skakun, Elena Yu. Tupikina

Institute of Chemistry, Saint Petersburg State University, Saint Petersburg, Russia

E-mail: aatitova1210@gmail.com

Introduction

Non-covalent interactions, including hydrogen bonds, are often used as bonding bridge between the building blocks of polymer materials [1]. Important types of such polymers are materials with adaptive properties, for example, with self-healing after changes in outer conditions (e.g. temperature or pressure). Such special behavior of these materials can be achieved due to the reversible character of hydrogen bonding formation [2]. Various electron-donating (EDG) and electron-withdrawing (EWG) groups located in the proximity of hydrogen bonds also have an influence on the physical and chemical properties.

Self-healing materials are perspective and still understudied field of research. Therefore, for smart planning a physical experiment, it is better to study the model structures theoretically and predict the parameters of hydrogen bonds in order to approach the synthesis of materials with adaptive properties more precisely and economically. It can be done using, for example, quantum chemical calculations.

Problems and solutions

In this work we investigated the geometry and different NMR parameters, for example, chemical shifts of protons involved in hydrogen bonds in dimers and larger oligomers. Chosen systems include one proton-donor and one proton-acceptor nitrogen atoms, which form two $\text{NH} \cdots \text{N}$ «head-to-tail» hydrogen bonds. Our goal was to analyze changes in the investigated parameters, estimate the influence of the substituents and also identify the cooperative/anticooperative behavior of the hydrogen bonds. This information can be applied to design of polymer adaptive materials with hydrogen bonds. Examples of used monomer structures, containing proton-donor and proton-acceptor nitrogen atoms, are shown in Figure 1.

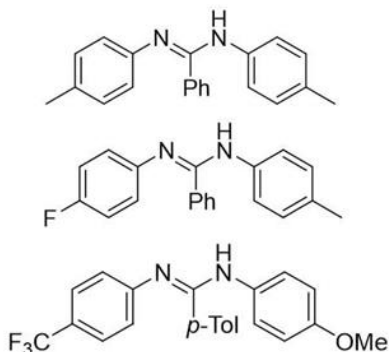


Figure 1. Examples of investigated monomer structures with different electron-donating and electron withdrawing groups on the benzene rings ($-\text{CF}_3$, $-\text{CH}_3$, $-\text{F}$, $-\text{OCH}_3$ etc.)

Calculations of dimers were performed with Gaussian16 software at B3LYP/6-311++G(d,p) level and with empirical dispersion correction (GD3BJ). NMR parameters were calculated at the same of level of theory using GIAO approach. Structures of oligomers were calculated with semi-empirical methods of quantum chemistry due to large size of such systems.

References

1. Hutchins, K. M. Functional materials based on molecules with hydrogen-bonding ability: Applications to drug co-crystals and polymer complexes. *R. Soc. Open Sci.* 5, (2018).
2. Van Gemert, G. M. L., Peeters, J. W., Söntjens, S. H. M., Janssen, H. M. & Bosman, A. W. Self-healing supramolecular polymers in action. *Macromol. Chem. Phys.* 213, 234–242 (2012).

Nitroxide radical sorption on MOF-808 for quantum bits

Aleksandr S. Tomilov^{1,2}, Anastasiya A. Yazikova^{1,2}, Artem S. Poryvaev², Matvey V. Fedin²

¹*Faculty of Natural Sciences, Novosibirsk State University, Novosibirsk, 630090, Russia*

²*International Tomography Center SB RAS, Novosibirsk, 630090, Russia*

E-mail: a.tomilov1@g.nsu.ru

Introduction

Quantum information processing has potential to become a revolutionary technology. Quantum computers, machines that can perform quantum calculations, consist of quantum bits (qubits). There are strict requirements for qubits, such as long coherence times and scalability of quantum systems. Qubit candidates include trapped ions, superconductors, spins in quantum dots and paramagnetic centers, etc. Molecular spin qubits (MSQs) based on paramagnetic molecules attract considerable interest because of the variety of such molecules. Moreover, their spins can be manipulated with electron paramagnetic resonance (EPR) pulses. EPR also allows studying paramagnetic materials to determine relaxation times and radical concentration, crucial for characterization of qubit candidates. MSQ systems can be scaled up with the use of metal-organic frameworks (MOFs). Their porous polymer structure allows for regular distribution of paramagnetic centers.

3-carboxy-PROXYL sorption on MOF-808

We decided to graft 3-carboxy-PROXYL molecules onto MOF-808 to create a MSQ candidate (fig. 1). Nitroxide radical 3-carboxy-PROXYL (c-Pr) was chosen due to its stability, while high porosity of MOF-808 makes it a perfect platform for radical sorption. Three syntheses were conducted with different loads of the radical and three samples with different concentrations of c-Pr were acquired.

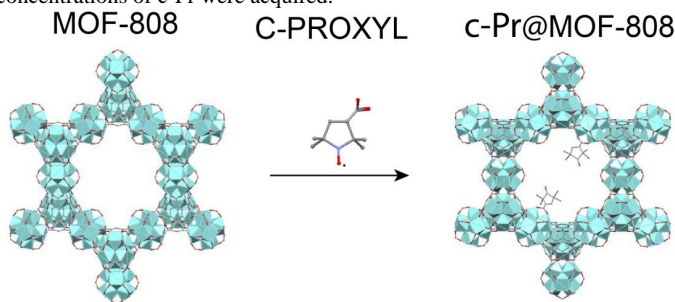


Figure 1. A scheme for synthesis of c-Pr@MOF-808

EPR studies of c-Pr@MOF-808

Continuous-wave EPR spectra were acquired for all three samples. They show that substances contain immobilized radical in two fractions. Low-load sample was also characterized with pulse EPR. Relaxation time was measured at temperatures between 80 and 300 K and showed high enough time T_2 for potential use of c-Pr@MOF-808 as a qubit. Rabi oscillations observed at room temperature exhibit possibility for spin manipulation in acquired substance, also supporting c-Pr@MOF-808 as a qubit candidate.

Acknowledgements

This work is supported by the Russian Science Foundation (grant № 22-73-10239).

Ionic Liquid Systems “[bimim]Cl/AlCl₃/H₂O” Studied by NMR and Quantum Chemistry

Milosh Ubovich, Vladimir V. Matveev, Vladimir I. Chizhik

Faculty of Physics, Saint-Petersburg State University, Russia

E-mail: v.matveev@spbu.ru

Introduction

Liquid electrolytes based on aluminum salts solutions in ionic liquids (ILs) are considered as prospective systems for new generation metal-ion batteries. The presence of water, which appears during the preparation of electrolytes, may have a negative effect on the properties of electrochemical devices. In many cases water cannot be removed by standard methods. It was shown that standard dehydration procedures were not reliable in the removal of water from the aluminum solvation shell [1, 2]. The mixtures of ionic liquid [bimim]Cl (1-butyl-3-methylimidazolium chloride, C₈H₁₅ N₂Cl) and aluminum chloride (AlCl₃) with different water concentrations was studied in the present work. The main purposes of this study are (1) the detection the existence of different solvate complexes of Al³⁺ with Cl⁻ in selected systems and (2) the estimation of the characteristic times of exchange processes by analysis the NMR data.

Experimental

The samples were prepared using crystalline hydrate AlCl₃·6H₂O and [bimim]Cl IL. The neat IL and the solution were undergone a standard drying procedure under low pressure at 80 °C. The water concentration was verified by ¹H spectra. The molar ratios were estimated for mixtures the “AlCl₃ – [bimim]Cl – H₂O” with different amounts of water. NMR measurements were carried out using Bruker Avance III 500 MHz Spectrometer at 500 MHz for ¹H nuclei (the examples of spectra see in Fig. 1), 130 MHz for ²⁷Al nuclei and 49 MHz for ³⁵Cl nuclei. All measurements were made in the temperature range between 293 and 363 K.

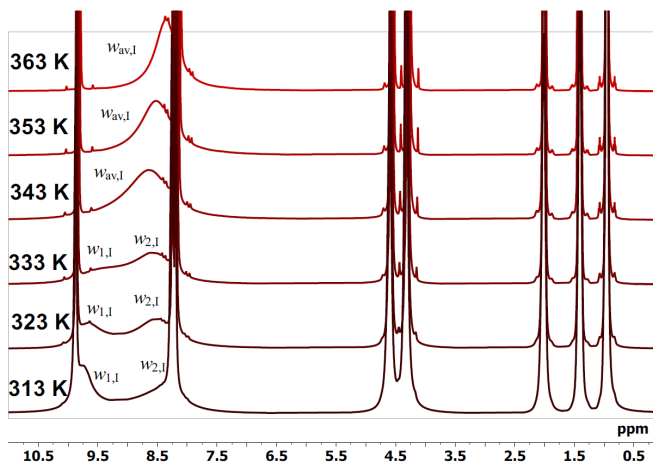


Figure 1. The ¹H spectra for the sample I (1Al³⁺ – 5.7[bimim]⁺ – 7.5H₂O).

Results

Several important features of the microstructure evolution of the “AlCl₃ – [bmim]Cl – H₂O” system under the variation of water concentration were discovered. The temperature dependences of spectra were also considered for the research system. The data obtained demonstrate that under certain conditions the Al³⁺ cation can strongly hold more than 6 water molecules in its surroundings. At the same time, the excess of Cl⁻ anions leads to the appearance of mixed solvate complexes with one and two anions near Al³⁺. Under the increase in the water content the integral intensities of water line near 9.7-9.8 ppm give the coordination number 6.0 (!) in the temperature range from 293 up to approximately 320 K that allows us to consider the cation Al³⁺ as fully hydrated. A model of the Al³⁺ cation environment in the studied system has been proposed on the basis of the data on the ¹H, ²⁷Al and ³⁵Cl spectra.

Our data make it possible to estimate the exchange time (τ_m) of water molecules between different substructures. For example, it can be determined that at high temperatures (more than 340 K): $\tau_m < 1$ ms.

In order to interpret the experimental data, Quantum chemical calculations were performed by Gaussian 09 Revision D.01 [3]. The chemical shifts in the ¹H and ²⁷Al spectra for each structure under consideration were calculated. The main results confirm that the Al³⁺ cation can hold more than 6 water molecules in its environment, and the excess of Cl⁻ anions leads to the appearance of mixed solvate complexes with one and two anions around Al³⁺ (see also [4]).

Acknowledgments

This work was supported by the Russian Science Foundation (project № 23-23-00049). All NMR measurements were carried out in the Resource Center "Magnetic Resonance Research Methods" of Research Park of Saint Petersburg State University.

References

1. Matveev V. V., Ievlev A. V., Vovk M. A., et al. – J. Mol. Liq. 2019. V. 278. P. 239.
2. Matveev V. V., Ievlev A. V., Šoltéssová M., et al. – Magn. Reson. Chem. 2021. V. 60. No. 2. P. 221.
3. Frisch M. J., Trucks G. W., Schlegel H. B., et al., Gaussian 09, Revision D.01. Gaussian, Inc., Wallingford CT, 2013.
4. Ubovich M., Matveev V. V., Vovk M. A., Chizhik V. I. – J. Phys. Chem. Lett. 2023. V. 14. P. 9324.

Liquid-liquid phase transition in the nanoconfined Ga-In-Sn eutectic alloy

A. A. Vasilev¹, D. Yu. Nefedov¹, A. V. Uskov¹, E. V. Charnaya¹, Yu. A. Kumzerov², A. V. Fokin²

¹*Physics Department, St. Petersburg State University, St. Petersburg 198504, Russia*

²*A.F. Ioffe Physico-Technical Institute RAS, St. Petersburg 194021, Russia*

E-mail: Allisher93529@yandex.ru

Introduction

The study of properties of gallium and gallium alloys in bulk and in nanocomposites are of great interest for modern applied physics [1, 2]. Structural transformations and size effects in such systems attract the increasing attention of investigators. In this regard, liquid-liquid phase transition (LLPT) in gallium alloys is of special interest due to the ability of gallium to be supercooled. Embedding such liquids in nanoporous matrices allows alloys to be supercooled to temperatures much lower than the melting temperatures, which raises expectations that LLPT can be found in liquids under nanoconfinement.

The present study has been carried out by using NMR technique, which is a powerful instrument for obtaining information about the internal structure of metallic liquids and solids. The ⁷¹Ga and ¹¹⁵In NMR measurements were performed for a ternary eutectic Ga-In-Sn alloy, embedded into porous alumina, with a view to study LLPT.

Experiment

The ternary eutectic Ga-In-Sn alloy with a composition of 75 at.% Ga, 17 at. % In and 8 at.% Sn was embedded into porous alumina with mean diameter of pores 11 nm under pressure up to 10 kbar. At room temperature, the confined alloy was in the melted state, which is in agreement with its phase diagram [3].

Studies were carried out using a Bruker Avance 400 NMR pulse spectrometer at magnetic field 9.4 T within a temperature range from 200 to 300 K. We observed NMR signals for the ⁷¹Ga and ¹¹⁵In isotopes. The NMR spectra were obtained as Fourier transforms of free-induction decays after 90° pulses. The Knight shift for gallium and indium isotopes was referenced to NMR signals from a GaAs single crystal and a In(NO₃)₃ molar solution respectively.

Results

The relative ⁷¹Ga and ¹¹⁵In NMR signal intensity from liquid alloy during the cooling-heating cycle is presented in Fig. 1. One can see two phase transition steps of gallium under both freezing and melting which demonstrates the complex structure of solid Ga-In-Sn.

The Fig. 2 shows the evolution of the ⁷¹Ga NMR spectrum. It can be seen that spectrum at the temperature 257K demonstrates two lines. One can conclude from the width of the lines that these components correspond to a liquid phase. The relative integral intensity of the high-frequency component increases, whereas the relative integral intensity of the low-frequency component decreases upon cooling. The last one disappears at the temperature 249 K.

NMR studies revealed changes in behavior of the ternary Ga-In-Sn alloy in comparison with the bulk alloy. It has been found that the splitting of ⁷¹Ga NMR lines in two components is followed by the gradual transformation of low-frequency signal into the high-frequency one upon cooling. The NMR measurements proved that the line splitting occurs due to LLPT under nanoconfinement within a temperature range where the coexistence of two spectral components is seen.

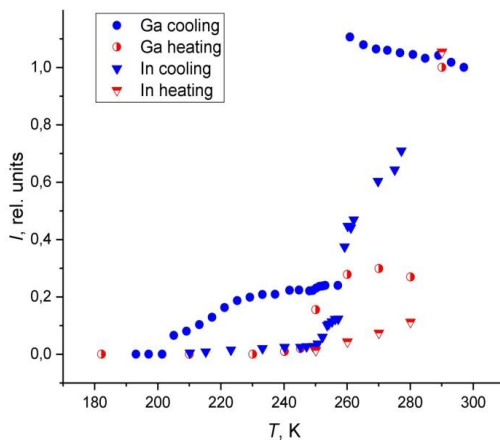


Figure 1. The temperature dependencies of the ^{71}Ga and ^{115}In signal relative integral intensities for the full freezing-melting cycle

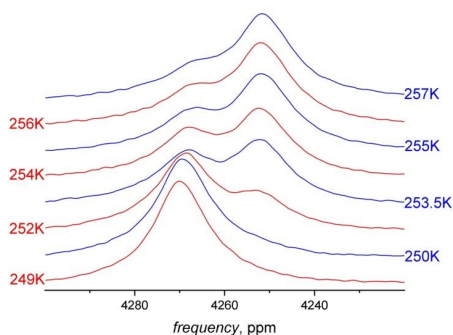


Figure 2. The evolution of the ^{71}Ga NMR spectrum

References

1. Z. Li, Y. Guo, Y. Zong, K. Li, S. Wang, H. Cao, C. Teng. *Nanomaterials* **11**, 2246 (2021).
2. G. Bo, L. Ren, X. Xu, Y. Du, S. Dou. *Adv. Phys.: X* **3**, 1446359 (2018).
3. Y. Plevachuk, V. Sklyarchuk, S. Eckert, G. Gerbeth, R. Novakovic, *J. Chem. Eng.* **59**, 757 (2014).

Acknowledgements

This work is supported by RSF (grant 21-72-20038). Measurements were carried out in SPbGU using the equipment of "Center for Diagnostics of Functional Materials for Medicine, Pharmacology and Nanoelectronics".

Dissipative dynamics of multiple-quantum NMR coherences in two-spin systems.

Sergey G. Vasil'ev¹, Ksenia Panicheva^{1,2}, Edward Fel'dman¹

¹*Federal Research Center of Problems of Chemical Physics and Medicinal Chemistry RAS, Ac. Semenov avenue 1, Chernogolovka, Moscow Oblast 142432, Russia*

²*Faculty of Fundamental Physical-Chemical Engineering, Lomonosov Moscow State University, GSP-1, Leninskie Gory, Moscow 119991, Russia*

E-mail: vasil'ev@icp.ac.ru, viesssw@mail.ru

Introduction

Coherent many-body quantum dynamics is the basis of the emerging quantum technologies including spin-based quantum information processing. In this regard, multiple-quantum (MQ) NMR coherences represent a handy model to investigate this dynamics. The MQ coherences among large group of spins in solids with extensive dipole-dipole interactions can be excited by a properly designed pulse sequence modifying the internal Hamiltonian [1]. Since single quantum coherence is the only magnetization that can be directly observed, the detection of MQ coherences is done indirectly through a two-dimensional experiment, comprising the excitation (preparation) period, the period of free evolution, reconversion (mixing) period, needed to transfer the unobservable MQ coherences to single-quantum magnetization prior to detection. The propagation of multiple-spin correlations and relaxation in multiple-spin clusters are directly observable in MQ NMR experiments. It was initially anticipated that only the number of correlated spins limits the achievable coherence order provided that the time of excitation is sufficient for interaction to become significant [1]. However, it was realized soon, that the intensities of the MQ coherences decrease with the increasing preparation time and this effect could not be solely explained by the accumulation of the experimental imperfections [2]. The discussion of this important phenomenon in the literature is limited.

Theoretical consideration

To address the question of dissipation during the excitation of MQ NMR coherences (on the preparation period) we chose relatively simple spin system consisting of two interacting ¹H spins. Real systems are unavoidably in contact with the environment, and the creation, evolution, and external manipulation of quantum coherence is always accompanied by its destruction through interaction with the environment [3]. The Hamiltonian in MQ NMR experiment is given by [1]:

$$H_{\text{MQ}} = D(I_1^y I_2^y - I_1^x I_2^x) = -\frac{D}{2}(I_1^+ I_2^+ + I_1^- I_2^-)$$

The dissipation in the system was accounted by the introduction of Lindblad equation[4]:

$$\frac{d\rho}{dt} = -i[H_{\text{MQ}}, \rho(t)] + \sum_{m=1}^4 \left\{ L_m \rho(t) L_m^\dagger - \frac{1}{2} L_m^\dagger L_m \rho(t) - \frac{1}{2} \rho(t) L_m^\dagger L_m \right\},$$

where the Lindblad operators for the two-spin system are chosen as

$$L_1 = \sqrt{\gamma} I_1^+, \quad L_2 = \sqrt{\gamma} I_1^-, \quad L_3 = \sqrt{\gamma} I_2^+, \quad L_4 = \sqrt{\gamma} I_2^-$$

The theoretical approach based on the Lindblad equation, which generalizes the von Neumann equation for open quantum systems, allows to include the influence of the environment on the system of interest without the explicit consideration of the complete system. For the two-spin system the theory predicts the oscillatory exchange of zero- and \pm second order MQ coherence intensities with the increasing excitation time, coinciding with the known results for isolated pairs, accompanied by the exponential decay of coherences, which is specific to the developed approach.

Experimental results and discussion

The experimental studies were performed on single crystals of gypsum ($\text{CaSO}_4 \cdot 2\text{H}_2\text{O}$) and hambergite ($\text{Be}_2\text{BO}_3\text{OH}$). Gypsum is a well-known diamagnetic crystal [5], in which the protons belong to two water molecules. The individual molecules are well-separated in space and there are two different noncollinear vectors connecting the protons in water molecules, resulting in two doublets in ^1H spectra with separation dependent on the orientation in the magnetic field. In hambergite structure the protons arrange in well-separated chains with constant distance between nearest protons and constant angle between chain and nearest neighbors (zigzag chain). The planes of the zigzags are parallel, so that the specific orientation exists at which every second vector connecting neighbors in the chain lies at the magic angle, which eliminates the dipolar coupling. In this situation, the chain transforms into a set of well-isolated spin pairs [6]. This orientation is shown in Fig. 1

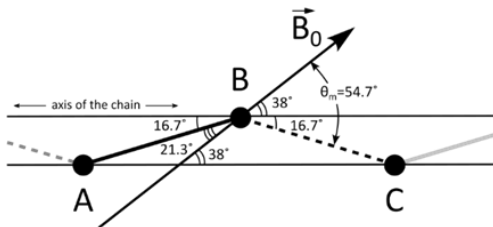


Figure 1. Illustration for a “magic orientation” of the hambergite crystal

The experiments were performed on a Bruker Avance III spectrometer operating at 400.2 MHz for ^1H . MQ NMR experiments [1] were performed for several different orientations of gypsum crystal (with different dipolar couplings in spin pairs) and a “magic orientation” of the hambergite crystal. Representative results are shown in Fig. 2 for hambergite crystal.

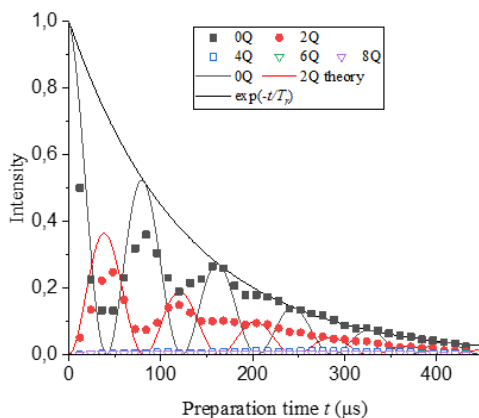


Figure 2. The evolution of ^1H MQ NMR coherence intensities in hambergite as a function of preparation time.

For both crystals the intensities of MQ NMR coherences are represented mainly by the zero- and second-order. The frequency of oscillations show good correlation with the dipolar splittings in single-quantum spectra. The intensities of MQ coherences decay in accordance with the exponential law predicted by the theory ($T_r=125 \mu\text{s}$ for hambergite and $T_r=150 \mu\text{s}$ for gypsum). Thus, the experimental decay of MQ coherences on the preparation period was successfully explained by the developed theory for ^1H spin pair weakly interacting with environmental ^1H spins. In the case of hambergite, the relaxation time of MQ coherences obtained in experiments closely correspond to the relaxation time due to the interactions with next nearest neighbors estimated independently from the simplified relaxation theory, which supports the dipole-dipole origin of the relaxation.

Acknowledgements

This work is performed as a part of a state task, State Registration No.124013000760-0.

References

1. J.Baum, M.Munowitz, A.N.Garroway, A.Pines, *J. Chem. Phys.*, 1985, 83, 2015-2025
2. K.K. Gleason, *Concepts Magn. Reson.*, 1993, 5, 199-216
3. J. M. Riga, C. C. Martens, *Chem. Phys.*, 2006, 322, 108-117
4. D. Manzano, *AIP Adv.*, 2020, 10, 025106
5. G. E. Pake, *J. Chem. Phys.*, 1948, 16, 327-336
6. G.A. Bochkin, E.B. Fel'dman, D.P. Kiryukhin, P.P. Kushch and S.G. Vasil'ev, *J. Magn. Reson.*, 2023, 350, 107415

Excitation of black spin wave solitons in an active ring resonator based on a ferromagnetic film

Vedernikov L. S., Stashkevich A. A., Tatsenko I. Y. Ustinov A. B.

¹*Department of Physical Electronics and Technology, St. Petersburg Electrotechnical University, St. Petersburg, 197376 Russia*

E-mail: lsv89314@mail.ru

Introduction

Envelope solitons, discovered in the 1980s [1-3], still remain a fascinating topic for study and a source of interest both for fundamental science and applications. The ability of these nonlinear wave packets propagating in ferromagnetic structures to preserve their shape without dispersive spreading makes them especially attractive for the rapidly developing field of magnonics [4-6]. Within this approach magnons, the quanta of spin waves (SW), are considered as carriers of information and, correspondingly, can potentially be used as energy efficient data carriers for low-power information processing, taking full advantage of novel wave-based computing technologies allowing operations with vector variables [7].

Experimental setup

Fig. 1 shows the experimental setup. The excitation of black spin wave envelope solitons was carried out by applying two microwave signals to the input of an active ring resonator. 5.5 μm thick a ferromagnetic film made of yttrium iron garnet with a saturation magnetization of 1950 G was used as a delay line. Permanent magnets were positioned so that they magnetized the film transversely to the propagation of waves, so that surface spin waves were excited in the film [8]. The external magnetic field strength was 1417 Oe. Two microstrip antennas used to excite and receive spin waves were located at a distance of 6 mm. The receiving antenna was connected to the exciting antenna feedback circuit, consisting of a broadband microwave amplifier and an adjustable attenuator, which adjusted the total gain in the G ring.

In this work, measurements were carried out below the self-oscillation threshold. In this case the gain of the ring does not exceed the losses arising during signal propagation. Spin waves in the delay line were excited by simultaneous supply of two microwave signals having different frequency. Due to the development of induced modulation instability envelope solitons were formed in the ring. To analyze solitons, a small part of the signal founded out of the ring and analyzed with a spectrum analyzer and oscilloscope.

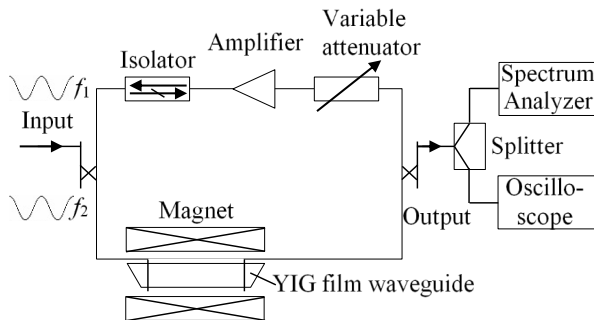


Figure 1. Schematic diagram of the experimental set-up.

Results

The amplitude-frequency characteristic of the active ring resonator is presented by red line in Fig.2. It features almost equidistant resonance peaks at frequencies for which the phase matching condition for the waves circulating in the ring is satisfied. Tis conditions can be described by the formula $k(\omega)d + \varphi_e = 2\pi n$, where k is the wavenumber, ω is the angular frequency and d is the distance between the antennas. It should be noted that the phase shift due to SW propagation in the delay line $k(\omega)d$ is much greater than that associated with the rest of the ring φ_e , i.e. the resonance frequencies are practically entirely determined by the predominant SW related contribution $k(\omega)d$. To boost the efficiency of the investigated nonlinear effects, the frequencies of the two input harmonic signals were chosen to coincide with resonance frequencies of the active ring.

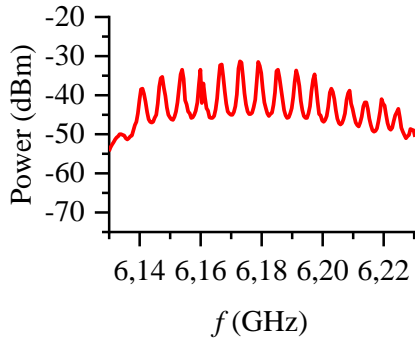


Figure 2. Amplitude-frequency characteristic of the active ring resonator

When two signals are supplied at frequencies $f_1 = 6.1852$ GHz and $f_2 = 6.166$ GHz with powers $P_1 = 15.5$ dBm and $P_2 = 13$ dBm, the formation of black solitons in the ring with period $T = 52.17$ ns and width $\tau = 12.15$ ns is observed. The observed solitonic waveform and corresponding frequency spectrum are shown in Fig. 3. Since the repetition period of black solitons is approximately three times less than the signal delay time $\tau_d = 162$ ns, we can say that during the delay time three pulses are formed, which indicates the emergence of a multi-soliton regime.

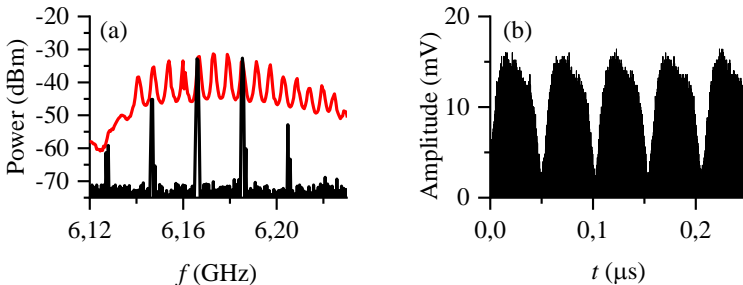


Figure 3. Spectrum (a) and waveform oscillograms for three solitons in the ring (b)

Acknowledgements

This work was supported by the Ministry of Science and Higher Education of the Russian Federation (grant number No. FSEE-2020-0005).

References

1. B. A. Kalinikos, N. G. Kovshikov, and A. N. Slavin, "Observation of spin wave solitons in ferromagnetic films," *Sov. Phys. -JETPLett.*, vol. 38, pp. 413-417, 1983 (*Pis'ma Zh. Eksp. Teor. Fiz.*, vol. 38, pp. 202-206, 1983).
2. B. A. Kalinikos, N. G. Kovshikov, and A. N. Slavin, "Multisoliton propagation of spin waves in ferromagnetic films," *Sov. Phys. -Solid State*, vol. 27, pp. 135-136, 1985 (*Fiz. Tverd. Tela*, vol. 27, pp. 226-228, 1985).
3. P. DeGasperis, R. Marcelli, and G. Miccoli, "Magnetostatic soliton propagation at microwave frequency in magnetic gamet films," *Phys. Rev. Lett.* vol. 59, pp. 481-487, 1987.
4. A. V. Chumak and H. Schultheiss, Magnonics: spin waves connecting charges, spins and photons, *J. Phys. D: Appl. Phys.* 50, 300201 (2017). DOI 10.1088/1361-6463/aa7715.
5. M Krawczyk and D Grundler, Review and prospects of magnonic crystals and devices with reprogrammable band structure, *J. Phys.: Condens. Matter* 26, 123202 (2014) DOI 10.1088/0953-8984/26/12/123202.
6. Anjan Barman et al., The 2021 Magnonics Roadmap, *J. Phys.: Condens. Matter* 33, 413001 (2021).
7. A. V. Chumak, V. I. Vasyuchka, A. A. Serga, and B. Hillebrands, Magnon spintronics, *NATURE PHYSICS* 11, 453 (2015) www.nature.com/naturephysics.
8. Gurevich A G and Melkov G A 1996 *Magnetic oscillations and waves* (SRC Press).

Ordering of water molecules in hydrated aluminophosphate AIPO-11 according to ^{27}Al solid-state NMR and DFT calculations

Ilya V. Yakovlev¹, Aleksandr A. Shubin², Evgeniy S. Papulovskiy¹, Aleksandr V. Toktarev¹, Olga B. Lapina¹

¹*Boreshkov Institute of Catalysis, p. Lavrentieva 5, 630090 Novosibirsk, Russia*

²*Institute of Solid State Chemistry and Mechanochemistry, ul. Kutateladze 18, 630090 Novosibirsk, Russia*

Lateral interactions between the adsorbed molecules play an important role in the physico-chemical properties of microporous catalysts and adsorbents. These adsorbate-adsorbate interactions influence the rates of chemical reactions, activation barriers, diffusion, dissipation and excitation of the reagents. Lateral interactions play an important role during the adsorption often leading to a decrease in the heat of adsorption. At the same time, identifying and characterizing such lateral interactions presents a very complicated problem due to the variety of their possible sources such as direct overlap of the adsorbate wave functions, surface-mediated indirect interactions and direct dipolar interaction.

This directs our interest to the zeolite-like aluminophosphate molecular sieve AIPO-11, which demonstrates a highly ordered process of hydration that we believe to be connected with the lateral interaction between the adsorbed H_2O molecules. This material is built from 4-, 6- and 10-membered one-dimensional channels with the dimensions of the largest 10-ring channel of roughly $4.4 \text{ \AA} \times 6.7 \text{ \AA}$. Upon hydration, the symmetry of the structure decreases from *Ima2* s.g. to *Pna2₁* resulting in five inequivalent Al sites with equal occupancies. According to previous ^{27}Al NMR measurements, exactly 1/5 of the 20 Al sites become octahedrally coordinated by water molecules, without forming any pentacoordinate species at any hydration state. Furthermore, the hydration of AIPO-11 proceeds strictly non-homogeneously, i.e. the sample always is a mixture of the fully hydrated and dehydrated phases at any hydration level. Such an interesting hydration behavior makes AIPO-11 a good candidate for the study of lateral interactions in microporous systems.

In this work, we study the sample of fully hydrated hydrothermally synthesized AIPO-11 using ^{27}Al solid-state NMR (both MAS and 3QMAS) in combination with DFT modelling of partially and fully hydrated aluminophosphate structures. We demonstrate that a strong lateral interaction directs the adsorption of water molecules on different Al sites in the AIPO-11 framework, which leads to the strict ordering of the octahedrally coordinated Al sites. Further, we use the models of the completely hydrated AIPO-11 to assign the experimentally observed signals in the ^{27}Al NMR spectrum to the structural Al sites in both hydrated and dehydrated AIPO-11 frameworks.

Acknowledgements

This work was supported by the Russian Science Foundation (RSF grant № 23-13-00151).

Scanning NV spectroscopy as a tool for the study of natural diamonds

Valentina V. Yakovleva¹, Kirill V. Likhachev^{1,2}, Roman A. Babunts¹, Sergey V. Titkov³, Pavel G. Baranov¹

¹*Ioffe Institute, Saint-Petersburg, 194021, Russia*

²*NArFU, Arkhangelsk, 163002, Russia*

³*(IGEM) RAS, Moscow, 119017, Russia*

E-mail: valya_yakovleva_1999@mail.ru

Introduction

Nowadays central research is focused on negatively charged nitrogen vacancy centers (NV centers), since it has been discovered that it is possible for them to register ODMR on single centers at room temperature [1]. However, the major part of research is related to NV centers in synthetic diamonds, where they were created artificially by radiation and annealing. This work is devoted to NV centers in natural diamonds, where they were formed naturally.

The NV centers were used as a tool for the investigation and identification of natural diamond single crystals and cryptocrystalline aggregates, called carbonado. Photoluminescence (PL) and (ODMR) spectroscopy at room temperature were used based on a scanning confocal microscope.

Features of natural diamonds

Distribution of NV-centers in natural diamond single crystals

When obtaining a map of the PL signal intensity distribution of NV centers in a diamond single crystal, it turned out that it was uneven; moreover, in many areas two systems of parallel stripes were observed (Fig. 1).

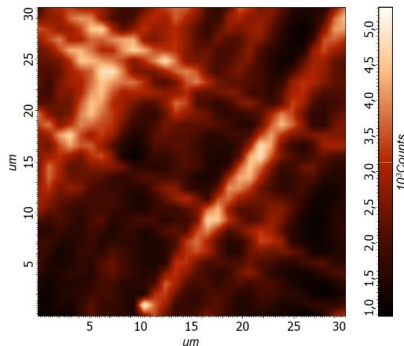


Figure 1. PL map of natural diamond single crystal

These stripes represent dislocation slip planes characteristic of plastically deformed diamonds [2].

Ratio of neutrally and negatively charged NV centers

Note that NV centers charge state plays a significant role in the study of them, since the energy structure of negative and neutrally charged NV centers takes on completely different forms. This NV^0/NV^- ratio becomes a necessary condition for assessing the possibilities of spin manipulation in a sample. Figure 2 shows the PL spectra of carbonado at several points. It can be seen that some spectra have a more intense zero-phonon PL line of NV^0 , while in others it may be completely absent.

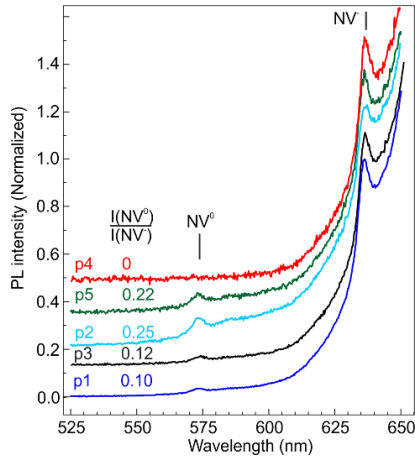


Figure 2. Ratio of NV^0 and NV zero-phonon lines intensities

Stresses and strains

One of the advantages of ODMR method is that it allows to locally determine such a parameter as the mechanical stress of the crystalline environment of the NV center. Figure 3 shows the stresses along the profile of a single crystal diamond plate. It can be seen that as one approach the center of the plate, the stresses increase.

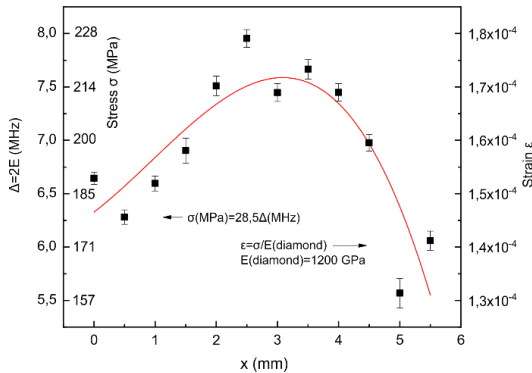


Figure 3. Distribution of stresses and strains along the profile of a diamond plate

Distance between the NV center and the nitrogen donor

Also, from the ratio of the intensities of the satellite and central lines in the ODMR spectrum, one can determine such an important parameter as the distance between the NV center and the nitrogen donor, which affects the decoherence of the NV center. These values were calculated along the same diamond plate profile (Fig. 4).

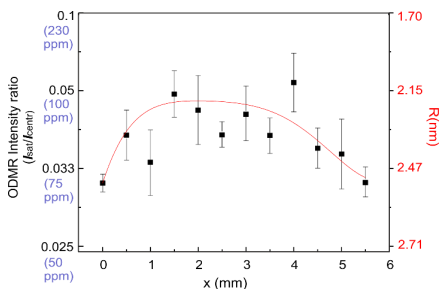


Figure 4. Distribution of distances between NV centers and nitrogen donors along the profile of a diamond plate

ODMR in magnetic field

An external magnetic field was used to study the orientation of micro- and nanocrystals in carbonado. The resulting spectrum was also compared with the spectrum of an artificial diamond polycrystal obtained by sintering detonation nanodiamonds at high temperatures and pressure (Fig. 5). The spectra differ in that in artificial diamond the lines are resolved much better and have greater intensity, because it contains a larger number of equally oriented nanocrystals.

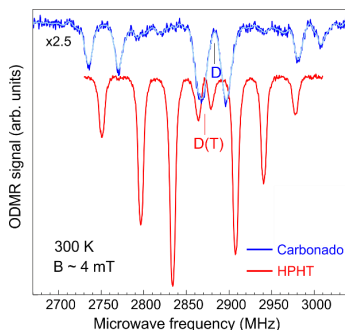


Figure 5. ODMR spectra in magnetic field of carbonado and an artificial diamond polycrystal

Conclusion

ODMR of NV centers in diamonds provides extensive information about their local properties. It is expected that this study will complement the existing geological information on the process of their formation, and will also be useful for developing a new method for creating NV centers in artificial diamonds.

Acknowledgements

This work is supported by the Russian Science Foundation (grant № 23-12-00152, <https://rscf.ru/project/23-12-00152/>)

References

1. A. Gruber, A. Drabenstedt, C. Tietz et al. – *Science*, **276** (5321), 2012-2014 (1997).
2. S.V. Titkov, V.V. Yakovleva, I.D. Breev et al. – *Diamond and Related Materials*, 136, 109938 (2023).

Solvent effects in hyperpolarization of ^{15}N nuclei in metronidazole and nimorazole antibiotics via SABRE-SHEATH

Anna P. Yi^{1,2}, Oleg G. Salnikov¹, Dudari B. Burueva¹, Nikita V. Chukanov¹, Igor V. Koptyug¹
¹Laboratory of Magnetic Resonance Microimaging, International Tomography Center SB RAS, Novosibirsk, Russia

²Department of Natural Sciences, Novosibirsk State University, Novosibirsk, Russia
 E-mail: anna.i@tomo.nsc.ru

Introduction

Nuclear magnetic resonance (NMR) spectroscopy and magnetic resonance imaging (MRI) are widely used in a broad range of applications in chemistry, biology and medicine. However, both these techniques possess a significant limitation of intrinsically low sensitivity caused by small population difference of nuclear spin energy levels (i.e., small degree of nuclear spin polarization) at thermal equilibrium [1]. An efficient way to overcome this problem is hyperpolarization techniques, which rely on transiently creating non-equilibrium polarization of nuclear spins allowing for enhancement of NMR signal up to several orders of magnitude [2]. One of the most promising hyperpolarization technique is Signal Amplification By Reversible Exchange (SABRE) [3] employing singlet spin order of a parahydrogen ($p\text{-H}_2$) molecule as a source of hyperpolarization. It is based on reversible binding of both $p\text{-H}_2$ and substrate molecules to an Ir complex accompanied by polarization transfer from $p\text{-H}_2$ -derived hydrides to a coordinated target molecule via spin-spin couplings (Fig. 1a) [4]. For prospective applications in medicine hyperpolarization of heteronuclei (e. g. ^{13}C , ^{15}N) is of importance. Polarization transfer to heteronuclei may be accomplished through an approach called SABRE in SHield Enables Alignment Transfer to Heteronuclei (SABRE-SHEATH) [5] to exploit ultralow magnetic fields creating with a mu-metal magnetic shield. This method allows to hyperpolarize a wide range of substrates without special tuning of experimental parameters for each substance and to achieve high polarization values [6].

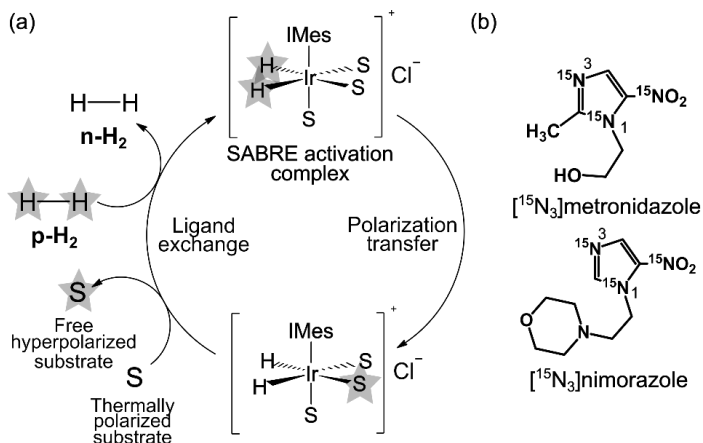


Figure 1. (a) Scheme of SABRE process. (b) To-be-hyperpolarized substrates $[^{15}\text{N}_3]$ metronidazole (on top) and $[^{15}\text{N}_3]$ nimorazole (at the bottom). Numbers 1 and 3 denote ^{15}N sites in the imidazole ring, corresponding designations ($^{15}\text{N}\text{-1}$ and $^{15}\text{N}\text{-3}$) are used further.

Metronidazole and nimorazole are of the great interest due to their ability to be reduced in anaerobic conditions, therefore they have prospects for clinical utilization as hypoxia radiosensitizers. Previously, studies of isotopically enriched [$^{15}\text{N}_3$]metronidazole [7] and [$^{15}\text{N}_3$]nimorazole [8] (Fig. 1b) hyperpolarization were carried out in methanol- d_4 as a solvent (which is a typical solvent for SABRE studies). However, this it is not the best choice for biomedical applications due to its toxicity and higher cost compared to nondeuterated solvents. Thus, herein, we systematically investigate the impact of solvent on SABRE-SHEATH performance and define optimal hyperpolarization conditions and lifetimes of [$^{15}\text{N}_3$]metronidazole and [$^{15}\text{N}_3$]nimorazole. We utilize three alcohol solvents: CD_3OD , CH_3OH , and $\text{C}_2\text{H}_5\text{OH}$.

Results and Discussion

The key parameters of SABRE-SHEATH experiments are polarization transfer field and temperature, moreover, the effects of these parameters are strongly connected with each other [9]. Here we started with the measurement of magnetic field profiles at four different temperatures with a 10°C increment (from 13 to 43°C for [$^{15}\text{N}_3$]metronidazole and from 23 to 53°C for [$^{15}\text{N}_3$]nimorazole) and then investigated temperature profiles at fixed magnetic field optimized at the previous step. For [$^{15}\text{N}_3$]metronidazole, the maximal ^{15}N polarization was observed at $\sim 23^\circ\text{C}$ and $0.7\ \mu\text{T}$ in methanol- h_4 and at $\sim 20^\circ\text{C}$ and $0.7\ \mu\text{T}$ in ethanol- h_6 . The optimal parameters for [$^{15}\text{N}_3$]nimorazole were 43°C and $0.55\ \mu\text{T}$ in methanol- h_4 and 33°C and $0.62\ \mu\text{T}$ in ethanol- h_6 . Defined optimal conditions were used further to measure polarization dependence on $p\text{-H}_2$ pressure and flow rate, buildup and decay kinetics in microtesla magnetic fields.

The hyperpolarized states of nitroimidazoles ^{15}N nuclei are known to persist for significantly longer time at high magnetic field in the range from hundreds millitesla to several tesla [9]. In this work we used $1.4\ \text{T}$ magnetic field of a benchtop NMR spectrometer for high field relaxation measurements. Importantly, $1.4\ \text{T}$ is close to typical magnetic fields of clinical MRI scanners. The longest relaxation was observed for the $^{15}\text{NO}_2$ sites. For the [$^{15}\text{N}_3$]metronidazole $^{15}\text{NO}_2$ and $^{15}\text{N-1}$ sites the longest decay times were observed in methanol- h_4 ($413 \pm 7\ \text{s}$ and $196 \pm 2\ \text{s}$, respectively), while for the $^{15}\text{N-3}$ site the longest decay was obtained in methanol- d_4 ($220 \pm 8\ \text{s}$). For [$^{15}\text{N}_3$]nimorazole the results were the opposite, i.e. the $^{15}\text{NO}_2$ and $^{15}\text{N-1}$ sites showed the highest T_1 in methanol- d_4 (349 ± 8 and $105 \pm\ \text{s}$, respectively) while for the $^{15}\text{N-3}$ site the longest relaxation was observed in methanol- h_4 ($93 \pm 1\ \text{s}$).

In addition it was observed that the maximal attainable polarization decreased from CD_3OD ($P_{^{15}\text{N,max}} = 7.6\%$) to CH_3OH ($P_{^{15}\text{N,max}} = 6.1\%$) and then to $\text{C}_2\text{H}_5\text{OH}$ ($P_{^{15}\text{N,max}} = 4.7\%$) for [$^{15}\text{N}_3$]metronidazole (the values averaged across three ^{15}N sites are presented here). For [$^{15}\text{N}_3$]nimorazole, the highest polarizations were observed in ethanol- h_6 ($P_{^{15}\text{N,max}} = 7.65\%$), while methanol- h_4 and methanol- d_4 provided similar polarization levels ($P_{^{15}\text{N,max}}$ of 6.1% and 5.8% , respectively).

Acknowledgements

This work was supported by the Russian Science Foundation (grant 21-73-10105).

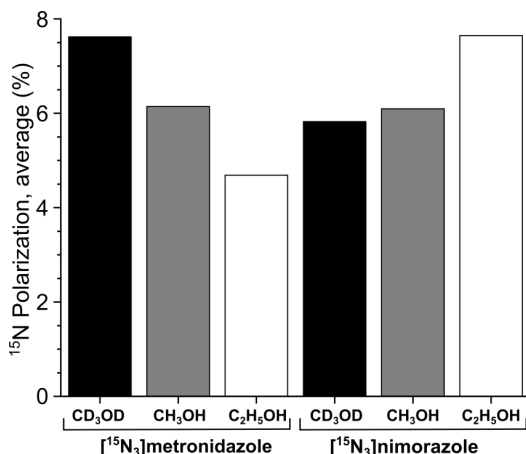


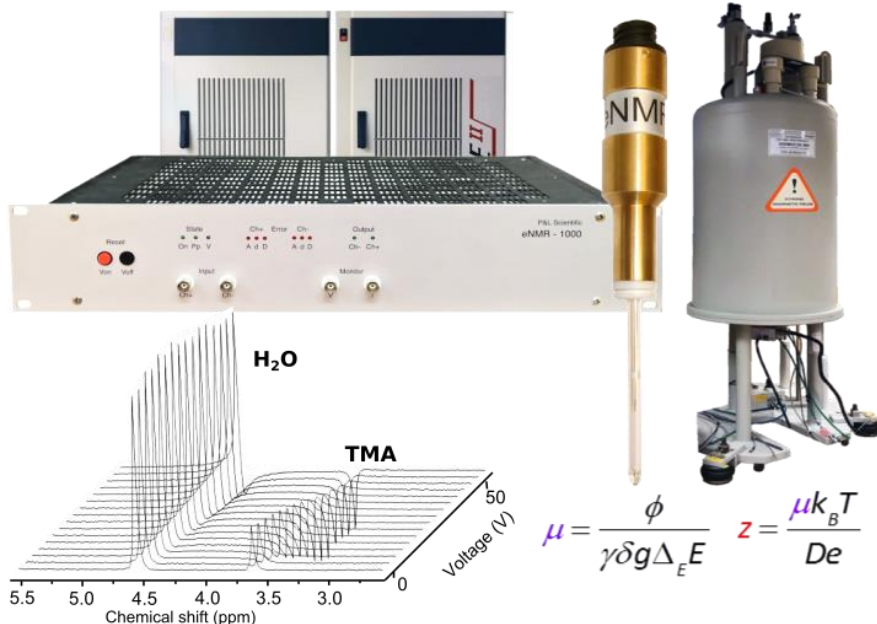
Figure 2. Histogram of average maximal ^{15}N polarizations for free [$^{15}\text{N}_3$]metronidazole (the left panel) and [$^{15}\text{N}_3$]nimorazole (the right panel) at optimized conditions in methanol- d_4 , methanol- h_4 and ethanol- h_6 (the values were averaged across three ^{15}N sites).

References

- Ardenkjaer-Larsen J.H. et al. Facing and Overcoming Sensitivity Challenges in Biomolecular NMR Spectroscopy // *Angew. Chemie - Int. Ed.* 2015. Vol. 54, № 32. P. 9162–9185.
- Eills J. et al. Spin Hyperpolarization in Modern Magnetic Resonance // *Chem. Rev.* 2023. Vol. 123, № 4. P. 1417–1551.
- Atkinson K.D. et al. Spontaneous transfer of Parahydrogen derived spin order to pyridine at low magnetic field // *J. Am. Chem. Soc.* 2009. Vol. 131, № 37. P. 13362–13368.
- Salnikov O.G. et al. Parahydrogen-based NMR signal amplification by reversible exchange (SABRE): Recent advances and applications // *Mendeleev Commun.* 2023. Vol. 33, № 5. P. 583–596.
- Theis T. et al. Microtesla SABRE enables 10% nitrogen-15 nuclear Spin polarization // *J. Am. Chem. Soc.* 2015. Vol. 137, № 4. P. 1404–1407.
- Colell J.F.P. et al. Generalizing, Extending, and Maximizing Nitrogen-15 Hyperpolarization Induced by Parahydrogen in Reversible Exchange // *J. Phys. Chem. C.* 2017. Vol. 121, № 12. P. 6626–6634.
- Shchepin R. V. et al. Hyperpolarizing Concentrated Metronidazole 15NO₂ Group over Six Chemical Bonds with More than 15 % Polarization and a 20 Minute Lifetime // *Chem. - A Eur. J.* 2019. Vol. 25, № 37. P. 8829–8836.
- Salnikov O.G. et al. 15N NMR Hyperpolarization of Radiosensitizing Antibiotic Nimorazole by Reversible Parahydrogen Exchange in Microtesla Magnetic Fields // *Angew. Chemie - Int. Ed.* 2021. Vol. 60, № 5. P. 2406–2413.
- Kiryutin A.S., Yurkovskaya A. V., Ivanov K.L. 15N SABRE Hyperpolarization of Metronidazole at Natural Isotope Abundance // *ChemPhysChem.* 2021. Vol. 22, № 14. P. 1470–1477.

Electrophoretic NMR assembly

Extending the capability of conventional NMR instruments



The electrophoretic mobility and the effective charge can be obtained by recording the variation of spectral phase by increasing electric field

Key features

- Well-established scientific background and proven technology
- Operates as add-on for any conventional NMR spectrometer and probe with gradient; requires no additional hardware or software
- Advanced sample cell and RF filter system
- Straightforward embedding of high voltage pulse generation in conventional NMR pulse programs
- Probe and user protection system

Specifications

Output voltage:	0 to ± 1000 V
Digital To Analogue converter size:	2×12 bit
Output current	
at ± 1000 V:	0 to ± 100 mA
at ± 500 V:	0 to ± 200 mA
Output power:	
Peak power	300 W
Mean power	30 W
Minimum/maximum pulse length:	$500 \mu\text{s} / 1 \text{ s}$
Duty cycle:	30 %
Output pulse shapes:	Rectangular
Slew rate:	Greater than $25 \text{ V} / \mu\text{s}$
Settling time (to 2%):	Less than $200 \mu\text{s}$ for 2 kV step
Stability	
Drift with time	Less than 200 ppm/hr, noncumulative
Drift with temperature	Less than 300 ppm/ $^{\circ}\text{C}$
RF Filters	10 MHz low pass
Power consumption:	80 W for 220 V AC
Dimensions of the main unit:	$430 \times 340 \times 90$ (fits in standard 19" rack); weight - 8 kg



Selected applications

Physical chemistry – ion pairing and association in simple and complex (polyelectrolytes) ionic mixtures.

Batteries and fuel cells - chemically selective measurement of ionic migration.

Biochemistry – biomolecular charge and association.

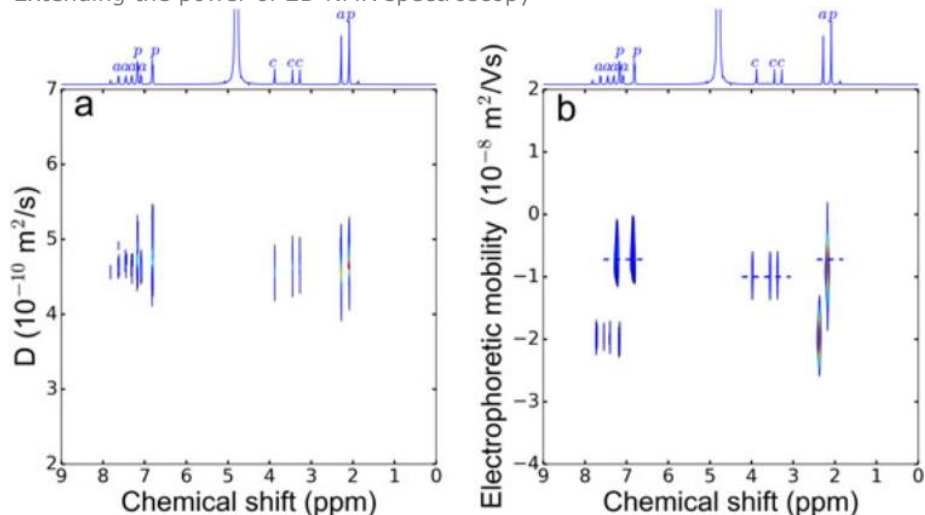
Analytical chemistry – electrophoretic analysis of complex ionic mixtures

Pharmaceutical chemistry – release and association of charged drugs

Metallorganic chemistry – the structure of supramolecular complexes from the observed charge

2D electrophoretic mobility spectroscopy (2D MOSY) based on eNMR

Extending the power of 2D NMR spectroscopy



Direct comparison of 2D DOSY (a) and 2D MOSY (b) experiments for a dissolved Thomapyrin® tablet clearly illustrates the superior performance of the 2D MOSY in selection of the different species

Selected articles for eNMR applications

Y. Fang, P. V. Yushmanov, and I. Furó, Assessing 2D electrophoretic mobility spectroscopy (2D MOSY) for analytical applications, *Magn. Reson. Chem.* 55 DOI: 10.1002/mrc.4558 (2017).

E. Bialik, B. Stenqvist, Y. Fang, Å. Östlund, I. Furó, B. Lindman, M. Lund, and D. Bernin, Ionization of cellobiose in aqueous alkali and the mechanism of cellulose dissolution, *J. Phys. Chem. Lett.* 7 5044-5048 (2016).

M. Giesecke, F. Hallberg, Y. Fang, P. Stilbs, and I. Furó, Binding of monovalent and multivalent metal cations to polyethylene oxide in methanol probed by electrophoretic and diffusion NMR, *J. Phys. Chem. B* 120 10358–10366 (2016).

M. Bielejewski, M. Giesecke and I. Furó, On electrophoretic NMR. Exploring high conductivity samples, *J. Magn. Reson.* 243 17-24 (2014).

L. Patel, O. Mansour, M. Crossman, P. Griffiths, Electrophoretic NMR characterization of charged side chain cationic polyelectrolytes and their interaction with the anionic surfactant, sodium dodecyl sulfate, *Langmuir* 2019, 35, 9233-9238

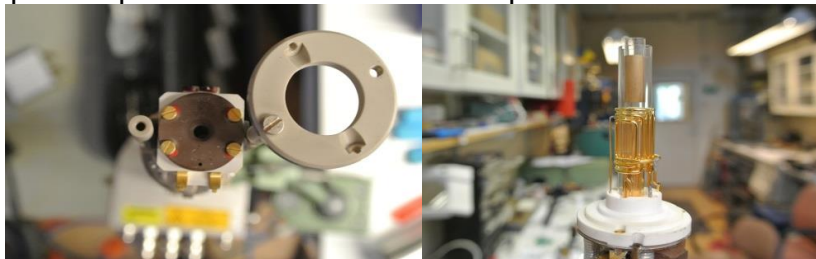
Our NMR services

Repair and modification of the NMR spectrometers and hardware components

- RF amplifiers
- Gradient units
- Synthesizer and SGU 400 - 1000 boards
- Power supplies and shim system
- Temperature and MAS controllers

Repair of the NMR probes:

- Solving arcing problems; bad sensitivity and RF tuning/matching
- Replacing broken glass and ceramics in the probe body
- Repairing certain gradient coils in diffusion and high-resolution probes
- Repair of MAS probes; arcing and spinning problem
- Repair of probe accessories for temperature control



Modification of the NMR probes

- Adaptation of an existing NMR probe to a different spectrometer or NMR frequency.
- Change of RF coil position and configuration
- Adaptation of temperature control components and connectors
- Change of body geometry, dimensions and mounting
- Modification NMR inserts used in several diffusion NMR probes (like Bruker Diff30) to different frequency or double-tuned configuration

Poster Session

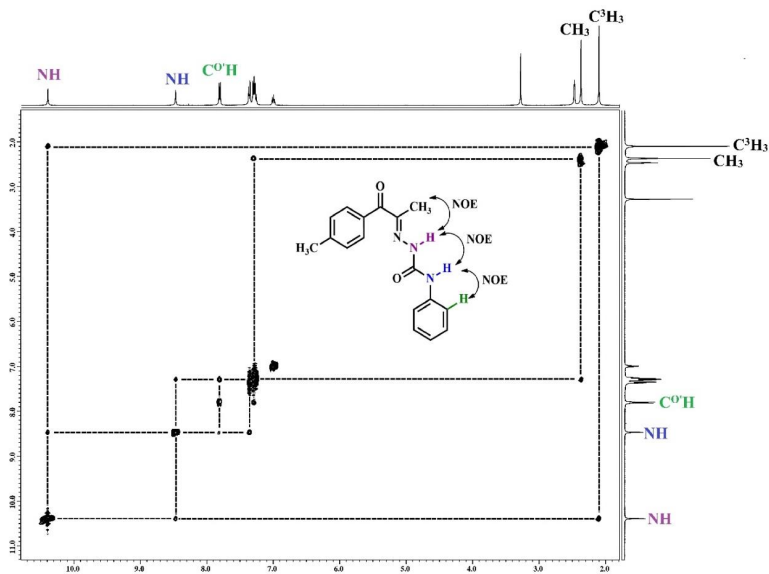


Figure 2. ^1H - ^1H NOESY spectrum of compound **4** ($\text{DMSO-}d_6$)

Assumptions made about the *E-s-trans* geometric configuration of the synthesized hydrazinecarboxamides series are validated by the X-ray structural analysis, as illustrated by compound **1** (Fig. 3).

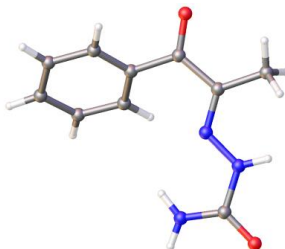


Figure 3. X-ray analysis of compound **1**

Hence, the structure of (2*E*)-2-(1-aryl-1-oxopropan-2-ylidene)hydrazinecarboxamides has been reliably confirmed through the results of the ^1H - ^1H NOESY experiment and further supported by X-ray structural analysis

References

1. Adyukov I.S., Pelipko V.V., Makarenko S.V. 1-Aryl-3-nitroprop-2-en-1-ones in reactions with substituted hydrazines // Book of abstracts Conference "New Emerging Trends in Chemistry (NewTrendsChem-2023)". Yerevan (Armenia). 24-28 September 2023. P. 98.

Behavior of magnetic nanoparticles of ferrofluid in a focused laser beam

Arseniy A. Alekseev¹, Ivan V. Pleshakov², Efim E. Bibik³, Igor V. Ilichev²

¹Higher School of Applied Physics and Space Technologies IET, Peter the Great St. Petersburg Polytechnic University, St. Petersburg, 195251, Russia

²Laboratory of Quantum Electronics, Ioffe Institute, St. Petersburg, 194021, Russia

³Faculty of Chemistry of Substances and Materials, St. Petersburg State Institute of Technology (Technical University), St. Petersburg, 190013, Russia

E-mail: arseniy.alekseev98@gmail.com

Introduction

The magnetic properties of ferrofluids (FF) – colloidal solutions of substances with a magnetic order – determine the every year increasing interest in these materials. These properties, in turn, set the optical characteristics of FF, which are expected to be used in a wide variety of optoelectronics devices [1]. In this regard, it is relevant to investigate the behavior of FF in laser beams and the possible formation of structures from nanoparticles that make up such samples. This work is devoted to studying the effect of laser light on drying drops of magnetite FF-solutions with various carrier media.

Experimental technique

Samples

Experiments were carried out with FFs containing solid phase in the form of magnetite (Fe_3O_4) nanoparticles with a characteristic size of about 10 nm. A fundamental role affecting the results was played by the method of stabilizing the colloid (i.e., preventing the particles from sticking together, consisting of the creation of a special layer on their surface) and, possibly, what the liquid medium was.

The work studied:

- commercial aqueous FF with an organic stabilizer and an organic oil additive (1);
- commercial FF based on kerosene with a polymer stabilizer and a synthetic oil additive (2);
- synthesized FF based on kerosene, stabilized by application to the nanoparticles surface surfactant in the form of a monomolecular layer of oleic acid (3);
- synthesized aqueous FF, stabilized by the creation a double electrical layer on the surface of nanoparticles (4).

The indicated numbering of the samples in parentheses is used below. (In the first two cases, the compositions of the stabilizer and additives were not specified by the manufacturer.) The liquids were diluted with the appropriate carrier to the concentrations of the solid phase n from 27 vol. % to 5 vol. %.

Methods

The fluid as drops was applied to a glass substrate and distributed in such a way as to form a layer with a thickness of about 1 mm, and then the radiation of a semiconductor laser with a wavelength of 650 μm and a nominal power of < 40 mW was focused on it. After drying for several hours, a trace of radiation exposure was formed on the surface of the sediment, which, depending on the sample, was either an aggregation of magnetite nanoparticles, in some cases strongly protruding above the surface, or a recess. The traces were studied using microscopes, one of which made it possible to obtain their pictures with illumination from above or below, and also to estimate the height of the aggregate h by

changing the depth of field, and the other, with a longer focal length, allowed record the sample image when turning it at an angle.

As an additional experimental method, laser correlation spectroscopy (LCS, described in [2]) was used, which made it possible to study FFs of the same composition, but with much lower concentrations of the solid phase, obtaining an estimate of the sizes of their constituent particles and agglomerates.

Results

Microphotographs illustrating the different nature of the action of laser light on FFs are shown in Fig. 1. It can be seen that in aqueous compositions 1 it leads to the appearance of an object strongly protruding in the direction of the beam (Fig. 1a) with a well-shaped lateral edge (Fig. 1b). Kerosene-based solutions give the opposite result: Fig. 1c demonstrates a hole in the focal area. A somewhat more complex picture is observed for samples 3 (Fig. 1d), which reveals, however, that near the focus is also occur the aggregation. The outcome for aqueous samples with ion stabilization 4 is similar to that obtained in the first case.

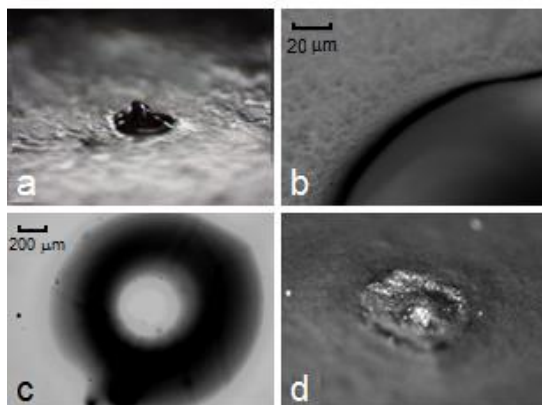


Figure 1. An examples of the effect of laser radiation on different samples: a) sample 1 with $n = 20\%$, inclined illumination, angle of about 15° ; b) sample 1 with $n = 12\%$, the edge of the protruding object formed by the light, illumination from above; c) sample 2 with $n = 10\%$, bottom illumination; and d) sample 3 with $n = 10\%$, inclined illumination, angle of about 15°

For protruding objects, it was possible to qualitatively determine the dependence of their height on the concentration of the initial liquid (Fig. 2), indicating an upward trend in h with an increase in n.

The appearance of aggregates in the form of a “protrusion” (Fig. 1), or, as in the case shown in Fig. 1d, “crater”, is in agreement with data of other works, where it was found that FF illumination can lead to clustering of nanoparticles [3-5]. The mechanism of this phenomenon is not completely clear, especially since the results of laser exposure to FF, as it is easy to see, are quite diverse. However, in general, it is considered that the attraction is provided by polarization induced in the material of the solid phase by the light. The opposite

effect under certain conditions may also be due to polarization or to heating. The latter, in turn, has different manifestations, determined by the sign of thermodiffusion coefficient [6,7].

When the different FFs are illuminated, competing processes of attraction and repulsion should occur in them differently, at that with the predominance of one, depending on characteristics of a sample. On the whole, this can explain the data of present work, based on which we assume that the nature of the observed phenomena should be associated not only with the core of the nanoparticle, but also with its coating, and moreover, possibly, with the surrounding carrier medium.

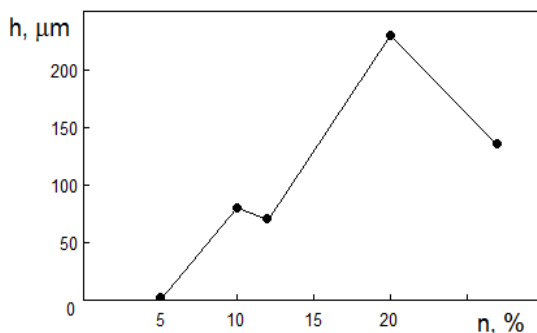


Figure 2. The dependence of the aggregate height on the concentration of the initial liquid

The above results are complemented by our experiments on LCS, provided preliminary information that the probe laser beam used in them can influence the colloid under study, changing the size of agglomerates.

Acknowledgement

The authors of the work thank A.V. Tronev for his help in the experiments.

References

1. J. Philip1, J. M. Laskar. – *J. Nanofluids*, **1**, 3-20 (2012).
2. S. Broillet, D. Szlag, A. Bouwens et al. – *Opt. Express*, **22**, 21944-21957 (2014).
3. B. Hoffmann, W. Köhler. – *J. Magn. Magn. Mat*, **262**, 289-293 (2003).
4. Xiangpeng Yang, Qian Li, Xiangshen Meng, Decai Li. – *ACS Omega*, **5**, 15821-15827 (2020).
5. B. Hoffmann, W. Köhler, M. Krekhova. – *J. Chem. Phys.*, **118**, 3237-3242 (2003).
6. Zi-Ming Meng, Hai-Ying Liu, Wei-Ren Zhao et al. – *J. Appl. Phys.*, **106**, 044905 (2009).
7. S. Alvès, G. Demouchy, A. Bee et al. – *Phil. Mag.*, **83**, 2059-2066 (2003).

UiO-66 framework with encapsulated spin probe: mechanistic study of sensitivity to mechanical pressure and guest molecules

Dmitry V. Alimov^{1,2}, Artem S. Poryvaev¹, Matvey V. Fedin¹

¹International Tomography Center SB RAS, 630090, Russia, Novosibirsk, Institutskaya, 3a

²Novosibirsk State University, 630090, Russia, Novosibirsk, Pirogova, 1

E-mail: d.alimov@g.nsu.ru

Metal-organic frameworks

Metal-organic frameworks (MOFs) are a promising class of compounds with high framework flexibility and great structural diversity. The ability to customize the functional properties of MOFs justifies the potential of their use, in particular, for the adsorption and storage of gases, catalysis, and the separation of gas and liquid-phase mixtures.

Encapsulated spin probe method

For many practical applications, parameters such as the shape and accessibility of pores are important. At the moment, to obtain this information, powder X-ray diffraction (PXRD) is most often used, which makes it possible to identify the phase composition of the material and identify structural changes under external influences or gas adsorption. However, PXRD allows one to obtain only information about the composition of the phases, but does not make it possible to draw a conclusion about the state of the pores and their accessibility to adsorbed molecules. In this work, we apply the method developed at LEPR ITC SB RAS for analyzing the spectra of stationary electron paramagnetic resonance (EPR), in which a spin probe is encapsulated in the pores of the MOFs at the synthesis stage. The EPR spectrum is influenced by the dynamics of the probe, reflecting its environment, which allows us to draw conclusions not only about the guest molecules, but also about the geometry of the MOFs framework.

EPR results

This paper presents the results of a study of a model system - MOF UiO-66 with encapsulated nitroxyl radical TEMPO. Spectra for TEMPO@UiO-66 in the presence/absence of air were obtained. In air and under vacuum EPR spectra are significantly different because paramagnetic oxygen from the air leads to a severe broadening of the nitroxide EPR spectrum (fig. 1). Suspending in hexane leads to the removal of air from pores and narrowing of the spectrum. All spectra can be simulated using characteristic parameters of mobile nitroxide. To simulate EPR spectra, we used a model based on the stochastic Liouville equation with ordered potential.

Although UiO-66 is a mechanically stable MOF up to 1.4 GPa EPR spectra changes at different pressures. Pressure > 0.13 GPa leads to a change of the EPR spectrum (fig. 2) due to the hindering of the nitroxide radical rotation. Deceleration of the radical is caused by occupation of cavity by free linkers of the collapsed ones.

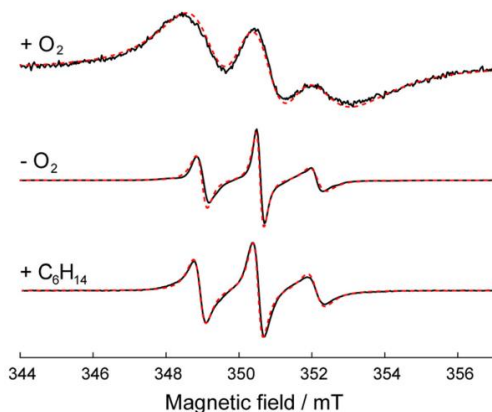


Figure 1. X-band room-temperature CW EPR spectra: TEMPO@UiO-66: open to the air (+O₂), evacuated and sealed off (O₂), impregnated with hexane, and kept exposed to air (+C₆H₁₄). Red dotted lines show simulated EPR spectra, where $g = [2.0090, 2.0085, 2.0055]$ and $A = [0.52, 0.52, 3.80]$ mT.

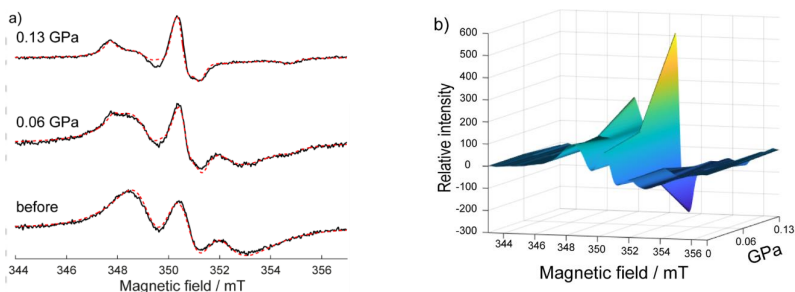


Figure 2 X-band room-temperature CW EPR spectra of TEMPO@UiO-66 measured after its exposure to different pressures of 0–0.13 GPa: 2D figure with spectra intensity normalized to 1 (a) and 3D figure with relative intensity of the EPR spectra normalized to the mass of the sample (b). Red dotted lines in (a) show simulated EPR spectra.

MD results

To interpret the dynamics of TEMPO, classical molecular dynamics (MD) simulations were performed. To simulate framework destruction, series of MD trajectories (298 K, 100 ns) were calculated for TEMPO in UIO-66 pore for the case of removal [0, 1, 2, 3] linkers and replacement [1, 2, 3] linkers on terephthalic acid.

Figure 3. TEMPO in UIO-66 pore. The nearest atoms of zirconium clusters visualized. Charge distribution in UIO-66 framework shown with color.

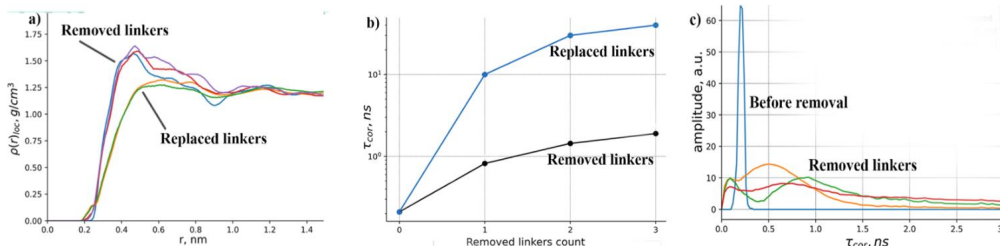
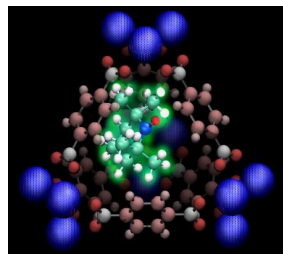


Figure 4. a) Local density of TEMPO. b) Dependence of rotational correlation time on amount of removed / replaced on terephthalic acid linkers; c) Inverse Laplace transform of rotational autocorrelational function of TEMPO calculated for different trajectories.

Despite the fact that local density of TEMPO environment decreases, rotational correlation time, on the contrary, increases (fig. 4). Reduced pore symmetry, decreases the probability of TEMPO “jumps” between pore windows. Interaction with OH groups of terephthalic acid causes significant immobilization. These observations explain existence of two fractions of TEMPO (mobile and immobile) obtained using EPR. The mobile fraction corresponds to TEMPO in pores with removed linkers, while the immobile fraction corresponds to a pores occupied by terephthalic acid. Inverse Laplace distribution of TEMPO ROTACF makes it possible to distinguish different types of radical movement for case of linkers removal: low-angle librations and “jumps” with large angles. Variations of the second one are the main reason for the increase in correlation time.

Acknowledgements

This work was supported by the Russian Science Foundation (No. 22-73-10239).

References

1. A. Sheveleva, A. Anikeenko, A. Poryvaev, D. Kuzmina, I. Shundrina, D. Kolokolov, A. Stepanov and M. Fedin, Journal of Physical Chemistry. 2017, 36, 19880-19886
2. R. Verploegh, A. Kulkarni, S. Boulfelfel, J. Haydak, D. Tang and D. Sholl, Journal of Physical Chemistry. 2019, 14, 9153-9167

Using NMR to establish experimental correlations between hydrogen bond strength and the chemical shift of the ^{31}P in complexes with phosphine oxide.

Omar Alkhuder¹, Peter M. Tolstoy¹, Mikhail A. Kostin¹

¹*Institute of Chemistry, St. Petersburg State University, St. Petersburg, Russia*

E-mail: omar.alkhuder2016@gmail.com

Introduction

Hydrogen bond formation is accompanied by changes in the geometric and spectroscopic properties of the interacting moieties. Hydrogen bonds are described based on their electronic structure, while all other parameters – energetic, geometric and spectroscopic – are consequences. As it is difficult to extract detailed electronic information, spectroscopic parameters become essential probes and markers of the geometric and energetic properties of complexes.

Phosphine oxides as probes

The spectroscopic properties of the P=O acceptor group of phosphine oxides can be used to characterize intermolecular complexes with their participation. The ^{31}P has spin $\frac{1}{2}$, 100% natural abundance and high gyromagnetic ratio ($\gamma = 17.235 \text{ MHz}\cdot\text{T}^{-1}$), as well as high sensitivity of the chemical shift to the formation of non-covalent interactions. For example, the range of chemical shifts of triphenylphosphine oxide is ca. 50 ppm, which is very useful for studies of hydrogen and halogen bonds [3, 4].

Phosphine oxides are used in ^{31}P NMR spectroscopy as probes to characterize the electron withdrawing properties of solvents and other compounds with Lewis acidity (so-called Gutmann-Beckett acceptor number scale) [1] and proton donating ability of compounds with Brønsted acidity [Ошибка! Закладка не определена.]. Previously, predicted ^{31}P NMR chemical shifts of phosphine oxides were used to theoretically estimate the strength of non-covalent interactions [Ошибка! Закладка не определена., 3 4].

Hydrogen bond strength and ^{31}P NMR chemical shift

In this work, we describe the experimental construction of a correlations between the hydrogen bond strength and the chemical shift of the ^{31}P for triphenylphosphine oxide (Fig. 1a) complexes with substituted phenols (Fig. 1b).

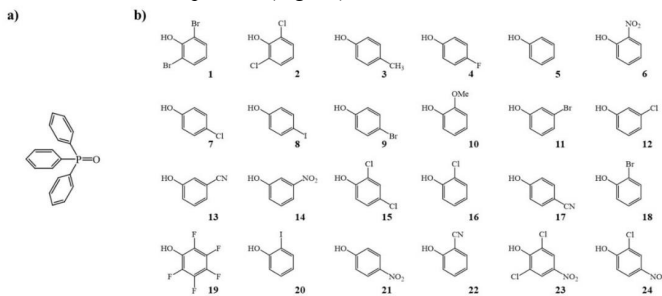


Figure 1. a) Triphenylphosphine oxide. b) Substituted phenols.

The complexes were studied in a polar aprotic solvent (liquefied freonic mixture $\text{CDF}_3/\text{CDF}_2\text{Cl}$), which is characterized by chemical inertness, low freezing point (<100 K), and low viscosity at low temperatures. The experiments were conducted using Bruker Avance III 500 NMR spectrometer at Center for Magnetic Resonance (St. Petersburg State University Research Park).

Two kinds of complexes were identified in low-temperature (100 K) ^1H and ^{31}P NMR spectra: 1:1 complexes (Fig. 2a), and 1:2 complexes (Fig. 2b). For example, Fig. 3 shows the signals of 1:1 and 1:2 complexes of triphenylphosphine oxide and 4-chlorophenol in ^1H and ^{31}P NMR spectra, while Fig. 4 shows a series of spectra recorded for solutions of Ph_3PO with various substituted phenols.

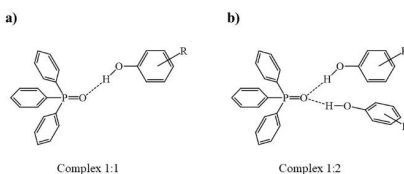


Figure 2. Structures of complexes formed in solution.

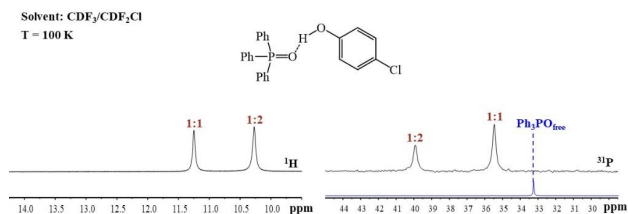


Figure 3. ^1H and ^{31}P NMR spectra recorded for solution of triphenylphosphine oxide and 4-chlorophenol (marked in black) and solution of triphenylphosphine oxide (marked in blue) in $\text{CDF}_3/\text{CDF}_2\text{Cl}$ solvent at 100 K.

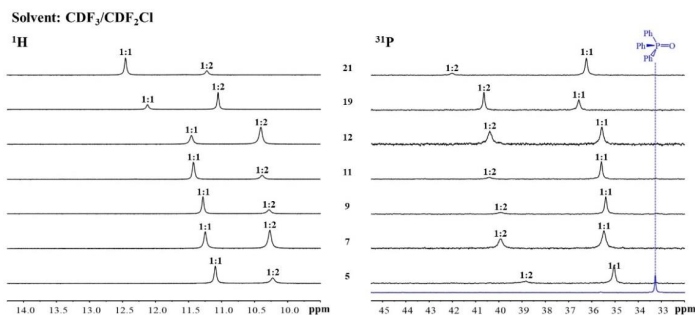


Figure 4. The series of ^1H and ^{31}P NMR spectra of triphenylphosphine oxide complexes with substituted phenols in $\text{CDF}_3/\text{CDF}_2\text{Cl}$ solvent at 100 K.

Using previously established correlation linking the ^1H NMR chemical shift changes upon complexation, $\Delta\delta\text{H}$, with the enthalpy of complexation, ΔH , given by the expression

$$-\Delta H(\text{in kJ} \cdot \text{mol}^{-1}) = 4.18 \cdot \Delta\delta\text{H}(\text{in ppm}) + 1.67 \quad (1)$$

we were able to propose a new correlation, this time with ^{31}P NMR chemical shift changes:

$$-\Delta H(\text{in kJ} \cdot \text{mol}^{-1}) = 16.9 \cdot \Delta\delta\text{P}^{0.45}(\text{in ppm}) \quad (2)$$

Fig. 5 shows the resulting relationship between hydrogen bond enthalpy and the change in ^{31}P NMR chemical shift, both in the 1:1 and 1:2 complexes.

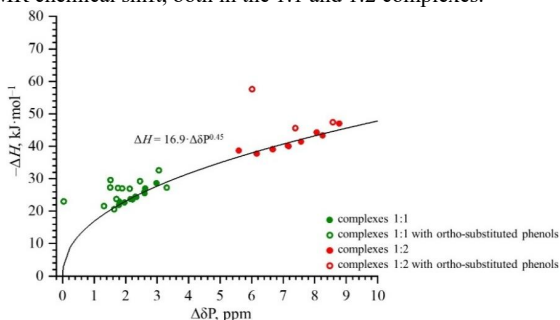


Figure 5. Correlation $\Delta H(\Delta\delta\text{P})$ for triphenylphosphine oxide complexes with substituted phenols. Green circles indicate 1:1 complexes and red circles indicate 1:2 complexes. The solid line corresponds to the approximation curve built according to Equation 2.

Interestingly, that data points corresponding to complexes with *ortho*-substituted phenols deviate from the general correlation (marked as open symbols in Fig. 5). We assume this effect may be explained the formation of an additional halogen bonds between P=O group and the *ortho*-substituent as schematically shown in Fig. 6.

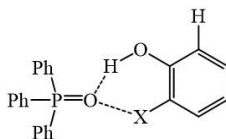


Figure 6. Proposed halogen bond between triphenylphosphine oxide and *ortho*-substituent in phenol.

Acknowledgements

This work is supported by the RSF grant 23-13-00095. The NMR spectra were recorded at the Center for Magnetic Resonance of SPbU Research Park.

References

1. E. Pires and J. M. Frailé, *Phys. Chem. Chem. Phys.*, 2020, 22, 24351–24358.
2. A.S. Ostras', D.M. Ivanov, A.S. Novikov, P.M. Tolstoy, *Molecules.*, 2020, 25, 1406.
3. J. A. McCune et al., *Phys. Chem. Chem. Phys.*, 2014, 16, 23233–23243.
4. E.R. Chakalov, E.Yu. Tupikina, E.V. Bartashevich, D.M. Ivanov, P.M. Tolstoy, *Molecules.*, 2022, 27, 4848.
5. M.A. Kostin, S.A. Pylaeva, P.M. Tolstoy, *Phys. Chem. Chem. Phys.*, 2022, 24, 7121.

6. J. Reuben, Journal of the American Chemical Society., 1986, 108, 1735–1738.

Study of the gastrointestinal tract using ^{19}F MRI

Nikolay V. Anisimov¹, Arina A. Tarasova², Lev L. Gervits³

¹*Faculty of Fundamental Medicine, Lomonosov Moscow State University, 119991, Russia*

²*Faculty of Physics, Lomonosov Moscow State University, 119991, Moscow, Russia*

³*Nesmeyanov Institute of Organoelement Compounds of the Russian Academy of Sciences, Moscow, Russia*

E-mail: anisimovnv@mail.ru

Experiments are described to study the gastrointestinal tract using ^{19}F MRI using capsules commonly used to deliver drugs into the body by ingestion. Depending on the type of capsule, the shell is expected to dissolve in either the stomach or small intestine. In our case, the capsules were filled with biologically inert (hydro- and lipophobic) liquid - perfluorodecalin (PFD), which act as a contrast MRI agent. By recording its signal using the ^{19}F MRI method at short time intervals, it is possible not only to monitor its localization in real time, but also to trace the dynamics of the decrease in the concentration of the administered drug [1, 2]. This dynamics can be associated with the intensity of biochemical and other processes occurring in the gastrointestinal tract and responsible for processing food and other substances entering the body, which, in turn, can be different under normal conditions and in the presence of diseases.

For ^{19}F MRI, a 3D-GRE sequence was used with the following parameters: TR/TE=50/3.5 ms, FA =30°. According to our data, the intensity of the processes of destruction of the shell of the swallowed capsule and the distribution of its contents inside the body depend on the posture of the subject (lying down or in another position) and the interval between the previous meal. In particular, this intensity is lower if the subject is in a supine position, and higher when the capsule is taken on an empty stomach compared to swallowing it after a meal.

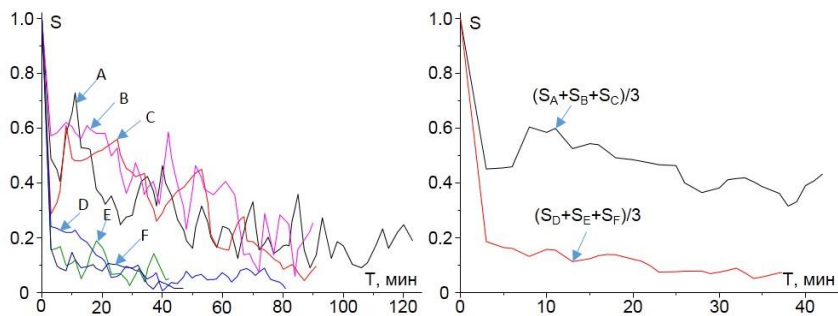


Figure 1 Change in the PFD signal over time when swallowing a capsule designed to dissolve in the stomach, for two scenarios: after a meal (A, B, C) and on an empty stomach (D, E, F). On the left are the original graphs, on the right are the averaged ones for each scenario (shortened interval)

For enteric capsules, a large range of delays was found between swallowing the capsule and its appearance at the entrance of the small intestine - 3-50 minutes. This is apparently due to differences in the filling of the stomach, and, as a consequence, to different speeds of its passage.

It is hypothesized that some specific features associated with the observed changes in the signal from the capsule may be due to the processes of fasting peristalsis.

Acknowledgements

This work is supported by the Interdisciplinary Scientific and Educational Schools of Moscow University «Molecular Technologies of the Living Systems and Synthetic Biology» and «Photonic and quantum technologies. Digital medicine». Access to electronic scientific resources was provided by Nesmeyanov Institute of Organoelement Compounds of the RAS with the support of Ministry of Science and Higher Education of the Russian Federation.

References

1. R. Schwarz et al. - Magn. Reson. Med., 48, 255–261 (2002)
2. T. Hahn et al. - Magn. Reson. Med., 66, 812–820 (2011)

Manifestations of spin coherence transfer in EPR spectra of nitroxide free radical solutions

Kev M. Salikhov, Marcel M. Bakirov, Ruslan B. Zaripov, Iskander T. Khairutdinov
Zavoisky Physical-Technical Institute, Federal Research Center "Kazan Scientific Center of the Russian Academy of Sciences", Kazan, Russia

E-mail: pinas1@yandex.ru

Introduction

One of the fundamental states of the modern paradigm of spin exchange in dilute solutions of paramagnetic particles is the formation of collective modes of motion of the magnetizations of subassemblies of particles with different resonant frequencies [1-3]. These collective modes arise due to the transfer of quantum coherence ("recoil" coherence) between the selected spin and the spin partner during their random collision in a dilute solution. This transfer is caused by Heisenberg spin exchange interaction during collision. For the two-frequency and three-frequency models (for example, ^{15}N and ^{14}N nitroxide radical, respectively), the properties of collective spin magnetization modes were studied in detail in [4]. Some new properties of collective modes were predicted.

In our work, it was experimentally confirmed that under conditions of fast spin exchange, the intensity of the outside components of the spectrum of ^{14}N nitroxide radical solution has a negative sign. Thus, new experimental results from the analysis of the EPR spectra of nitroxyl radicals in solution were obtained that confirm the formation of collective modes.

Experimental system and conditions

Aqueous solutions of the nitroxyl radical 4-Hydroxy-2,2,6,6-tetramethylpiperidine 1-oxyl, Tempol were studied. CW EPR spectra of samples were carried out at different concentrations at temperatures of 298K, 340K on EMX Bruker spectrometer.

Using the nonlinear regression method, the experimental lines were decomposed by the sum of the Lorentz absorption and dispersion lines:

$$J_{exp} = \sum_n \left(J_{abs\ n} \frac{\Delta\omega}{(\omega - \Omega_n)^2 + \Delta\omega^2} + J_{disp\ n} \frac{\omega - \Omega_n}{(\omega - \Omega_n)^2 + \Delta\omega^2} \right), \quad (1)$$

where Ω_n resonant frequency, $\Delta\omega$ - Lorentz line half-width, $J_{abs\ n}$, $J_{disp\ n}$ - absorption and dispersion lines amplitudes, n - collective mode number. In the case of the ^{14}N nitroxyl radical, the value of Ω_n in the absence of exchange interaction takes three values: $-A_0$, 0 , A_0 . The value of hyperfine splitting A_0 in the experiment is 17 G.

Figure 1 shows the experimental CW EPR spectra of ^{14}N Tempol solution at two different concentrations and their decomposition into Lorentzian absorption and dispersion lines. It should be noted that 60-70 mM/l concentration corresponds to the beginning of exchange narrowing regime. The decomposition of spectrum (Fig.1.B) gives negative amplitudes of the Lorentz absorption lines of side components of the spectrum. This means that these collective magnetization modes are in the radiation mode, their integral intensity becomes negative. This behavior of side components is consistent with the theoretical prediction made in [4].

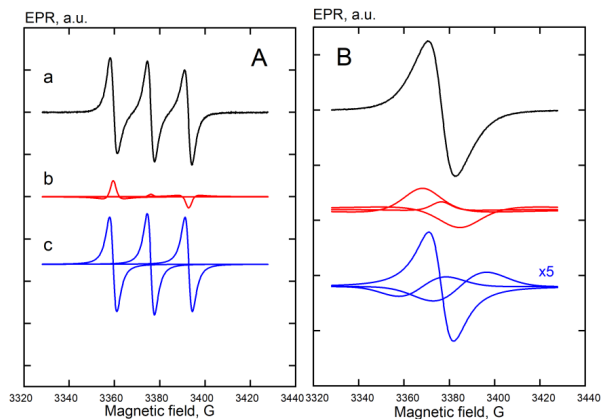


Fig.1. Decomposition of experimental spectra of an aqueous solution of Tempol ^{14}N 10 mM/l (A) and 71 mM/l (B) at 340 K using (1): a. Initial view of the experimental spectrum; b. Contribution of the dispersion line shape; c. Contribution of the absorption line.

Acknowledgements

This study was supported by the Russian Science Foundation (grant #22-72-10063, <https://rscf.ru/project/22-72-10063/>).

References

1. Yu.N. Molin, K.M. Salikhov, K.I. Zamaraev. Spin Exchange. Principles and Applications in Chemistry and Biology. – Springer Verlag, Berlin, 1980.
2. K.M. Salikhov. – UFN (Physics Uspekhi), 189, 1017-1043 (2019).
3. K.M. Salikhov. Fundamentals of spin exchange. Story of a paradigm shift. – Springer International Publishing, 2019.
4. K.M. Salikhov. – Appl. Magn. Reson., 47, 1207–1228 (2016)

The effect of the counterion and substituent in the ligand on the properties of the Fe(II)–Fe(III) heptanuclear complex

*E.E. Batueva*¹, *A.R. Sharipova*², *E.N. Frolova*², *L.I. Savostina*^{1,2}, *L.V. Bazan*²,
*M.A. Cherosov*¹, *R.G. Batulin*¹, *O.A. Turanova*^{1,2}, *A.N. Turanov*^{1,2}

¹*Institute of Physics, Kazan Federal University, Kazan, Russia*

²*Zavoisky Physical-Technical Institute, FRC Kazan Scientific Center of RAS, Kazan, Russia*

E-mail: kathrin200001@gmail.com

Introduction

The aim of searching for materials with predetermined properties is relevant. This can be achieved by knowing in advance the relationship between the structure of a molecule and its physicochemical properties. The properties of the resulting compounds are directly influenced by the variation of counterions and substituents in ligands.

The effect of counterions and substituents in ligands on the magnetic properties of three Fe(II)-Fe(III) heptanuclear complexes with the general structural formula $[\text{Fe(II)(CN)}_6\{\text{Fe(III)(L)}\}_6]\text{X}_2$ (Fig. 1), where L are dianions of pentadentate N3O2-donating Schiff bases: $\text{H}_2\text{L} = \text{N,N-bis(1-hydroxy-2-benzyliden)-1,7-diamino-4-azaheptane}$ (H_2Salten), $\text{X} = \text{Cl}$ (**1**), $\text{H}_2\text{L} = \text{H}_2\text{Salten}$, $\text{X} = \text{NCS}$ (**2**), $\text{H}_2\text{L} = \text{N,N-bis(1-hydroxy-4-octadecyloxy-2-benzyliden)-1,7-diamino-4-azaheptane}$, $\text{X} = \text{Cl}$ (**3**) have been considered in this work.

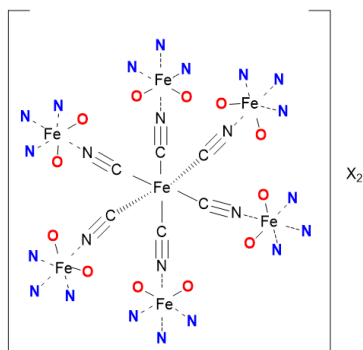


Figure 1. The general structural formula of the complex with no L

Results

Three complexes have been studied by EPR (in the temperature range from 4 to 340 K) and magnetometry (from 5 to 200 K). It has been found that spin-crossover properties appear at the replacing chlorine anyone with thiocyanate anions in the complex. Thermotropic liquid crystalline properties arise in the complex when long alkoxy chains are added to the ligand. A liquid crystalline thermotropic phase for complex **3** has been identified by polarizing microscopy. The structure and properties of the synthesized compounds have been modeled by *ab initio* methods.

Spin-crossover complexes have great potential to become the basis for the development of contrast agents with new properties for MRI.

Molecular dynamic simulation of complexes lysine-based dendrimers with fullerenes C₆₀

Valeriy V. Bezrodnyi¹, Sofia E. Mikhtaniuk², Emil I. Fatullaev², Oleg V. Shavykin^{1,2,3}, Igor M. Neelov^{1,2} and Nadezhda N. Sheveleva¹

¹St. Petersburg State University, 7/9 Universitetskaya nab., 199034 St. Petersburg, Russia

²St. Petersburg National Research University of Information Technologies, Mechanics and Optics (ITMO University), Kronverkskiy pr. 49, 197101 St. Petersburg, Russia

³Tver State University, Zhelyabova St., 33, 170100 Tver, Russia

⁴Institute of Macromolecular Compounds RAS, Bolshoi pr.31, 199004, St.Petersburg, Russia
E-mail: kupala-89@mail.ru

Classical dendrimers are structured like stars, branching out from a central core with each generation. They have a well-defined molecular weight, nanoscale size, low polydispersity, and multivalency. These dendrimers find application in various industries, medicine, and pharmaceuticals due to their exceptional characteristics [1]. They are considered containers for carrying drugs and genetic material by forming complexes with different bioactive molecules [2]. The wide range of dendrimer chemical structures and their modifiability aid in creating delivery systems with desired properties for various drug molecules[3]. The bonding between dendrimers and guest molecules determines the formation of these complexes, whether by physical containment or encapsulation through mechanisms like hydrophobic, electrostatic interactions, or hydrogen bonding [4] dendrimer-based system can also help achieve controlled and targeted delivery to specific tissues and organs [5]. Dendrimer structures protect the transported molecules from premature enzymatic degradation and early release and helps cross the biological membranes, improving their pharmacokinetics and bioavailability [6–10].

Structure

To illustrate the relative positioning of dendrimer and fullerene molecules in the complex, snapshots of these systems at the conclusion of the simulation (after 500 ns) are shown in Figure 2. It can be clearly seen that in all cases, the fullerene is located inside the dendrimer or, at least, between its branches. The additional visual analysis of snapshots confirms that after the first approach to the dendrimer, the fullerene molecule stays in contact with it all the time. This is in good agreement with the results presented in Figure 1.

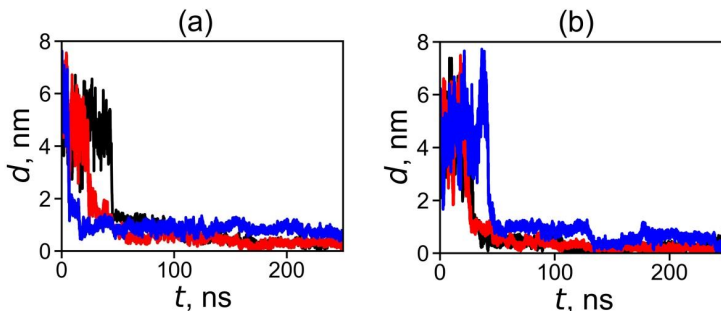


Figure 1. Distance between the centers of mass of the dendrimer and fullerene molecules in the system: a) Lys-2Gly + C₆₀, b) Lys-2Gly + C₇₀.

Based on the obtained trajectories, it is possible to calculate the equilibrium characteristics of the complexes and the dendrimer and fullerene molecules included in them (see Table 1).

Table 1: The asphericity α , the radius of gyration R_g of the dendrimer, and the dendrimer–fullerene complex, as well as mean square distance d between the centers of mass of the fullerene and dendrimer.

Dendrimer/Fullerene	α	R_g	d
Lys-2Gly	0.013	1.24	-
Lys-2Gly + C ₆₀	0.006	1.04	0.51
Lys-2Gly + C ₇₀	0.006	1.08	0.57

According to Table 1, for both complexes, the values of asphericity are smaller compared to that of dendrimer.

The sizes of the complexes can be effectively characterized by one characteristic—the radius of gyration (R_g). Also, to describe the structure of the resulting complexes, it will be sufficient to use the radial distribution functions described below.

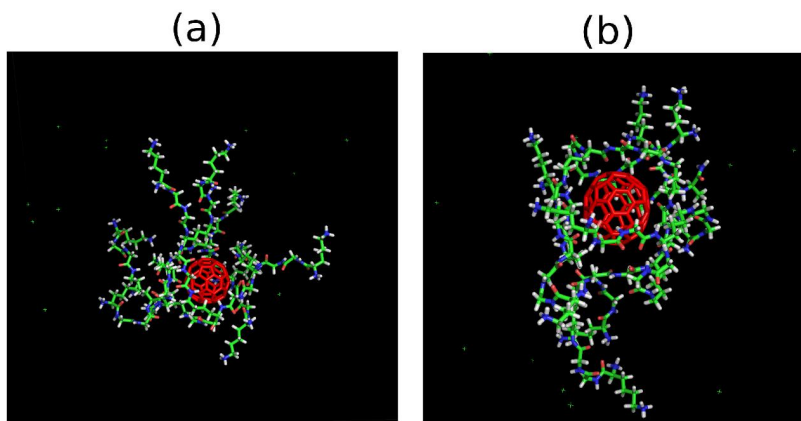


Figure 2. Snapshots of the dendrimer–fullerene system after 500 ns of simulation: a) Lys2Gly+C₆₀, b) Lys2gly+C₇₀.

It can be clearly seen that the relative positions of the dendrimer and fullerene in different complexes differ. For both cases with Lys-2Gly dendrimers (Figure 3a,b), the shape of the $\rho(r)$ can be clearly seen that dendrimer encapsulates fullerene quite well. In this case, the atoms of the Lys-2Gly dendrimer are displaced from the center of the mass region by fullerene and replaced by fullerene atoms.

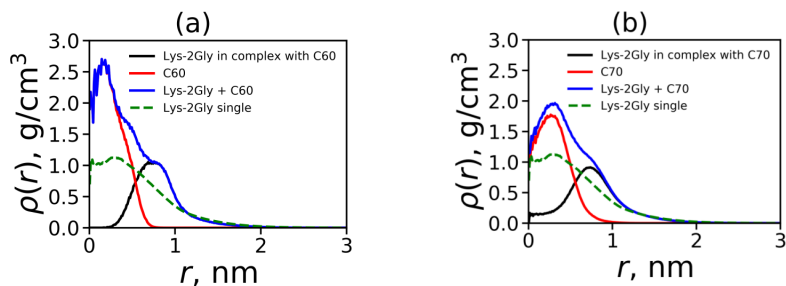


Figure 3. Density distribution for the dendrimer, fullerene, and the dendrimer–fullerene complex: a) Lys-2Gly + C60, b) Lys-2Gly + C70

References

- González Corrales, D.; Fernández Rojas, N.; Solís Vindas, G.; Santamaría Muñoz, M.; Chavarría Rojas, M.; Matarrita Brenes, D.; Rojas Salas, M.F.; Madrigal Redondo, G. Dendrimers and Their Applications. *J. Drug Deliv. Ther.* 2022, 12, 151–158. [CrossRef]
- Ziamba, B.; Borowiec, M.; Franiak-Pietryga, I. There and Back Again: A Dendrimer's Tale. *Drug Chem. Toxicol.* 2022, 45, 2169–2184. [CrossRef] [PubMed]
- Samad, A.; Alam, M.; Saxena, K. Dendrimers: A Class of Polymers in the Nanotechnology for the Delivery of Active Pharmaceuticals. *Curr. Pharm. Des.* 2009, 15, 2958–2969. [CrossRef] [PubMed]
- D'Emanuele, A.; Attwood, D. Dendrimer-Drug Interactions. *Adv. Drug Deliv. Rev.* 2005, 57, 2147–2162. [CrossRef] [PubMed]
- Madaan, K.; Kumar, S.; Poonia, N.; Lather, V.; Pandita, D. Dendrimers in Drug Delivery and Targeting: Drug-Dendrimer Interactions and Toxicity Issues. *J. Pharm. Bioallied Sci.* 2014, 6, 139–150. [CrossRef] [PubMed]
- Allen, T.M.; Cullis, P.R. Drug Delivery Systems: Entering the Mainstream. *Science* 2004, 303, 1818–1822. [CrossRef]
- Sosnik, A.; Carcaboso, A.; Chiappetta, D. Polymeric Nanocarriers: New Endeavors for the Optimization of the Technological Aspects of Drugs. *Recent Pat. Biomed. Eng.* 2008, 1, 43–59. [CrossRef]
- Tyshenko, M.G. Medical Nanotechnology Using Genetic Material and the Need for Precaution in Design and Risk Assessments. *Int. J. Nanotechnol.* 2008, 5, 116–123. [CrossRef]
- Veldhoen, S.; Laufer, S.; Restle, T. Recent Developments in Peptide-Based Nucleic Acid Delivery. *Int. J. Mol. Sci.* 2008, 9, 1276–1320. [CrossRef]
- Cheng, Y.; Xu, T. The Effect of Dendrimers on the Pharmacodynamic and Pharmacokinetic Behaviors of Non-Covalently or Covalently Attached Drugs. *Eur. J. Med. Chem.* 2008, 43, 2291–2297. [CrossRef]

Spin-Dependent Interactions of Fe₂O_n (n=1-6) Clusters with H₂ and O₂ Molecules

K.V. Bozhenko ¹, A.N. Utenyshev ¹, L.G. Gutsev ¹, S.M. Aldoshin ¹, and G.L. Gutsev ²

¹ Federal Research Center of Problems of Chemical Physics and Medicinal Chemistry, Russian Academy of Sciences, Chernogolovka, Moscow region, 142432 Russia

² Department of Physics, Florida A&M University, Tallahassee, FL 32307, United States

E-mail: bogenko@icp.ac.ru

Introduction

The geometry and electronic structure of the Fe₂O_n (n=1-6) clusters and the products of their interaction with H₂ and O₂ in the gas phase have been calculated by the density functional theory method [1, 2]. It can be expected that iron oxide nanoparticles with magnetic properties like those of Fe₂O₃, Fe₂O₄ and Fe₂O₅ clusters could be used to create sensors for detecting oxygen molecules.

Computational details

Calculations were performed by the density functional theory method in the generalized gradient approximation (DFT-GGA) with the GAUSSIAN-09 program [3] using the 6-311+G* basis set. The BPW91 functional consisting of the Becke exchange and the Perdew–Wang correlation was chosen as the exchange-correlation functional. The choice of this functional and basis set was justified by the previous estimate of their efficiency in calculations of 3d-metal monoxides MO and dioxides MO₂ (M = Sc–Zn)], where good agreement was found between the experimental data and the results of calculations by other methods considering the electron correlation energy. The logic of the search for the ground states of Fe₂O_n (n=1-6) clusters and compounds formed after their interaction with H₂ and O₂ was as follows. For each cluster, probable geometric structures were generated, and full state optimization was performed with these geometries for all possible spin multiplicity values. The state with the lowest total energy was taken as the ground one for the given cluster. Local total spin moments on atoms were calculated using the basis set of natural atomic orbitals.

Results and Discussion

For oxides with an odd number of oxygen atoms

It has been found that in the Fe₂O₃ + O₂ → Fe₂O₅ and Fe₂O₅ + H₂ → Fe₂O₅H₂ reactions, the initial total spin magnetic moments are not conserved, and a transition occurs from the antiferromagnetic state of the reactants to the ferrimagnetic state of the products in the first case and to the antiferromagnetic state in the second. Such a switching of the total spin magnetic moment of the reaction products of two reactants is extremely unusual. The property to change the magnetic moments of iron oxide clusters during their interaction with H₂ can be used in modeling the chemical composition of sensors for detecting hydrogen molecules. Analogously, it can be expected that iron oxide nanoparticles with magnetic properties like those of Fe₂O₃ and Fe₂O₅ clusters could be used to create sensors for detecting oxygen molecules. The activation barriers for the Fe₂O_{2n+1} + H₂ and Fe₂O_{2n+1} + O₂ reactions are relatively low, which indicates the absence of significant obstacles to the reactions.

For oxides with an even number of oxygen atoms

It has been shown that the total spin magnetic moments of the ground states of the products and initial complexes do not coincide in two of the four reactions considered. Such a change in the spin magnetic moments of the ground states of the reactants in going to the

products takes place in the $\text{Fe}_2\text{O}_4 + \text{H}_2 \rightarrow \text{Fe}_2\text{O}_4\text{H}_2$ and $\text{Fe}_2\text{O}_4 + \text{O}_2 \rightarrow \text{Fe}_2\text{O}_4\text{O}_2$ reactions with relatively low activation barriers (~ 20 kcal/mol). It can be assumed that iron oxide nanoparticles, similar in their properties to those of the Fe_2O_4 cluster, can be used as sensors for detecting H_2 and O_2 molecules.

References

1. K.V. Bozhenko, A.N. Utenyshev, L.G. Gutsev, L.G. Gutsev, S.M. Aldoshin. Spin-Dependent Interactions of Fe_2O_n Clusters with H_2 and O_2 Molecules. *Russian Journal of Inorganic Chemistry*, 2022, Vol. 67, No. 12, pp. 2003–2008. © Pleiades Publishing, Ltd., 2022. (Russian Text © The Author(s), 2022, published in *Zhurnal Neorganicheskoi Khimii*, 2022, Vol. 67, No. 12, pp. 1789–1794.)
2. K.V. Bozhenko, A.N. Utenyshev, L.G. Gutsev, L.G. Gutsev, S.M. Aldoshin. Nonempirical Modeling of Interactions of Fe_2O_2 and Fe_2O_4 Clusters with H_2 and O_2 Molecules. *Russian Journal of Inorganic Chemistry*, 2023, Vol. 68, No. 10, pp. 1453–1459. © Pleiades Publishing, Ltd., 2023. (Russian Text © The Author(s), 2023, published in *Zhurnal Neorganicheskoi Khimii*, 2023, Vol. 68, No. 10, pp. 1454–1461.)
3. M. J. Frisch, G. W. Trucks, H. B. Schlegel, et al., Gaussian 09, Revision C.01. (Gaussian, Inc., Wallingford CT, 2009).

Microstructure and molecular mobility in the LiCl-CsCl-H₂O ternary system according to molecular dynamics simulations

Cheremensky S.O., Egorov A.V.

Department of Nuclear-Physics Research Methods, Faculty of Physics, Saint-Petersburg State University

E-mail: st087373@student.spbu.ru

Introduction

In recent years, ternary aqueous solutions are considered as perspective electrolytes for batteries. One of the most promising systems is LiCl-CsCl-H₂O [1]. To improve our understanding of the nature of ternary solutions, it would be extremely important to describe the structure of such systems at the molecular level. In the present work, the molecular dynamics simulations of LiCl-CsCl-H₂O ternary solution were carried out.

Methodology

At all, 8 systems were considered: 6 ternary and 2 binary solutions. The composition of the model systems is presented in Table 1.

Table 1. The composition of the model systems

System	number of ions/molecules				Concentration, mol/kg		Ratio Li:Cs
	<i>Li</i> ⁺	<i>Cs</i> ⁺	<i>Cl</i> ⁻	<i>H</i> ₂ <i>O</i>	LiCl	CsCl	
Ternary	100	300	400	900	6.2	18.5	1:3
	300	100	400	900	18.5	6.2	3:1
	200	200	400	900	12.3	12.3	2:2
	80	320	400	900	4.9	19.7	1:4
	320	80	400	900	19.7	4.9	4:1
	312	88	400	900	19.2	5.4	3.5:1
Binary	400	0	400	900	24.7	0	-
	0	400	400	900	0	24.7	-

The MDynaMix v.5.0 package was used for modeling [2]. All systems were simulated in the isothermal-isobaric ensemble (temperature - 25°C, pressure - 1 atm.) in a cubic cell with periodic boundary conditions. The SPC/E model of the water molecule was used [3]. To describe the model *Li*⁺, *Cs*⁺ and *Cl*⁻ ions, the potentials described in [4-6] were employed. The equations of motion were solved using Verlet method with a time step of 2 fs. The Coulomb interaction potentials were calculated using Ewald summation method. Constant temperature and pressure were maintained using Nose-Hoover algorithm. For each system the equilibration time was equal to 1 ns, following simulation time – 1 ns. For subsequent processing, the coordinates of all particles in the system were recorded every 20 fs.

Results

Based on the simulation data, the radial distribution functions between different components of the solution were calculated, the coordination numbers of ions, the average residence times of water molecules in the hydration shells of ions, as well as the self-diffusion coefficients of solution components and the times of H₂O molecules reorientation were

estimated. Special attention was paid to the effect of changing the ratio of cations on the peculiarities of the solution microstructure and components mobility in LiCl-CsCl-H₂O ternary system.

References

1. M. Turgeman, V. Wineman-Fisher, F. Malchik, A. Saha, G. Bergman, B. Gavriel, T.R. Penki, A. Nimkar, V. Baranauskaite, H. Aviv, M.D. Levi, M. Noked, D.T. Major, N. Shpigel, D. Aurbach - Cell Reports Physical Science 3, 100688 (2022).
2. P. Lyubartsev, A. Laaksonen. – Comp. Phys. Comm., 128, 565-589 (2000).
3. H.C.J. Berendsen, J.R. Grigera, T.P. Straastma – J. Phys. Chem., Vol.91, 6269, (1987).
4. L.X. Dang – J. Chem. Phys., v. 96, p. 6970, (1992).
5. L.X. Dang – CPL v. 227, pp. 211-214, (1994).
6. D.E. Smith, L.X. Dang – J. Chem. Phys., v. 100 (5), p. 3757, (1994).

ANATOLIA: NMR Software for Total Lineshape Analysis

Dmitry A. Cheshkov^{1,2}, Dmitry O. Sinitsyn³, Vyacheslav A. Chertkov⁴

¹*Lomonosov Institute of Fine Chemical Technologies, MIREA - Russian Technological University, 86 Vernadsky Ave., 119571 Moscow, Russia*

²*State Scientific Research Institute of Chemistry and Technology of Organoelement Compounds, 38 Shosse Entuziastov, 105118 Moscow, Russia*

³*Research Center of Neurology, 80 Volokolamskoye Shosse, 125367 Moscow, Russia*

⁴*Department of Chemistry, Moscow State University, Moscow 119991, Russia*

E-mail: dcheshkov@gmail.com

https://github.com/dcheshkov/ANATOLIA/

Introduction

“Yet another spectrum iterator... That’s it.” but it’s fast, robust, user friendly* free open source software, available for public downloading for Linux, Windows, Mac OS, FreeBSD.

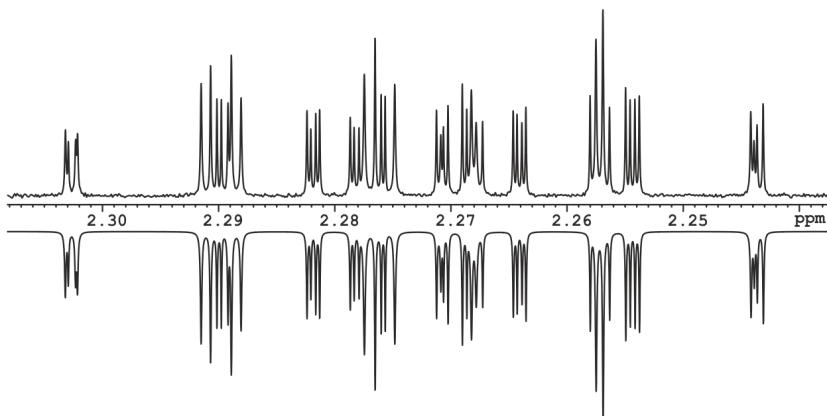
Software Description

ANATOLIA [1, 2] is a software for total lineshape analysis of fine multiplet structure of one-dimensional NMR spectra of spin- $\frac{1}{2}$ systems. It is capable of analyzing non-first order spectra with strongly coupled spins, since it is based on quantum mechanical formalism for spin systems. For local minima elimination a sequence of decreasing additional Lorentz broadenings is applied, as it has been implemented in VALISA [3] and thoroughly studied in [4]. To optimize the parameters of the spin system, the highly computationally efficient Powell algorithm BOBYQA [5] is used for multidimensional nonlinear optimization.

As input ANATOLIA requires an experimental spectrum (currently Bruker TopSpin NMR dataset format supported only) with defined regions containing multiplets for total lineshape fitting, text file (Input_Data.txt) describing the spin system and optimization control parameters, and also a separate text file with parameter values, containing the initial/resulting values of the spin system parameters, i.e. resonant frequencies and scalar spin-spin coupling constants. The structure of the spin system description section allows us to equate the values of resonance frequencies between chemically equivalent spins and equate the values of coupling constants in accordance with the magnetic equivalence and/or symmetry of the spin system. Detailed user manual is given in [1], some practical applications of ANATOLIA can be found in [6, 7]. A typical result of fitting of ^1H NMR spectrum is presented in the figure below.

Experimental (top) and theoretical (bottom) spectra of H-3t multiplet of α -tetrahydrofuroic acid (600 MHz, 0.5M methanole- d_4 solution, 303K).

*According to the authors of [6].



Acknowledgements

This work is supported by the Lomonosov Institute of Fine Chemical Technologies, MIREA - Russian Technological University.

References

1. Cheshkov D.A., Sheberstov K.F., Sinitsyn D.O., Chertkov V.A. ANATOLIA: NMR software for spectral analysis of total lineshape. *Magn.Reson.Chem.*, 2018, 56, 449-457. DOI: 10.1002/mrc.4689.
2. <https://github.com/dcheshkov/ANATOLIA/>; <http://anatolia.nmrclub.ru/>
3. Zubkov S.V., Golotvin S.S., Chertkov V.A. VALISA: a new procedure for total lineshape analysis of NMR spectra. Conformational analysis of trans-1,2-dibromocyclopentane. *Russ. Chem. Bull.*, 2002, 51(7), 1222-1230. DOI: 10.1023/A:1020948412771.
4. Cheshkov D.A., Sinitsyn D.O., Sheberstov K.F., Chertkov V.A. Total lineshape analysis of high-resolution NMR spectra powered by simulated annealing. *J. Magn. Reson.*, 2016, 272, 10-19. DOI: 0.1016/j.jmr.2016.08.012.
5. Powell M.J.D. The BOBYQA algorithm for bound constrained optimization without derivatives. Technical report, Department of Applied Mathematics and Theoretical Physics University of Cambridge, 2009.
6. Edgar M., Zeinali F., Mojally M., Hughes C., Riaz S., Weaver G.W. NMR spectral analysis of second-order ^{19}F - ^{19}F , ^{19}F - ^1H and ^{13}C - ^{19}F coupling constants in pentafluorobenzene and tetrafluoro-4-(morpholino)pyridine using ANATOLIA. *J. Fluor. Chem.*, 2019, 224, 35-44. DOI: 10.1016/j.jfluchem.2019.04.018.
7. Cheshkov D.A., Sinitsyn D.O. Total line shape analysis of high-resolution NMR spectra. *Ann.Rep. NMR Spectrosc.*, 2020, 100, 61-96. DOI: 10.1016/bs.annmr.2019.11.001.

^1H and ^{13}C NMR spectra of bioactive glassy polymorphic N-heterobiphenylene acetate binuclear complexes of Zn^{2+} and Cd^{2+}

*Viktor N. Demidov*¹, *Alexandra G. Ivanova*¹, *Alexandr A. Matveev*¹, *Tatiana B. Pakhomova*²,

*Irina B. Glebova*¹, *Anna Yu. Mylnikova*¹, *Sofia V. Paston*³, *Evgenya V. Bogomolova*⁴

¹Laboratory of Inorganic Synthesis, I.V. Grebenshchikov Institute of Silicate Chemistry of the Russian Academy of Sciences, Makarov Emb., 2, 199034, Saint Petersburg, Russia

²Department of Inorganic Chemistry, St. Petersburg State Technological Institute (Technical University), Moskovsky pr., 24-26/49 lit. A, 190013, Saint Petersburg, Russia

³Department of Molecular Biophysics and Polymer Physics, St. Petersburg State University, Ulyanovskaya Str., 1, 198504, Peterhof, Russia

⁴Laboratory of Systematics and Geography of Fungi, V.L. Komarov Botanical Institute of the Russian Academy of Sciences, prof. Popova Str., 2, 197376, Saint Petersburg, Russia

E-mail: vndemidov@mail.ru

Introduction

Zn^{2+} and Cd^{2+} ions are bioactive, moreover, Zn^{2+} ions are biogenic agents [1], and Cd^{2+} ions are toxic and carcinogenic [2]. 1,10-Phenanthroline mononuclear Zn^{2+} coordination compounds are actively being investigated as potential antibacterial, antifungal and antitumor agents [3]. In recent decades, due to the growing resistance of bacteria, fungi and tumors to the action of antibiotics and traditional drugs based on purely organic substances, interest in metal-medicinal agents has increased [4-6]. Among such agents, mononuclear complexes of d-elements with 1,10-phenanthroline derivatives, as well as 1,10-phenanthroline binuclear bridge structures, occupy an important place [4]. Cd^{2+} complexes inhibiting the growth of tumor cells *in vitro* and *in vivo* are of interest as active potential drugs in antitumor therapy [3], including neutron capture therapy.

We systematically investigate compounds of a new apo-1,10-phenanthrocyanine class: metallo-N-heterobiphenylenes – glassy polymorphic *electron-rich* binuclear 1,10-phenanthrocyanines (bi-1,10-phenanthrolylenes) $\text{L}_n(\text{phen})_m\text{M}(\mu\text{-N-biphen})\text{M}(\text{phen})_m\text{L}_n(\text{OAc})_n$ of d-elements (M) Zn^{2+} ($[\text{Ar}]3\text{d}^{10}$), Cd^{2+} ($[\text{Kr}]4\text{d}^{10}$), Co^{2+} ($[\text{Ar}]3\text{d}^7$), Mn^{2+} ($[\text{Ar}]3\text{d}^5$), Ni^{2+} ($[\text{Ar}]3\text{d}^8$), Cr^{3+} ($[\text{Ar}]3\text{d}^3$) (phen = 1,10-phenanthroline, L – secondary amine ligands, OAc^- - acetate groups) [7-9]. In their structure, they contain bridging chromophores – pharmacophore ligands of $\mu\text{-N-biphen}$, which are characterized by the presence of temperature-accessible lowest electronic biradical triplet states T_{low} . [10, 11]. We found that 1,10-phenanthrocyanines of Zn^{2+} , Cd^{2+} , Co^{2+} and Mn^{2+} exhibit biocidal properties. They inhibit some micromycete fungi and have an effective biostatic effect as antifouling agents of metal surfaces in river water. 1,10-Phenanthrocyanines of Zn^{2+} also exhibit cytostatic properties. In this work, NMR spectroscopy methods were used to identify the structure of the binuclear acetate compounds of Zn^{2+} and Cd^{2+} of the new 1,10-phenanthrocyanine class, in comparison with their mononuclear 1,10-phenanthroline precursors. 1,10-Phenanthrocyanines of Zn^{2+} also exhibit cytostatic properties. In this work, NMR spectroscopy methods were used to identify the structure of the binuclear acetate compounds of Zn^{2+} and Cd^{2+} of the new 1,10-phenanthrocyanine class, in comparison with their mononuclear 1,10-phenanthroline precursors.

Synthesis of Zn^{2+} and Cd^{2+} binuclear N-heterobiphenylene complexes

The production of glassy nanoscale polymorphic binuclear chromophore 1,10-phenanthrocyanines Zn^{2+} and Cd^{2+} with pharmacophore bridging ligands **(phen) n M(μ -N-biphen)M(phen) n (OAc) $_4$ ($n = 0-2$)** was carried out using the original methodology of metal-assisted non-dehydrogenative $C(sp^2)H$ coupling coordinated 1,10-phenanthroline in acetate complexes of d-elements [7-9]. The synthesis of binuclear chromophore 1,10-phenanthrocyanines Zn^{2+} and Cd^{2+} was carried out in melts at a temperature of 200-205 °C, heating the corresponding simple mononuclear 1,10-phenanthroline precursors for 25-30 minutes. As a result of the $C(sp^2)H$ coupling of coordinated 1,10-phenanthroline, after cooling the black-purple melts, the compounds were obtained in a glassy state. 1,10-Phenanthrocyanines are highly soluble in chloroform, DMFA and DMSO at room temperature with the formation of intensely colored purple-violet solutions. The composition of the compounds, according to the data of the elemental analysis, corresponds to the formulas given (Fig. 1, **1-3**, **a** $M = Zn^{2+}$, **b** $M = Cd^{2+}$). IR spectra of substances (in tablets with KBr, 2000-400 cm^{-1}) confirm the coordination of 1,10-phenanthroline to Zn^{2+} and Cd^{2+} ions, respectively.

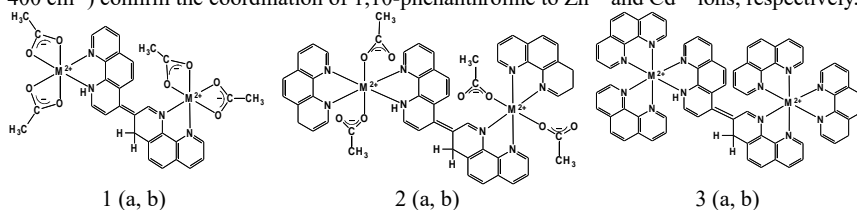


Figure 1. Coordination environment of 1,10-phenanthrocyanine of Zn^{2+} and Cd^{2+} **1-3** (a, b).

NMR spectroscopy of Zn^{2+} and Cd^{2+} binuclear N-heterobiphenylene complexes

The 1H and ^{13}C NMR spectra of solutions in deuterated organic solvent DMSO- d_6 and D_2O of binuclear 1,10-phenanthrocyanines (bi-1,10-phenanthrolylenes) of Zn^{2+} and Cd^{2+} **(phen) $_n$ M(μ -biphen)M(phen) $_n$ (OAc) $_4$ ($n = 0-2$, 1-3 a, b)** with pharmacophore bridging ligands (Fig. 3) in comparison with mononuclear 1,10-phenanthroline precursors **M(phen) $_n$ (OAc) $_2 \cdot 2H_2O$ ($M = Zn^{2+}$ и Cd^{2+} , $n = 1-3$).**

Measurements of the NMR spectra of Zn^{2+} and Cd^{2+} complexes were carried out on an NMR spectrometer Bruker 500 MHz Avance III at the Magnetic Resonance Research Methods Resource Center of the St. Petersburg Science Park of St. Petersburg State University.

Results and Discussion

The 1H and ^{13}C NMR spectra of glassy binuclear 1,10-phenanthrocyanines (bi-1,10-phenanthrolylenes or N-heterophenylenes) of Zn^{2+} **2**, **3** and Cd^{2+} **2a**, **3a** show signal sets of a significantly more complex structure than mononuclear acetate 1,10-phenanthroline precursors corresponding to both 1,10-phenanthroline ligands and bridged 1,10-phenanthrocyanines (bi-1,10-phenanthrolylenes). The latter contain *dihydro*-bi-1,10-phenanthroline fragments, which appear in the 1H NMR spectra in the range 5.0-7.5 ppm. The detection of signals belonging to the bridge chromophores of **μ -biphen** was performed on the basis of NMR spectra of Zn^{2+} and Cd^{2+} **1a** and **1b** compounds that do not contain pure 1,10-phenanthroline ligands.

Conclusions

The study of ^1H and ^{13}C NMR spectra of glassy binuclear 1,10-phenanthrocyanines (bi-1,10-phenanthrolylenes or N-heterophenylenes) of Zn^{2+} and Cd^{2+} in DMSO-d_6 solutions shows that, compared with their simple mononuclear precursors, binuclear chromophore complexes contain bridging ligands of a significantly more complex nature than 1,10-phenanthroline. These are *electron-rich* pharmacophore 1,10-phenanthrocyanine C–C-dimers. These bridging ligands modify the biocidal action of mononuclear 1,10-phenanthroline precursors. The studied binuclear compounds can be used as modulators of microbial activity, in particular, as «soft» biostatic antifouling agents.

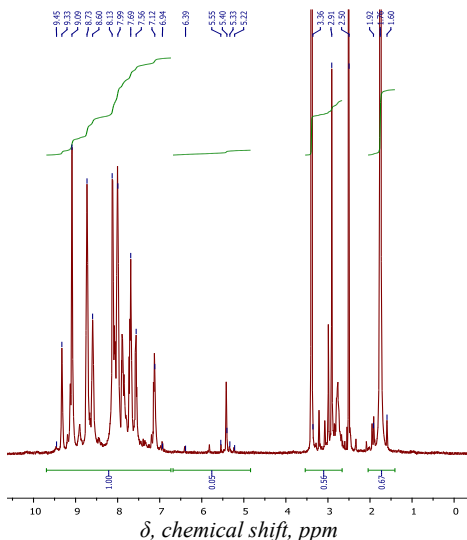


Figure 2. ^1H NMR spectrum of Cd^{2+} complex **1b** in DMSO-d_6

Funding

The work was carried out at the ISC RAS within the framework of the theme of the state budget: “Phys.-chem. bases of inorg. synthesis of micro- and nanostruct. non-organic, organo-non-organic and ceramic materials and coatings for bio-, energy- and resource-saving technol.” (1023033000122-7-1.4.3); as well as by V.L. Komarov Botanical Institute of the Russian Academy of Sciences, state budget theme: 125013100892-3, “Biodiversity, ecology and struct. and funct. features of fungi and fungi-like protistes”.

Acknowledgements

The authors thank Prof. Doct. of Biol. Scie. V.V. Sharoiiko (Lab. of Biomed. Chem., Institute of Chemistry, St. Petersburg St. University, Universitetsky pr., 26, 198504, Peterhof, and Department of General and Bioorganic Chemistry, Pavlov First Saint Petersburg State Medical University, L’va Tolstogo str., 6–8, 197022, Saint Petersburg, Russia) for the study of cytotoxicity activity of Zn(II) complexes.

References

1. N. P. Bitytskiy. Trace elements of higher plants. – St. Petersburg Univ., St. Petersburg, 2020.
2. B. L'Azou, I. Passagne, S. Mounicou, and al. – *Tox. Res.*, 3 (1), 32-41 (2014).
3. I. S. Golubeva, A. E. Barmashov, A. A. Rudakova, and al. – *Ross. Bioterap. J.*, 16 (3), 75-78 (2017).
4. L. Viganor, O. Howe, P. McCarron, and al. – *Curr. Top. in Med. Chem.*, 17 (11), 1280-1302 (2017).
5. I. S. Sousa, T. D. P. Vieira, R. F. S. Menna-Barreto, and al. – *J. Fungi*, 9, 356, 22 p. (2023).
6. M. O'Shaughnessy, J. Hurley, S. C. Dillon, and al. – *J. Biol. Inorg. Chem.*, 28, 153-171 (2023).
7. V. N. Demidov, V. G. Puzenko, A. I. Savinova, and al. – *News MIFCT*, 2 (3), 36-43 (2007).
8. V. N. Demidov. – *Doct. Diss.*, St.-Petersburg Techn. Inst. (Tech. Univ.), St.-Petersburg (2010).
9. V. N. Demidov, S. A. Simanova, A. I. Savinova, at al. – *Russ. J. Gen. Chem.*, 79 (12), 2807-2814 (2009).
10. V. N. Demidov, S. M. Sykharzhevskiy, S. V. Paston, at al. – *News St.-Petersburg Univ. Phys., Chem.*, 4 (62) (2) 138-145 (2017).
11. V. N. Demidov, S. M. Sukharzhevsky, T. B. Pakhomova, at al. – *Appl. Magn. Reson.*, 54, 1015–1051 (2023).

Effect of the coordination centers and the solvents on the parameters of the ^1H and ^{13}C NMR spectra of Zn^{2+} and Cd^{2+} acetate mononuclear complexes with 1,10-phenanthroline

*Viktor N. Demidov*¹, *Alexandra G. Ivanova*¹, *Irina N. Tsvetkova*¹, *Evgeny M. Kosobuko*¹,
*Evgenya V. Bogomolova*², *Sofia V. Paston*³, *Vadim I. Voschikov*¹, *Yaroslav A. Khamidulin*¹,
*Larisa N. Efimova*¹, *Tatiana B. Pakhomova*⁴

¹Laboratory of Inorganic Synthesis, I.V. Grebenshchikov Institute of Silicate Chemistry of the Russian Academy of Sciences, Makarov Emb., 2, 199034, Saint Petersburg, Russia

²Laboratory of Systematics and Geography of Fungi, V.L. Komarov Botanical Institute of the Russian Academy of Sciences, prof. Popova Str., 2, 197376, Saint Petersburg, Russia

³Department of Molecular Biophysics and Polymer Physics, St. Petersburg State University, Ulyanovskaya Str., 1, 198504, Peterhof, Russia

⁴Department of Inorganic Chemistry, St. Petersburg State Technological Institute (Technical University), Moskovsky pr., 24-26/49 lit. A, 190013, Saint Petersburg, Russia
E-mail: vndemidov@mail.ru

Introduction

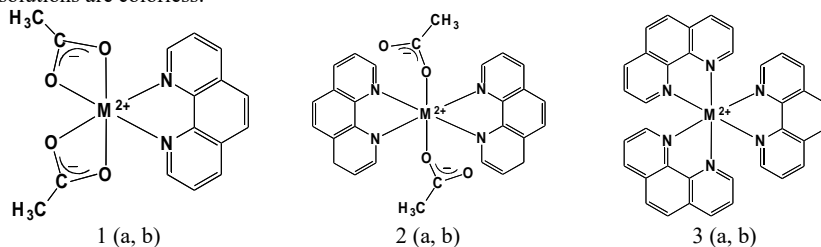
Mononuclear coordination compounds of Zn^{2+} with 1,10-phenanthrolines have recently been investigated as potential antibacterial, antifungal and antitumor agents [1]. Interest in metallo-medicinal agents is increasing due to the growing resistance of bacteria, fungi and tumors to the action of antibiotics and traditional drugs [2-4]. Mononuclear complexes of d-elements with 1,10-phenanthroline derivatives occupy an important place among such agents [2]. Cd^{2+} complexes inhibiting the growth of tumor cells are of interest as active potential drugs in antitumor therapy [1].

Acetate 1,10-phenanthroline complexes are the precursors of the compounds of the new apo-1,10-phenanthrocyanine class systematically studied by us: metallo-N-heterobiphenylenes – glassy electron-rich binuclear 1,10-phenanthrocyanines (bi-1,10-phenanthrolylenes) $\text{L}_n(\text{phen})_m\text{M}(\mu\text{-N-biphen})\text{M}(\text{phen})_m\text{L}_n(\text{OAc})_l$ of d-elements (M) Zn^{2+} ($[\text{Ar}]3\text{d}^{10}$), Cd^{2+} ($[\text{Kr}]4\text{d}^{10}$), Co^{2+} ($[\text{Ar}]3\text{d}^7$), Mn^{2+} ($[\text{Ar}]3\text{d}^5$), Ni^{2+} ($[\text{Ar}]3\text{d}^8$), Cr^{3+} ($[\text{Ar}]3\text{d}^3$) (phen = 1,10-phenanthroline, L – secondary amine ligands, OAc – acetate groups) [5-7]. In their structure, compounds of the new class contain bridging chromophores – pharmacophore ligands of $\mu\text{-N-biphen}$, which are characterized by the presence of temperature-accessible lowest electronic biradical triplet states T_{low} . [8, 9]. We have established that mononuclear 1,10-phenanthroline acetates of Zn^{2+} , Cd^{2+} , Co^{2+} and Mn^{2+} exhibit strong biocidal properties. They effectively inhibit some micromycete fungi. In this work, the NMR spectra of ^1H and ^{13}C mononuclear 1,10-phenanthroline acetate compounds of Zn^{2+} and Cd^{2+} were studied in order to use the data obtained to analyze similar spectra of binuclear complexes of a new class – N-heterobiphenylenes.

Synthesis of Zn^{2+} and Cd^{2+} mononuclear 1,10-phenanthroline acetate complexes

The synthesis of mononuclear 1,10-phenanthroline precursors of Zn^{2+} and Cd^{2+} $\text{M}(\text{phen})_n(\text{OAc})_2 \cdot 2\text{H}_2\text{O}$ ($\text{M} = \text{Zn}^{2+}$ and Cd^{2+} , $n = 1-3$) was carried out by complexation of $\text{M}(\text{OAc})_2 \cdot 4\text{H}_2\text{O}$ acetates with 1,10-phenanthroline monohydrate in aqueous solutions $n = 1$ at a temperature of 90-95 ° C, or in melts $n = 2, 3$ at a temperature of 110-115 ° C, heating mixtures of starting substances for about 1 hour in stoichiometric ratios. According to the data of the elemental analysis, the composition of the compounds corresponds to the formulas given (Fig. 1, **1-3**, **a** $\text{M} = \text{Zn}^{2+}$, **b** $\text{M} = \text{Cd}^{2+}$). The IR spectra of substances (in tablets with

KBr, 2000–400 cm^{-1}) indicate the coordination of 1,10-phenanthroline to Zn^{2+} and Cd^{2+} ions, respectively. The compounds are highly soluble in water at room temperature. The resulting solutions are colorless.



1 (a, b)
2 (a, b)
3 (a, b)
Figure 1. Coordination environment of 1,10-phenanthroline complexes of Zn^{2+} and Cd^{2+} 1-3 (a, b).

NMR spectroscopy of Zn^{2+} and Cd^{2+} mononuclear 1,10-phenanthroline acetate complexes

The ^1H and ^{13}C NMR spectra of solutions in D_2O and deuterated organic solvent DMSO-d_6 of mononuclear Zn^{2+} and Cd^{2+} 1,10-phenanthroline precursors: $\text{M}(\text{phen})_n(\text{OAc})_2 \cdot 2\text{H}_2\text{O}$ ($\text{M} = \text{Zn}^{2+}$ и Cd^{2+} , $n = 1-3$, 1-3 a, b) (Fig. 3) of binuclear 1,10-phenanthrolyanines (bi-1,10-phenanthrolylenes) $(\text{phen})_n\text{M}(\mu\text{-biphen})\text{M}(\text{phen})_n(\text{OAc})_4$ ($n = 0-2$) with pharmacophore bridging ligands were studied.

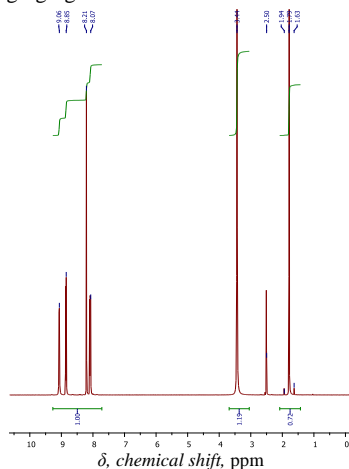


Figure 2. ^1H NMR spectrum of Zn^{2+} complex **3a** in DMSO-d_6

Measurements of the NMR spectra of Zn^{2+} and Cd^{2+} complexes were carried out on an NMR spectrometer Bruker 500 MHz Avance III at the Magnetic Resonance Research Methods Resource Center of the St. Petersburg Science Park of St. Petersburg State University.

Results and Discussion

The ^1H and ^{13}C NMR spectra of simple mononuclear 1,10-phenanthroline acetates of Zn^{2+} **1-3** and Cd^{2+} **1a-3b** in D_2O and DMSO-d_6 contain a set of signals characteristic of

coordinated 1,10-phenanthroline. The coordination of 1,10-phenanthroline to Zn^{2+} and Cd^{2+} ions has almost no effect on the chemical shifts of the signals of hydrogen atoms in the heteroaromatic region. While the nature of the solvent significantly affects them. And during the transition from D_2O to $DMSO-d_6$, the proton signals of the heteroaromatic ring shift to a weak field. The largest shifts in proton signals were detected for the binary solvent D_2O – $DMSO-d_6$ (1:1).

Conclusions

The study of NMR spectra of 1H and ^{13}C acetate mononuclear 1,10-phenanthroline complexes in D_2O solution and $DMSO-d_6$ solution shows that 1,10-phenanthroline acts in all cases as a bidentate chelating ligand.

As our biological studies show, these mononuclear 1,10-phenanthroline compounds can be used as strong inhibitors of the activity of microorganisms (fungi) and highly organized creatures, in particular, as «hard» fungicides and biocidal antifouling agents.

Funding

The work was carried out at the ISC RAS within the framework of the theme of the state budget: “Phys.-chem. bases of inorg. synthesis of micro- and nanostruct. non-organic, organo-non-organic and ceramic materials and coatings for bio-, energy- and resource-saving technol.” (1023033000122-7-1.4.3); as well as by V.L. Komarov Botanical Institute of the Russian Academy of Sciences, state budget theme: 125013100892-3, “Biodiversity, ecology and struct. and funct. features of fungi and fungi-like protists”.

Acknowledgements

The authors thank Prof. *Doct. of Biol. Scie. V.V. Sharoiko (Lab. of Biomed. Chem., Institute of Chemistry, St. Petersburg St. University, Universitetsky pr., 26, 198504, Peterhof, and Department of General and Bioorganic Chemistry, Pavlov First Saint Petersburg State Medical University, L'va Tolstogo str., 6–8, 197022, Saint Petersburg, Russia)* for the study of cytotoxicity activity of $Zn(II)$ complexes.

References

1. I. S. Golubeva, A. E. Barmashov, A. A. Rudakova, and al. – *Ross. Bioterap. J.*, **16** (3), 75–78 (2017).
2. L. Viganor, O. Howe, P. McCarron, and al. – *Curr. Top. in Med. Chem.*, **17** (11), 1280–1302 (2017).
3. I. S. Sousa, T. D. P. Vieira, R. F. S. Menna-Barreto, and al. – *J. Fungi*, **9**, 356, 22 p. (2023).
4. M. O'Shaughnessy, J. Hurley, S. C. Dillon, and al. – *J. Biol. Inorg. Chem.*, **28**, 153–171 (2023).
5. V. N. Demidov, V. G. Puzenko, A. I. Savinova, and al. – *News MIFCT*, **2** (3), 36–43 (2007).
6. V. N. Demidov. – *Doct. Diss., St.-Petersburg Techn. Inst. (Tech. Univ.), St.-Petersburg* (2010).
7. V. N. Demidov, S. A. Simanova, A. I. Savinova, at al. – *Russ. J. Gen. Chem.*, **79** (12), 2807–2814 (2009).
8. V. N. Demidov, S. M. Sykharzhevskiy, S. V. Paston, at al. – *News St.-Petersburg Univ. Phys., Chem.*, **4** (62) (2) 138–145 (2017).
9. V. N. Demidov, S. M. Sukharzhevsky, T. B. Pakhomova, at al. – *Appl. Magn. Reson.*, **54**, 1015–1051 (2023).

Preparation and characterization of pervaporation membranes based on sodium alginate modified by Zn(BIM)

Maria E. Dmitrenko¹, Anna I. Kuzminova¹, Roman R. Dubovenko¹, Alexandra M. Korovina¹, Anton S. Mazur¹, Konstantin N. Semenov¹, Tatiana V. Plisko¹, Anastasia V. Penkova¹
¹Saint Petersburg State University, Saint-Petersburg, Russia
E-mail: m.dmitrienko@spbu.ru
<https://go.spbu.ru/rgpenkova>

Introduction

Pervaporation attracts much attention as a promising method for separation, concentration and purification of low molecular weight substances. However, the rapid development of this process requires novel mixed matrix materials and effective supported (composite) membranes based on them. However, before the creation of a supported (composite) membrane, it is necessary to study the effect of the introduced modifier on the structure and morphology of polymeric material, which will significantly change the membrane physicochemical and transport properties. This can be easily done by spectroscopic methods.

Results

In the present work, novel mixed matrix pervaporation membranes based on sodium alginate (SA) modified with Zn-based metal-organic framework (Zn(BIM)) were prepared for the enhanced pervaporation dehydration. The structural changes of the developed membranes were studied by spectroscopic methods. The interaction between Zn(BIM) and SA was confirmed by nuclear magnetic resonance (NMR) method. The additional characterization of the samples was carried out by scanning electron and atomic force microscopies, thermogravimetric analysis, and swelling experiments. Transport properties of membranes were tested in pervaporation dehydration of isopropanol.

Acknowledgements

The authors acknowledge Saint-Petersburg State University for a research project 11602266. The experimental work was facilitated by the equipment from the Resource Centers for Nanotechnology, Magnetic Resonance, Cryogenic Department, Thermogravimetric and Calorimetric Research Centre, Centre for Physical Methods of Surface Investigation, Centre for Innovative Technologies of Composite Nanomaterials, Computing Centre, Chemical Analysis and Materials Research Centre, and Centre “Nanofabrication of Photoactive Materials (Nanophotonics)” at the St. Petersburg State University.

Low-field bench-top NMR study of magnetic cellulose microspheres for spiking of circulating tumor cells

*Anastasia S. Dmitrieva*¹, *Boris P. Nikolaev*^{2,3}, *Ludmila Yu. Yakovleva*², *Viacheslav S. Fedorov*^{2,4}, *Maxim Shevtsov*^{2,4}

¹*Saint-Petersburg State Institute of Technology, St. Petersburg, Russian Federation*

²*Institute of Cytology of the Russian Academy of Sciences (RAS), St. Petersburg, Russian Federation*

³*Saint-Petersburg Technopark, Engineering Centre API, Saint-Petersburg, Russian Federation*

⁴*Personalized Medicine Centre, Almazov National Medical Research Centre, Akkuratova Str. 2, 197341 Saint Petersburg, Russia*

E-mail: dmitriyeva03@bk.ru

Introduction

Circulating tumor cells (CTCs) have received significant attention as emerging biomarkers for cancer progression and evaluation of the efficacy of therapeutic interventions. Therefore, the development of novel methods for highly efficient spiking of CTCs from the patients biological samples is of high importance. In the current study, the properties of magnetic cellulose microspheres are being investigated as a matrix for conjugation with 14-mer peptide (TKDNNLLGRFELSG) being developed for detection of malignant cells that overexpress the plasma membrane-associated heat shock protein (mHsp70). Targeted cellulose microcarriers are particularly designed to spike the mHsp70-positive CTCs with subsequent separation by magnetic field.

Results and discussion

Cellulose microbeads with high ratio of porous surface/volume were formed by emulsification and condensation of cellulose solution in oil in correspondence with special technology procedure. Particles structure is represented by tortuous network of large and very tiny pores. Large pores (\varnothing 100 – 1000 nm) ensure light water capillary saturation in solution. Gel-like thin-porous structure of beads provides intense exchange of external solvent with adsorbed water in cellulose body. The prepared biocompatible cellulose porous microspheres are magnetized by inclusion of superparamagnetic iron oxide nanoparticles (SPIONs) in pores through the reaction of iron oxide co-precipitation from impregnated salt solution Fe(+2), Fe(+3).



Figure 1. Light microscope view of microspherical cellulose nonmagnetic particles (a) and loaded by SPIONs (b), magnification x40.

A large darkening area in the microphotoimage (b) indicates the possible aggregation of iron oxide nanoparticles in macroscopic magnetic structures of a ferrimagnetic nature.

The superparamagnetic nature was confirmed by nonlinear magnetic response and MRI study.

^1H NMR spectra were recorded and proton relaxation times were measured on a Spinsolve 60 spectrometer (Magritek) created on the base of Halbach magnet system with magnetic field of 1.4 T. The probes of aqueous cellulose microbead suspension (\varnothing 500-800 μm) were placed in a standard ampoule with a diameter of 5 mm. The spectra were recorded at room temperature, without rotating the sample. TMS was used as a standard for measuring the chemical shift. When recording the spectra, the one pulse program was used, the number of accumulations was 2 – 1000, the delay time between pulses varied in the range of 2 – 5 s. Relaxation times T1, T2 were measured using by inversion recovery and Carr-Purcell – Meiboom – Gill pulse sequence.

NMR signal distorted by the presence of inhomogeneities in the static magnetic field was investigated. NMR signal from magnetic suspension was detected during the sedimentation of magnetic beads in magnet hole. The data were obtained by periodic scanning in time interval of 4 s. The magnet was shimmed before measurement adjusting 2H optimal resonance of deuterowater. Chemical shift and line form change were observed during the process of sedimentation what cause the continual change in magnetic susceptibility distribution Figure 2.

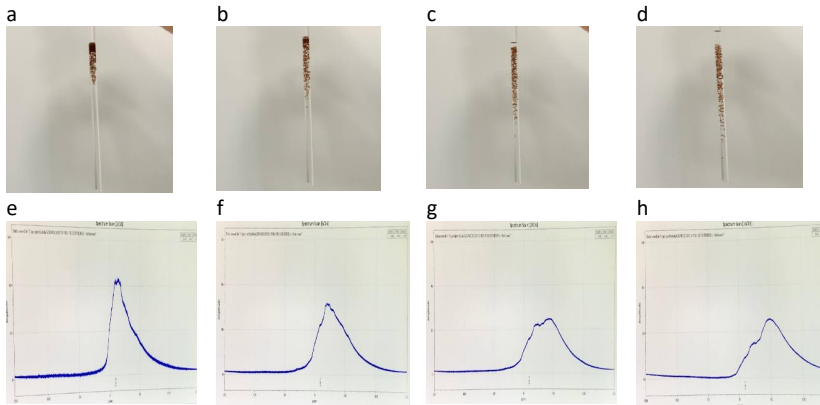


Figure 2. Process of magnetic cellulose deposition (a – d), dynamic changes of NMR spectrum from magnetic suspension during its deposition (e – h), a,e corresponds to 2 s, b,f – 6 c, c,g – 10 s, d,h – 14 s after the start of deposition.

Change of chemical shift of external and internal solvent in spheroid magnetic suspension is described by relations [1]

$$\begin{aligned}\delta v_{in} &= -(1 - \sigma)(N_2 - N_1)\Delta\chi v_0 \\ \delta v_{out} &= \sigma\Delta\chi(N_2 - N_1)v_0\end{aligned}$$

where δv_{in} , δv_{out} – the difference of resonance frequency relative standard, $\Delta\chi$ – difference of magnetic susceptibility, σ – volume fraction of spheroids, N_1 , N_2 – magnetization factors.

The varying magnetic susceptibility of the magnetic suspension in-cylinder ampule (5 mm) affect the NMR signal in correspondence with theoretical predictions [1]. NMR spectrum of final dense deposited magnetic layer have large line width about 20 kHz. The general line view is shown in Figure 3.

The large microbead magnetization was confirmed by high rates of water proton relaxation. The shortage of transverse relaxation times T2, T2* indicates the large magnetic

field distortion created by magnetic bead clusters. This effect is increased by high magnetic moment of beads and static spin-dephasing mechanism of relaxation in environment of magnetic clusters inside microbeads. For external water protons the magnetic cellulose particles can be considered as separate magnetic dipoles which induce nonhomogeneous static magnetic field that leads to broadening of resonance line. The measured short time T_2^* (0,1 ms) arises from formation of magnetite particles in small pores, retainment of water molecules in gel environment of magnetic iron oxide and nonrestricted water exchange in pores. Due to effective transverse relaxation magnetic cellulose microspheres significantly enhance the contrast of MR images of gel phantoms and may serve as negative contrast agent [2].

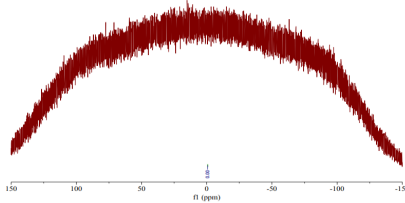


Figure 3. NMR spectrum of densely deposited microspherical magnetic cellulose.

For randomly packed spherical beads, the local internal magnetic field gradient scales with the pore size. The visual picture of sedimentation of microbeads in NMR sample in the absence of constant magnetic field is presented in Figure 2. Nonmagnetic cellulose microbeads generate another NMR response after placing into receiver cell.

The signal from “external” (free) water had a chemical shift of 5.51 ppm (3 Hz), wide line of “internal” strongly bound water was not observed in low field opposite the early results in field 7.1 T. The signal of strongly bound water molecules broadens so much that it becomes unobservable.

Conclusion

Magnetic cellulose microbeads provide shortage of transverse relaxation times T_2 , T_2^* of water protons due to specific particle structure, high content of magnetic nanoclusters of magnetite, static-dephasing regime relaxation and intense molecular interchange in perturbed magnetic field induced by iron oxide. NMR analysis of magnetic cellulose microbeads in low field depends on the instant space configuration of spheroids in cylinder cell detector.

Acknowledgments

This work was supported by Saint-Petersburg Technopark Fund. Authors are grateful for helpful advices and efforts of I. Voevodiva, N.Skvortzov, M.Pokrovsky, Y.Marchenko.

Funding: *This work was financially supported by the Ministry of Science and Higher Education of the Russian Federation (Agreement No. 075-15-2022-301).*

References

1. I.Yu. Marchenko, B.P. Nikolaev, Magnetic heterogeneity of porous materials and its manifestation in NMR spectra / Proceedings of SPbGETU "LETI", 2019, No.1B, pp. 35-40.
2. A. Kosogornova, B. Nikolaev, L. Yakovleva, V. Fedorov, A. Mazur, M. Shevtsov Synthesis and NMR relaxometry studies of self-assembling nanoclusters of SPIONs conjugated with bioactive ligands, St.Petersburg State University, 19 Int.School-Conference “Magn.Res. and its applications, Proceedings,2022,p.102-104.

Structure and physicochemical properties of carboxymethyl cellulose/Zn-based MOF membrane

Roman Dubovenko, Mariia Dmitrenko, Anna Kuzminova, Anna Mikulan, Margarita

Puzikova, Artem Selyutin, Anton Mazur, Anastasia Penkova

Institute of Chemistry, St. Petersburg State University, St. Petersburg, Russia

E-mail: r.dubovenko@spbu.ru

<https://go.spbu.ru/rgpenkova>

Introduction

Membrane reactors have garnered significant attention in various industrial processes due to their numerous advantages. These reactors offer enhanced reaction efficiency and selectivity by continuously removing reaction products, leading to improved conversion rates and minimizing unwanted side reactions. The compact design of these systems combines the reaction and separation processes into a single unit, simplifying the overall system and reducing the required equipment size. Additionally, membrane reactors operate under milder conditions, ensuring safety and enabling the use of sensitive catalysts.

In addition to these benefits, membrane reactors facilitate process intensification, resulting in shorter process times, higher throughput, and increased overall process efficiency. The versatility of these reactor systems makes them suitable for a wide range of industries, including petrochemicals, pharmaceuticals, chemical synthesis, and environmental applications. In this study, we created a promising membrane based on carboxymethyl cellulose modified with a metal-organic framework (ZnBIM) for carrying out a hybrid process of “pervaporation + esterification” for the production of ethyl acetate.

Results

The incorporation of a Zn(BIM) modifier, known for its porous structure, into the polymer matrix has resulted in an enhancement of transport performance. This improvement can be attributed to the alteration of the hydrophilic-hydrophobic characteristics of the membrane surface and an increase in the available free volume between polymer chains. To evaluate the developed composite membranes, comprehensive characterization techniques such as Fourier-transform infrared spectroscopy (FTIR), thermogravimetric analysis (TGA), nuclear magnetic resonance (NMR), scanning electron microscopy (SEM), atomic force microscopy (AFM), computational tools (quantum chemical calculations) were employed. The hydrophilic-hydrophobic properties of the membrane surface were assessed by measuring the water contact angles using the sessile drop method. Furthermore, the impact of the modifying additive on the transport properties of the membranes was investigated through a hybrid process of ethyl acetate synthesis involving esterification reaction and pervaporation, carried out at a temperature of 60°C.

Acknowledgements

This work is supported by the Russian Science Foundation (grant № 20-79-10064, <https://rscf.ru/project/20-79-10064/>). The experimental work was facilitated by the equipment from the Resource Centers for Nanotechnology, Magnetic Resonance, Cryogenic Department, Thermogravimetric and Calorimetric Research Centre, Centre for Physical Methods of Surface Investigation, Centre for Innovative Technologies of Composite Nanomaterials, Computing Centre, Chemical Analysis and Materials Research Centre, and Centre “Nanofabrication of Photoactive Materials (Nanophotonics)” at the St. Petersburg State University

Device for determining the characteristics of the magnetic field of a permanent magnet. Preliminary results.

*Pavel Shandybin¹, Anna Dyatlovich¹, Anna Hurshkainen¹, C. Cabal Mirabal^{1,2}
ITMO University, St. Petersburg, Russia¹
MRI Department Cuban Neuroscience Center²
a.a.dyatlovich@yandex.ru*

Introduction

Magnetic Resonance Imaging (MRI) have demonstrated it powerfully for the medical diagnostic and others transcendental research during decade [1]. However, its health impact has been restricted by access to MRI equipment. Fortunately, new imaging, electronic, signal and image processing technologies have allowed, in recent years, the development of mobile and low-cost equipment that expands access to MRI studies for those in need [1, 2]. Our work is located in the characterization of low field permanent magnet (0.069 T) with configuration C. The parameters to measure in our experimental conditions are:

1. The stability of the magnetic induction B_0 of the magnet over time and its dependence on the ambient temperature in the environment of the magnet.
2. Homogeneity in the region of interest (ROI) determining the zonal and tesseral spherical harmonics that determine the inhomogeneity and the possible concrete ways to compensate them.
3. The isomagnetic center of the ROI.
4. As is well known for MRI, the existence of orthogonal gradients (G_x , G_y , G_z) is essential. Our task is also to characterize the intensity and linearity of the G_s in the ROI, the isocenter of the three G_s . It is also possible to determine the effectiveness of the coils fed with direct current.

The work describes the mechanical coordinate system used for such characterizations and provides preliminary data obtained.

Requirements to mechanical coordinate system

When analyzing the homogeneity of the magnetic field, the inhomogeneities are decomposed into spherical harmonics [3]. They can be divided into 2 types i.e along Z, zonal harmonics and orthogonal around Z direction, tesseral harmonics. The geometry of the mechanical system should allow the simple measurement the intensity map and consequently the inhomogeneity in the ROI.

Additionally, mechanical system should be made of non-metallic materials to avoid affecting the magnetic field inside the magnet. Also, the system must be accurate and robust enough to ensure that the sensor is accurately positioned at the point. Finally, it must be handy to make quick measurements as they are made manually (since it would take a long time to develop an automated system).

The region of interest is a vertical cylinder with a height of ≤ 27 cm and a diameter of ≤ 12 cm. Its axis is located in the magnetic isocenter of the magnet, which in the best case should coincide with the geometric isocenter.

Mechanical coordinate system

For the characterization of the stationary and gradient magnetic fields a mechanical system was developed.

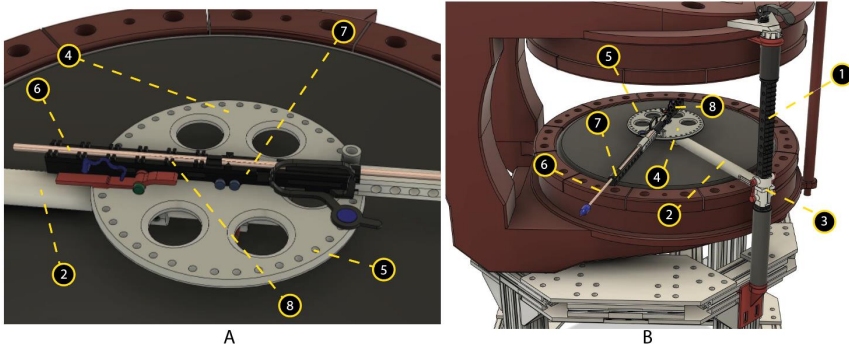


Figure 1. Mechanical coordinate system, A - general view, B - detailed disk image.

A cylindrical coordinate system with a vertical axis passing through the geometric isocentre of the magnet was chosen for magnetic field measurements. In order to place the sensor at the same location each time, a mechanical system with fixation devices has been developed (Figure 1). For height fixation, the vertical beam¹ holding the sensor is made with height holes at 1 cm increments. To maintain the strength, the holes are placed one by one on different sides. The sensor is placed in the centre of the magnet with a tube (2) running from the vertical beam (1) to the geometric isocentre. The beam and the tube are connected using a fixture (3) that allows the system to be positioned at a certain height. At the end of the tube (2) is placed a disk (4) with holes (5) in diameter to position the sensor by angle. The angle between the holes (5) is 9 degrees. The disk (4) is attached to the horizontal tube using a plastic nail printed on a 3D printer. Finally, the sensor (6) is directly inserted into a holder (7) fixed in the centre of the disk (4). To be able to measure in a cylindrical coordinate system with different radii, there are 2 cm spaced dividers (8) on the holder (7). This system allows measurements in cylindrical coordinate systems with radii from 2 to 12 cm.

Parts of the mechanical system were printed from acrylonitrile butadiene styrene (ABS) plastic using 3D printing. Thick water pipes were used for the supporting cylindrical structures.

Measurement results

To measure the magnetic field inside the magnet, a Three-Dimensional Gauss Meter DX-360 with a Hall sensor. Simultaneously, temperature measurements were made in the vicinity of the magnet. Using a positioning mechanical system, the sensor was fixed inside the magnet and stability measurements were made for 95 hours. Using a Python program, data from the gaussmeter were written to a file every 20 seconds.

The data obtained were used to plot the time dependence of the magnetic field modulus (Figure 2). After 40 hours of the experiment, the magnetic field tends to stability. This may be related to the stabilization of the magnet temperature.

Table 1 shows the average and maximum values of magnetic field deviations at the geometric center of the magnet for 1, 24 and 95 hours in different units. The instability within an hour is in the range of 3.45-12.12 ppm. One MRI scan is performed for an average of 30 minutes. Thus, the magnetic system has sufficient stability for clinical studies.

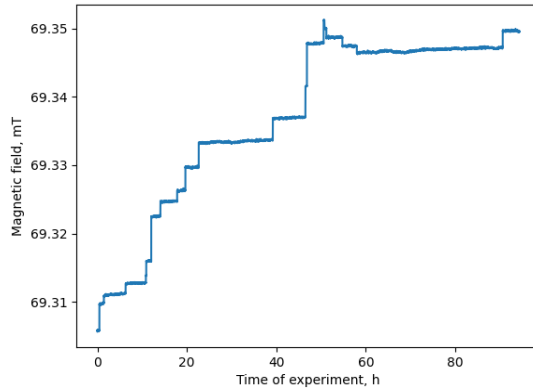


Figure 2. Magnetic field in the magnet as dependence on the time of experiment.

Table 1. Stability of magnetic field in different units.

Time interval (hours)	Mean ΔB (mT)	Max ΔB (mT)	Mean $\frac{\Delta B}{B}$	Max $\frac{\Delta B}{B}$	Mean $\Delta \nu$ (Hz)	Max $\Delta \nu$ (Hz)	Mean, ppm	Max, ppm
1	2.39e-4	8.41e-4	3.45e-6	1.21e-5	10.18	35.81	3.45	12.12
24	4.05e-3	1.59e-2	5.84e-5	2.29e-4	172.52	676.46	58.38	228.93
95	1.23e-2	4.56e-2	1.78e-4	6.57e-4	525.01	1941.02	177.67	656.89

Conclusion

The mechanical system created in our work allows us to measure zonal and tesseral harmonics, and it also places the gaussmeter sensor quite firmly and accurately at a given point in space within the magnet.

Long-term field measurements have shown that the stability of the magnetic field is sufficient for further measurements of magnetic field homogeneity, magnetic isocenter search, and gradient coil analysis. The long-term measurement data showed that the stability of the magnetic field within an hour is at an average of 3 ppm, with a maximum of 12 ppm, which is sufficient for clinical MRI studies.

Acknowledgements

This work is supported by Priority 2030 Federal Academic Leadership Program.

References

1. Kimberly, W.T., Sorby-Adams, A.J., Webb, A.G. et al. Brain imaging with portable low-field MRI. *Nat Rev Bioeng* 1, 617–630 (2023).
2. Guallart-Naval, T.; O'Reilly, Thomas; Algarin, Jose et al. Benchmarking the performance of a low-cost Magnetic Resonance Control System at multiple sites in the open MaRCoS community. (2022).
3. I. Frollo, P. Andris, A. Krafčík, D. Gogola and T. Dermek, Magnetic Field Homogeneity Adjustment for Magnetic Resonance Imaging Equipment, *IEEE Transactions on Magnetism*, vol. 54, no. 5, pp. 1-9, May 2018, Art no. 6500309.

Local ordering and mobility of water molecules in the micropores of a 3D zeolite with mordenite structure by molecular dynamics simulation

M.I. Egorova, D.A. Mizyulin, A.V. Egorov, M.G. Shelyapina

Department of Nuclear-Physics Research Methods, Faculty of Physics, Saint-Petersburg State University

E-mail: maryaverina@gmail.ru

Atomistic molecular dynamics simulations are widely used for studying water behavior in the micropores of various zeolites. However, a detailed understanding of the main regularities in the formation of local water microstructure, as well as factors affecting its molecular mobility in such systems is still missing. In the present study we focus on the differences in the behavior of water molecules in the different fragments of the micropores of a 3D zeolite with mordenite structure.

Simulations were carried out in the *NVT* ensemble using the *MDynaMix* package [1]. The simulated system was a fragment of mordenite consisted of $2 \times 2 \times 4$ elementary cells filled with 384 water molecules. Periodic boundary conditions were used in all three dimensions. The mordenite was considered as a rigid system. Interactions between mordenite and water atoms were a sum of Coulomb and Lennard-Jones (6-12) potentials. Corresponding parameters for mordenite atoms were taken from Refs. [2, 3]. Three different water models: three-site rigid SPC/E [4], three-site flexible SPC-F [5], and five-site rigid TIP5P [6], were considered. In each case all water molecules, based on their initial location in the different fragments of the pores, were divided into 4 subgroups, the phase trajectories of which were analyzed independently. All systems were simulated over the temperature range from 298 to 163 K. The temperature was decreased in the following steps: 283, 263, 243, 223, 203, 183, and 163 K. At each step, the equilibration time was 1.0 ns, the following production run – 1.0 ns.

Based on the simulation data, it was possible to identify several substructures of water in the different fragments of the micropores of a 3D zeolite with mordenite structure and estimate their characteristic lifetimes. Diffusivity and rotational reorientation of water molecules belonging to different substructures were studied in detail.

Acknowledgements

This work is supported by the Russian Science Foundation (grant #23-23-00448).

References

1. A. P. Lyubartsev, A. Laaksonen. – *Comp. Phys. Comm.*, **128**, 565-589 (2000).
2. S. Grimme. – *J. Comput. Chem.*, **27**, 1787-1799 (2006).
3. H. Fang, P. Kamakoti, P. I. Ravikovitch, et al. – *Phys. Chem. Chem. Phys.*, **15**, 12882-12894 (2013).
4. H. J. C. Berendsen, J. R. Grigera, T. P. Straatsma. – *J. Phys. Chem.*, **91**, 6269-6271 (1987).
5. K. Toukan, A. Rahman. – *Phys. Rev. B*, **31**, 2643-2648 (1985).
6. M. W. Mahoney, W. L. Jorgensen. – *J. Chem. Phys.*, **112**, 8910-8922 (2000).

The effect of DyF₃ particles on the magnetic relaxation of ³He nuclei

A. M. Garaeva, E. M. Alakshin, E.I. Boltenkova, K.R. Safiullin, I. V. Romanova, M.S. Tagirov
 Kazan Federal University, Institute of Physics, Kazan, Russia
 E-mail: adeliagaraeva84@gmail.com

Dysprosium fluoride DyF₃ is a dipole ferromagnet with an easy magnetization axis along the [010] axis of the crystal lattice; the ferromagnetic ordering temperature is 2.55 K along the [010] axis for single crystal [1]. The compound has unique properties that allow it to be used as a high-field contrast agent for MRI [2] and as an additive to Nd-Fe-B magnets to increase coercive force [3].

Particles of DyF₃ and LaF₃ with a size of 20 nm were obtained by hydrothermal synthesis using a nitrate reaction [4], particles with a size of 220 nm × 150 nm were obtained by a chloride reaction [5]. Control of the chemical composition and confirmation of crystallinity was carried out by X-ray phase analysis on a Bruker D8 Advance Cu K α diffractometer, $\lambda=1.5418$ Å. Based on photographs taken by transmission electron microscopy on a HitachiHT Exalens microscope, the shape and characteristic size of particles in the resulting powders were determined.

In this work, the effect of a powder of magnetic DyF₃ particles on the rate of longitudinal and transverse relaxation of helium-3 nuclei in the adsorbed layer, in the bulk of the liquid, and with adsorbed helium-4 was studied. The DyF₃ particle powder was diluted with LaF₃ particles. The measurements were carried out at temperatures in the range of 1.5-3 K in fields of 173 and 505 mT. In the case of liquid helium-3, in the presence of an adsorbed layer of helium-3, a two-component relaxation of longitudinal and transverse magnetization is observed. A possible explanation for this phenomenon is proposed.

This work was supported by the Russian Science Foundation (project no. 23-72-10039).

References

1. Savinkov A. V. et al. *Journal of Physics: Condensed Matter*, 2008, 20, 48, 485220.
2. González Mancebo D. et al. *Particle & Particle Systems Characterization*, 2017, 34, 10, 1700116.
3. Xu F. et al. *Scripta Materialia*, 2011, 64, 12, 1137-1140.
4. Alakshin E. M. et al. *Journal of Nanomaterials*, 2016, 2016, 7148307
5. Alakshin E. et al. *Nanoscale*, 2022, 14, 31, 11353-11358.

Automated method of MRI image segmentation

Dilyara R. Gareeva

Kazan University, Institute of physics, Department of Physics of Molecular Systems, Biotechnical Systems and Technologies, Kazan, Kremlevskaya 16a, 420111, Russian Federation

E-mail: dilyaragareeva@yandex.ru

Introduction

Currently, the field of medical image analysis is growing significantly, and tasks such as organ segmentation, disease detection, or anomaly identification on medical images are becoming more voluminous and labor-intensive, especially for doctors themselves. The existing situation may affect the timeliness of establishing a patient's diagnosis and the duration of their recovery. In my work, I will pay special attention to the segmentation task, namely the ability to automate it and make the process of processing MRI scans less complex and time-consuming.

U-Net

The U-Net is considered one of the standard CNN architectures for image segmentation tasks, where it is necessary not only to determine the class of the entire image but also to segment its regions by class, i.e. create a mask that will separate the image into multiple classes. I have chosen the classical U-Net architecture, which has proven to be excellent in solving issues related to semantic segmentation.

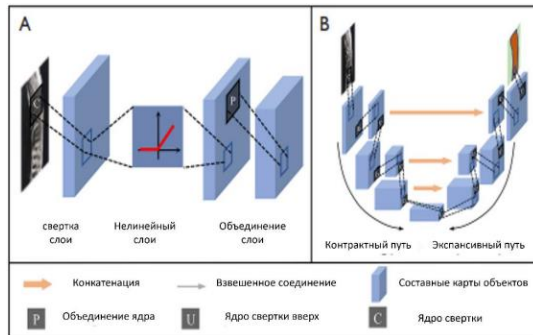


Figure 1. CNN and U-Net network architecture ((A) - CNN, (B) - U-Net)

Training the U-Net model on MRI images of the spine

U-Net training

The network is trained using the stochastic gradient descent method based on input images and their corresponding segmentation maps. Due to convolutions, the output image is smaller than the input signal by a constant border width. The per-pixel soft-max function computes energy based on the final feature map along with the cross-entropy function. Cross-entropy calculated at each point is determined as follows:

$$E = \sum_{x \in \Omega} \omega(x) \log(p_{l(x)}(x))$$

The boundary is determined using morphological operations. Then, a weight map is calculated:

$$\omega(x) = \omega_c(x) + \omega_0 \cdot \exp\left(-\frac{(d_1(x) + d_2(x))^2}{2\sigma^2}\right)$$

Where ω_c is the weight map for balancing class frequencies, d_1 is the distance to the boundary of the nearest cell, and d_2 is the distance to the boundary of the second nearest cell.

Processing and presentation of results

In this study, MRI images from 100 patients were manually segmented. Typically, segmentation took 1 hour per patient.

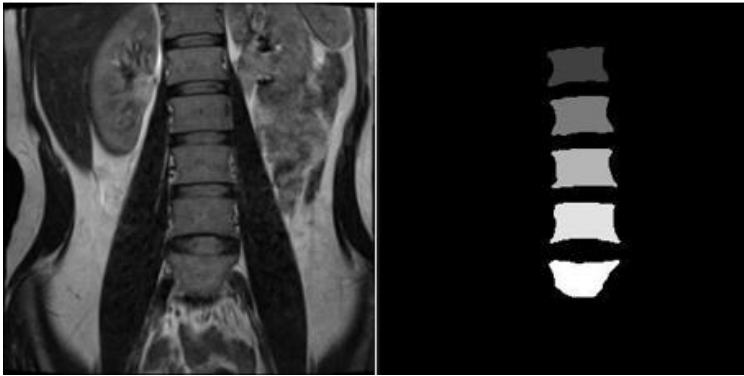


Figure 2. Example of manually segmented vertebrae (left image - MRI image of the spine, right image - mask)

Predicted masks were obtained from the output of the trained model:

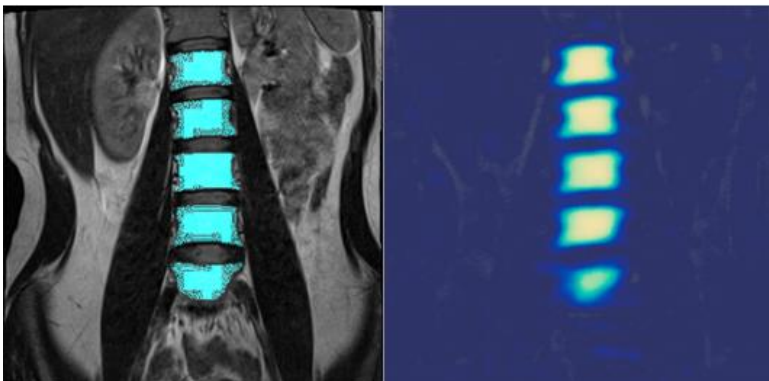


Figure 3. Location of the binary mask in the image (left) and the predicted mask (right)

As a tool for evaluating the quality of the model's performance, the Dice coefficient (Sorensen–Dice coefficient) was chosen. The Dice coefficient (DSC) is defined by the following formula:

$$Dice(X, Y) = \frac{2|X \cap Y|}{|X| + |Y|}$$

Where X is the predicted mask, and Y is the ground truth mask on the current image. $|X|$ denotes the cardinality of set X (the number of elements in this set), and \cap denotes the intersection of X and Y .

Below is a graph of the Dice coefficient, as well as a graph of the loss – function (helps the model find optimal parameters by minimizing the error on the training data):

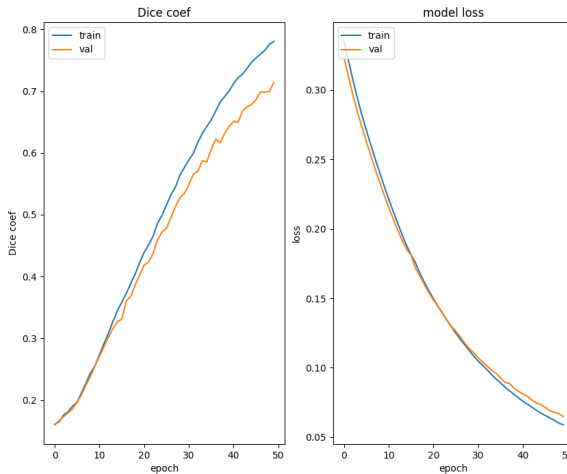


Figure 4. The Dice coefficient (left graph) and the loss - function (right graph) are shown on the image

Acknowledgements

I express my gratitude to Ilyasov Kamil Akhatovich and Alhabeeb Muhammad Habib for their support and assistance

References

1. Alhabeeb M. Habeeb. Quantitative methods for analyzing magnetic resonance tomographic data. – Kazan, 2023. – P.37.
2. Semantic segmentation based on U-Net architecture and determining the distance between objects. - <https://habr.com/ru/articles/746842/>
3. U-Net: neural network for image segmentation. - <https://neurohive.io/ru/vidy-nejrosetej/u-net-image-segmentation/>

Nuclear Overhauser effect in determining the configuration of nitrofuran-3-carboxylates semicarbazones

Gomonov K. A., Pelipko V. V., Baichurin R. I., Makarenko S. V.

Herzen State Pedagogical University of Russia, Department of Organic Chemistry, Laboratory of Nitrocompounds, Center of collective use at the Faculty of Chemistry "Instrumental methods for the study of nitro compounds, coordination, biologically active substances and nanostructured substances"

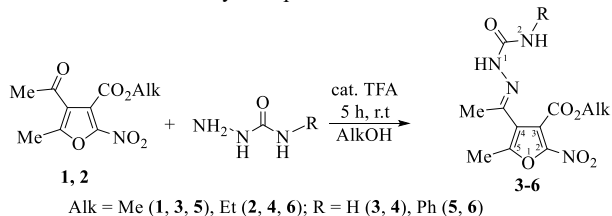
48 Moyka River Embankment, Saint Petersburg 191186, Russia

E-mail: kohrgpu@yandex.ru

<http://kohrgpu.ru>, <http://ckpo.herzen.spb.ru/?page=organic-chemistry>

Previously, it was shown that of the interaction of furan-3-carboxylates with substituted hydrazines, furan-3-carboxylate hydrazones with *E-s-cis*-configuration are formed [1].

As the interaction result of acetyl-containing 2-nitrofuran-3-carboxylates **1,2** with semicarbazide hydrochloride and its phenyl-substituted analogue, we obtained 2-nitrofuran-3-carboxylates semicarbazones **3-6** with a yield up to 88%.



The synthesized 2-nitrofuran-3-carboxylates semicarbazones **3-6**, according to the ^1H and $^{13}\text{C}\{^1\text{H}\}$ NMR spectra, are formed stereohomogeneously. The correct assignment of signals in the ^1H and $^{13}\text{C}\{^1\text{H}\}$ NMR spectra of compounds **3-6** is confirmed by the results of ^1H - ^{13}C HMQC and HMBC NMR experiments.

However, semicarbazones **3-6** can exist in the form of *E*- and *Z*-isomers relative to the C=N bond, as well as *s-cis*- and *s-trans*-conformers (Fig. 1).

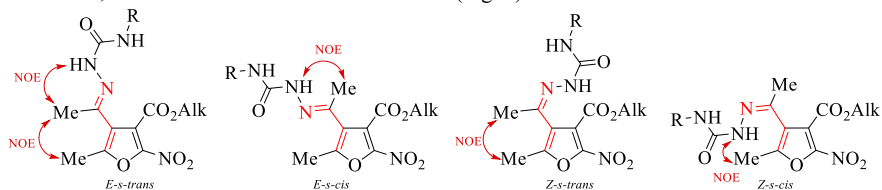


Figure 1. Hypothetical NOE in nitrofuran-3-carboxylate semicarbazones molecules

The aim of this work is to determine the geometric configuration of the obtained semicarbazones **3-6** using ^1H - ^1H NOESY NMR spectroscopy experiment.

The results of ^1H - ^1H NOESY experiments for semicarbazones **6** carried out with varying mixing times ($\tau = 0.5$ -1.5 s) indicate the presence of a nuclear Overhauser effect (NOE) between the amino group proton N^1H and the protons of methyl group ones to the azomethine bond

($\text{Me}-\text{C}=\text{N}$). Also, the presence of NOE between the methyl group protons of the furan ring and the azomethine bond. This makes it possible to determine the *E-s-trans*-configuration of

the fragment $C^5=C^4-C=N$ (Fig. 2). In addition, the spectra also contain a cross-peak of the amino group proton N^2H with both the proton of the benzene ring H^o and the methylene protons of the ester group, which also give a cross peak with each other.

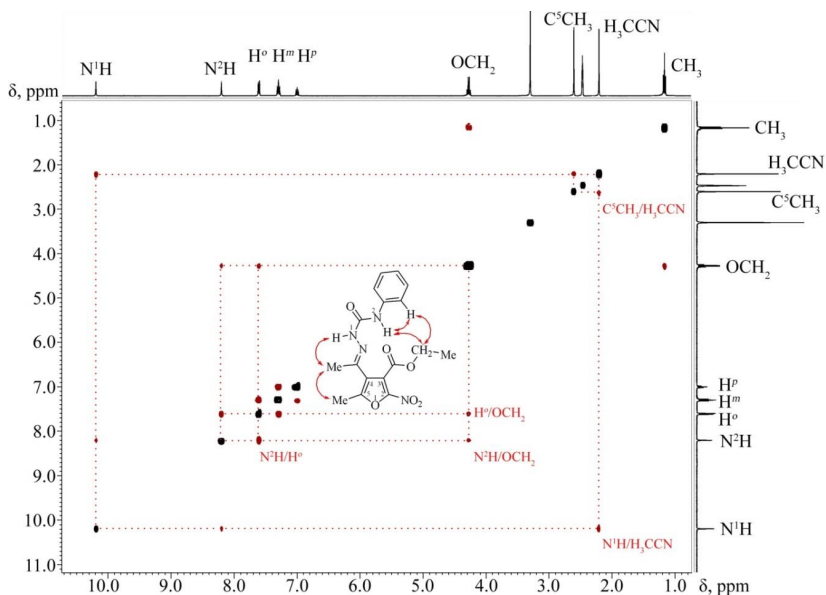


Figure 2. NOE in nitrofuran-3-carboxylates semicarbazones 6

Thus, according to NMR data, the configuration of the synthesized 2-nitrofuran-3-carboxylates semicarbazones was established and their structure was confirmed using X-ray diffraction analysis on example of compound 6.

The studies were carried out at the Central Collective Use Center at the Faculty of Chemistry of the Herzen State Pedagogical University of Russia on the Jeol ECX-400A spectrometer (Royal probe) with an operating frequency of 399.78 (1H), 100.53 (^{13}C) MHz at standard experimental settings, using the solvent signal as an internal standard.

Acknowledgements

The research was supported by an internal grant of the Herzen State Pedagogical University of Russia (project № 3VG).

References

- Gomonov K.A., Pelipko V.V., Baichurin R.I., Makarenko S.V. Carbonyl-containing furan-3-carboxylates in the synthesis of original mono- and biheterocyclic structures // Book of abstracts Conference "New Emerging Trends in Chemistry (NewTrendsChem-2023)". Yerevan (Armenia). 24-28 September 2023. P. 80.

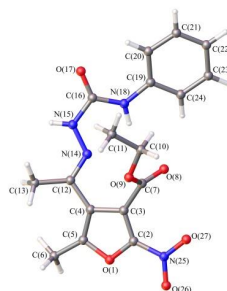


Figure 3. X-ray diffraction analysis of compound 6

The detecting of correlations between NMR spectra of ligno-carbohydrate complexes in dissolved and solid state

Ilya A. Grishanovich, Semyon L. Shestakov, Yuliya A. Sypalova, Alexander Yu. Kozhevnikov
 Core facility center "Arktika", Northern (Arctic) federal university named after
 M.V. Lomonosov, Arkhangelsk city, Russian Federation
 E-mail: i.grishanovich@narfu.ru

Most of technical lignins, unlike the lignins isolated with laboratory methods, are insoluble in the solvents, used in NMR spectroscopy. Thus, the study of technical lignins with NMR spectroscopy is possible mostly for solid-state samples.

CP/MAS method distorts the quantitative ratio of integral intensities of signals in ^{13}C -NMR spectra, due to the transferring of magnetization from hydrogen nuclei to carbon nuclei, linked to them.

We registered ^{13}C -NMR spectra of several lignin samples in dissolved and solid state in order to test the presence of correlations between the intensities of corresponding signals. We selected and fixated the chemical shifts ranges for integration of signals intensities in all spectra. The reference of spectral signals to atom groups in substances was implemented according to the literature data (Table 1). All intensities were normalized on mass with the purpose to exclude its influence on calculation results.

Table 1. Integrated ranges of chemical shifts and atom groups, corresponding to them.

Range, ppm	Groups
162.8 – 142.6	Ar-CH=CH-CHO
142.6 – 120.0	H _{2,6}
120.0 – 95.1	G ₂ ; S _{2,6} ; PhGly; GlcU
95.1 – 67.8	β -5 (phenylcoumarone); S β -O-4 E; S β -O-4 T; β - β (resinol); G β -O-4 E+T; α -CO/ β -O-4; BE; β -O-4/ α -OH
67.8 – 45.7	γ -ethers; OMe; Hk

The integration of spectra signals was implemented with the tools of spectrometer software. After integration of signals and their normalization on samples masses we calculated the ratio of integral intensities of signals in liquid (I_l) and solid (I_s) samples in corresponding chemical shifts ranges (Table 2).

Table 2. The ratio of integral intensities of corresponding ranges of chemical shifts in ^{13}C -NMR spectra of analyzed lignins.

Chemical shift, ppm	I_s/I_l		
	Soda-ethanol lignin	DMSO lignin	Alkali lignin
162.8 – 142.6	0.091	0.060	0.075
142.6 – 120.0	0.088	0.048	0.062
120.0 – 95.1	0.063	0.033	0.069
95.1 – 67.8	0.087	0.070	0.192
67.8 – 45.7	0.110	0.108	0.137

At the current stage of research, the comparison of integral intensities in corresponding ranges did not allow confirming the presence of correlations between

intensities of NMR signals in liquid and solid lignins samples. The possible reason could be a presence or absence of lignins fragments, as well as contaminants of extraneous substances, which presence in sample depends on the method of isolation. For example, technical lignins contain significantly higher concentration of carbohydrates, than lignins isolated with laboratory methods. The main carbohydrates signals appear in ranges of 120.0 – 95.1 ppm and 95.1 – 67.8 ppm. We attempted to separate carbohydrates signals from signals of lignin fragments and calculate their fraction in general integral intensity with application of HSQC NMR spectroscopy, but the subtraction of carbohydrates fraction of intensity did not change the resulting ratio.

In addition to the processing of spectral curves with integration methods, we processed the array of spectra with statistic methods, using the principal components analysis (PCA). The analysis demonstrated the presence of some tendencies, for example, the samples of ethanol and sodic lignins group both among liquid and among solid-state spectra (Fig. 1). It can indicate both the similarity of the structures of these samples, and the supposing presence of the correlations of spectral data for samples in dissolved and solid state.

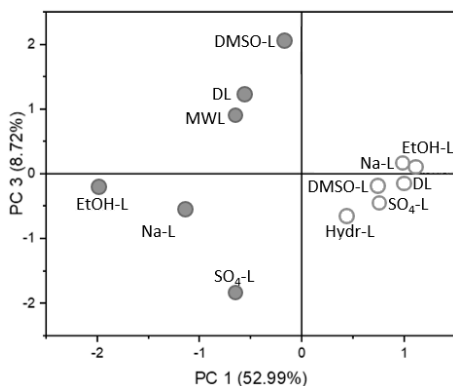


Figure 1. PCA for obtained ^{13}C -NMR spectra (PC3/PC1). Gray circles – dissolved samples, white circles – solid samples. DMSO-L – lignin isolated by dimethylsulfoxide, EtOH – soda-ethanol lignin, Na-L – alkali lignin, DL – dioxanelignin, Hydr-L – hydrolyzed lignin, SO_4 -L – kraft lignin, MWL – milled wood lignin.

The obtained results substantiate the application of more deep mathematical analysis of spectral data for detection of the unobvious regularities, for example, PLS or OPLS methods, however such algorithms require more amount of data for analysis.

The further work in this field supposes the improvement of samples purity (the decrease of contaminants content), the adjustment of experiment conditions, the extension of the studied substances set, and the advancement of mathematical processing of obtained experimental data array.

Acknowledgements

This research was funded by the Russian Science Foundation, grant number 22-13-20015. Instrumentation of the Core Facility Center «Arktika» of Northern (Arctic) Federal University was used in this work.

Investigation of Lovastatine with transition metal by NMR

Islamov T.R., Aganova O.V., Julmetov A.R., Klochkov V.V.

Institute of Physics, Kazan Federal University, Kazan, 420008 Russia

E-mail: relifer2000@mail.ru

Introduction

One of the current tasks is to find ways to modernize existing drugs in order to reduce their toxicity by adding metals to their structure. The choice of ligand for the synthesis of the metal complex will allow you to adjust lipophilicity, solubility and reactivity, thereby enhancing the positive properties of the drug and reducing toxicity [1]. Statins are the most common class of drugs used to lower low-density lipoprotein cholesterol levels.

Object

The statin group is represented by a wide variety of molecules that differ in medical activity, solubility, etc. Lovastatin is the first approved HMG-CoA reductase inhibitor, clinical trials of which have provided evidence of the ability of drugs in this class to reduce morbidity and mortality associated with cardiovascular diseases [2]. Its structure with the numbering of carbon atoms is presented in Figure 1 a.

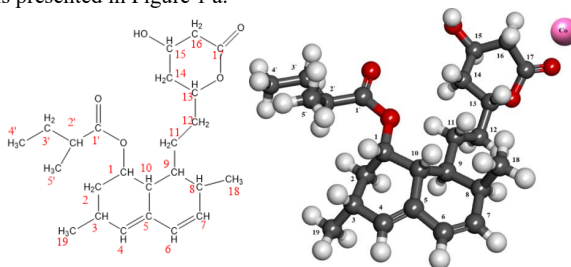


Fig. 1. Structural formula of Lovastatin (a) and schematic representation of the cobalt (Co^{+2}) – lovastatin complex (b).

The main requirement for a ligand is low toxicity of the ion. Transition group metals, such as cobalt, are present in the body as part of vitamin B₁₂ and are involved in hematopoiesis [1,2].

Method

The study of complex formation in the cobalt (Co^{+2}) - lovastatin system was carried out using one-dimensional ¹H NMR spectroscopy within the framework of the approach discussed in our previous works [3,4].

Recording of ¹H NMR spectra of lovastatin in deuterated acetone at various concentrations of cobalt chloride CoCl₂ (cobalt/lovastatin: 1/5, 1/10) was carried out on a Bruker Avance II 500 NMR spectrometer at a temperature of 308 K. ¹H NMR spectrum was recorded using 90° pulse, delay between pulses 2 with spectral width 10 ppm. The correlation of one-dimensional spectra was performed using TopSpin software.

Result

The one-dimensional ¹H NMR spectrum of the prepared solutions is shown in Fig. 2.

The ^1H NMR spectra of lovastatin in a solution of deuterated acetone (a) and in a solution of deuterated acetone with the addition of Co^{+2} ions (b and c) have a number of differences. The following changes are observed in the NMR spectra: the ^1H NMR signal ^{15}CH changes in intensity (while the integral intensity remains unchanged), the ^{16}CH signal shifts towards higher ppm. The shift of the ^1H NMR signal of ^{16}CH during the transition from sample a to sample b (ion/statin ratio 1/10) is 2.6 ppm; at a concentration of 1/5, the ^1H NMR signal disappears. Changes in the ^1H NMR signals of the remaining protons of lovastatin are insignificant. The spatial proximity of paramagnetic Co^{+2} ions leads to a decrease in the proton relaxation time, which, in turn, causes a broadening of the spectral lines. Thus, it can be assumed that cobalt is predominantly located near the 15-16th carbon atoms (Figure 1 b).

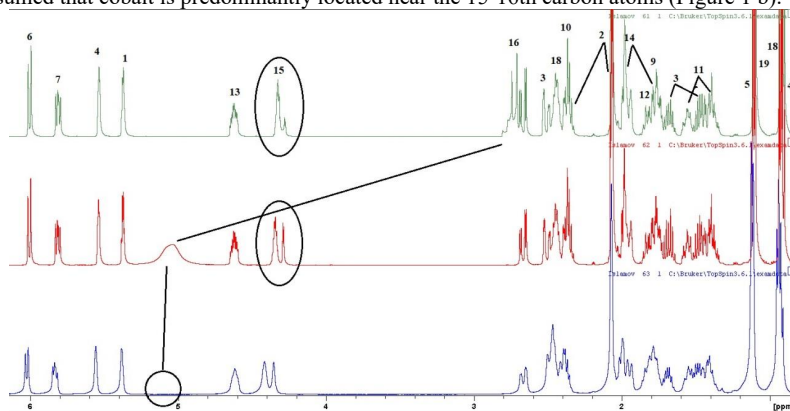


Fig. 2. NMR spectra (^1H , 500 MHz) of lovastatin in deuterated acetone (a – lovastatin, b – lovastatin solution with cobalt chloride in a ratio of 1/10, c – lovastatin mixed with cobalt chloride in a ratio of 1/5)

Acknowledgments

The work was supported by the subsidy allocated from the Kazan Federal University Strategic Academic Leadership Program (PRIORITY-2030).

References

1. Kuranova N. N. et al. Complexation of Gold (III) with Pyridoxal 5'-Phosphate-Derived Hydrazones in Aqueous Solution //Molecules. – 2022. – T. 27. – №. 21. – C. 7346.
2. Hamelin B.A., Turgeon J. Hydrophilicity/lipophilicity: relevance for the pharmacology and clinical effects of HMG-CoA reductase inhibitors. // Trends Pharmacol. Sci. England, 1998. Vol. 19, № 1. P. 26–37.
3. Abdrakhmanov, Rustam, Modeling the Co^{2+} Binding to Amyloid Peptide $\text{A}\beta_{13-23}$ in Water Environment by NMR Spectroscopy [text] / Rustam Abdrakhmanov, Dmitriy Blokhin, Konstantin Usachev, Vladimir Klochkov// BioNanoScience. – 2018.- V. 8, Issue 1.- P. 423-427. DOI 10.1007/s12668-017-0475-2. IF = 1.08 Scopus.
4. Tarasov, A.S. The effect of gadolinium ion on micelles and reverse micelles by NMR spectroscopy [text] /A.S. Tarasov, I.Z. Rakhmatullin, G.S. Shurshalova, A.V. Klochkov, K.A. Il'yasov, V.V. Klochkov// BioNanoScience.- 2021. – V.11, Issue1. - P.136-141. Q4; SiteScore = 2.20. (Scopus). <https://doi.org/10.1007/s12668-020-00813-2>.

Multi-point magnetic field mapping device to passive shimming of NMR permanent magnet

Ivanov A. A., Skirda V. D., Alexandrov A. S., Ivanov D. S., Doroginiczky M. M., Valiullin A. L., Berdnikov V. A.

¹*Institute of Physics, Kazan Federal University, Kazan*

E-mail: anatoly.ivanov1@gmail.com

Introduction

Measurement and visualization methods based on the principles of nuclear magnetic resonance (NMR) require a static magnetic field with high homogeneity in the entire volume of the object [1]–[3]. But in practice, there is no magnet (permanent or electric) that can produce a perfectly uniform magnetic field, so achieving the highest possible homogeneity is a common goal in magnetic resonance equipment design.

To achieve the highest possible level of magnetic field homogeneity of the particular given permanent magnet, a magnetic field map meter layout has been developed to promptly control the spatial distribution of the field strength in the magnet gap. Controlling the magnetic field is crucial for adjusting the initial homogeneity of the magnet during device manufacturing and for servicing the magnetic system during long-term use. The adjustment of the magnetic field homogeneity (shimming) involves multiple and iterative changes in the magnetic field configuration, followed by the necessary subsequent control of the obtained result. Therefore, it is crucial to measure the magnetic field at multiple points in space within the shortest time and with the appropriate precision. Such interactivity cannot be achieved in practice using regular magnetic field meters, which also require precise positioning of the measuring sensor in the mapped space. In addition to interactivity, another important requirement for a magnetic field mapping device is sufficient measurement accuracy, which should reach at least 10 ppm from the mean value of the magnetic field.

Multi-point magnetic field mapping device design and construction

The accuracy and speed requirements for developed device are achieved by measuring the frequency of the nuclear magnetic resonance (NMR) signal at multiple spatial points. To accomplish this, the magnetic field sensor includes multiple coils that receive the NMR signal, whose frequency reflects the magnetic field strength value at a given point. One advantage of using NMR signals is the ability to measure magnetic field strength with high precision, which can even surpass the required measurement accuracy in this particular case. The measurement process is greatly speeds up by the fact that the NMR signal sensor is constructed as a plane with 17 coils attached to it, serving as a multi-point magnetic field sensor. Accordingly, to measure the field at more points and in other planes of space, it is sufficient to move the sensor along only one axis, which speeds up data acquisition and simplifies the measurement process.

Figure 1 shows a general view of the sensor design, which consists of three parallel boards, on the first of which coils are fixed and to which their common wire is connected, on the second board all capacitors are located, and on the third board there is a connector, by which the sensor is connected to the coil switching board. Such separation of sensor elements on several boards was required due to the necessity of spatial separation of capacitors from measuring coils, because magnetic impurities contained in the metal of capacitor leads disturbs the static magnetic field in close range.

The block diagram of the magnetic field map meter is shown in Figure 2, where the following blocks are shown: A1 - sensor consisting of 17 identical circuits (one is shown), A2

- connecting loop that transmits the signal to the coil circuit board A3, which in turn transmits the signal of the selected circuit to the RX/TX switch board A4, power amplifier A5, receiver A6 and digital control board A7.

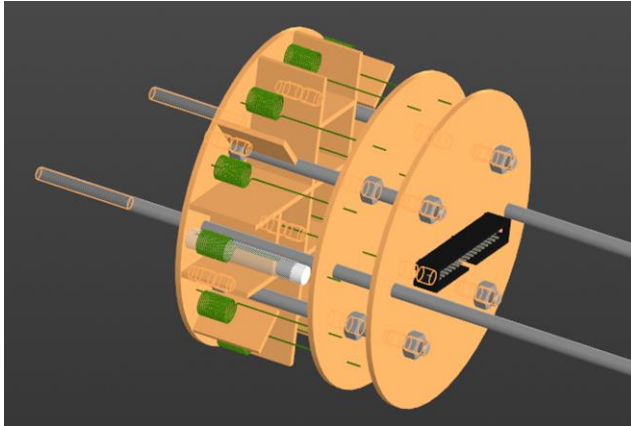


Figure 1. General view of the sensor design

The block diagram of the magnetic field map meter is shown in Figure 2.

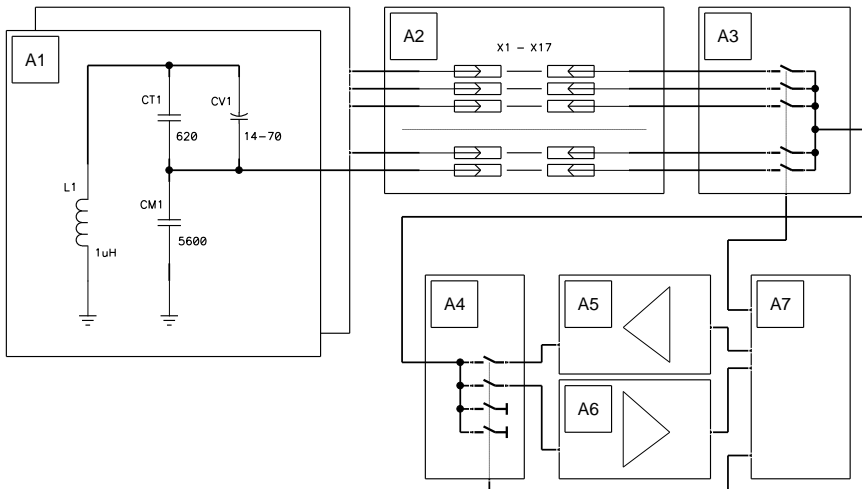


Figure 2. Magnetic field map meter block diagram

As shown in this block diagram, the coil used for the measurement at the current point is alternately connected by switches first to a power amplifier, which generates a short powerful pulse of high frequency field in the coil, and then to a receiver path, which amplifies

the NMR signal to a level sufficient for digitization and transmission to a digital unit. The digitized NMR signal is then processed to measure its frequency and determine the value of the magnetic field strength. At this stage, the resulting signal is multiplied by the apodization function and then converted to the frequency domain using the Fast Fourier Transform (FFT).

As a result, a multi-point magnetic field mapping device was developed, which allows measuring the magnetic field strength corresponding to the proton resonance center frequency of 6.7 MHz in the range of 150 kHz and with an accuracy not lower than 10 ppm of the average magnetic field value.

Acknowledgements

The work was carried out at the expense of funds, subsidies, allocated to the Kazan Federal University for the implementation of the state task in the field of scientific activity (project № FZSM-2023-0016).

References

1. А., Абрагам. Ядерный магнетизм / Абрагам А. Издательство Иностранной Литературы. — 1963. — 551 с.
2. Фаррар, Т. Импульсная и Фурьеспектроскопия ЯМР. Пер. с англ. Б.А. Квасова / Т. Фаррар, Э. Беккер; Под ред. Э. И. Федина. — Мир, 1973. — 162 с.
3. Квантовая радиофизика: магнитный резонанс и его приложения. Учеб. пособие. 2-е изд., перераб. Под ред. В. И. Чижика. – СПб.: Изд-во С.-Петерб. Ун-та, 2009. 700 с.

Synthesis and macromonomer structure analysis by ¹H NMR spectroscopy

M.V. Kadnikov^{1,2}, P.A. Fetin², I.M. Zorin², N.V. Tsvetkov¹

¹Faculty of Physics, Saint Petersburg State University, Saint Petersburg, Russia

²Institute of Chemistry, Saint Petersburg State University, Saint Petersburg, Russia

E-mail: mkadnikov199991@gmail.com

Introduction

One of the main Green Chemistry approaches in recent years is carrying out organic cross coupling reactions in water, since water is the most common and safe solvent on our planet. One of the promising approaches for carrying out such reactions is the use of surfactants, micelles of which are capable of solubilizing poorly soluble organic substrates and catalysts in water, while their local concentration increases, which can accelerate the reaction. Some of the most promising substances as such micellar catalysts are comb-like polyelectrolytes, due to their extremely low threshold aggregation concentrations. Therefore, the task of synthesizing such substances seems to be one of the most important in the context of Green Chemistry, while the NMR spectroscopy method is key in the analysis of any organic substances.

Method

To obtain target cationic surfactant macromonomers containing a methoxypolyethylene glycol fragment of various lengths, 4 stages of synthesis were carried out (Fig. 1). The precursors and each of the intermediate products were characterized by ¹H NMR spectroscopy. Based on the obtained macromonomers, polymers were synthesized that accelerated the Suzuki reaction in water. The degree of conversion of functional groups was also determined by ¹H NMR spectroscopy.

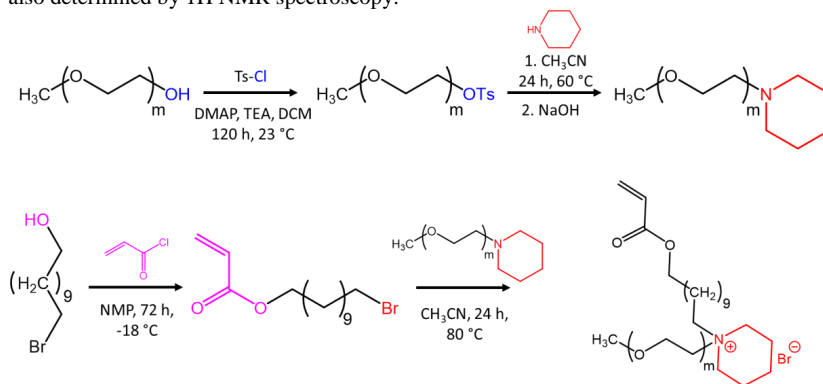


Figure 1. Scheme of macromonomers synthesis

Acknowledgements

Synthesis and study of self-organized structures were supported by the RSF № 21-73-10132. The work was supported by the research park of St. Petersburg state university: RC of Magnetic resonance and cryogenic department.

Synthesis and characterization of membranes based on polyether block amide modified by MIL-125

*Anna S. Kariakina¹, Anna I. Kuzminova¹, Roman R. Dubovenko¹, Maria E. Dmitrenko¹,
Konstantin N. Semenov¹, Anastasia V. Penkova¹*

¹Saint Petersburg State University, Saint-Petersburg, Russia

E-mail: st110579@student.spbu.ru

<https://go.spbu.ru/rgpenkova>

Introduction

Recently, membrane technologies have been widely used in water treatment processes as highly efficient, environmentally friendly and resource-saving methods. One of the most promising membrane processes is pervaporation, an environmentally friendly method in which the separation of liquid substances occurs during their evaporation through the membrane. Pervaporation makes it possible to separate azeotropic mixtures, as well as mixtures of near-boiling and thermally unstable substances using compact modular equipment at low energy costs. To implement more advanced water treatment using membrane methods, improved materials and highly efficient membranes based on them are required. One of the most relevant approaches to improving the transport properties of membranes is their modification. The use of polyether block amide (PEBA) as a membrane material is due to the possibility of varying the ratio of blocks, which makes it possible to obtain polymers and, accordingly, polymer membranes with different properties.

Results

In this work, membranes based on PEBA modified with a metal–organic framework (MOF) were developed. The MOF MIL-125 was used as a modifier. MIL-125 is a Ti-based MOF obtained from metal ions Ti and 1,4-benzenedicarboxylic acid. The unique properties of this MOF, such as high porosity, excellent chemical and thermal stability, can positively and significantly affect the characteristics of the PEBA.

The physico-chemical properties of the membranes were studied using nuclear magnetic resonance, Fourier transform infrared spectroscopy, scanning electron microscopy, atomic force microscopy, thermogravimetric analysis, swelling experiments and measurement of the contact angle with water.

The transport properties of the developed membranes were investigated during the initial separation of the isopropyl alcohol/water mixture (5/95 wt. %). The composition of the initial mixture and permeate is determined by the gas chromatographic method. For the developed membranes, the positive effect of the introduced modifier on transport characteristics was noted.

Acknowledgments

The authors acknowledge Saint-Petersburg State University for a research project 11602266. The experimental part was carried out with the participation of resource centers: Interdisciplinary Resource Center in the field of Nanotechnology, Thermogravimetric and Calorimetric research methods, Cryogenic Department, Geomodel, Magnetic resonance research methods, Innovative technologies of composite nanomaterials, X-ray diffraction research methods, Methods of substance composition analysis, St. Petersburg State University Computing Center, Physical Methods of surface research, Nanoconstruction of photoactive materials St. Petersburg State University.

Structural transformations of pore water based on nuclear magnetic resonance in the filtration consolidation theory of fine-grained soils

Regina E. Dashko¹, Darya L. Kolosova¹, Anton S. Mazur², Alexandr V. Ievlev³

¹Faculty of Geological Prospecting, Saint Petersburg Mining University, Saint Petersburg 199106, Russia

²Resource center MRMI of Research park Saint-Petersburg State University, Russia

³Department of Nuclear Physics Research Methods, Saint Petersburg State University, 199034, 7/9, Universitetskaya nab., Saint Petersburg, Russia

E-mail: regda2002@mail.ru, a.ievlev@spbu.ru

Introduction

The safety of construction and operation of buildings and structures for various purposes, as well as the study of operational recourses of architectural and historical monuments on water- and water-gas-saturated fine-grained, primarily clay soils, largely depends on the calculations parameters of their stability. The non-alternative concept of filtration consolidation described by K. Terzaghi in 1925 is considered in the practice of designing new constructions, reconstruction and restoration of cultural heritage monuments. The hypothesis describes an ideal model of water-saturated clay soil with no structural bonds and with bulk water in its pores. The hypothesis was developed by many Russian and foreign scientists, taking into account the knowledge of the nature of the dispersed soils strength and the anomalous properties of water.

The crystallochemical structure of bulk water was proved by J.D. Bernal and R.H. Fowler in 1933 [1]. Further theoretical and experimental study of water was carried out to evaluate its structural changes under the influence of various physical effects [3, 4]. However, the results of these studies have been not used in the theory and practice of the filtration consolidation, as well as in the sections of engineering geology and geotechnics.

The maximal amount of “physically bound water is characterized by the maximum molecular moisture capacity of clay soils ($W_{m \max}$). This parameter is determined by the method of pressing thin layers of water-saturated clay samples under standard pressure. It is assumed that at a water content (W) exceeding $W_{m \max}$, the soil contains free water, therefore filtration consolidation of clay soils takes place. It should be noticed that $W_{m \max}$ is close to plastic limit of clay soils (W_p). In soil science W_p has a physical meaning and corresponds to the beginning of withering of root system, because its vacuum system with a large rarefaction cannot absorb soil moisture.

It is known that in the practice of designing structures for various purposes, it is necessary to calculate allowable pressures, in which it is assumed that the soil works under the action of compressive stresses, so all deformations are considered as damped in time. The design pressure should not exceed the allowable pressure, which is calculated by the following formula:

$$p_a = \frac{\pi}{ctg\varphi + \varphi - \frac{\pi}{2}} \left(0,25b\gamma + \frac{c}{tg\varphi} + \gamma' h_f \right) + \gamma' h_f,$$

where φ, c – angle of internal friction and cohesive strength of soils, b, h_f – width and depth of the foundation, γ, γ' - specific weight of the soil below and above the bottom of the excavation.

As follows from the analysis of this formula, the main parameters of the properties that determine its value are the soil shear strength parameters: φ and c . Currently, it is recommended to estimate φ and c only on consolidated samples of water-saturated clay soils: consolidated-drained tests. This testing scheme assumes high values of φ and determines an overestimation of p_a .

Observations of changes in the physical state of clay soils at the base of operating structures or structurally unsafe buildings have shown that deformations of buildings occur not due to the consolidation, but due to the spreading of soils [2]. Clay soils deform as a quasi-plastic substance. It was concluded that water is inert to the acting pressure. This statement was proved during experimental studies of water-saturated clay soils using nuclear magnetic resonance (NMR) facilities in the 1980s by Prof. R.E. Dashko under the supervision of Prof. V.I. Chizhik at the Department of Nuclear Physics Research Methods of Saint Petersburg State University [2]. In these studies, the longitudinal relaxation time (T_1) of water-saturated clay soils of different granulometric and mineral compositions, as well as their physical state, was determined. $T_1 = n \cdot 10^{-3}$ sec corresponds to a decrease of this parameter by three orders in comparison with bulk water. In the study of clay soils with W close to W_p (or $W_{m \max}$) no water in the liquid state was recorded.

Experiment

In continuation of this work, a series of experiments were carried out to measure the spin-lattice relaxation time of water protons in water-saturated clay soil at the liquid limit (according to the provisions of engineering geology and soil mechanics) using two instruments at frequencies of 89 MHz and 300 MHz. The research results are shown in Figures 1a and 1b. In Fig. Figure 1a shows the dependence of the intensity of the spectral line on the interval between rf pulses, and 1b shows the process of integration of a broad line characteristic of strongly bound protons. Similar studies will be continued in future works.

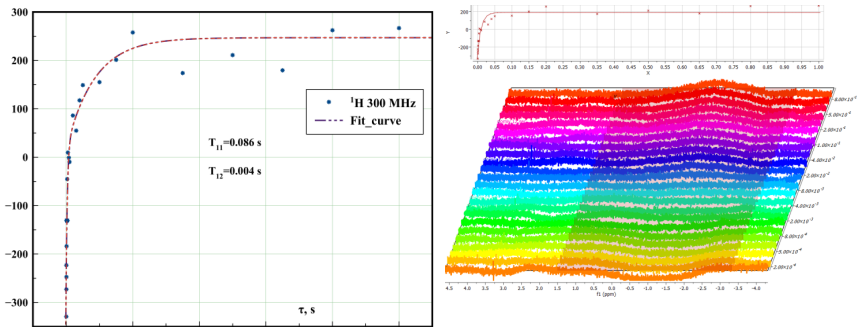


Figure 1. Relaxation dependence ^1H

In addition to the relaxation data, a solid-state spectrum is also presented with rotation of a sample of water-saturated clay at a magic angle with a rotation frequency of 12.5 kHz, recorded on the device at a frequency of 400 MHz. The results of such studies are shown in Figure 2.

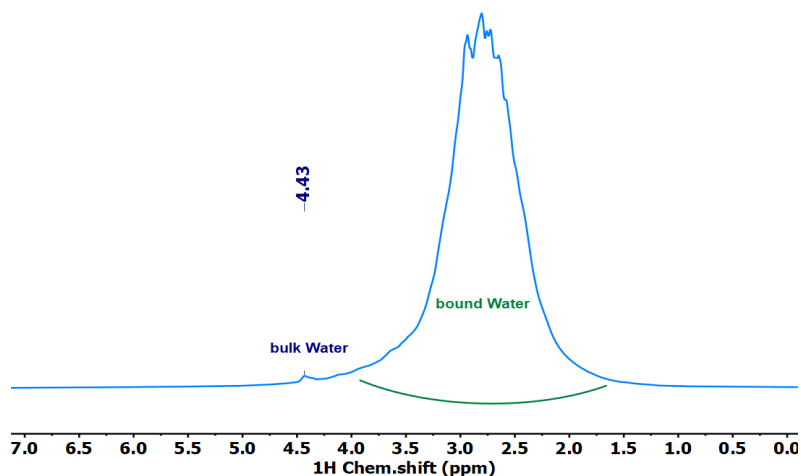


Figure 2. ^1H spectrum recorded with a rotation frequency of 12,5 kHz. Satellites are not shown.

Analysis of Figure 2 makes it possible to establish that the proton spectrum contains a mixture of broad lines from water associated to varying degrees with the active centers of clay particles (layered aluminosilicates), while in the region of 4.43 ppm an insignificant line of bulk water is visible. In addition, spectra were recorded on ^1H , ^2D , ^{23}Na , ^{27}Al , ^{29}Si nuclei at different rotation rates; a detailed analysis of such studies will be given in the next work.

Acknowledgements

This work is supported by internal grant of St. Petersburg State University initiative project (ID 100349765). This scientific research was carried out at the "Center for Magnetic Resonance Research" of the Science Park of St. Petersburg State University.

References

1. Bernal J.D., Fowler R.H. A theory of water and ionic solution, with particular reference to hydrogen and hydroxyl ions. *The Journal of Chemical Physics*, 1933. Vol. 1, No. 8, pp. 515-548, <https://doi.org/10.1063/1.1749327>.
2. Dashko R.E. Engineering-geological analysis and assesment of water-saturated clayey rocks as a base for structures. Publishing house of the Institute "Georekonstrukciya", Saint Petersburg (in Russian). – Publishing house of the Institute "Georekonstrukciya", Saint Petersburg, 2015.
3. Deryagin B.V., Churaev N.V. *New properties of liquids* (in Russian). – Nauka, Moscow, 1971.
4. Mecik M.S. Properties of thin films between mica plates. Poverhnostnye sily v tonkih plenkah i dispersnyh sistemah (in Russian): In collection of papers IV surface forces conference, Moscow, 1972, p. 189.
5. Terzaghi K. *Erdbaumechanik auf bodenphysikalischer grundlage*. Publisher of F. Deuticke, Vienna, Austria, 1925.

Influence of the operating regime on performances of the magnonic reservoir computer

Alexandr V. Kondrashov¹, Mikhail Kostylev², Alexey B. Ustinov¹

¹Department of Physical Electronics and Technology, Saint Petersburg Electrotechnical University "LETI", St. Petersburg, 197022, Russia

²Department of Physics, University of Western Australia, Crawley, Western Australia 6009, Australia

E-mail: avkondrashov@etu.ru

Introduction

A recurrent neural network (RNN) is a special type of the artificial neural networks which can be used for processing the data of time series such as speech, chaotic waveforms, etc. The main disadvantages of RNN are difficult and energy sufficient training process, as well as the complexity of RNN hardware realization. Physical reservoir computers (RC) is a concept of recurrent neural network that is free of this disadvantage [1]. In this case, only the weights of output layer must be trained through a simple linear regression procedure. The main requirements for material that can be used as a base for physical RC are the nonlinearity of the response of the physical system and availability of short-term memory.

Magnonics is an area of research where interest in RC is steadily growing [2] due to the wide variety of nonlinear processes in ferromagnetic materials and relatively low decay rate of oscillations. Recently, physical RC based on magnonic active ring oscillators (MARO) have been proposed [3-5]. Completion of conventional short-term memory (STM) and parity check (PC) tests revealed modest performance of the first experimentally implemented MRC. Later, numerical modeling [4] helped optimizing the physical parameters of the active ring. This led to a significant increase in the performance characteristics [5]. However, fine-tuning of physical parameters is a complex problem.

In this work, we experimentally investigate the possibility of improving RC by changing the construction of RC main element, as well as by using operating regime based on transient between the active and passive state of MARO.

Experimental setup

The block-diagram of a magnonic RC (MRC) based on a magnonic active ring oscillator is shown in Fig. 1(a). This concept was proposed in Ref. [3]. A spin-wave delay line (SWDL) based on yttrium iron garnet (YIG) film is used as a nonlinear node of the magnonic physical RC. The film is 5.2 μm thick, 15 mm long and 2 mm wide. A magnetic field of 760 Oe is applied to the film in its plane providing propagation of so-called magnetostatic surface spin wave (MSSW). The planar microwave waveguides are used as antennas for excitation and detecting of MSSW. Spin waves travelling in the film provides both the nonlinearity of the response and availability of short-term memory.

The feedback loop of the ring includes an electronically tunable attenuator (ETA), a microwave amplifier, a directional coupler, and a variable attenuator. The ETA is used to enter input data into the reservoir. Its attenuation coefficient depends on the voltage at its control ports. In order to fan out a small portion of the signal for analyzing it in the time domain, a directional coupler is used. We rectify the microwave signal with a zero-bias Schottky diode and register the rectified signal with an oscilloscope.

The improvement of RC performances can be achieved through increasing the MRC response amplitude and the spin wave relaxation time in the ring. Previously investigated MRC on MARO operated in self-generation regime. Due to this, the response amplitude was

limited by the available amplification gain range. The self-generation threshold determined the lower limit G_l of the range, and the spin wave modulation instability threshold set the upper limit G_h . As a result, the gain range was relatively small.

The use of a *metallized* yttrium iron garnet film allows increasing considerably the modulation instability threshold [6], thus increasing upper limit of ring gain. To make response amplitude even higher we have set the lower limit of gain to negative value, which means that self-generation stopped after the transition process finished. In this work, we experimentally investigate the dynamics in MAROs based on metallized and free (without metallization) films and compare the computational capabilities of the MRCs.

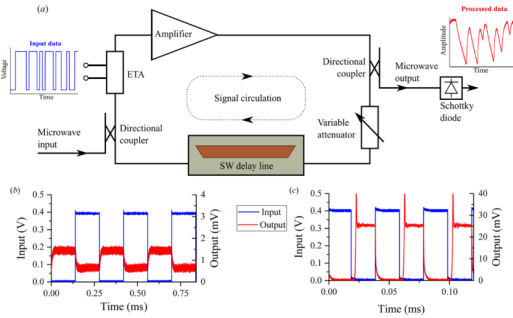


Figure 1. The MRC experimental setup (a); operating principles of the MRC for MARO based on free (b) and metallized (c) film. Panels demonstrate waveforms for the following gains: (b) - $G_h = 0.13$ dB, $G_l = 0.03$ dB; (c) - $G_h = 0.62$ dB, $G_l = -0.14$ dB.

Results and discussion

Figure 1(b,c) demonstrates the change of MRC response to the same periodical signal if we add metallization and change lower limit of gain to negative value. For example, maximum available amplitude of the MRC response for free film configuration is approximately 1 mV. Metallization of the film allows using higher value of G_h that increased maximum of response voltage from 1.5 mV up to 25 mV. Switching to negative gain G_l makes response voltage equal zero. It means that response amplitude increases 25 times. Worth mentioning that decreasing of lower limit of gain provides increase in MARO relaxation time as well as growth of MRC short-term memory. Therefore, using metallized film as a base for MRC and application of negative gain might give the higher MRC performances.

To study this, we employ the short-term memory (STM) task and the parity check (PC) task to evaluate the short-term memory and nonlinear properties of devices. These tasks characterize physical RCs by the value of capacity. Higher capacity means better RC. The STM capacity characterizes the memory effect only. The result of execution of the PC task depends on both short-term memory and nonlinearity. Details of the procedure of completing both tasks can be found in Ref. [4-6].

For both tasks, we use random binary pulse sequences consisting of 2000 bits as an input signal. The voltage corresponding to each bit of the sequence is applied to the control port of ETA during a fixed time interval T_{pulse} . We refer to this time interval as the pulse duration.

During the experimental investigation T_{pulse} was varied from 100 ns to 10 μ s. The values of G_h was set as close as possible to the modulation instability threshold. Higher value

of G_h in metallized configuration provides higher power of the signal circulating in the MARO, that makes nonlinearity of MRC higher. The values of G_l for both configuration were chosen according to the following. The maximum values of G_l translate into a response amplitude of at least 0.5 mV. The magnitude of the most negative G_l is roughly equal to the magnitude of the most positive G_l . In addition, we select two more G_l values slightly above or slightly below the self-generation threshold.

Obtained results show that increase of pulse duration leads to decrease of STM capacity and increase of PC capacity. The reason for this behavior is that the reservoir's memory depth is limited by the time of transition between the steady states, which corresponds to G_h and G_l . By the end of the transition time, the memory contents are erased. Thus, when using shorter pulses, it is possible to fit more pulses in the transition time which is equivalent to growth of short-term memory. In contrast, if the input pulses are too short, there is not enough time for the nonlinearity of the ring response to them to develop. This yields PC capacity values below 1. An increase of the pulse duration makes the shape of the output waveforms more complex. This increases the PC capacity.

Figures 4(a) and 4(b) demonstrate the influence of the ring gain G_l on the STM and PC capacities. Input pulse durations for the graphs are 0.1, 0.2 and 5 μ s. Increasing the gain yields a slight decrease in the capacities due to decrease of relaxation time. For MRC based on the metallized film, the largest values of the capacities are observed for G_l values well below the self-generation threshold. The maximum registered STM and PC capacities are 2.15 and 1.17, respectively.

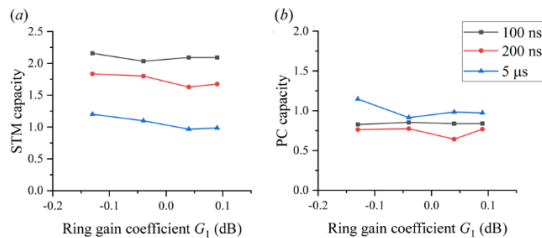


Figure 2. Influence of the ring gain coefficient G_l on the capacities for the metallized film configuration (a) and free film configuration (b)

Acknowledgements

The work of St. Petersburg Electrotechnical University was supported by the Ministry of Science and Higher Education of the Russian Federation (grant number No. FSEE-2020-0005).

References

1. K. Nakajima, I. Fischer. Reservoir computing. – Springer, Singapore, 2021.
2. G. Tanaka, et al. – Neural Networks, 115, 100-123 (2019).
3. S. Watt, and M. Kostylev. – Physical Review Applied, 13, 034057 (2020).
4. A. A. Nikitin, A. A. Nikitin, A. B. Ustinov, S. Watt, and M. P. Kostylev. – Journal of Applied Physics, 131, 113903 (2022).
5. A. V. Kondrashov, A. A. Nikitin, A. A. Nikitin, M. Kostylev, and A. B. Ustinov. – Journal of Magnetism and Magnetic Materials, 563, 169968 (2022)
6. A. E. Kozin, A. B. Ustinov. – Technical Physics, 64, 265-269 (2019)

Identification of glucofrangulin A in *Rhamnus frangula* L. by ^1H NMR spectroscopy.

Vasilij G. Vasil'ev, Anzhelika V. Sheremeta, Vasilij A. Ivlev, Sergey V. Goryainov, Luiza A. Miridonova, Alina Y. Polukhina, Anastasia A. Murtazina, Ekaterina A. Krivosheeva
¹Peoples' Friendship University of Russia (RUDN University), 6 Miklukho-Maklaya Street, Moscow, 117198, Russian Federation
 E-mail: krikate2000@mail.ru

Introduction

According to the Russian State Pharmacopoeia (Edition 14), thin-layer chromatography is the main method for determining the authenticity of *Ramnus frangula* L. raw material [1]. Widespread methods for qualitative and quantitative assessment of the content of the main biologically active substances in the plant under study, described in the literature are spectrophotometric methods, such as UV spectroscopy and chromatographic methods, in particular HPLC. However, all the presented methods have a number of significant disadvantages, among which are time-consuming, multi-step sample preparation and the necessity to have and use standard samples. The recent ones are often quite expensive, as well as difficult to obtain in the current logistics of imported international supplies. In this work, an alternative method of NMR spectroscopy is proposed for the identification of target analytes, which does not need authentic standard samples and also does not require difficult sample preparation.

Rhamnus frangula

Rhamnus frangula (*Frangula alnus* Mill. syn. *Ramnus frangula* L.) is a shrub usually up to 7 m high [2,3]. It is a light-loving species that thrives in temperate forests, mainly in slightly acidic, moist soils. *Ramnus frangula* L. has been used in folk medicine due to its extremely laxative effect of the bark or decoctions of the black berries since the Middle Ages [4].

The dried bark of the stem and branches contains anthraquinone compounds (derivatives of emodol, chrysofanol, frangulin, frangulosides A and B, formed as a result of partial hydrolysis of glycofrangulosides A and B), alkaloids such as arcepavine, tannins and flavonoids [5,6]. The main biologically active compounds are atracene derivatives - emodin, frangulin A, frangulin B, glucofrangulin A and glucofrangulin B.

Identification of glucofrangulin A

Ramnus frangula L. is a medicinal plant that is rich in glucofrangulin compounds. These compounds have been shown the importance for human health in gastrointestinal tract [7,8].

This study attempted to identify and semi-quantitatively determine glucofrangulin A in *Ramnus frangula* L. extract by ^1H NMR spectroscopy.

The solvent used in this work was dimethyl sulfoxide- d_6 ($\geq 99.9\%$, Sigma-Aldrich, CAS No. 2206-27-1) and a commercial sample of *Ramnus frangula* L.

The main experiment was carried out on a JNM ECA-600 NMR spectrometer (JEOL, Japan) with an operating frequency for protons of 600 MHz under the following conditions: relaxation delay - 10 sec., points - 32768, sweep - 22 ppm, acquisition time - 1.98 sec., scans - 16, angle - 45°.

Post-registration processing of ^1H NMR spectra was analyzed using Delta IV software (Japan). The phase, baseline and signal integration were adjusted manually.

Identification of organic substances by ^1H NMR spectroscopy is obtained either by comparing the spectrum of the analyzed compound with the spectrum of a standard sample, or

by matching the spectral characteristics of the test sample with the data described in the literature. We chose the second option, since we did not have the required standard samples of anthracene derivatives.

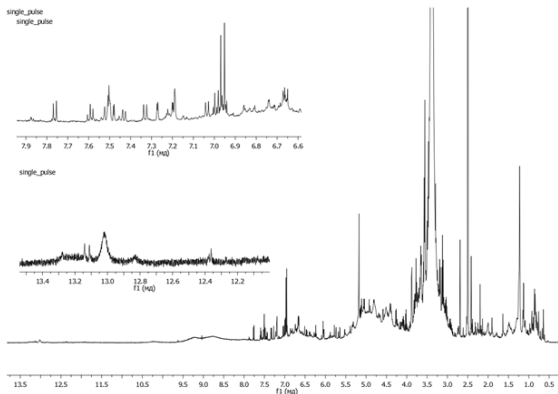


Figure 1. ^1H NMR spectrum of *Ramnus frangula* L. in DMSO-d_6 also shows increased spectrum fragments of 6.6 - 7.9 ppm and 12.2 - 13.4 ppm

To identify glucofrangulin A, signals from its protons at positions H-7, H-5 and OH-1 were used, appearing at 7.28 and 13.00 ppm, consequently. We selected a signal at 7.26 ppm for the quantitative determination of glucofrangulin A in the extract of *Ramnus frangula* L.

For the quantitative determination of glucofrangulin A, the signal of residual protons of DMSO-d_6 solvent, which was pre-calibrated using a standard sample of benzoic acid, was chosen as a comparison signal.

Quantification was performed by comparing the integrated intensities of the target bioactive agent with the DMSO-d_6 residual proton signal.

The content of glucofrangulin A in the tested commercial sample of *Ramnus frangula* L. is determined equal to 2.09 ± 0.07 %.

Considering the area from 11.7 to 13.5 ppm ^1H NMR spectrum of *Ramnus frangula* L. extract in DMSO-d_6 , where protons of hydroxyl groups in positions 1 and 8 of anthraquinone derivatives appear, since they form an intramolecular hydrogen bond with the oxygen of the neighboring carbonyl group, we can conclude that the extract under study contains at least 8 more anthraquinone derivatives, which could be determined using these signals if their standard samples were available.

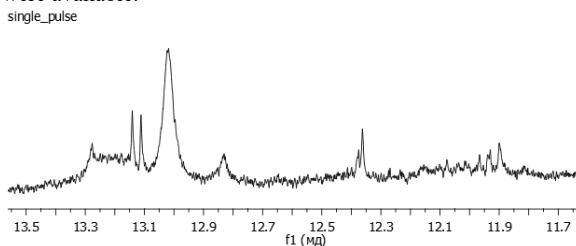


Figure 2. Selected area 11.7 - 13.5 ppm ^1H NMR spectrum of *Rhamnus frangula* in DMSO-d_6 .

Practical application

In summary, there are several analytical techniques that can be used to identify and characterize the glucofrangulin compounds of *Ramnus frangula* L. including HPLC, LC-MS, FTIR spectroscopy, NMR spectroscopy. These techniques can provide valuable information about the structure, composition, and properties of the anthraquinones compounds, which can be used to better understand their biological activities and potential health benefits.

It is proposed to use this approach for determination of glucofrangulin A in extracts from leaves of *Rhamnus frangula* L. by ^1H NMR spectroscopy as an alternative method for the qualitative determination. Using the considered signals, it is also possible to quantify the glucofrangulin A content in *Ramnus frangula* L. by ^1H NMR spectroscopy because this method is free from complicated sample preparation, derivatization and the need for standard samples.

Acknowledgements

This paper has been supported by the RUDN University Strategic Academic Leadership Program.

References

1. Russian State Pharmacopoeia (Edition 14). Available at: <https://docs.rucml.ru/feml/pharma/v14/vol4/>
2. T. G. Tutin, Flora Europaea, Volume 2: Rosaceae to Umbelliferae, T. G. Tutin, et al., eds. (Cambridge University Press, 1968), p. 245.
3. C. Gucker, Frangula alnus. Fire Effects Information System (2008). Available at: <http://www.feis-crs.org/feis>
4. G. Hatfield, Hatfield's Herbal: The Curious Stories of Britain's Wild Plants (Penguin, UK, 2009).
5. CABI, Frangula alnus (alder buckthorn) (2015). Invasive Species Compendium. Available at: <http://www.cabi.org>
6. G. del Campo, I. Berregi, R. Caracena, J. I. Santos. Quantitative analysis of malic and citric acids in fruit juices using proton nuclear magnetic resonance spectroscopy. Anal. Chim. Acta. – 2006, 556, pp. 462–468.
7. K. Bolmgren, O. Eriksson. Oikos 124, 639 (2015).
8. A. Tardieu, W. De Man, H. This. Using one-dimensional (1D) and two-dimensional (2D) quantitative proton (^1H) nuclear magnetic resonance spectroscopy (q NMR) for the identification and quantification of taste compounds in raw onion (*Allium cepa* L.) bulbs and in aqueous solutions where onion tissues are soaked. Anal. Bioanal. Chem. – 2010, 398, pp. 3139–3153.

Novel membranes based on poly(ester-block-amide) modified with Ho-MOFs.

Anna I. Kuzminova¹, Anna S. Karyakina¹, Maria E. Dmitrenko¹, Semen S. Egorov¹, Anton S. Mazur¹, Anastasia V. Penkova¹

¹Saint Petersburg State University, Saint-Petersburg, Russia

E-mail: a.kuzminova@spbu.ru

<https://go.spbu.ru/rgpenkova>

Introduction

Pervaporation is one of the most popular membrane processes that allows the separation of low molecular weight components, including isomer mixtures, azeotropic mixtures, and thermally unstable mixtures. Besides high selectivity, pervaporation is an environmentally-friendly and low energy consuming process with inexpensive and compact equipment. The rapid development of pervaporation requires the search for novel membrane materials with desired properties. One of the effective methods for improving the transport properties of pervaporation membranes is the development of the mixed – matrix membranes (MMMs). The development of MMMs consists in modification of the polymer matrix by introduction of an inorganic filler, that leads to getting tailoring properties. MMMs combine the simplicity of preparation of polymer membranes with the superior properties of inorganic particles.

Results

In the present work the novel membranes based on poly(ester-block-amide) (PEBA) were prepared by introducing in the polymer matrix the Ho-based metal-organic frameworks (Ho-MOFs): Ho-1,3,5-H₃btc, Ho-1,2,4-H₃btc, Ho-1,2-H₂bdc, Ho-1,3-H₂bdc, Ho-1,4-H₂bdc. The improvement of the transport properties of the PEBA/Ho-MOFs membranes was expected due to the structure and hydrophilic/hydrophobic properties of the Ho-MOFs. The characterizations of the polymer samples were studied by nuclear magnetic resonance (NMR), Fourier-transform infrared spectroscopy (FTIR), scanning electron microscopy (SEM), atomic force microscopy (AFM), thermogravimetric analysis (TGA), swelling experiments, and contact angle measurement. Transport properties of the developed membranes were investigated for water treatment by pervaporation.

Acknowledgements

This research was funded by the Russian Science Foundation, grant number 23-29-00473, <https://rscf.ru/en/project/23-29-00473/>. The experimental work of this study was facilitated by the equipment from the Resource Centre of Geomodel, Chemical Analysis and Materials Research Centre, Centre for X-ray Diffraction Methods, Magnetic Resonance Research Centre, Centre for Innovative Technologies of Composite Nanomaterials, Nanophotonics Centre, Computer Centre, Cryogenic department, Thermogravimetric and Calorimetric Research Centre and the Interdisciplinary Resource Centre for Nanotechnology at the St. Petersburg State University.

Investigation of the interaction of polyvinyl alcohol and tetraethoxysilane in dimethyl sulfoxide by NMR spectroscopy

Olga S. Lezova^{1,*}, *Ruslan I. Baichurin*², *Olga A. Shilova*^{1,3,4}, *Alexandra G. Ivanova*¹, *Stanislav I. Selivanov*^{5,1}

¹ *Institute of Silicate Chemistry of the Russian Academy of Sciences, 199034, Russia, St. Petersburg, nab. Makarova, 2*

² *Herzen State Pedagogical University of Russia, 191186, St. Petersburg, Moika Emb., 48*

³ *St. Petersburg State Electrotechnical University "LETI" named after V.I. Ulyanov (Lenin), 197376, Russia, St. Petersburg, Professora Popova str., 5*

⁴ *St. Petersburg State Institute of Technology (Technical University), 190013, Russia, St. Petersburg, Moskovsky Prospekt, 26*

⁵ *Laboratory of Biomolecular NMR, St. Petersburg State University, 199034, Russia, St. Petersburg, Moika River embankment 48*

E-mails: ^{1,}os_zar@mail.ru; ⁵nmr.group.spbu@gmail.com*

Introduction

The development of a competitive ion-conducting membrane material for a hydrogen-air solid polymer fuel cell (SPFC) is a fairly urgent task [1, 2]. Ion-conducting membranes for SPFC can be divided into three main groups: membranes based on perfluorinated sulfonated polymers, membranes based on polycondensation polymer systems and hybrid (organo-inorganic) membranes. The most interesting of them are hybrid membranes, which contain inorganic components in the polymer matrix, including those obtained by hydrolysis and condensation of tetraethoxysilane (TEOS), which contribute to an increase in moisture capacity, temperature and chemical stability of the membrane material [3]. Currently, a significant number of foreign and domestic scientific groups are engaged in the development of ion-conducting hybrid membranes based on various polymer materials – sulfonated or phosphorylated aromatic and aliphatic polymers [4]. As a rule, to achieve sufficient proton conductivity aromatic polymers require a high level of sulfation, which is due to the low acidity of the sulfogroups in the aromatic ring. Such a high level of sulfonation usually makes them excessively swollen and even soluble in water, which can lead to the loss of mechanical strength [5, 6]. Aliphatic polymers, on the contrary, are sulfated moderately. The ion-conducting membrane material based on a modified aliphatic polymer polyvinyl alcohol (PVA) is quite promising. Such material is technologically advanced and, after its modification, has high ionic conductivity, thermal stability and a fairly low cost.

The analysis of the literary data showed a limited number of scientific publications devoted to the production and study of hybrid membranes based on sulfonated PVA modified by TEOS in an aqueous medium [7, 8], and practically no scientific articles aimed at studying the interaction of PVA and TEOS in an organic medium – dimethyl sulfoxide (DMSO). The analysis of such systems is most carried out by using the methods of liquid-phase/solid-phase nuclear magnetic resonance (NMR) spectroscopy.

Previously, using the liquid-phase synthesis method, we obtained an ion-conducting hybrid membrane material based on furfural-crosslinked PVA modified by aminosulfonic acid (ASA) and TEOS and studied its composition and structure using ¹H NMR spectroscopy. However, due to the multicomponent nature of the system, it was not possible to determine exactly how the process of interaction between PVA and TEOS proceeded. Since this process underlies the synthesis of new ion-conducting hybrid membranes based on PVA, obtaining at

least qualitative or even semi-quantitative information about the mechanism of their interaction by NMR spectroscopy methods could provide additional useful information about possible ways to improve the performance of the finished membrane material.

The purpose of this work was to obtain and study the PVA-TEOS model system in DMSO- d_6 with and without distilled water using one-dimensional (^1H , ^{13}C) and two-dimensional (COSY, J-COSY and NOESY) liquid-phase NMR spectroscopy. Three the model systems with different ratio of components were selected (Table 1).

Table 1. Ratio of components of the PVA-TEOS model system

Sample 1	Sample 2	Sample 3
PVA 0.0022 g + TEOS 5 μl in DMSO- d_6	PVA 0.0022 g + TEOS 5 μl + H $_2$ O 5 μl in DMSO- d_6	PVA 0.0023 g + TEOS 10 μl in DMSO- d_6

Experiments and results

Figure 1 shows the NMR (^1H and ^{13}C) and 2D spectrum J-COSY of the system PVA-TEOS (Sample 3) in DMSO- d_6 , obtained on a 400 MHz spectrometer at room temperature for 2 days after mixing the components. They indicate the presence of 3 types of OH group signals, which are designated by the letters “a”, “b” and “c” and belong to the PVA proton. Moreover, each of these groups consists of several overlapping doublet signals with the same values of the vicinal constants $^3J_{(\text{HO-CH})}$, but different for “a”-, “b”- and “c”- signals in the following sequence: $^3J_{(\text{HO-CH})}^{\text{a}} < ^3J_{(\text{HO-CH})}^{\text{b}} < ^3J_{(\text{HO-CH})}^{\text{c}}$ (Figure 1-1). This is clearly visible in a fragment of the J-COSY spectrum (Fig. 1-2), which shows the exact values of these constants from 3.9 to 6.0 Hz. The total intensity of all OH signals in the region of 4.7 – 4.1 ppm. is comparable with the intensity of the broadened O-CH- signal of PVA protons in the region of 3.9 – 3.7 ppm. and is 2 times less than the total intensity of the broadened signals in the region of 1.6 – 1.1 ppm, belonging to the protons of -CH $_2$ - groups of PVA.

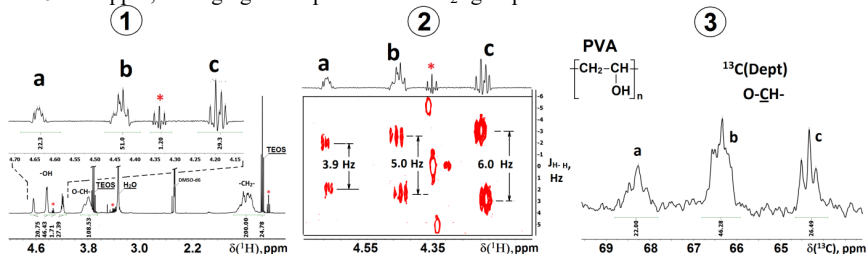


Figure 1. ^1H NMR spectrum (1), fragments of the J-COSY (2) and ^{13}C (DEPT-135) (3) spectra of the PVA-TEOS system in DMSO- d_6 , recorded during the first two days after the preparation of sample 3 (ethanol (EtOH) is formed by the reaction of PVA with TEOS and spectra its signals are depicted by red asterisk)

In the ^{13}C NMR spectrum in the region of 69 – 63 ppm, which contains carbon signals of O-CH groups, as well as in the proton spectrum, three signals with a complex structure are observed at 68, 66 and 64 ppm. Based on this, we can conclude that PVA is a structurally heterogeneous polymer. This can be explained by the fact that in dimethyl sulfoxide strong hydrogen bonds arise between PVA and the solvent, which significantly slow down the rate of OH-proton exchange and the vicinal constants $^3J_{\text{OH-CH}}$ are observed in the form of doublets. In addition, hydrogen bonds apparently cause a downfield shift of the OH group proton signal by 0.5 ppm. and a decrease in the vicinal constant $^3J_{\text{OH-CH}}$ by approximately 2 Hz while going from stereoisomer “c” to “a”.

Good resolution of the signals of OH protons of stereoisomers “a” – “c” made it possible to determine the position of the signals of O-CH- and -CH₂- groups in the overlapping regions of 4.7 – 4.1 (Fig. 2-1) and 1.6 – 1.1 ppm. (Fig. 2-2), respectively, with the help of COSY method. In the EXSY-NOESY spectrum, along with exchange cross-peaks between the signals of OH-protons (including water), NOE cross-peaks of the same positive polarity as the exchange cross-peaks are observed between the signals of OH-protons and the signals of O-CH- and -CH₂- group. The coincidence of the sign of the exchange and NOE cross-peaks indicates the negative Overhauser effects and the polymeric nature of PVA existing under conditions of the spin diffusion limit ($\omega_0\tau_c > 1$) [9].

NMR analysis of the PVA-TEOS system also showed that the process of their interaction includes the formation of one (or more) intermediate products and proceeds depending on the ratio of these components with different rates. To prove this, experimental dependences of the composition of the PVA-TEOS system on time were obtained for all three samples, which lasted for six months (Fig. 2-4 and 2-5).

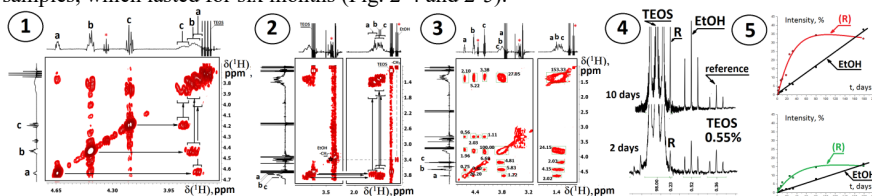


Figure 2. Fragments of COSY (1 and 2) and EXSY-NOESY (3) spectra of PVA-TEOS system in DMSO-*d*₆, recorded during the first two days after the preparation of the sample 3. High-field part of ¹H NMR spectrum of the sample 1 after two and ten days (4) and (5) – dependences of triplet intensities on the time for intermediate R and product EtOH measured relatively to ¹³C_α-satellite triplet of TEOS for sample 1 (high) and sample 2 (low)

Conclusion

In the PVA-TEOS system in DMSO-*d*₆ the multiplet structure of the signals of hydroxyl protons was discovered and studied using NMR methods, which made it possible to identify the overlapping signals of the corresponding methine and methylene protons of PVA. The formation of the intermediate (R) with low molecular weight and the final (EtOH) product of the interaction of PVA with TEOS in DMSO-*d*₆ was discovered and their complete NMR identification was carried out.

Acknowledgments

This work was within the framework of the topic of the state assignment № 1023033000122-7-1.4.3. S.I.S. acknowledges Saint-Petersburg State University for a research grant 116883049. Physicochemical studies were carried out using the equipment of the Center for Collective Use «Physical and chemical methods for the study of nitro compounds, coordination, biologically active substances and nanostructured materials» of the Interdisciplinary Resource Center for Collective Use «Modern physical and chemical methods for the formation and study of materials for the needs of industry, science and education» of Herzen State Pedagogical University of Russia.

References

1. G.G. Gagliardi, A. Ibrahim, D. Borello, A. El-Kharouf. – *Molecules*. 2020. V. 25(7). Art. № 1712. DOI: 10.3390/molecules25071712.
2. U.M. Zavorotnaya, I.I. Ponomarev, Y.A. Volkova, V.V. Sinitsyn. – *Membranes*. 2023. V. 13(5). Art. № 485. DOI: 10.3390/membranes13050485.
3. N. Mahato, H. Jang, A. Dhyani, S. Cho. – *Polymers*. 2020. V. 12(11). Art. № 2480. DOI: 10.3390/polym12112480.
4. R.R. Choudhury, J.M. Gohil, K. Dutta. – *Polymers for Advanced Technologies*. 2021. V. 32(11). P. 4175-4203. DOI: 10.1002/pat.5431.
5. W. Li, A. Manthiram. – *J. Power Sources*. 2010. V. 195(4). P. 962-968. DOI: 10.1016/j.jpowsour.2009.08.096.
6. C.Y. Wong, W.Y. Wong, K.Sh. Loh, W.R. Wan Daud, K.L. Lim, M. Khalid, R. Walvekar. – *Polymer reviews*. 2019. V. 60(1). P. 171-202. DOI: 10.1080/15583724.2019.164151.
7. Y.-N. Zhao. – *e-Polymers*. 2013. P. 115-123. DOI: 10.1515/epoly.2013.2013.1.115
8. J. Muller, B. Prelot, J. Zajac, S. Monge. – *Reactive and Functional Polymers*. 2019. V. 144. Art. № 104364. DOI: 10.1016/j.reactfunctpolym.2019.104364.
9. V.A. Likić. – *Concepts in Magnetic Resonance*. 1996. V. 8(6). P. 423-436. DOI: 10.1002/(SICI)1099-0534(1996)8:6<3C423::AID-CMR3%3E3.0.CO;2-0.

All-optical scanning spectroscopy of anti crossing of electron and nuclear spin levels in a SiC crystal of hexagonal polytype

Kirill V. Likhachev, Igor.P. Veyshkort, Maxim.V. Uchaev, Anastasia.V. Batueva, Valentina.V. Yakovleva, Alexander.S. Gurin, Roman.A. Babunts, Pavel.G. Baranov
 Ioffe Institute, 194021 St. Petersburg, Russia

The wide-gap semiconductor silicon carbide (SiC) has a family of quartet spin color centers (V-centers, spin $S=3/2$), in which a unique mechanism of optically induced alignment (polarization) of the populations of spin levels at room temperature and above - up to 300 °C is realized. The main polytype for applications in quantum technologies is 4H-SiC, in which spin centers with $S=3/2$ with the mentioned properties are realized [1-4].

Optically induced spin alignment allows optical detection of magnetic resonance (ODMR) and optical registration of level anticrossing (LAC) signals by photoluminescence (PL) intensity, the latter not requiring microwave power [5, 6]. The technique of optical detection of spin transitions leads to a gigantic increase in sensitivity, up to the ability to detect single spins at room temperature [7, 8]. LAC spectroscopy of spin centers with $S=3/2$ in SiC is a promising tool for creating magnetic field and temperature sensors with the possibility of spatial resolution in the submicron range, as well as for magnetic field sensors operating under high temperature and radiation conditions, including outer space [9].

We present the results of the study of coloring centers with spin $3/2$ in hexagonal polytype 4H-SiC. Centers with spin $S=3/2$ were introduced into a single crystal of 4H-SiC with low nitrogen concentration by irradiating the crystal with electrons of 2 MeV energy and $\sim 10^{18}$ cm⁻² flux. It is accepted to denote the coloring centers with spin $S=3/2$ by the corresponding zero-phonon lines (ZPLs); in our experiments we study V2 centers in 4H-SiC.

Fig. 1 (a) shows the LAC signals for spin V2 centers, $S=3/2$, in the ground state (GS) recorded in the $B \parallel c$ orientation at room temperature from the change in photoluminescence intensity in a 4H-SiC single crystal with natural isotope content. The upper spectrum (blue color) corresponds to the LAC signals as a derivative of the magnitude of the varying magnetic field with an amplitude of ~ 0.1 Gs. The lower spectrum (red color) represents the LAC signals recorded using low-frequency modulation of the intensity of the excitation laser light. The upper part (Figure 1 b) shows a schematic of energy levels in the magnetic field for even-numbered silicon isotopes with zero nuclear magnetic moment: $S=3/2$, $I=0$, $D=35$ MHz= 11.7×10^{-4} cm⁻¹, $\Delta=2D=70$ MHz= 23.4×10^{-4} cm⁻¹. The lower part of the figure (Fig. 1 (c)) shows the scheme of energy levels in the magnetic field taking into account the superfine interactions with one nucleus of ²⁹Si isotope located in the second coordination sphere relative to the silicon vacancy included in the spin center (SiNNNN): $S=3/2$, $I=1/2$, $A=9$ MHz= 3×10^{-4} cm⁻¹= 3.2 G.

In this work we demonstrate all-optical spectroscopy of superfine interactions under ambient conditions in a SiC crystal with natural isotope content. All possible anti-crossings of spin levels in the ground state in the system of superfine interactions with one nucleus of the silicon isotope ²⁹Si falling into the second coordination sphere relative to the silicon vacancy included in the structure of the quartet spin center have been registered. The effect of purely nuclear transitions on the photoluminescence intensity of the quartet spin centers was found. The presented studies open the possibility for all-optical spectroscopy of superfine interactions in a wide range of quartet spin centers in other SiC polytypes. There is a suggestion that based on the spectroscopy of superfine interactions a new unique direction for the development of

sensors with all-optical vector magnetometry with micron and submicron spatial resolution will be developed.

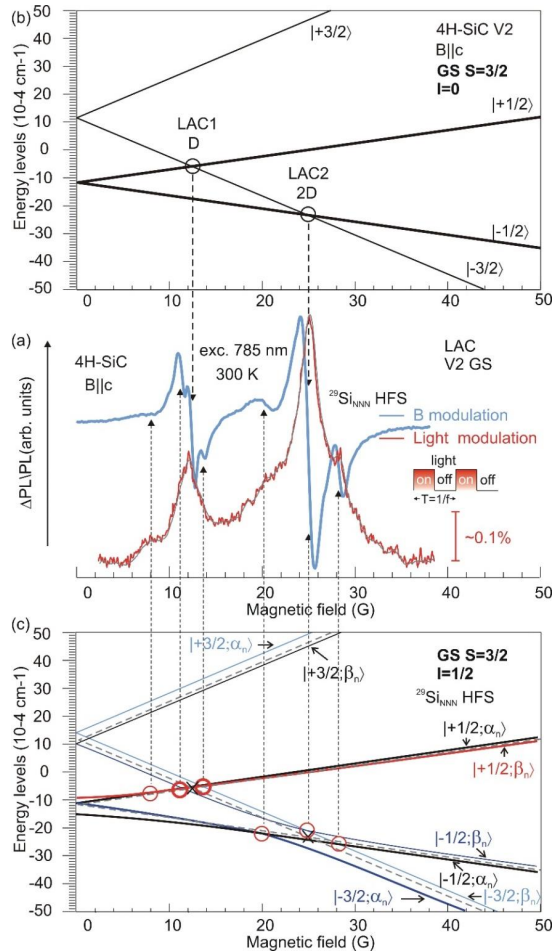


Figure 1. (a) LAC level anti crossing signals recorded from the change in the FL intensity of V2 spin centers in the ground state (GS) in 4H-SiC single crystal with natural isotope content. The upper spectrum (in blue) shows the LAC signals as a derivative of the magnitude of the scanning magnetic field recorded with low-frequency modulation of the magnetic field (amplitude ~ 0.1 Gs); the lower spectrum (in red) shows the LAC signals recorded using low-frequency modulation of the excitation laser light intensity. (b) Schematic of energy levels in a magnetic field for even-numbered silicon isotopes. (c) Schematic of energy levels in the magnetic field taking into account superfine interactions with a single nucleus of the ^{29}Si isotope.

Acknowledgements

This work was supported by the Russian Science Foundation № 23-12-00152 (<https://rscf.ru/project/23-12-00152/>)

References

1. P. G. Baranov, I. V. Il'in, E. N. Mokhov, M. V. Muzafarova, S. B. Orlinskii, J. Schmidt, JETP Lett. **82**, 441 (2005).
2. P. G. Baranov, A. P. Bundakova, I. V. Borovykh, S. B. Orlinskii, R. Zondervan, J. Schmidt, JETP Lett. **86**, 202 (2007).
3. P. G. Baranov, A. P. Bundakova, A. A. Soltamova, S. B. Orlinskii, I. V. Borovykh, R. Zondervan, R. Verberk, J. Schmidt, Phys. Rev. B **83**, 125203 (2011).
4. W. F. Koehl, B. B. Buckley, F. J. Heremans, G. Calusine, and D. D. Awschalom, *Science*, **332**, 84 (2011).
5. A. N. Anisimov, R. A. Babunts, S. V. Kidalov, E. N. Mokhov, V. A. Soltamov, P. G. Baranov, Spin Centers in SiC for All-Optical Nanoscale Quantum Sensing under Ambient Conditions, JETP Letters **104**, 82–87 (2016).
6. D. Simin, V. A. Soltamov, A. V. Poshakinskiy, A. N. Anisimov, R. A. Babunts, D. O. Tolmachev, E. N. Mokhov, M. Trupke, S. A. Tarasenko, A. Sperlich, P. G. Baranov, V. Dyakonov, G. V. Astakhov, All-Optical dc Nanotesla Magnetometry Using Silicon Vacancy Fine Structure in Isotopically Purified Silicon Carbide, Phys. Rev. X **6**, 031014 (2016).
7. M. Widmann, S.-Y. Lee, T. Rendler, N. T. Son, H. Fedder, S. Paik, L.-P. Yang, N. Zhao, S. Yang, I. Booker, A. Denisenko, M. Jamali, S. A. Momenzadeh, I. Gerhardt, T. Ohshima, A. Gali, E. Janzen, and J. Wrachtrup, Nat. Mater. **14**, 164 (2015).
8. P. G. Baranov, H.-J. von Bardeleben, F. Jelezko, J. Wrachtrup, Magnetic Resonance of Semiconductors and Their Nanostructures: Basic and Advanced Applications (Springer Series in Materials Science, Volume 253, Springer-Verlag GmbH Austria, 2017) Chap. 6.
9. C. J. Cochrane, J. Blacksberg, M. A. Anders, P. M. Lenahan, Vectorized magnetometer for space applications using electrical readout of atomic scale defects in silicon carbide, Scientific Reports **6**, 37077 (2016).

Synthesis and ^1H - ^1H spectroscopy NOESY studies of (*E*)-(2-chloro-2-phenylvinyl)diaminophosphine oxide

*Lobova A.M.*¹, *Egorova A.V.*², *Egorov D.M.*¹, *Baichurin R.I.*³

¹ St. Petersburg State Institute of Technology (Technical University), St. Petersburg, Russia

² St. Petersburg Federal Research Center of the Russian Academy of Sciences, St. Petersburg, Russia

³ Herzen State Pedagogical University of Russia, St. Petersburg, Russia

E-mail: diekerze54@gmail.com

Introduction

As sure as a two of the most useful methods for determination and confirmation structures of compounds are – X-ray diffraction and the NMR spectroscopy. The benefit of the second method is the possibility to carried out in solutions and in the crystalline state. Also NMR is giving possibilities for studding the weak magnetic interactions.

Results and Discussion

Here we investigate the reaction between secondary aliphatic amines and β -chlorophenylvinylphosphonic acid dichloride (Fig. 1).

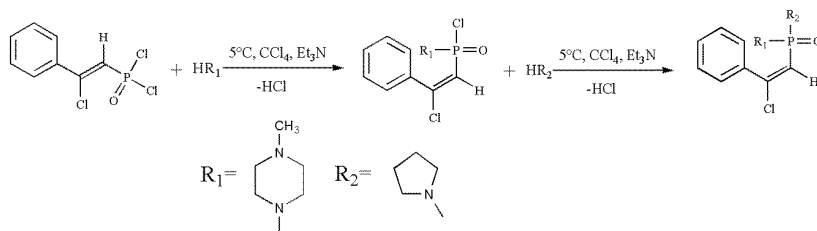


Figure 1. Scheme for the synthesis of (*E*)-(2-chloro-2-phenylvinyl)diaminophosphine oxide

Previously, using two-dimensional ^1H - ^1H NOESY spectroscopy, it was proven that in the reaction of β -chlorophenylvinylphosphonic acid dichloride with various aliphatic alcohols, *Z*-isomers of *O*-functionalized phosphonates are selectively formed [1]. Thus, in the ^1H - ^1H NOESY spectrum of di(prop-2-yl) [(*Z*)-2-chloro-2-phenylethenyl]-phosphonate, there is nuclear Overhauser effect between the *ortho*-proton of the aromatic ring and the =CH moiety (Fig. 2). For the *E*-isomer, such effect is not possible.

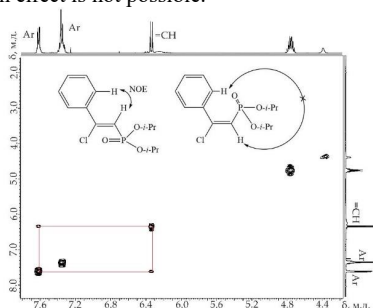


Figure 2. ^1H - ^1H NOESY di(prop-2-yl) [(*Z*)-2-chloro-2-phenylethenyl]-phosphonate

We assumed that the reaction of aliphatic amines with β -chlorophenylvinylphosphonic acid dichloride would proceed with the formation of products of a similar structure. But in contrast, the synthesis of substituted diaminephosphine oxide is characterized by the formation of the *E*-isomer, as evidenced by the absence of a cross-peak between the proton of the vinyl bond and the proton of the phenyl ring, as in Fig. 2. However, the initially selected parameters with a mixing time of 0.5 sec did not allow us to accurately establish the correlation of signals between the vinyl fragment and the protons of secondary amines. When the mixing time was increased to 1 sec, a cross-peak of the proton of the vinyl bond and the multiplet corresponding to the proton of the pyrrolidine ring closest to the phosphorus atom could be observed in the $^1\text{H} - ^1\text{H}$ NOESY spectrum (Fig. 3).

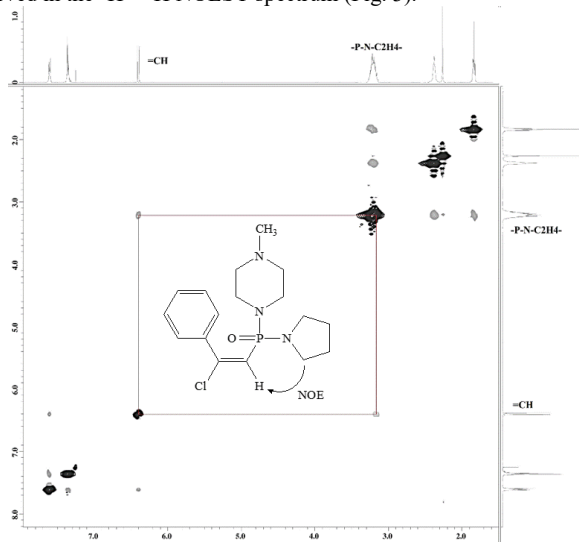


Figure 3. $^1\text{H} - ^1\text{H}$ NOESY of (*E*)-(2-chloro-2-phenylvinyl)diaminephosphine oxide

This ratio of cross-peaks indicates that the primary attack by a secondary aliphatic amine on the acid chloride molecule of β -chlorophenylvinylphosphonic acid occurs at the chlorine atom located closer to the double bond.

The use of two-dimensional $^1\text{H} - ^1\text{H}$ spectroscopy NOESY has proven itself as a method for monitoring the structure of the resulting phosphonate. In the course of further research, it will be used to establish at what point isomerization occurs; monitoring on the ^{31}P nucleus will perhaps make it possible to understand through which intermediate structures the reaction proceeds.

Acknowledgements

This study was supported by within the state assignment of Ministry of Education and Science of the Russian Federation for 2022-2024 (No. 122041100086-5).

References

1. A. V. Egorova, D. M. Egorov, N. O. Sonin, I. E. Kolesnikov, D. V. Pankin, A. A. Manshina, R. I. Baichurin, – *Russ. J. Gen. Chem*, 92, 92, 2191–2196 (2022).

Molecular dynamics simulation of sulfur compound extraction from a model fuel

Kenan K. Mammadhasanov¹, Andrei V. Komolkin¹, Sabina A. Seidova², Minaver D. Ibragimova², Vagif M. Abbasov², Huseyn J. Huseynov²

¹Faculty of Physics, Saint Petersburg State University, 199034, St. Petersburg, Russia

²Y. H. Mammadaliyev Institute of Petrochemical Processes of Ministry of Science and Education of Republic of Azerbaijan, AZ 1025, Baku, 30 Khojaly ave., Azerbaijan

E-mail: mammadhasanov@yandex.ru

E-mail: sabina.seidova.ai@mail.ru

Introduction

The current stage of oil refining and petrochemicals development is characterized by increasing attention of scientists and practitioners to the development of pollution-free technologies. Such directions include technologies for purification of oil fractions for various purposes by liquid extraction with the use of ionic liquids as solvents, which have a complex of specific properties due to the unique combination of cations and anions in them.

Sulfur compounds are one of the main sources of sulfur dioxide, which is a pollutant of the atmosphere, and therefore strict limits on their content in fuels have been adopted worldwide.

Many review articles are known to show the extraction potential of ionic liquids in the process of fuel desulfurization [1]. In particular, the use of ionic liquids in the processes of extraction, oxidative and combined desulfurization of diesel fraction has been investigated. It was established that high degree of extraction of high molecular weight sulfur compounds (thiophene derivatives) in the process of hydrodesulfurization at mild conditions is impossible.

To select the optimal extractant and to understand its high extraction capacity with respect to the undesirable fuel components to be removed, a molecular dynamic modeling method is used [2]. In paper [3] the process of desulfurization of thiophene and benzothiophene from the composition of model fuel (dodecane) by various imidazolium-based ionic liquids was studied by molecular dynamic method and the influence of the cation alkyl chain length and anion type on the desulfurization degree was shown.

Research work carried out at the Institute of Petrochemical Processes on extraction purification of oil fractions using different ionic liquids as an extractant showed high extraction ability of the ionic liquid based on N-methylpyrrolidone and acetic acid – N-methylpyrrolidonium acetate.

Taking into account that the ionic liquid N-methylpyrrolidonium acetate is obtained by chemical modification of the extractant used on an industrial scale – N-methylpyrrolidone, comparative studies were carried out to determine the efficiency of the process of extraction purification of diesel fraction with both extractants. The results of these studies indicated a relatively high selectivity of the ionic liquid to undesirable sulfur compounds of real and model fuels.

Computer model

In order to reveal the principle of extraction of heterocyclic sulfur compounds from the model fuel composition by the molecular dynamics method, the process of extraction purification of the system n-hexane, thiophene, meta-xylene (1,3-dimethylbenzene) and N-methylpyrrolidonium acetate and N-methylpyrrolidone was modeled.

Molecular dynamic modeling was performed using the AKMD program, and calculations were performed with OPLS-AA force field. In order to determine the optimal cleaning parameter, the system temperature was varied between $-25\text{ }^{\circ}\text{C}$ and $+25\text{ }^{\circ}\text{C}$, under the assumption that the system temperature may not correspond to the real temperature. Two models are taken for the simulation:

I – hexane (1900 molecules), thiophene (20 molecules), meta-xylene (300 molecules), ionic liquid (2200 N-methylpyrrodonium cations and 2200 acetate anions);

II – hexane (1900 molecules), thiophene (20 molecules), meta-xylene (300 molecules), N-methylpyrrolidone (2200 molecules).

Simulation time of system I was $0.73\text{ }\mu\text{s}$, while system II was $0.39\text{ }\mu\text{s}$. A layered structure was chosen as initial conditions: one flat layer housed the fuel (hexane+thiophene+meta-xylene mixture) and the other layer housed the extractant.

Results and discussion

The results of modeling of system I at 248 K showed that $(60\pm 12)\%$ of thiophene molecules are in contact with the surface of the ionic liquid or dissolved in it. Hexane molecules are not dissolved in the ionic liquid. The result showed that despite the high content of sulfur component in the model fuel (10 wt%) the ionic liquid shows high absorption capacity towards thiophene. The final distribution of thiophene in the simulation cell is shown in the Figure 1.

In the system II, the extraction coefficient was $(70\pm 10)\%$. At high temperature of 298 K some molecules of N-methylpyrrolidone dissolved in the fuel. This corresponds to the introducing the nitrogen-containing compounds to the fuel (Figure 2).

Experiments shows that raffinate output is higher for ionic liquid extractant.

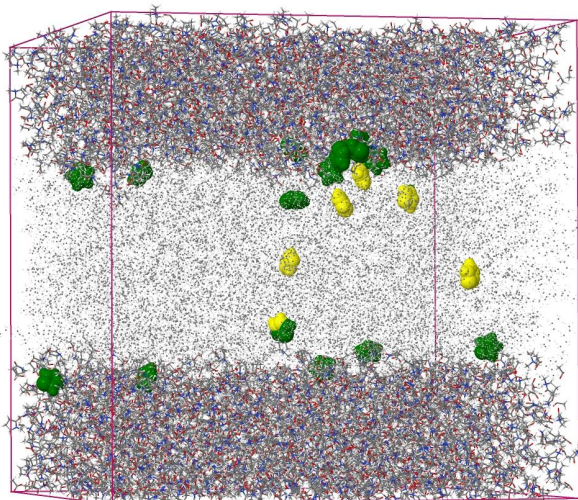


Figure 1. Snapshot of the system I. Thiophene molecules are shown in green (atoms are shown as a sphere of van der Waals radius) at a distance of less than $6\text{ }\text{\AA}$ from the ionic liquid and in yellow inside fuel. Hexane are shown with dots, ionic liquid is in the bottom and top.

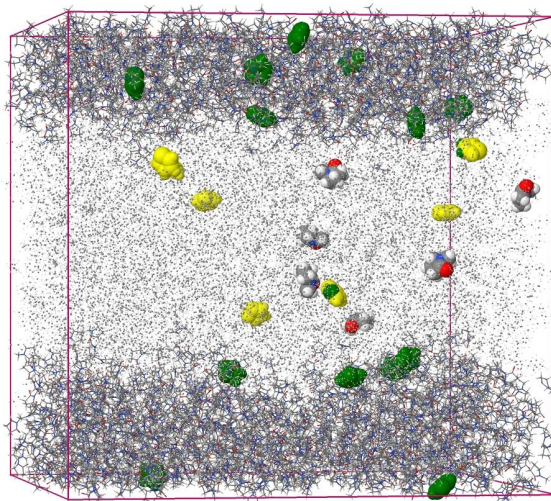


Figure 2. Snapshot of the system II. Thiophene molecules are shown in green (atoms are shown as a sphere of van der Waals radius) at a distance of less than 6 \AA from the N-methylpyrrolidone and in yellow inside fuel. Hexane are shown with dots. N-methylpyrrolidone is in the bottom and top, the dissolved molecules are shown with spheres.

Acknowledgements

This work is supported by Russian Science Foundation (RSF): grant 23-23-00430.

References

1. Seidova S.A. Ekstraktsionnyye metody ochistki motornogo topliva [Extraction methods of cleaning of motor fuel]. *Khimiya i khimicheskaya tekhnologiya* [Chemistry and chemical technology], 2019, no. 10, pp. 30-39 (in Russian).
2. Mammadhasanov K. K., Seyidova S. A., Ibrahimova M. D. et.al. Simulation of ionic-liquid extractive purification process of thiophene and m-xylene from their mixture with n-hexane by the molecular dynamics method // *Modern Physics Letters B*, 2023, Vol. 37, No. 30, 2350139.
3. Singh M.B., Harmalkar A.U., Prabhu S.S., Pai N.R. Molecular dynamics simulation for desulphurization of hydrocarbon fuel using ionic liquids // *Journal of Molecular Liquids*, 2018, Vol. 264, p.490-498.

Magnetic parameters of magnetosomes inside Magnetotactic Bacteria *Magnetospirillum* spp.

V. A. Ryzhov¹, V. V. Deriglazov¹, D. S. Grouzdev², V. V. Koziaeva^{3,4}, I. A. Kiselev¹, I. I. Larionov¹, K. G. Gareev^{4,5}, N. O. Sitkov^{4,5}, T. M. Zimina^{4,5}, Ya. Yu. Marchenko¹, V. S. Fedorov^{4,7}, M. A. Shevtsov^{4,6,7}

¹Petersburg Nuclear Physics Institute, National Research Centre “Kurchatov Institute”, Gatchina, Russia; ryzhov_va@pnpi.nrcki.ru

²SciBear OU, Tartu mnt 67/1-13b, Kesklinna Linnaosa, 10115 Tallinn, Estonia;

³Research Center of Biotechnology of the RAS, Institute of Bioengineering, 119071 Moscow, Russia;

⁴Institute of Cytology of the Russian Academy of Sciences, 194064 Saint Petersburg, Russia

⁵Department of Micro and Nanoelectronics, Saint Petersburg Electrotechnical University “LETI”, 197376 St. Petersburg, Russia

⁶Center of Translational Cancer Research (TranslTUM), Klinikum Rechts der Isar, Technical University

Munich, 81675 Munich, Germany

⁷Personalized Medicine Centre, Almazov National Medical Research Centre, 197341 Saint Petersburg, Russia

E-mail: 046_slava@mail.ru; marchenko_yv@pnpi.nrcki.ru

Introduction

Magnetotactic bacteria are a group of organisms deeply studied in the last years due to their interesting magnetic behavior and potential applications in theranostics, hyperthermia and biosensor devices due to intracellular chains of submicron-sized membrane-enclosed magnetic particles called magnetosomes [1].

Materials and methods

Magnetic parameters of magnetosomes inside the bacteria of the genus *Magnetospirillum* fixed by 5% formalin in the nutrient medium were estimated by the measurements: (i) of nonlinear longitudinal response to a weak ac magnetic field (NLR-M2) with registration of the second harmonic of magnetization [2] for MSR-1, LBB-42, AMB-1, SP-1, BB-1, and SO-1 strains; and (ii) of electron magnetic resonance (EMR) spectra with the special X-band spectrometer for wide-line registration [3] for the BB-1, MSR-1 and AMB-1 strains. To trace the evolution of the magnetic state of magnetosomes during long-term storage, freshly prepared samples (S1) and samples after a year of storage at 40 C (S2) were studied.

Results

The stable single-domain state of magnetic centers in magnetosomes indicating their proximity to superparamagnetic (SPM) regime was found by NLR-M2 at the scan frequency 0.02 Hz of the steady magnetic field. This allowed for a semi-quantitative analysis of M2 data with the formalism based on the numerical solution of the kinetic Fokker–Planck equation for SPM particles. Processing the NLR-M2 data evidenced the presence of two kinds of magnetosomes: (i) with the large magnetic moment (“heavy”, monodispersed mode) and (ii) with the comparatively small magnetic moment (“light”, dispersed mode), in both the S1 and S2 samples. The EMR spectra are formed mostly by the “heavy” fraction for both samples. In the “light” fraction, the formation of magnetosome aggregates occurs, accompanied by the suppression of their magnetic moment by dipolar correlations, in accordance with the M2

data, therefore their contribution to the EMR spectra is quite small. The presence of two peaks in the spectra evidences the presence of conventional uniaxial magnetic anisotropy in the magnetosomes. The appearance of one or two additional peaks in the spectra in the S2 samples of some strains instead of a broad diffuse line, on the one hand, suggests their instability at long storage even being fixed by formalin and sealed in the nitrogen atmosphere and, on the other hand, evidences that destruction of the magnetosome chains at long storage occurred not randomly [4]. The Atomic Force Microscopy assessment of the state of the ensemble of bacteria in the medium after the long-term storage carried out for one typical strain (BB-1) confirmed this finding and showed partial degradation of the native magnetosomal chain into shorter chains forming aggregates.

Acknowledgements

The research was carried out within the state assignment of Ministry of Science and Higher Education of the Russian Federation (theme №1023031500037-7-1.6.8;1.6.1;1.6.2;1.6.3).

References

1. Gareev K. G. et al. Magnetotactic Bacteria and Magnetosomes: Basic Properties and Applications. *Magnetochem.* 7, 86, 2021.
2. Ryzhov V.A., Larionov I.I., Fomichev V.N., On the spurious signal in the longitudinal nonlinear susceptibility of magnets at the second harmonic of excitation frequency, *Tech. Phys.* 41, 620, 1996.
3. Ryzhov V.A., Zavatskii E.I., Solov'ev V.A., Kiselev I.A., Fomichev V.N., Bikineev V.A. Spectrometer for studying broad dipole transitions in magnets and the Hall conductivity at microwave frequencies in conducting materials, *Tech. Phys.* 40, 71, 1995.
4. Ryzhov V., Deriglazov V., Grouzdev D., Kozaieva V., Kiselev I., Larionov I., Gareev K., Sitkov N., Zimina T., Marchenko Y., and Shevtsov M.. Biogenic Nanomagnetic Carriers Derived from Magnetotactic Bacteria: Magnetic Parameters of Magnetosomes Inside *Magnetospirillum* spp. *Appl. Sci.* 13(4), 2431, 2023.

Theoretical relationship between proton spin-spin magnetic relaxation time (T_2) and dynamic viscosity.

Yulianela Mengana Torres, Manuel A. Lores Guevara, Juan C. García Naranjo, Yamilka Alonso Geli, Fabián Tamayo Delgado.

Center for Medical Biophysics, Universidad de Oriente, Cuba.

yulianela.mengana@uo.edu.cu

Introduction

Nuclear Magnetic Resonance (NMR) has been employed to determine η in protein solutions [1]. Endre and Kuchel proposed in 1986 the measurement of the rotational correlation time of glycine and glutathione molecules present in the intracellular medium marked with C13 from the longitudinal relaxation time (T_1) of this nucleus. This allowed determining the hemoglobin viscosity using spherical or symmetric ellipsoid configurations [2]. However, this is a complex method, which requires at least a 4-hour incubation to achieve the marking of intracellular molecules. The present work proposes a method based on NMR, similar to one previously developed by our group for blood plasma [3], to determine the dynamic viscosity in solutions of hemoglobin and blood serum. This method overcome the aforementioned limitations of the current approaches by reducing the amount of sample by an order of magnitude and does not require washing the instruments between successive measurements.

Materials and methods

Hemoglobin and serum samples were obtained by classical methods [4, 5] from fresh venous whole blood, collected by venipuncture and immediately heparinized. For the construction of the calibration curve and the study of the control individuals, whole blood was obtained from volunteer donors in the provincial blood bank. For the proton NMR measurements, Hb and serum samples of 500 μ l were used and the experiment was carried out on a LapNMR console from Tecmag. T_2 was measured using the Carr Purcell Meiboom Gill (CPMG) pulse sequence with 800 echoes, a resonance frequency of 4.07MHz (6 and 12 μ s as pulse lengths for the 90° and 180° pulses respectively, echo time of 500 μ s). All measurements were made at 20 °C and the values reported, as usual, in mPas. A student test (t-test) was used to compare means with $\alpha = 0.005$. The values of η were reported according to: $\eta = \bar{\eta} \pm t_{1-\alpha/2, n-1} s / \sqrt{n}$ where $\bar{\eta}$ is the mean value of η , n the number of samples, s the deviation standard, $t_{1-\alpha/2, n-1}$ the percentile of the Student distribution with n-1 degrees of freedom and $\alpha = 0.001$.

Results and Discussion

From CPMG experiment $1/T_2$ can be determined as follow:

$$\frac{1}{T_{2m}} = \frac{1}{T_2} + \frac{DG^2\gamma^2\tau^2}{3} \quad (1)$$

$$D = \frac{kT}{6\pi\eta_{Hb}a}$$

From the previous analysis $1/T_{2m} = 1/T_2$ and $R_2 = 1/T_2$ can be described using a two sites water exchange model [9, 12]:

$$R_2 = P_{bulk}R_{2w}^{bulk} + P_b\delta \left[3\tau_R + \frac{5\tau_R}{1 + (\omega_0\tau_R)^2} + \frac{2\tau_R}{1 + 4(\omega_0\tau_R)^2} \right]$$

$$\delta = \frac{3}{20} \left(\frac{\mu_0}{4\pi} \right)^2 \frac{\gamma^4 \hbar^2}{b^6} \quad (2)$$

Here R_{2w}^{bulk} is the transverse magnetic relaxation rate of the protons at the solvent. P_b and P_{bulk} are the fractions of bound (b) and free (bulk) water respectively ($P_b + P_{bulk} = 1$). Additionally; τ_R is the rotational correlation time of the protein, ω_0 is the frequency of resonance, μ_0 is the magnetic permeability of the vacuum, \hbar is the Planck's constant divided by 2π and b the inter proton distance at the water molecule. In this model the bound water has been considered irrotationally bound to the Hb and the dipolar interaction between protons at the water molecule as the dominant contribution to T_2 . P_b can be calculated as a function of the number of available sites for the binding of water molecules to the Hb (h), the molecular weight of the macromolecule (M), the molarity of water (N_w), the fraction of volume occupied by the molecules of the prototein at one sample volume of 0.5 ml (ϕ) and the protein concentration (C) in gl^{-1} [9]:

$$\begin{aligned}
 P_b &= \frac{h C}{MN_w(1-\phi)} \\
 \phi &= \frac{N_A V_{Hb} C}{2000M} \\
 V_{Hb} &= \frac{4\pi r_{Hb}^3}{3}
 \end{aligned} \tag{3}$$

In Eq. (3) r_{Hb} and V_{Hb} are the radius and the volume of the Hb molecule and N_A is the Avogadro's number. It can be demonstrated that, for the C values used in Fig. 1, $\phi \ll 1$.

In the solution of Hb η_{Hb} is a function of C according to the Mooney's generalized equation (Eq. (5)) [13, 14], where η_0 is the absolute dynamic viscosity of the solvent and $A=2.77$ ml/g and $B=1.2$ ml/g are related with the geometry of the protein and the intermolecular interactions respectively.

On the other hand, τ_R can be described using the Debye's model (Eq. (5)) [9, 14].

$$\eta_{Hb} = \eta_0 \exp\left(\frac{AC}{1-BC}\right) \tag{4}$$

$$\begin{aligned}
 C &= \frac{\ln\left(\frac{\eta_{Hb}}{\eta_0}\right)}{\left[A + B \ln\left(\frac{\eta_{Hb}}{\eta_0}\right)\right]} \\
 \tau_R &= \frac{4\pi r_{Hb}^3}{3kT} \eta_{Hb}
 \end{aligned} \tag{5}$$

Using the Eqs. from (3) to (5), the Eq. (2) can be rewritten as follow:

$$\begin{aligned}
 R_2 &= R_{2w}^{bulk} + \delta_1 \delta_2 \eta_{Hb} \frac{\ln\left(\frac{\eta_{Hb}}{\eta_0}\right)}{\left[A + B \ln\left(\frac{\eta_{Hb}}{\eta_0}\right)\right]} \left[3 + \frac{5}{1 + (\delta_2 \omega_0)^2 \eta_{Hb}^2} + \frac{2}{1 + 4(\delta_2 \omega_0)^2 \eta_{Hb}^2} \right] \\
 \delta_1 &= \frac{1000h}{MN_w} \left(\frac{\mu_0}{4\pi}\right)^2 \frac{\gamma^4 \hbar^2}{b^6} \\
 \delta_2 &= \frac{4\pi r_{Hb}^3}{3kT}
 \end{aligned} \tag{6}$$

In the Eq. (6) the constant 1000 appears to guarantee the proper dimensional unit (s.) at the second term of the right hand member. Additionally, $P_{bulk} \approx 1$ without losing rigor [1].

The physical model most commonly used to describe proton magnetic relaxation in protein solutions is the two sites water exchange model [6]; which considers two types of water: the water bound to the macromolecular surface (b) and the free water (bulk). In this model the bound water is considered as irrotationally bound to the protein surface, such as its residence time (τ_{res}) is much bigger than the macromolecular rotational correlation time (τ_R) and much shorter than the measured values of ωT and the longitudinal proton magnetic relaxation time (T_1). Then, a fast exchange of water molecules between the bound and free water states will be established; and, for heterogeneous protein solutions, can be calculated as follow [4-7]:

$$R_2 = P_{bulk} R_{2w}^{bulk} + \sum_i P_b^i R_{2b}^i \quad (8)$$

In the Eq. (8) R_{2w}^{bulk} and R_{2b} represent the transverse proton magnetic relaxation rates of the free and bound water protons respectively. P_b and P_{bulk} are the fractions of bound and free water, such as $\sum_i P_b^i + P_{bulk} = 1$. P_b can be calculated using the following equation [3, 12, 15, 16]:

$$P_b^i = \frac{h_i C_i}{M_i N_w (1 - \phi_i)} \quad (9)$$

Where M and C are the molecular weight in g Mol⁻¹ and the concentration in g l⁻¹ of the protein respectively, $N_w = 55.5$ Mol l⁻¹ is the molarity of water, and h_i represents the number of sites available for the water binding to the protein surface. ϕ is the partial volume occupied by the protein in the total volume of the sample. In one heterogeneous protein solution i runs by the different types of proteins at the solution, in the case of blood serum (S) $i =$ albúmin (Al) and Globulins (Gb) [17]. Starting from all the analyzed above the Eq. (8) can be rewritten as follow [15-18]:

$$\begin{aligned} R_2^S &= R_{2w}^{bulk(S)} + \sum_i \frac{g_i^S}{M_i} C_i^S \\ g_i^S &= 0.018 h_i \left(R_{2b}^{i(S)} - R_{2w}^{bulk(S)} \right) \\ R_2^S &= R_{2w}^{bulk(S)} + \left[\frac{g_{Al}^S}{M_{Al}} C_{Al}^S + \frac{g_{Gb}^S}{M_{Gb}} C_{Gb}^S \right] \end{aligned} \quad (10)$$

The blood serum has been considered an extremely diluted solution of proteins ($P_{bulk} \approx 1$, $\phi \ll 1$) [15-17] and g_i^S is constant, in the range of concentration from zero to the physiological concentration (Fig. 2), for albumin and globulins [15].

If we consider to C_{Al}^S and C_{Gb}^S as a function of the total concentration of proteins in blood serum (C_{tot}^S) [16]:

$$\begin{aligned}
 R_2^S &= R_{2w}^{bulk(S)} + C_{tot}^S \left[\frac{1}{\sigma + 1} \left(\frac{\sigma g_{Al}^S}{M_{Al}} + \frac{g_{Gb}^S}{M_{Gb}} \right) \right] \\
 C_{tot}^S &= C_{Al}^S + C_{Gb}^S \\
 \sigma &= \frac{C_{Al}^S}{C_{Gb}^S} \\
 C_{Gb}^S &= \frac{C_{tot}^S}{\sigma + 1} \\
 C_{Al}^S &= \frac{\sigma C_{tot}^S}{\sigma + 1}
 \end{aligned} \tag{11}$$

In one extremely diluted solution of proteins η_S is a function of C_{tot}^S in agreement with the Einstein's equation [10]:

$$\begin{aligned}
 \eta_S &= \eta_0^S (1 + 2.5\nu^S C_{tot}^S) \\
 C_{tot}^S &= \frac{\eta_S}{2.5\nu^S \eta_0^S} - \frac{1}{2.5\nu^S}
 \end{aligned} \tag{12}$$

Where η_0 is the absolute dynamic viscosity of the solvent, at the absolute temperature T , and ν is the mean value of the contributions from the specific partial volumes of the albumin and globulins. Mixing Eqs. (11) and (12) we obtain:

$$R_2^S = \eta_S \left[\frac{1}{2.5\nu^S \eta_0^S (\sigma + 1)} \left(\frac{\sigma g_{Al}^S}{M_{Al}} + \frac{g_{Gb}^S}{M_{Gb}} \right) \right] + R_{2w}^{bulk(S)} - \left[\frac{1}{2.5\nu^S (\sigma + 1)} \left(\frac{\sigma g_{Al}^S}{M_{Al}} + \frac{g_{Gb}^S}{M_{Gb}} \right) \right] \tag{13}$$

Conclusions

Was obtained a relationship between the inverse of T2 and viscosity.

References

1. M. A. Lores-Guevara, C. A. Cabal-Mirabal, R. N. Muller, S. Laurent, F. Tamayo-Delgado, J. C. García-Naranjo. *Appl. Magn. Reson.* **A 53**, 387 (2022) <https://doi.org/10.1007/s00723-021-01452-w>
2. S. Meiboom, D. Gill. *Rev. Sci. Instrum.* **A29**, 688 (1958) <https://doi.org/10.1063/1.1716296>
3. J.S. D'Arrigo. *Am. J. Physiol.* **A235**, C109 (1978) <https://doi.org/10.1152/ajpcell.1978.235.3.C109>
4. M. Lores, C. Cabal. *Appl. Magn. Reson.* **A28**, 79 (2005) <https://doi.org/10.1007/BF03166995>
5. K. Monkos. *Int. J. Biol. Macromol.* **A16**, 31 (1994) [https://doi.org/10.1016/0141-8130\(94\)90008-6](https://doi.org/10.1016/0141-8130(94)90008-6).
6. M. Lores, C. Cabal, O. Nascimento, A.M. Gennaro. *Appl. Magn. Reson.* **A30**, 121 (2006) <https://doi.org/10.1007/BF03166986>
7. D.J. Wright, E. Jenkins. *Blood.* **A36**, 516 (1970) <https://doi.org/10.1182/blood.V36.4.516.516>
8. R. S. Menon, P. S. Allen. *Biophys. J. A* **57**, 389 (1990) [https://doi.org/10.1016/S0006-3495\(90\)82555-8](https://doi.org/10.1016/S0006-3495(90)82555-8)
9. P. S. Allen, M. E. Castro, E. O. Treiber, J. A. Lunt, D. P. J. Boisvert. *Phys. Med. Biol.* **A 31**, 699 (1986) <https://doi.org/10.1088/0031-9155/31/7/001>.
10. K. J. Olszewski. *Acta Physica Polonica A.* **A82**, 487 (1992) <https://doi.org/10.12693/APhysPolA.82.487>
11. M. A. Lores-Guevara, Y. Rodríguez-Almira, E. R. Pérez-Delfín. *Revista Cubana de Química.* **A XIV**, 3 (2002)

Study of pervaporation membranes based on polyelectrolyte complex of sodium alginate/polyethylenimine modified with graphene oxide

Olga Mikhailovskaya¹, Xeniya Sushkova¹, Anna Kuzminova¹, Roman Dubovenko¹, Anton Mazur¹, Anastasia Penkova¹, Mariia Dmitrenko¹

¹ St. Petersburg State University, 7/9 Universitetskaya nab., Saint Petersburg 199034, Russia

E-mail: mihajlovskaya.olga.1@yandex.ru

<https://go.spbu.ru/rgpenkova>

Introduction

Pervaporation is a promising membrane method for separation of liquid mixtures of low molecular weight substances. The selectivity and efficiency of this process largely depends on the choice of membrane material. Polyelectrolyte complexes (PEC) are one of the progressive materials for the manufacture of pervaporation membranes for dehydration purposes. Also PEC-based membranes are actively modified by introducing various nanoparticles to improve their characteristics. One of the most widely used are carbon nanoparticles.

The aim of this study was to develop pervaporation membranes based on PEC of sodium alginate (SA)/polyethylenimine (PEI) modified with graphene oxide (GO) for enhanced dehydration of bio-alcohols. To evaluate the formation of PEC and interaction of it with GO, the structure of obtained composites and membranes based on them was studied by spectroscopic methods (FTIR and nuclear magnetic resonance (NMR) spectroscopies). Also samples were characterized by scanning electron and atomic force microscopies, thermogravimetric analysis, etc. Membrane performance was tested in pervaporation dehydration of ethanol in the wide concentration range.

It was shown that the increase of PEI content in the PEC composition led to the rise of permeation flux and decrease of selectivity of PEC membrane compared to the pristine SA membrane. The introduction of GO into PEC membrane allowed increase of permeation flux maintaining the selectivity at high level.

Acknowledgements

The study was supported by the Russian Science Foundation grant No. 23-73-01070, <https://rscf.ru/project/23-73-01070/>. The experimental work was facilitated by equipment from the Resource Centers for Nanotechnology, Magnetic Resonance, Cryogenic Department, Thermogravimetric and Calorimetric Research Center, Center for Physical Methods of Surface Investigation, Center for Innovative Technologies of Composite Nanomaterials, Chemical Analysis and Materials Research Center, and Center "Nanofabrication of Photoactive Materials (Nanophotonics)" at the St. Petersburg State University.

Novel composite carboxymethyl cellulose/MIL-125 pervaporation membranes: synthesis and characterization

Anna I. Mikulan¹, Anna I. Kuzminova¹, Maria E. Dmitrenko¹, Roman R. Dubovenko¹, Anton S. Mazur¹, Anastasia V. Penkova¹

¹Saint Petersburg State University, Saint-Petersburg, Russia

E-mail: st097675@student.spbu.ru

https://go.spbu.ru/rgpenkova

Introduction

Membrane processes are one of the most promising areas in modern technology for processing various types of raw materials and separating components. Membrane technologies are becoming more energy efficient and environmentally friendly compared to traditional separation methods. Pervaporation is a membrane method used to separate liquid mixtures containing low molecular weight components. Using pervaporation, it is possible to separate mixtures of isomers, azeotropic mixtures and thermally unstable mixtures. The rapid development of pervaporation requires the search for new highly efficient membrane materials. The creation of mixed matrix membranes (MMMs) is of particular interest as a promising way to improve the transport characteristics of polymer membranes by introducing an organic and/or inorganic modifier. This option allows you to obtain unique membrane materials by combining the properties of the components.

Results

In this work, the novel membranes based on carboxymethyl cellulose (CMC) were prepared by introducing the metal-organic framework MIL-125 into the polymer matrix. The resulting membrane has improved transport characteristics for pervaporation dehydration. The most important tool for the investigation membrane structural changes is the nuclear magnetic resonance (NMR) method. NMR allowed us to evaluate the interaction between MIL-125 and CMC, confirming the complex structure of the resulting material. For detailed characterization were additionally used such methods as scanning electron microscopy, atomic force microscopy, infrared Fourier spectroscopy and thermogravimetric analysis, swelling experiments and contact angle measurements. The transport properties of MMMs were investigated for the pervaporation separation of the water-isopropanol mixture. It has been shown that the modified MIL-125 CMC-based membrane has a significantly improved permeability compared to the original CMC membrane.

Acknowledgements

The authors acknowledge Saint-Petersburg State University for a research project 11602266. The experimental work of this study was facilitated by the equipment from the Resource Centre of Geomodel, Chemical Analysis and Materials Research Centre, Centre for X-ray Diffraction Methods, Magnetic Resonance Research Centre, Centre for Innovative, Technologies of Composite Nanomaterials, Nanophotonics Centre, Computer Centre, Cryogenic department, Thermogravimetric and Calorimetric Research Centre and the Interdisciplinary Resource Centre for Nanotechnology at the St. Petersburg State University.

Cis-trans isomerization in cyclosporin C dissolved in acetonitrile

Guzel A. Minnullina, Sergey V. Efimov, Vladimir V. Klochkov

Institute of Physics, Kazan Federal University, Kazan, 420008 Russia

E-mail: g.minnullina2010@yandex.ru

Introduction

Cyclosporin is an 11-amino acid cyclic peptide with pharmacologically valuable properties which has a variety of actual and potential applications: for example, cyclosporin A (CsA) is widely used in immunosuppressive therapy in organ transplantation [1]. There are analogues of CsA that have the same properties, but with weaker side effects; other modifications of cyclosporin's formula can subdue its physiological action. Experiments with cyclosporin C (CsC) showed that it has strong immunosuppressive activity, but remains less nephrotoxic than CsA [2].

Cyclosporins demonstrate conformational flexibility, and different molecular structures usually coexist in polar solvents. When administered inside, cyclosporin is distributed into a number of conformers containing both active and unneeded forms; these forms may possess different properties and activity. Thus, for the possibility of increasing drug efficacy and maximizing the concentration of the required conformer, it is necessary to learn more about how structure of cyclosporins changes and distribution into diverse conformers occurs. The aim of this work was to observe the conformational behavior of CsC (Fig. 1) in deuterated acetonitrile (CD_3CN) by NMR spectroscopy and to determine the parameters of conformational exchange using the theory described in [3].

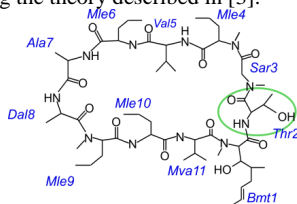


Figure 1. Chemical structure of cyclosporin C

Method

NMR measurements were carried out on a Bruker Avance III HD 700 spectrometer (Center of Shared Facilities of Kazan Federal University). Solution was prepared in deuterated acetonitrile (CD_3CN), the sample concentration was 1.4 mM (for all conformers). Two-dimensional spectra (DQF-COSY, TOCSY, ROESY, HSQC and HMBC) were recorded at the temperature of 25°C. Exchange spectroscopy (EXSY) spectra were obtained at different temperatures from 12 to 38°C, the mixing times were in the range from 0.15 to 0.35 s. A series of one-dimensional 1H NMR spectra was taken at the temperatures from 12 to 38°C in the spectral window of 12 ppm and spectral resolution of 0.257 Hz per data point.

Results and Discussion

Total signal assignment was obtained for the major conformer of CsC. Another set of 11 α -CH peaks with weaker intensity was also observed in the HSQC spectrum, which allowed identification of the second conformer. Four pairs of signals were selected for further analysis of chemical exchange: threonine Thr2 NH – Thr2* NH, valine Val5 NH – Val5* NH, alanine Ala7 NH – Ala7* NH, and leucine Mle9 α – Mle9* α (Fig. 2).

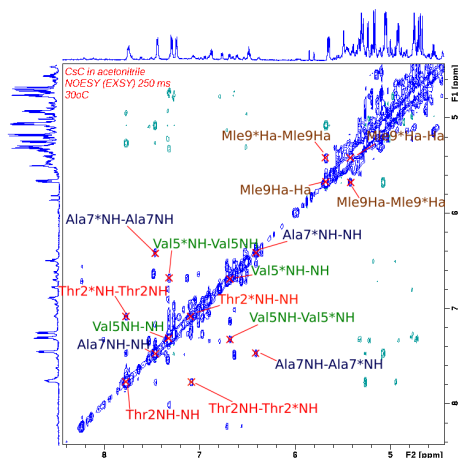


Figure 2. ^1H - ^1H NOESY (EXSY) spectrum of CsC at 30°C. Signals of the minor (second) conformer are marked with the asterisk (*)

The most significant difference in chemical shifts for the same amide proton in different conformers was 1.07 ppm for the pair Ala7 NH – Ala7* NH at 26°C. A large variation of the chemical shift (in the order of 1 ppm) for a certain atom in different forms of the molecule should represent a drastic difference in the local magnetic environment. We can expect thus that alanine Ala7 and threonine Thr2 are close to the place where *cis-trans* isomerization of a peptide bond occurs. This may be either the adjacent amino acid residue or a more distant segment of the peptide chain which turns out to be close in space due to oblate shape of the cyclosporin's ring.

The rates of conversion of the major and minor conformers to each other, the summary exchange rate and the energy difference ΔG_0 were calculated at different temperatures. The activation energy of the minor form ΔG^\ddagger obtained from all analyzed spectral peaks is approximately the same: 77 ± 2 kJ/mol. The energy difference between the stable conformations found from 1D spectra was approximately 8×10^2 J/mol for Mle9 H α signal and $(4.2\text{--}5.4) \times 10^3$ J/mol for NH signals. These findings are indicative of *cis-trans* isomerization occurring in one or several sites of the peptide backbone in polar solvent (acetonitrile, $\epsilon = 37.5$).

Acknowledgements

The work was supported by the Russian Science Foundation (project no. 24-23-00427).

References

1. M. Hamawy, S. Knechtle. Overview of the Actions of Cyclosporine and FK506. *Transplantation Reviews*, 2003, Vol. 17 (4), P. 165-171.
2. N. Sadeg, C. Pham-Huy, P. Rucay et al. In Vitro and In Vivo Comparative Studies on Immunosuppressive Properties of Cyclosporines A, C, D and Metabolites M1, M17 and M21. *Immunopharmacology and Immunotoxicology*, 1993, Vol. 15, P. 163-177.
3. C. Perrin, T. Dwyer. Application of Two-Dimensional NMR to Kinetics of Chemical Exchange. *Chemical Reviews*, 1990, Vol. 90 (6), P. 935–967.

Determination of diosmin in *Hyssopus officinalis* L.: opportunity of ^1H NMR spectroscopy.

Vasily G. Vasil'ev, Anzhelika V. Sheremeta, Vasily A. Ivlev, Sergey V. Goryainov, Luiza A. Miridonova, Alina Y. Polukhina, Anastasia A. Murtazina, Ekaterina A. Krivosheeva
¹Peoples' Friendship University of Russia (RUDN University), 6 Miklukho-Maklaya Street, Moscow, 117198, Russian Federation
 E-mail: 1032201854@pfur.ru

Introduction

Hyssop (*Hyssopus officinalis* L.) is a branched subshrub that can reach heights up to 60 cm. It belongs to the Lamiaceae family. Initially, the plant was widespread in the Mediterranean and Central Asia. Now it can be found in Russia in a wild state. As a rule, hyssop is founded in the forest and steppe zones of the European part of our country, in the Caucasus and Altai. The plant prefers to grow on dry hills and rocky places.

Hyssop contains essential oil, flavonoids (diosmin, hyssopin, hesperidin), tannins and bitter substances, resins, gum, triterpene acids (ursolic and oleanolic) and others. Most of them are determined by HPLC-UV, spectrophotometry (phenolic compounds), and HPLC-MS. The big disadvantage of the methods is necessary to use a reference sample and long sample preparation time. NMR spectroscopy requires short sample preparation time (only extraction) and reference samples and is successfully used for the identification and quantification of substances.

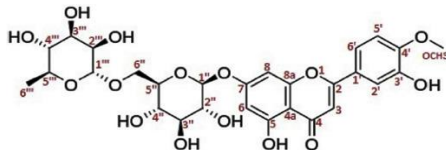


Figure 1. The chemical structure of diosmin [4]

There are several methods that can be used to identify and characterize the polyphenolic compounds of *Hyssopus officinalis* L. [3]. In the research [4] ultraviolet–visible (UV) spectroscopy was used to determine the total flavonoid content of hyssop leaves and one-dimensional nuclear magnetic resonance (NMR) spectroscopy was used to elucidate diosmin structure.

The flavonoid composition of the hyssop plant was studied using high-performance liquid chromatography and NMR spectroscopy in research [5]. The presence of diosmin as the main flavone was detected. The maximum levels of this compound are found in the sepals and leaves, which account for 51 and 40.5%, respectively, of the total diosmin content of the whole plant.

METHODOLOGY

Crushed leaves of a commercial sample of hyssop were analyzed in this research. The following solvents and reference samples were used: dimethyl sulfoxide- d_6 ($\geq 99.9\%$, Sigma-Aldrich, CAS number 2206-27-1), a reference sample of diosmin (CAS number 520-27-4). The samples were analyzed on a spectrometer JEOL JNM ECA-600, Japan.

RESULTS

In our previous work [6], we developed a method for identifying diosmin in hyssop. In this study, the technique was applied to 4 commercial samples of *Hyssopus officinalis* L. and confirmed the diosmin content in them, which was also examined and quantified. To

determine the amount of diosmin in the tested samples, 4 ^1H NMR spectra were obtained (Fig. 2).

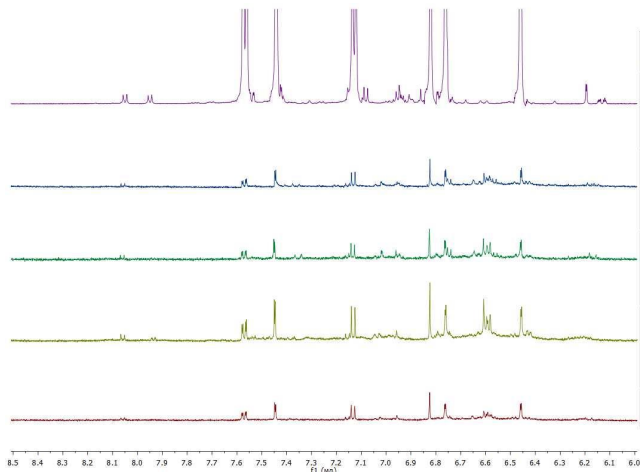


Figure 2. Stack of ^1H NMR spectra in DMSO-d_6 : 1) leaf extract of *Hyssopus officinalis* L. from commercial sample №1; 2) leaf extract of *Hyssopus officinalis* L. from commercial sample №2; 3) leaf extract of *Hyssopus officinalis* L. from commercial sample №3; 4) leaf extract of *Hyssopus officinalis* L. from commercial sample №4; 5) standard sample of diosmin

To estimate the diosmin content in the extract of *Hyssopus officinalis* L. by ^1H NMR spectroscopy, we used a doublet signal at 7.44 ppm. Quantitative determination was carried out by comparing the integral intensity of the target biologically active substance with the signal of residual protons of DMSO-d_6 .

The values obtained as a result of integration were entered into an Excel table for further calculations. Three parallel measurements were carried out for the studied *Hyssopus officinalis* L. leaf extract for each commercial samples. Quantification was performed by comparing the integrated intensities of the target analyte with the DMSO-d_6 residual proton signal. Thus, quantitative results of diosmin determination in samples 1-4 are presented in the Table 1.

Table 1. Results the quantitative determination of diosmin in extracts from leaves of *Hyssopus officinalis* L. by ^1H NMR

Sample №	% diosmin
1	$0,75 \pm 0,04\%$
2	$0,66 \pm 0,03\%$
3	$0,60 \pm 0,03\%$
4	$1,24 \pm 0,04\%$

CONCLUSIONS

A method for the identification and quantitative determination of diosmin in *Hyssopus officinalis* L. by NMR spectroscopy has been developed. The conditions for sample preparation and registration of ^1H NMR spectra have been selected. The obtained results can also be used for the determination of diosmin in other samples of plant origin.

ACKNOWLEDGEMENTS

This paper has been supported by the RUDN University Strategic Academic Leadership Program.

References

1. F. Fathiazad, S. Hamedeyzdan. A Review on *Hyssopus officinalis* L.: Composition and Biological Activities. – African Journal of Pharmacy and Pharmacology. – 2011, 5(17), pp. 1959-1966.
2. S. Kumar, A. K. Pandey. Chemistry and biological activities of flavonoids: an overview. – Sci. World J. – 2013.
3. M. N. Ivashev, O.A. Andreeva, V.A. Bandjukova, T.D. Dragaleva. Extraction of diosmin from plants of the genus *Vicia* and *Hyssopus officinalis* and its effect on blood coagulation (in Russian). – Pharm. Chem. J. – 1995, 10, pp. 39-41.
4. Z. Soheilikhah, M. Modarresi, N. Karimi, A. Movafeghi. Qualitative and quantitative analysis of diosmin content of hyssop (*Hyssopus officinalis*) in response to salinity stress. – Heliyon. – 2021, 7(10), p. e08228.
5. F. R. Marin, A. Ortuño, O. Benavente-Garcia, J. A. Del Rio. Distribution of flavone glycoside diosmin in *Hyssopus officinalis* plants: changes during growth. – Planta medica. – 1998, 64(2), pp. 181-182.
6. A.V. Sheremeta, V.A. Ivlev, A.A. Murtazina, A.Y. Polukhina, L.A. Miridonova, V.G. Vasil'ev. Identification of diosmin in *Hyssopus officinalis* L. by ^1H NMR spectroscopy. – Magnetic resonance and its applications. – 2023, pp. 233-235.

Cell size dependence of hydrodynamic radius of PAMAM dendrimers G2 in methanol

Amina D. Muratova, Andrey V. Komolkin, Denis A. Markelov

Department of Nuclear-Physics Research Methods, Faculty of Physics, Saint-Petersburg State University

E-mail: st087242@student.spbu.ru

Introduction

Dendrimers are monodisperse regularly branched macromolecules. Due to the perfect tree structure, dendrimers have a number of unique properties: a spherical shape that persists under various external conditions, the ability to free up spaces inside the macromolecule for encapsulation, for example, drugs, as well as a large number of end groups that can be modified at the last stage of synthesis. These properties make these macromolecules in demand in various fields.

The study of diffusion properties is necessary for the practical usage of dendrimers. However, the investigation of the diffusion properties of dendrimers by the molecular dynamics (MD) method using the standard method (using mean square displacement, MSD) in solutions has to take into account various factors such as the size of the modeling cell and the length of the trajectory [1,2]. At the same time, as has been shown for carboxilane dendrimers, [1,2] the rotational diffusion of the dendrimer is less sensitive to the simulation conditions. The aim of this work is to verify the conclusions obtained for carboxilane dendrimers for the PAMAM dendrimer of the second generation. Namely, the study of the influence of modeling parameters on translational and rotational diffusion.

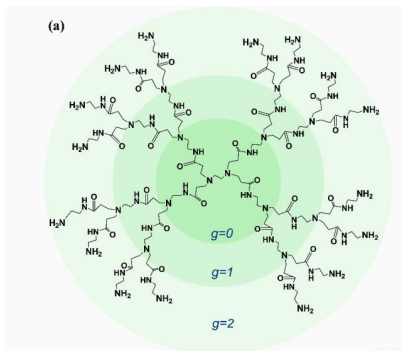


Figure 1. Structures of the second generation dendrimers ($G = 2$, with 16 terminal groups) polyamidoamine (PAMAM) [3]

Molecular dynamics simulation details

The studied PAMAM dendrimer of the second generation was modeled using the GROMACS package[5-9] and dissolved in methanol. Periodic boundary conditions and the OPLSaa force field [10] were used. To study the effect of boundary conditions, a dendrimer molecule was mixed with a different number of molecules of methanol solvent in the range of 4000-20000 molecules. Energy minimization and further modeling were performed with each system. V-rescale thermostat and Berendsen barostat were utilized for simulation of NPT ensemble at 300 K. Each system was equilibrated for one microsecond.

After that, the simulation was continued for 3 microseconds in order to obtain a equilibrium trajectory. This trajectory was used for analysis.

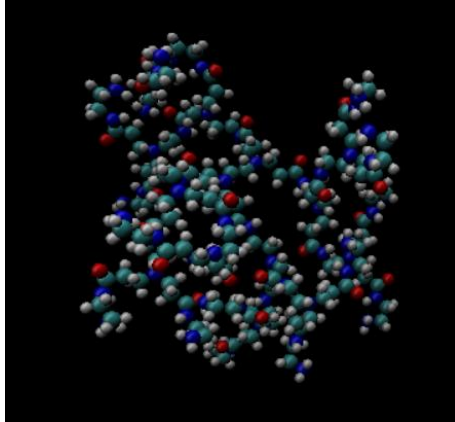


Figure 2. Screenshot, the dendrimer molecule PAMAM

Radius of gyration, R_g , of the dendrimer within the error range 1.07 ± 0.08 nm is in good agreement with the experimental data 1.18 ± 0.02 nm [4].

Simulation results

The hydrodynamic radius of the molecule was calculated for each system using several methods. The first method is based on the analysis of translational diffusion and the use of the Stokes-Einstein equation, from which the hydrodynamic radius, R_h , can be estimated using the following equation:

$$R_h = \frac{k_B T}{6\eta_{solv} D}, \quad (1)$$

where T is temperature, k_B is the Boltzmann constant, D is the diffusion coefficient, and η_{solv} is the viscosity of the solvent.

When the diffusion mode is reached, the diffusion coefficient D can be calculated using the Einstein formula, where the RMS displacement MSD is calculated along the modeling trajectory as a function of time:

$$\lim_{t \rightarrow \infty} (MSD) = 6Dt, \quad (2)$$

where t is time. As it was expected R_h decreases with growing simulation box.

In the second approach, to account for the influence of the simulation box size, we recalculated the hydrodynamic radius using an equation involving the linear cell size L :

$$\frac{1}{R_h^L} = \frac{1}{R_h} + \frac{2.837}{L}, \quad (3)$$

where R_h^L is the hydrodynamic radius calculated taking into account the simulation box size, L is the linear box size, and R_h is the hydrodynamic radius obtained during simulation. The values obtained give significantly lower results, smaller than R_g .

In the third method we utilized rotational diffusion to estimate R_h of the PAMAM dendrimer by the following formula:

$$\tau_{rot} = \frac{4\pi\eta_{sol}R_h^3}{3k_B T} \quad (4)$$

where τ_{rot} is characteristic time of dendrimer rotation as a whole, T is temperature, k_B is the Boltzmann constant, η_{sol} is the viscosity of the solvent and R_h is the hydrodynamic radius.

As was established for carboxilane dendrimers, [1-2] the rotational diffusion of the dendrimer is less sensitive to the modeling condition. This conclusion was also verified for the PAMAM dendrimer. The hydrodynamic radius was calculated using the following equation:

The obtained results show that the hydrodynamic radius of G2 PAMAM dendrimers obtained from the analysis of rotational diffusion does not depend on the size of the simulation cell. The first method, based on the Stokes-Einstein equation, gives correct results only for huge size of the simulation cell. The hydrodynamic radius decreases as the size of the box increases. The adjustment according to equation 3 gives low results, less than the radius of inertia R_g .

Acknowledgements

This work is supported by the Russian Science Foundation (grants no. 23-13-00144). The simulations were performed at the Computer Resource Center of Saint Petersburg State University.

References

1. N.R. Khusnutdinova, D. A. Markelov. Hydrodynamic radius of dendrimers in solvents, *Phys. Chem. Chem. Phys.*, 2023,25, 28220-28229.
2. N.R. Khusnutdinova, D. A. Markelov. Cell size dependence of hydrodynamic radius of carboxilane dendrimers in chloroform – Book of proceeding “Magnatic Reasonance and its applications.Spinus-2024” St.Petersburg, April 1-5, 2024.
3. N.N. Sheveleva, Andrei V. Komolkin and Denis A. Markelov. Influence of the Chemical Structure on the Mechanical Relaxation of Dendrimers. *Polymers* 2023, 15(4), 833.
4. S.Rathgeber, T.Pakula, V.Urban. Structure of star-burst dendrimers: a comparison between small angle x-ray scattering and computer simulation results. *J Chem Phys.* 2004 Aug 22;121(8):3840-53.
5. M. J. Abraham, T. Murtola, R. Schulz, S. Pa’ll, J. C. Smith, B. Hess and E. Lindahl, *SoftwareX*, 2015, 1–2, 19–25.
6. S. Pa’ll, M. J. Abraham, C. Kutzner, B. Hess and E. Lindahl, *Lecture Notes in Computer Science (including subseries Lecture Notes in Artificial Intelligence and Lecture Notes in Bioinformatics)*, 2015.
7. B. Hess, C. Kutzner, D. Van Der Spoel and E. Lindahl, *J. Chem. Theory Comput.*, 2008, 4, 435–447.
8. H. Berendsen, D. van der Spoel and R. van Drunen, *Comput. Phys. Commun.*, 1995, 91, 43–56.
9. E. Lindahl, B. Hess and D. van der Spoel, *J. Mol. Model.*, 2001, 7, 306–317.
10. W.L. Jorgensen, J. Tirado-Rives, Potential energy functions for atomic-level simulations of water and organic and biomolecular systems, *Proc. Natl. Acad. Sci.* 102 (19) (2005) 6665–6670.

From Theory to Practice: Extracting spin-spin coupling constants from highly complex NMR multiplets

Nichugovskiy A.I., Cheshkov D.A.

Lomonosov Institute of Fine Chemical Technologies, MIREA - Russian Technological University, 86 Vernadsky Ave., 119571 Moscow, Russia

E-mail: ainichugovskiy@gmail.com

<https://github.com/dcheshkov/ANATOLIA/>

The study of the structural features and stereochemistry of molecules by nuclear magnetic resonance (NMR) spectroscopy primarily relies on the use of indirect spin-spin coupling constants (J values). Advances in technology, particularly the introduction of high-field magnets, have significantly simplified this task, reducing it to the analysis of first-order multiplets from which the J values can be directly extracted without substantial difficulty. However, due to the ever-increasing complexity of molecules under investigation and the widespread adoption of benchtop NMR spectrometers in research practice, the need to analyze non-first-order spectra and multiplets of complex structure remains relevant. The same considerations apply to multiplets caused by chemically equivalent but magnetically nonequivalent groups of spins, such as in AA'XX' systems. Various techniques, including the introduction of deuterium into the molecule or selective signal suppression, are employed to address these challenges, although these approaches may not always be effective, can be time-consuming, and in some cases, impossible. An alternative solution is the analysis of the total lineshape of NMR spectra.

For example, the ^1H NMR spectrum of a D-glucose isonitrile derivative (Fig. 1) exhibits strong non-first-order effects corresponding to the ABCDX spin system, which persist even on a 600 MHz instrument, making it impossible to directly determine the stereochemical configuration of the anomeric center from the multiplet structure. Therefore, we conducted an analysis based on the total lineshape of the proton spectrum with selective decoupling $^1\text{H}\{\text{H-sel, X}\}$ from the proton at H-5. The spectrum was analyzed within the ABCD spin system using the ANATOLIA software, allowing the determination of vicinal J values. It was found that the J value between the anomeric proton and the proton at the C-2 atom of D-glucose isonitrile is 9.25 Hz, indicating a β -configuration of the anomeric center.

Another example is the investigation of the stereochemical structure of bicyclo[2.2.1]heptanes, characterized by extremely complex ^1H NMR multiplets. The most effective approach for this investigation is indeed the analysis of the total lineshape of resonant multiplets. Framework compounds, such as vinyl norbornene (VNB) and its derivatives, are of interest to chemistry and organic synthesis due to their unique structural properties and reactivity. Knowledge of the spin-spin coupling constants for compounds of this class can enhance understanding of intramolecular interactions, conformational dynamics, and assist in the development of new analytical methods and structural studies of organic compounds.

In particular, VNB, obtained by the Diels-Alder reaction between butadiene and cyclopentadiene, forms as a mixture of exo and endo isomers. Determining the orientation of the vinyl substituent in such molecules can be achieved based on the values of J constants, the extraction of which without total lineshape spectrum analysis is not feasible.

The ^1H NMR spectrum of VNB deuterobenzene solution contains two sets of signals corresponding to exo- and endo-isomers. Spectrum analysis using the ANATOLIA program allowed for the identification of all spin-spin coupling constants between spins. This enabled the unequivocal confirmation of the presence of endo and exo isomers and the refinement of chemical shift values for overlapping signals.

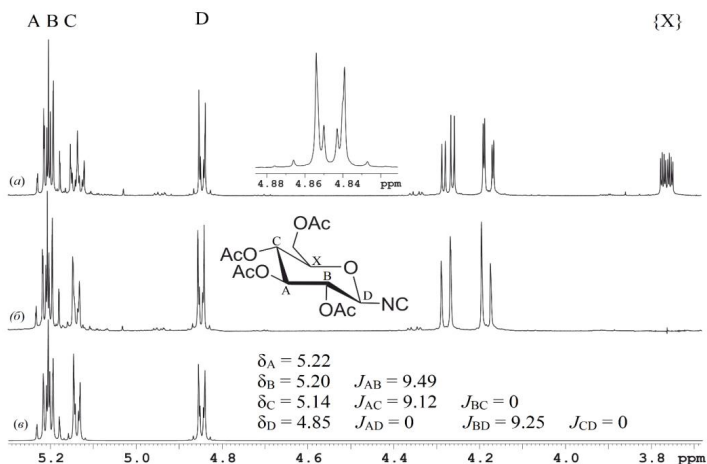


Fig. 1: (a) The ^1H NMR spectrum of a D-glucose derivative; (b) the $^1\text{H}\{^1\text{H}, \text{sel}\}$ NMR spectrum of a D-glucose derivative; (c) the calculated $^1\text{H}\{^1\text{H}, \text{sel}\}$ NMR spectrum of a D-glucose derivative.

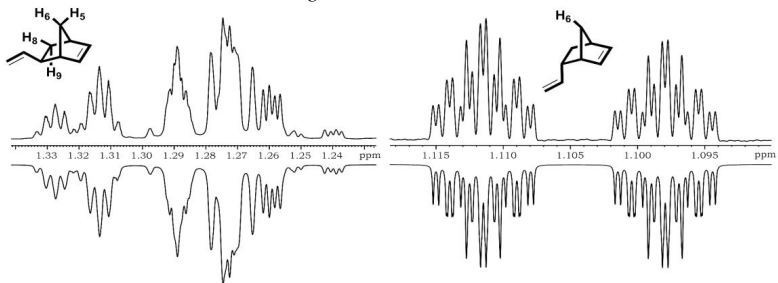


Fig. 2: Comparison of actual and calculated ^1H NMR spectra of exo- and endo-vinyl norbornenes.

Acknowledgements

This work is supported by the Lomonosov Institute of Fine Chemical Technologies, MIREA - Russian Technological University.

References

- Cheshkov D.A., Sheberstov K.F., Sinitsyn D.O., Chertkov V.A. ANATOLIA: NMR software for spectral analysis of total lineshape. *Magn.Reson.Chem.*, 2018, 56, 449-457. DOI: 10.1002/mrc.4689.
- <https://github.com/dcheshkov/ANATOLIA/>; <http://anatolia.nmrclub.ru/>
- Nichugovskiy A. I. et al. Synthesis of Isonitrile Derivatives of Diglycerides and Carbohydrates as Intermediates for Multicomponent Ugi Reaction. *Russian Journal of Bioorganic Chemistry.*, 2021, 47, 929-93. DOI: 10.1134/S1068162021040166.

Studies of EPR relaxation of NV centers in diamonds

Yury V. Bogachev, Vasily I. Zubkov, Anna V. Solomnikova I, Anastasiya V. Nikitina^{1,2},
Stanislav M. Suharzevskiy²

¹St.-Petersburg Electrotechnical University, St.-Petersburg, Russia

²Magnetic Resonance Research Centre, St.-Petersburg State University, St.-Petersburg, Russia

E-mail: Yu.Bogachev@mail.ru

Introduction

Currently, a significant number of studies are being conducted related to the prospect of using the quantum states of diamond NV centers as elementary units – qubits (q-bits) in a quantum computer [1]. The quantum states of the unpaired electrons of such systems depend on the interaction of electron spins with each other, and on the interaction with the surrounding nuclear spins, as well as on the dynamics of spin systems over time, just as decoherence occurs with any interaction of the system with the environment in the process of information exchange [2, 3]. Thus, this leads to decoherence of the quantum states of unpaired electrons, which manifests itself in an inhomogeneous broadening of the electron paramagnetic resonance (EPR) lines. The line width determines the spread of resonant frequencies. The most informative parameters for evaluating decoherence effects are the spin-lattice T_1 , spin-spin T_2 and effective spin-spin T_2^* relaxation times.

Experiments and Results

EPR studies of synthetic diamond samples of NDT company (Sestroretsk, Russia) grown by the HPHT method were carried out. EPR experiments were performed on spectrometer Bruker Elexsys E580 EPR in the Magnetic Resonance Research Centre of St.-Petersburg State University, Russia.

We have analyzed the stationary saturation of inhomogeneously broadened EPR lines of NV centers in HPHT diamond sample (Fig.1) using the method proposed in [4] when modulating the magnetic field at a frequency of ω_m under conditions of adiabatically slow passage ($\omega_m \ll T_2^{-1}, T_1^{-1}$).

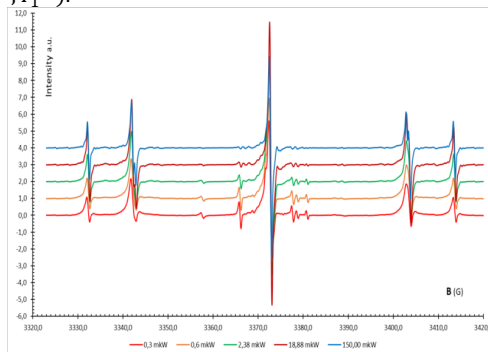


Figure 1. EPR spectra of NV centers in diamond under various microwave power

In accordance with [4], we assume that the inhomogeneously broadened resonance line consists of spin packets that do not interact with each other, each of which is characterized by a Lorentz absorption line

$$g(\omega - \omega') = \frac{T_2}{\pi} \frac{1}{1 + (\omega - \omega')^2 T_2^2}, \quad (1)$$

where ω' is the resonant frequency of the spin packet, ω is the frequency of the alternating magnetic field. The frequency distribution function of the packets is approximated by a Gaussian curve

$$h(\omega' - \omega_0) = \frac{1}{\pi^{1/2}} \frac{1}{\Delta\omega_r} \cdot \exp\left[-\left(\frac{\omega' - \omega_0}{\Delta\omega_r}\right)^2\right] \quad (2)$$

Then the absorption signal:

$$I = \frac{\pi}{2} H_1 \chi_0 \omega_0 \int_{-\infty}^{\infty} \frac{g(\omega - \omega') h(\omega' - \omega_0)}{1 + \pi \gamma^2 H_1^2 T_1 g(\omega - \omega')} d\omega' \quad (3)$$

where χ_0 is the static magnetic susceptibility, H_1 is the amplitude of the alternating microwave field. The analysis of the function (3) leads to the expression [4]:

$$I_1 = \chi_0 \omega_0 \sqrt{\frac{T_2}{T_1}} \frac{s}{\gamma b \sqrt{1+s^2}} \int_0^{\infty} J_1(\alpha A_m) \sin(\gamma \alpha) \exp\left(-\frac{\alpha^2}{4} - \alpha \cdot \frac{\sqrt{1+s^2}}{b}\right) d\alpha. \quad (4)$$

As a result of the analysis of the function (4) using computer simulation of the saturation curves of the first harmonic of the absorption signal ($A_m \ll 1$) depending on s^2 and b , a simpler and more accurate method was proposed [4] for determining the relaxation times T_1 and T_2 of inhomogeneously widened EPR lines.

This method uses the normalized saturation curves $I_{1m}/I_{1mm} = f(s^2/s_m^2)$, where I_{1mm} is the maximum value of the function I_{1m} at $s = s_m$. The ratio $s^2/s_m^2 = H_1^2/H_{1m}^2 = P_{\omega}/P_{\omega m}$. The values s_m , H_{1m} and $P_{\omega m}$ correspond to the maximum of the saturation curve. P_{ω} is the microwave power incident on the sample in the resonator of the EPR spectrometer.

The graph of the simulated dependence $I_{1m}/I_{1mm} = f(s^2/s_m^2)$ for $A_m = 0.1$ and various values of b is shown in Figure 2 (theoretical saturation curves are marked in black).

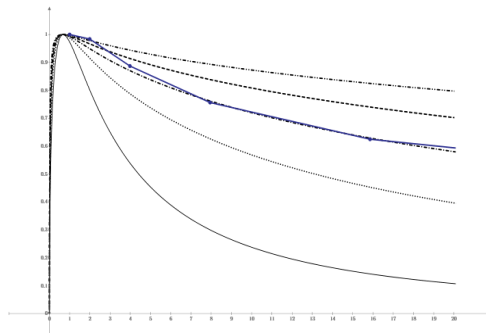


Figure 2. Normalized saturation curve

To construct such an experimental graph, the stationary saturation of the microwave power of the leftmost low-field line of the ultrathin structure of the EPR spectrum of a synthetic diamond was investigated. As a result of analyzing the signal intensity of the leftmost low-field line of the ultrathin structure of these EPR spectra at different microwave power, a normalized steady-state saturation curve for this EPR line was constructed, shown in Figure 2 in blue. From comparing the experimental and modelled normalized saturation curves $I_{1m}/I_{1mm} = f(s^2/s_m^2)$ for different values of the number of spin packets b shown in Figure 2, we find that with a sufficiently high degree of accuracy, the number of spin packets

involved in the inhomogeneous broadening of the EPR lines of the studied diamond sample, is equal to 25. According to the found value b from the calibration graph of the dependence $s_m = f(b)$, constructed in [4], we find the value $s_m=2.5$ corresponding to our experiment. The value s_m is associated with the relaxation times T_1 and T_2 by the ratio $S_m^2 = \gamma^2 \cdot H_{1s}^2(T_1 \cdot T_2)$.

The value of $H_{1s}^{1,0}$, corresponding to the maximum of the saturation curve, is associated with the microwave power P_{om} incident on the sample by the ratio:

$$(H_{1s}^{1,0})^2 = 2 \cdot 10^{-3} \cdot P_{\text{om}} \cdot Q_L \cdot \eta \cdot \frac{V_{\omega}}{V_s}$$

This expression can be converted to the form $H_{1s}^2 = K \cdot P_{\text{om}}$, where H_{1s}^2 is expressed in Gauss, P_{om} - in Watts. For the cylindrical resonator type TE₀₁₁ used in our EPR spectrometer with Q-factor $Q_L = 12000$, the coefficient K is on the order of one, that is, $K = 1 \text{ Gs}^2/\text{W}$. Thus:

$$S_m^2 = \gamma^2 \cdot H_{1s}^2(T_1 \cdot T_2) = \gamma^2 \cdot K P_{\text{om}}(T_1 \cdot T_2)$$

The spin-spin relaxation time of a single spin packet is related to the effective relaxation time T_2^* by the ratio $T_2 = b \cdot T_2^*$, where b is the number of spin packets in a nonuniformly widened EPR line.

The time T_2^* , in turn, is determined by the width of the inhomogeneously widened EPR line:

$$T_2^* = \frac{1,3131 \cdot 10^{-7}}{g \cdot \Delta H_{pp}^0}$$

where ΔH_{pp}^0 is the width of the EPR line in the absence of saturation.

In our experiment, for HPHT diamond $\Delta H_{pp}^0 \approx 0.66$, the g-factor for the NV center is approximately equal to 2.0. Calculations using the above formulas give the value $T_2 = 2,5 \cdot 10^{-6}$ c.

Substituting the experimentally found values $S_m = 2.5$, $P_{\text{om}} = 15 \cdot 10^{-5}$ W, $T_2 = 2,5 \cdot 10^{-6}$ c, $K = 1 \text{ Gs}^2/\text{W}$ and $\gamma = 0.88 \cdot 10^7$ Hz / Gs into equation (27), we obtain $T_1 = 5,4 \cdot 10^{-5}$ c.

The values of relaxation times found in our experiment are consistent with the values of T_1 and T_2 found by the pulsed EPR method [5] for the NV centers in diamonds. The difference in the values of T_1 may be due to the different nature and concentration of the studied paramagnetic centers, different structures of the sample matrices.

Conclusion

Determining the spin-lattice T_1 and spin-spin T_2 EPR relaxation times of NV centers in synthetic diamonds by the method of stationary saturation of inhomogeneously widened EPR lines will allow us to investigate the mechanisms of decoherence of the quantum states of these paramagnetic centers and evaluate the possibility of using nanodiamonds in the creating the element base of quantum computers.

Acknowledgments

This study was supported by the state assignment for the Saint Petersburg Electrotechnical University "LETI" (theme No. FSEE-2024-0005).

References

1. A. P. Nizovtsev, S. Y. Kilin, F. Jelezko, T. Gaebel, I. Popa, A. Gruber, J. Wrachtrup. - *Opt. Spectrosc.*, 99 (2), 233–244 (2005).
2. J. R. Maze, J. M. Taylor, M. D. Lukin. - *Phys. Rev. B*, 78, 094303 (2008).
3. E. Bauch, S. Singh, J. Lee, C. A. Hart, J. M. Schloss, M. J. Turner, J. F. Barry, L. M. Pham, N. Bar-Gill, S. F. Yelin, R. L. Walsworth. - *Phys. Rev. B*, 102, 134210 (2020).
4. Bogachev Yu.V., Nikitina A.V. - *LETI Transactions on Electrical Engineering and Computer Science*, 8, 16-20 (2016).
5. S. Kollarics, F. Simon, A. Bojtor, K. Koltai, et al. - *Carbon*, 188, 393-400 (2022).

EPR of magnetic nanoparticles in water dispersions

Yury V. Bogachev¹, Marina N. Shishkina¹, Anastasiya V. Nikitina^{1,2}

¹St.-Petersburg Electrotechnical University, St.-Petersburg, Russia

²Magnetic Resonance Research Centre, St.-Petersburg State University, St.-Petersburg, Russia

E-mail: Yu.Bogachev@mail.ru, nastya_nikitina1996@mail.ru

Introduction

Currently, the study of the physical properties and structure of promising MRI theranostic agents [1] based on aqueous dispersions of magnetic iron oxide nanoparticles is of considerable interest. In connection with the use of these substances in immuno-magnetic analysis [2], in NMR diagnostics (DMR method [1]), questions arise related to the aggregation of magnetic nanoparticles (MNPs) in a magnetic field, with the properties of the coating of nanoparticles, conjugation processes with various molecular compounds focused on capturing analyzed objects.

Experiments and Results

EPR studies of superparamagnetic iron oxide nanoparticles in aqueous suspensions (in distilled water and physiological solutions (a phosphate buffer with $pH = 7.0$ was used)) were carried out depending on their size and concentration. The synthesis of superparamagnetic iron oxide nanoparticles was carried out under heterophase conditions from solutions of ferrous and trivalent iron according to the Elmore-Massart scheme. EPR measurements were performed on a compact ESR-MINI-10 (SPbETU, Russia) spectrometer in St.-Petersburg Electrotechnical University, Russia and Bruker Elexsys E580 EPR spectrometer in the Magnetic Resonance Research Centre of St.-Petersburg State University, Russia.

A comparative analysis of the EPR spectra of suspensions of iron oxide nanoparticles in both distilled water and aqueous physiological solutions (Fig. 1) shows the following patterns:

- with an increase in the concentration of iron oxide nanoparticles, the intensity and "effective" width of EPR signals increase;
- the shape of the EPR lines contains two components – narrow and wide signals with different g -factor, overlapping each other.

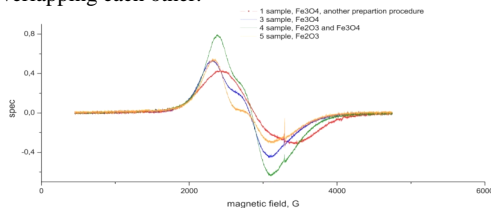


Figure 1. EPR spectra of suspensions of iron oxide nanoparticles in water solutions

Modeling and analysis of experimental EPR spectra showed that the observed EPR spectra are due to aggregates of polydisperse nanoparticles containing different numbers of particles and having different fractal dimensions. Most likely, the experimental EPR spectra are due to aggregates of polydisperse iron oxide nanoparticles, when the smallest particles are located in the center of the aggregate, followed by larger particles, and the largest are located on the periphery.

Since the MRI contrasting ability of MNPs increases with increasing magnetization of the core of nanoparticles, studies of the magnetic properties of nanoparticles depending on the

composition of the core have been conducted. It has been found that saturation magnetization (relative to unalloyed magnetite) increases with the introduction of manganese ions into the crystal lattice. The highest magnetization value corresponded to the composition $Mn_{0.3}Fe_{2.7}O_4$. At the same time, the absence of magnetic hysteresis for the magnetization curve indicated the superparamagnetic state of these particles. To reduce the aggregation effects, $Mn_{0.3}Fe_{2.7}O_4$ nanoparticles were stabilized in the form of colloidal solutions using a number of polyelectrolytes (PDDA, CH60, CH60-PEG, CH60-Dex). Studies of the effect of various MNP coatings on the EPR spectra of their aqueous dispersions show that EPR spectra consisting of a superposition of two EPR signals are transformed into a single Gaussian line with different widths and g -factor values depending on the type of coating (Table 1).

Table 1. EPR data of MNPs in aqueous dispersions

Sample	d_{HD}, nm	g -factor	$\Delta H_{pp}, Gs$
Mn _{0.3} Fe _{2.7} O ₄ /PDDA	86,1	2,1717	480 - 530
Mn _{0.3} Fe _{2.7} O ₄ /CH60	196,6	2,0865	550-600
Mn _{0.3} Fe _{2.7} O ₄ /CH60-PEG	216,6	2,0786	600-650
Mn _{0.3} Fe _{2.7} O ₄ /CH60-DEX	214,3	2,1167	650-700

The application of polyelectrolyte shells to $Mn_{0.3}Fe_{2.7}O_4$ nanoparticles made it possible to obtain stable sols of these particles. The best stabilizing effect was observed for $Mn_{0.3}Fe_{2.7}O_4$ /PDDA nanoparticles, while the hydrodynamic diameter of the particles relative to other particles had the smallest size. The EPR signal width for $Mn_{0.3}Fe_{2.7}O_4$ /PDDA nanoparticles had the lowest value. NMR relaxation studies for aqueous dispersions of stabilized MNPs samples showed the highest value of the transverse relaxation time T_2 in samples with $Mn_{0.3}Fe_{2.7}O_4$ /PDDA nanoparticles, which also indicates their lower ability to aggregate.

The following trends are typical for all the stabilized samples studied.

A decrease in the sample temperature from 289 K to 100 K led to a broadening of the EPR line and a shift of its g -factor to higher values.

EPR measurements of the same sample after standing for one month showed a slight broadening of the EPR signal and a decrease in signal intensity. The value of the g -factor did not change at the same time.

An increase in the size of nanoparticles from tens of nanometers to the micron level led to a significant broadening of the EPR lines.

Comparison of EPR line widths and g -factors for uncoated (Fig. 1) and coated magnetic nanoparticles (Table 1) shows that when aggregating magnetic nanoparticles, there is a significant broadening of the EPR lines and their displacement to the region of higher values of g -factors (to the region of lower magnetic fields).

Conclusion

Thus, EPR studies of aqueous dispersions of magnetic nanoparticles allow us to evaluate their MRI contrasting capabilities, stabilizing properties and aggregation ability.

References

1. Yu. V. Bogachev, V. V. Frolov, V. I. Chizhik. Magnetic resonance theranostics (in Russian). – SPbETU “LETI” Publ., St.-Petersburg, 2020. 224 p.
2. P. Nikitin, A. Orlov, M. Nikitin, P. Vetoshko, B. Gorshkov. Immunoassays Based on Magnetic Nanolabels. - *Book of abstracts of the 8th European Conference on “Magnetic Sensors and Actuators” (Bodrum, Turkey, 4-7 July 2010)*, p. W30.36.

Analysis of NOESY spectra to obtain accurate information on the structure and dynamics of some 5,7-substituted pyrazolo[1,5-a]pyrimidine derivatives in solution

*Daria S. Novikova*¹, *Anmar Al Mustafa*¹, *Vyacheslav G. Tribulovich*¹, *Ruslan I. Baichurin*², *Stanislav I. Selivanov*^{3,4}

¹Laboratory of Molecular Pharmacology, St. Petersburg State Institute of Technology, 190013 St. Petersburg, Russia

²Department of Organic Chemistry, Herzen State Pedagogical University of Russia, 191186 St. Petersburg, Russia

³Laboratory of Biomolecular NMR, St. Petersburg State University, 199034 St. Petersburg, Russia

⁴Department of Organic Chemistry, St. Petersburg State Institute of Technology, 190013 St. Petersburg, Russia

E-mails: dc.novikova@gmail.com (D.S.N.), nmr.group.spbu@gmail.com (S.I.S.)

Introduction

The nuclear Overhauser effect (NOE) is one of the most popular phenomena, which is currently intensively used to solve structural and dynamic problems in organic and bioorganic chemistry. This interest is due to the extremely strong sensitivity of the cross-relaxation rate σ_{ij} between the magnetic nuclei "i" and "j" on the distance between them r_{ij} , and also due to the dependence of σ_{ij} on the motion of the vector r_{ij} , which is determined by the overall rotational diffusion and intramolecular mobility of this pair of nuclei: $\sigma_{ij} \sim \tau_c^{\text{eff}}(r_{ij})^{-6}$, where τ_c^{eff} is the effective correlation time of overall diffusional and internal motions.

A lot of experimental and methodological problems of obtaining, processing and interpreting NOE data have been discussed during the last sixty years. The accuracy of quantitative estimates of interproton distances and the need for correct averaging of the results of their measurements in the presence of intramolecular dynamic processes that are fast within the NMR time scale hold a special place among these problems [1–3]. Ignoring the established methodology leads to a violation of one of the important I. Solomon requirements on the invariance of the interproton distance r_{ij} with time in the canonical description of the NOE phenomenon [4]. Another well-known requirement is the spherical shape of the studied molecule in solution, which ensures the absence of rotational diffusion anisotropy and the fulfillment of the requirement on the same correlation times τ_c for all pairs of magnetic nuclei compared with each other in a given molecule. Thus, the selection and correct use of existing approaches to eliminate or compensate factors leading to quantitative errors in the estimation of experimental distances based on NOE are important for the practical application of this NMR tool for studying the structure and dynamics of molecules in solution.

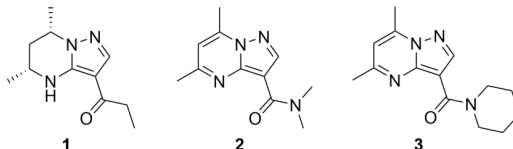


Figure 1. Structures of the studied pyrazolopyrimidine derivatives

This report presents the use of NOESY data to study in detail some 5,7-substituted pyrazolo[1,5-a]pyrimidine derivatives in solution (Fig. 1). Compound **1** was recently used to evaluate the possibility of accurately (within $\pm 5\%$ error) measuring the long-range distance $r_{2,6\text{eq}}$, which exceeds 6 Å [5]. It was shown that the main source of experimental errors is the

distortion of integral intensities when using the Whittaker smoother procedure [6]. So another algorithm was proposed for determining the exact values of volume integrals in NOESY spectra. In this work, these methodological features of data processing were applied in structural and dynamical studies.

Results and Discussions

Compounds **1–3** turned out to be extremely convenient models to analyze the problems of registration and processing of cross-peaks in NOESY spectra. Our efforts to further study structural features of compound **1** were aimed at determining the exact values of the distances between the H_{6eq} proton and protons H_{5ax} and H_{7ax} apparently symmetrically located relative to it (Fig. 2a).

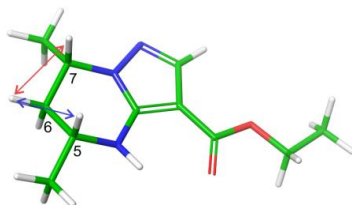


Figure 2. Spatial structure of compound **1**, obtained by conformational search and subsequent geometry optimization, where two-ended arrows indicate considered distances

The procedure of optimizing the geometry of the molecule **1** consistently produced a small difference between the distances $r_{6eq-5ax}$ and $r_{6eq-7ax}$ (blue and red arrows, respectively, in Fig. 2). Since this difference indicates a slight asymmetry in the location of the axial protons H_5 and H_7 with respect to the equatorial proton at position 6, we tried to use NOE to determine whether the calculated values of these distances correspond to the reality or are a consequence of optimizing method errors. To solve this problem Isolated Spin Pair Approximation (ISPA) and Peak Amplitude Normalization for Improved Cross-relaxation (PANIC) approaches were used to process the NOESY data obtained at short mixing times. These approaches are based on the use not the absolute values of the volume integrals of the corresponding cross-peaks, but their normalized values relative to the volume integrals of the diagonal cross-peaks.

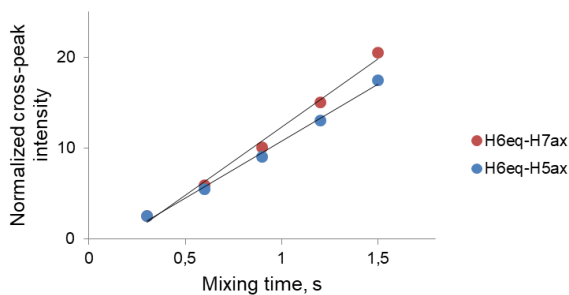


Figure 3. Graphical dependence of the normalized cross-peak intensity (S_{ij}/S_{ii}) on the mixing time τ_m for the distances $r_{6eq-7ax}$ (red points) and $r_{6eq-5ax}$ (blue points)

However, when using the minimum possible mixing time of 0.3 s for considered distances in two identical experiments, almost the same result was obtained within the measurement accuracy. Therefore, similar measurements of the normalized cross-peaks were conducted at longer mixing times. The results obtained were used to plot the dependence of normalized cross-peak intensities on mixing time (Fig. 3), which allowed estimating the corresponding cross-relaxation rates. Then we experimentally evaluated the difference in the corresponding distances using one of the calculated distances as a reference one within the considered pair. Consequently, the experimental difference in distances between considered protons turns out to be 30% higher than that obtained by the previously performed calculations [5]. Thus, it can be stated that the distance $r_{6eq-5ax}$ is really greater than the $r_{6eq-7ax}$ distance.

A similar study of the NOESY spectra of compounds **2** and **3** was carried out to determine the distances between H_2 and H_6 protons located in the rigid part of these molecules with the mobile protons of the methyl groups at positions 5 and 7, as well as with the mobile protons of the amide fragments. In this case, for quantitative estimates of cross-relaxation rates, effective values of the distances averaged by rapid exchange of mobile protons of methyl groups to the protons H_2 and H_6 were used. This report discusses various methods for obtaining and correctly processing data from NOESY spectra of such dynamic systems.

Conclusions

The presented results show the possibility of quantitative estimates of interproton distances in small molecules in solution between rigid protons, as well as between rigid and mobile protons with the high accuracy based on NOESY data using ISPA and PANIC approaches.

Acknowledgements

This work was supported by the Russian Science Foundation (project no. 23-13-00344). S.I.S. acknowledges St. Petersburg State University for research grant 116883049. The work was performed using the equipment of the Engineering Center of the St. Petersburg State Institute of Technology and the Research Equipment Park of the Herzen State Pedagogical University of Russia.

References

1. S. I. Selivanov, A. G. Shavva. – *Russ. J. Bioorg. Chem.*, 28(3), 194-208 (2002).
2. S. I. Selivanov, A. Y. Solov'ev, S. N. Morozkina, A. G. Shavva. – *Russ. J. Bioorg. Chem.*, 33(3), 302-309 (2007).
3. S. I. Selivanov, S. Wang, A. S. Filatov, A. V. Stepakov. – *Appl. Magn. Reson.*, 51, 165-182 (2020).
4. I. Solomon. – *Phys. Rev.*, 99, 559-565 (1955).
5. D. Novikova, A. Al Mustafa, T. Grigoreva, S. Vorona, S. Selivanov, V. Tribulovich. – *Molecules*, 28, 6584 (2023).
6. P. H. C. Eilers. – *Anal. Chem.*, 75, 3631-3636 (2003).

Structural Investigations of Fibril-Forming Peptide Fragments of Semenogelin1 Protein

Daria A. Osetrina, Aydar G. Bikmullin, Aydar R. Yulmetov, Timur A. Mukhametzyanov, Vladimir V. Klochkov¹, Dmitriy S. Blokhin

¹*Kazan Federal University, Kremlevskaya Str., 18, 420008, Kazan, Russia*

E-mail: d.sanchugova@yandex.ru

Introduction

Although the human immunodeficiency virus (HIV) was discovered more than 40 years ago, it continues to threaten public health around the world. Sexual intercourse is the most common mode of HIV transmission. Human semen has been shown to contain amyloid fibrils that multiply the infectivity of HIV virions. [1]

Amyloid fibrils in seminal fluid are formed from peptide fragments of the semenogelin1 (SEM1) protein (SEM1(45-107), SEM1(49-107), SEM1(68-107), SEM1(86-107)). SEM1 is secreted in the seminal vesicles and during ejaculation is cleaved into small peptide fragments by internal proteases. [2] The amyloid fibrils formed by SEM1 are cationic bridges that reduce electrostatic repulsion between the charged surfaces of HIV virions and target cells.

In this work, the spatial structures of all four amyloid-forming peptides of the semenogelin1 protein in monomeric form (SEM1(45-107), SEM1(49-107), SEM1(68-107), SEM1(86-107)) and the structures of the N-domains of the three peptides studied (SEM1(45-67), SEM1(49-67), SEM1(68-85)) were determined for the first time. High-resolution nuclear magnetic resonance (NMR) spectroscopy, circular dichroism (CD) spectroscopy and molecular dynamic (MD) modelling were used as research methods. This work also involved the modelling of the SEM1(68-107) dimer using molecular dynamics in the GROMACS [3] software and metadynamics using the PLUMED [4] library for GROMACS.

Results

SEM1(86-107) and SEM1(86-107)+DPC complex in solutions were studied by NMR spectroscopy. The obtained spatial restrictions (inter-nuclear distances) were used as input data for calculations of the structures of the investigated objects. Analysis of the structure of the SEM1(86-107) peptide and circular dichroism spectra showed that this peptide has a disordered secondary structure. [5] While the SEM1(86-107) peptide with dodecylphosphocholine micelle has a helix.

2D and 3D NMR spectra were obtained for the peptide SEM1(68-107) and used to relate chemical shifts. Chemical shift assignments were completed for 34 of the 40 amino acid residues. A full assignment could not be made due to uninformative NMR spectra for some amino acid residues. This is explained by the high mobility of the peptide in these sites. Therefore, to solve this problem, an approach based on the use of experimental constraints of individual peptide fragments found in the full-length study object was applied. [6] Therefore, it was necessary to study the N-terminal domain of SEM1(68-107), the SEM1(68-85) peptide.

¹H, ¹³C and ¹⁵N chemical shift assignments were carried out for the SEM1(68-85) peptide using two-dimensional NMR spectroscopy. The obtained spatial constraints were used to calculate the structure of SEM1(68-85) in the XPLOR-NIH program [7] using the nonlinear annealing method. A file with the spatial constraints of SEM1(68-85) and SEM1(86-107) was created to calculate the spatial structure of SEM1(68-107). The calculation was also performed in the XPLOR-NIH program using the non-linear annealing method. Molecular dynamic modelling was also performed for SEM1(68-107) in the

GROMACS package. The simulation duration was 350ns. Basically, the peptide has a disordered secondary structure, but there are fragments that have helical regions.

Modelling of the dimer SEM1(68-107) in the GROMACS package was also performed, as well as metadynamics using the PLUMED library. Two monomers were placed in a box with water at maximum distance from each other. The monomer was taken from the obtained structures after MD modelling. Metadynamics was used to construct the free energy profile of the dimer system. The distance between the centres of mass of the dimer and the number of close contacts between Ca atoms were chosen as collective variables.

The primary structure of SEM1(45–107) differs from SEM1(49–107) only by the presence of four amino acids residues. A clear difference was observed in the rate of the amyloid formation process using fluorescence spectroscopy of thioflavin T. We observed a more intense aggregation process of SEM1(45-107) compared to SEM1(49-107). This did not allow us to study the structures of the peptides in monomeric form. Therefore, the N-domains of these peptides were studied by NMR spectroscopy and molecular dynamics (MD) modelling of full-length peptides was done.

Two-dimensional NMR spectra were recorded for each of the N-domains of the peptides. They were analyzed and data were obtained to calculate spatial structures. Both peptides have a predominantly disordered structure, but SEM1(45-67) has a helix. To calculate the full-length peptides SEM1(45-107) and SEM1(49-107), files were created with constraints derived from previous studies of the N domains of SEM1(45-67) and SEM1(49-67) and the peptide SEM1(68-107). All SEM1(45-107) structures contain helical fragments at the N-terminus. MD simulations confirm the presence of a helical fragment at the N-terminus of SEM1(45-107) compared to SEM1(49-107). Therefore, four additional residues stabilize the helical motif SEM1(45-107).

Conclusions

Studies of the spatial structures of SEM1(45-107), SEM1(49-107), SEM1(68-107), SEM1(86-107) and their N-domains (SEM1(45-67), SEM1(49-67) and SEM1(68-85)) show that all peptides possess a disordered structure, but the SEM1(45-107) peptide contains a helical fragment at the N-terminus, which was also observed for the SEM1(45-67) peptide fragment. The high hydrophobicity of SEM1(45-107), associated with the presence of the first four amino acid residues, leads to the formation of a stable helical region and a propensity for further aggregation, which increases the rate of fibril formation. Consequently, four additional residues stabilise the helical motif of SEM1(45-107), which contributes to the formation of a stabilised hydrophobic region. The higher hydrophobicity of SEM1(45-107) ensures that the peptides are prone to interactions leading to rapid aggregation rates.

Also studies of the SEM1(86-107) peptide with a lipid membrane surface model lead to the formation of a helical region. This can be explained by the interaction of the peptide with the surface of the DPC micelle. The appearance of the helical fragment helps to rearrange the hydrophilic sites.

Modelling of the SEM1(68-107) dimer in the GROMACS package was also performed, as well as metadynamics using the PLUMED library. The duration of dimer modelling was 1000ns. During this time, conformational changes occurred in the structure of each peptide in the dimer: a beta-bend was formed, changing the direction of the main chain by 180 degrees. There are also stable helical regions parallel to each other. These conformational changes are characteristic of germinal core formation during the lag phase of amyloid peptide oligomerisation, and we observe an intermediate state before beta sheet aggregation. Indeed, the formation of an amyloidogenic assembly containing helical regions is a key step in fibril formation.

Acknowledgements

This work is supported by the Russian Science Foundation (D.S. Blokhin, project no. 20-73-10034)

References

1. Quantitation of human immunodeficiency virus type 1 infection kinetics. / D. S. Dimitrov, R. L. Willey, H. Sato [et al.] // *Journal of Virology*. – 1993. – Vol. 67, № 4. – P. 2182-2190.
2. Semen-derived amyloid fibrils drastically enhance HIV infection. / J. Munch, E. Rucker, L. Standker [et al.] // *Cell* – 2007. – Vol. 131, № 6. – P. 1059-1071.
3. Pronk, S. GROMACS 4.5: A high-throughput and highly parallel open source molecular simulation toolkit. / S. Pronk, S. Pall, R. Schulz, et al. // *J. Bioinform.* – 2013. – V. 29. – P. 845-854.
4. Bonomi, M. PLUMED: A portable plugin for free-energy calculations with molecular dynamics. / M. Bonomi, D. Branduardi, G. Bussi, et al. // *Computer Physics Communication*. – 2010 – V. 180 (10). – P. 1961-1972.
5. D. Sanchugova, et al., The Structure of Fibril-Forming SEM1(86-107) Peptide Increasing the HIV Infectivity. *BioNanoScience*, 2021, Vol. 11, P. 182–188.
6. Schmitz, T. NMR-Based Structural Characterization of a Two-Disulfide-Bonded Analogue of the FXIIIa Inhibitor Tridegin: New Insights into Structure-Activity Relationships. / T. Schmitz, A. A. P. George, B. Nubbemeyer, et al. // *Int. J. Mol. Sci.* – 2021. V. 22, P. 880.
7. Schwieters, C. D. Using Xplor – NIH for NMR molecular structure determination. / C. D. Schwieters, J. J. Kuszewski, G. M. Clore // *Prog. Nucl. Magn. Reson. Spectrosc.* – 2006. – V. 48. – P. 47-62.

Study of the thermochromic behavior of nitro-substituted symmetric bis-spiropyran of the indoline series using dynamic NMR methods

I.V. Ozhogin, A.S. Kozlenko, A.D. Pugachev, V.S. Dmitriev, P.B. Chepurnoy, G.S. Borodkin
 Institute of Physical & Organic Chemistry, Southern Federal University,
 Russian Federation, 344090 Rostov-on-Don, Stachka ave., 194/2
 E-mail: iozhogin@sfnu.ru

Introduction

Spiropyrans are a well-known and promising class of organic photochromes [1, 2], capable of isomerization from the spirocyclic (SP) to the brightly colored merocyanine (MC) form. One of the most interesting and little studied derivatives of the spiropyran series are bis-spiropyrans (BSP), in which the photochromic centers are connected through a common electronic π -system. These systems are of great interest to researchers, since sequential or parallel isomerization of their photoactive fragments potentially allows these systems to exist in the form of three or more isomers [3, 4], which makes them prototypes of multi-state molecular switches of optical, electrical, magnetic and other properties of systems based on them. The goal of this study was to obtain a symmetrical BSP of the indoline series containing a nitro group in the central pyranochromene fragment of the molecule and to study the mechanisms of its thermal isomerization (Fig. 1).

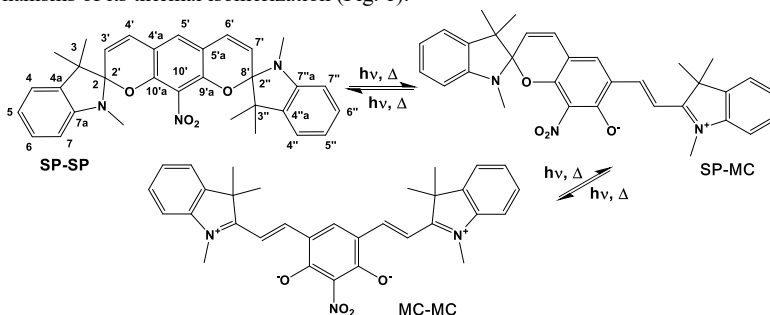


Figure 1. Isomerization transformations of the target BSP

Synthesis and study of the structure and isomerization mechanisms of the target BSP

The symmetrical indoline BSP **3** was prepared by refluxing aldehyde **1** with two equivalents of 1,2,3,3-tetramethyl-3*H*-indolium perchlorate **2** in methanol in the presence of triethylamine as a deprotonating agent (Fig. 2).

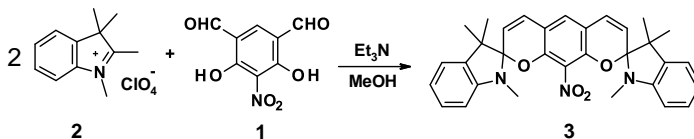


Figure 2. Synthesis of symmetrical BSPs of the indoline series

The structure of the resulting compound was studied using NMR spectroscopy. ^1H NMR spectra recorded in various deuterated solvents contained signals from proton-

containing groups characteristic of both spirocyclic (SP-SP) and merocyanine (SP-MC and/or MC-MC) forms of BSP, which indicated the presence of equilibrium between these isomers in solution (Fig. 1). At the same time, the ratio of isomers changed significantly depending on the polarity of the solvent and temperature. Thus, in weakly polar CDCl_3 in the temperature range from +10 to +50 °C (283 – 323 K), the proton signals of the three main BSP isomers (SP-SP, SP-MC and MC-MC) were detected in close ratios. Fig. 3 shows the fragments of ^1H NMR spectra, representing the areas of manifestation of indicative signals of N-methyl groups. About 2.7 ppm the signals of the N-Me groups of the completely closed SP-SP isomer are located. Similar signals of the closed fragment of the SP-MC form appeared as singlets in the region of 2.75 – 2.77 ppm, and the corresponding signals of the open fragment of the molecule – at 3.59 – 3.61 ppm. In the most downfield region there are N^+-Me groups' signals of the twice opened MC-MC isomer, which appear in the form of broadened singlet signals with maxima in the range of 3.70 – 3.79 ppm.

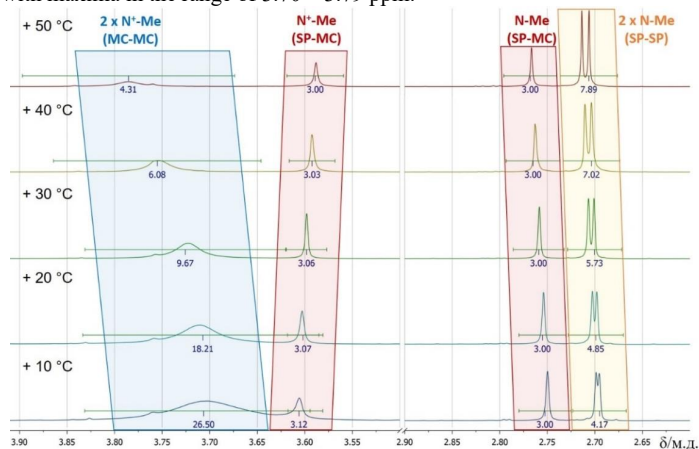
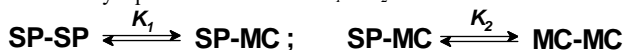


Figure 3. Fragments of ^1H NMR spectra of BSP recorded in CDCl_3 in the temperature range from +10 to +50 °C

Analysis of the integral intensities of characteristic signals made it possible to establish the ratio of the main forms of BSP in a CDCl_3 solution at different temperatures. It was found that with decreasing temperature the doubly opened MC-MC isomer stabilizes, while heating of solution up to 50 °C leads to the predominance of the completely closed SP-SP form. The concentration of singly opened merocyanine SP-MC usually takes intermediate values, which is associated with the involvement of this isomer in two equilibrium processes at once, characterized by equilibrium constants K_1 и K_2 :



Based on the data obtained, we calculated the equilibrium constants of the isomerization processes (K_1 и K_2), after which, according to the Van't Hoff equation, we plotted graphs of the logarithms of the equilibrium constants $\ln K$ on the inverse temperature $1/T$ (Fig. 4), which made it possible to calculate ΔH^0 of the corresponding processes. It was found that both isomerization processes accompanied by ring opening ($\text{SP-SP} \rightarrow \text{SP-MC}$ and $\text{SP-MC} \rightarrow \text{MC-MC}$) are exothermic ($\Delta H^0 = -3.0$ and -7.7 kcal/mol, respectively). Accordingly,

an increase in temperature shifts the equilibrium of both processes towards partial or complete cyclization of merocyanines.

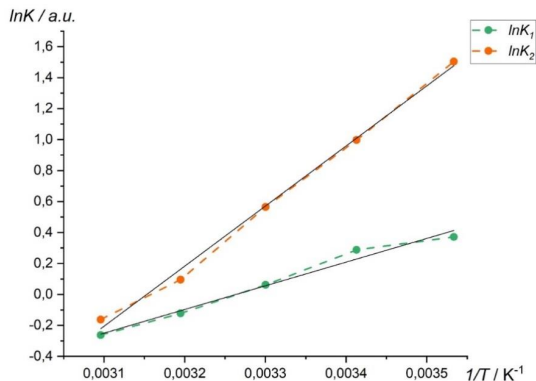


Figure 4. Graph of logarithms of the equilibrium constants $\ln K$ versus reciprocal temperature $1/T$

Similar studies carried out in polar deuterated solvents such as CD_3CN and $\text{DMSO-}d_6$ showed that the dominant form at room temperature was the doubly opened MC-MC. In the ^1H NMR spectra recorded in CD_3CN in the temperature range from +10 to +50 °C, the ratio of MC-MC and SP-SP isomers varied from 40:1 to 10:1, and the peaks of the SP-MC isomer were difficult to detect. A similar picture was observed in NMR spectra recorded in $\text{DMSO-}d_6$: the dominant form at 30 °C was the doubly opened MC-MC (88 mol.%), but the second place was taken by the singly open isomer SP-MC (about 10 mol.%), and the content of the SP-SP form did not exceed 2%.

Thus, we have shown that the synthesized symmetrical indoline BSP with a nitro group in the central pyranochromene fragment of the molecule exists in the equilibrium of MC-MC, MC-SP and SP-SP isomers in organic solvents. It is important to note that at room temperature the doubly opened MC-MC form predominates. Using NMR spectroscopy, it was shown that an increase in temperature leads to a shift in equilibrium towards spirocyclic isomers, since both isomerization processes accompanied by ring opening (SP-SP \rightarrow SP-MC and SP-MC \rightarrow MC-MC) are exothermic ($\Delta H^\circ = -3.0$ and -7.7 kcal/mol, respectively).

Acknowledgements

This study was financially supported by the Russian Science Foundation grant No. 21-73-10300, <https://rscf.ru/project/21-73-10300/>, and carried out at Southern Federal University.

References

1. A. S. Kozlenko, I. V. Ozhogin, A. D. Pugachev, M. B. Lukyanova, I. M. El-Sewify, B. S. Lukyanov. – *Top. Curr. Chem.*, 381, 8 (2023).
2. J. K. Rad, Z. Balzade, A. R. Mahdavian. – *J. Photochem. Photobiol. C: Photochem. Rev.*, 51, 100487 (2022).
3. F. Nourmohammadian, A. A. Abdi. – *Bull. Korean Chem. Soc.*, 34, 1727 (2013).
4. E. L. Mukhanov, I. V. Dorogan, A. V. Chernyshev, S. O. Bezuglyi, I. V. Ozhogin, M. B. Lukyanova, B. S. Lukyanov. – *Int. J. Photoenergy*, 2013, 752949 (2013).

Relaxation of the ^1H multiple-quantum (MQ) NMR coherences during the excitation period in gypsum single crystal.

Ksenia Panicheva^{1,2}, *Sergey G. Vasil'ev*¹, *Edward Fel'dman*¹

¹*Federal Research Center of Problems of Chemical Physics and Medicinal Chemistry RAS, Ac. Semenov avenue 1, Chernogolovka, Moscow Oblast 142432, Russia*

²*Faculty of Fundamental Physical-Chemical Engineering, Lomonosov Moscow State University, GSP-1, Leninskie Gory, Moscow 119991, Russia*

E-mail: vasiliev@icp.ac.ru, viesssw@mail.ru

Introduction

Multiple-quantum (MQ) NMR coherences [1] serve a testbed for many concepts in questions associated with quantum information. They served as a model of a large qubit register [2], were used to investigate the multi-qubit quantum state transfer [3], many-particle entanglement [4], scrambling [5], etc. In MQ NMR spectroscopy the behavior of multispin/multiple-quantum coherent states is observed. These states emerge because of the cooperative action of internal interactions (dipole-dipole interactions, DDIs) and intentionally designed series of radio-frequency pulses [1]. MQ NMR experiment used in the present study [1] consists of 4 steps: the preparation period, at which the MQ coherences emerge, the polarization spreads among larger number of observable coherences and the number of spins contributing to any given coherence grows with increasing time τ ; the period of free evolution (optional), at which the coherences develop under the internal interactions; the mixing period, at which the unobservable MQ coherences are transformed into observable single-quantum coherences by applying the pulse sequence identical to the preparation period, but with the $\pi/2$ phase shift of all pulses to invert the sign of the Hamiltonian; and finally the detection period, consisting typically of $\pi/2$ pulse, is used to detect the magnetization. The MQ coherences are detected indirectly by repeating the whole experiment multiple times with increasing phases of pulses of the preparation period each time by a fixed value $\Delta\phi$ between 0 and 2π , which is selected according to the desired maximum coherence order to be detected, $\Delta\phi = 2\pi / 2n_{\text{max}}$.

The goal of the present study was the experimental investigation of the dynamics and relaxation of MQ NMR coherences in dipolar coupled ^1H spin pairs in gypsum single crystal and comparison of the results with the theory for open quantum systems based on the Lindblad equation developed in our group.

Experimental results and discussion

The experiments were performed on a Bruker Avance III spectrometer operating at 400.2 MHz for ^1H nuclei. Gypsum, $\text{CaSO}_4 \cdot 2\text{H}_2\text{O}$, single crystal was used as a sample for investigation. This is a well-known diamagnetic crystal lacking a significant amount of NMR-active isotopes except for ^1H [6]. All protons in the structure are equivalent and belong to the two water molecules. The distance between the protons within a single water molecule is much smaller than the distance between different water molecules. The separation between protons in water molecule is 1.54 Å. The vectors connecting the protons of two water molecules in the structure are not collinear. In general, the ^1H NMR spectrum consists of two pairs of doublets, which may collapse or overlap at some orientations of the crystal in the external magnetic field. The ^1H NMR spectra obtained at different orientations, which were subsequently investigated in MQ experiments are shown in Fig. 1. The signals on the detection period of MQ NMR experiment were first Fourier transformed in the direct

dimension. The signals belonging to the different components of the doublets were integrated and then the second Fourier transformation was performed to obtain the MQ spectra.

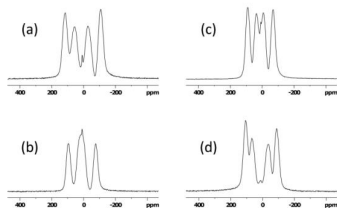


Figure 1. The ^1H NMR spectra of gypsum obtained at different positions in the external magnetic field.

The intensities of MQ coherences corresponding to different dipole-dipole couplings (7 in total) were obtained as the function of preparation time. The intensities of MQ coherences corresponding to the outer doublet shown in Fig. 1(d) are demonstrated in Fig. 2.

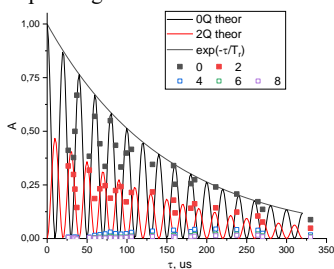


Figure 2. The intensities of ^1H MQ NMR coherences in gypsum crystal as the function of preparation time. Points represent the experimental data. Solid lines are theoretical curves.

The MQ NMR spectra consist mainly of zero- and second order coherences. It was found that the oscillatory behavior of these coherences with increasing preparation time is governed by the dipolar coupling in the spin pair for different orientations of the crystal. The decay of MQ coherences of zero- and second- orders are well described by the exponents with the same relaxation time T_r in agreement with the theoretical predictions (solid lines in Fig. 2). The obtained relaxation time values $T_r = 150 \pm 15 \mu\text{s}$ are similar for different orientations.

The obtained results show that the interaction of investigated system (isolated spin pair) with the environment is inevitable. With increasing preparation time the experimental the MQ intensity distributes beyond the correlation among two spins. The Higher order coherences appear and the overall intensity of MQ coherences decay. The intensities of the MQ coherences of the order higher than 2 depend on the orientation of the crystal in the external magnetic field. Even in this case the developed theory gives a good approximation of the experimental data for zeroth and second order MQ coherences.

Acknowledgements

This work is performed as a part of a state task, State Registration No.124013000760-0.

References

1. J.Baum, M.Munowitz, A.N.Garroway, A.Pines, *J. Chem. Phys.*, 1985, 83, 2015-2025
2. M. Lovric', H.G. Krojanski, D. Suter, *Phys. Rev. A.*, 2007, 75, 42305
3. E.B. Fel'dman, A.N. Pechen, A.I. Zenchuk, *Phys. Lett. A*, 2007, 413, 127605
4. S. I. Doronin, E. B. Fel'dman, I. D. Lazarev., *Physical Review A*, 2019, 100, 022330
5. M. Gartner, P. Hauke, A. M. Rey., *Phys. Rev. Lett.*, 2018 120, 040402
6. G. E. Pake, *J. Chem. Phys.*, 1948, 16, 327-336

Determination of regio- and stereochemistry of spiropyrrolizine oxindoles using NMR spectroscopy methods

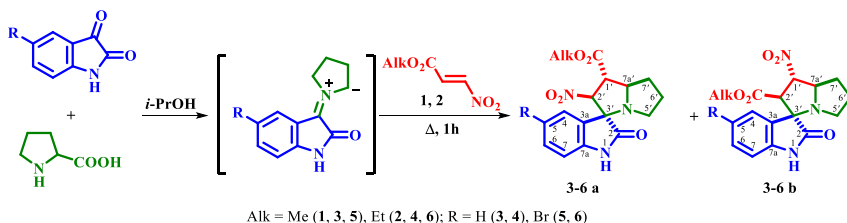
Pelipko V. V., Baichurin R. I., Makarenko S. V.

Herzen State Pedagogical University of Russia, Laboratory of nitro compounds, Center of collective use at the Faculty of Chemistry "Instrumental methods for the study of nitro compounds, coordination, biologically active substances and nanostructured substances" 48 Moyka River Embankment, Saint Petersburg 191186, Russia

E-mail: kohrgpu@yandex.ru

http://kohrgpu.ru

A study of the nitroacrylates **1**, **2** interaction with isatinproline ylides upon boiling for 1 hour in isopropyl alcohol showed that the reaction leads to the formation of regioisomeric spirooxindoles **3-6**, similar to the reactions of 3,3,3-trihalo-1-nitropropenes [1] or β -nitrostyrenes [2]. Spiropyrrolizine oxindoles **3-6** were isolated from the reaction as a mixture of two regioisomers in the ratio $a : b = 2 : 1$ (by ^1H NMR spectra). Individual major isomers of spiropyrrolizine oxindoles **3-6a** was isolate by recrystallization.



The rigidly fixed structure of the isolated spiropyrrolizine oxindoles **3-6a** makes them very attractive objects for studying the structure using 2D NMR spectroscopy experiments.

In the ^1H NMR spectra of individual compounds **3-6a** the proton ($\text{H}^{2'}$) at the carbon atom associated with the nitro group appears as a doublet at 5.59-5.61 ppm (3J 11.1-11.3 Hz), in turn, the proton ($\text{H}^{1'}$) at the carbon atom associated with the alkoxycarbonyl group resonated as a doublet of doublets at 3.96-4.21 ppm (3J 9.2-9.3, 3J 11.1-11.3 Hz), which allows them to be characterized as regioisomers **a** (Fig. 1).

This assignment of signals in the ^1H NMR spectra is confirmed by the results of studying these substances using the ^1H - ^1H COSY NMR method. Thus, in the ^1H - ^1H COSY spectrum of compound **6a**, cross peaks are observed between the signals of the pyrrolizine ring protons $\text{H}^2/\text{H}^{1'}$, $\text{H}^{1'}/\text{H}^{7a}$, $\text{H}^{7a}/\text{H}^{7'}$, $\text{H}^{7'}/\text{H}^6$, $\text{H}^6/\text{H}^{5'}$, which confirms the presence of spin-spin interaction between them (Fig. 2).

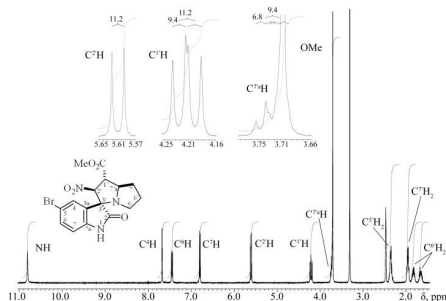
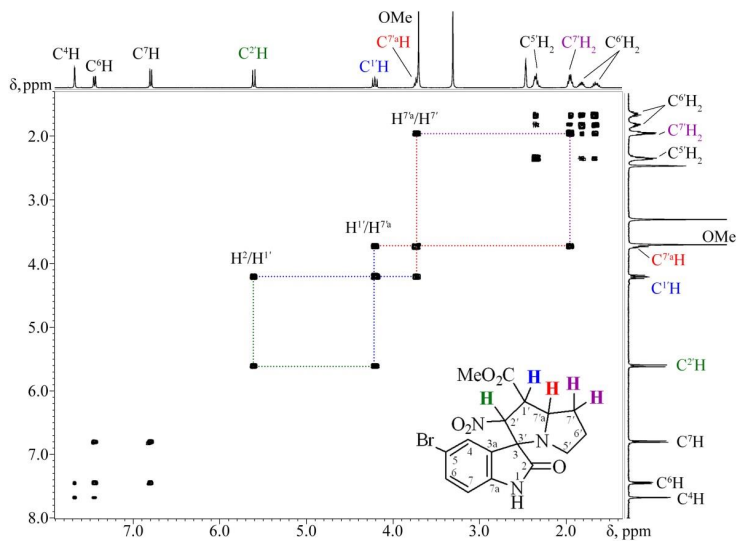
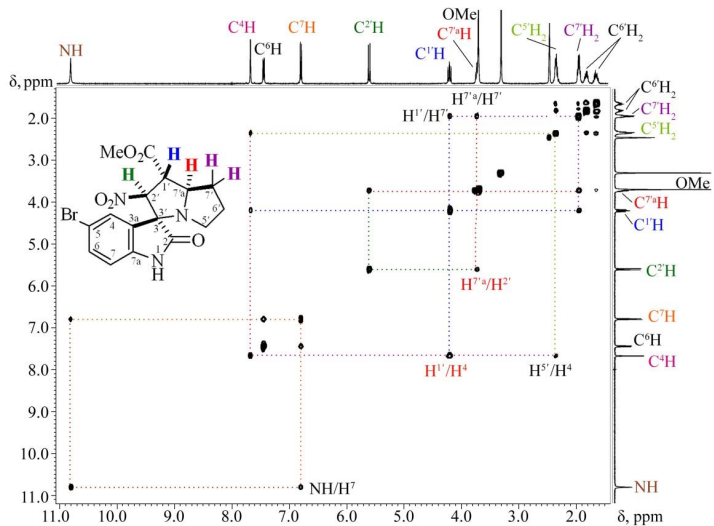


Figure 1. ^1H NMR spectrum of compounds **6a** (DMSO- d_6)



The fine structure of the obtained individual spiropyrrolizine oxindoles **3-6a** was studied using a ^1H - ^1H NOESY NMR experiment. Results of ^1H - ^1H NOESY experiments for individual diastereomers, obtained with a variable value of mix. time (τ 0.5, 1, 1.5, 2 sec), demonstrate NOE correlations of protons H^1/H^4 and $\text{H}^{7a}/\text{H}^{2'}$ (Fig. 3).



The presence of these correlations indicates that for diastereomer **a** such an arrangement of spirocycles is realized in which the proton of the pyrrolizine ring (H^1) at the carbon atom associated with the alkoxy carbonyl group and the proton of the indole ring (H^4) are as close as possible in space (Fig. 4).

Thus, the study of individual isomers of spiropyrrolizine oxindoles 3-6a using 1H - 1H COSY and NOESY NMR spectroscopy experiments made it possible to establish their regeo- and stereochemistry.

The studies were carried out in the Center of collective use at the Faculty of Chemistry of the Herzen State Pedagogical University of Russia on the Jeol ECX-400A spectrometer (Royal Probe) at 399.78 (1H) and 100.53 (^{13}C) MHz with standard experimental settings. The residual signals of a non-deuterated solvent (for 1H nuclei) or the signals of a deuterated solvent (for ^{13}C nuclei) were used as a standard.

Acknowledgments

This work was financially support by the Ministry of Education of Russia (project no. VRFY-2023-0003).

References

1. A. Y. Barkov, N. S. Zimnitskiy, V. Y. Korotaev, I. B. Kutyashev, V. S. Moshkin, V. Y. Sosnovskikh. – *Tetrahedron*, 72(43), 6825-6836 (2016).
2. B. Gayen, A. Banerji. – *Monatshefte für Chemie-Chemical Monthly*, 145, 1953-1965 (2014).

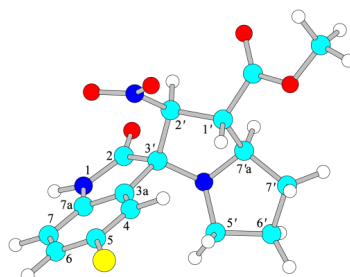


Figure 4. Spatial model of compound **6a** (HyperChem, MM+)

Investigation of polyvinylpyrrolidone–hydroxyapatite composites by NMR and EPR methods

*Alina Petrova*¹, *Fadis Murzakhanov*¹, *George Mamin*¹, *Oleg Gnezdilov*¹, *Inna Fadeeva*²,
*Marat Gafurov*¹

¹*Institute of Physics, Kazan Federal University*

²*A.A. Baikov Institute of Metallurgy and Material Science, Russian Academy of Sciences, Moscow*

E-mail: *mamatovaalinka@mail.ru*

Introduction

Synthetic calcium hydroxyapatite (HAP) with the chemical formula $\text{Ca}_{10}(\text{PO}_4)_6(\text{OH})_2$ is widely used for medical purposes due to its good biocompatibility and maximum chemical similarity with natural bone. However, the use of pure HA in modern implantology is limited due to its low strength characteristics and insolubility. The synthesis of bioresorbable composite materials (organomineral composites) is one of the most difficult problems in regenerative medicine and materials sciences. In this work, we applied electron paramagnetic resonance (EPR) and nuclear magnetic resonance (NMR) to study the properties of organomineral composite films [1] synthesized in situ in a solution of the bioresorbable polymer polyvinylpyrrolidone (PVP).

The spectra obtained by EPR and NMR

For HA, PVP and PVP-HA, the EPR signal was not observed due to the absence of paramagnetic centers in the structure of materials, which confirms the purity of the starting materials. After X-ray irradiation of HA powders, an EPR spectrum containing three lines was recorded at X-band frequency range (Fig. 1). Spectroscopic parameters of the EPR spectrum made it possible to attribute the detected signal to the well-studied NO_3^{2-} -stable species in HA [1, 2]. PVP samples were also examined after X-ray irradiation (Fig. 2, red lines) and photoinduced EPR at low temperatures (Fig. 3), since it is known that exposure to visible light does not lead to the formation of stable radicals in HA [3], but in the polymer chain of PVP [4]. In the W-band, due to the better spectral resolution, a three-line PVP pattern was observed (Fig. 2). He showed the localization of an unpaired electron on the PVP nitrogen atom. In the X-range, the three-line pattern for PVP has not been solved again.

As can be seen from Figure 2 (blue lines), the EPR spectrum of PVP-HA contains only the spectrum of NO_3^{2-} radicals in HA, and the EPR spectrum component from PVP was not observed.

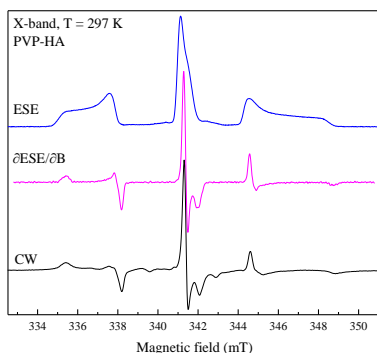


Figure 1. Comparison of EPR spectra of PVP-HA sample detected in ESE (blue upper curve) and cw (black lower curve) after X-ray irradiation in the X-band at $T = 297$ K. Middle curve was obtained by differentiating the ESE EPR spectrum.

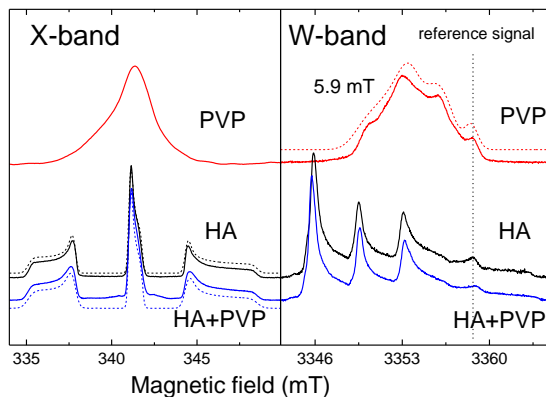


Figure 2. EPR spectra obtained by detecting the ESE of samples after X-ray irradiation: X-band at the left panel, W-band at the right panel. The red lines show the spectra of PVP, the black lines – of HA, and the blue lines – of PVP-HA. The dotted lines show the approximation of the EPR spectra.

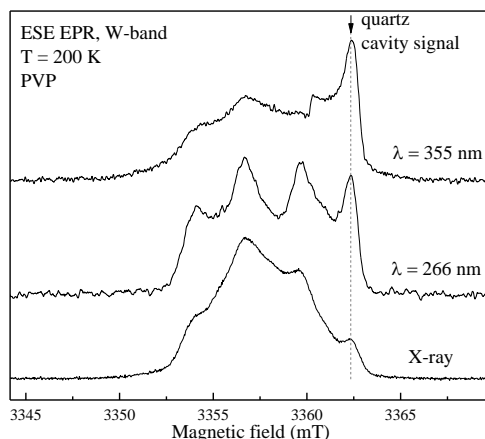


Figure 3. Photo-induced (by lasers with the wavelengths of 355 and 266 nm) and X-ray induced ESE EPR spectra at $T = 200$ K of PVP in the W-band. The dotted line belongs to the quartz tube of the sample holder.

The ^1H NMR spectra for PVP and PVP-HA are shown in Fig. 4. The ^1H MAS-NMR spectrum of the PVP consists of one unresolved NMR signal at 2.4 ppm associated with the CH_2 groups of the pyridine ring and the polymer chain. The CH groups of the polymer chain contributed to the signal at about 5 ppm, while the CH_3 end groups make a small contribution in the region of 0.5-1.5 ppm. On the ^1H NMR spectrum in Fig. 6, the contributions of these chemical groups appeared as small shoulders to the right and left of the main NMR signal.

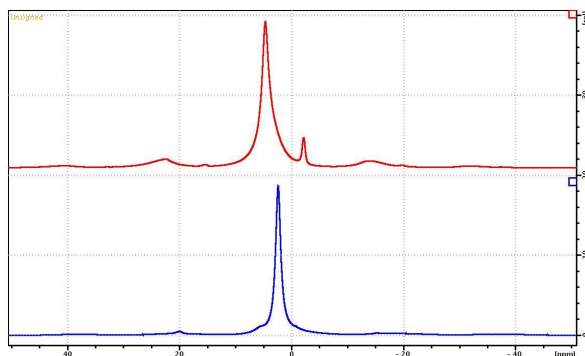


Figure 4. ^1H NMR spectra of samples of PVP (blue curve) and, PVP-HA (red curve) samples.

Figure 7 shows the $^{13}\text{C}\{^1\text{H}\}$ MAS-NMR spectra of the PVP on ^{13}C during proton decoupling, obtained using the pulse programs cp (red) and hpdec (blue), respectively. The MAS-NMR $^{13}\text{C}\{^1\text{H}\}$ spectrum of PVP-HA has the same form as in Fig. 6, only the signal-to-noise ratio is several times lower. The NMR signals of the aliphatic region for cross-polarization have a resolution worse than for the ^{13}C NMR spectrum with proton suppression.

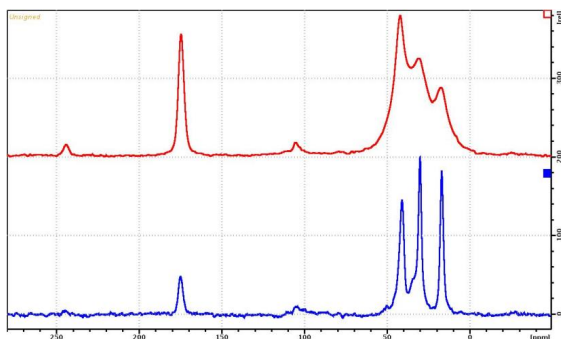


Figure 7. MAS-NMR spectra of $^{13}\text{C}\{^1\text{H}\}$ cp (red) and hpdec (blue) of the PVP. The rotation frequency of the sample is 7kHz.

The use of EPR in two frequency ranges made it possible to determine with high accuracy the spectroscopic parameters of photoinduced and radiation-induced paramagnetic centers (PC)–based on nitrogen in HA, PVP and PVP-HA composite. It is shown that PVP does not significantly affect the EPR parameters of radiation PC and their relaxation times in GA. Photoinduced PC were found only in PVP. In the ^1H NMR spectra, two signals (4.7 ppm and 2.15 ppm) attributed to “free” water and hydroxyl groups are observed in composites with rotation at a magic angle, respectively; A single line was observed for ^{31}P . NMR relaxation measurements for ^1H and ^{31}P showed that relaxation attenuations are multicomponent processes that can be described by three contributions (times) of transverse relaxation. The results obtained show that magnetic resonance methods can be used to control the quality of synthesis of PVP-HA composites and, potentially, to track the processes of their resorption [5].

Acknowledgements

The work was carried out with the support of the RSCF project grant No. 23-63-10056.

References

1. Gafurov M., Biktagirov T., Yavkin B., Mamin G., Filippov Y., Klimashina E., Putlayev V. and Orlinskii S. Nitrogen-containing species in the structure of the synthesized nano-hydroxyapatite // JETP letters, 2014, V. 99, P.196-203.
2. Shurtakova D. V., Mamin G. V., Gafurov M. R. The study of synthetic tricalcium phosphate by EPR and DFT methods // Magn. Reson. Solids, 2023, V. 25, P. 23201.
3. Gabbasov B., Gafurov M., Starshova A., Shurtakova D., Murzakhanov F., Mamin G., Orlinskii S. Conventional, Pulsed and High-Field Electron Paramagnetic Resonance for Studying Metal Impurities in Calcium Phosphates of Biogenic and Synthetic Origins // J. Magnetism and Magnetic Materials, 2019, V. 470, P. 109–117.
4. Radtsig V. A. MODERN ACHIEVEMENTS IN MECHANICAL ENZYMATIVE PROCESSING OF PLANT RAW MATERIALS //Khim. Fiz., 2004, V. 23, № 10, P. 70–109. (in Russian)
5. Petrova A. Magnetic Resonance Based Analytical Tools to Study Polyvinylpyrrolidone—Hydroxyapatite Composites / A. Petrova, G. Mamin, O. Gnezdilov, I. Fadeeva, O. Antonova, A. Forysenkova, V. Antoniac, J. Rau, and M. Gafurov // Polymers - 2023. – Vol.15, Is.22. – 4445. – DOI: 10.3390/polym15224445

Application of 2D NMR experiments for identification of alkyl 5-nitro-7,12-dioxo-7,12-dihydroindeno[1,2-a]fluorene-6-carboxylates

Pilipenko I. A.,^a Selivanov S. I.,^b Pelipko V. V.,^a Baichurin R. I.,^a Makarenko S. V.^a

^aHerzen State Pedagogical University of Russia, Department of Organic Chemistry, Laboratory of Nitrocompounds, Center of collective use at the Faculty of Chemistry "Instrumental methods for the study of nitro compounds, coordination, biologically active substances and nanostructured substances"

48 Moyka River Embankment, Saint Petersburg 191186, Russia

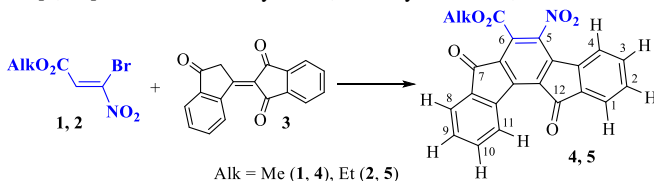
E-mail: kohrgpu@yandex.ru

<http://kohrgpu.ru>, <http://ckpo.herzen.spb.ru/?page=organic-chemistry>

^b St. Petersburg State University, Laboratory of Biomolecular NMR St. Petersburg, 199034, Russia

E-mail: nmr.group.spbu@gmail.com

The interaction of alkyl 3-bromo-3-nitroacrylates **1**, **2** we have studied with the original representative of cyclic CH acids - bindone ([1,2'-biindenylidene]-1',3,3'(2H)-trione) **3** – led to the preparation of previously unknown alkyl 5-nitro-7,12-dioxo-7,12-dihydroindeno[1,2-a]fluorene-6-carboxylates **4**, **5** with yields of 60, 90%.



In the ¹H NMR spectra of synthesized polyaromatic products **4**, **5**, proton signals of three isolated spin systems (an alkoxy carbonyl group and two 1,2-disubstituted benzene rings) are observed, and the aromatic systems partially overlap with their signals at 7.53 (2H) and 7.62 (2H) m.d. (Fig. 1).

The study of compound **5** by ¹H-¹H *J*-COSY NMR spectroscopy showed that the multiplet at 7.53 m.d. is formed by two triplet signals, and the multiplet at 7.62 m.d. is formed by a doublet and a triplet (Fig. 2). One should note the presence of two additional (symmetrical) signals (marked in red) in the ¹H-¹H *J*-COZY spectrum in the region of two overlapping triplet signals (*t+t*), which, apparently, is a consequence of the strong coupling in the system of three proton signals at 9.05 d, 7.69 t, 7.53 m (ABX system), which manifests itself in such an unexpected way in this

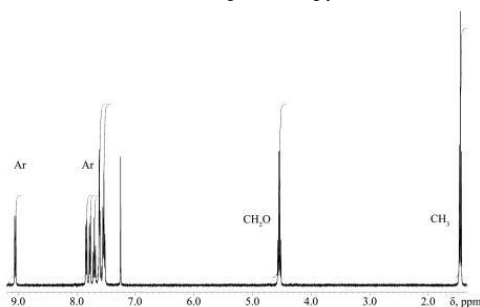


Figure 1. ¹H NMR spectrum of ethyl 5-nitro-7,12-dioxo-7,12-dihydroindeno[1,2-a]fluorene-6-carboxylate **5**

experiment.

The study of the same compound **5** by the ^1H - ^1H dqf-COSY NMR spectroscopy allowed us to hypothesize that the observed signals belong to the corresponding protons in the structure of the molecule (Fig. 3). In the ^1H NMR spectrum, a doublet at 9.05 m.d. can be attributed to the proton H^{11} , which is under the deshielding effect of the anisotropy of the neighboring carbonyl group ($\text{C}^{12}=\text{O}$). Consequently, the cross peaks observed in the ^1H - ^1H dqf-COSY spectrum relate to proton signals: 7.83 d (H^1), 7.77 d (H^8), 7.69 t (H^{10}), 7.62 m (H^3 and H^4), 7.53 m (H^2 and H^9), 4.54 q (CH_2O) and 1.45 t (CH_3).

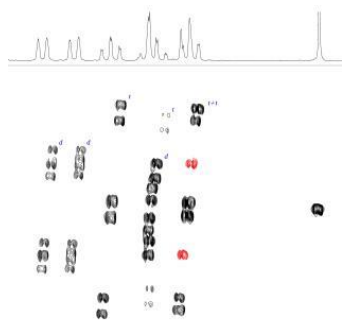


Figure 2. The fragment of ^1H - ^1H COSY spectrum of compound **5**.

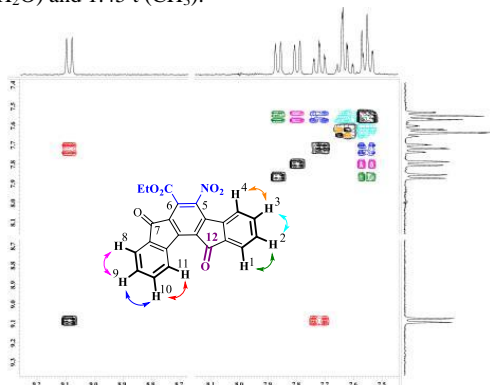


Figure 3. The fragment of ^1H - ^1H COSY spectrum of compound **5**

Our accepted assignment of proton signals correlates with the results of X-ray diffraction analysis performed for compound **4**. Thus, proton H^{11} is located near the carbonyl group ($\text{C}^{12}=\text{O}$), falls into its deshielding region and undergoes a shift to a low field compared to other protons. At the same time, the proton H^4 is located near the nitro group, which is removed from the plane of the cycle and cannot show a deshielding effect to it.

The studies were carried out at the Central Collective Use Center at the Faculty of Chemistry of the Herzen State Pedagogical University of Russia on the Jeol ECX-400A spectrometer (Royal probe) with an operating frequency of 399.78 (^1H), 100.53 (^{13}C) MHz at standard experimental settings, using the solvent signal as an internal standard.

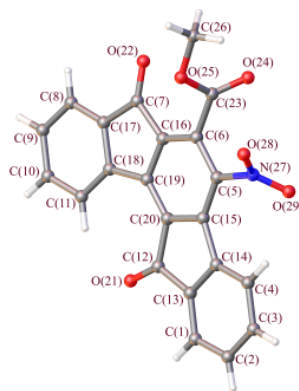


Figure 4. X-ray diffraction analysis of compound **4**

Acknowledgements

The research was supported by an internal grant 116883049 of the Saint-Petersburg State University.

Development and characterization of novel nanofiltration membranes based on polyacrylonitrile modified with Zr-MOFs.

*Margarita E. Puzikova¹, Anna I. Kuzminova¹, Maria E. Dmitrenko¹, Roman R. Dubovenko¹,
Alexandra M. Korovina¹, Anton S. Mazur¹, Anastasia V. Penkova¹*

¹Saint Petersburg State University, Saint-Petersburg, Russia

E-mail: st095099@student.spbu.ru

https://go.spbu.ru/rgpenkova

Introduction

Nanofiltration is a pressure-driven membrane process between reverse osmosis and ultrafiltration, and is used for removing solutes with a molecular weight in the range of 200–1000 g/mol. Nowadays, nanofiltration is actively used for water softening and disinfection, pre-treatment, nitrate, and color removal, mainly, for heavy metal ions removal from wastewater. In this regard, there is a need to develop new improved membranes. One of the most interesting ways to make membranes is to create a mixed matrix membranes. It is a promising modification method, consisting in the introduction of an organic/inorganic component into the polymer matrix.

In the present work the novel membranes based on polyacrylonitrile (PAN) were prepared by introducing metal-organic framework (Zr-MOFs): MIL-140A, MIL-140A-AcOH-EDTA and MIL-140A-AcOH. The improvement of the transport properties of the membranes based on PAN modified with Zr-MOFs was expected due to the porous structure, hydrophilic/hydrophobic properties, good chemical and thermal stability of the Zr-MOFs. The most important investigation of Zr-MOFs inclusion in PAN matrix is analysis of membranes by spectroscopic methods. Among these methods, nuclear magnetic resonance (NMR) helps to track the change in the PAN-matrix due to modification by Zr-MOFs. The additional characterizations of the polymer samples were studied by Fourier-transform infrared spectroscopy, scanning electron microscopy, atomic force microscopy, thermogravimetric analysis, and swelling experiments. Transport properties of the developed membranes were investigated by nanofiltration during separation of water, which included Cu^{2+} , Pb^{2+} , Cd^{2+} .

Acknowledgements

This work is supported by Scholarship of the President of the Russian Federation CII-2506.2022.1. The experimental work of this study was facilitated by the equipment from the Resource Centre of Geomodel, Chemical Analysis and Materials Research Centre, Centre for X-ray Diffraction Methods, Magnetic Resonance Research Centre, Centre for Innovative Technologies of Composite Nanomaterials, Nanophotonics Centre, Computer Centre, Cryogenic department, Thermogravimetric and Calorimetric Research Centre and the Interdisciplinary Resource Centre for Nanotechnology at the St. Petersburg State University.

Temperature evolution of spin-phonon coupling efficiency under magnetic saturation for sodium quadrupole nuclei in a NaF crystal

Andrey M. Rochev, Vladimir M. Mikushev, Elena V. Charnaya, Akim D. Zagovorich

Faculty of Physics, St. Petersburg State University, St. Petersburg

E-mail: v.mikushev@spbu.ru

Introduction

The efficiency of the nuclear spin-phonon coupling in NMR is defined quantitatively by the nuclear spin-lattice relaxation (SLR) rate. In solid dielectric samples, local relaxation is drastically accelerated near paramagnetic defects and impurities, which occur in real crystals [1]. Even in the case of a small number of such paramagnetic centers in a "nominally pure" crystalline material, the "impurity" mechanism of nuclear SLR is effective due to participation of the spin diffusion. Within the thermodynamic approach, the condition of the noticeable contribution of impurity SLR involving spin diffusion can be written as:

$$|\alpha_{loc} - \alpha_l| < |\langle \alpha_l \rangle - \alpha_l|, \quad (1)$$

where α_l is the inverse lattice temperature, $\langle \alpha_l \rangle$ average inverse spin temperature in the sample, α_{loc} inverse local spin temperature near paramagnetic centers. The violation of this condition near some paramagnetic centers removes the contribution of these centers to nuclear SLR. Total SLR of quadrupole nuclei in insulating solids is due to a sum of the impurity contribution mentioned above and the "lattice" mechanism [2], which is realized through modulations of interatomic distances by thermal phonons and dominates at room temperature. The rate of total SLR is given by:

$$(T_1^{\Sigma})^{-1} = (T_1^{lat})^{-1} + (T_1^{imp})^{-1}, \quad (2)$$

where the $(T_1^{lat})^{-1}$ term is determined by the spin-phonon coupling in crystals with an ideal lattice and $(T_1^{imp})^{-1}$ is the rate of "impurity" relaxation.

A method has been suggested for dividing the SLR mechanisms of quadrupole nuclei [3] by suppressing the impurity contribution with additional acoustic or electric resonance continuous fields, which tend to reverse the inequality (1). It is of great interest to extend the suggested method over standard pulse NMR spectrometers using known inversion recovery or saturation recovery procedures supplemented with magnetic excitation at the Larmor frequency [4, 5].

Sample and experiment

The samples were cut from a single crystal of sodium fluoride NaF along the axes of symmetry of the fourth order. The composition of the crystal under study was tested for the presence of growth impurities and electronic centers. The results of the sample testing, the information on a Bruker Avance III 400 spectrometer optimized for solids, and the measurement procedure are described in detail in [6].

Results and discussion

The dependence of the relative integral intensity of the ^{23}Na NMR signal $Z(t)=A(t)/A^{st}$ on the time interval t between the 180° and 90° pulses was measured under application of additional weak long electromagnetic pulses at the Larmor frequency, which produced saturation of the sodium nuclear spin system to the value Z^{st} in the range from 1 to 0.1. The

saturation factor is defined here as $Z^{st}=A^{st}/A_0$, where A^{st} and A_0 are the integral intensities of the NMR signals in equilibrium after a single 90° pulse under additional saturating excitation and without it.

When the spin temperature averaged over the crystal volume is negative, which corresponds to $Z(t)<0$, the restoration of nuclear magnetization follows the exponential law

$$Z(t) = Z^{st} [1 - b \exp(-t/\tau_1)], \quad (3)$$

where b is a numerical coefficient ($1 < b < 2$). For the positive average spin temperature ($Z(t) > 0$), the magnetization recovery could be better described not by a single exponential, unlike [5], but by the sum of two exponentials for any factors Z^{st} of continuous saturation:

$$Z(t) = Z^{st} \left\{ 1 - \left[\rho \exp(-(t-t_0)/\tau_1) + (1-\rho) \exp(-(t-t_0)/\tau_2) \right] \right\}, \quad (4)$$

where ρ is the weighting coefficient characterizing the fraction of nuclei, which relax with relaxation time τ_1 . The emergence of the second exponential with a longer time of nuclear magnetization recovery demonstrates a decrease in the efficiency of spin-phonon coupling for a part of nuclei and corresponds to a decrease in the ^{23}Na SLR rate. The experimental values of ρ at 90 K are shown in Fig. 1a. The results obtained showed that the time τ_2 is longer than τ_1 . Moreover, the second exponential appeared only at Z^{st} below a particular continuous saturation.

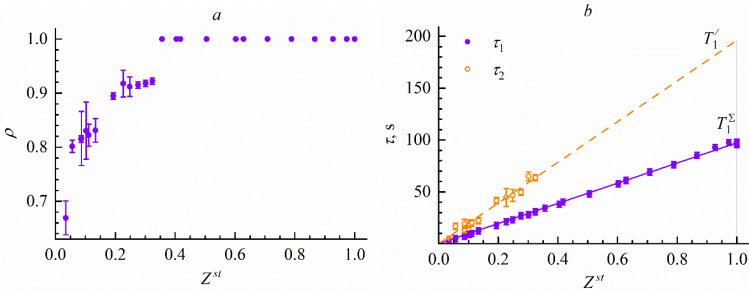


Figure 1. The dependences of ρ (a) and the ^{23}Na restoration times (b) on the ^{23}Na saturation factor Z^{st} .

The dependences of the restoration times τ_1 and τ_2 on the saturation factor Z^{st} is shown in Fig. 1b. Since the general analysis of relaxation under continuous saturation, which neglects the role of impurities, predicts the linear decrease of the restoration time with decreasing the saturation factor

$$\tau = T_1^\Sigma / Z^{st}, \quad (5)$$

the straight line shown for the $\tau_1(Z^{st})$ dependence in Fig. 1b should be extended to T_1^Σ at $Z^{st} = 1$. This agrees with the experimental data obtained. The emergence of the contribution to nuclear spin relaxation with τ_2 , which is longer than τ_1 (see Fig. 1b), means the suppression of the impurity relaxation as a result of strong enough saturation. Such suppression can occur only at positive spin temperatures. When impurity relaxation breaks down, nuclear relaxation runs only due to spin-phonon coupling as in crystals with perfect structure. Then the straight line, which fits the $\tau_2(Z^{st})$ dependence in Fig. 2b, should extend to T_1^{int} at $Z^{st} = 1$. However, in the presence of various types of paramagnetic centers in the sample, the suppression of the

contribution of the impurity mechanism to SLR may be only partial, since the condition (1) remains being fulfilled for some centers. In this case the dependence $\tau_2(Z^{if})$ should correspond to the time $T_1' < T_1^{lat}$.

Fig. 2 shows the experimentally obtained values of the SLR rates of Na nuclei for various temperatures. Also, for clarity, the theoretical curve T_1^{lat} for the "lattice", spin-phonon mechanism of SLR, linked to the experimental value T_1' at 293 K, is drawn [2]:

$$(T_1^{lat})^{-1} = C \int_0^{\frac{k_B \theta_D}{\hbar}} \omega^6 \frac{\exp\left(\frac{\hbar \omega}{k_B T}\right)}{\left[\exp\left(\frac{\hbar \omega}{k_B T}\right) - 1\right]^2} d\omega. \quad (6)$$

For the temperature range from room temperature to 120 K, the SLR time of ^{23}Na nuclei after suppression of the impurity contribution is quite well described by the dependence for the "lattice" mechanism. With further cooling the sample, relaxation accelerates due to an increase in the relaxation efficiency near paramagnetic centers because the product $(\tau_{PC}\omega_0)$ approaches 1, where τ_{PC} is the relaxation time of the paramagnetic center, ω_0 is the Larmor frequency of nuclear spins. This means an increase in the efficiency of the "impurity" contribution to SLR [1].

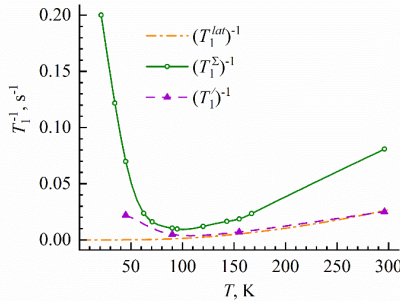


Figure 2. Temperature dependence of the SLR rate of ^{23}Na nuclei.

Acknowledgements

The measurements were carried out using the equipment of the Resource Centers of the St. Petersburg State University Scientific Park "Center for Diagnostics of Functional Materials for Medicine, Pharmacology and Nanoelectronics".

References

1. G. R. Khutsishvili. – Sov. Phys. Uspekhi, 8, 743-768 (1966).
2. A. R. Kessel'. Nuclear Acoustic Resonance - Nauka, Moscow, 1969 [in Russian].
3. P. Yu. Efitsenko, V. M. Mikushev, E. V. Charnaya. - JETP Lett., 54, 587-589 (1991).
4. E. V. Charnaya, V. M. Mikushev, A. M. Ulyashev, D. A. Yas'kov. – Physica B: Condens. Matter, 292, 109-113 (2000).
5. V. M. Mikushev, E. V Charnaya, M. K. Lee, L.-J. Chang. – Results Phys., 12, 1202 (2019).
6. V. M. Mikushev, A. M. Rochev, E. V Charnaya. - Acoust Phys, 69, 782-787 (2023).

Organocatalytic synthesis of Michael adducts of the sesquiterpene lactone arglabin and their 2D NMR structural analysis

Alexey V. Salin, Andrey A. Shabanov, Elizaveta V. Kartashova

A.M. Butlerov Institute of Chemistry, Kazan Federal University, Kremlevskaya 18, Kazan, 420008, Russian Federation

E-mail: salin555@mail.ru

Introduction

Arglabin **1** is a natural sesquiterpene lactone of the guaianolide class isolated for the first time by Adekenov from *Artemisia glabella* Kar. *et* Kir., a species of wormwood [1]. Arglabin shows promising cytotoxic activity against different cancer cell lines and is used in medicine to treat breast, colon, ovarian and lung cancers. The anticancer activity of arglabin is attributed to the ability to inhibit farnesyl transferase which leads to the activation of the RAS proto-oncogene, a process that is believed to cause many types of human tumors.

The Michael addition of amines to the conjugated olefinic bond represents a promising strategy to improve pharmacokinetic profile and increase biological activity of arglabin and other medicinally important sesquiterpene lactones. The Michael adducts formed serve as prodrugs, which release the parent lactone via the *retro*-Michael reaction under biological conditions.

Recently we reported the stereoelectronic effect in the addition reaction of tertiary phosphines to α -methylene lactones [2]. This effect originates from the locked *s-cis*-geometry of these Michael acceptors that favors for the additional stabilization of zwitterionic intermediate by electrostatic interaction between phosphonium and enolate oxygen centers. In this work, using the stereoelectronic effect we performed diversity-oriented synthesis of Michael adducts derived from sesquiterpene lactone arglabin with nitrogen- and carbon-centered pronucleophiles.

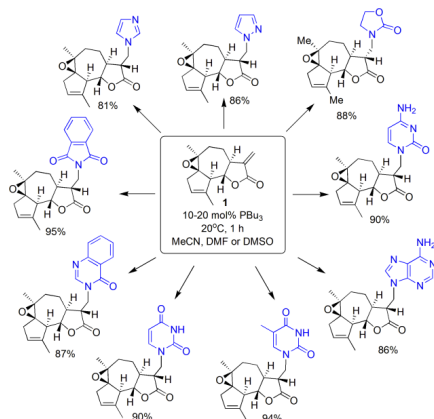
Results and Discussion

Tri-*n*-butylphosphine efficiently catalyzes addition of various biologically and medicinally important *aza*-heterocycles, such as: pyrazole, phthalimide, 2-oxazolidinone, 4-quinazolinone, and nucleobases to arglabin **1**. By employing 10 mol% of the catalyst, the reactions proceed at ambient temperature with more or less noticeable heat evolution and furnish *aza*-Michael adducts in excellent yields within 1 h (Scheme 1). Other functional groups presented in the arglabin core tolerate well the phosphine organocatalysis. The reactions were found to be highly chemo- and diastereoselective, as confirmed by ^1H and $^{13}\text{C}\{^1\text{H}\}$ NMR spectra of the crude reaction mixtures. With multifunctional *aza*-heterocycles like nucleobases, the addition occurred exclusively at the N9 atom of purine ring or the N1 atom of pyrimidine ring.

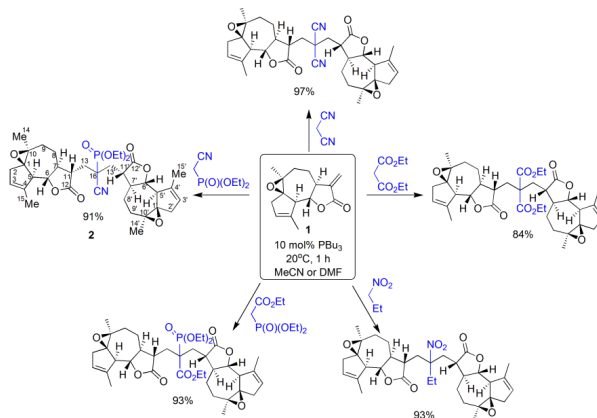
Then, similar reaction conditions were employed for the addition of CH-acids (diethyl malonate, malononitrile, 1-nitropropane, and Horner reagents) to arglabin. These reactions were found to give bisadducts with novel quaternary carbon center in excellent yields (Scheme 2). The ability of tri-*n*-butylphosphine to provide chemo- and stereoselective formation of these bisadducts under very mild conditions is quite remarkable.

The structures of all Michael adducts were deduced from ^1H , ^{13}C NMR, 2D NMR (^1H - ^1H COSY, NOESY, HSQC, HMBC) spectra. In NOESY spectra, all arglabin derivatives show

diagnostic cross-peaks between β -H6 and β -H11, α -H7 and α -H5, α -H14 and α -H5, α -H14 and α -H7 useful for stereochemical assignments (Figure 1).



Scheme 1. Synthesis of Michael adducts of arglabin with aza-heterocycles



Scheme 2. Synthesis of bisadducts of arglabin with CH-acids

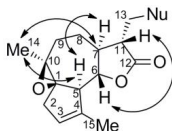


Figure 1. NOE correlations for Michael adducts of arglabin

According to the NOESY spectra, absolute configuration of the newly formed stereocenter C11 is *R* in the *aza*-Michael adducts, and *S* – in the adducts derived from CH-

acids. Tables 1 and 2 show signal assignments in ^1H and $^{13}\text{C}\{^1\text{H}\}$ NMR spectra of adduct **2** made from the analysis of 2D NMR spectra. Both arglabin moieties are diastereotopic and give double set of signals in ^1H and $^{13}\text{C}\{^1\text{H}\}$ NMR spectra.

Table 1. Signal assignment in ^1H NMR spectrum of **2** (CDCl_3 , 400 MHz)

H atom	Chemical shift (δ , ppm), multiplicity, and integral intensity
H3, H3'	5.60-5.53 (m, 2H)
2POCH ₂	4.41-4.23 (m, 4H)
H6	4.14 (t, $J=10.0$ Hz, 1H)
H6'	4.07 (t, $J=10.0$ Hz, 1H)
H5	2.91 (br d, $J=10.6$ Hz, 1H)
H5'	2.83 (br d, $J=10.6$ Hz, 1H)
H _A 9, H _A 9', H11	2.80-2.68 (m, 3H)
H _A 13, H11'	2.67-2.51 (m, 2H)
H _B 13, H _A 13', H _B 13', H _B 9, H _B 9', H _A 8, H _A 8', H _B 8, H _B 8', H7, H _A 2	2.25-1.67 (m, 11H)
H15, H15'	1.92 (br s, 6H)
H _A 2', H _B 2, H _B 2', H7'	1.65-1.19 (m, 4H)
POCH ₂ CH _{3A}	1.41 (t, $J=7.1$ Hz, 3H)
POCH ₂ CH _{3B}	1.40 (t, $J=7.1$ Hz, 3H)
H14	1.34 (s, 3H)
H14'	1.33 (s, 3H)

Table 2. Signal assignment in $^{13}\text{C}\{^1\text{H}\}$ NMR spectrum of **2** (CDCl_3 , 100.6 MHz)

C atom	Chemical shift (δ , ppm)	C atom	Chemical shift (δ , ppm)
C12/C12'	177.8/177.6	C11	43.6 (d, $J_{\text{PC}}=7.0$ Hz)
C4/C4'	140.6/140.3	C11'	43.4 (d, $J_{\text{PC}}=5.0$ Hz)
C3/C3'	125.0/124.9	C16	40.4 (d, $J_{\text{PC}}=142.9$ Hz)
CN	118.4 (d, $J_{\text{PC}}=16.1$ Hz)	C9/C9'	39.7/39.6
C6/C6'	83.0/82.8	C8/C8'	33.4/33.2
C1/C1'	72.4/72.3	C13	30.8 (d, $J_{\text{PC}}=4.0$ Hz)
POC _A H ₂	65.0 (d, $J_{\text{PC}}=8.0$ Hz)	C13'	30.7 (d, $J_{\text{PC}}=4.0$ Hz)
POC _B H ₂	64.8 (d, $J_{\text{PC}}=7.0$ Hz)	C2/C2'	22.8/22.7
C10/C10'	62.7/62.5	C14/C14'	22.3 (both)
C5/C5'	53.4/52.1	C15/C15'	18.32/18.29
C7/C7'	52.0/51.9	POCH ₂ CH ₃	16.5 (d, $J_{\text{PC}}=6.0$ Hz)

Acknowledgements

This work was supported by Russian Science Foundation (grant #23-23-00029).

References

1. S. H. Lone, K. A. Bhat, M. A. Khuroo. – *Chem.-Biol. Interact.*, **240**, 180-198 (2015).
2. A. V. Salin, A. A. Shabanov, K. R. Khayarov, R. I. Nugmanov, D. R. Islamov. – *J. Org. Chem.*, **88**, 11954-11967 (2023).

Characterization of novel dense membranes based on chitosan modified by MIL-125

Kirill A. Salomatin¹, Anna I. Kuzminova¹, Danila D. Myznikov¹, Mariia E. Dmitrenko¹, Roman R. Dubovenko¹, Artem A. Selyutin¹, Anton S. Mazur¹, Alexandra Yu. Pulyalina¹, Anastasia V. Penkova¹

¹Saint Petersburg State University, Saint-Petersburg, Russia

E-mail: st106790@student.spbu.ru

https://go.spbu.ru/rgpenkova

Introduction

Recently, membrane processes are quickly growing up. At the same time, industry requires effective membrane materials based on biopolymers for separation of mixtures used in many areas. In addition, the issue of environmental safety is on the agenda, the impact of industrial development on it becomes more and more controlled. Therefore, the industry is improving its production methods by using novel technologies to improve productivity and efficiency of processes, and make them environmentally friendly and economically beneficial. Pervaporation is one of the most advanced and rapidly developing membrane processes applied for the separation of mixtures with low molecular weight components, azeotropic mixtures, isomer mixtures and other due to its excellent characteristics: environmental friendliness, low energy consumption and compact modular equipment. To improve the transport properties of membrane material the mixed matrix membranes (MMMs) are being developed. The process consists in modifying of the polymer matrix by introduction of inorganic compound that leads to crosslinking of polymer fibers.

Results

In this work biopolymer chitosan was selected for the development of novel dense membranes for the separation of water/isopropanol mixture. Metal-organic framework MIL-125 was used for modification of chitosan polymer matrix. Structure and physicochemical properties of the developed membranes were investigated by Fourier-transform infrared spectroscopy, scanning electron microscopy, atomic force spectroscopy, thermogravimetric analysis, swelling degree, contact angle and nuclear magnetic resonance (NMR). NMR spectroscopy is important method that shows what effect the introduction of modifier and cross-linking agents has on the bond length and structure of membrane, also it allows to confirm the embedding of the modifier in the polymer structure. All that are important to explain the changes of selectivity, permeation flux and other parameters of the membrane. It was demonstrated that the creation of MMMs led to notable improvement of the membrane transport properties due to significant changes in membrane inner and surface structure.

Acknowledgements

The authors acknowledge Saint-Petersburg State University for a research project 11602266. The experimental work of this study was facilitated by the equipment from the Resource Centre of Geomodel, Chemical Analysis and Materials Research Centre, Centre for X-ray Diffraction Methods, Magnetic Resonance Research Centre, Centre for Innovative Technologies of Composite Nanomaterials, Nanophotonics Centre, Cryogenic department, Thermogravimetric and Calorimetric Research Centre and the Interdisciplinary Resource Centre for Nanotechnology at the St. Petersburg State University.

Structure and mobility of the lipid system in water-ionic liquid mixtures: magnetic resonance measurements and molecular dynamics simulations

A.N. Sashina¹, A.R. Khakimzyanova¹, A.M. Khakimov², A.V. Filippov³, A.V. Khaliullina¹

¹Kazan Federal University, Kremlevskaia str, 18, Kazan, 420008, Russia

²Institute of Civil Engineering, Kazan State University of Architecture and Engineering, Kazan, Russia

³Division of Chemical Engineering, Luleå University of Technology, Luleå, Sweden

E-mail: ANSashina@stud.kpfu.ru

Introduction

An ionic liquid (IL) is a salt in the liquid state. They usually consist of an organic cation and an organic or inorganic anion. They have unique properties such as thermal and chemical resistance, good solubility, high ionic conductivity, etc. Recently, the interaction of these liquids with phospholipids and their use in transdermal and oral drug delivery has been actively researched [1]. The options for interaction between ILs and biological membranes are different. ILs with long hydrocarbon tails self-organize into micelles, which are then absorbed on the surface of the cell membrane. Short-tailed ILs are more mobile and can integrate into the membrane spontaneously [2]. They can be used as permeability enhancers for transdermal delivery of drugs. Research into the interaction between these liquids and phospholipids is important for understanding their potential toxicity to cells and the environment. In this work, we discuss the features of the structure, phase behavior and molecular mobility of the system consisting of lecithin and water-ethylammonium nitrate (EAN) mixtures studied by nuclear magnetic resonance (NMR) and molecular dynamics methods.

NMR measurements

The ³¹P NMR line shape analysis revealed two lipid phases in the systems: lamellar and isotropic phases. The ³¹P NMR spectrum for lecithin in pure D₂O has a “bilayer” shape. With the addition of ionic liquid to water-ionic liquid mixtures, the fraction of the ³¹P NMR spectrum with a “bilayer” line shape decreases, while the spectral intensity of the “isotropic” component increases. And the ³¹P NMR spectrum of lecithin in pure EAN only has an “isotropic” component.

Diffusion NMR experiments were carried out using the pulsed-field gradient method. The self-diffusion coefficient (SDC) value related to lipids in pure EAN can be associated with lipids which undergo isotropic motion observed by ³¹P NMR. The hydrodynamic radius calculated using the Stokes-Einstein equation corresponds to the micellar size of lipid particles. The SDC related to lipids in pure D₂O may be associated with the movement of lipids with bilayer arrangements observed in the ³¹P NMR spectra. The hydrodynamic radius corresponds to the vesicular size of lipid particles. As the portion of D₂O in the D₂O-EAN solvent mixture increases, the self-diffusion coefficients related to the ionic liquid and lipids increase, i.e. the system becomes more mobile, which may be due to a decrease in viscosity.

According to NMR relaxometry data, the transverse magnetization decay for the lipids in D₂O-EAN mixtures (in the ratios from 80/20 to 20/80), are due to the sum of contributions from three components. This indicates the presence in the system of components with different molecular mobility: “liquid-phase” components and components associated with fast movement of diffusing lipids and with slow movement of lipids.

Computer modeling methods

The method of molecular dynamics shows that lecithin molecules assemble into a micelle in water. This micelle remains stable and compact during the entire calculated time (30 ns). Water molecules are mainly concentrated on the surface of the micelle, with the majority of hydrogen bonds formed with the phosphate group. In a mixture of IL and water, the micelle becomes cylindrical during the first 10 ns. At the same time, an increase in the average area per phospholipid was observed. Within the next 20 ns, this phospholipid structure remains unchanged. The analysis reveals that the cation penetrates deep into the micelle along with water. The changes in structure can be explained by the weakening of the interaction between lecithin molecules due to the presence of ILs molecules. When lecithin interacts only with EAN molecules, the micelle disintegrates. The disintegration of the structure may be due to Coulomb interactions between the cation of EAN and the phosphate part of phospholipid, and between the anion of EAN and choline.

Self-diffusion coefficients (SDCs) for lecithin molecules were calculated in the investigated systems. The comparative analysis of the SDCs revealed a correlation between values obtained by molecular dynamics and NMR methods [3].

References

1. Kubota, K. The molecular assembly of the ionic liquid/aliphatic carboxylic acid/aliphatic amine as effective and safety transdermal permeation enhancers / K. Kubota, A. Shibata, T. Yamaguchi // *European Journal of Pharmaceutical Sciences*. – 2016. – V. 86. – P. 75-83.
2. Imidazolium salts mimicking the structure of natural lipids exploit remarkable properties forming lamellar phases and giant vesicles / P. Drucker, A. Ruhling, D. Grill [et al.]. // *Langmuir*. – 2017. – V. 33. – № 6. – P. 1333-1342.
3. A lipid system in the ionic liquid – water mixtures studied by magnetic resonance measurements and molecular dynamics / A.V. Khaliullina, A.R. Khakimzyanova, A.N. Sashina [et al.]. // *Kazan science week. “Spin Physics, Spin Chemistry and Spin Technology”*, (September 25–30, 2023, Kazan). – Kazan, 2023. – P. 242.

Study of ionic-liquid extraction of arenes from petroleum fractions by UV spectroscopy method

Sabina A. Seidova, Minaver D. Ibragimova, Vagif M. Abbasov, Huseyn J. Huseynov, Ulviya J. Yolchueva

Y. H. Mammadaliyev Institute of Petrochemical Processes of Ministry of Science and Education of Republic of Azerbaijan, AZ 1025, Baku, 30 Khojaly ave., Azerbaijan

E-mail: sabina.seidova.ai@mail.ru

E-mail: minaver-ibrahimova@rambler.ru

Introduction

As is known, the environmental problem of the oil industry is associated with environmental pollution by substances obtained from the consumption of petroleum products and their purification from undesirable components by various methods, in particular extraction using volatile organic solvents.

A modern approach to solving this problem is to replace the volatile organic solvents used in the extraction process with environmentally acceptable solvents - ionic liquids that have high selectivity towards undesirable components of petroleum feedstock, in particular aromatic hydrocarbons.

Research conducted at the Institute of Petrochemical Processes on the use of formate and acetate ionic liquids as extractants has shown significant success in the process of extracting aromatic hydrocarbons from petroleum fractions [1, 2].

Knowledge of the content of various aromatic hydrocarbons is very important, based on this, in this material, the composition (mono-, bi-, tri- and polycyclic) and content of aromatic hydrocarbons in distillate and oil fractions purified by ion-liquid extraction method are analyzed using UV spectroscopy.

Research method

UV spectral analysis of the samples was carried out on a UV/Vis 6850 spectrophotometer from JENWAY in the spectral region of 190-1100 nm. Mercury lamps and incandescent lamps were used as excitation sources. The studies were carried out at room temperature using a standard solvent - hexane; the quantitative composition of the samples was calculated using the appropriate method [3].

Results and discussion

A process of stepwise purification of diesel distillate based on 70% mass of straight-run diesel fraction and products of secondary oil refining - 15% mass of light gas oil coking and 15% of the mass of catalytic cracking (27.7% mass of arenes) at room temperature, as well as transformer oil distillate T -1500 at 60°C (28.6% mass of arenes) using at each stage an equal amount of raw material and ionic liquid -N-methylpyrrolidoneacetate and a contact time of 1 hour was carried out. The resulting solutions of samples and solvent were poured into rectangular quartz cuvettes with a diameter of 1 cm, then UV spectra were recorded, while the Bouguer-Lambert-Beer law was observed.

The research results showed that in the process of two-stage ionic-liquid extraction purification of diesel distillate and three-stage extraction of oil distillate, tricyclic aromatic hydrocarbons (phenanthrenes and anthracenes) are almost completely removed from the composition of the distillates under study (Diagram). In this case, the degree of dearomatization of fuel and oil distillate is 79.78% mass and 90.87% mass, respectively.

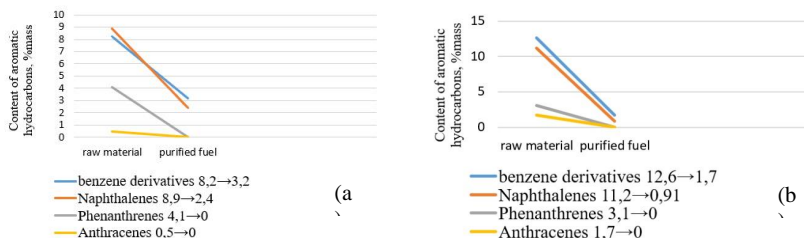


Diagram. Change in the content of aromatic hydrocarbons during two-stage extraction purification of diesel distillate (a) transformer oil distillate T-1500 (b) with *N*-methylpyrrolidoneacetate ionic liquid

References

1. M.D.Ibragimova, S.A.Seidova, S.G.Aliyeva Issledovaniye ostatochnogo sodержaniya aromaticsikh uglevodorodov v sostave dizel'nogo topliva posle ekstraktsionnoy ochistki. SOCAR Proceedings, 2022, 3, 101-105. (in Russian)
2. S.A.Seyidova Justification of high efficiency of ionic liquid in the process of extraction cleaning of diesel fraction. Processes of Petrochemistry and Oil-Refining, 2019, 3, 291-296.
3. A.P.Mamedov, R.A.Dzhafarova, M.A.Nadzhafova Spektral'no-lyuminesstentnyye svoystva, EPR i fotokhimiya nefteproduktov, 2014. 328 s. (in Russian)

Study of intramolecular dynamics of β -enaminone using NMR, UV and DFT methods

*Amina F. Shaidullina*¹, *Michael Yu. Volkov*², *Alsu R. Sharipova*², *Olga A. Turanova*², *Ludmila I. Savostina*^{1,2}, and *Alexander N. Turanov*^{1,2}

¹*Institute of Physics, Kazan Federal University, 420008 Kazan, Russia*

²*Zavoisky Physical-Technical Institute, Federal Research Center Kazan Scientific Center of RAS, Kazan 420029, Russia*

E-mail: *shaidullina.amina@yandex.ru*

β -Enaminones are widely used in pharmacology. Different *cis*- and *trans*-geometric isomers of β -enaminones can have different biological activities, therefore determining the geometry of β -enaminone molecules is important from the point of view of both fundamental and applied science.

In this work, the structure of β -enaminone 1-phenyl-3-(8-quinolylamino)prop-2-en-1-one was studied by NMR, UV spectroscopy and DFT calculations. 1D and 2D ¹H and ¹³C NMR spectra of the studied substance dissolved in carbon tetrachloride, deuterated acetone and deuterated dimethyl sulfoxide were recorded at room temperature using a Bruker Avance 400 NMR spectrometer. Analysis of 1D and 2D NMR spectra showed that the molecules of the studied compound are in the ketone form of the *cis*- isomer. Irradiation of these solutions with UV light with $\lambda = 365$ nm did not lead to *cis-trans* isomerization of their molecules, but resulted in the appearance of a brown precipitate in the solutions. The ¹H NMR spectrum of the brown precipitate, recorded in a solution of deuterated chloroform, indicates its heterocyclic composition.

Using the ORCA software package [1], the geometries of all isomers and tautomers of the molecules of the studied substance were optimized and the energies of their states were found by the CAM-B3LYP functional [2] and the def2-TZVP basis set [3]. The results showed that the energetically more stable form of this β -enaminone is the *cis*- isomer, but the difference in energy between its *cis*- and *trans*- isomers is not large, about 0.1 eV. Figure 1 shows the optimal geometries of *cis*- and *trans*- isomers.

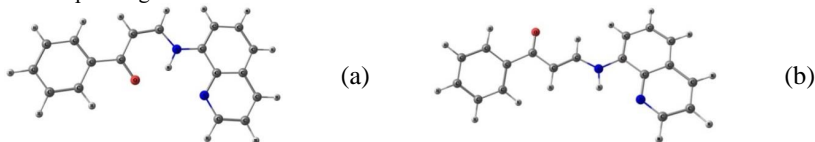


Figure 1. Optimized geometries of *cis*- (a) and *trans*- (b) isomers calculated by DFT calculations without taking into account the solvent.

On the base of the experimental results and DFT calculations it was established that in solutions, regardless of the polarity of the solvent, the studied compound exists in the ketone form of the *cis*- isomer.

References

1. Yanai, T.; Tew, D. P.; Handy, N. C. (2004) A new hybrid exchange– correlation functional using the Coulomb-attenuating method (CAM-B3LYP) Chem. Phys. Lett., V.393, 51-57.
2. Weigend, F. (2005) Balanced basis sets of split valence, triple zeta valence and quadruple zeta valence quality for H to Rn: Design and assessment of accuracy Phys. Chem. V.7, Iss.18. 3297-3305.
3. Neese, F. (2012) The ORCA program system. WIREs Comput Mol Sci. 2 73– 78.

Adsorption of glycerol at Brønsted sites in mordenite: A density functional theory study

M.G. Shelyapina*, E.P. Maksimova, A.V. Egorov

Saint Petersburg State University, 7/9 Universitetskaya nab., Saint Petersburg 199034, Russia

E-mail: marina.shelyapina@spbu.ru

Biomass is a rich source of renewable carbon, which can be converted into environmentally friendly fuels and chemicals [1]. Glycerol, the main by-product of biodiesel production (about 10 wt.%) [2], is a very attractive "green" building block that can be used to produce various chemicals with high added value. The effectiveness and selectivity of the reactions is determined by the catalyst. Zeolites are highly effective catalysts for a number of chemical reactions, including glycerol conversion reactions, namely in its dehydration, esterification, and aromatization [2-4]. The study of microporous zeolites has shown their effectiveness in the reaction of direct carboxylation of glycerol [5]. At the same time, the ratio of the Brønsted and Lewis acid sites is important for the selectivity of the reaction [4]. Mordenite is well-known catalysts for many important reactions. Its catalytic properties are largely determined by the structure of its pores, cationic form, as well as the distribution of acid centers. According to a number of experimental and theoretical studies, for the protonated form of mordenite, Brønsted acid sites are formed on the oxygen atoms O2 and O7 of the mordenite framework, oriented towards the center of the 12-membered ring [6,7].

The density functional theory is widely used to study the adsorption of organic molecules and their catalytic transformations on active sites of zeolites. However, studies of glycerol adsorption are very few. The main difficulty lies in the fact that the glycerol molecule framework is very flexible, see Fig. 1(a), that leads to the appearance of various conformations. It is convenient to describe the structure of the glycerol molecule framework in terms of α , β and γ conformations, determined through the relative orientation of two molecular groups $-\text{CH}_2(\text{OH})$ and $\text{CH}(\text{OH})$ groups [8], see Fig. 1(b).

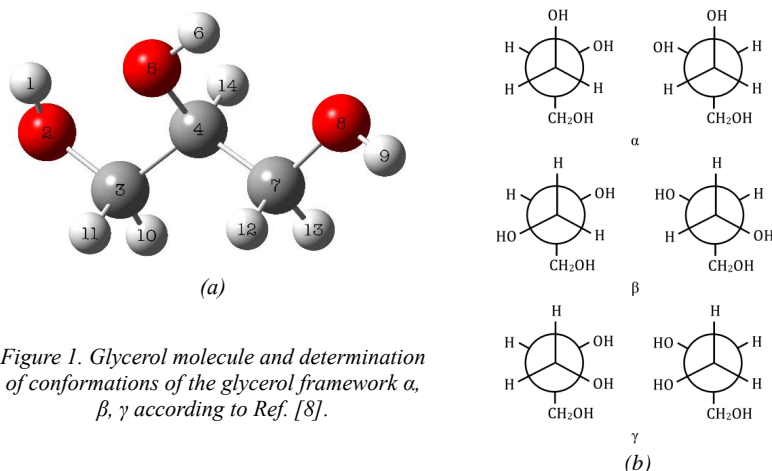


Figure 1. Glycerol molecule and determination of conformations of the glycerol framework α , β , γ according to Ref. [8].

In the α -conformation, the oxygen atom of the $\text{CH}_2(\text{OH})$ group is almost in the trans position for the carbon atom $-\text{CH}(\text{OH})\text{C}-$ groups. In the β -conformation, the oxygen atoms of the two groups are in the trans position. In the γ -conformation, the oxygen atom of the $-\text{CH}_2(\text{OH})$ group is in a position almost trans to the hydrogen atom of the $-\text{CH}(\text{OH})\text{C}-$ group. Thus, a glycerol molecule can have six different types of framework conformations, which are designated as $\alpha\alpha$, $\alpha\beta$, $\alpha\gamma$, $\beta\beta$, $\beta\gamma$ and $\gamma\gamma$. At the same time, in this classification, regardless of the orientation of the hydrogen of the OH group, pairs of the type $\alpha\beta$ and $\beta\alpha$ are considered to be the same conformer.

In this work, we report the results of our theoretical studies of the adsorption of glycerol molecules on the Brønsted centers of mordenite. To simulate the Brønsted site, the Si atom in one of the T4 positions was replaced by Al. The charge compensating proton was placed in a 12-membered ring on an O2 bridged oxygen atom connecting the tetrahedra T4 (Al) and T2(Si), with the orientation of the O-H bond in the direction towards the main mordenite channel. Calculations were carried out using Gaussian 16 package within the framework of density functional theory with B3LYP-D3 functional, designed specifically to account for non-covalent interactions. When modeling the lattice of zeolite and the adsorbed glycerol molecule, a three-fold valence-split basis 6-311G was used for all atoms. When optimizing the geometry, the coordinates of the atoms of the zeolite framework, excluding the atoms forming the Brønsted site, were fixed. The positions of the Al and Si atoms connected to the O2 atom, as well as the oxygen atom O2 and the hydrogen atom localized on it, were optimized.

It was found that the adsorption energy is sensitive to the initial conformation of the glycerol molecule and ranges from -44.0 (for the $\beta\beta$ conformation) to -64.7 kcal/mol (for the $\alpha\gamma$ conformation). In some cases, under the influence of nanoconfinement, the conformation of the glycerol molecule changes. It has been shown that the adsorption of glycerol through the primary OH group is more energetically advantageous for mordenite, see Fig. 2. The high energy of glycerol adsorption is due to the transfer of a proton from the Brønsted site of the zeolite to glycerol with the formation of a hydrogen bond, as well as the formation of up to four additional hydrogen bonds with oxygen atoms of the zeolite framework.

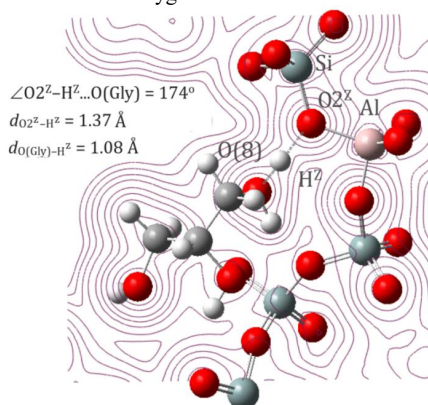


Figure 2. Fragment of the charge density distribution for the $\alpha\gamma(\text{O8})$ conformation of glycerol adsorbed at the Brønsted site. For better visualization, some of the atoms of the zeolite framework have been removed.

Acknowledgements

This work was supported by the Russian Science Foundation (grant No 23-23-00448). The calculations were carried out using computational facilities provided by Computing Centre of the Research Park of Saint Petersburg State University (<http://cc.spbu.ru/en>).

References

1. C.M. Lok, J. Van Doorn, G. Aranda Almansa. – *Renew. Sustain. Energy Rev.* **113**, 109248 (2019).
2. S. He, K. Zuur, D.S. Santosa, A. Heeres, C. Liu, E. Pidko, H.J. Heeres. – *Appl. Catal. B Environ.* **281**, 119467 (2021).
3. L.H. Chen, M.H. Sun, Z. Wang, W. Yang, Z. Xie, B.L. Su. – *Chem. Rev.* **120**, 11194 (2020).
4. Z. Wang, L. Wang, Y. Jiang, M. Hunger, J. Huang. – *ACS Catal.* **4** (2014) 1144–1147.
5. V.S. Marakatti, A.B. Halgeri. – *RSC Adv.* **5** (2015) 14286–14293.
6. G. Sastre, N. Katada, M. Niwa. – *J. Phys. Chem. C.* **114** (2010) 15424–15431/
7. Bhan, A.D. Allian, G.J. Sunley, D.J. Law, E. Iglesia. – *J. Am. Chem. Soc.* **129**, 4919 (2007).
8. O. Bastiansen. – *Acta Chem. Scand.* **3**, 415 (1949)

Study on biodegradability of carrageenan/starch/nanocellulose food films

Xeniva D. Sushkova¹, Maria E. Dmitrenko¹, Anna I. Kuzminova¹, Anna Y. Mikulan¹, Anton S. Mazur¹, Roman R. Dubovenko¹, Anastasia V. Penkova¹

¹Saint Petersburg State University, Saint-Petersburg, Russia

E-mail: st111000@student.spbu.ru

<https://go.spbu.ru/rgpenkova>

Introduction

The growth in food production and demand has led to the development of new packaging materials that are useful in extending the shelf life of food products and improving their quality during transportation, storage and distribution, as well as minimizing harm to the environment and human health. Thus, edible films are being used as potential eco-friendly alternative for the difficult-to-degrade plastic materials in the food packaging, but their physicochemical and mechanical properties still have limitations and require further improvement.

In the present work, biodegradable nanocomposite films based on carrageenan and starch, reinforced with nanocellulose were developed and studied for the application as a bio-based food packaging system. Nanocellulose was incorporated into the film matrix to enhance the mechanical properties. Aloe vera gel, glycerin and sesame oil were also included to the film's composition as plasticizers to provide and antibacterial properties, moisture resistance and flexibility. The film samples were characterized by various analysis methods (spectroscopic, microscopic, thermogravimetric analysis (TGA), measurements of contact angle and mechanical properties, etc). The biodegradability test of the developed films was also conducted, and the sample structure before and after were studied by nuclear magnetic resonance (NMR) spectroscopy. This method has proven to be beneficial and informative tool in studying the biodegradation of films, since the changes in the content and structure of the film matrix at different stages of the experiment were clearly determined.

Acknowledgements

The study was carried out with the financial support of the Russian Federation represented by the Ministry of Science and Higher Education of the Russian Federation, grant number 075-15-2022-1231 on 18 October 2022. The experimental work was facilitated by the equipment from the Resource Centers for Nanotechnology, Magnetic Resonance, Thermogravimetric and Calorimetric Research Centre, the Centre for Innovative Technologies of Composite Nanomaterials, Chemical Analysis and Materials Research Centre, and the Centre for "Nanofabrication of Photoactive Materials (Nanophotonics)" at the St. Petersburg State University.

Spectral characteristics of the complex of cyclosporin C (CsC) with Dy³⁺ ions and DPC micelles in aqueous solution determined by NMR spectroscopy

Artjom S. Tarasov¹, Sergey V. Efimov¹, Vladimir V. Klochkov¹

¹Institute of Physics, Kazan Federal University, Kazan, Kremlevskaya Str., 18, Russian Federation

E-mail: tarasov_as2010@mail.ru

Introduction

The spectral characteristics of cyclosporin C (CsC) complex with Dy³⁺ ions incorporated into a dodecylphosphocholine (DPC) micelle in deuterated water (D₂O) were investigated by high-resolution NMR spectroscopy. The study focused to finding the interaction between CsC and Dy³⁺ ions within DPC micelle. By employing a combination of one-dimensional (¹H, ¹³C) and two-dimensional (¹H-¹H TOCSY, ¹H-¹³C HSQC) NMR techniques, we were able to provide information on the spectral features and possible interactions in the CsC-Dy³⁺ complex. This work contributes to the growing body of knowledge on the spectral characterization of complex biomolecular systems and holds promise for further investigations in drug design and development.

The study of the influence of metal ions on biologically active molecules and cell membrane is relevant, as the interaction of metal ions with organic compounds leads to various biological effects [1, 2].

Cyclosporins are natural or synthetic organic biologically active compounds consisting of 11 amino acids. The cyclosporin family is quite diverse and includes more than 20 different molecules [3, 4]. Cyclosporin C (CsC) (Fig. 1) was used in this study because it has different permeability and showed a different biological action on organic objects compared to another cyclosporins [4, 5].

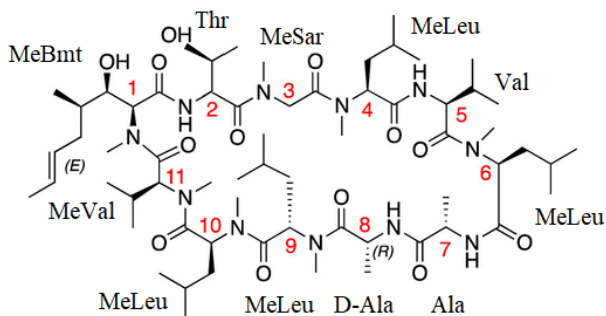


Figure 1. Chemical structure of CsC (from [4])

DPC micelle was used to dissolve CsC in D₂O and imitate cell membrane. Micelle based on DPC is a spherical aggregate of molecules in which hydrophilic heads are on the surface and in contact with water, and the hydrophobic tails of the fatty acids of these molecules are inside the sphere and only contact with each other or with hydrophobic compounds co-dissolved with the lipid. Usually it is used as a simplified membrane model (Fig. 2) [2].

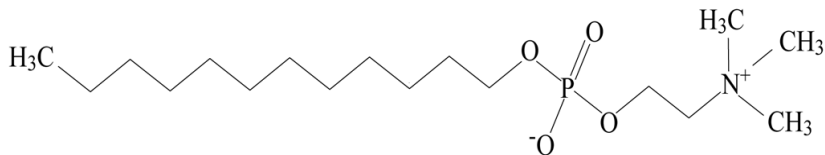


Figure 2. Chemical structure of dodecylphosphorylcholine (DPC) (from [2])

Method

NMR measurements were carried out on a Bruker Avance III HD 700 spectrometer (700 MHz for ^1H , 175 MHz for ^{13}C). All samples were prepared in standard 5-mm NMR tubes. The solution volume was 0.6 ml. Solution was prepared in D_2O , the sample concentration of CsC was 1.5 mM, concentration of DPC was 46.6 mM. Two-dimensional spectra (^1H - ^1H TOCSY, ^1H - ^{13}C HSQC) were recorded at the temperature of 298 K. TOCSY mixing time was 0.35 s. The spectral window was 12 ppm. A series of one-dimensional ^1H and two-dimensional ^1H - ^{13}C HSQC NMR spectra was acquired with 2 sets of $\text{Dy}(\text{NO}_3)_3$ salt concentration in probe (1.0 mM, and 2.0 mM).

Results and Discussion

Total signal assignment was obtained for ^1H - ^{13}C HSQC spectra CsC with different concentrations (1 mM, 2 mM) of $\text{Dy}(\text{NO}_3)_3$ in micellar solution in D_2O (Fig. 3). The initial HSQC spectra of CsC – DPC – D_2O was assigned accordingly with previous results [3]. By adding Dy^{3+} ions in the CsC – DPC – D_2O system, it was revealed that CsC and DPC micelle were affected by surrounding Dy^{3+} ions. This influence can be described by shifts of certain peaks in the HSQC spectrum and additional line broadening. An attempt to characterize quantitatively the effect of Dy^{3+} ion based on measuring the signal volume in HSQC spectrum was made. In this research we may predict that system CsC – DPC has possible site of binding with Dy^{3+} ion: the influence of the ion on NMR spectra is prominent in residues MeLeu₄ (NCH₃ group), Val₅, MeLeu₆, Ala₇, D-Ala₈ (CH α groups). Analysis of relaxation time T_1 in the system CsC – DPC – Dy^{3+} and obtaining spatial structure of the complex are planned for further investigations.

Acknowledgements

The work was supported by the Russian Science Foundation (project no. 24-23-00427). V.V. Klochkov also acknowledges the support from the Kazan Federal University Strategic Academic Leadership Program (PRIORITY-2030).

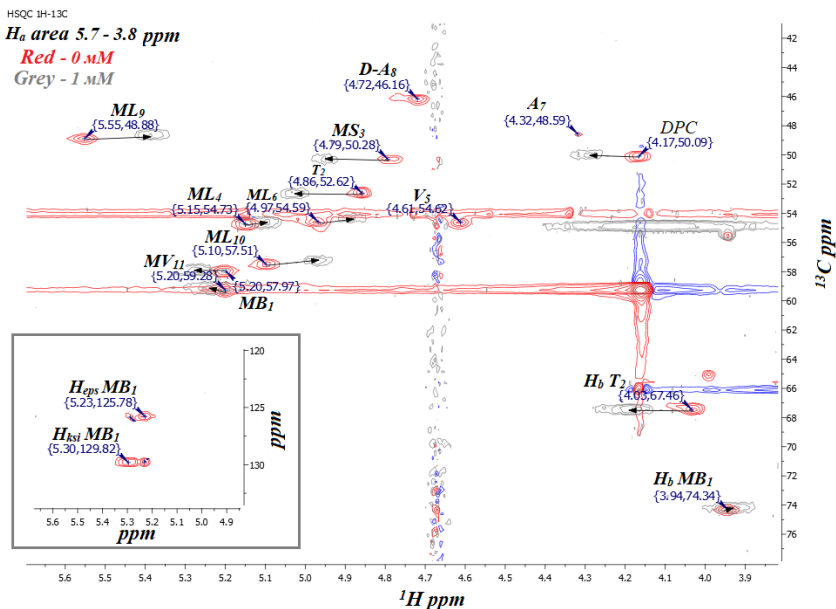


Figure 3. Fragment of ^1H - ^{13}C HSQC NMR spectrum of CsC-DPC with different concentrations of $\text{Dy}(\text{NO}_3)_3$ (red, 0 mM Dy^{3+} ; grey, 1 mM Dy^{3+}) in D_2O (700 MHz, 298 K)

References

1. F.S. Santana, et al. – Chem. Sci., Vol. 13, Issue 20, Pages 5860-5871 (2022).
2. A.S. Tarasov, et al. – BioNanoScience, Vol. 11, Issue 1, Pages 136-141 (2021).
3. S.V. Efimov, et al. – Biochemical and Biophysical Research Communications, Vol. 526, Issue 4, Pages 1054-1060 (2020).
4. K.M. Corbett, et al. – J. Med. Chem., Vol. 64, Issue 18, Pages 13131-13151 (2021).
5. M. Moussaïf, et al. – Appl Environ Microbiol., Vol. 63, Issue 5, Pages 1739-1743 (1997).

Spatial structure of taxifolin's diastereomers via NMR analysis

Roman P. Terekhov¹, Amir Taldaev^{2,3}, Eduard V. Bocharov^{3,4}, Denis I. Pankov¹,
Anastasiya D. Savina¹, Irina A. Selivanova¹

¹Nelyubin Institute of Pharmacy, Sechenov First Moscow State Medical University, Moscow, 8-2 Trubetskaya str., Russia

²Institute of Biomedical Chemistry, Moscow, 10-8 Pogodinskaya str., Russia

³Research Center for Molecular Mechanisms of Aging and Age-Related Diseases, Moscow

⁴Institute of Physics and Technology, Dolgoprudny, 9 Institutskiy per., Russia

⁵Shemyakin-Ovchinnikov Institute of Bioorganic Chemistry of the Russian Academy of Sciences, Moscow, 16-10 Miklukho-Maklaya str., Russia

E-mail: terekhov_r_p@staff.sechenov.ru

<https://colab.ws/labs/782>

Introduction

Taxifolin is a promising object for drug development. This compound is characterized by two chiral centers in positions 2 and 3, which result in two diastereomeric configurations: *trans*- and *cis*-isomers. A wide range of biological activity has been observed for *trans*-taxifolin [1]. At the same time, there is a lack of knowledge regarding pharmacological properties of *cis*-taxifolin. Previously, a *cis*-isomer-enriched sample of taxifolin was generated [2-3]. Obtaining the structural parameters of this diastereomer could prove fruitful for pharmacological screening *in silico* [4]. NMR spectroscopy can be utilized for this purpose.

The objective of this study was to assess the structural parameters of taxifolin diastereomers *via* NMR spectroscopy.

Methods

The *cis*-isomer-enriched sample of taxifolin was obtained using a spray drying approach [2-3] from active pharmaceutical ingredient (Lavitol[®], 99.1%, Ametis JSC, Blagoveshchensk, Russia).

The analyzed sample, weighing 15 mg, was dissolved in 450 μ L of deuterated methanol (99.8%, Cambridge Isotope Laboratories, Tewksbury, MA, USA). NMR spectra were acquired at 298 K on an 800-MHz Bruker Avance III NMR spectrometer (Billerica, MA, USA) equipped with a TXI triple resonance probe. The mixing time in the NOESY experiment was 400 ms. The ¹H were analyzed with CcpNmr software [5].

Results and Discussion

Regardless of configuration, the 1D NMR ¹H spectrum profile of taxifolin in MeOH-*d*₄ with water includes five signals, which are associated with the following hydrogen atoms (Figure 1): H8 (δ = 5.90 ppm; 1H; d), H6 (δ = 5.94 ppm; 1H; d), H5' and H6' (δ = 6.86 ppm; 6H; m), H2' (δ = 6.99 ppm; 1H; d), and OH5 (δ = 11.75 ppm; 1H; s). Additionally, *trans*-taxifolin can be identified by signals of hydrogen atoms in the chiral centers: H3 (δ = 4.52 ppm; 1H; d) and H2 (δ = 4.93 ppm; 1H; d). In contrast, in *cis*-taxifolin, these signals have other characteristics: H3 (δ = 4.20 ppm; 1H; d) and H2 (δ = 5.31 ppm; 1H; d). The spin-spin coupling constant between hydrogen atoms in positions 2 and 3 for *trans*- and *cis*-DHQ were 12.00 Hz and 2.40 Hz, respectively, resulting in dihedral angles of 154° and of 64°, respectively.

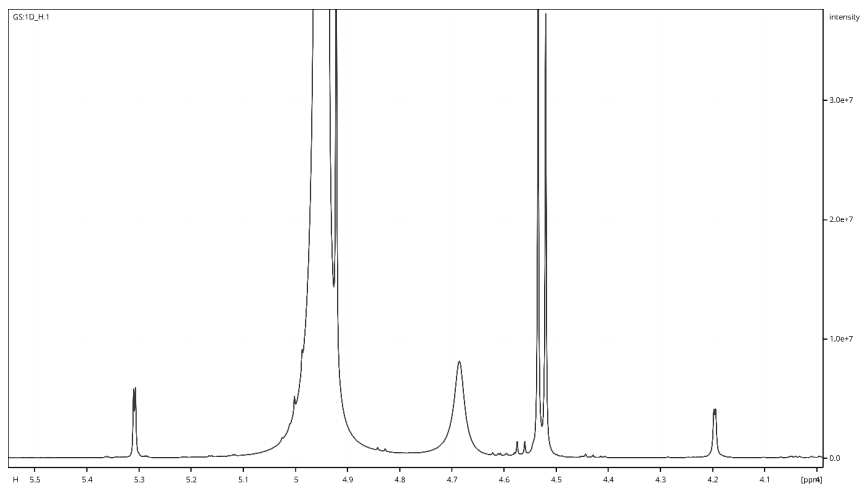


Figure 1. 1D NMR ^1H spectrum of *cis*-isomer-enriched taxifolin

The interatomic distances for conformers of taxifolin diastereomers were calculated based on the intensity of cross-peaks of the NOESY spectrum (Figure 2). In *trans*-taxifolin, the lengths between H2 and H8, H2', and H6, were 3.52 Å, 2.75 Å, and 2.50 Å, respectively. In *cis*-taxifolin, the same interatomic distances were 3.41 Å, 3.14 Å, and 2.88 Å, respectively. The lengths between H3 and OH5, H2', and H6' were 3.98 Å, 2.74 Å, and 2.86 Å for the *trans*-isomer and 3.58 Å, 3.43 Å, and 3.15 Å for the *cis*-isomer, respectively. The interatomic distances between hydrogen atoms in positions 2 and 3 were 3.14 Å and 2.40 Å for *trans*- and *cis*-taxifolin, respectively.

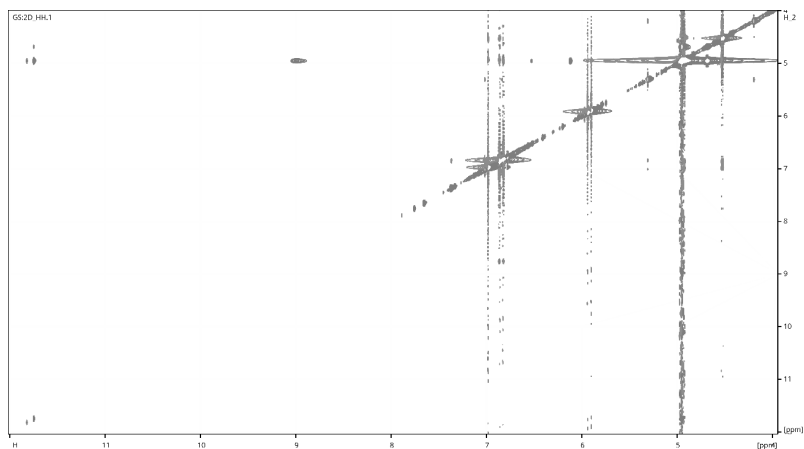


Figure 2. 2D NOESY spectrum of *cis*-isomer-enriched taxifolin

The results of structural data are summarized in Figure 3.

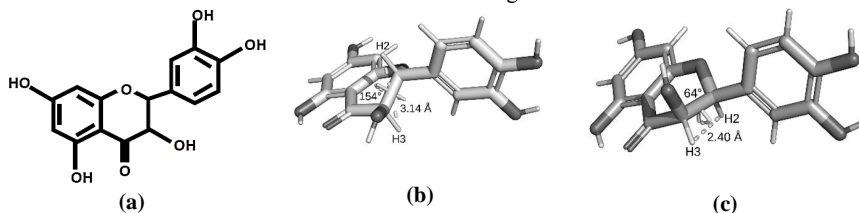


Figure 3. Taxifolin: (a) structural formula, (b) conformation of *trans*-isomer; (c) conformation of *cis*-isomer

Conclusion

The structural data of the conformers of taxifolin diastereomers in liquid media were obtained *via* NMR spectroscopy. These data can be used in the screening of biological activity through molecular modelling.

Acknowledgements

This work was financed by the Russian Science Foundation (No 075-15-2022-305), <https://rscf.ru/project/23-75-01130/>

References

1. A. Das, R. Baidya, T. Chakraborty, A.K. Samanta, S. Roy. – *Biomed. Pharmacother.*, **142**, 112004 (2021).
2. R.P. Terekhov, I.A. Selivanova, N.A. Tyukavkina, I.R. Ilyasov, A.K. Zhevhlakova, A.V. Dzuban, A.G. Bogdanov, G.N. Davidovich, G.V. Shylov, A.N. Utenishev, D.Yu. Kovalev, A.A. Fenin, T.G. Kabluchko. – *Molecules*, **25**(22), 5437 (2020).
3. A. Taldaev, R.P. Terekhov, I.A. Selivanova, D.I. Pankov, M.N. Anurova, I.Yu. Markovina, Z. Cong, S. Ma, Z. Dong, F. Yang, Y. Liao. – *Sci. Pharm.*, **90**(4), 67 (2022).
4. A.Kh. Taldaev, I.D. Nikitin, R.P. Terekhov, I.A. Selivanova. – *Drug Dev. Registr.*, **12**(2), 206-210 (2023).
5. S.P. Skinner, R.H. Fogh, W. Boucher, T.J. Ragan, L.G. Mureddu, G.W. Vuister. – *J. Biomol. NMR*, **66**, 111-124 (2016).

Structure of the amyloidogenic peptide SEM2(49-107) by NMR spectroscopy

Anastasia A. Troshkina, Dmitriy S. Blokhin, Vladimir V. Klochkov

Kazan Federal University, Kremlevskaya Str., 18, 420008 Kazan, Russia

E-mail: trosha29.00@mail.ru

Introduction

As is well known [1], the human immunodeficiency virus (HIV) remains one of the major public health challenges worldwide. Once inside in the human body, this virus attacks and disrupts the cells of the immune system. As a result, acquired immune deficiency syndrome (AIDS) may develop. Some research has shown that semen contains peptides that form amyloid, which significantly increases the risk of infection.

The mechanism of transmission of viral infection has not been fully studied. When describing the interaction between HIV virions and human target cells, these are considered to be negatively charged particles which will have electrostatic repulsive forces.

Human seminal fluid is considered the main factor in increasing HIV activity. Only about 0.1% of viral particles are infectious in laboratory conditions, this is due to the limited rate of attachment of viruses to host cells [2]. In natural conditions, HIV transmission is ineffective and occurs only in 1% of cases.

However, researchers have found [3] that certain components of seminal fluid can form amyloid fibrils. The cationic surface of these amyloid fibrils functions as an electrostatic bridge, allowing the attachment of the virus to human cells. As a result, an increased infectious activity of HIV has been linked to the presence of these amyloid fibrils within the seminal fluid.

It is currently known that semen amyloid fibrils are formed from small peptide fragments of the proteins PAP (prostatic acid phosphatase), Semenogelin 1 (SEM1) and Semenogelin 2 (SEM2).

A class of two highly homologous amyloids formed from peptide fragments of semenogelin 1 (SEM 1) and semenogelin 2 (SEM 2) proteins were identified. After ejaculation, the SEM proteins are rapidly cleaved by internal proteases into short peptide fragments SEM2(45-107), SEM2(49-107), SEM2(68-107), SEM1(45-107), SEM1(49-107), SEM1(68-107), SEM1(86-107).

In this study, one of these peptide fragments, SEM2(49-107), was investigated. To better understand the molecular interaction mechanism between SEM2 (49-107) and viral particles and cells, it is essential to determine its three-dimensional structure [4]. This will contribute to the development of drug inhibitors that reduce the risk of HIV infection [5].

Experimental section

Materials

The sample was a peptide SEM2(49-107) consisting of 59 amino acid residues corresponding to 49-107 amino acid residues of the human protein semenogelin 2. The single-letter amino acid sequence of the peptide SEM2(49-107), is as follows:

MFGQKDQHQHTKSKGSFSIQHTYHVDINDHDWTRKSQQYDLNALHKATKSKQ
HLGGSQQLLEHHHHH

To inhibit the fibrillation of the peptide during the final stages of synthesis, 0.2% sodium dodecyl sulfate (SDS) was added to the buffer solution (25 mM Bis-Tris pH 6.0) [6].

Methods

The 1D (^1H), 2D (^1H - ^{15}N) and 3D (^1H - ^{13}C - ^{15}N) NMR spectra of the SEM2 (49-107) peptide (C=0.46mM, H₂O+D₂O/ 90%+10%) were carried out on NMR spectrometer with a 700 MHz frequency (Bruker, AVANCE III 700) equipped with a quadruple resonance (^1H ,

^{13}C , ^{15}N , ^{31}P) CryoProbe at temperature of 293K. Data processing was performed using the Bruker Topspin 3.6 software. Chemical shifts (^1H , ^{13}C , ^{15}N) were assigned based on NMR spectra. All spectra were analyzed in the CCP-NMR program. During the experiments, no changes were observed in the ^1H NMR spectra of the peptide SEM2 (49-107). Based on this, it is assumed that there have been no structural changes in the peptide.

Results and discussions

The 2D ^1H - ^{15}N HSQC experiment was used to determine the chemical shifts of the nitrogen ^{15}N signals and assign their spin systems. The 3D (^1H - ^{13}C - ^{15}N) experiments were used to reconstruct the amino acid sequences: HNCO, HN(CO)CA, HNCA, HN(CA)CO, HN(CO)CACB, HNCACB, HN(CO)CC, TOCSY, to find the H^{N} , N, CO signals of the main chain, and the C_α , C_β , H_α , H_β signals of the side chains. The obtained values of chemical shifts for various amino acids were compared to the literature data [7].

The assignment of signals from nuclei ^1H , ^{13}C , and ^{15}N for atoms in the main and side chains of the SEM2(49-107) peptide was performed for 46 of the 59 amino acid residues (85%). The spectra did not contain signals of amide proton H^{N} in the center of the chain between 72 (Asp) and 78 (Thr) amino acids and 86 (Asp) and 88 (Asn). This may be due to their high conformational mobility and rapid chemical exchange of amide protons H^{N} and deuterium of the solvent for these residues. Based on the data of chemical shifts values of ^1H and ^{13}C it can be predicted that this peptide contains alpha-helices fragments at the C-terminus (Figure 1).

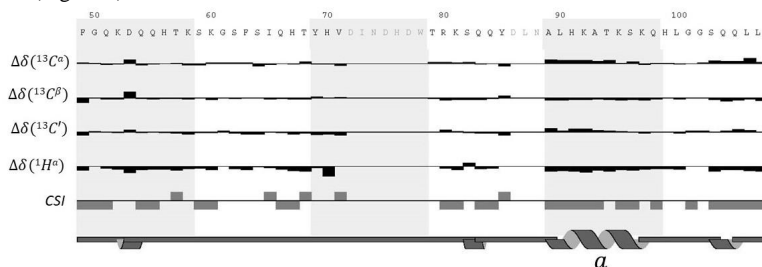


Figure 1. Prediction of the secondary structure of the SEM 2 peptide (49-107). The figure shows the SEM2 (49-107) sites predicted as α -helical (ribbon) at the C-terminus of the peptide. Chemical shift index (CSI) consensus calculated using the CCPNMR drawn as vertical bar chart

To assess the mobility of the SEM2 (49-107) peptide, a series of NMR relaxation experiments were performed. Specifically, a phase-sensitive 2D ^1H - ^{15}N HSQC experiment was used to measure relaxation times T_1 and T_2 at various delay times. The relaxation delays to measure R_1 were 0.01, 0.05, 0.1, 0.2, 0.4, 0.6, 0.8, 1.2, 1.6, and 2.0 s; and to measure R_2 the values were 0, 16, 32, 48, 64, 96, 128, 160, 192 and 256 ms. Based on these experiments, values for the longitudinal and transverse relaxation rates R_1 and R_2 were determined.

The observed difference in the R_2/R_1 rate values suggests that there is a variation in mobility and conformational dynamics along the peptide sequence. Specifically, it indicates that the C-terminal end of the peptide has less mobility compared to the N-terminal end.

In addition, the R_2/R_1 rate values indicate that there is secondary structure in the form of an alpha helix within the amino acid range of 89 (Ala) to 98 (Gln). This suggests that this region of the peptide adopts a relatively constrained conformation, which is consistent with the results of the secondary structure analysis.

Acknowledgements

This work was supported by the Russian Science Foundation (D.S. Blokhin, project no. 20-73-10034). V. Klochkov also acknowledges the support from the Kazan Federal University Strategic Academic Leadership Program (PRIORITY-2030).

References

1. Münch J. et al. Semen-derived amyloid fibrils drastically enhance HIV infection //Cell. – 2007. – V. 131. – №. 6. – P. 1059-1071.
2. Castellano L. M., Shorter J. The surprising role of amyloid fibrils in HIV infection //Biology. – 2012. – V. 1. – №. 1. – P. 58-80.
3. Usmani S. M. et al. Direct visualization of HIV-enhancing endogenous amyloid fibrils in human semen //Nature communications. – 2014. – V. 5. – №. 1. – P. 3508.
4. Ortega M., Ances B. M. Role of HIV in amyloid metabolism //Journal of Neuroimmune Pharmacology. – 2014. – V. 9. – P. 483-491.
5. Bergman P. et al. Amyloid formation: functional friend or fearful foe? //Journal of internal medicine. – 2016. – V. 280. – №. 2. – P. 139-152.
6. Bikmullin, A. The data of heterologous expression protocol for synthesis of 15N, 13C-labeled SEM1(68–107) peptide fragment of homo sapiens
7. 63 semenogelin1. / A. Bikmullin, E. Klochkova, F. Krasnovid, D. Blokhin. //MethodsX. – 2021. – V. 8. – P. 101512.
8. K. Wuthrich, NMR of proteins and nucleic acids. New York: Wiley-VCH, 1986.

Investigation of the features of the interaction of water molecules and saccharides in aqueous solutions by NMR

Daria Tsukhlova, Daria Melnikova, Vladimir Skirda

Department of Molecular Physics, Institute of Physics, Kazan Federal University, Kazan 420008, Russian Federation

E-mail: daryaparfenova@mail.ru

Introduction

In the field of scientific research, of particular interest is the study of aqueous solutions of saccharides. There is a large list of works devoted to the possibilities of using saccharides in medicine and pharmacology to create new drugs and improve treatment methods [1], in the food industry as substitutes and additives [2], in the chemical industry to obtain other popular compounds and materials [3].

The study of the characteristics of saccharides during their dissolution plays an important role in determining their structural and functional properties, which will improve the efficiency of their use. The mechanisms underlying the interaction of water molecules and saccharides remain poorly understood [4]. Important information about the patterns of interaction of molecules in aqueous solutions of saccharides can be obtained from studies devoted to the study of the mobility of water and saccharide molecules.

Method and objects of research

The purpose of current work was to study the features of the interaction of water molecules and saccharides in aqueous solutions using nuclear magnetic resonance method. The monosaccharides D-xylose, D-mannose and the disaccharide sucrose were chosen as the objects of study in this work.

To determine the relaxation times in the system under study, the Carr-Purcell-Meiboom-Gill sequence and inversion-recovery sequence were used. A stimulated echo sequence was used to determine the self-diffusion coefficients of water and saccharide molecules.

Results and discussion

It was found that the spin-spin relaxation of water molecule protons is characterized by an anomalously strong concentration dependence for studied saccharide solutions (Fig. 1).

As additional results, the fulfillment of the condition for rapid exchange between the protons of water molecules and the protons of the hydroxyl groups of saccharides is shown for all experimental data and in the entire studied concentration range.

The work was carried out on the equipment of the Federal Center of Shared Facilities for physical and chemical research of substances and materials (FCSF) KFU Bruker AVANCE 400 MHz spectrometer optimized for microtomography, solid state and self-diffusion.

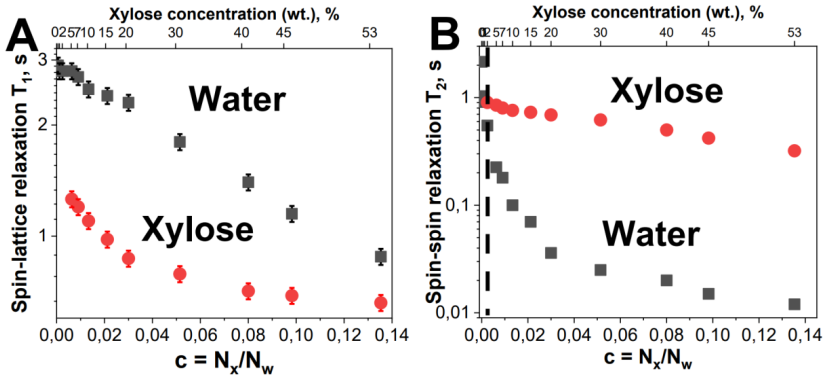


Figure 1. Concentration dependences of the spin-lattice (A) and spin-spin (B) relaxation times of water and xylose molecules; the dotted line marks the xylose concentration, starting from which the spin-spin relaxation time of water molecules becomes less than the relaxation time of saccharide

References

1. Yu W., Zhang N., Li C.: *Curr. Pharm. Des.* 15, 3826–3836 (2009)
2. Röhrig C.H., Choi S.S., Baldwin N.: *Crit. Rev. Food Sci. Nutr.* 57, 1017–1038 (2017)
3. Hengtao T., Zheng Z., Zhi C., Xin J., Liangzhi L.: *Mol. Catal.* 531, 112672 (2022)
4. Heugen U., Schwaab G., Bründermann E., Havenith M.: *PNAS.* 103, 12301-12306 (2006)

Molecular Mobility in Mixtures of Ethylammonium and Aluminum Nitrates by Molecular Dynamics Simulations in Interests of Interpreting NMR Data

Milosh Ubovich, Andrei V. Egorov, Vladimir. I. Chizhik

Faculty of Physics, Saint-Petersburg State University, Russia

E-mail: ubovich.milosh@yandex.ru

Introduction

The interest in the research of alkylammonium nitrate protic ionic liquids (AN PILs) has significantly risen in the recent several decades. PILs consist of only ions and they are in a liquid state at relatively low temperatures (up to approximately 100 °C). These compounds attract the attention due to their incredible properties, such as high thermal stability, low vapor pressure, high boiling point, etc. PILs are employed in various electrochemical applications (for example, lithium ion batteries, fuel cells, etc.). Also AN PILs have relatively low cost and toxicity, and in addition they are outlined by a special combination of properties.

Ethylammonium nitrate (EAN, $[\text{C}_2\text{H}_5\text{NH}_3^+][\text{NO}_3^-]$) is an interesting AN PIL to study. EAN consists of ethylammonium cation (EA^+ , see Fig.1) and nitrate anion (NO_3^-). Mixtures of EAN and aluminum nitrate $\text{Al}(\text{NO}_3)_3$ salt were chosen as the research objects.

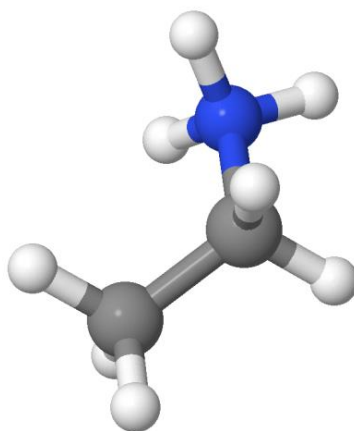


Figure 1. The schematic representation of the ethylammonium nitrate cation (hydrogen – white, nitrogen – blue, carbon – grey)

A detailed research of the mixture of EAN and aluminum nitrate by molecular dynamics (MD) simulations was carried out in Ref. [1]. Despite the interesting results obtained, the authors in this paper did not investigate molecular mobility of the systems.

It is worth paying attention to the study [2], which shows that even in systems with well-dried aluminum nitrate, Al^{3+} is surrounded by 6 water molecules. It is necessary after working out the methodology on the systems studied in the present work, to study with the help of the MD simulations data the system in which this environment will be taken into account. Firstly, to check model parameters, the mixtures without water (as a test system) were simulated. After that, the mixtures EAN and $\text{Al}(\text{NO}_3)_3$ were simulated with an environment around the aluminum cation in the form of six water molecules (see Fig. 2).

To study the mechanisms of changes in molecular mobility, when adding $\text{Al}(\text{NO}_3)_3$ to the EAN, the attempt was implemented by the MD simulations. The investigation purpose was not only to quantify the kinetic characteristics of the components in the mixture at their different ratios but also to identify the relationship between the peculiarities of the local structure of mixtures and the character of processes of rotational reorientations of ions.

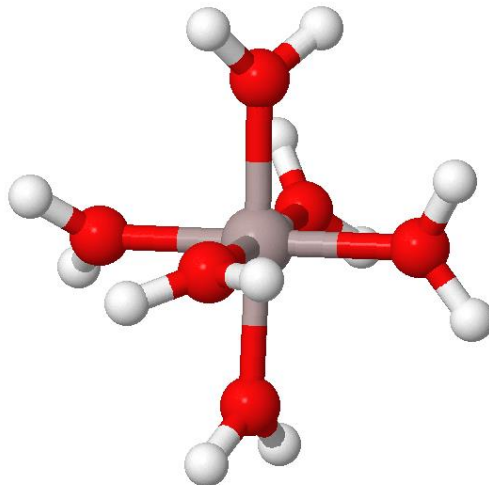


Figure 2. An example the schematic representation of the aluminum cation surrounded by 6 water molecules (hydrogen – white, oxygen – red, aluminum – light brown)

Simulation details and results

The mixtures containing EAN and $\text{Al}(\text{NO}_3)_3$ were simulated by the MD method. MDynaMix package [3] was used in the present investigation. The simulation was carried out in a cubic cell with periodic boundary conditions in the NPT ensemble at 298 K and 1 atm. The temperature was kept constant with a Nose-Hoover thermostat [4, 5]. The pressure was maintained with a Hoover barostat [6]. The EA^+ cation was simulated applying the potentials described in Ref. [7, 8]. A model nitrate anion was treated as a 4-site planar structure with the central nitrogen atom and three oxygen atoms at the distance of 1.22 Å with all O-N-O angles of 120° [9]. Its intermolecular interactions were described by the sum of Coulomb and Lennard-Jones (6-12) potentials. Three different potential parameter sets were considered (see Refs. [7, 10, 11]). The interaction potential of the model aluminum ion was also the sum of Coulomb and Lennard-Jones (6-12) potentials (the potential parameters were described in Ref. [12]). Three-site SPC/E [13] water model was considered in the present study. Simulation time was 1 ns.

The density of mixtures, radial distribution functions, self-diffusion coefficients and reorientation times of the intramolecular vectors of the nitrate anion have been obtained from MD simulations data. A detailed analysis of the influence of added aluminum nitrate on the translational motions of the system components and on the processes of reorientation of the nitrate anion has been fulfilled. The molecular mobility in the mixtures is also compared with and without taking into account the aqueous environment.

The results obtained are ready to compare with experimental NMR data (NMR diffusometry and NMR relaxation).

Acknowledgments

This work was supported by the Russian Science Foundation (project № 23-23-00049).

References

1. Gomez-Gonzalez V., Docampo-Alvarez B., Montes-Campos H., et al. – Phys. Chem. Chem. Phys. 2018. V. 20. No. 28. 19071.
2. Matveev V. V., Ievlev A. V., Vovk M. A., et al. – J. Mol. Liq. 2019. V. 278. 239.
3. Lyubartsev A. P., Laaksonen A. – Comp. Phys. Comm. 2000. V. 128. No. 3. P. 565.
4. Nose S. – Mol. Phys. 1984. V. 52. No. 2. P.255.
5. Martyna G. J., Tobias D. J., Klein M. L. – J. Chem. Phys. 1994. V. 101. No. 5. P. 4177.
6. Martyna G. J., Tuckerman M. E., Tobias D. J., et al. – Mol. Phys. V. 87. No. 5. P. 1117.
7. Umehayashi Y., Chung W.-L., Mitsugi T., et al. – J. Comput. Chem. Jpn. 2008. V. 7. No. 4. P. 125.
8. Choe J., Kim K., Chang S. – Bull. Korean Chem. Soc. 2000. V. 21. P. 200.
9. Ebner C., Sansone R., Hengrasmee S., et al. – Int. J. Quant. Chem. 1999. V. 75. P. 805.
10. Megyes T., Balint S., Peter E., et al. – J. Phys. Chem. B. 2009. V. 113. No. 13. P. 4054.
11. Laaksonen A., Kovacs H. – Can. J. Chem. 1994. V. 72. P. 2278.
12. Faro T. M. C., Thim G. P., Skaf M. S. – J. Chem. Phys. 2010. V. 132. P. 11450.
13. Berendsen, H. J. C.; Grigera, J. R.; Straatsma, T. P. – J. Phys. Chem. 1987. V. 91. No. 24. 6269.

Transition metals in wide-band-gap semiconductor β - Ga_2O_3 identified by high-frequency electron paramagnetic resonance

Yu. A. Uspenskaya, A. S. Gurin, D. D. Kramushchenko, I. V. Ilyin, A. V. Batueva, P. G. Baranov, R. A. Babunts

Ioffe Institute, Saint Petersburg, Russia

E-mail: yulia.uspensskaya@mail.ioffe.ru

Introduction

Gallium oxide in the β phase is a wide-band-gap semiconductor with a bandgap of 4.7 eV. Both bulk single crystals and epitaxial layers of beta-gallium oxide (β - Ga_2O_3) can be used in various fields: from power electronics to solar-blind UV detectors. One of the attractive features of the Ga_2O_3 system is its high radiation resistance, making it suitable for use in space applications.

Results and discussion

Transition metal ions may be either deliberately or unintentionally introduced into the crystal during the growth process due to their presence in source materials, and these impurities largely determine the electrical and optical properties of the crystal. Recently, the results of electron paramagnetic resonance (EPR) research of commercial samples of nominally undoped β - Ga_2O_3 bulk crystals were published [1]. The study demonstrate that the Fermi level position, varied by means of electron irradiation, is one of the critical parameters that determines the charge and spin states of transition elements, such as iron and chromium.

The charge states of non-Kramers Fe^{2+} ions ($S = 2$) and Fe^{3+} ions ($S = 5/2$) in the octahedral and tetrahedral positions of the crystal lattice in a commercial substrate of semi-insulating gallium oxide β - Ga_2O_3 before and after proton irradiation with an energy of 15 MeV have been identified by high-frequency EPR (Fig. 1) [2].

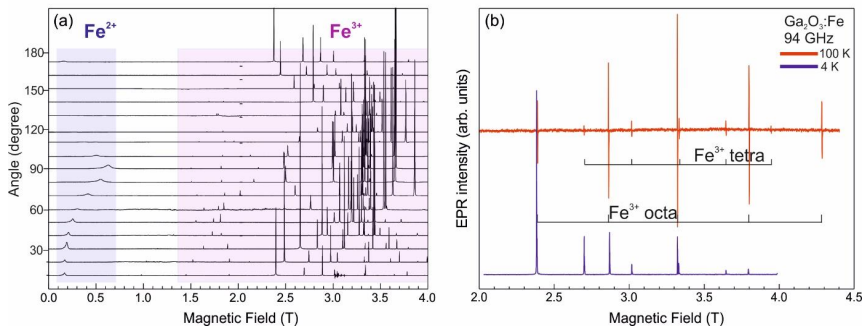


Figure 1. EPR spectra of semi-insulating $\text{Ga}_2\text{O}_3:\text{Fe}$ crystal recorded at 94 GHz. (a) Orientation dependence of EPR signals of Fe^{3+} and Fe^{2+} ions. (b) The fine structure of lines for Fe^{3+} ions in octahedral and tetrahedral positions is indicated.

Fig. 1 (a) presents the orientation dependence of EPR signals of Fe^{3+} and Fe^{2+} ions in a $\text{Ga}_2\text{O}_3:\text{Fe}$ crystal detected in the continuous-wave mode at a frequency of 94 GHz at a temperature of 4 K. A significant asymmetry of intensities of EPR lines with respect to the center in the $g = 2$ region is observed in the EPR spectra of Fe^{3+} ions. This is attributable to

the Boltzmann distribution of populations of spin levels. One may gain a better understanding of these EPR spectra by examining Fig. 1 (b), which shows the fragment of EPR spectra of Fe^{3+} ions detected in the continuous-wave mode at low (4 K) and high (100 K) temperatures. It is evident that the high-temperature spectrum is almost symmetric with respect to its center, since the influence of the Boltzmann factor is greatly decreased. The fine structure of lines for Fe^{3+} ions in octahedral and tetrahedral positions is also seen. It has determined unambiguously that there are two charge states for iron, Fe^{2+} and Fe^{3+} , in the semi-insulating material. Protons irradiation with an energy of 15 MeV and a dose of $\sim 10^{14} \text{ cm}^{-2}$ does not lead to any change in intensity or shape of the EPR spectra, that indicates a high radiation resistance of semi-insulating $\beta\text{-Ga}_2\text{O}_3$.

Acknowledgements

This work was supported by the Russian Science Foundation № 22-12-00003, <https://rscf.ru/project/22-12-00003/>.

References

1. R. A. Babunts, A. S. Gurin, E. V. Edinach, H.-J. Drouhin, V. I. Safarov, P. G. Baranov. – *J. Appl. Phys.*, **132**, 155703 (2022).
2. R. A. Babunts, A. S. Gurin, E. V. Edinach, Yu. A. Uspenskaya, P. G. Baranov. – *Tech. Phys. Lett.*, **49**, 12-14 (2023).

Formation of 2-aminospiropyrazolinium and linear compounds at β -aminopropioamidoximes alkylsulfochlorination

Ljudmila A. Kayukova¹, [Azamat Yerlanuly](#)¹, Aidana M. Duisenali¹, Anna V. Vologzhanina², Yelizaveta O. Belyankova³

¹JSC «A.B. Bekturov Institute of Chemical Sciences», 050010 Almaty, Kazakhstan

²A. N. Nesmeyanov Institute of Organoelement Compounds, Russian Academy of Sciences, 119991 Moscow, Russia

³Kazakh British Technical University, 050010 Almaty, Kazakhstan

E-mail: azaraze8575@mail.ru

Introduction

Amidoximes carry the potential for several possible reaction directions: at the oxygen atom of the oxime group, at the amine nitrogen atom; the formation of rearranged products is also likely. In the arylsulfochlorination of β -aminopropioamidoximes we discovered previously unknown products – arylsulfonates of spiroprazole compounds [1,2]. During alkylsulfochlorination the formation of spiroprazole sulfonates is less likely than during arylsulfochlorination, and the main products should be as we were proposed alkylsulfochlorination products at the oxygen atom of the amidoxime group.

Materials and methods

The reagents were purchased from Sigma-Aldrich and were used without purification. FT-IR spectra were obtained on a Thermo Scientific Nicolet 5700 FTIR instrument (Thermo Fisher Scientific, Inc., Waltham, MA, USA) in KBr pellets. The ¹H- and ¹³C-NMR spectra of the compounds 3–9 were acquired on a Bruker Avance III 500 MHz NMR spectrometer (Bruker, BioSpin GmbH, Rheinstetten, Germany). The signals of the residual undeuterated solvents were used as a reference for the ¹H-NMR (2.50 ppm) and ¹³C-NMR (39.5 ppm) spectra. The solvents for the synthesis, recrystallization, and TLC analysis (ethanol, 2-PrOH, benzene, chloroform) were purified according to the standard techniques.

Results and Discussion

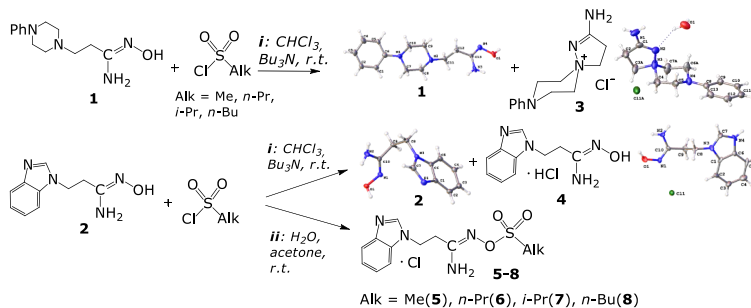
We fulfilled alkylsulfochlorination of β -aminopropioamidoximes [β -aminogroup: 4-phenylpiperazin-1-yl (1) and benzimidazol-1-yl (2)]. Alkyl substituents in a row of alkylsulfonyl chlorides were: methyl, *n*-propyl, *i*-propyl, *n*-butyl. Alkylsulfochlorination was carried out in chloroform at r.t.; for the HCl binding released in the reaction tributylamine was used as a base.

After the reaction was complete (as evidenced by TLC) crystalline products were isolated in the yields >50%. Similarly with arylsulfochlorination of β -aminopropioamidoximes, it was assumed that in the case of β -(Ph-piperazin-1-yl)propioamidoxime (1) 2-aminospiropyrazolylammonium alkylsulfonates can be isolated, and for β -(benzimidazol-1-yl)propioamidoxime (2) O-alkylsulfonates should be obtained (Scheme 1).

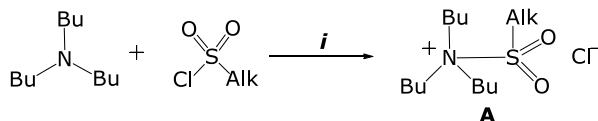
But in accordance with ¹H and ¹³C NMR spectroscopy and X-ray diffraction data, under the indicated conditions (*i*), in the reaction of β -aminopropioamidoximes 1,2 with a row of alkylsulfochlorides (Alk = Me, *n*-Pr, *i*-Pr, *n*-Bu) starting amidoximes 1,2, hydrochloride 4 were isolated and in the case of *n*-butylsulfochlorination of amidoxime 1 the second identified product was 2-amino-8-phenyl-1,5,8-triazaspiro[4.5]dec-1-en-5-ium chloride (3) described in the work [3].

Obviously Bu₃N used in the reaction to bind the HCl liberated in the reaction binds the alkylsulfonyl group of the sulfochlorides into an alkylsulfonyl tributylammonium

chloride (A) due to competitive relationships with the nucleophilic centers of the amidoximes 1,2 and no sulfochlorination products of β -aminopropioamidoximes were detected (Scheme 2).

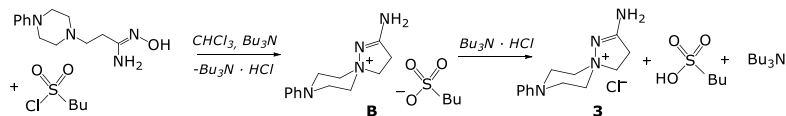


Scheme 1. β -Aminopropioamidoximes alkylsulfochlorination



Scheme 2. Binding of alkylsulfonyl chloride reagents with tributylamine under reaction conditions (i)

The formation of 2-aminospiropyrazolammonium chloride 3 can be explained by the initial formation of 2-aminospiropyrazolylammonium *n*-butylsulfonate (B) and Bu_3N hydrochloride and the subsequent ion exchange reaction between them (Scheme 3).



Scheme 3. Formation of 2-aminospiropyrazolammonium chloride 3 under conditions (i)

We revised the reaction scheme for the β -aminopropioamidoximes alkylsulfochlorination and decided to carry out it without a base since the substrate molecule contains a binding center for HCl – the nitrogen atom of the β -amino group.

The reaction of β -(benzimidazol-1-yl)propioamidoxime (2) with alkylsulfonylchlorides was carried out in a mixture of water:acetone (5:1) (conditions ii). As a result, hydrochlorides of alkylsulfochlorination products 5–8 were obtained in the yields of 40–85%.

Hydrochlorides 5–7 are a caramel-like mass for which it is impossible to determine the m.p.; only *O*-butylsulfonate of β -(benzimidazol-1-yl)propioamidoximehydrochloride (8 is a crystalline substance with the m.p. 84 °C. At this time, we do not yet have X-ray single crystals of hydrochloride 8; it's on crystallization.

Evidence of the occurrence of β -(benzimidazol-1-yl)propioamidoxime (2) alkylsulfochlorination in the IR spectra is the presence of asym. and sym. bands of stretching vibrations of the sulfonate group in the regions ν 1347–1361 cm^{-1} and ν 1160–1194 cm^{-1} . A wide band of stretching vibrations of the ammonium bond $\text{N}(+)\text{--H}$ in the region of 2700 cm^{-1} ; bands of stretching vibrations of $\text{C}=\text{C}$, $\text{C}=\text{N}$ bonds with very strong intensity, bending vibrations of N-H bonds of the NH_2 group in the region of 1636 – 1658 cm^{-1} are present in the IR spectra of the hydrochlorides 5–8.

In the ^1H NMR spectra signals of sulfonylalkyl groups of hydrochlorides of O-alkylsulfonyl derivatives 5–8 are present at δ , ppm: 3.50 (s, 3H, CH_3) (5); 1.00 (t, $J = 7.0$ Hz, 3H, $\text{CH}_3\text{CH}_2\text{CH}_2$), 1.40 (m, 2H, $\text{CH}_3\text{CH}_2\text{CH}_2$), 1.48 (m, 2H, $\text{CH}_3\text{CH}_2\text{CH}_2$) (6); 1.00 [d, $J = 7.0$ Hz, 6H, $\text{CH}(\text{CH}_3)_2$], 3.55 (m, 1H, $\text{CH}(\text{CH}_3)_2$) (7); 0.80 [t, $J = 7.0$ Hz, 3H, $\text{CH}_2(\text{CH}_2)_2\text{CH}_3$], 1.40 (m, 4H, $\text{CH}_2(\text{CH}_2)_2\text{CH}_3$), 2.80 [m, 2H, $\text{CH}_2(\text{CH}_2)_2\text{CH}_3$] (8).

The triplet signals of the $\alpha\text{-CH}_2$ and $\beta\text{-CH}_2$ protons of the methylene groups of compounds 5–8 are in the range δ 2.22–2.80 ppm and 3.95–4.78 ppm, respectively. The signal of olefin proton of the imidazole ring is present in the region δ 9.50–9.60 ppm. The remaining benzimidazole $\text{C}_{\text{sp}^2}\text{-H}$ protons give multiplet signals in the region of δ 7.20–8.27 ppm. Wide singlet proton signals of NH_2 group of the hydrochlorides 5–8 are present at δ 7.00 ppm.

In the ^{13}C NMR spectra of the hydrochlorides 5–8 the signals of sulfonylalkyl groups are at δ , ppm: 39.70 (CH_3); 12.45, 18.47, 53.52 (*n*-Pr); 15.82, 48.72 (*i*-Pr); 13.30, 20.52, 25.41, 47.07 (*n*-Bu). The carbon atoms of the $\text{C}=\text{N}$ bond of amidoxime groups have signals in a narrow region at δ 156.6–157.2 ppm. Carbon atoms of benzimidazole ring C_{sp^2} give groups of 6 signals, one of which has an intensity of 2C in the region δ 113.00–142.37 ppm. Signals of carbon atoms of α - and β -methylene groups were found at $\sim \delta$ 30 and 43 ppm, respectively.

Conclusion

The reaction of alkylsulfochlorination of β -aminopropioamidoximes compared to arylsulfochlorination has its own peculiarities. The presence of tributylamine as a base does not lead to the interaction between reagents and substrates, because products contained either original amidoximes and its hydrochlorides or 2-aminospiropyrazolylammonium chloride [in the case of butylsulfochlorination of β -(4-phenylpiperazin-1-yl)propioamidoxime]. Carrying out alkylsulfochlorination without a base made it possible to obtain hydrochlorides of O-sulfoalkyl- β -(benzimidazol-1-yl)propioamidoximes.

Acknowledgements

This study was supported by the Committee of Science of the Ministry of Science & High Education of the Republic of Kazakhstan (Grant IRN AP14870011). The research is carried out using the equipment of the NMR Laboratory and X-ray Center of A. N. Nesmeyanov Institute of Organoelement Compounds, Russian Academy of Sciences, Moscow, Russia and Kazakh British Technical University, Almaty, Kazakhstan.

References

1. L. A. Kayukova, G. P. Baitursynova, E. M. Yergaliyeva, et al. – *Chem. J. Kaz.*, 74, №2, 22–32 (2021).
2. L. A. Kayukova, A. V. Vologzhanina, P. Dorovatovskii, et al. – *Molecules*, 27, 2181 (2022).
3. L. A. Kayukova, A. V. Vologzhanina, P. Dorovatovskii, et al. – *Int. J. Mol. Sci.*, 24, 11315 (2023).

Using Microwave and Field Gradient Pulses for binary coding of the Transverse Magnetization

Ruslan B. Zaripov, Iskander T. Khairutdinov

Zavoyskiy Physical-Technical Institute, Federal Research Center "Kazan Scientific Center of the Russian Academy of Sciences", Kazan, Russia

E-mail: rb.zaripov@knc.ru

Introduction

The binary coding system is the basis of digital computing. It uses only two characters 0 and 1. An important aspect in the development of digital devices is the bit depth of the binary code. The number of digits defines the range of numbers that can be represented in this code. Each digit in the binary code represents a bit of information. In recent decades, the use and implementation of quantum bits have been actively studied. Electronic and nuclear spins are good model systems for testing certain ideas in the implementation of quantum logical operations. It is known that degeneracy is eliminated and two states of electron spin can be manipulated in a magnetic field due to the Zeeman effect. In this work, the possibility of writing a number in binary code on a free induction signal in a tetracyanoethylene radical is shown.

Experimental system and conditions

Tetracyanoethylene (TCNE) is an organic compound. In [1, 2], the use of this system for implementing quantum memory algorithms on electron spins was demonstrated. In this compound, the electron density of an unpaired electron is evenly distributed with respect to four equivalent nitrogen nuclei ^{14}N ($I = 1$). Therefore in electron paramagnetic resonance (EPR) spectrum a liquid solution of TCNE reveals 9 lines due to hyperfine interaction (HFI). The steady-state EPR spectrum can be described by the spin Hamiltonian:

$$\hat{H} = \omega_0 S_z + a S_z \sum_{i=1}^4 I_{iz}, \quad (1)$$

where S_z and I_{iz} ($i \in [1...4]$) are operators of projections onto the spin z axis of the electron and the spins of nitrogen nuclei, respectively, ω_0 is the Zeeman frequency of an electron in a constant magnetic field B_0 which is directed along the z axis, a is the HFI constant. The number of HFI lines in the spectrum in the case of magnetically equivalent nuclei is $2nI + 1$, where n is the number of nuclei, I is the nuclear spin.

In this work, along with a microwave (MW) pulse, the studied system was irradiated by magnetic field gradient (MFG) pulses. After the first MW pulse (the pulse length was 16 ns) at certain times (based on which signals are to be suppressed or recovered), pulses were applied creating a MFG of one direction or another. Since a commercial spectrometer is not equipped with blocks for creating a MFG, a homebuilt version was implemented [2, 3].

Beat peaks as bits in memory

The supply of a MW pulse leads to the appearance of a free induction decay (FID). In the case of nonselective excitation, each spin packet (HFI component) gives its own FID signal. Sum of all the FIDs give an interference pattern. The FID's peaks (beat peaks) can be used to store the value of a binary digit. The maximum number of beats gives the maximum digit of the number and therefore the maximum value of the number to be stored in quantum memory. For binary encoding we will take the presence of the FID peak as 1 and its absence

as 0. The number of bits is limited by observing a peak with an intensity of 10% of the initial amplitude.

In a liquid solution, there are ensembles of spins that are uniformly randomly arranged in space. The MFG pulse changes the Zeeman rotational frequency of the electron precessing around the z axis by an amount that depends on the magnitude of the gradient. In this case, there are transitions of spins from one ensemble to another, which destroy the beats.

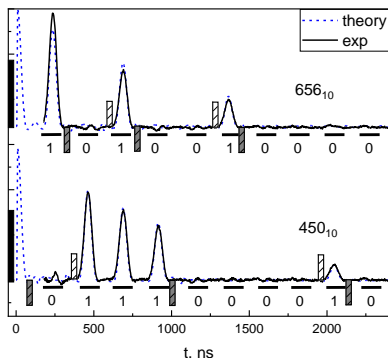


Fig. 1. Experimental (black) and theoretical (dashed blue) dependences of FID. Time intervals for storing the digit value are marked with black segments. Digit values are given below the bars. The black rectangle marks the initial MW pulse.

Examples of encoding the decimal numbers 450 and 656 in binary form of binary numbers 0111000010 and 101001000 are shown in figure 1. The figure shows that the combination of gradient (white rectangle) and antigradient (gray rectangle) pulses makes it possible to successfully encode binary numbers. The quality of the restored signals does not depend on the set values of the bits and their position. This indicates the effective action of gradient and anti-gradient pulses. On the other hand, it should be noted that a small part of the signal from the spin system is still preserved due to the imperfection of MFG pulses. Experimental signals are easily reproduced using simulation, which indicates a good correspondence to the chosen theoretical model and its reliability.

Acknowledgements

We are grateful to V.I. Morozov (Arbuzov Institute of Organic and Physical Chemistry, FRC Kazan Scientific Center, Russian Academy of Sciences) for the TCNE anion-radical. The experiments were carried out on the basis of the Collective Spectro-Analytical Center for Physical and Chemical Studies of the Structure, Properties, and Composition of Substances and Materials; FRC Kazan Scientific Center; Russian Academy of Sciences. This study was supported by the Russian Science Foundation (grant #22-72-10063, <https://rscf.ru/project/22-72-10063/>).

References

1. K. I. Gerasimov, S. A. Moiseev, V. I. Morosov, R. B. Zaripov. – *Phys. Rev. A*, 90, 042306 (2014).
2. K. I. Gerasimov, S. A. Moiseev, R. B. Zaripov. – *Appl. Magn. Reson.*, 48, 795 (2017).
3. R. B. Zaripov, I. T. Khairutdinov. – *JETP Letters*, 118, 826 – 833 (2023).

Relaxation dispersion of water protons in magnetic fields ranging from 10 mT to 16.4 T for Gd-containing materials proposed as new MRI contrast agents

Ivan Zhukov¹, Anton Popov^{2,3}, Alexander Baranchikov³, Yulia Gorbunova^{3,4}, and Alexandra Yurkovskaya¹

¹*International Tomography Center SB RAS, Novosibirsk, Russia*

²*Institute of Theoretical and Experimental Biophysics RAS, Pushchino, Russia*

³*Kurnakov Institute of General and Inorganic Chemistry RAS, Moscow, Russia*

⁴*Frumkin Institute of Physical Chemistry and Electrochemistry RAS, Moscow, Russia*

E-mail: i.zhukov@tomo.nsc.ru

Introduction

Magnetic resonance imaging (MRI) is a safe and non-invasive technique that visualize the interior of non-conducting bodies by representing the distribution of proton spin density. The contrast of an MRI image is limited by a small equilibrium proton spin polarisation and the relaxation properties of protons in a particular tissue. In particular, the speed of an MRI scanning is determined by the longitudinal nuclear spin relaxation rate $R_1 = 1/T_1$. Relaxation rates vary significantly between different tissues and body fluids. To enhance the contrast of MRI images, gadolinium-based contrast agents are commonly used to modify the relaxation parameters R_1 , R_2 and R_1/R_2 ratio, thus improving the contrast of MRI images. However, the injection of a contrast agent can lead to severe adverse effects due to the lability of gadolinium complexes and the toxicity of free Gd^{3+} ions [1]. Therefore, it is important to develop efficient contrast agents that provide equivalent relaxation enhancement with a lower concentration of Gd-containing substances.

Materials and Methods

The relationship between the magnetic field and the relaxation enhancement of water protons was investigated for two types of Gd-containing materials: Gd-doped CeO_2 nanoparticles and Gd-based phthalocyanine complexes. $Ce_{0.8}Gd_{0.2}O_{1.9}$ nanoparticles were synthesized using microwave-hydrothermal and polyol-mediated methods [2]. Estimates based on X-ray powder diffraction and transmission electron microscopy data indicate that the resulting $Ce_{0.8}Gd_{0.2}O_{1.9}$ nanoparticles had sizes of 5 nm and 2.5 nm, respectively. Structures of Gd-based phthalocyanine complexes $[Gd\{L(crown)_4\}]^*4$ DBU and $Gd\{L(ArO)_8\}I_8$ are shown in Fig. 1. The sol of nanoparticles in water or dry powder samples were dissolved in freshly distilled H_2O up to concentrations of atomic gadolinium 0.07, 0.21, and 0.63 mM for CeO_2 nanoparticles and 0.1, 0.2, and 0.3 mM for phthalocyanine complexes. The resulting solution was loaded into an NMR tube and sealed under ambient air pressure with a plastic cap. D_2O was not added to solutions because the sufficient spectral resolution was obtained with default shim values, and the drift of the spectrometer's magnetic field was negligible.

The dependence of the longitudinal relaxation rate R_1 of water protons on the magnetic field was measured using a custom-engineered fast-field cycling setup installed on top of a high-resolution 700 MHz NMR spectrometer (Bruker) for each NMR sample. The magnetic field for relaxation B_{rel} was varied from 10 mT to 16.4 T. A five-step protocol (Fig. 2a) was used to measure $T_1 = 1/R_1$ [3]. In the first step, the sample restores equilibrium magnetization at the detection field B_0 ; an optional 180° RF pulse was applied if relaxation field $B_{rel} > 1$ T. Next, the sample is transferred to field B_{rel} , where it rests for the variable relaxation delay τ . Finally, the sample is transferred back to the detection field B_0 (step four), where free induction decay is recorded after application of 90° RF pulse (step five).

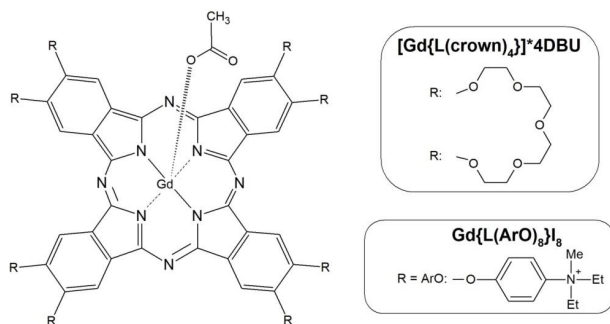


Figure 1. Structures of Gd-based phthalocyanine complexes $[Gd\{L(\text{crown})_4\}]^*4\text{DBU}$ and $Gd\{L(\text{ArO})_8\}I_8$

The dependences of H_2O NMR signal intensity on the relaxation delay in each magnetic field B_{rel} were fitted by single-exponent function. The resulting concentration-dependent relaxation rates $R_1(B, [Gd]_{\text{sample}}) = 1/T_1(B)$ were approximated using the linear function: $R_1(B, [Gd]_{\text{sample}}) = r_{1,\text{sample}}(B) \times [Gd] + R_1(\text{H}_2\text{O})$, where $R_1(\text{H}_2\text{O}) = 0.35 \text{ s}^{-1}$ is the relaxation rate of pure water, $[Gd]$ is the concentration of atomic gadolinium, and $r_{1,\text{sample}}(B) \text{ s}^{-1}\text{mM}^{-1}$ is the sample-specific relaxivity showing the efficiency of relaxation rate enhancement by the specific relaxant. Relaxivity is demonstrated by the slope of the linear approximation of the concentration dependence of relaxation rates. An example of such approximation for the $[Gd\{L(\text{crown})_4\}]^*4\text{DBU}$ complex is shown in Fig. 2b.

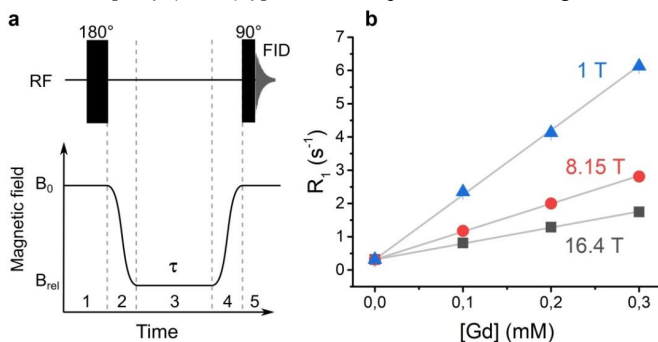


Figure 2. a. The protocol used to measure relaxation rates R_1 . b. Relaxation rates R_1 measured for $[Gd\{L(\text{crown})_4\}]^*4\text{DBU}$ samples in fields 16.4 T (squares), 8.15 T (circles), and 1 T (triangles). Lines show the result of linear approximation of R_1 vs Gd concentration.

Results and Discussion

Fig. 3 shows the dependence of relaxivity (or paramagnetic relaxation enhancement, PRE) of the studied materials on the magnetic field.

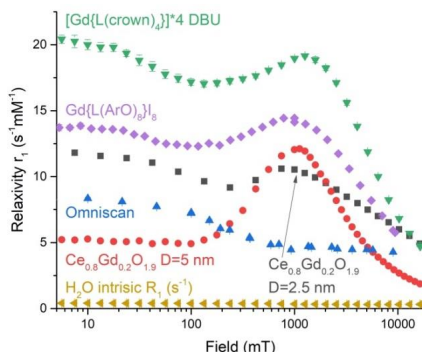


Figure 3 Field dependence of paramagnetic relaxation enhancement of water protons.

PRE arises from the dipolar interaction between the electron and nuclear spins, which is stochastically modulated by the particle motions [4]. At low magnetic fields $B_{rel} < 0.5$ T, the relaxation rate of solvent protons located in the inner coordination sphere of the paramagnetic complex is enhanced due to the increase in the electron spin relaxation rate. For Gd-complexes in this regime the electron spin relaxation is caused by fluctuations of the zero-field splitting (ZFS) interaction, which is the dominant term of the electron spin Hamiltonian [4]. PRE is transmitted to the bulk of the solvent through the exchange of solvent molecules between the inner- and outer- coordination spheres of the paramagnetic complex. The efficiency of the inner sphere relaxation enhancement gradually decreases as the magnetic field increases. This is because the relaxation rate of the electron spin decreases when the electron Zeeman interaction exceeds the ZFS interaction, assuming the anisotropy of the electron g -factor is negligible. At high field the proton relaxation rate is enhanced mostly due to the mutual translational diffusion of the electron and nuclear spins in the outer-sphere of the paramagnetic complex [4]. The relative weights of the contributions from the inner- and outer-sphere mechanisms of PRE depend on the ZFS interaction parameters, the magnetic field strength, the rotational diffusion correlation time and the average time spent by the solvent molecules in the inner coordination sphere of the paramagnetic complex. Nearly coinciding local maxima of relaxivity of the studied relaxants at ~ 1 T indicate the similarity of the parameters of zero-field splitting interaction and the value of rotational diffusion correlation time for all studied materials, except for the compact Omniscan complex, which rotates much faster than bulky nanoparticles and paramagnetic complexes.

In conclusion, the relaxivity of all proposed relaxant materials exceeds that of the commercially available contrast agent Omniscan in modern medical MRI scanners at 1.5 and 3 T. Additionally, nanocrystalline Gd-doped ceria oxide particles demonstrated good biocompatibility with human mesenchymal stem cells, which are potential therapeutic agents for the treatment of socially relevant diseases [2].

Acknowledgements

This work is supported by the Russian Science Foundation (grant #23-73-01101).

References

1. M. Rogosnitzky, S. Branch. – *BioMetals*, **29**, 365–376 (2016).
2. A. L. Popov et al. – *Molecules*, **28**, 1165 (2023).
3. I. V. Zhukov et al. – *Physical Chemistry Chemical Physics*, **20**, 12396–12405 (2018)
4. D. Kruk, J. Kowalewski. – *Journal of Magnetic Resonance*, **162**, 229–240 (2003)

Poems about School

* * *

Чижик-Spinus, где ты был?
– «Я сигнал за хвост ловил!
Сделал я ему “Фурье” –
Закружилось в голове!»

Цели Spinus’а просты:
Дать научные мосты!
Пусть у вас здесь будет шанс
Пообщаться «в резонанс»!

В Школе здесь научат всех
Сочетать с наукой смех,
Дисотеки с Э-Пе-эР,
Я-Ка-эР и Я-эМ-эР!

В Школе много новых лиц,
Будем превращать их в птиц:
Вдруг хотя б одной из ста
Дастся «Нобель-высота»!

2010

* * *

Spinus, Spinus, where you were?
Did you dive in the Resonance world?
– “Yes! I dived with my great joy –
Resonance is a pleasant toy!”

“Spinus” school invited you
To look for a knowledge clue.
We will show the signal birth
In the field of our Earth!

If you wish to have success,
At the School achieve progress!
We will teach you all to fly
In the scientific sky!

We desire you to get
Many victories-побед!
It will be a good surprise
If you catch the Nobel prize!

2010

Author Index

- Abbasov V.M.*, 261, 317
Adyukov I.S., 186
Aganova O.V., 235
Alakshin E.M., 227
Aldoshin S.M., 205
Alexandrov A.S., 237
Alieva A.F., 74
Alimov D.V., 191
Alizadeh F.T., 74
Alkhuder O., 194
Alonso Geli Ya., 54, 122, 266
Anisimov N.V., 58, 197
Araujo Duran Y., 54, 122
Arkhipova A.S., 61
Babenko S.V., 156
Babunts R.A., 34, 66, 175, 256, 338
Badrieva Z., 63
Baichurin R.I., 186, 231, 252, 259, 287, 298, 305
Baishya B., 47
Bakirov M.M., 199
Baranchikov A., 345
Baranov P.G., 66, 175, 256, 338
Batueva A.V., 66, 256, 338
Batueva E.E., 201
Batulina R.G., 201
Bazaikin V.Y., 68
Bazan L.V., 201
Belousov M.V., 94
Belyankova Y.O., 340
Berdnikov V.A., 237
Bezrodnyi V.V., 202
Bibik E.E., 188
Bikmullin A.G., 290
Blokhin D.S., 290, 330
Bocharov E.V., 327
Bogachev Yu.V., 282, 285
Bogomolova E.V., 211, 215
Bohtenkova E.I., 227
Bondarev S.A., 94
Borodkin G.S., 293
Bozhenko K.V., 205
Bruil E.A., 63, 146
Bunkov Yu., 37
Burov D., 139
Burueva D.B., 100, 156, 178
Bystrov S.S., 71
Cabal Mirabal C., 82, 85, 119, 124, 139, 223
Ceccolini I., 125
Charnaya E.V., 35, 166, 308
Chepurinov P.B., 293
Cheremensky S.O., 207
Cherosov M.A., 201
Chertkov V.A., 209
Cheshkov D.A., 209, 280
Chinaka O.A., 61
Chizhik V.I., 32, 164, 335
Chukanov N.V., 156, 178
Çolak B., 129
Cruz Vadell H., 54, 122
Dashko R.E., 242
Demidov V.N., 211, 215
Deriglazov V.V., 264
Dmitrenko M.E., 218, 222, 241, 251, 270, 271, 307, 314, 323
Dmitrienko E.V., 61
Dmitriev A.A., 104
Dmitriev D.S., 159
Dmitriev V.S., 293
Dmitrieva A.S., 219
Doğan E., 129
Doroginizky M.M., 237
Dubovenko R.R., 218, 222, 241, 270, 271, 307, 314, 323
Duisenali A.M., 340
Dyatlovich A., 223
Efimov S.V., 272, 324
Efimova L.N., 215
Egorov A.V., 207, 226, 320, 335
Egorov D.M., 259
Egorov S.S., 251
Egorova A.V., 259
Egorova M.I., 226
Eldarova S.H., 74
Fadeeva I., 301
Fatullaev E.I., 202
Fedin M.V., 163, 191
Fedorov V.S., 219, 264
Fedotov A., 139
Fel'dman E.B., 77, 168, 296
Fetin P.A., 79, 240
Fetina V.I., 79
Filippov A.V., 315
Fokin A.V., 166

- Fomenko V.V.*, 102
Frolova E.N., 201
Gafurov M.R., 143, 301
Garaeva A.M., 227
García Cruz C., 54, 122
García Naranjo J.C., 124, 266
Garea-Llano E., 82
Gareev K.G., 264
Gareeva D.R., 228
Gervits L.L., 58, 197
Glebova I.B., 211
Gnezdilov O., 301
Gomonov K.A., 231
Gonzalez Dalmau E., 82, 85, 119
Goribunova Yu., 345
Goryainov S.V., 248, 274
Grigorieva E.V., 61
Grishanovich I.A., 233
Gromova N.R., 88
Grouzdev D.S., 264
Grunin L., 39
Gulyaev M.V., 159
Gurin A.S., 66, 256, 338
Gutsev G.L., 205
Gutsev L.G., 205
Hajiyeva G.A., 74
Hurshkainen A., 139, 223
Huseynov H.J., 261, 317
Ibragimova M.D., 261, 317
Ievlev A.V., 91, 242
Ilichev I.V., 188
Ilyin I.V., 338
Islamov T.R., 235
Ivanov A.A., 237
Ivanov D.S., 237
Ivanova A.G., 211, 215, 252
Ivanova M., 39
Ivlev V.A., 248, 274
Japharova R.A., 74
Julmetov A.R., 235
Kadnikov M.V., 79, 240
Kariakina A.S., 241, 251
Kartashova E.V., 311
Kay L.E., 125
Kayukova L.A., 340
Khairutdinov B.I., 151
Khairutdinov I.T., 199, 343
Khakimov A.M., 315
Khakimzyanova A.R., 315
Khaliullina A.V., 315
Khamidulin Ya.A., 215
Kharkov B.B., 94, 125
Khrustalev A.A., 71
Kirilenko V. D., 71
Kirilov I., 39
Kiryutin A.S., 96, 109, 126, 152
Kiselev I.A., 264
Klochkov V.V., 235, 272, 290, 324, 330
Kolosova D.L., 242
Kolyagin Yu.G., 106
Komlev V.S., 143
Komolkin A.V., 4, 68, 70, 261, 277, 279
Kondrashov A.V., 245
Kononenko E.S., 100
Kononova P.A., 102
Koptyug I.V., 100, 156, 178
Korovina A.M., 218, 307
Koshman V.E., 104
Kosobuko E.M., 215
Kostin M.A., 194
Kostylev M., 245
Kostyukov I.A., 106
Kovtunova L.M., 100
Kozhevnikov A.Yu., 233
Koziaeva V.V., 264
Kozinenko V., 96
Kozinenko V.P., 109, 126
Kozlenko A.S., 293
Kramushchenko D.D., 338
Krivosheeva E.A., 248, 274
Kumzerov Yu.A., 166
Kupriyanov P., 129
Kupriyanova G., 112
Kuzmichev A., 116
Kuzminova A.I., 218, 222, 241, 251, 270, 271, 307, 314, 323
Kuznetsova E.I., 77
Lapina O.B., 174
Larionov I.I., 264
Laurent S., 124
Lazarev I.D., 77
Levkina A.D., 125
Lezova O.S., 252
Likhachev K.V., 66, 175, 256
Lobova A.M., 259
Lores Guevara M.A., 54, 119, 122, 124, 266
Lukzen N.N., 152
Luzik D.A., 125
Makarenko S.V., 186, 231, 298, 305

- Maksimova E.P.*, 320
Mamin G.V., 143, 301
Mammadhasanov K.K., 261
Maraşlı A., 129
Marchenko Ya.Yu., 264
Markelov Danil A., 126
Markelov Denis A., 68, 88, 277
Matveev A.A., 211
Matveev V.V., 133, 164
Mazur A.S., 218, 222, 242, 251, 270, 271, 307, 314, 323
Melnikova D., 333
Mengana Torres Yu., 266
Mershev L., 112
Mikhailovskaya O., 270
Mikhtaniuk S.E., 202
Mikulan A.I., 222, 271, 323
Mikushev V.M., 308
Minnullina G.A., 272
Miridonova L.A., 248, 274
Mishra S.K., 47
Mizyulin D.A., 226
Monet Alvarez D.E., 122
Mozzhukhin G., 112, 129
Mukhametzyanov T.A., 290
Mukhin K.A., 133
Muller R.N., 124
Muratova A.D., 277
Murtazina A.A., 248, 274
Murzakhanov F.F., 143, 301
Mustafa A.A., 287
Mylnikova A.Yu., 211
Myznikov D.D., 314
Neelov I.M., 202
Nefedov D.Yu., 35, 166
Nichugovskiy A.I., 280
Nikitina A.V., 282, 285
Nikolaev B.P., 219
Novikova D.S., 287
Osetrina D.A., 290
Ozhogin I.V., 293
Pakhomova T.B., 211, 215
Panicheva K., 168, 296
Pankov D.I., 327
Papulovskiy E.S., 174
Paston S.V., 211, 215
Pavlova O.S., 159
Pelipko V.V., 186, 231, 298, 305
Penkova A.V., 218, 222, 241, 251, 270, 271, 307, 314, 323
Pergat A.V., 151
Pestova O.N., 133
Pestryaev E.M., 136
Petrakova N.V., 143
Petrova A., 301
Pilipenko I. A., 305
Pirogov Yu.A., 41, 159
Pistrak A.G., 159
Pleshakov I.V., 188
Plisko T.V., 218
Podkorytov I.S., 94, 125
Pokhvisheva N.V., 91
Polukhina A.Y., 248, 274
Polyakov N.E., 61, 102, 104
Popov A., 345
Poryaev A.S., 163, 191
Pugachev A.D., 293
Pugovkin V., 139
Pulyalina A.Yu., 314
Puzikova M.E., 222, 307
Rameev B., 112, 129
Rochev A.M., 308
Rodriguez de la Cruz N.Ju., 124
Romanova I.V., 227
Ryabikov K.N., 159
Ryzhov V.A., 264
Sadovnikova M.A., 143
Safullin K.R., 227
Salabert Revilla A., 122
Salakhutdinov N.F., 102
Salikhov K.M., 43, 199
Salikov V.A., 94
Salin A.V., 311
Salnikov O.G., 178
Salomatin K.A., 314
Sashina A.N., 315
Savina A.D., 327
Savostina L.I., 201, 319
Seidova S.A., 261, 317
Selivanov S.I., 252, 287, 305
Selivanova I.A., 327
Selyutin A.A., 222, 314
Selyutina O.Yu., 61, 102, 104
Semenov K.N., 218, 241
Shabanov A.A., 311
Shaidullina A.F., 319
Shandybin P., 223
Sharipova A.R., 201, 319
Sharipova L.V., 146
Shavykin O.V., 202

- Shchelokova A.V.*, 146
Shelyapina M.G., 45, 226, 320
Sheremeta A.V., 248, 274
Shestakov S.L., 233
Shevelev O.B., 100
Sheveleva N.N., 202
Shevtsov M.A., 219, 264
Shilova O.A., 252
Shishkina M.N., 285
Shubin A.A., 174
Shuntian L., 40
Sinitsyn D.O., 209
Sitkov N.O., 264
Skakun M.A., 161
Skirda V.D., 237, 333
Skovpin I.V., 156
Skripnikov L.V., 120
Skrynnikov N.R., 94, 125
Skvortsova P.V., 151
Snadin A.V., 152
Solomnikova A.V., 282
Somoano Delgado L., 54, 122
Sóñora Mengana A., 154
Stashkevich A.A., 171
Stepišnik J., 46
Suarez Beyries L.C., 54, 122
Suarez Olivares A.T., 122
Suharzewskiy S.M., 282
Suryaprakash N., 47
Sushkova X.D., 270, 323
Sviyazov S.V., 156
Sypalova Yu.A., 233
Tagirov M.S., 227
Taldaev A., 327
Tamayo Delgado F., 54, 122, 124, 266
Taran T.T., 159
Tarasov A.S., 324
Tarasov V.P., 159
Tarasova A.A., 58, 197
Tatsenko A.A., 171
Terekhov R.P., 327
Titkov S.V., 175
Titova A.A., 161
Toktarev A.V., 174
Tolstoy P.M., 194
Tomilov A.S., 163
Torres-Martínez L.R., 54
Trepakova A.I., 100
Tribulovich V.G., 287
Troshkina A.A., 330
Tsukhlava D., 333
Tsvetkov N.V., 240
Tsvetkova I.N., 215
Tupikina E.Yu., 161
Turanov A.N., 201, 319
Turanova O.A., 201, 319
Tyutyukin K.V., 91
Ubovich M., 164, 335
Uchaev M.V., 256
Ulyanova M., 61
Uskov A.V., 35, 166
Uspenskaya Yu.A., 338
Ustinov A.B., 171, 245
Utenyshev A.N., 205
Valiullin A.L., 237
Vasil'ev S.G., 77, 168, 296
Vasilev A.A., 35, 166
Vasil'ev V.G., 248, 274
Vedernikov L.S., 171
Vetoshko P., 116
Veyshtort I.P., 256
Volkov M.Yu., 319
Vologzhanina A.V., 340
Voschikov V.I., 215
Yakovlev I.V., 174
Yakovleva L.Yu., 219
Yakovleva V.V., 175, 256
Yazikova A.A., 163
Yerlanuly A., 340
Yi A.P., 178
Yolchueva U.J., 74, 317
Yulmetov A.R., 290
Yurkovskaya A.V., 96, 109, 126, 152, 345
Yushmanov P., 48
Zagovorich A.D., 308
Zaripov R.B., 199, 343
Zhouravleva G.A., 94
Zhukov I., 345
Zimina T.M., 264
Zolotov D. R., 71
Zorin I.M., 79, 240
Zubkov V.I., 282

Magnetic Resonance and its Applications

Proceedings

Saint Petersburg State University
April 1-5, 2024

Подписано в печать 27.03.2026. Формат $60 \times 84^{1/16}$.
Бумага офсетная. Гарнитура Times. Печать цифровая.
Усл. печ. л. 42,85. Тираж 150 экз. Заказ № 446; .

Отпечатано в Издательстве ВВМ.
198095, Санкт-Петербург, ул. Швецова, 41.